Sio-Iong Ao · Gi-Chul Yang
Len Gelman *Editors*

Transactions on Engineering Technologies

Springer

Transactions on Engineering Technologies

Sio-Iong Ao · Gi-Chul Yang
Len Gelman
Editors

Transactions on Engineering Technologies

Springer

Editors
Sio-Iong Ao
International Association of Engineers
Hong Kong
Hong Kong

Len Gelman
Cranfield University
Cranfield, Bedfordshire
UK

Gi-Chul Yang
Department of Multimedia Engineering
Mokpo National University
Chonnam
Korea, Republic of (South Korea)

ISBN 978-981-10-1087-3 ISBN 978-981-10-1088-0 (eBook)
DOI 10.1007/978-981-10-1088-0

Library of Congress Control Number: 2016931995

Printed on acid-free paper

This Springer imprint is published by Springer Nature
The registered company is Springer Science+Business Media Singapore Pte Ltd.

Preface

A large international conference on Advances in Engineering Technologies and Physical Science was held in London, UK, 1–3 July 2015, under the World Congress on Engineering 2015 (WCE 2015). The WCE 2015 is organized by the International Association of Engineers (IAENG); the Congress details are available at: http://www.iaeng.org/WCE2015. IAENG is a non-profit international association for engineers and computer scientists, which was found originally in 1968. The World Congress on Engineering serves as good platforms for the engineering community to meet with each other and to exchange ideas. The conferences have also struck a balance between theoretical and application development. The conference committees have been formed with over three hundred committee members who are mainly research center heads, faculty deans, department heads, professors, and research scientists from over 30 countries. The congress is truly global international event with a high level of participation from many countries. The response to the congress has been excellent. There have been more than 700 manuscript submissions for the WCE 2015. All submitted papers have gone through the peer-review process, and the overall acceptance rate is 51 %.

This volume contains 39 revised and extended research articles written by prominent researchers participating in the conference. Topics covered include mechanical engineering, wireless networks, knowledge engineering, manufacturing engineering, and industrial applications. The book offers the state of art of tremendous advances in engineering technologies and physical science and applications, and also serves as an excellent reference work for researchers and graduate students working on engineering technologies and physical science and applications.

Sio-Iong Ao
Gi-Chul Yang
Len Gelman

Contents

Preparation, Characterization and Molecular Transport of a Supported Silica Membrane for Gas Separation

Ngozi Nwogu and Edward Gobina

Abstract This paper presents the synthesis and hydrodynamic characteristics of a surface-modified ceramic membrane. The porous support consists of gamma-alumina and a titanium wash-coat. Single gas permeation through the membranes was measured at 298 and 373 K using H_2, N_2, Ar, CO_2 and CH_4. The membranes showed separation factors that are consistent with Knudsen diffusion mechanism. Structural characteristic and pore size distribution of the modified silica membrane were analyzed with liquid nitrogen adsorption at 77 K to obtain gas adsorption/desorption isotherm of membrane materials. The adsorption/desorption curve for the surface-modified silica ceramic membrane showed a type IV/V isotherm which indicates a mesoporous structural make-up. Scanning electron microscopy (SEM) images show that membrane surface has a dense silica film and were defect-free. Energy dispersive x-ray analysis (EDXA) confirms the formation of silica films and indicating the presence of C, O, Al, Si, Cl and Ti elements on the modified support. H_2 permselectivity to N_2 ($H_2/N_2 = 4.37$) is higher than the ideal Knudsen value of 3.74. Results from the experiments have helped explain the effect of dissimilarity in the mass-transfer on the gas permeation through the hybrid ceramic membranes.

Keywords Silica membrane · Dip-coating · Gas permeance · Membrane characterization · Transport mechanisms · Permselectivity · Ideal separation factor · mesoporous structure

N. Nwogu · E. Gobina (✉)
School of Engineering, Centre for Process Integration and Membrane Technology (CPIMT), The Robert Gordon University, Aberdeen AB10 7GJ, UK
e-mail: e.gobina@rgu.ac.uk

N. Nwogu
e-mail: n.c.nwogu@rgu.ac.uk

S.-I. Ao et al. (eds.), *Transactions on Engineering Technologies*,
DOI 10.1007/978-981-10-1088-0_1

Nomenclatures

q Flow rate (mol sec^{-1})
A_s Membrane surface area (m^2)
ΔP Pressure difference (pa)
P_1 Pressure at feed side
P_2 Pressure at permeate side
K Permeance (mol sec^{-1} m^{-2} pa^{-1})
α_{jf} Selectivity of j to f

1 Introduction

The separation of gases by selective transport through inorganic ceramic membranes is a vibrant and fast growing field in membrane technology [1–3]. In membrane-based gas separation process, components are separated from their mixtures by their difference in permeation through the membranes. A number of benefits, including low capital and operational costs, lower energy requirements and ease of operation are offered by membrane separation [4–6]. As a result, gas separation by membrane process has attained high importance in the industrial setting in terms of cost-effectiveness, as gases occupy an important space in the chemical feed stock industry. Current applications of membrane-based gas separation include oxygen enhancement, hydrogen purification and recovery, natural gas processing, removal of carbon dioxide from flue gas and volatile organic compounds from effluent streams [3, 7, 8]. Cost-effective and energy efficient carbon dioxide separation methods are vital for general industrial processes and for applications involving CO_2 recovery for further utilization. The most commonly used CO_2 removal processes involve chemical and physical absorption using amines. Cryogenic process and pressure swing adsorption (PSA) are the most commonly used methods utilized in hydrogen separation purification. However, both processes require large amount of energy and therefore a major disadvantage that has been reported by some researchers [9–11]. Furthermore, the application of silica membranes in membrane reactors, using catalytically active or passive membranes has proved to be very promising by the continuous separation of the hydrogen product from the reaction system [12–14]. Koutsonikolas et al. [15] compared the thermal and chemical stability of polymer membranes to silica membranes and reported that silica membranes have shown excellent permeability and selectivity characteristics in gas separations especially for small gas molecules like H_2 and He over the larger ones; for example N_2 and CO_2. In another literature, Li and Uhlhorn [16, 17] stated that the foremost and operational silica membrane with high quality for gas separation was fabricated in the 1980s. The preparation was carried out using the sol-gel technique. The process involved the immersion of a porous support made of alumina in a silicon dioxide sol-gel followed by drying to attain a particular pore size

structure. As a result, they suggested silica as the best choice in terms of porous support modification due to its high thermal stability. Similarly, De Lange et al. [18, 19] established that sol-gel modification process of mesoporous membranes of pore size between 1 and 25 nm in a silica polymeric solution was successful in the preparation of microporous membranes. The formation of a very thin top layer in the range of 50–100 nm resulted in very high gas permeation rates. However, further findings showed that silica membrane formed through sol gel was quite unstable in the presence of water at elevated temperature resulting in ageing which is a major disadvantage. In the quest for a solution to this problem Li and Uhlhorn [16, 17] suggested a more superior membrane material, titanium which is less sensitive to water although less thermally firm than silica.

For porous membranes, the International Union of Pure and Applied Chemistry (IUPAC) approvals [20, 21] membrane pores are categorized into three distinct types: micropores having diameter less than 2 nm, mesopores, diameter greater than 2 nm but less than 50 nm and macropores with diameter more than 50 nm [22]. Practically speaking, investigational gas adsorption isotherms fall into six groups. Most importantly, adsorption isotherms for microporous solids tallies with types I while types IV and V isotherms corresponds to features which are characteristic of mesoporous solids (especially ceramics). Additionally for the type VI and V, the adsorption process indicates macroporous solids, but at an elevated relative pressure, the amount of adsorption increases sharply due to the capillary condensation mechanism in the mesopores [23, 22]. In this study, the ceramic support used is tubular in shape comprising of both alumina and titania material. These porous ceramic materials are well known in nature and are of high mechanical strength. In this regard, surface modification through dip-coating technique using appropriate functional groups is a suitable way of the alteration of the membrane structure to achieve the desired membrane performance. More current patents explain inorganic membranes comprising of a ceramic support, like Al_2O_3, with a deposited separating layer made of silica, alumina or zirconia for modification purposes [24–26].

The objective of this paper therefore is to discuss the structural characteristics and permeation of gases through a supported silica inorganic ceramic membrane. It is a well-known that ceramic membranes are better supports due to their superior thermal and mechanical properties compared to polymer systems. The study further provides a useful insight for materials formulation and fabrication of a high performance silica membrane for gas separation especially for application in hydrogen separation and application in carbon capture applications. This also allows for operation at higher temperatures and greater transmembrane pressure differences.

2 Experimental

The gas permeation experiment was performed using the supported silica inorganic membrane prepared through a successive dip-coating procedure [27] to achieve the desired membrane pore size modification. The commercial alumina support layer

Fig. 1 Photograph of support

has an internal diameter of 7 mm, an outer diameter of 10 mm and a nominal pore diameter of 15 nm. The membranes were 368 mm long with an impermeable 50 mm at both ends. Single gas permeation through the membranes was measured at 298 and 373 K respectively. The gases used for the gas transport tests include: nitrogen (N_2), hydrogen (H_2), argon (Ar), carbon dioxide (CO_2) and methane (CH_4) respectively. The gases were delivered by BOC, UK. The membrane design involved the formation of a thin separating layer on the outside surface of the tube made up of silica and fashioned through a successive dip-coating technique to form composite ceramic membrane. The silica solution consisted of 900 ml of 2-methylbutane and 100 ml of silicon elastomer. A mixture of the above stated quantity of Iso-pentane, silicone elastomer and 10 ml of curing agent was used which prevents a cross linking between silica molecules. The mixture was then carefully poured into a graduated beaker and placed on a magnetic stirrer for 30 min until a clear solution was obtained. The entire mixture was stirred continuously until complete homogeneity was achieved. The final solution was then poured into a 1000 ml graduated cylinder. This process is a patented innovation by Gobina [25–28]. Figure 1 is a picture of the support while Fig. 2 describes the immersion of the support in a silica - based solution for modification purposes.

Figure 3 shows a picture of the experimental rig used for gas transport test. Prior to and after the modification, the ceramic membrane was placed in stainless steel shell housing with graphite rings as seals to prevent gas leakages and at the same time enhance accuracy of data obtained. Digital pressure gauges were connected to the reactor at strategic points on the flow line to measure feed, permeate and retentate pressures. Flow rates of the permeating gases were measured and recorded using a digital flow meter.

One of the key parameters dictating membrane performance is the gas permeance, K through the membrane expressed as:

$$\mathrm{K} = \frac{q}{\mathrm{A_S}\Delta P} \tag{1}$$

where, q the gas flow rate through the membrane (moles/sec), A_s the membrane surface area (m^2) and Δp the pressure difference across the membrane (bar).

The separation factor for component j over f, that is the membrane's preference for passing one gas species and not another is expressed as:

$$\propto_{jf} = \frac{K_j}{K_f} \tag{2}$$

Fig. 2 Support immersion

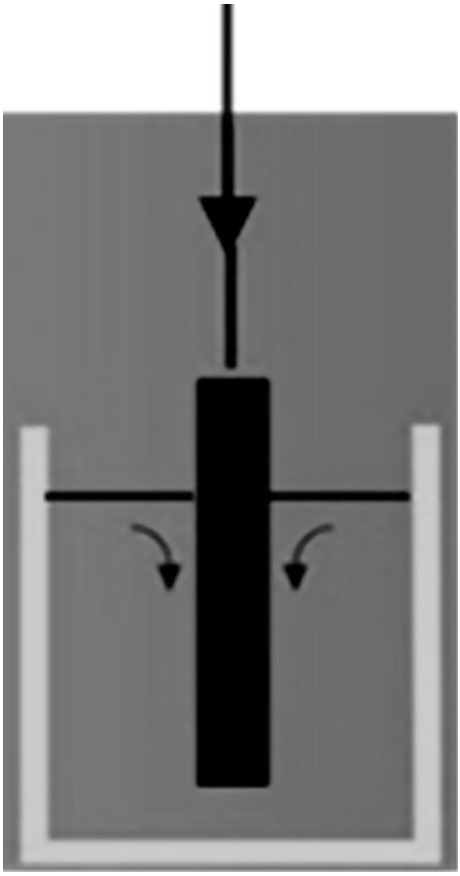

Fig. 3 Experimental rig

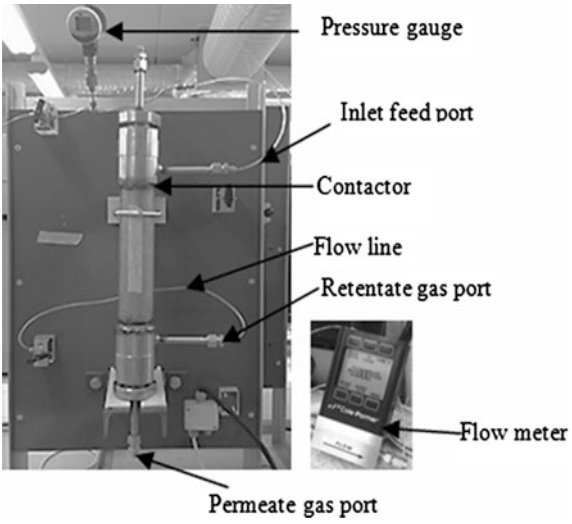

Where α is the ideal gas selectivity for pure gases, K_j, the permenace of the more permeating gas and K_f, the permeance of the less permeating gas. For various membranes, there is a trade-off between selectivity and permeability. A highly permeable membrane tends to have low selectivity and vice versa [29].

The structural characterisation of support and modified membranes was done by employing probe molecules in this case nitrogen at a low temperature of 77 K to adsorb on the pore within the membrane pores. These measurements were acquired using gas sorption system analyser (Quantachrome Instruments Florida, USA). However, before this was done, the process of degassing was carried out to remove unwanted components present by subjecting the surface of the material to an elevated temperature of about 300 °C. A difference in the weight before and after degassing was also obtained. Due to its simplicity the Brunauer-Emmett-Teller (BET) gas adsorption model has become the most widely exploited technique used for the determination of the surface area of finely-crushed sample of support and modified membrane. To enable accurate evaluation, gas adsorption isotherms and hysteresis are displayed in graphical form with the amount of nitrogen adsorbed plotted against the relative pressure as shown in Figs. 4 and 5 [30, 31].

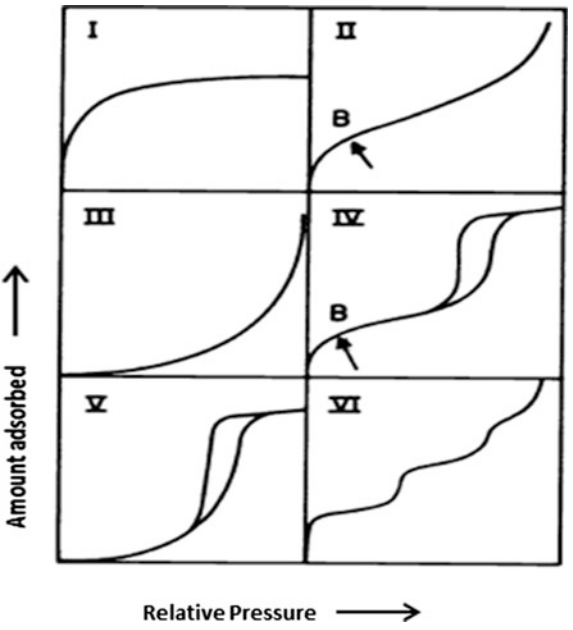

Fig. 4 The various kinds of physisorption isotherms

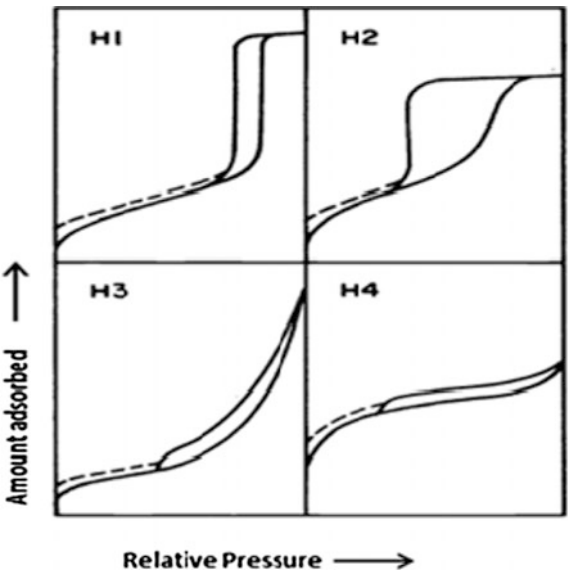

Fig. 5 Types of hysteresis

3 Results and Discussion

The structural characteristic of the support and the supported silica membrane were analyzed using nitrogen adsorption method to determine the surface and the pore size distribution. The plots of the amount of gas adsorbed (volume at STP (cc/g) against relative pressure (P/P_0) is shown in Fig. 6 for support and Fig. 7 for the silica supported membrane. As observed, two colors are displayed in the plots. The blue depicts desorption line and the red represents the adsorption. The hysteresis of the support has a close resemblance to type H1 loop in Fig. 5 above. The adsorption and desorption lines are identical, thus according to [31] indicates that the membrane has large pores which are features of support. For the silica supported membrane in Fig. 7, it can be seen that there is an enlargement in the loop similar to that of type IV isotherm where the adsorption process initiates, but at an elevated relative pressure, the amount of adsorption increases sharply due to the capillary condensation formation in the mesopores, this is in accordance as reported by [31]. This result is similar to work done by [32]. The BET summary and BJH method of desorption for support and silica membrane are shown in Table 1. From multi-points chosen at random, plots obtained gave a surface area of 0.161 m^2/g for the support and 1.068 m^2/g for the silica membrane. This change in the membrane surface area is attributed to the silica modification effect on the support. Further investigation on the determination of the pore diameter of both the support and silica membrane was carried out. The result further confirms the pore diameter determined using the Barrette-Joyner-Halenda (BJH) method of desorption. From the values obtained, there was a clear difference between the pore diameter of

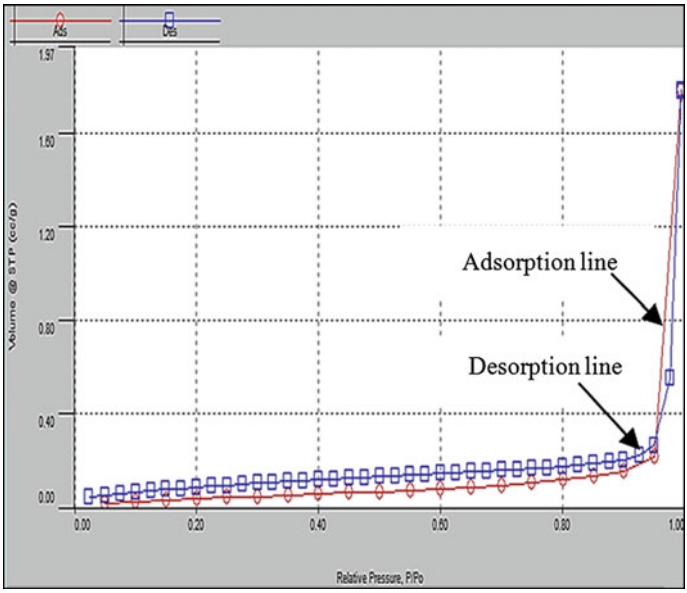

Fig. 6 Plot of linear isotherm of gas adsorption and desorption for fresh membrane

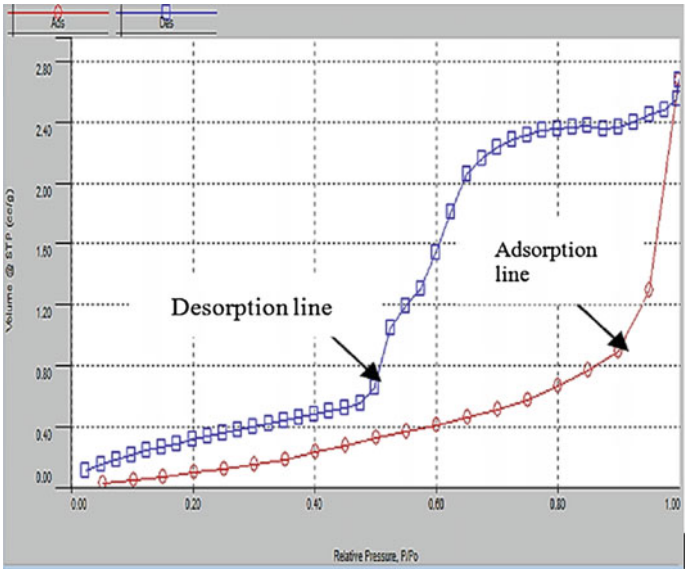

Fig. 7 Plot of linear isotherm of gas adsorption and desorption for silica membrane

Table 1 BET summary and BJH method of desorption for support and silica membrane

	Support	Silica membrane
Surface area (m^2/g)	0.161	1.068
Pore diameter (nm)	15	3.136

support and the pore diameter after modification indicating the characteristic features of a mesoporous membrane of pore diameter (between 2 and 50 nm).

4 Morphology of Support and Silica Membrane

The morphology of the membrane before and after coating was obtained using a Zeiss EVO LS10 variable pressure scanning electron microscope (SEM) while the elemental composition was obtained with the Oxford instrument INCA Energy dispersive x-ray analyser (EDXA). The images obtained are shown in Figs. 8 and 9 respectively. The modified support surface indicates the presence of deposited silica. These images show that the support is coarse in nature exposing the particle of the support whereas once modified smoother and lighter surface is formed. EDXA analysis of the ceramic support and modified support further confirms that silica was not present in the support, but after the sequential dipping, silica (Si) was identified as indicated on the micrograph. Other elements present are C, O, Al, Cl and Ti elements. The presence of Si in the film is due to the deposition of the silica solution on the surface of the ceramic support.

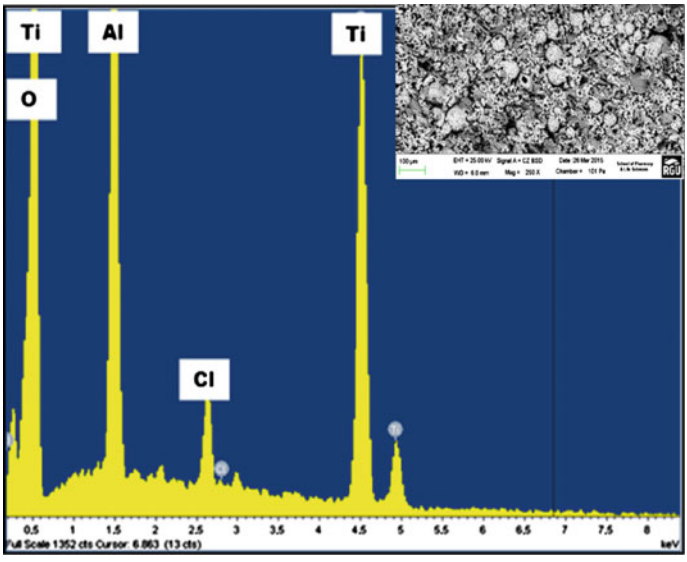

Fig. 8 SEM and EDXA micrograph of a ceramic support

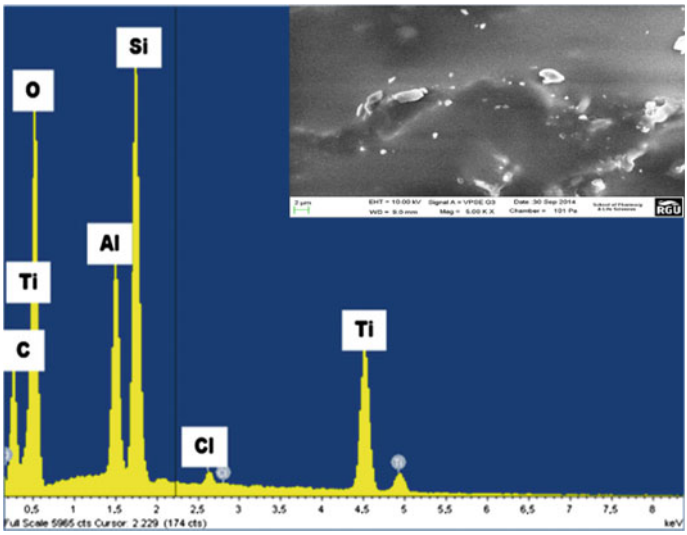

Fig. 9 SEM and EDXA micrograph of a thin silica layer deposited on top of the support fresh support

Table 2 Elemental percentage composition of the modified membrane

Element	C	O	Al	Si	Cl	Ti
Percentage composition (%)	31.97	26.74	5.81	32.21	0.08	3.20

Table 2 presents the composition of the various elements obtained from the EDXA and confirms the presence of Si and O having their elemental percentage composition as 32.21 and 26.7 % in the modified ceramic support.

The differences in single gas permeances versus the mean pressure expressed as $(P_1 + P_2)/2$ through the supported silica membrane were studied. Figures 10 and 11 shows the relationship for H_2, N_2, CH_4 and Ar permeances and the mean pressure at a temperature of 298 and 473 K. As can be observed H_2 gas maintained the highest permeance at each of the investigated temperatures. Again individual gas permeance decreased with the mean pressure, in this scenario; viscous contribution is not quite relevant. However all indication tends towards Knudsen diffusion mechanism which occurs when the mean free path of the gas molecules is much bigger that the pore diameter of the membrane pore walls through which the gases permeate. In this circumstance, the gases with lower molecular weight will be favoured which can be identified in mesopores. An analysis of permselectivity measurements on the modified membrane was explored (for H_2 over CO_2, N_2 and CH_4 as a function of feed pressure. This is illustrated in Fig. 12. Results obtained shows the permselectivity or the separation factor, obtained as the ratio of the permeance of the more preferred gas, in this case H_2 to that of the less preferred gas (N_2, CH_4 and CO_2).

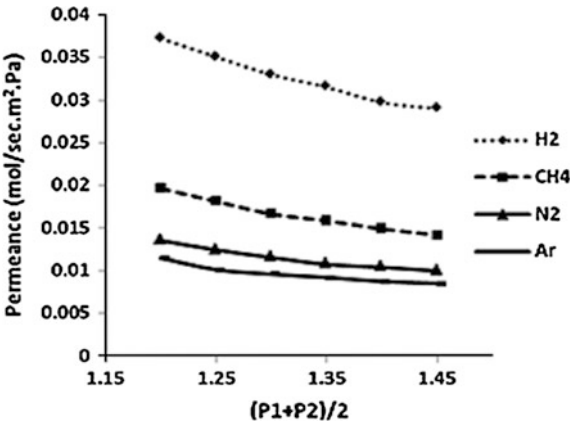

Fig. 10 H_2, CH_4, N_2 and Ar permeance as a function of mean pressure at 298 K

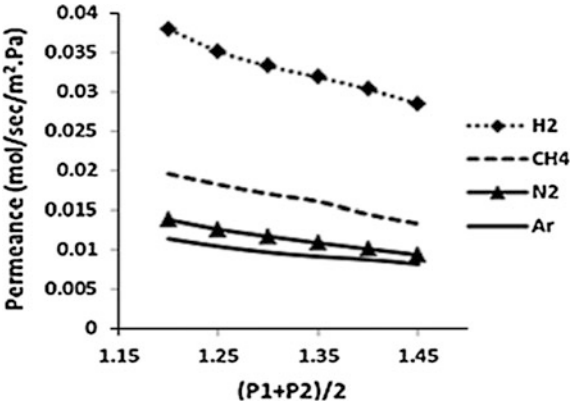

Fig. 11 H_2, H_2, CH_4, N_2 and Ar permeance as a function of mean pressure at 473 K

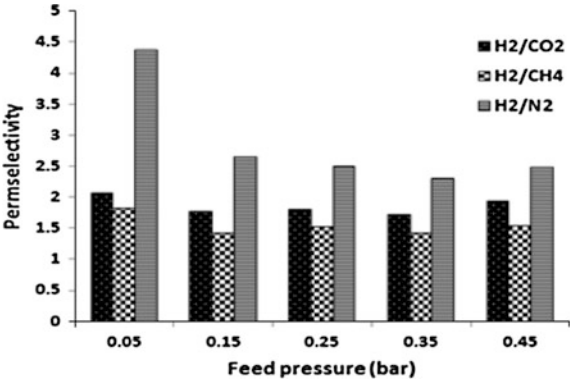

Fig. 12 H_2 permselectivity measurements as a function of feed pressure at room temperature

A high selectivity value of 4.37 at a relatively low pressure of 0.05 bar was obtained for H_2 over N_2 compared to a much lower selectivity values of 2.08 and 1.82 over CO_2 and CH_4 respectively. This confirms that more H_2 was recoverable from N_2 than from the other gases.

5 Conclusion

The structural characterization of a commercially available support and a coated silica membrane using BET and BJH models has been studied. The BET from multi-point chosen at random gave a surface area of 0.16 m^2/g for the support, whereas, for the supported silica membrane, there was an increment in the surface area to 1.068 m^2/g. The silica membrane exhibited a type IV/V isotherm indicating that the membrane has a mesoporous structure. This also shows that there is a significant influence of the silica modification of the support. From the values obtained with respect to the pore size estimation, there was a clear difference between the pore diameter of the support (15 nm) and the pore diameter after modification (3.136 nm) indicating the characteristic features of a mesoporoos membrane of pore diameter between 2 and 50 nm. Coating condition largely influenced the membrane performance for H_2 separation. A high selectivity value of 4.37 at a relatively low pressure of 0.05 bar was obtained for H_2 over N_2 compared to a much lower selectivity values of 2.08 and 1.82 over CO_2 and CH_4 respectively. This confirms that more H_2 was recoverable from N_2 than from the other gases. The SEM and EDXA experiments showed the presence of silica dense coating on the membrane surface and the chemical composition respectively. Permeation experiments conducted at temperatures 298 and 473 K, in relation to the mean pressure show that the supported silica membrane can operate at high temperatures. Results of this study demonstrate the potential for using this membrane in membrane reactors including applications that require operation at relatively high temperatures.

Acknowledgment The author wishes to express sincere thanks to the Centre for Process Integration and Membrane Technology of Robert Gordon University for procuring the fresh membrane and Gas sorption system analyser used for the study.

References

1. Rousseau ERW (2009) Handbook of separation process technology. Wiley, New York
2. Nunes SP, Peinemann K (2006) Membrane technology: in the chemical industry. Wiley, New York
3. Chung T, Jiang LY, Li Y, Kulprathipanja S (2007) Mixed matrix membranes (MMMs) comprising organic polymers with dispersed inorganic fillers for gas separation. Prog Polym Sci 32(4):483–507

4. Paul DR, Yampol'skii YP (1993) Polymeric gas separation membranes. CRC press, Boca Raton
5. Stern SA (1994) Polymers for gas separations: the next decade. J Membr Sci 94(1):1–65
6. Mulder M (1996) Basic principles of membrane technology. Springer, Berlin
7. Ho WW, Sirkar KK (1992) Membrane handbook. Springer, Berlin
8. Kesting RE, Fritzsche A (1993) Polymeric gas separation membranes. Wiley, New York
9. Chen HZ, Thong Z, Li P, Chung T (2014) High performance composite hollow fiber membranes for CO_2/H_2 and CO_2/N_2 separation. Int J Hydrogen Energy 39(10):5043–5053
10. Yang S, Choi D, Jang S, Kim S, Choi D (2008) Hydrogen separation by multi-bed pressure swing adsorption of synthesis gas. Adsorption 14(4–5):583–590
11. Hinchliffe AB, Porter KE (2000) A comparison of membrane separation and distillation. Chem Eng Res Des 78(2):255–268
12. Khatib SJ, Oyama ST (2013) Silica membranes for hydrogen separation prepared by chemical vapor deposition (CVD). Sep Purif Technol 111:20–42
13. Baptista P, Tomás M, Silva C (2010) Plug-in hybrid fuel cell vehicles market penetration scenarios. Int J Hydrogen Energy 35(18):10024–10030
14. El-Sharkh M, Tanrioven M, Rahman A, Alam M (2010) Economics of hydrogen production and utilization strategies for the optimal operation of a grid-parallel PEM fuel cell power plant. Int J Hydrogen Energy 35(16):8804–8814
15. Koutsonikolas D, Kaldis S, Sklari S, Pantoleontos G, Zaspalis V, Sakellaropoulos G (2010) Preparation of highly selective silica membranes on defect-free γ-Al_2O_3 membranes using a low temperature CVI technique. Microporous Mesoporous Mater 132(1):276–281
16. Li K (2007) Ceramic membranes for separation and reaction. Wiley, New York
17. Uhlhorn R, Huis In't Veld M, Keizer K, Burggraaf A (1989) High permselectivities of microporous silica-modifiedγ-alumina membranes. J Mater Sci Lett 8(10):1135–1138
18. De Lange R, Hekkink J, Keizer K, Burggraaf A (1995) Permeation and separation studies on microporous sol-gel modified ceramic membranes. Microporous Mater 4(2):169–186
19. De Lange R, Kumar K, Hekkink J, Van de Velde G, Keizer K, Burggraaf A et al (1994) Microporous SiO_2 and SiO_2/MO_x (M = Ti, Zr, Al) for ceramic membrane applications: a microstructural study of the sol-stage and the consolidated state. J Sol-Gel Sci Technol 2(1–3):489–495
20. Rouquérol J, Avnir D, Fairbridge C, Everett D, Haynes J, Pernicone N, Ramsay JDF, Sing KSW, Unger KK (1994) Recommendations for the characterization of porous solids (Technical Report). Pure Appl Chem 66(8):1739–1758
21. Sing KSW, Everett DH, Haul RAW, Moscou L, Pierotti RA, Rouquérol J, Siemieniewska T (1985) Physical and biophysical chemistry division commission on colloid and surface chemistry including catalysis. Pure Appl Chem 57(4):603–619
22. Choma J, Kloske M, Jaroniec M (2003) An improved methodology for adsorption characterization of unmodified and modified silica gels. J Colloid Interface Sci 266 (1):168–174
23. Rouquerol J, Rouquerol F, Llewellyn P, Maurin G, Sing KS (2013) Adsorption by powders and porous solids: principles, methodology and applications. Academic Press, London
24. Ku AY, Ruud JA, Molaison JL, Schick LA, Ramaswamy V (2008) Functionalized inorganic membranes for gas separation. US Patent 7,396,382
25. Gobina E (2006) Apparatus and method for separating gases. US Patent 7,048,778, 23 May 2006
26. Basile A, Gugliuzza A, Iulianelli A, Morrone P (2011) Membrane technology for carbon dioxide (CO_2) capture in power plants. In: Basile A, Nunes SP (eds) Advanced membrane science and technology for sustainable energy and environmental applications. Woodhead Publishing, Cornwall, pp 113–159
27. Karkare M (2008) Nanotechnology: fundamentals and applications. IK International Pvt Ltd

28. Gobina E (2007) Apparatus and method for separating gases. US Patent 7,297,184, 20 Nov 2007
29. Robeson LM (2008) The upper bound revisited. J Membr Sci 320(1):390–400
30. Nwogu NC, Kajama MN, Osueke G, Gobina E (2015) Structural characteristic and permeation of gases through a supported silica inorganic ceramic membrane. In Proceedings of the World Congress on Engineering, London, UK, 1–3 July 2015. Lecture notes in engineering and computer science, pp 245–248
31. Sing KS (1985) Reporting physisorption data for gas/solid systems with special reference to the determination of surface area and porosity (Recommendations 1984). Pure Appl Chem 57 (4):603–661
32. Smart S, Liu S, Serra JM, Diniz da Costa JC, Iulianelli A, Basile A (2013) Porous ceramic membranes for membrane reactors. Woodhead Publishing, Cornwall

Functional Validation of Demagnetizing Factor of Quasi-Solid and Solid Magnets (Phenomenological Approach)

Anna A. Sandulyak, Darya A. Sandulyak, Vera A. Ershova, Maria N. Polismakova and Alexander V. Sandulyak

Abstract We managed to get the following results: we have confirmed the commonality of the functional view of the demagnetizing factor for quasi-solid and solid ferromagnetic cylindrical samples dependence on their relative dimension; the view is exponential with the radical of the relative dimension being the argument. Also the second argument is in addition revealed is a weak power function of magnetic permeability of substance of a magnetic. Expanded functional dependence for the demagnetizing factor which it is possible to use at the solution of a wide range of scientific and practical tasks is received. It is noted that for rather narrow range of values of magnetic permeability, for example, characterizing quasisolid "substance" of a matrix magnetic, the functional coefficient degenerates in a constant.

Keywords Demagnetizing factor · Magnetic permeability · Relative dimension · Relative level of magnetization

A.A. Sandulyak (✉) · D.A. Sandulyak · V.A. Ershova · M.N. Polismakova
A.V. Sandulyak
Moscow Technological University, Stromynka 20, Moscow, Russia
e-mail: anna.sandulyak@mail.ru

D.A. Sandulyak
e-mail: d.sandulyak@mail.ru

V.A. Ershova
e-mail: v.ershova@mail.ru

M.N. Polismakova
e-mail: gradient-m@mail.ru

A.V. Sandulyak
e-mail: a.sandulyak@mail.ru

S.-I. Ao et al. (eds.), *Transactions on Engineering Technologies*,
DOI 10.1007/978-981-10-1088-0_2

1 Introduction

Level of magnetization of ferromagnetic (ferrimagnetic, antiferromagnetic) bodies, as we know, depends not only on intensity of the magnetizing field and properties of material of a ferromagnetic, but also on its form.

When we magnetize a magnetic sample (body) of a particular form, there are poles formed at the edges of the sample which create an internal demagnetizing field, opposed to the external magnetizing one. A corresponding quantitative parameter characterizing this phenomenon is called a demagnetizing factor N (also known as the demagnetization coefficient which essentially is a parameter of magnetization suppression); this factor relates the demagnetizing field intensity with the sample magnetization. For example, the analytically calculable values of N for a ball, a cross-wisely magnetized long cylinder and a thin plate amount to $N = 1/3$, $N = 1/2$, $N = 1$ [1–4] respectively.

For the samples of other forms (for example, often used cylindrical), the factor is defined experimentally. In such a case it is always actual to obtain analytical (describing some experimental data) dependences apt for various calculations applicable to different samples of particular shapes and sizes.

To ascertain how great the influence of the demagnetizing factor N on the level of sample magnetization is, it is enough to turn to a classical expression for N:

$$N = \frac{1}{\mu_N - 1} - \frac{1}{\mu - 1}, \tag{1}$$

which shows the connection of N and magnetic permeability of the matter μ and that of the sample—body μ_N [1, 5–9]. Then, by the formula obtained in (1):

$$\frac{\mu_N}{\mu} = \Lambda = \frac{1}{\mu}\left[\frac{\mu - 1}{(\mu - 1)N + 1} + 1\right] \tag{2}$$

for a particular sample we can define such essential parameters as a relative level of magnetic permeability μ_N/μ and thus, a relative level of magnetic induction B_N/B, i.e. their real (reduced) values in comparison with potential ones. Herewith, the identity of these parameters, viz. $\mu_N/\mu = B_N/B = \Lambda$ follows from $B_N = \mu_0\mu_N H$ and $B = \mu_0\mu H$, where μ_0 is a magnetic constant and H is the magnetizing field intensity.

Basing on formula (2) we can illustrate (Fig. 1) to which extent the level of sample-body magnetization Λ depends on the demagnetizing factor N, e.g. for the samples with greatly varying values of magnetic permeability of their matter, say with $\mu = 5$, $\mu = 10$ and $\mu = 100$. We can clearly see in Fig. 1 that N is really the factor which even with seemingly small values, let alone increased or big ones, is able to sufficiently suppress the magnetic properties of the magnet. The N value of a given sample-body in its turn varies with its form and is mainly defined experimentally, as stated above.

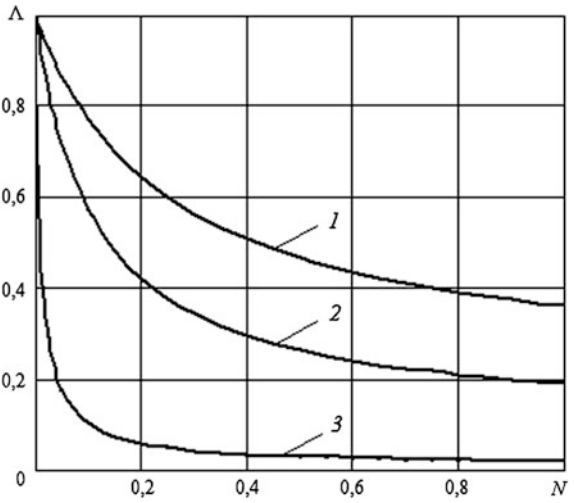

Fig. 1 Demonstrating the influence of the demagnetizing factor of the magnet sample (body) on the relative level of its magnetization; 1 − μ = 5, 2 − μ = 10, 3 − μ = 100

As to the employing certain obtained experimental data on N (most often these are the values for longitudinally magnetized cylindrical samples with given values of length L and diameter D, i.e. the relative dimension L/D), provided the data is in good supply, it will be necessary to derive a relevant generalizing formula for calculating N. Such a formula with introduced dimensionless argument L/D may be integrated in formula (2), thus instantiating it for the samples of any particular form in question.

2 Results for Samples of Quasisolid Ferromagnetics

Among the formulae connecting N and L/D parameter, one original equation is noteworthy, it is the one obtained for specific magnets: porous (granular) samples [10], for which (as for quasi-solid bodies) the issue of a demagnetizing factor influence has been less well understood than for solid magnets. A systematic study of the matter is necessary due to increased use of matrix magnetic separators, or filter-type separators [11–16]. The magnetized matrix (a loading of granules) performs a targeted capture of ferroparticles (ferroimpurities). Thus, as applied to the sample bodies of these magnets (a loading of ball-bearing balls) of a cylindrical form of various L/D values, field dependences of induction have been obtained experimentally. In paper [10], using these data in and proceeding to field dependencies of permeability, we calculated explicit values of N by (1). A respective processing of these data revealed that N dependency on L/D has an exponential view but with such a rather unusual argument as a radical of the relative dimension [10]:

$$N = \exp\left(-k_N \sqrt{\frac{L}{D}}\right), \tag{3}$$

with the value of coefficient $k_N \cong 1.5$ integrated in (3); it is for the studied quasi-solid samples in a comparatively narrow range of $\mu = 6.9–8.5$.

Moreover, formula (3) proved to be highly applicable not only to the samples of a granular medium, but also to various quasi-solid cores of ball-granule chains as well (as to an element of a bundled chains in a real granular medium [10]). Meanwhile, the values of metal volume concentration γ for a conditionally cut out core of the balls chain are different (in contrast to granular media, where $\gamma \cong 0.6$). They vary from $\gamma = 0.66$ for a solitary chain up to $\gamma \to 1$ when thinning out at its core part in a paraxial area of the chain, i.e. with a sharp decrease of a wedge-gap between the granules and thus with approximation of the core to the state of a solid metal.

This fact should be considered especially noteworthy as it gives grounds to assume that the obtained relation (3) may prove true not only for quasi-solid but also for solid magnet samples as well.

To test the assumption, it is necessary to have at one's disposal relevant experimental data on the demagnetizing factor N, e.g. for solid cylindrical samples in relation to their relative dimension L/D.

For this purpose, we can use classical experimental data (Kifer, Chen, Brug, Goldfarb, described in [4] and shown in Fig. 2). Here, if we again employ the results obtained for the samples with reciprocally far too different values of magnetic permeability of their matter (Fig. 2), e.g. $\mu = 5$, $\mu = 10$ and $\mu = 100$ congruently to the case considered above, then by formula (2) for starters we can find a relative level of magnetization Λ (Fig. 3), but now depending on L/D.

It can be seen that with reduction of relative dimension L/D of the sample and judging by the decrease of Λ parameter (Fig. 3), its magnetic properties (μ_N and B_N) are more and more giving into the magnetic properties of the matter (μ and B). And vice versa, with increase of L/D magnetic properties of the sample and its matter come closer, and with this growth μ zone of almost complete convergence moves towards bigger values of L/D. So, for relatively low values of $\mu = 5–10$ (Fig. 3, curves 1 and 2) magnetic properties of the sample and its matter practically become sufficiently close with $L/D \approx 10$. As for increased and big values of μ, e.g. for $\mu = 100$ (Fig. 3, curve 3) this kinship is reached with higher values of L/D. By the way, this is why a well-known rule is justified, it being the rule that recommends taking quite long samples ($L/D \geq 50$) to study magnetic properties of such materials in case when we use cylindrical instead of classic toroidal samples.

Having factual data on the demagnetizing factor N for cylindrical magnets (let us repeat, the values lie in a rather wide range of magnetic permeability of the matter $\mu = 5–100$), with the data obtained with various values of relative dimension L/D of these samples (Fig. 2), we can now test the above stated assumption on a possible universalization of expression (3), i.e. making it applicable to the samples of solid magnets. For this purpose, the data represented in Fig. 2 (curves 1–3) have to be

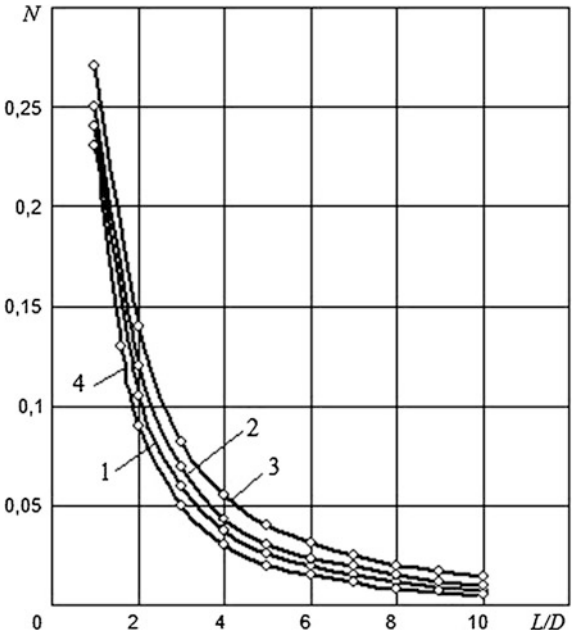

Fig. 2 Generalizing in [4] experimental data on the demagnetizing factor of ferromagnetic cylindrical samples varying with their relative dimension; curves *1*, *2*, and *3* correlate to values $\mu = 5$, $\mu = 10$, $\mu = 100$ respectively, curve *4*, the value of μ in [7] is regrettably not stipulated

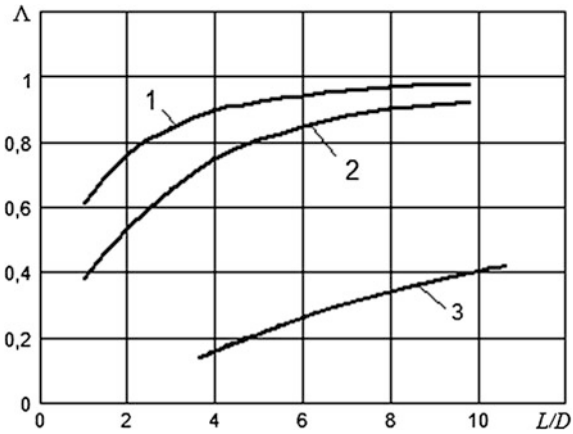

Fig. 3 Illustration of the alterations in values of the sample magnetization relative level depending on their relative dimension, by data in Fig. 2 with using (2); 1 − $\mu = 5$, 2 − $\mu = 10$, 3 − $\mu = 100$

represented in the same semi-logarithmic coordinates which are used for granular magnets [10], assuming the radical of relative dimension *L/D*, i.e. $\sqrt{L/D}$ (Fig. 4) to be an argument. Herewith, the mandatory reference point of $N = 1$ with $L/D \rightarrow 0$ just as in the case for a thin plate should serve the principle check point [10].

In these coordinates the data on *N* are seen to linearize quite well, thus signifying the validity of relation (3) and now even for solid magnets as well. It means we can

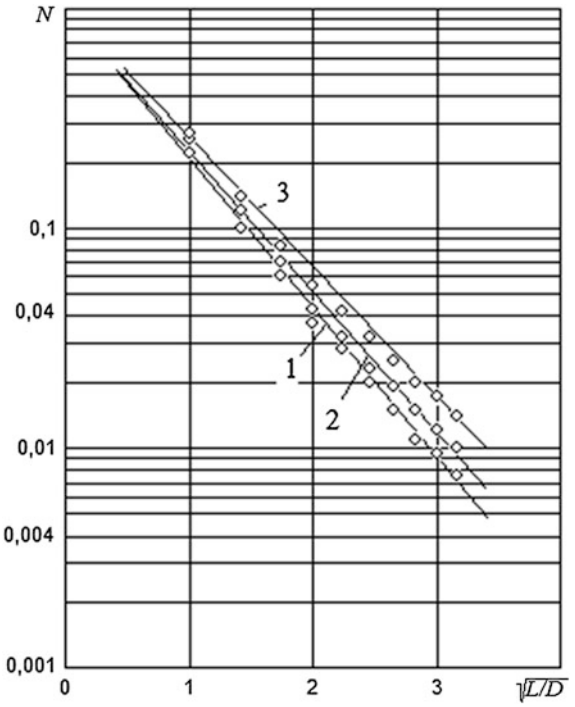

Fig. 4 Data on the demagnetizing factor of the samples (Fig. 2) represented in semi-logarithmic coordinates as related to the radical of their relative dimension. The linearization phenomenon is the manifestation of exponential dependence

speak of the exponential relation of N with the indicated argument-radical ($\sqrt{L/D}$) as of a universal regularity.

At the same time, judging by the stratification taking place (for various μ) dependences of N on L/D and (Fig. 2 and according to Fig. 4), it is necessary to talk about the k_N parameter entering expression (3), not as to a constant, but functional parameter here. In the analyzed range μ = 5–100 communication of k_N with μ was close to weak sedate (Fig. 5):

$$k_N = \frac{1.7}{\mu^{0.05}}. \tag{4}$$

Then after substitution (4) in (3) expression for the demagnetizing factor of a continuous sample registers more expanded, than (3):

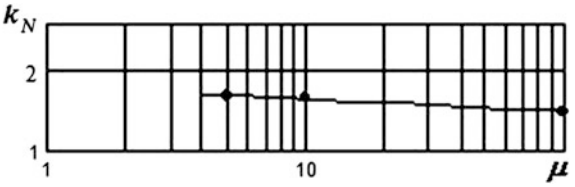

Fig. 5 Illustration (in logarithmic coordinates) weak influence of magnetic permeability of substance of a magnetic on the size of the k_N parameter entering a settlement formula (3)

$$N = \exp\left(-\frac{1.7}{\mu^{0.05}} \cdot \sqrt{\frac{L}{D}}\right). \tag{5}$$

at least, fair for (Fig. 2) range of values of magnetic permeability for substance of a magnetic analyzed here μ = 5–100.

For rather narrow range of values μ, for example, characterizing quasisolid "substance" of a matrix magnetic ($\mu \approx$ 6–9), the functional coefficient of k_N, in fact, degenerates in a constant, and the formula (5) will be transformed to simpler, private formula (3) with $k_N \cong 1.5$ value as it is stated above.

3 Conclusion

The original functional dependence (3) instigated the current research aimed at enhancing the understanding of the role and behavioural patterns of the demagnetizing factor for various magnetic bodies. Obtained for specific magnets, viz. granular ferromagnetic samples (as quasi-solid magnets) and 'packed' cores of granules chains (as the constituting elements of these magnets), the formula indicates exponential connection between demagnetizing factor N and the radical of their relative dimension, $\sqrt{L/D}$.

The assumption about a possible applicability of this functional dependence (3) with respect to solid samples proved to be valid for the most part. We managed to get the following results from the analysis of a number of experimental dependences of the demagnetizing factor N for solid ferromagnetic cylindrical samples on their relative dimension L/D:

- We have confirmed the commonality of the functional view (3) of the demagnetizing factor N for quasi-solid and solid ferromagnetic cylindrical samples dependence on their relative dimension L/D; the view is exponential with the radical of the relative dimension $\sqrt{L/D}$ being the argument.
- Also the second argument is in addition revealed is a weak power function of magnetic permeability of substance of a magnetic, namely $\mu^{0.05}$ (for indicated range μ = 5–100).
- Expanded functional dependence for the demagnetizing factor (true for range μ = 6–9), which it is possible to use at the solution of a wide range of scientific and practical tasks is received.
- It is noted that for rather narrow range of values of magnetic permeability, for example, characterizing quasisolid "substance" of a matrix magnetic, the functional coefficient degenerates in a constant $k_N \cong 1.5$.

References

1. Smistrup K, Hansen O, Bruus H, Hansen M (2005) Magnetic separation in microfluidic systems using microfabricated electromagnets—experiments and simulations. J Magn Magn Mater 293:597–604
2. Presuel-Moreno FJ, Sagues AA (2009) Bulk magnetic susceptibility measurements for determination of fly ash presence in concrete. Cem Concr Res 39(2):95–101
3. Anhalt M, Weidenfeller B, Mattei JL (2008) Inner demagnetization factor in polymer-bonded soft magnetic composites. J Magn Magn Mater 320:844–848
4. Sandulyak A, Sandulyak D, Ershova V, Kiselev D, Sandulyak A (2015) Finding out the commonalities in functional expressions for demagnetizing factor of quasi-solid and solid magnets. Lecture notes in engineering and computer science. In: Proceedings of the world congress on engineering 2015, WCE 2015, pp 1183–1185. London, UK, 1–3 July 2015
5. Nandy K, Chaudhuri S, Ganguly R, Puri IK (2008) Analytical model for the magnetophoretic capture of magnetic microspheres in microfluidic devices. J Magn Magn Mater 320:1398–1405
6. Goleman R (2004) Macroscopic model of particles' capture by the elliptic cross-section collector in magnetic separator. J Magn Magn Mater 272–276:2348–2349
7. Chen D-X, Brug JA, Goldfarb RB (1991) Demagnetizing factors for cylinders. IEEE Trans Magn 27(4):3601–3619
8. Chen D-X, Pardo E, Sanchez A (2006) Fluxmetric and magnetometric demagnetizing factors for cylinders. J Magn Magn Mater 306:135–146
9. Bose S, Datta A, Ganguly R, Banerjee M (2013) Lagrangian magnetic particle tracking through stenosed artery under pulsatile flow condition. J Nanotechnol Eng Med 4:031006-1–031006-10
10. Sandulyak AA, Ershova VA, Ershov DV, Sandulyak AV (2010) On the properties of short granular magnets with unordered granule chains: a field between the granules. Solid State Phys 52(10):1967–1974
11. Sandulyak AA, Sandulyak AV (2006) Prospects of employing magnetic filter-separators for purifying ceramic suspensions. Glass Ceram 11:34–37
12. Newns A, Pascoe RD (2002) Influence of path length and slurry velocity on the removal of iron from kaolin using a high gradient magnetic separator. Miner Eng 15:465–467
13. Rayner JG, Napier-Munn TJ (2003) A mathematical model of concentrate solids content for the wet drum magnetic separator. Int J Miner Process 70:53–65
14. Norrgran D (2008) Magnetic filtration: producing fine high-purity feedstocks. Filtr Sep 45 (6):15–17
15. Zezulka V, Straka P, Mucha P (2004) A magnetic filter with permanent magnets on the basis of rare earth. J Magn Magn Mater 268:219–226
16. Furlani EP, Sahoo Y, Ng KC, Wortman JC, Monk TE (2007) A model for predicting magnetic particle capture in a microfluidic bioseparator. Biomed Microdevices 9(4):451–463

Real Time Thermo Racing Tyre Model

Flavio Farroni, Aleksandr Sakhnevych and Francesco Timpone

Abstract New structure elements have been developed and implemented in the TRT thermo-dynamic tyre model. The updated model aims to provide a complete tool to study and understand all the phenomena concerning the tyre behaviour in thermal transient conditions, since all the elements constituting its structure are modelled. The computational cost, connected to a more complex model to manage, has been decreased by simplifying the mesh of the previous model version and, thus, by reducing the state vector length so making it suitable for real time analyses.

Keywords Strain energy loss · Tyre diffusivity evaluation · Tyre sidewall thermal behaviour · Tyre structure implementations · Tyre structure thermodynamic characterization · Tyre temperature real-time estimation · Tyre thermodynamics modelling · Tyre test procedures

1 Introduction

The characterization of the tyres is an essential issue for the formulation of vehicle dynamics models, since the tyres allow the interaction with the road and are interested by the fundamental slip related phenomena [1, 2].

Nowadays everyone playing a role in automotive sector is looking for the optimal solution in order to model and to understand the tyres behaviour in both experimental and simulation environments. The ability to predict the interior temperature distribution, and thus the grip behaviour of the tyre [3], is fundamental in

F. Farroni · A. Sakhnevych · F. Timpone (✉)
Department of Industrial Engineering, University of Naples Federico II,
Via Claudio 21, 80125 Naples, Italy
e-mail: francesco.timpone@unina.it

F. Farroni
e-mail: flavio.farroni@unina.it

A. Sakhnevych
e-mail: ale.sak@unina.it

S.-I. Ao et al. (eds.), *Transactions on Engineering Technologies*,
DOI 10.1007/978-981-10-1088-0_3

terms of the vehicle handling improvement and of the asset optimization according to highly variable outdoor testing conditions [4].

The new implementations to the already existing TRT thermo-dynamic model have a key purpose: to add new structure elements and, thus, to enhance and optimize the physical response, but not at the expense of the real-time simulation.

2 TRT—Thermo Racing Tyre Model

The model, called Thermo Racing Tyre (TRT) [5, 6] was developed in collaboration between the Department of Industrial Engineering of the University of Naples Federico II and a top ranking motorsport team.

The model is three-dimensional and takes into account of the following thermo-dynamic phenomena:

heat generation due to:

- tyre-road tangential interaction, known as "Friction Power";
- effect of tyre cyclic deformation during the rolling, known as "SEL" (strain energy loss);

heat exchange with the external environment due to:

- thermal conduction between the tread and the road;
- forced convection of the surface layer with the outside air;
- natural convection of the inner liner with the inner air;

heat conduction between the tyre layers due to the temperature gradient.

2.1 Tyre Modelling

As in the original version, the tyre, modelled as slick, is considered as unrolled in the circumferential direction along x-axis, lacking of sidewalls and grooves (Fig. 1). Its parallelepiped shape is constituted by three layers in the radial direction z, indicated as surface (outer surface of the tyre structure), bulk (intermediate layer), and inner liner (inner coating).

Each layer is discretized by means of a grid, whose nodes represent the points in which the temperature can be determined in real time. To the generic i-th node a parallelepiped volume V_i is associated, equal to

$$V_i = \Delta x \cdot \Delta y \cdot \Delta Z_{m,i} \tag{1}$$

in which Δx and Δy are respectively the dimensions along the longitudinal-circumferential and the transversal-wide directions, while the quantity $\Delta Z_{m,i}$ represents the thickness of a node's mass associated to i-th layer along the radial one.

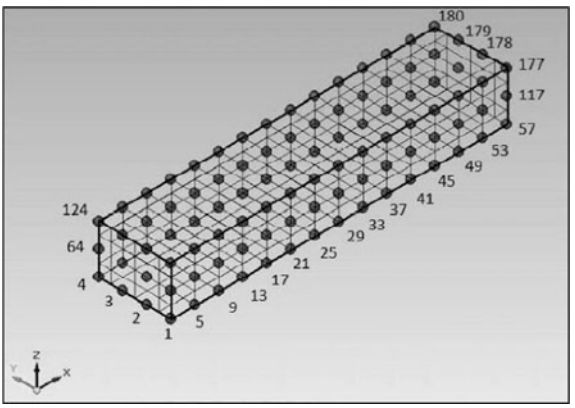

Fig. 1 Discretization of the tyre. Each layer is subdivided in 15 elements in longitudinal direction x and in 4 elements in transversal direction y. Thus, the entire tyre results discretized in 180 elements (but nevertheless the discretization could be easily modified)

With special regard to the tyre's structure, in which visco-elastic vulcanized polymers and fillers mainly constitute the tread and the carcass also includes reinforcements, two zones of homogeneous material have been identified and characterized by the following physical parameters along the radial direction:

- density ρ
- specific heat c_v
- thermal conductivity K

where, in particular, the variability of the last two terms with temperature is taken into account. Thus, each node has a mass expressed as follows:

$$m_i = C \cdot \rho \cdot V_i \tag{2}$$

where the dimensionless C coefficient depends on its position in the grid.

2.2 Base Hypotheses

With the aim of modelling heat dynamics and tyre layers temperature distribution, the following assumptions have been adopted:

- road: schematized as a geometric plane without irregularities, isotropic and homogeneous in all its characteristics, whose surface temperature is equal to T_r
- contact area: assumed to be rectangular, whose dimensions are the width W of the tread and the length L_a depending on the tyre radial stiffness and on the normal load applied
- camber angle: assumed equal to zero
- linear variation of the contact patch extension related to the value reached under the application of the static load by means of an appropriate set of coefficients

- motionless tyre with variable boundary conditions
- neglection of the radiation heat transfer mechanism.

2.3 Thermodynamic Model

The developed thermodynamic tyre model is based on the use of the diffusion equation of Fourier applied to a three-dimensional domain.

The complexity of the transient thermo-dynamical phenomena under study and the degree of accuracy required implies the dependence of the thermodynamic quantities, and in particular of the thermal conductivity, on the temperature. Furthermore, the non-homogeneity of the tyre has made it necessary to consider the variation of the above parameters also along the thickness.

Therefore, the Fourier equation takes the following formulation [7]:

$$\frac{\partial T}{\partial t} = \frac{\dot{q}_G}{\rho \cdot c_v} + \frac{1}{\rho \cdot c_v} \cdot \left(\frac{\partial^2 k(z,T) \cdot T}{\partial x^2} + \frac{\partial^2 k(z,T) \cdot T}{\partial y^2} + \frac{\partial^2 k(z,T) \cdot T}{\partial z^2} \right) \tag{3}$$

Writing the balance equations for each generic node needs the modelling of heat generation and of heat exchanges with the external environment.

2.4 Heat Exchange

The heat exchange between the tyre and the external environment, remembering that the radiation mechanism is neglected by hypothesis, it can be classified as follows:

- Heat exchange with the road

The thermal exchange between the tread and the asphalt has been modelled through Newton's formula [8], schematizing the whole phenomenon by means of an appropriate coefficient of heat exchange. The term for such exchanges, for the generic *i*-th node will be equal to:

$$H_c \cdot (T_r - T_i) \cdot \Delta X \cdot \Delta Y \tag{4}$$

where:

- H_c is the convective heat transfer coefficient, estimated for the track testing conditions $\left[\frac{\mathrm{W}}{\mathrm{m^2\,K}}\right]$;
- T_r is the track temperature [K].

- Heat exchange with the outside/inside air

The whole mechanism of the heat transfer between a generic surface and a moving fluid at different temperatures is described by natural and forced convection equations. The convection heat transfer is expressed by Newton's law of cooling, as before:

$$h_{conv} \cdot \left(T_{fluid} - T_i\right) \cdot \Delta X \cdot \Delta Y \tag{5}$$

Therefore, the heat exchange with the outside air is modelled by the mechanism of forced convection, occurring when there is relative motion between the car and the air, and by natural convection, when such motion is absent.

Natural convection is also employed to characterize the heat transfer of the inner liner with the inflating gas. The determination of the convection coefficient h, both forced h_{forc} and natural h_{nat}, is based on the classical approach of the dimensionless analysis [8, 9].

Supposing the tyre invested by the air similarly to a cylinder invested transversely from an air flux, the forced convection coefficient is provided by the following formulation [9, 10]:

$$h_{forc} = \frac{K_{air}}{L} \cdot \left[0.0239 \cdot \left(\frac{V \cdot L}{v_{air}}\right)^{0.805}\right] \tag{6}$$

in which:

- $K_{air}\ \left[\frac{\mathrm{W}}{\mathrm{m\,K}}\right]$ is air conductivity, evaluated at an average temperature between the effective air one and outer tyre surface one;
- $V\ \left[\frac{\mathrm{m}}{\mathrm{s}}\right]$ is considered to be equal to the forward speed of the vehicle (air speed is supposed to be zero);
- $v_{air}\ \left[\frac{\mathrm{m}^2}{\mathrm{s}}\right]$ is the kinematic viscosity of air, empirically obtained as:

$$\begin{aligned} v_{air} = (5 \times 10^{-10} \cdot T_{m,air}^3 - 10^{-6} \cdot T_{m,air}^2 \\ + 0.0008 \cdot T_{m,air} + 0.135) \times 10^{-4} \end{aligned} \tag{7}$$

- $L\ [\mathrm{m}]$ is the characteristic length of the heat transfer surface;
- $T_{m,air}[\mathrm{K}]$ is the arithmetic mean between the temperatures of the tyre outer surface and the external air in relative motion.

The values of h_{forc} evaluated with the above approach are close to those obtained by means of CFD simulations [11].

The natural convection coefficient h_{nat}, however, can be expressed as:

$$h = \frac{Nu \cdot k_{air}}{L} \tag{8}$$

in which, for this case:

$$Nu = 0.53 \cdot Gr^{0.25} \cdot Pr^{0.25} \tag{9}$$

2.5 Heat Generation

As concerns the tyre, the heat is generated in two different ways: for friction phenomena arising at the interface with the asphalt and because of stress-deformation cycles to which the entire mass is subjected during the exercise (SEL).

- Friction power

The first heat generation is connected with the thermal power produced at tyre-road interface because of interaction; in particular, it is due to the tangential stresses that, in the sliding zone of the contact patch, do work dissipated in heat. Friction power can be associated directly to the nodes involved in the contact with the ground, and it is calculated as referred to global values of force and sliding velocity, assumed to be equal in the whole contact patch:

$$FP = \frac{F_x \cdot v_x + F_y \cdot v_y}{A} \tag{10}$$

where a part of this thermal power is transferred to the tyre and the remaining to the asphalt.

Since F_x and F_y are global forces between tyre and road, and it is not known the contribution of each node to these interaction forces, heat generated by means of friction power mechanism transferred to the tyre has been equally distributed to all the nodes in contact with the ground. The model allows uneven local heat distributions as soon as local stresses and velocities distributions are known.

- Strain Energy Loss

The energy dissipated by the tyre Q_{SEL} because of cyclic deformations is due to a superposition of several phenomena: intra-plies friction, friction inside singular plies, nonlinear visco-elastic behaviour of all rubbery components, etc.

During the rolling, the entire tyre is subjected to the cyclic deformations with a frequency corresponding to the tyre rotational speed. During the motion, portions of tyre, entering in sequence in the contact area, are subjected to deformations, which cause energy loss and then heat dissipation.

In the model, the amount of heat generated by deformation (SEL) is estimated through experimental tests carried out deforming cyclically the tyre in three directions (radial, longitudinal and lateral) [12]. Estimated energies do not exactly coincide with the ones dissipated in the actual operative conditions, as the deformation mechanism is different; it is however possible to identify a correlation between them on the basis of coefficients estimated from real data telemetry.

2.6 Contact Area Calculation

The size and the shape of the contact area are function of the vertical load F_z, of the inner pressure p_{in} and of the camber γ and toe φ angles.

The contact area is assumed to be rectangular in shape with constant width W, equal to the tread's one, and length L_a, variable with the above mentioned parameters, except the toe angle. The number of nodes in contact is then calculated from the effective area of contact, which is obtained, taking into account actual vertical load and inflating pressure, on the basis of the results provided by FEM simulations and pressure sensitive films [13].

2.7 Constitutive Equations

The power balance equations, on heat transfers, are written for each elementary mass associated to each node, and differ in relation to their position inside the grid.

The heat conductivity between the surface and the bulk layers is indicated with k_1, while with k_2 is indicated the heat conductivity associated to the exchange between the bulk and the inner liner layer.

In the model, the tyre is considered motionless and the boundary conditions rotating around it to take into account the fact that elements belonging to the surface layer will be affected alternatively by the boundary conditions corresponding to the contact with the road and to the forced convective exchange with the external air.

As an example, heat balance equations for the surface node 2 are graphically reported in Figs. 2 and 3, recalling that, for the performed discretization, the nodes adjacent to node 2 are 6 and 58 along the x direction, 1 and 3 along the y direction and 62 along the z direction.

The previous images show the thermal powers, exchanged in all directions respectively for the two cases, only for node 2: road contact (Fig. 2) and contact with the external air (Fig. 3).

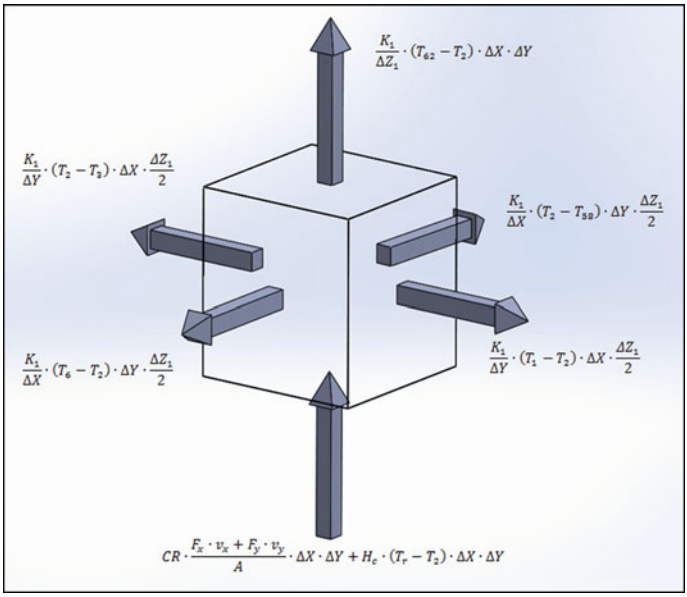

Fig. 2 Thermal powers exchanged in all directions for the control volume associated with node 2, assumed in contact with the road. It is possible to notice the term identifying the cooling with the road, characterized by the presence of the Hc coefficient, and the one connected to the tyre-road interaction

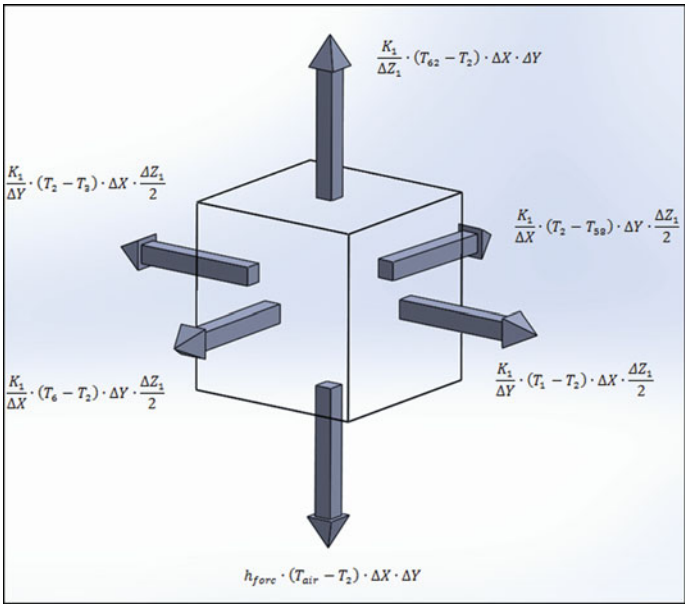

Fig. 3 Thermal powers exchanged in all directions for the control volume associated with node 2, assumed in contact with the external air. Note the absence of the generative term and the presence of the term identifying the exchange with the outside air, characterized by h_{forc} coefficient

Finally, the matrix equation at the basis of the model is:

$$\begin{pmatrix} \frac{\partial T_1}{\partial t} \\ \frac{\partial T_2}{\partial t} \\ \frac{\partial T_3}{\partial t} \\ \cdots \\ \cdots \\ \frac{\partial T_n}{\partial t} \end{pmatrix} = \begin{pmatrix} b_1 \\ b_2 \\ \cdots \\ \cdots \\ \cdots \\ b_n \end{pmatrix} + \frac{1}{\rho \cdot c_v} \begin{pmatrix} a_{11} & \cdots & a_{1n} \\ a_{21} & \cdots & a_{2n} \\ \cdots & & \cdots \\ \cdots & & \cdots \\ \cdots & & \cdots \\ \cdots & & \cdots \\ a_{n1} & & a_{nn} \end{pmatrix} \cdot \begin{pmatrix} T_1 \\ T_2 \\ \cdots \\ \cdots \\ \cdots \\ T_n \end{pmatrix} \tag{11}$$

in which a_{ij} is the generic coefficient, relative to the energy balance equation of the node i, that multiplies the j-th node temperature, while b_i is the generic coefficient not multiplying nodes temperatures.

Generally, to properly operate in order to provide the tyre temperature distribution, the model requires the following input data: normal, longitudinal and lateral tyre-road interaction forces, longitudinal and lateral sliding speeds, forward speed at the wheel centre, air and road temperature. The structural characteristics and the thermal properties of the tyre and the thermal conductivity of the track are also required.

Some of these data result from the telemetry measurements available for different tracks and are preliminarily analysed in order to check their reliability; others, such as in particular the ones related to structural and thermal characteristics of the tyre, are estimated on the basis of measurements and tests conducted on the tyres [14].

In addition to surface, bulk and inner liner temperature distributions, the model also provides the thermal flows involving the tyre, such as the flow due to the external air cooling, the one due to the cooling with the road, the one with the inflation air as well as the flows due to friction, hysteresis and exchanges between the different layers.

3 New TRT Implementations

In the latest versions, Thermo Racing Tyre has been simplified in order to reduce the number of equations to solve and so to decrease the computation burden. The changes concerned the substitution of the node grid on the internal layers (bulk and inner liner) with a singular node configuration.

The performance gain, obtained with the above-mentioned simplification, has been employed to run the iterations concerning the sidewalls nodes. These new elements, constituting the tyre structure, have been introduced in the model to estimate more accurately the temperature of the inner liner, since the latter is actively involved in the convective heat exchange with the external and the internal airflow [15, 16].

3.1 TRT—Simplified Mesh

The classic TRT was a discrete three-dimensional model, discretized by means of a grid, whose nodes represented the points in which the temperature was determined instant by instant, as shown in Fig. 1.

The number of nodes of the grid was given by the product ($numX \cdot numY \cdot numZ$) where $numX$ represented the number of nodes along the x direction, $numY$ the number of nodes along the y direction and $numZ$ was the number of nodes along the z direction. Nodes enumeration had been carried out starting from the first layer in contact with the road, proceeding transversely.

Over time, TRT's three-layer configuration was simplified as following (Fig. 4):

- *Surface* (grid of nodes in blue): outer surface of the tyre, made up of a grid of nodes, whose number is given by the product ($numX \cdot numY$);
- *Bulk* (parallelepiped in black): intermediate layer modelled as a singular node;
- *Inner liner* (parallelepiped in magenta): inner layer modelled as a singular node.

Considering the model within a thermo-mechanical chain, regarding respectively the bulk and inner layers, a detailed temperature distribution of these zones is unnecessary anymore because of their thermal inertias. This consideration allowed to simplify the discretization, reducing respectively the bulk and the inner layers to single nodes. With this, the computational burden is decreased and consequently TRT can be used in real time applications [17] without any difficulties.

In fact, the number of state variables and therefore of Eq. (11) has been reduced from n to $(n/3 + 2)$. The above simplification was made preserving the heat transfers between the layers, whose inertial and thermal material properties, as density, conductivity and specific heat, were respectively attributed to singular nodes.

To take into account the simplification adopted, the bulk and inner liner nodes only allow the heat exchange along the radial direction of the tyre; therefore the tangential heat transfers inside the single interior tiers have been supposed absent. In particular, since the bulk and the inner nodes are assumed to have the heat exchange area along the radial direction equal to the rectangle, whose dimensions

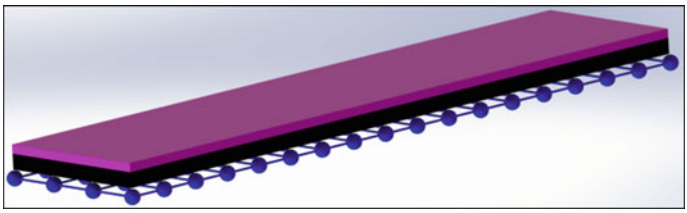

Fig. 4 Simplified mesh, adopted for tyre structure. While the surface layer is still modelled as a grid of nodes (in *blue*), the bulk (in *black*) and the inner (in *magenta*) ones have as singular node configuration (color figure online)

coincide with tyre circumferential length and width, the heat balance equations can be respectively written as:

$$\rho \cdot c_v \cdot W \cdot L \cdot \Delta Z_{m,bulk} \cdot \frac{\Delta T_{bulk}}{\Delta t} = \dot{Q}_{SEL} + \frac{k(z,T)}{\Delta Z} \cdot (T_{inner} - T_{bulk}) \cdot W \cdot L + \frac{K_1}{\Delta Z_1} \cdot \left(T_{surf,avg} - T_{bulk}\right) \cdot W \cdot L \tag{12}$$

$$\rho \cdot c_v \cdot W \cdot L \cdot \Delta Z_{m,inner} \cdot \frac{\Delta T_{inner}}{\Delta t} = \dot{Q}_{SEL} + h_{forc} \cdot \left(T_{gas} - T_{inner}\right) \cdot W \cdot L + \frac{k(z,T)}{\Delta Z} \cdot (T_{bulk} - T_{inner}) \cdot W \cdot L \tag{13}$$

where $T_{surf,avg}$ is the mean temperature value of the entire surface layer. The above-mentioned equations are therefore developed in order to write a complete set of normal-form Eq. (11), as follows:

$$\frac{\Delta T_{bulk}}{\Delta_t} = \frac{1}{\rho \cdot c_v} \cdot \left[\frac{\dot{Q}_{SEL}}{W \cdot L \cdot \Delta Z_{m,bulk}} + \frac{k(z,T)}{\Delta Z_{m,bulk} \cdot \Delta Z} \cdot (T_{inner} - T_{bulk}) + \frac{k(z,T)}{\Delta Z_{m,bulk} \cdot \Delta Z} \cdot \left(T_{surf,avg} - T_{bulk}\right) \right] \tag{14}$$

$$\frac{\Delta T_{inner}}{\Delta t} = \frac{1}{\rho \cdot c_v} \cdot \left[\frac{\dot{Q}_{SEL}}{W \cdot L \cdot \Delta Z_{m,inner}} + \frac{h_{forc}}{\Delta Z_{m,inner}} \cdot \left(T_{gas} - T_{inner}\right) + \frac{k(z,T)}{\Delta Z_{m,inner} \cdot \Delta Z} \cdot (T_{bulk} - T_{inner}) \right] \tag{15}$$

3.2 TRT—Sidewalls Implementation

To estimate more accurately the temperature distribution even of the deepest tyre layers, usually not easily measurable on-line, an innovative structure configuration was adopted. The evolved tyre structure includes the presence of the sidewalls, actively involved in the convective heat exchanges with the external airflow and the inner gas fluid threads inside the wheel. Inside the chamber, the tyre sidewalls thermally interact with the inner gas, that is in its turn involved in the heat convective exchange with the inner liner.

As shown in Fig. 5, the TRT tyre structure with sidewalls implementation is still considered unrolled. The sidewalls have been discretised as two parallelepiped shaped single node layers. In this way their nodes, called *surface* (in green) and *bulk* (in yellow), for a right tyre, are respectively in contact with the external air flux and with the inner gas contained inside the wheel chamber. It is also necessary to

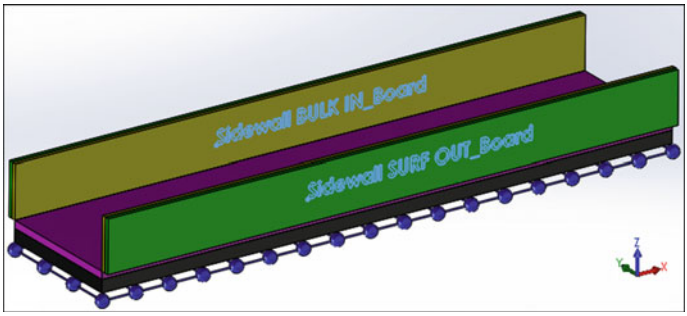

Fig. 5 Particular diversification between the in_board and out_board nodes for a right tyre is obtained regarding their position towards the vertical longitudinal plane *xz* of the vehicle reference system (color figure online)

highlight that the same sidewall nodes are diversified in *in_board* and *out_board*, regarding their position towards the vertical longitudinal plane of symmetry of the vehicle (in_board and out_board sidewalls are correspondingly the nearest and the farthest ones); therefore the thermal convective powers, respectively investing the sides of the tyre, will be different.

The sidewalls take in account both the conductive and the convective heat exchanges. In particular, as regards the external sidewall nodes, the convective exchange rate with the external airflow is obtained from the heat transfer area A_{Side}, calculated knowing the CAD of the tyre; meanwhile, the internal sidewall nodes are involved in the convective heat exchange with the inner gas fluid threads. The heat balance equations related to respectively the sidewall layer's external and internal nodes are:

$$\rho \cdot \Delta V_{Side,surf} \cdot c_v \cdot \frac{\Delta T_{Side,surf}}{\Delta t} = h_{forc} \cdot \left[T_{air} - T_{Side,surf}\right] \cdot A_{side} + \frac{k(z,T)}{\Delta Z} \cdot \left(T_{Side,bulk} - T_{Side,surf}\right) \cdot A_{side} \tag{16}$$

$$\rho \cdot \Delta V_{Side,bulk} \cdot c_v \cdot \frac{\Delta T_{Side,bulk}}{\Delta t} = h_{forc} \cdot \left[T_{gas} - T_{Side,bulk}\right] \cdot A_{side} + \frac{k(z,T)}{\Delta Z} \cdot \left(T_{Side,surf} - T_{Side,bulk}\right) \cdot A_{side} \tag{17}$$

Equations (16) and (17) are further developed as follows:

$$\frac{\Delta T_{Side,surf}}{\Delta t} = \frac{1}{\rho \cdot c_v} \cdot \left[\frac{h_{forc}}{\Delta Z_{m,Side,surf}} \cdot \left[T_{air} - T_{Side,surf}\right] + \frac{k(z,T)}{\Delta Z \cdot \Delta Z_{m,Side,surf}} \cdot \left(T_{Side,bulk} - T_{Side,surf}\right)\right] \tag{18}$$

$$\frac{\Delta T_{Side,bulk}}{\Delta t} = \frac{1}{\rho \cdot c_v} \cdot \left[\frac{h_{forc}}{\Delta Z_{m,Side,bulk}} \cdot \left[T_{gas} - T_{Side,bulk} \right] + \frac{k(z,T)}{\Delta Z \cdot \Delta Z_{m,Side,bulk}} \cdot \left(T_{Side,surf} - T_{Side,bulk} \right) \right] \tag{19}$$

4 Experimental Characterizations

In order to properly reproduce the tyre temperature trends achievable on the track and to be predictive in the mere simulation, the TRT model has to be conveniently characterized. In this way the Thermo Racing Tyre model is able to provide both the most deepened analysis, aimed to optimize the performance of the whole tyre, and the real-time simulations with the driving simulator [18].

The tyre is characterized according to the two main test branches:

- structural: evaluation of the contribution of the heat generation caused by the specific carcass composition and the particular disposition of the different tyre layers (such as steel belt chords and nylon cover plies, inside the tread and the sidewalls);
- thermal: evaluation of the main thermal characteristics, such as the thermal diffusivity and the specific heat of the various layers inside the tread and the sidewalls.

4.1 Strain Energy Loss (SEL) Characterization

The SEL (Strain Energy Loss) is the energy dissipated by the tyre as a result of the cyclic deformations. This dissipation is caused by a superposition of several phenomena, such as intra-plies friction, friction inside plies, non-linear visco-elastic behaviour of all rubbery composite components.

SEL test are commonly employed to take into account the heat generation linked with tyre structure deformation caused by rolling, traction, braking and steering.

Experimental data are used to identify the parameters of an analytical function that allows to estimate in the TRT thermal model the heat produced by the SEL phenomena as a function of the acquired ad estimated vehicle variables (wheel angular speed, tyre/road interaction forces, slip indices).

The cyclic deformations, whom the system is subjected to, occur with a frequency linked to the tyre rotational speed. During the rotation, indeed, tyre's portions enter continuously into the contact area, and, as a result, they are subjected to large deformations, causing energy loss and then heat dissipation within the entire tyre structure [19].

In the model, the amount of heat generated by the deformation (SEL) is estimated through experimental tests, cyclically deforming the tyre in three directions

(radial, longitudinal and lateral). In this way, the rolling resistance dispersions and the tangential tyre/road interaction losses are properly reproduced.

In order to determine the above mentioned mechanical characteristics of an automotive pneumatic tyre, two different test sequences have especially been developed: radial and tangential procedures.

- Radial test
  This type of test is realized by stressing the tyre with a pavement shaped plate along the radial direction per diverse load and frequency values. In order to have a complete characterization of the phenomena in every operating condition, this procedure is repeated per different tyre pressures and the tyre temperature initial conditions.
  The vertical load and the corresponding displacement response are acquired to evaluate the hysteresis cycle in every tyre typical operating condition. In other words, it is possible to determine the tyre normal interaction characteristics as, for example, its radial stiffness.
- Tangential test
  In the tangential test, the tyre is stressed with a pavement shaped plate along the longitudinal and the lateral directions per diverse load e frequency values. If a proper radial load value is applied, it is possible to avoid the relative motion between the tyre and the plate surface in reciprocal contact.
  It is important, indeed, to evaluate only the quantity of the heat linked to the tyre structure deformation (and not others like the one linked to the friction). That is why, in this type of test, it is mandatory to avoid the slip motion between the pavement shaped plate and the tyre.
  Once the plate is correctly placed with an established amount of constant radial preload, a specifically designed sequence of diverse load amplitudes in both longitudinal and lateral directions, is applied.

The typical output is a cycle, evaluated in a force versus displacement diagram at different frequency values, where the area is calculated in steady state conditions, considered as an index of the dissipated power converted in heat, is represented in Fig. 6.

4.2 Thermal Diffusivity Characterization

In order to determine the value of the tyre thermal diffusivity and to obtain a more accurate temperature profile in simulation, the following experiments are performed.

A fundamental parameter for the tyres thermodynamic characterization is the thermal diffusivity [20], which embraces together the thermal conductivity, the density and the specific heat. The estimation of this parameter is complex and hard

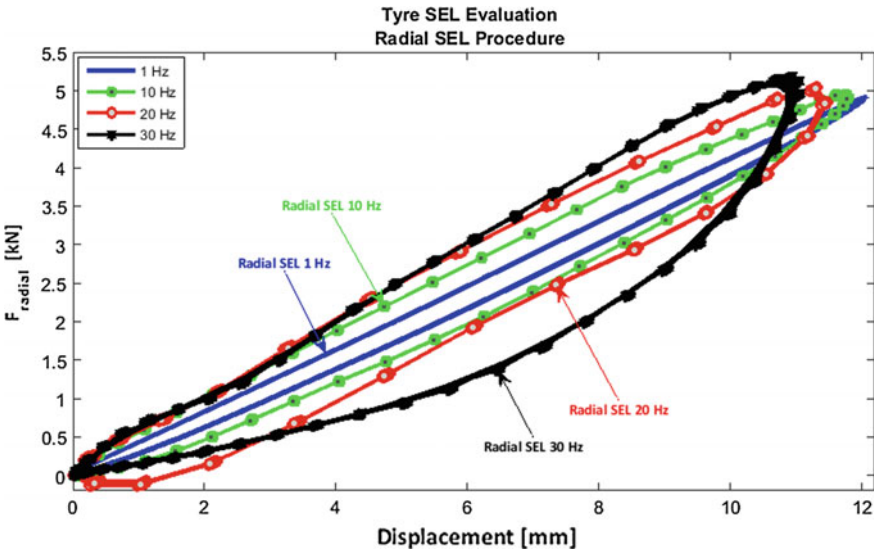

Fig. 6 Radial SEL evaluation at the 5 kN value of sinusoidal radial load shows a typical tyre structural behavior as the increasing area and stiffness (slope) values at increasing frequency

to determine, due to its variability from tyre to tyre and to its intrinsic temperature dependence.

To this purpose, a non-destructive test procedure has been developed [21]. This non-destructive test is performed on the entire tyre and allows the determination of the thermal diffusivity via the heat supply on the tread surface through a specific powered laser and then by measuring the temperatures reached during the test on both the tread and the inner surfaces.

With the use of the proper layout instrumentation, in Fig. 7, it possible to estimate:

- the radial temperature gradient within the whole thickness of the tyre;
- the trend of the circumferential temperatures on the external tread layer, close to the laser focal spot;
- the trend of the circumferential temperatures on the internal innerliner layer.

In the following Fig. 8, a comparison of the temperature trends of the surface and inner surfaces of two different tyres, equally heated by the same laser power of 1 W, is represented.

The results of the mentioned tests, are used to identify the above mentioned thermodynamic parameters via the especially developed TRT Lab model.

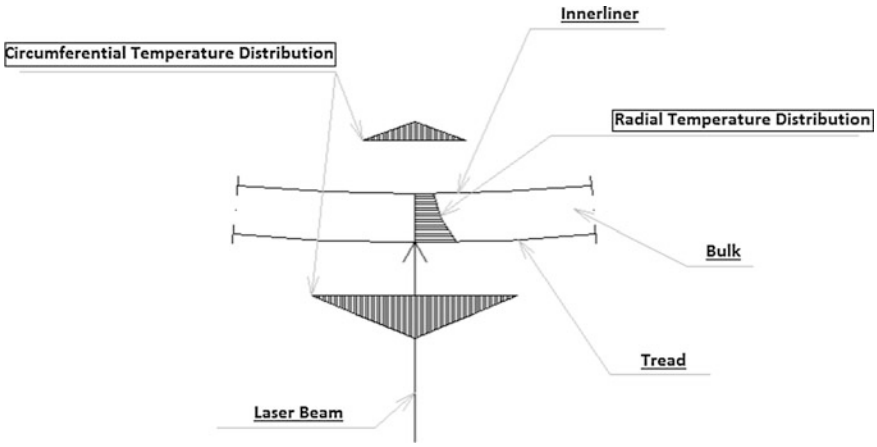

Fig. 7 Two thermocameras are pointed to the external tread and the internal innerliner surfaces to acquire the radial and the circumferential temperature gradients, while the laser power heat warms up the tyre thickness mass

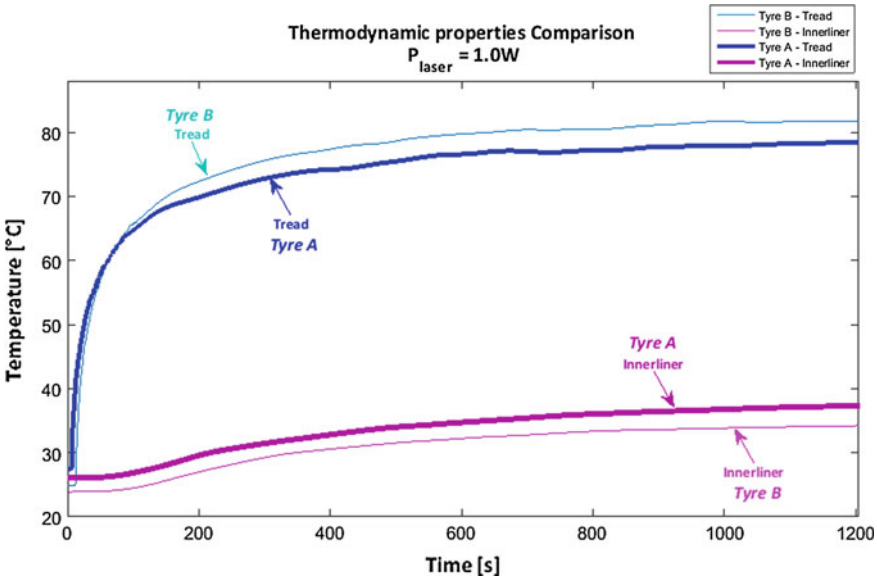

Fig. 8 The diagrams reproduce the temperature registered in correspondence of the area directly hit by the laser spot on both tread and innerliner layers, per different tyre compounds

5 Results

First of all, a comparison between the fully discretized version of TRT and the mononodes one is illustrated. Other things being equal, the above models have negligible differences between temperature trends for all the tyre layers, as shown in Fig. 9.

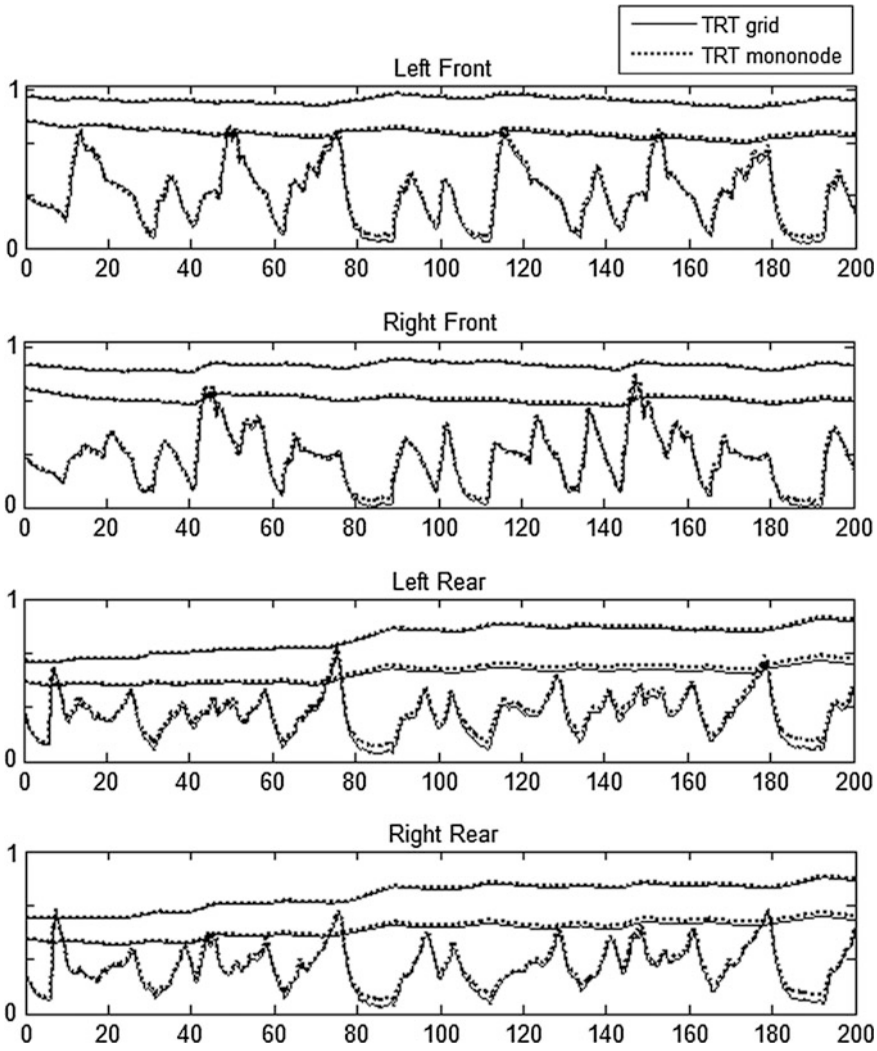

Fig. 9 The comparison between the TRT model and the simplified singular node configuration version shows negligible differences between the temperature trends of all three-tyre layers

In Fig. 10, the temperature trends of all the tyre layers of the new-modelled TRT with the sidewalls implementation for all the four wheels, are illustrated (it must be highlighted that in the above figures the temperature values are dimensionless because of confidentiality agreements).

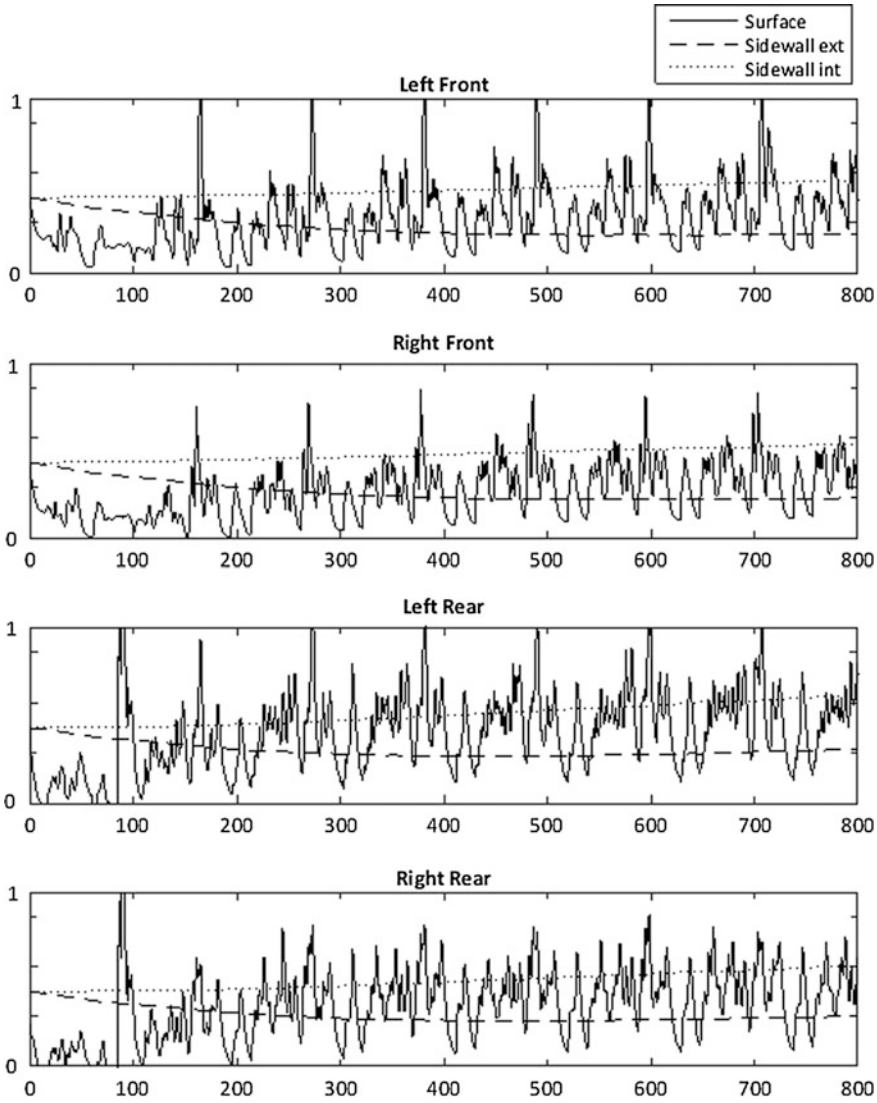

Fig. 10 The temperatures of both the external layers, the tread and the sidewall surfaces, and the internal ones, the bulk/inner and sidewall plies, are close concerning the mean values, while the thermal dynamics is different due to the different physical phenomena they are involved with. The temperature of the tread layer is characterized by higher dynamics, while the sidewall's internal and external surfaces interact with different environments, in particular with the tyre internal chamber and with the external air flow

As expected, the mean temperature values of respectively the internal (tread bulk/inner and sidewall bulk) and the external (tread surface and sidewall surface) tyre layers are fairly close. The difference in the thermal shapes of the external layers is due to their position inside the tyre structure: the tread layers, especially the surface one, are subjected to the instant thermal powers generated by the tyre/road interaction; meanwhile a slow temperature trend induced concurrently by the rolling fatigue effect and by the convective heat exchanges characterizes the sidewalls dynamics. That is why, the internal tyre strata seem to have a slow temperature ascent during the rolling motion of the wheel, while the tread surface layer is characterized by an oscillating profile.

6 Conclusions

The adoption of a new simplified tyre configuration and the implementation of an opportune mesh allowed to obtain a complete tyre temperature distribution in all the tyre working conditions, being able to fit the response of the model to the telemetry data, minimizing moreover the computer resources expended. In this way, the updated model aims to provide a tool useful to study and understand all the thermal phenomena concerning the tyre during its interaction with both the external environment and the internal chamber. In fact, the factors like the inflating gas pressure, since its influence on the tyre rolling fatigue, can be optimized with the above instrument.

It has to be highlighted that, to be used in a predictive manner, the model needs an initial tuning phase to be carried out only once for each season, because of changes in car setup and tyres construction. Once developed through this operation, known all inputs, the results obtained are in good agreement with the telemetry data, with reference to the various operating conditions of the different tracks.

References

1. Pacejka HB (2006) Tyre and vehicle dynamics. Butterworth-Heinemann, Oxford
2. Guiggiani M (2014) The science of vehicle dynamics. Springer, Berlin
3. Farroni F, Russo M, Russo R, Timpone F (2014) A physical–analytical model for a real-time local grip estimation of tyre rubber in sliding contact with road asperities. Proc Inst Mech Eng Part D J Automobile Eng 228(8):958–972
4. Wright P (2001) Formula 1 technology. SAE
5. Farroni F, Giordano D, Russo M, Timpone F (2014) TRT: thermo racing tyre a physical model to predict the tyre temperature distribution. Meccanica 49(3):707–723
6. Farroni F, Sakhnevych A, Timpone F (2015) An evolved version of thermo racing tyre for real time applications. Lecture notes in engineering and computer science. proceedings of the world congress on engineering 2015, 1–3 July 2015, London, U.K., pp 1159–1164
7. Kreith F, Manglik RM, Bohn MS (2010) Principles of heat transfer, 6th ed. Brooks/Cole, USA

8. Van der Steen R (2007) Tyre/road friction modeling. Ph.D. thesis, Eindhoven University of Technology
9. Brown AL, Wickliffe LE (1980) Parametric study of convective heat transfer coefficients at the tire surface. Tire Sci Technol 8:37–67
10. Gillespie TD (1992) Fundamentals of vehicle dynamics. SAE
11. Derome D, Blocken B, Carmeliet J (2007) Determination of surface convective heat transfer coefficients by CFD. In: 11th Canadian conference on building science and technology, Banff, Alberta
12. Brancati R, Strano S, Timpone F (2011) An analytical model of dissipated viscous and hysteretic energy due to interaction forces in a pneumatic tire: theory and experiments. Mech Syst Signal Process 25(7):2785–2795
13. Gabel G, Moldenhauer P, Kroger M (2008) Local effects between the tyre and the road. ATZautotechnology 8(4):48–53
14. Farroni F, Rocca E, Timpone F (2013) A full scale test rig to characterize pneumatic tyre mechanical behaviour. Int Rev Mech Eng (I.RE.M.E.) 7(5):841–847
15. Calabrese F, Baecker M, Galbally C, Gallrein A (2015) A full thermo-mechanical tire model for advanced handling applications. SAE 2015 world congress, Detroit, USA
16. Devaraj S, Ramprasath T, David SJ (2013) A study on fluid dynamic properties of a passenger tyre tube by using CFD. Int J Emerg Technol Adv Eng 3(10)
17. Balaguru P, Krishna Mohan N, Sathiyagnanam AP (2011) Neural network based analysis of thermal properties rubber composite material—pneumatic tire. In: Lecture notes in engineering and computer science: proceedings of the world congress on engineering 2011, WCE 2011, 6–8 July 2011, London, U.K., pp 2015–2019
18. Gerardo M, Sarria M (2011) Real-time concurrent constraint calculus: the complete operational semantics. Eng Lett 19(1):38–45
19. Muhammad AK, Okamoto S, Lee JH (2015) Computational simulations and experiments on vibration control of a flexible two-link manipulator using a piezoelectric actuator. Eng Lett 23 (3):200–209
20. Frantzen M, Ng AHC, Moore P (2011) A simulation-based scheduling system for real-time optimization and decision making support. Robot Comput Integr Manuf 27(4):696–705
21. Allouis C, Amoresano A, Giordano D, Russo M, Timpone F (2012) Measurement of the thermal diffusivity of a tire compound by mean of infrared optical technique. Int Rev Mech Eng 6:1104–1108

The Method of Determining Velocity by Measuring the Vehicle-Body Deformation Plane Approximation Method

Przemysław Kubiak, Marek Woźniak, Карпушкин Виктор Геннадьевич, Piotr Jóźwiak, Gustavo Ozuna, Szymon Madziara, Mateusz Najbert and Andrzej Szosland

Abstract Crash test vehicle are mainly defining the relationship between the speed of the vehicle in the early phases of the collision and the energy necessary for the deformation occurs. Vehicle speed at the start of the collision is determined by comparing the body deformation cars ``and their kinetic energy. After reviewing the methods used to date, a new approach to the calculation of the EES was proposed. The new algorithm allows the parameter EES to obtain a high accuracy on the basis of known factors A, B, G, b_k.

P. Kubiak (✉) · M. Woźniak · P. Jóźwiak · S. Madziara · M. Najbert · A. Szosland
Department of Vehicles and Machine Design, Technical University of Lodz, 116 Żeromskiego, 90-924 Lodz, Poland
e-mail: przemyslaw.kubiak@p.lodz.pl

M. Woźniak
e-mail: marek.wozniak.1@p.lodz.pl

P. Jóźwiak
e-mail: piotr.jozwiak@p.lodz.pl

S. Madziara
e-mail: 171243@edu.p.lodz.pl

M. Najbert
e-mail: 174616@edu.p.lodz.pl

A. Szosland
e-mail: andrzej.szosland@p.lodz.pl

К.В. Геннадьевич
Факультет машиностроения, Новгородский государственный университет имени Ярослава Мудрого, Великий Новгород ул. Большая Санкт-Петербургская, д. 41, Великий Новгород, 173003, Russia
e-mail: endomorf1990@gmail.com

G. Ozuna
Department of Industrial and Systems Engineering, University of Sonora, Hermosillo, Mexico
e-mail: gozuna@industrial.uson.mx

S.-I. Ao et al. (eds.), *Transactions on Engineering Technologies*,
DOI 10.1007/978-981-10-1088-0_4

Keywords Car accidents · Coefficient of restitution · Crash test · Distortion factor · Equivalent speed energy · NHTSA · Vehicle speed

1 Introduction

Currently, the vehicles were the result of the work of engineers and scientists to a group of more than 100 years. However, a growing number of vehicles, together with the lack of driving skills and poor quality of infrastructure, leading to a large number of collisions. Since 1990, only in Poland, the number of vehicles increased by 62.6%. In 1990-2009, there were more than 1 million 61 thousand accidents that left 126,000 people have died and more than 1 million 336 thousand injured. The greatest number of road accidents take place in Germany, Italy and the UK, which is directly related to the number of vehicles in these countries. Poland, with 44.196 accidents, occupies 6th place. However, the largest number of deaths per 100 accidents recorded in Poland-10, 3 and Lithuania-9.9. These statistics clearly indicates a problem with traffic safety on our roads.

So far, the existing methods for determining the vehicle speed based on measurements of the deformation of the vehicle body are applied linear models. This means that the relationship between the EES searched (the energy equivalent to the speed defined as the kinetic energy lost during the collision of the vehicle), and the value of the coefficient C_s (corresponding to the mean value of the six points of the deformation of the body) was linear,

It has been determined that the critical factors for this analysis is the coefficient b_k and slope constituting the above-mentioned linear relationship. His constant value corresponds to the assumption of linear behavior of the system response to internal forces during a collision deformation of the vehicle.

However, for a fixed coefficient b_k on the basis of tables for a given class of vehicles leads to an error in the assessment of the EES more than 12%, which prevents the practical application of this method in case of actual collisions. Using nonlinear model and b_k coefficient calculated from the regression equation polynomial, for the first time in this publication, a mathematical model of the relationship b_k factor of two variables: C_s -The average deformation of the body and (L_t) -the deformation field width, we obtained the EES improving estimation accuracy of the average error of approx. 6% [1–4].

For this purpose, the above relationship approximately in the plane of the second order in three dimensional space. As in the previous publications describing vehicles compact class experimental data from the database NHTSA collected crash test confirmed the non-linear relation b_k coefficient on the average deformation of the vehicle body, C_s. In addition, the study provides a description of the relationship zb_k coefficient (slope of the curve illustrating the dependence of the speed V_t to C_s) and the width of the zone of deformation, L_t.

This relationship, which has not been previously studied, is visible in the form of three teams graph showing the relationship b_k on C_s. The implementation of this method of description, in spite of a smaller base for cars Subcompact compared to the previously described compact class, in addition to improved accuracy of determination of EES and, at the same time, has led to the independence of the error description C_s, L_t and m vehicle parameters.

The method used herein involves three separate stages. In a first step, the tabulated values b_k for the group of cars Subcompact taken as equal to 26 m / s / m, corresponding to a linear gradient with a continuous process compared V_t vs. C_s. In the second stage, as in previous publications concerning small cars, the polynomial approximation b_k the formula C_s was used while second degree polynomial. This step corresponds to the nonlinear without depending b_k factor in the deformation zone width L_t. In the third step, the compound was introduced to a b_k values calculated using a function of two variables (C_s, L_t) approximately two-dimensional plane of the second stage. This approach resulted not only to improve the accuracy of estimation of speed (EES smaller average error), but above all, independent of the error parameters of vehicles, such as C_s, L_t and m. The database was repeatedly cleaned for the purposes of the calculation. Extreme cases, and those shaded image b_k the formula C_s in the form of double units are omitted. The prepared data allowed the extraction b_k (C_s) compound using a polynomial of the second degree. Such prepared database also provides a good starting point to bring together data from the plane of the second degree. This plane describes the relationship b_k factor on the C_s and L_t . This document introduces the relationship b_k on the car deformation zone width L_t . This relationship, in the form of two branches, is presented on a plot of velocity as a function of EES C_s parameters of the car. Speed value for the parameter width of the deformation of the body L_t = 1500 (mm) are above those for L_t = 1000 (mm). At the same time, there is clearly visible increase in information on the nonlinearity with increasing L_t of [4-6].

In the case described, Subcompact Car class, relatively small database was available (with less than 200 cases). This makes it difficult to achieve the full potential of the model plane approximation. In the case of larger size of the database it is possible to complete the approximation of plane dimension greater than two, which of course contributes to the improved accuracy of the description and its independence from the other parameters of the model. Particular attention was paid to the distribution of errors. It is the nature of the normal distribution or similar to her. This justifies the use of the standard deviation of the parameter as a measure of the dispersion of error around the mean. It is this value than the average obtained in the statistical description, which is the most important parameter indicating the accuracy of determining the speed of the EES in the model. The database of small size is determined by a relatively small improvement parameter in turn goes to the description in the second degree polynomial, and then by plane approximation. Increased database like the one in the previously described compact cars to allow

greater improvement of this parameter, as we move to more advanced methods of description. This effect can be further enhanced through the plane of degree higher than two to describe. The calculations in this case may lead to more accurately understand the dependence of b_k factor not only in the L_t parameter, but perhaps also on the mass of the vehicle, m. the current data do not allow such a discussion. the aim is to present the proposed method of approximation b_k inclination of the plane in order to determine the speed of the EES the vehicle. Further research directions authors will also be identified [7–10].

2 Method for Determination of Velocity Vehicle Collision

The database for this calculation has been made available by the NHTSA for subcompact cars. The database is the result of measurements performed in crash tests, and in the present case, consists of 191 records. The database contains basic parameters, such as vehicle weight, year of manufacture, as well as the speed at which the vehicle was accelerated during the study.

It was assumed that a collision was central and easy, and therefore phase restitution neglected, which leads to deformation, assuming entirely of plastic during the impact. Before the adoption of the definition of kinetic coefficient of restitution as the ratio of the relative velocity and the collision taken with a negative sign , this assumption leads to the omission of the relative speed of vehicles after the collision. This assumption is fulfilled, the specifically, the greater the distortion factor C_s in [4, 11].

A collision deformation results, which may be described as a decrease in the profile body 6 points C_1 - C_6 arranged along the front surface of the body, and with parameter width of the cavity, L_t calculated in a plane perpendicular to the axis of the vehicle.

Constant linear relationship EES Case C_s -defined as the ratio b_{gk} -was expected. Specifies the initial value for the EES $C_s = 0$. Thus, it is the ratio of the speed at which, despite the collision, without deformation / paragraph there yet . this corresponds perfectly elastic collision. the value of this ratio has been set at 11 (km / h) or 3.05 (m / s).

Based on the tables and the database NHTSA, the average value b_k parameters representing the slope of the regression line calculated speed EES on an average coefficient of strain C_s -was assumed to be 26 m / s / m. As a specific value, in accordance with the procedure established in line meaning A, B, G, C_s, the coefficients α β calcd for subsequent cases.

As in the previous case, to the car class Compact dependence of the average strain C_{are} on the mass m of the vehicle, and the speed V_t also removed. This compound was shown in Fig. 1 which confirms the non-linear behavior C_p (V_t) function [10, 12, 13, 15, 16].

That is, the speed before the impact, V_t, can not be determined with a constant slope coefficient b_k. This problem and its solution will be explained in the following

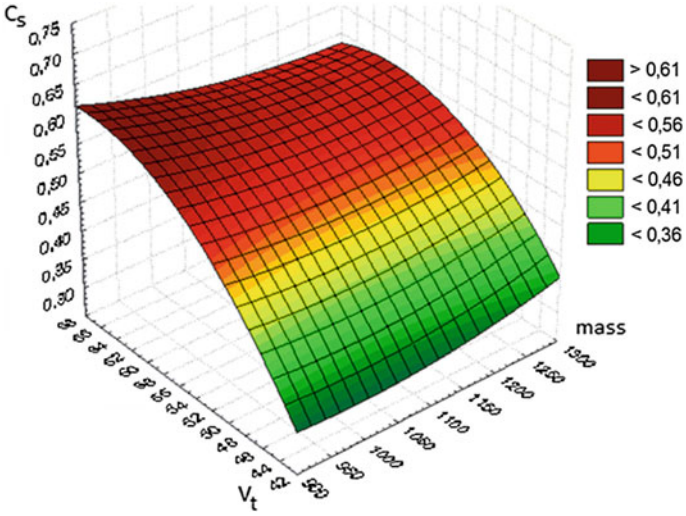

Pussy. 1 Dependence of C_s on the vehicle speed and mass base NHTSA

chapters. Here, as in the case of a compact vehicle class diagram of the calculation are presented, leading to the determination of EES and vehicle speed for determining the error.

$$A = \frac{m \cdot b_{sg} \cdot b_k}{L_t} \tag{1}$$

$$B = \frac{m \cdot b_k^2}{L_t} \tag{2}$$

$$G = \frac{A^2}{2 \cdot B} \tag{3}$$

where:

m	vehicle weight,
b_{sg} = 3.05 (m / s)	Flexible speed collision,
b_k	a constant slope, 27 m / s / m,
L_t	Breadth of deformation (m).

Strain describes the parameters in the following form on:

$$C_s = \frac{\frac{C_1}{2} + C_2 + C_3 + C_4 + C_5 + \frac{C_6}{2}}{5} \tag{4}$$

Then, work deformation calculated:

$$W_{def} = \frac{L_t}{5} \cdot \left(\frac{A \cdot \alpha}{2} + \frac{B \cdot \beta}{2} + 5 \cdot G \right) \tag{5}$$

and then the speed EES looking determined:

$$EES = \sqrt{\frac{2 \cdot W_{def}}{m}} \tag{6}$$

The error in this estimation speed, calculated as a relative error, obtained from the formula:

$$Error = (EES - V_r)/V_r \tag{7}$$

where the speed V_t is the actual value of speed crash tests for the case. The following was obtained for the linear model: determination failure EES 0.09 ± 0.12 for asymmetry = 0.53 and = 0.42 kurtosis.

The histogram shows the distribution of error (the Kolmogorov-Smirnov test) distribution is a normal distribution (Fig. 2).

The distribution is flattened, the asymmetry on the right side, in most cases is below average. This study shows a linear dependence on the EES C_s ratio is unsatisfactory from the point of view of practical applications, resulting in an error of 12%, assuming a normal distribution. That is, assuming that an averaged value of b_k = 26 m / s / m for transport class Subcompact prevents the use of the above calculations for determining the velocity of a vehicle collision based on the geometry of the indentation of the body [2, 14].

Another argument against the linear method is the strong dependence of the error on the C_s and L_t coefficients (Fig. 3).

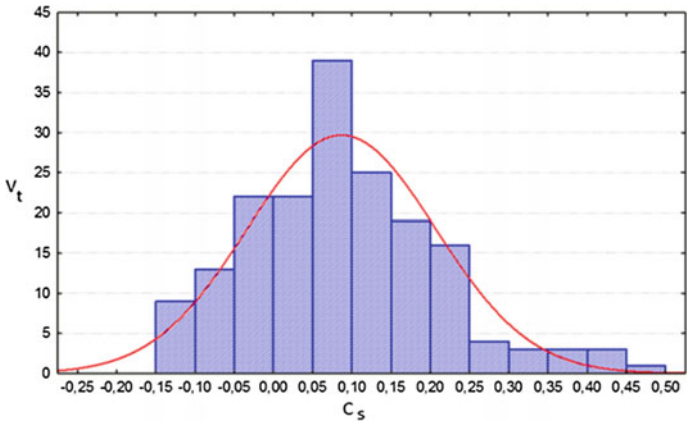

Pussy. 2 Histogram of error in the linear model V_t (C_s relationship)

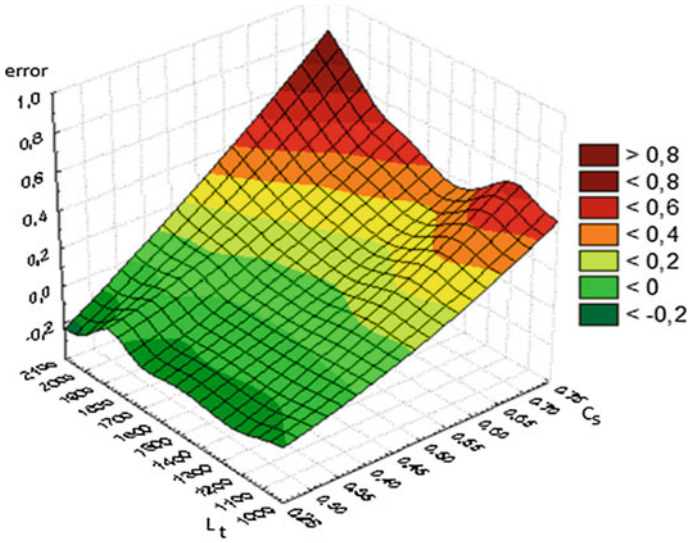

Pussy. 3 A strong dependence of error of determining the speed of the vehicle on the C_s and L_t coefficients-linear model

However, this method can not be used for actual measurements, where speed is not known. This procedure is only possible in case of crash tests where the EES is known before the collision and its measurement model is the subject of control of the correctness of calculations. The chart below shows the relationship determination failure EES error determined from the formula containing the speed factor b_k -The slope of the curve is shown in Fig. 4.

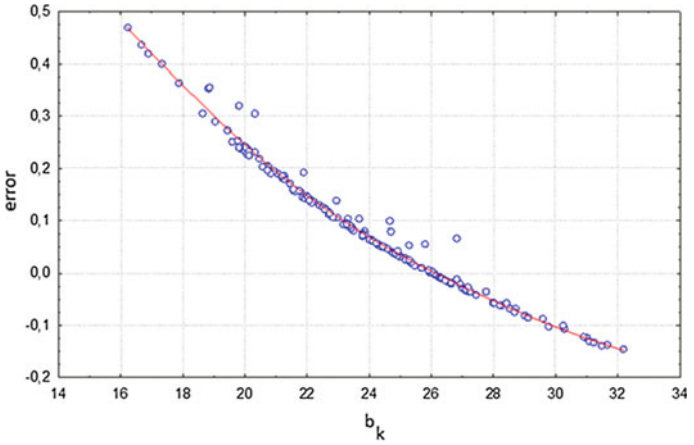

Pussy. 4 The dependence of error of determining the speed EES Linear Model b_k values for the zoom speed containing EES [4]

3 The Proposed Method Velocity Determination in the Course of Collision

This chapter presents a method developed by the authors, which is associated with the mining of the relationship b_k the slope of the curve at C_s parameter deformation of the experimental data. In the present case, that is, Subcompact cars class, this relationship shows the two teams that are averaged by the approximation of the experimental data with second-degree polynomial. the result approximation studied the same data set. The resulting compound was plotted as a non-linear speed value as a function of the average EES deformation parameter C_s. Application results will

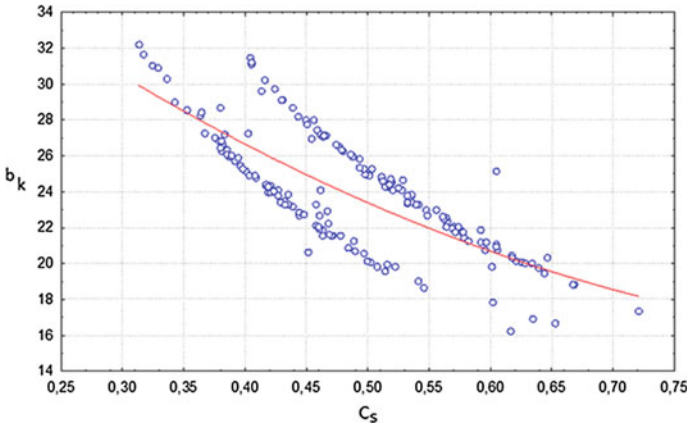

Pussy. 5 Close relations of the slope b_k compared to the average deformation parameter C_s with second-degree polynomial

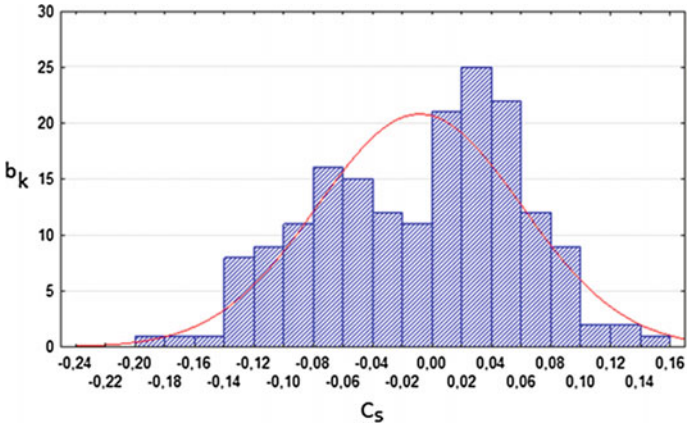

Pussy. 6 Histogram of error distribution EES on the approximation of the average relationship coefficient b_k versus the average strain C_s with second-degree polynomial

be possible in the case of refilling the database of the new cases, the results of crash tests NHTSA [4 , 6 , 11] (Fig. 5).

Thus defined, the coefficient b_k (a downward slope with an increase in C_s - nonlinear relationship), the other factors, namely, the work of deformation, velocity EES and the determination of the relative error were calculated.

For non-linear model, the following was obtained:

Error determine the EES: 0.008 ± 0.69
where = -0.25 skewness, kurtosis = -0.67.

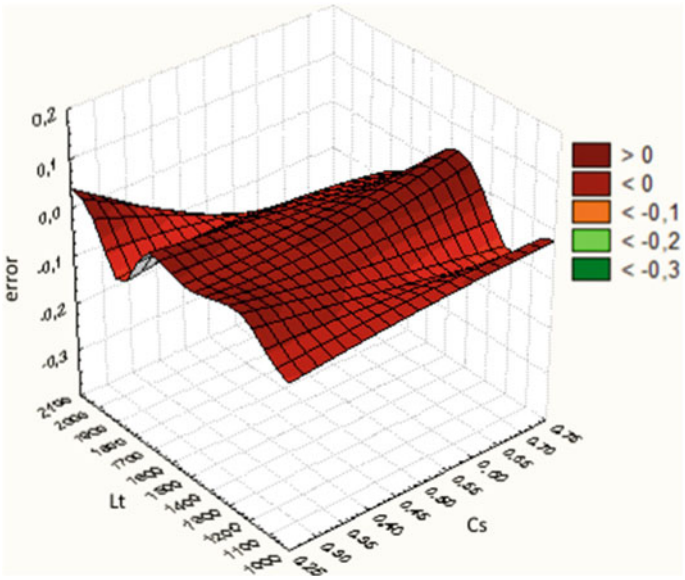

Pussy. 7 The dependence of the error detecting speed of the vehicle to C_s and $L_t$coefficients

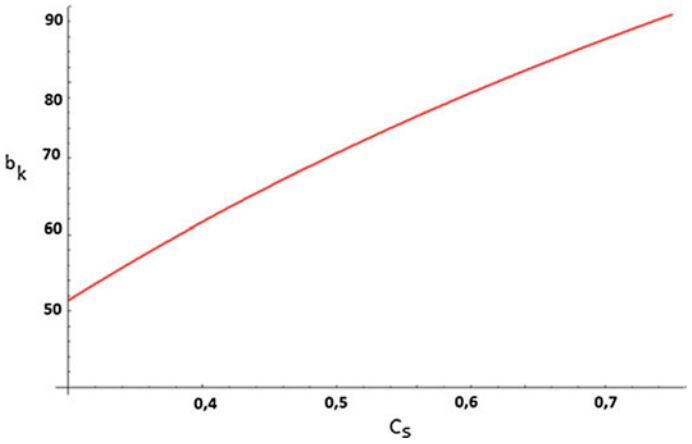

Pussy. 8 The speed relationship of the vehicle to C_s distortion factor

Histogram of the error of the approximate polynomial is shown in Fig. 6.

In this case, the distribution is not normal. It has a slender shape, and asymmetry of the right side, and the majority of the cases below the average.

The estimated dependence b_k coefficient on average C_s deformation values, a new model was created non-linear. It is characterized by not only a very small estimation error EES about 6.9%, but also reduced the dependence of error on the activity of C_s and L_t values as shown in Fig. 7. In this model, the non-linear

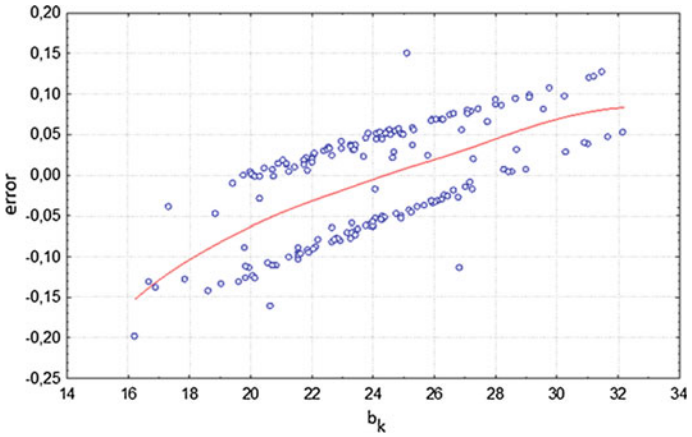

Pussy. 9 The dependence of the error in determining the speed of EES non-linear model with respect to b_k factor

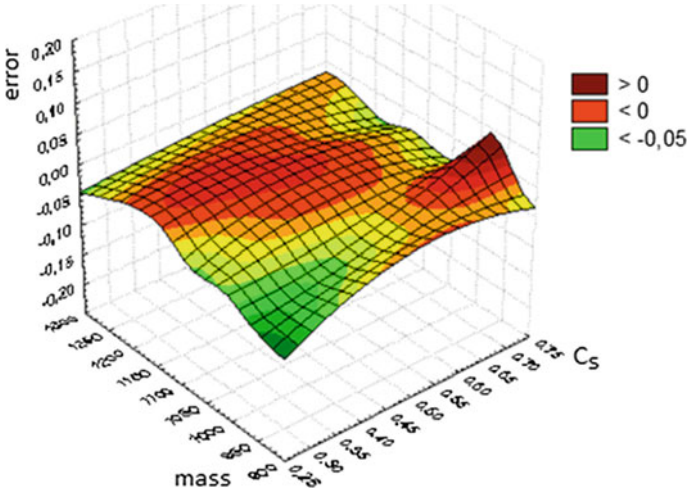

Pussy. 10 The dependence of the error for determining the speed of the vehicle to the weight coefficients C_s and non-linear model

dependency on the velocity of the EES C_s ratio will be presented in the selected range (0.3-0.75) (Fig. 8, 9 and 10); [17, 18].

These charts show weak relationship EES speed error obtained in the nonlinear model to C_s ratio and vehicle weight. It should be noted dependence on the error in the C_s and L_t parameters, in particular the design of new additions to the database [4].

4 Verification of the Assumption Collision Velocity Determination

This publication shows the dependence of the slope b_k parameter width of the deformation of the body, L_t. This relationship for a compact class car was visible in the form of three bands in the graph showing the relationship between b_k and an average C_s factor.

For class cars Subcompact into account two teams are observed in Fig. 5. Now, Subcompact car class, the effect of L_t parameter in determining the non-linear relationship b_k coefficient on average deformation of the body C_s has been fully taken into account.

In this new model description, the improved accuracy of determining the speed of the EES, as well as to further reduce the dependence of the error term for L_t, C_s performance and vehicle mass m have been achieved (see Fig. 11).

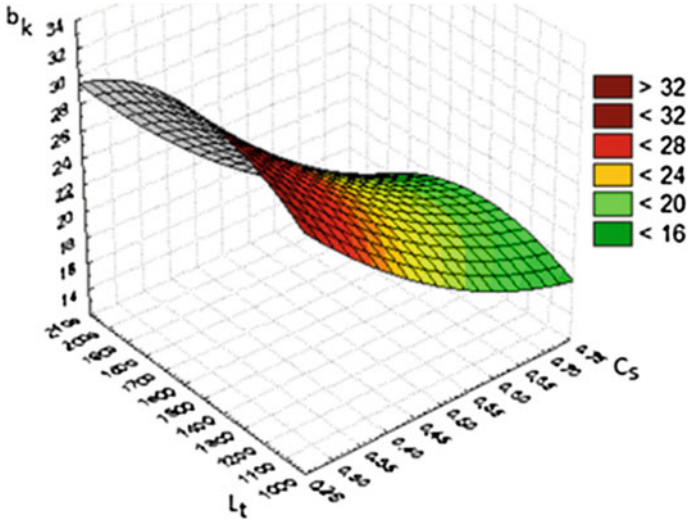

Pussy. 11 Dependence b_k coefficient on the C_s and L_t coefficients at the same time. Approximation with the plane of the second degree

EES determine the speed error: 0.007 ± 0.065, = -0.07 skewness, kurtosis = -0.82.

Error distribution histogram (Fig. 12):

Within the defined model, a reduced dependence on the error in the vehicle speed EES parameters L_t, C_s, and C_s at a weight (mass) is obtained (Fig. 13).

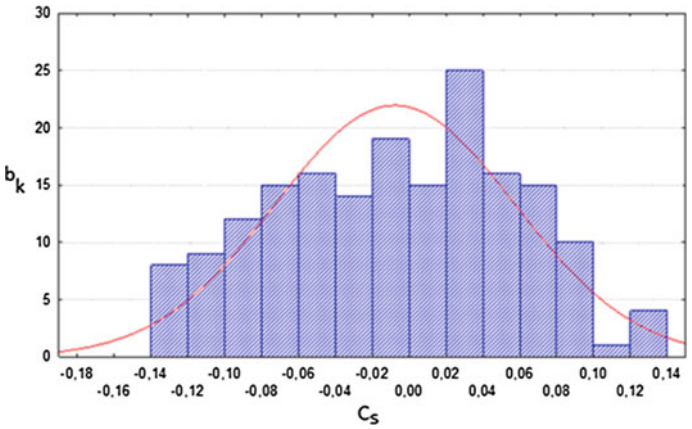

Pussy. 12 Histogram of the error for determining the EES on the approximation of the relationship b_k coefficient relative to the average strain C_s and a width L_t of the plane of the second stage

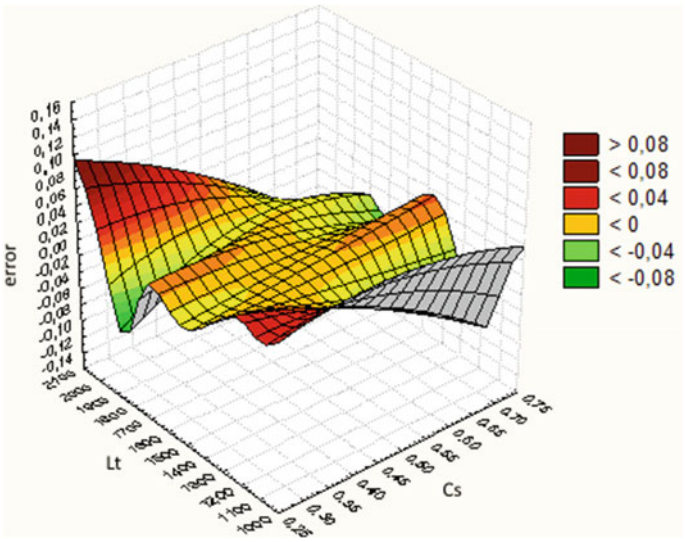

Pussy. 13 Weak dependence of error of determining the speed of the vehicle on the coefficients $C_s$and L_t methods -The closer to the plane of the second degree

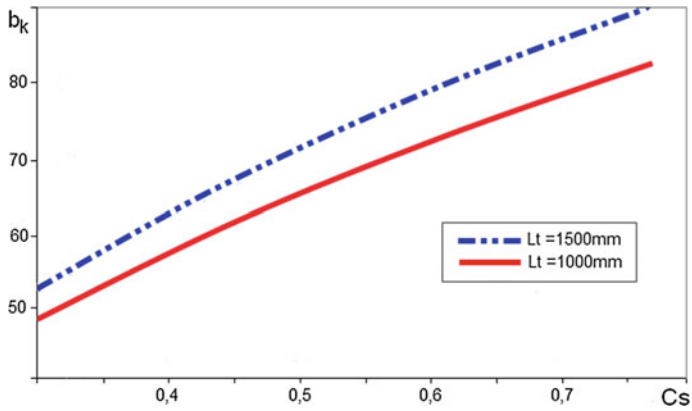

Pussy. 14 The dependence of the vehicle speed EES vs. deformation coefficient C_s -The model b_k slope closer to the plane of the second degree. *The red* line L_t = 1000 mm, and the *blue* line L_t = 1500 mm (Figure color online)

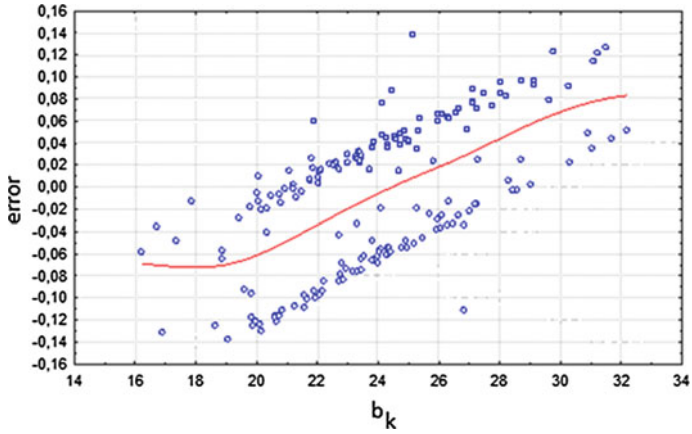

Pussy. 15 The dependence of error of determining the speed of the EES in the approximation model of the aircraft in relation to b_k ratio defined by the formula containing EES

Assuming the a b_k magnification, closer to the plane of the second stage defined by the equation given in Fig. 11, the dependence of the speed of the vehicle in relation to C_s coefficient is plotted for the two L_t coefficient values before 1000 and 1500 mm, respectively, which is shown in Fig. 14. This shows that the non-linear nature of the relationship between vehicle speed and the distortion factor C_s increases with the width of the deformation (L_t). at the same time, the increase in L_t finds higher speeds EES obtained for the same value of C_s. It should also be noted that in the case of an L_t values for the vehicle in question is a class Subcompact (1132 mm, 1991 mm) (Fig. 15).

5 Conclusions and Future Work

The authors constructed a model of non-linear body and respond deformation during impact. This model is based on non-linear speed collision on the distortion factor C_s and L for $_t$, observed on the basis of NHTSA. This model provides a significant improvement in the rate of accuracy of determination by ± 6% of poor the dependence of the estimation error of the speed at the C_s, L_t parameters and weight. The relationship between the $b_{k\ angle}$ anglefactor and the deformation coefficients C_s and L_t assumed in the model obtained by approximating to the plane of the second stage. The process described for the first time takes into account the units shown in Fig. 4 as a result of the hidden relationship b_k factor to L_t of the parameter.

The objective set by the artists was achieved. Further research will be directed to the further stages of the verification of the results obtained in the calculation speed disrupted for more new cases Subcompact cars NHTSA database, and for other classes of vehicles. The authors plan to build statistical tools that enable even more accurate determination of the speed of the EES mainly by analyzing the function of the profile deformation, which will bring more accurate results than achieved with the currently used model for the measurement of strain at 6 checkpoints.

Confirmation This work was supported by MNISW / 2014 / DIR / 374 GP II.

Reference

1. Prochowski L, Unarski J Wach W, J Wicher (2008) Fundamentals of accident reconstruction Road. WKiŁ, Warsaw
2. Day TD, Hargens RL (2014) Discusses how to ED-CRASH computers delta-V. SAE Technical Paper Series, 870069
3. Cromack JR Lee SN (1974) study of cohesion rate of deformation of the vehicle. SAE 740299
4. Kubiak P Wozniak M, Karpushkin V Jozwiak P Ozun G Madziara S, Najbert M, Szosland A (2015) The method for determining the speed by measuring the deformation of the vehicle body in the plane approximation. In: Proceedings of the World Congress on Engineering 2015 2015 pp WCE 1097-1101. London, UK, 1-3 July 2015
5. Crash3 assembly (1986) Accident Investigation Division NCSA, NHTSA
6. Kubiak P Wozniak M Jablonski R Ozun G, de la Fuente P (2014) Determination of deformation energy using NHTSA rigidity factor 4 (4): 188-193. IJEIT ISSN: 2277-3754
7. Chen S, Mulgrew B Grant PM (1993) Technique cluster for digital communications channel equalization using a radial basis function network. IEEE Trans Neural Netw 4: 570-578
8. Duncombe Jagiellonian University (1959) Infrared navigation, Part I: feasibility study. IEEE Trans Electron Devices 11: 34-39
9. The increase in Ph V, Fugger Th F Jr, Marcosky J (1992) Truck scales damage and the impact on the injury analysis. SAE 920602
10. Kubiak P Szosland A Awrejcewicz J Zagrodny B (2013) Estimation of injury to the driver and passenger in the car accident on the basis of the method of accident reconstruction. In: 12th Conference on the theory of dynamical systems and applications, Lodz, pp 259-270
11. Nelson WD (1981) History and evolution of classification deformation collision. SAE J224

12. Lin CY, Wu M, Bloom JA Cox IJ M Miller (2001), rotation, scaling, watermarks and translations resilient public image. IEEE Trans Process Image 10: 767-782
13. Campbell KL (1974) Basis of energy intensity of the collision. SAE 740565
14. Siddall DE, Day TD (1996) Update categories Lass vehicle. SAE 960897
15. Mc Henry R (1997) Effects of restitution in the application of the coefficient of crushing. SAE 970960
16. Kończykowski W (1993) playback and analysis of the course of the accident Road, SRTSiD Paris-Warsaw
17. McHenry RR (1973) computer program for reconstruction of highway accidents. SAE 730980
18. Kubiak P, M Wozniak, Ozun G (2014) Determination of the energy required to deform the cars body by applying the NHTSA machine rigidity materials technologies 1 (8): 38-40. ISSN 1313-0226

Novel Composite Inorganic Ceramic Membranes for Gas Separations and Environmental Applications

Shehu Habiba, Okon Edidiong and Edward Gobina

Abstract Composite ceramic inorganic membranes have been prepared using different types of support with the aim to achieving high selectivity for lower hydrocarbons. Upon modification of the support, the morphology was examined using Scanning Electron Microscopy (SEM), which showed a reduction in the pore radius and pore size distribution. Energy Dispersive X-ray Diffraction (EDAX) was used to determine the elemental composition of the membrane. Gas permeation tests were carried out with inorganic ceramic membrane consisting of a ceramic support and a zeolite layer. The permeance of nitrogen, carbon dioxide, helium, methane, propane and argon through the membrane at varying pressures was determined. The effect of the mean pressure of up to 0.1 MPa on the molar flux of the gases at 294 K was determined.

Keywords Characterization · Composite membranes · Knudsen flow · Permeability · Permeance · Selectivity

Nomenclatures

Symbols

E_{diff} Activation energy (J mol^{-1})
E_e Activation energy for activated gas translational diffusion (J mol^{-1})
D_∞ Arrhenius-type pre-exponential factor (m^2 s^{-1})
$\bar{P}$ Average pressure drop across the membrane (Pa)
B Constant representing Knudsen flow

S. Habiba · O. Edidiong · E. Gobina (✉)
School of Engineering, Centre for Process Integration and Membrane Technology (CPIMT), The Robert Gordon University Aberdeen, Aberdeen AB10 7GJ, UK
e-mail: e.gobina@rgu.ac.uk

S. Habiba
e-mail: h.shehu@rgu.ac.uk

O. Edidiong
e-mail: e.p.okon@rgu.ac.uk

S.-I. Ao et al. (eds.), *Transactions on Engineering Technologies*,
DOI 10.1007/978-981-10-1088-0_5

A Constant representing viscous flow
D Diffusivity ($m^2\ s^{-1}$)
D_g Diffusion coefficient
Ds Fick's diffusivity constant
N Flux (mol $s^{-1}\ m^{-2}$)
M Gas molecular mass (g mol^{-1})
N_g Gas translational diffusion
K Knudsen number
S Membrane area (m^2)
R Molar gas constant (8.314 J $mol^{-1}\ K^{-1}$)
Q Molar gas flow rate (mol s^{-1})
J Permeability (mol m $m^{-2}\ s^{-1}\ Pa^{-1}$)
ΔP Pressure drop across the membrane (Pa)
d_p Pore diameter (m)
N_s Surface flux
D_o The intrinsic or corrected diffusivity
T Temperature (K)

Greek Symbols

Å Angstrom
μ_m Average velocity (m s^{-1})
$\boldsymbol{\lambda}$ Mean free path of gas molecule (m)
r_p Membrane Pore radius (m)
Γ Thermodynamic correction factor

1 Introduction

Gaseous hydrocarbons that are prevalent under increased pressure are solution gases in oil reservoirs. At equilibrium, they are in solution with the liquid hydrocarbon phase. These hydrocarbon gases are usually conserved but in some cases their storage is considered uneconomical and the gases are flared which is not an ideal practice. The impact of gas flaring cannot be over emphasized, it can cause detrimental effects to the environment [1], and these effects are highlighted below:

Emissions of methane and carbon dioxide: The main gases responsible for global warming are carbon dioxide and methane with methane being about 35 times more potent than carbon dioxide. The reduction of the volume of gases wasted by flaring without compromising oil production can be achieved by exploiting gas conservation opportunities [2].

Nitrous oxide emissions in the presence of volatile organic compounds: The emissions of nitrous oxides in the presence of volatile organic compounds can lead to the formation of ground level ozone which can have a toxic effect to the vegetation and humans as well. Nitrogen oxide is a major contributor to acid rain as well.

Sulfur dioxide and hydrogen sulphide emissions: Hydrogen sulfide is a corrosive toxic gas that can be oxidized rapidly to sulfur dioxide, which is a contributor to acid rain. Many efforts have been made in the last couple of years to develop an effective method for the separation and subsequent removal of impurities from natural gas.

There are ongoing researches on the use of nano-composite ceramic membranes to separate gaseous mixtures hence making it one of the emerging technologies that is growing fast. Their use has grown considerably both academically as well as industrially and they can be used for several applications. They are generally more expensive to fabricate than polymeric membranes but they can withstand more rigorous separation conditions that include high temperatures or corrosive solvents [3]. Ceramic membranes do not only have higher thermal and chemical stability but also have higher permeability as well [4]. There are several types of support used for these membranes. These include zeolites, silica, alumina and stainless steel [5]. The various use of ceramic membranes include hydrogen separation and purification to get ultra-pure hydrogen, recovery of CO_2 from natural gas and power station flue gases and oxygen or nitrogen enrichment of air [6, 7].

Ceramic membranes that are available commercially generally have a pore size of 5 nm or bigger [8]. With the modification of these ceramic membranes the pore size may be reduced to near molecular dimensions, enabling separation of components based on the differences in molecular sizes or in the shape of the components [9]. There are various methods that can be used for the modification including deposition that aims at the formation of porous or non-porous layer on the surface. Further processing by means such as annealing, carbonization or plasma treatment can follow the modification for further optimization. Examples of deposition techniques include: chemical vapor deposition (CVD), sol-gel deposition, Langmuir-Blodgett (LB) deposition, spin coating and self-assembly [3].

Gas permeation by Knudsen diffusion varies inversely with the square root of the molecular weights of the gases. Hence an ideal separation for a mixture of binary gases is equal to the inverse of the square root of their molecular mass ratio [10]. The transportation equation that comprises of Knudsen and viscous flow is given by:

$$J = A\bar{P} + B \tag{1}$$

According to Eq. (1), A is the constant representing viscous flow while B is the constant representing non-viscous flow, $\bar{P}$ is the average pressure across a membrane and J is the permeability of the membrane and it is calculated using the equation:

$$J = \frac{Q}{S} . \bar{P} \tag{2}$$

where Q is the flow rate in mol s^{-1} and S is the membrane area in m^2. The pore radius of the membrane can be determined using the formula [11]:

$$r_p = \frac{16 . A . \mu}{3 . B} \sqrt{8RT/\pi M} \tag{3}$$

where M is the molar mass of the gas (g mol^{-1}), R is the molar gas constant (8.314 mol^{-1} J K^{-1}), T is the temperature in (K) and μ is the viscosity (Pa s^{-1}) of the gas.

The Knudsen number is given by:

$$K = d_p/\lambda \tag{4}$$

where d_p is the pore diameter (m) and λ is the mean free path of the molecules (m). The Knudsen number determines the flow regime of the membrane. When the diameter of the pores is lower than the mean free path of the molecules then Knudsen flow is dominant [11]. The assumption made using this model is that there is negligible pressure drop due to the relatively small length of the capillaries [12].

Gas transport through α-Al_2O_3 support can involve both Knudsen and viscous flow when the interaction between the gas and the pore walls of a porous membrane is negligible [13]. A plot of gas permeability against the mean pressure drop is depicted in Fig. 1; this is for a membrane that is free of defects.

According to Fig. 1, the intercept B at the axis ordinate represents the contribution of Knudsen flow and in membrane 1 gas transport takes place in a region of Knudsen flow and thus for a defect free membrane, the gas permeability remains unchanged with increase in trans membrane mean pressure. The contribution due to viscous flow is represented by membrane 2 while membrane 3 is a representation of both Knudsen and viscous transport mechanism [13].

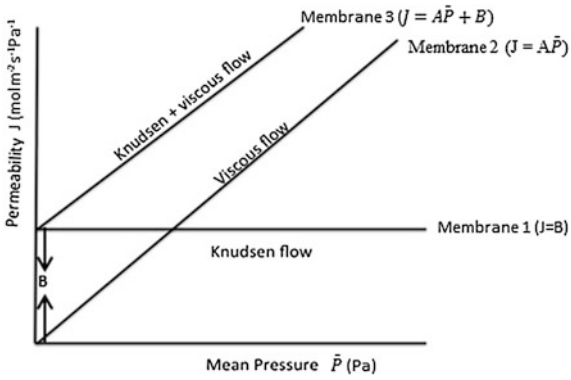

Fig. 1 The contributions of Knudsen diffusion and viscous flow [13]

For a commercial ceramic membrane, at elevated temperatures and low pressures the most likely transport mechanism employed is the Knudsen flow. Molecular sieving does not take place since the pore sizes are larger than the gas molecules [14]. The transport of gases through only Knudsen diffusion has been found to be inhibitive on the selectivity of a separating system. To overcome this difficulty, various efforts to promote other modes of transport have been made by surface modification [6]. The choice of membrane material greatly affects the permeation flux and selectivity of different gases as they move through the membrane [15]. In this research work the morphology of the silica and zeolite membrane was determined using the Scanning Electron Microscope (SEM).

The process of mass transport through a membrane varies for different membrane materials. For a zeolite layer gas transport is as a result of the following five steps [16, 17].

- Adsorption of the substance on the outer surface of the membrane
- Mass transport from the outer surface into the zeolite pore
- Diffusion through intra-crystalline zeolite
- Mass transport out of the zeolite pores to the external surface
- Desorption from the outer surface to the bulk.

Adsorption and desorption of the species from the outer surface of the zeolite layer depends on the permeation conditions (temperature and pressure), type of crystalline material and the nature of the chemical specie. Steps 2, 3 and 4 are usually activated processes [18].

Intra crystalline permeation through a zeolite membrane can be described using various approaches [19]. The Fickian approach uses the concentration gradient as the driving force in a membrane while for the Maxwell-Stefan (MS) approach the driving force is the gradient of the thermodynamic potential. The MS approach allows for the approximation of the flux through the membrane for multicomponent gas mixtures by using the information from single gas permeations [20]. For the permeation of single gas components through a zeolite membrane in a wide range of temperatures, the Fickian approach can be followed and the assumption that the total flux N is the combination of the surface flux N_s which takes place at low to medium temperatures and the activated gaseous flux N_g which is prevalent at high temperatures [16, 17, 21, 22].

$$N = N_s + N_g \tag{5}$$

2 Experimental

A schematic diagram of the membrane flow apparatus used for the permeation test for the gases is presented in Fig. 2. Four different gases: carbon dioxide, helium, nitrogen and argon were used for the permeability through a porous ceramic membrane at various trans-membrane pressures [22].

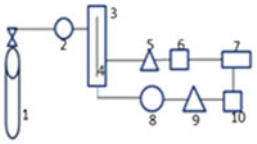

1 Gas feed
2 Pressure guage
3 membrane reactor
4 membrane
5 flow meter
6 Retentate
7 Gas chromatograph
8 Pressure guage
9. Flow meter
10 Permeate

Fig. 2 Schematic diagram of a membrane permeation flow system

2.1 Preparation of the Silica Membrane

The dip coating method (Fig. 2) was used to modify the membrane. In this method, the support layer which comprises of a porous alumina which is dipped into a solution consisting of Silicone elastomer, curing agent and isopentane in the ratio 10:1:100 respectively. The mixture was first homogenized with magnetic stirring for 2 h before the support is dipped for 1 h with constant stirring to prevent the mixture from gelling. The membrane was air dried for 30 min and thermally treated at 333 K for 2 h prior to permeation test. The dip-coating set up is shown in Fig. 3 and the composition of the solution used for membrane modification is given in Table 1 [22].

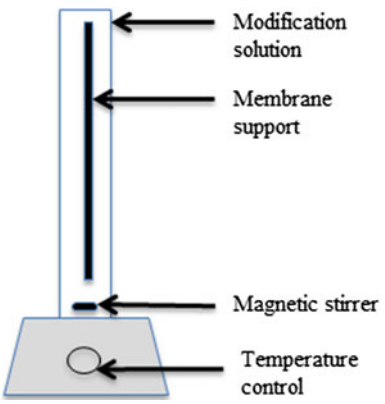

Fig. 3 Membrane modification using the dip-coating process

Table 1 Composition of the dip-coating modification solution

Silicone elastomer	50 ml
Curing agent	5 ml
Isopentane	500 ml

Table 2 Composition of the modification solution for zeolite membrane

Chemical	Amount (ml)
Aluminium oxide	10
Sodium hydroxide	14
Deionised water	798
Silicone oxide	1

2.2 Preparation of the Zeolite Membrane

For the zeolite membrane preparation, a solution containing silicone oxide, aluminium oxide, sodium oxide and deionized water was prepared and homogenized at room temperature for 20 h. The amount of each substance used is given in Table 2. Zeolite crystals were deposited on alumina support that is subsequently dipped into the solution and kept for 20 h at 343 K using a similar system as described in Fig. 3. The membrane was washed with deionized water and the pH of the rinse water was monitored. When the rinse water pH was neutral the membrane was air dried for 20 min and thermally treated in the oven at 338 K for 2 h prior to permeation test [22].

2.3 Membrane Characterization

The morphology of the membrane was determined by the use of the scanning electron Microscope (SEM) and the elemental composition of the membrane was confirmed using Energy Dispersive X-Ray Analysis (EDAX).

3 Results and Discussion

3.1 Gas Permeation of Silica Membrane

The gas flow rate through the silica membrane was used to calculate the permeance using Eq. (2) and the plot of permeance against the pressure drop is shown in Fig. 4.

It is observed that the permeance decreased with increase in feed pressure, CO_2 has the lowest permeance but the highest molecular weight and He has the lowest molecular weight but highest permeance, hence this follows an inverse relationship between molecular weight and permeance which follows the flow mechanism of Knudsen flow [16]. At pressures higher than 0.1 bar the plot indicate a flow that is consistent with Knudsen flow for a membrane that is free from defects as shown in Fig. 1. The order of molecular weights is $CO_2 > Ar > N_2 > He$. Nitrogen and argon have close permeance as can be observed in Fig. 4 but their molecular weights are not close. This could imply that a different flow mechanism was responsible for the transport of these gases across the membrane.

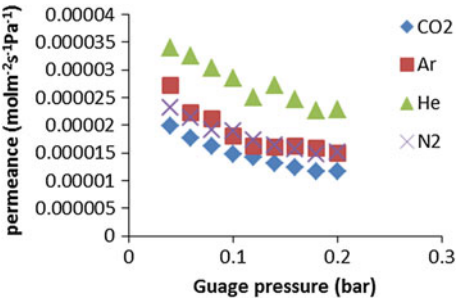

Fig. 4 Effect of pressure on gas permeance of silica membrane at 298 K

From Eqs. (1) and (3), the pore radius of the membrane was calculated.

The slope (A) of the graph is the viscous contribution, while the intercept (B) is the contribution due Knudsen flow. From Fig. 5, the pore radius and the mean free path of the molecules was calculated and represented in Table 3.

Theoretically the pore radius of the membrane is supposed to be the same and independent of the type of gas. However, as can be seen in Table 3, there is variation with He giving the highest value and CO_2 giving the lowest. Hence the membrane will have a distribution of pore sizes and different gases will flow through these pores at different rates depending on the resistance to flow. From Table 3, it can be seen that the calculated pore radius is much lower than the mean free path, which implies that the dominant flow of the gases is Knudsen flow.

In Table 4, the Knudsen selectivity was calculated using the square root ratios of the molecular weights of the gases. These are presented in Fig. 5 and compared with the pure gas selectivity values based on the permeability ratio.

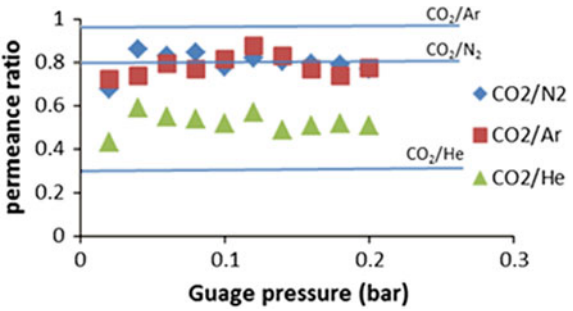

Fig. 5 Permselectivity with CO_2 at room temperature

Table 3 Pore radius of the membrane and mean free path of the gases

	rp(m)	λ(m)
Ar	0.037×10^{-10}	1.48×10^{-4}
He	0.312×10^{-10}	6.24×10^{-4}
N_2	0.044×10^{-10}	2.93×10^{-4}
CO_2	0.029×10^{-10}	1.99×10^{-4}

Table 4 Knudsen selectivity calculated using the molecular weights of the gases

Gases	Knudsen selectivity
CO_2/N_2	0.799
CO_2/Ar	0.952
CO_2/He	0.302

The Knudsen selectivity calculated has higher values for CO_2/Ar at all the pressures investigated than the experimental Knudsen selectivity calculated using the ratio of the gas permeability. This could indicate another flow mechanism should be employed for the separation of these gases. For CO_2/He, the Knudsen selectivity calculated is lower than the experimental value that could indicate a good separation of helium if this performance were to be replicated in a mixed gas stream.

A plot of the permeance against the inverse of the square root of the molecular weights of the gases is given in Fig. 6.

The graph is not linear as expected for Knudsen flow mechanism.

To further explain the flow mechanism that the membrane exhibited, Fig. 7 is a plot of gas permeance against the kinetic diameter of the gas molecules to see if the mechanism could be molecular sieving. According to Pandey and Chauhan [10] the smaller molecules will permeate while the larger molecules will be retained.

The order of the kinetic diameter of the gases starting from the largest is $N_2 > Ar > CO_2 > He$. It can be seen that nitrogen having the highest kinetic diameter is permeating at a rate that is higher than argon and carbon dioxide which both have lower kinetic diameters. Figure 7 proves that the membrane did not exhibit molecular sieving flow mechanism.

Nitrogen and argon have similar permeance although they possess different molecular weights. This could indicate there is a different flow mechanism that is responsible for the flow of these gases. The flux of nitrogen was determined and showed an increase in flux with the increase in temperature.

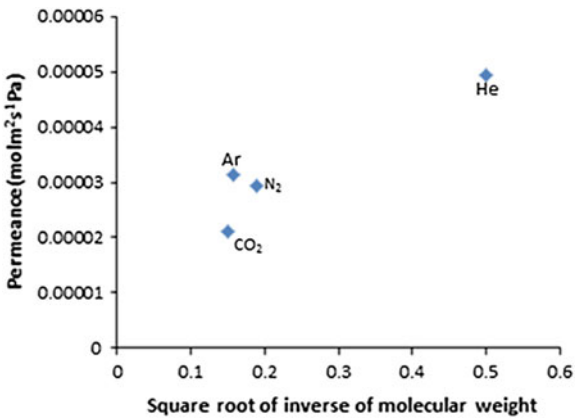

Fig. 6 Permeance against inverse of the square root of the molecular weights of the gases

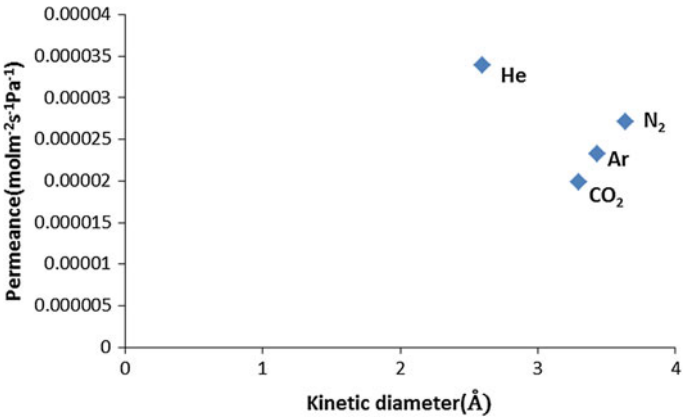

Fig. 7 Permeance at 298 K and 2 kPa against kinetic diameter

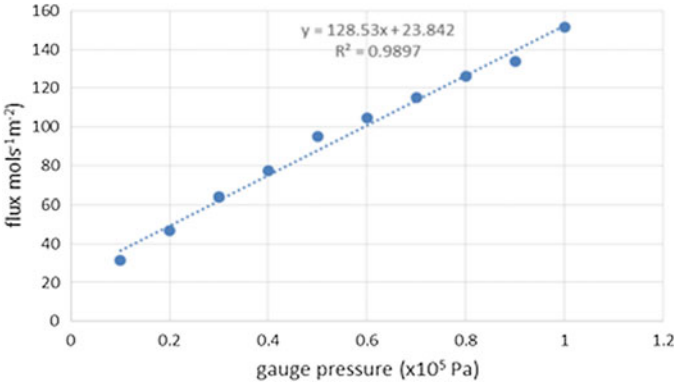

Fig. 8 Effect of gauge pressure on the flux of nitrogen at 298 K using silica layer

The flux of nitrogen as depicted in Fig. 8 increases linearly with increase in pressure, and it has a good correlation coefficient of 0.9897. The other gases (carbon dioxide, argon and helium) also had high fluxes at higher pressures.

3.2 Gas Permeation of Y-Type Zeolite Membrane

The flux of propane, nitrogen and methane was determined through the zeolite layer. Figure 9 depicts the flux of nitrogen and Fig. 10 shows the permeances of propane, nitrogen and methane against the gauge pressure.

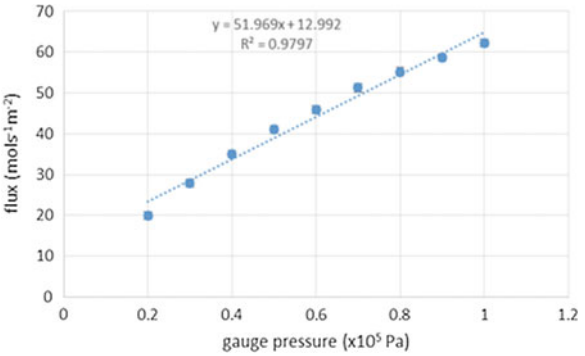

Fig. 9 Effect of gauge pressure on the flux of nitrogen at 298 K using zeolite layer

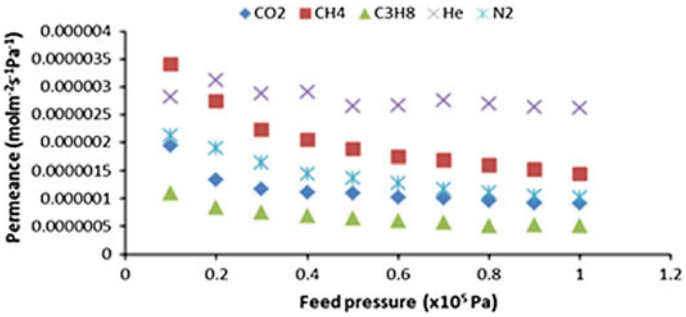

Fig. 10 Effect of pressure on gas permeance of zeolite membrane at 298 K

Compared to the plot in Fig. 4, the values fit more closely to membrane 1 where the permeance J = B as described in Fig. 1.

3.3 Membrane Characterization

The SEM images were collected in order to have an insight on the morphology of the selective layer. The cross section of the α–Al_2O_3 ceramic membrane support is shown in Fig. 11 and the surface of the synthesized membranes is shown Fig. 12a for the silica and Fig. 12b for the zeolite membrane.

The thickness of the membrane can be estimated as 6 ± 0.2 µm.

The images in Fig. 12 show the pore structure of the silica that is deposited on the aluminium support. Both the silica and zeolite are deposited on the support unevenly which could suggest that the pore size distribution could be unequal at different points of the membrane

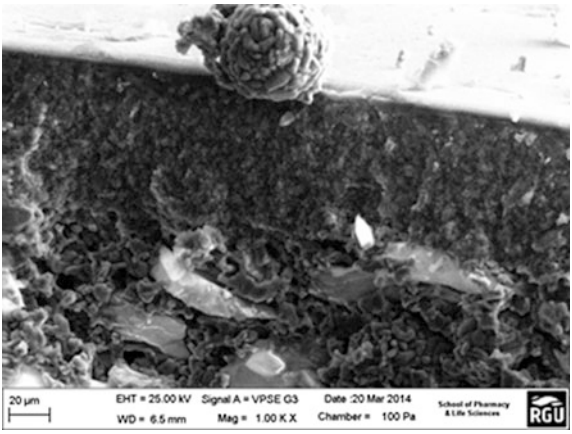

Fig. 11 Cross section image of α–Al_2O_3 membrane support

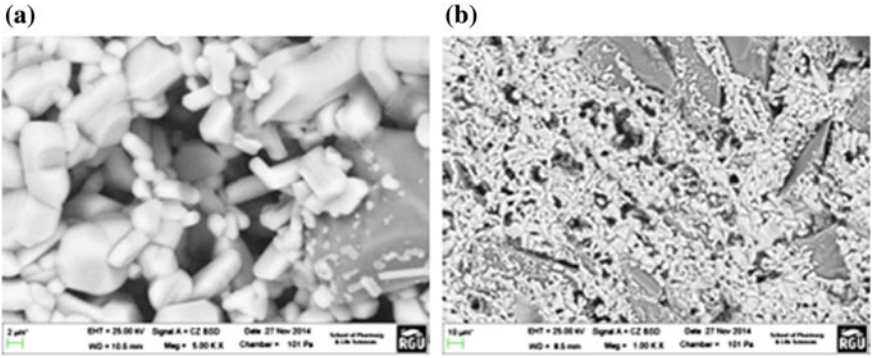

Fig. 12 The outer surface of silica (**a**) and zeolite (**b**) membrane

4 Conclusion

An investigation on gas separations efficiency of inorganic membranes has been carried out. The support was modified and the flow mechanism of the membrane was investigated. On the basis of the results obtained it can be concluded that the main mechanism governing the flow of gases through the modified silica membrane was Knudsen flow although there is evidence that another flow mechanism come to play. Further work will be carried out to determine how to modify a membrane support to achieve a specific flow mechanism. Studies from literature and preliminary experimental work have shown that for the separation of lower hydrocarbons, zeolite membranes have more efficacy than the silica or alumina ones. From the

SEM images observed there is a need to modify the deposition of pore modifying agents on a membrane support to achieve a defect free membrane with an even pore size distribution over the entire effective length of the membrane

Acknowledgements The conference was sponsored by IDEAS Research Institute, The Robert Gordon University Aberdeen, United Kingdom. The Authors of this paper acknowledge the center for Process Integration and Membrane Technology at RGU for providing the research infrastructure and the School of Pharmacy Life Science for the SEM/EDAX analysis.

References

1. Abedini R, Nezhadmoghadam A (2010) Application of membrane in gas separation processes: its suitability and mechanisms. Pet Coal 52(2):69–80
2. Tarmoon I (1999) Middle east oil show, 20–23 February
3. Schüth F, Sing KSW, Weitkamp J (2002) Handbook of porous solids. Wiley-Vch, Weinheim
4. Huang P, Xu N, Shi J, Lin Y (1997) Recovery of volatile organic solvent compounds from air by ceramic membranes. Ind Eng Chem Res 36(9):3815–3820
5. Li H, Schygulla U, Hoffmann J, Niehoff P, Haas-Santo K, Dittmeyer R (2013) Experimental and modeling study of gas transport through composite ceramic membranes. Chem Eng Sci 111:20
6. Baker RW (2000) Membrane technology. Wiley Online Library, New York
7. Powell CE, Qiao GG (2006) Polymeric CO_2N_2 gas separation membranes for the capture of carbon dioxide from power plant flue gases. J Membr Sci 279(1):1–49
8. Singh RP, Way JD, McCarley KC (2004) Development of a model surface flow membrane by modification of porous vycor glass with a fluorosilane. Ind Eng Chem Res 43(12):3033–3040
9. Van de Graaf JM, Kapteijn F, Moulijn JA (1999) Modeling permeation of binary mixtures through zeolite membranes. AIChE J 45(3):497–511
10. Pandey P, Chauhan R (2001) Membranes for gas separation. Prog Polym Sci 26(6):853–893
11. Julian A, Juste E, Chartier T, Del Gallo P, Richet N (2007) Catalytic membrane reactor: multilayer membranes elaboration. Catalytic membrane reactor: multilayer membranes elaboration. In: Proceedings of the 10th international conference of the european ceramic society, p 718–722
12. Gobina EN, Oklany JS, Hughes R (1995) Elimination of ammonia from coal gasification streams by using a catalytic membrane reactor. Ind Eng Chem Res 34(11):3777–3783
13. Li A, Zhao H, Gu J, Xiong G (1997) Preparation of γ-$A1_2O_3$ composite membrane and examination of membrane defects. Sci China B Chem 40(1):31–36
14. Sidhu PS, Cussler E (2001) Diffusion and capillary flow in track-etched membranes. J Membr Sci 182(1):91–101
15. Bernardo P, Drioli E, Golemme G (2009) Membrane gas separation: a review/state of the art. Ind Eng Chem Res 48(10):4638–4663
16. Burggraaf A (1999) Single gas permeation of thin zeolite (MFI) membranes: theory and analysis of experimental observations. J Membr Sci 155(1):45–65
17. Den Exter M, Jansen J, van de Graaf J, Kapteijn F, Moulijn J, Van Bekkum H (1996) Zeolite-based membranes preparation, performance and prospects. Stud Surf Sci Catal 102:413–454
18. Barrer RM (1990) Porous crystal membranes. J Chem Soc Faraday Trans 86(7):1123–1130

19. Krishna R, Van Baten J (2006) Describing binary mixture diffusion in carbon nanotubes with the Maxwell-Stefan equations. An investigation using molecular dynamics simulations. Ind Eng Chem Res 45(6):2084–2093
20. Basile A (2013) Handbook of membrane reactors: fundamental materials science, design and optimisation. Elsevier, UK
21. Xiao J, Wei J (1992) Diffusion mechanism of hydrocarbons in zeolites—I. Theory. Chem Eng Sci 47(5):1123–1141
22. Shehu H, Okon E, Gobina E (2015) The use of nano-composite ceramic membranes for gas separations. In: Proceedings of the world congress on engineering, London, UK, WCE 2015, 1–3 July 2015. Lecture Notes in Engineering and Computer Science, pp 1225–1229

Effect of Titanium on Gouging Abrasion Behavior and Hardness of Austenitic Manganese Steel

Eduardo R. Magdaluyo, Jr, Marthony S. Ausa and Robert J. Tinio

Abstract The gouging abrasion resistance, hardness and microstructural properties of austenitic manganese steel were investigated as influenced by the varying amount of titanium addition. The gouging abrasion of the steel sample with 0.1 % titanium had the least amount of material loss and showed the highest work hardening effect. The alloying process to 0.2 % was detrimental to its mechanical properties. There was an increase in the hardness from 0 to 0.1 % titanium addition and a decrease at 0.2 % titanium content. Metallurgical surface examination of the unmodified austenitic manganese steel revealed the formation of manganese sulfide micronodules and grain boundary carbide. The titanium modified austenitic manganese steel showed titanium-containing precipitates, which increases the strength and toughness of the steel material as well as the resistance of the material to slip and plastic deformation through the precipitation hardening and grain size refinement mechanisms.

Keywords Austenitic manganese steel · Ferrotitanium addition · Gouging · Grain size refinement · Hardness · Precipitation hardening

1 Introduction

The high austenitic manganese or Hadfield steel has been widely utilized in numerous engineering applications in mining, quarrying, earthmoving, steelmaking, and railroading as well as in the manufacturing of cement and clay products

E.R. Magdaluyo, Jr (✉) · M.S. Ausa · R.J. Tinio
Department of Mining, Metallurgical and Materials Engineering,
University of the Philippines, Velasquez Street Corner C.P. Garcia Avenue,
1101 Diliman, Quezon City, Philippines
e-mail: ed.magdaluyojr@coe.upd.edu.ph

M.S. Ausa
e-mail: martz_619@yahoo.com

R.J. Tinio
e-mail: tinio_robert@yahoo.com

S.-I. Ao et al. (eds.), *Transactions on Engineering Technologies*,
DOI 10.1007/978-981-10-1088-0_6

due to its excellent wear resistance with high strength and ductility. It is an extremely tough alloy and has built up an enviable record as an outstanding material for resisting severe service conditions that combines abrasion and heavy impact. It can perform best in gouging abrasion conditions such as in dragline brackets, gyratory rock crushers, roll crushers, jaw crushers and among others, where toughness is a prime requirement. The machining of this type of steel is difficult because of its hardness, low thermal conductivity and strain hardening behavior [1–4].

One of the primary mechanisms in the deterioration of metal castings involved in many industrial applications is the abrasive wear. Gouging abrasion is one type of wear that results from the combination of high stress or low stress abrasions with some degree of impact and load. The metal surface receives prominent gouges and grooves when massive objects are being forced with pressure against each other. Gouging abrasion also places a premium on the toughness and sometimes at the expense of harder and more abrasion resistant alloys [5, 6].

The material composition of the metal castings varies widely depending on the type and conditions of the target applications. The basic criteria for the material selection should be high resistant to wear and tear as well as showing the best response when exposed to other factors such as working temperature and corrosion conditions [7]. The incorporation of the different alloying elements into the steel matrix has been done to improve further the wear resistance of the metallic materials. For the Hadfield manganese steel, it is a solid solution of carbon and manganese in χ iron. While the nominal composition of the Hadfield manganese steel is 1.2 % carbon and 12–13 % manganese, in commercial products, the carbon ranges from 1.0 to 1.4 % and the manganese content between 10 and 14 % in accordance with the ASTM-A128 specification [8].

The high work hardening properties of the austenitic manganese steel can only be maximized under high load impact. Under low stress condition, its work hardening properties are poor and the yield stress is low. Accordingly, the initial deformation is high in service, and therefore, it is not well suited for parts that must resist plastic deformation. Solution and precipitation strengthening are typically used to improve the yield strength of the Hadfield manganese steel by the addition of alloying elements such as Cr, Mo and V [9, 10].

This study aims to develop an austenitic manganese steel alloyed with varying amount of titanium [11]. The effect on the gouging abrasion resistance of austenitic manganese steel using a laboratory scale jaw crusher set-up and the change in the Rockwell hardness value were also investigated. The formation of the secondary phase or inclusions in the austenitic matrix and its effect with the grain size were also studied.

2 Experimental Procedure

A 200 kg of manganese returns, 300 kg of steel craps, 30 kg of high-carbon ferromanganese steel, 47.5 kg of low-carbon ferromanganese and 3 kg of ferrosilicon were melted in an induction furnace to obtain the typical composition of the manganese steel. The spectrometric analysis of the obtained cast manganese steel is shown in Table 1. The manganese steel melt was modified by successive alloying with ferrotitanium, following the 0.05, 0.1 and 0.2 % of titanium content. Table 2 shows the amount of ferrotitanium being added to the manganese steel melt.

The modified and unmodified manganese steels were cast into the prepared furan sand molds as seen in Fig. 1. The tapping temperature of the unmodified manganese steel was 1550 °C while titanium modified manganese steel was at 1770 °C. Both modified and unmodified manganese steels were poured at 1450 °C. The castings were allowed to cool for 24 h. The modified and unmodified manganese steels were austenitized in an industrial muffle furnace at a temperature of 1050 °C for 2 h.

The different set of samples was then soaked for 15 min in a water tank fitted with submersible pumps for quenching process. The quenched austenitic manganese steel jaw plates were machined down to the specified dimensions of 240 × 115 × 20 mm. The samples with dimensions of 25 × 25 × 12.5 mm were also obtained, being used as jaw crusher plates for the gouging abrasion test.

Appropriate preparation of the metallographic specimens was also done in order to obtain the microstructure and surface morphology of the austenitic manganese steel. The use of 3 % nital followed with viella etchants revealed the microstructural

Table 1 Chemical composition of the unmodified manganese steel

Composition	Weight percent
C	1.0715
Si	0.4837
Mn	11.324
P	<0.0130
S	<0.0074
Cr	0.6247
Ni	0.0704
Mo	0.0718
Al	0.0060
Sn	<0.6729
V	<0.0320

Table 2 Variation of ferrotitanium additions in the manganese steel

% titanium	Ferrotitanium equivalent (kg)
0	0
0.05	0.18
0.1	0.30
0.2	0.70

Fig. 1 Furan sand molds being utilized in the production of manganese steel

details and were taken using the metallurgical microscope and scanning electron microscope (SEM).

The number of grains per square millimeter was calculated based on the Jeffries Planimetric method of grain size determination according to the ASTM E112 [12]. The gouging performance of the modified and unmodified austenitic manganese steel jaw plates was evaluated using the modified jaw crusher gouging abrasion set-up. The process involved feeding manually the ore into the jaw crusher, with equal amount of 450 kg being crushed using each jaw plate. The Rockwell C hardness was also determined before and after the gouging resistance test for all the steel samples.

3 Results and Discussions

The ideal austenitic structure of the high manganese steel is a carbide-free and the carbon and manganese are homogenously distributed across the austenite matrix. However, carbides exist at the grain boundaries. Figure 2 shows the photomicrograph of the modified manganese steel which revealed a non-uniform distribution of carbides in the austenitic matrix. High concentration of carbide particles was noticeable at the grain boundaries. The relative abundance of alloying element has resulted to high degree of manganese sulfide micronodules and grain boundary carbides in austenite matrix.

Figure 3 shows the energy dispersive X-ray (EDX) analysis of the austenitic manganese steel with 0.1 % titanium addition. The presence of titanium, manganese and iron can be seen in the spectrum. Titanium modified manganese steel showed manganese sulfide micronodules, titanium inclusions and grain boundary carbides in austenite matrix. The grey particles were nonmetallic inclusions, while the dark spots were shrinkage pores. The inner matrix may contain pearlite, acicular carbides, martensite, meta-stable austenite and other unstable austenitic compositions. The outer portion of the surface of the austenitic manganese steel has relatively high hardness compared to the midsection area which is more ductile. Grain

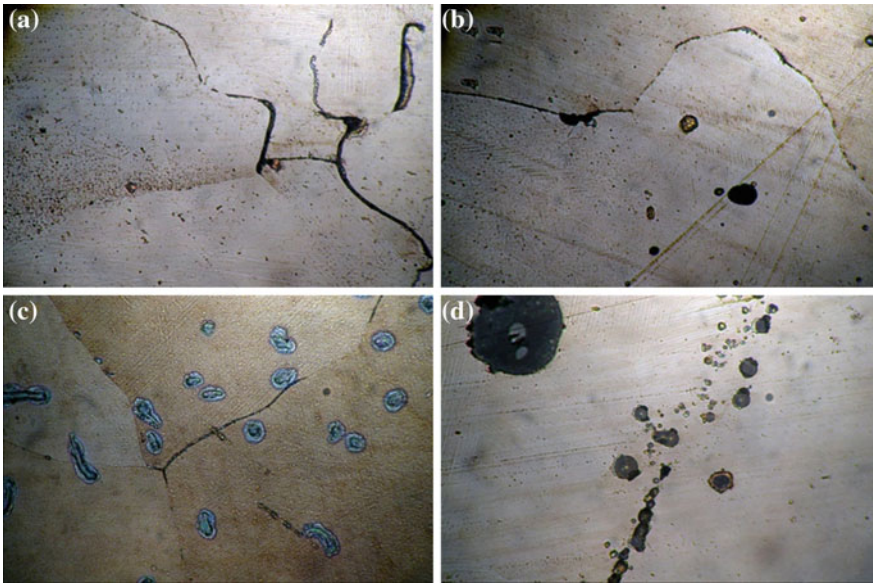

Fig. 2 Microstructure of austenitic manganese steel with **a** 0 %, **b** 0.05 %, **c** 0.1 % and **d** 0.2 % titanium addition taken at 1000× magnification

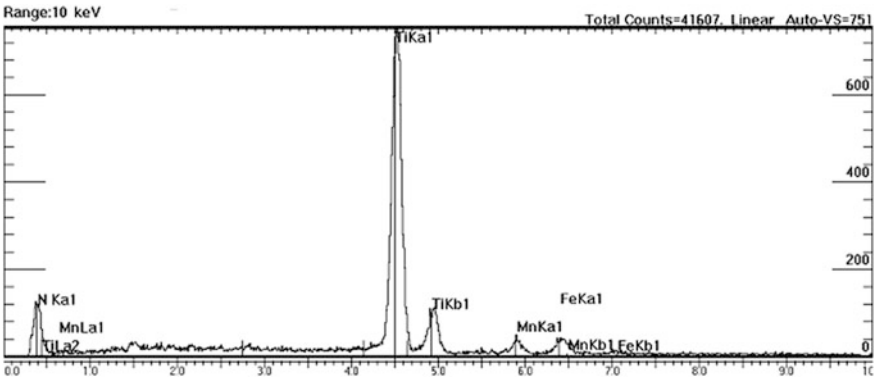

Fig. 3 Energy dispersive X-ray (EDX) spectrum of the austenitic manganese steel with 0.1 % titanium addition

size at the outer portion of the casting was finer and getting coarser grained towards the central area.

Figure 4 shows the effect of titanium in the initial Rockwell C hardness value of the Hadfield manganese steel. There was an increasing hardness from 0 to 0.1 % titanium addition but decreasing at 0.2 %. Correspondingly, Fig. 5 shows the mass loss of each jaw plate after the gouging abrasion test simulation was done. The jaw plate with 0.1 % titanium has the least amount of material loss. The low wear

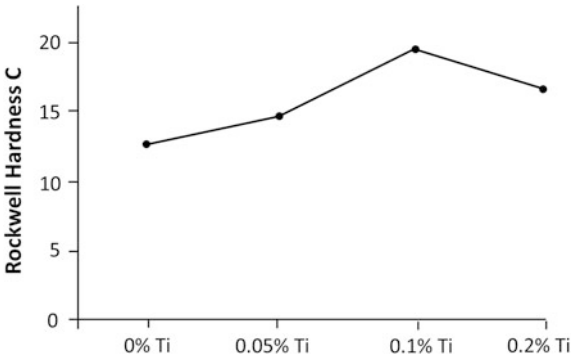

Fig. 4 Initial Rockwell C hardness values of the austenitic manganese steel

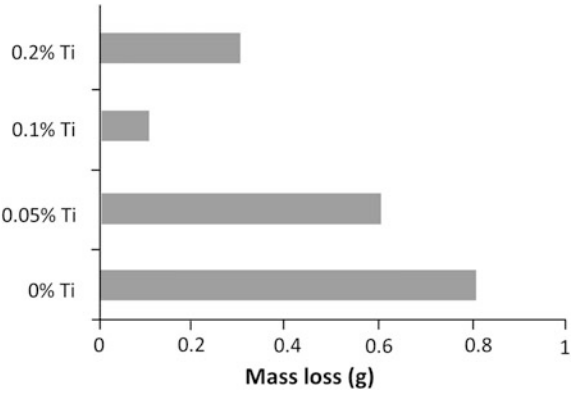

Fig. 5 Mass loss after gouging abrasion test of the austenitic manganese steel

loss of the jaw plate with 0.1 % titanium can be explained by solid solution strengthening effect of the titanium inclusions.

The angular impurities as shown in Fig. 6 are titanium inclusions. The scanning electron microscopy (SEM) image of manganese steel with 0.1 % titanium contained the most number of impurities. These titanium inclusions go into solid solution imposing lattice strains on the surrounding host atoms. Thus, there is a lattice strain field interaction between dislocations and the impurities, consequently, dislocation movement is restricted.

The increase in the Rockwell C hardness of the jaw plate after the gouging abrasion test confirmed the work hardening behavior of the austenitic manganese steel as shown in Fig. 7. The jaw plate containing 0.1 % titanium has the highest increase in Rockwell C hardness value. The difference in the hardness values can be explained by the grain refinement characteristics because of the titanium addition. Photomicrographs of unmodified and modified manganese steel were taken at same magnification (25×) for comparison. Figure 8 shows the microstructural grain distribution of the titanium-modified austenitic manganese steel.

The manganese steel with 0.1 % titanium size has the smallest grain size. The fine grain size influences the mechanical properties; it is harder and stronger

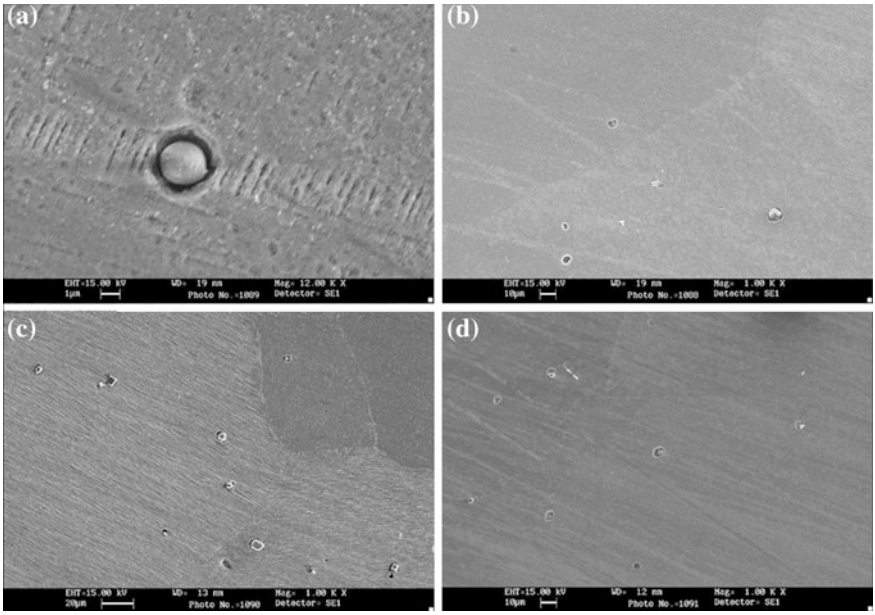

Fig. 6 Surface morphology of the austenitic manganese steel with **a** 0 %, **b** 0.05 %, **c** 0.1 % and **d** 0.2 % titanium addition

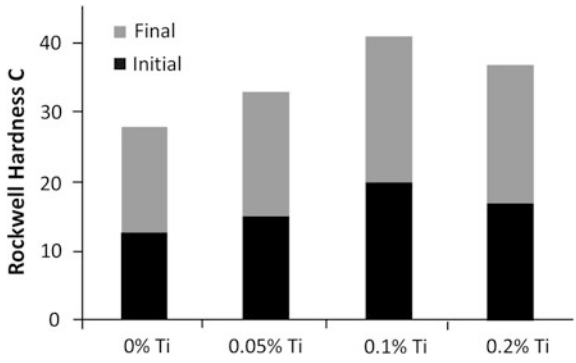

Fig. 7 Comparison of the final and initial Rockwell C hardness values

compared to the one that is coarse grained. Fine grained material has a higher total grain boundary area to impede dislocation motion. The average grain size of the modified and unmodified manganese steel is shown in Table 3. The incorporation of 0.1 % titanium has the best result for the refinement of grain size of austenitic manganese steel. In addition, it has been reported that the fine grain size can inhibit the formation of deformation twins in low stacking-fault energy type such as the Hadfield manganese steel [13].

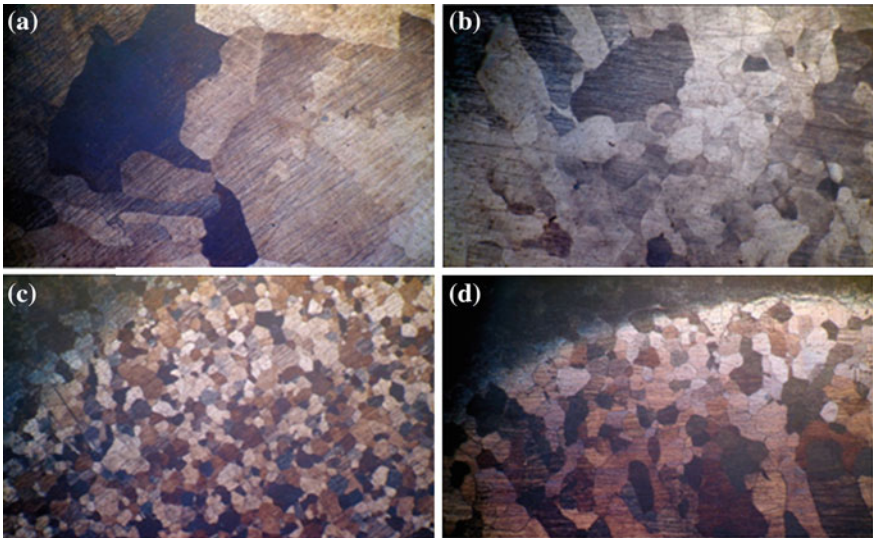

Fig. 8 Microstructure of austenitic manganese steel with **a** 0 %, **b** 0.05 %, **c** 0.1 % and **d** 0.2 % titanium addition

Table 3 Average grain size of the manganese steel

Manganese steel with % titanium	Number of grains/mm^2	Average grain area (mm^2)	Average grain diameter (mm)
0 % titanium	2.25	0.444	0.666
0.05 % titanium	6.50	0.154	0.392
0.1 % titanium	39.25	0.025	0.158
0.2 % titanium	15.00	0.067	0.259

4 Conclusion

The alloying of titanium to the austenitic manganese steel can be used to improve its gouging abrasion resistance and hardness properties. The alloying process can cause titanium precipitates in the matrix of the austenite phase. The Hadfield manganese steel with 0.1 % titanium addition rendered the highest work hardening effect through the precipitation strengthening and grain size refinement mechanisms.

Acknowledgment The authors would like to express their appreciation to the Tiger Machinery and Industrial Corporation (TMIC), especially to Mr. Michael C. Ang, for the use of materials and facilities as well as their engineers for extending their technical expertise. Sincere thanks and gratitude are also extended to the UP DMMME faculty and staff, especially to Prof. Brian Buenaventura for the assistance. The financial support from the Commission on Higher Education (CHED) is also highly appreciated.

References

1. Canadinc D, Sehitoglu H, Maier HJ, Chumlyakov YI (2005) Strain hardening behavior of aluminum alloyed Hadfield steel single crystals. Acta Mater 53:1831–1842
2. Kivak T (2014) Optimization of surface roughness and flank wear using the Taguchi method in milling of Hadfield steel with PVD and CVD coated inserts. Measurement 50:19–28
3. Avery H (1981) Metal handbook: austenitic manganese steel, 8th edn. ASM International
4. Lv B, Zhang F, Li M, Hou R, L. Qian L and Wang T (2010) Effects of phosphorus and sulfur on the thermoplasticity of high manganese austenitic steel. Mater Sci Eng A, 527:5648–5653
5. Tolfree D (2004) Investigation of gouging abrasion resistance of materials in mining industry. MS Thesis, University of British Columbia
6. Neale M (2001) The tribology handbook, 2nd edn. Elsevier Publishing
7. Neale M, Gee M (2001) Guide to wear problems and testing for industry. William Andrew Publishing
8. ASTM A128 (2007) Standard specification for austenitic manganese steel. ASTM International
9. ASM Handbook (1993) Properties and selection: irons, steels and high-performance steels, 10th edn., vol 1. ASM International
10. Wen YH, Peng HB, Si HT, Xiong RL, Raabe D (2014) A novel high manganese austenitic steel with higher work hardening capacity and much lower impact deformation than Hadfield manganese steel. Mater Des 55:798–804
11. Magdaluyo E Jr, Ausa M, Tinio R (2015) Gouging abrasion resistance of austenitic manganese steel with varying titanium. In Proceedings of the World Congress on Engineering WCE, London, UK, 1–3 July 2015. Lecture notes in engineering and computer science, pp 1279–1282
12. ASTM E112 (2007) Standard test methods for determining average grain size. ASTM International
13. Yuan X, Chen L, Zhao Y, Di H, Zhu F (2015) Influence of annealing temperature on mechanical properties and microstructures of a high manganese austenitic steel. J Mater Process Technol 217:278–285

The Methods for Optimum Pressure Computing in Elastic-Creep Microdefect Materials

Maxim Anop, Evgenii Murashkin, Vladislav Mikhalichuk and Marina Polonik

Abstract The present study is devoted to the problem of optimal loading pressure computing by the prescribed displacements vector. The mathematical model of finite elastocreep deformations is used. The boundary value problem of residual stresses forming in microdefect material was considered. Integro-differential equations for the external pressure, irreversible deformations and displacements were derived. The optimization algorithms for this problem was proposed. The optimal strain-stress state parameters were computed and analyzed.

Keywords Blind undirected search · Creep · Elasticity · Finite strain · Microdefect · Residual stress · Swarm intelligence method · Zero-order optimization

E. Murashkin (✉)
Institute for Problems in Mechanics of the Russian Academy of Sciences, Vernadsky Avenue 101, Building 1, Moscow 119526, Russia
e-mail: evmurashkin@gmail.com

E. Murashkin
Bauman Moscow State Technical University, 2nd Baumanskaya Street 5/1, Moscow 105005, Russia

E. Murashkin
National Research Nuclear University MEPhI (Moscow Engineering Physics Institute), Kashirskoye shosse 31, Moscow 115409, Russia

E. Murashkin
Moscow Technological University, Vernadsky Avenue 78, Moscow 119454, Russia

M. Anop · V. Mikhalichuk
Institute of Automation and Control Processes of the Far Eastern Branch of the Russian Academy of Science, Radio Street 5, Vladivostok 690041, Russia
e-mail: manop@dvo.ru

V. Mikhalichuk
e-mail: 19vlad91@dvo.ru

M. Polonik
Far Eastern Federal University, Suhanova Street 8, Vladivostok 690950, Russia
e-mail: polonic@dvo.ru

S.-I. Ao et al. (eds.), *Transactions on Engineering Technologies*,
DOI 10.1007/978-981-10-1088-0_7

1 Preliminary Remarks

Similar problems arise in the stress-strain state calculation of the metal forming processes. In the design of ship hulls and aircraft are widely used panels and profiles of hardly-deformed aluminum alloys. Traditional methods of formation of such structural elements often leads to the appearance of the plastic breaks, cracks and other damages. Thus, the effective way of this fabrication is metal forming under creep and low strain rates. These processes ensures the production of construction with high accuracy, which reduces the complexity of assembly and welding, and increase the residual life and the quality of construction [1].

The mathematical description of the thermomechanical treatment of construct materials is faced with the need to consider the elastic properties of materials at all stages of the product life cycle. Consideration of the problems in the classical models of small deformations is impossible when the relative shape change of the body is large. One such typical application is the problem of modeling processes of deformation metals in vicinity of micropore under the action of intense pressure. In this case, we are forced to assume large deformation. Experiments for significant increasing the long-term strength of metal products after the treatment under hydrostatic pressure are well known [2]. Attempts to simulate such process of the micropores "healing" in the metal have been made repeatedly. In [3] such problems are considered on the basis of the framework of large elastic-plastic deformation. In this case, the adaptability effect to periodic loading on the cycle "loading and unloading" was elucidated in [3].

Since classic work Lee [4], lots of plastic flow frameworks with large reversible and irreversible deformations were built [4–14]. Lot of them use a Lagrangian description [6, 7, 9–12]. But in this case the results of mathematical modeling are physically difficult interpreted. If we want to build a framework of the flow in Eulerian descriptions, then we are faced with two fundamental problems. The first problem is identification of irreversible and reversible components of the total strain tensor. The second problem is definition of irreversible strain source (irreversible strain rate tensor). The mathematical model which proposed in [5] and detail described in [15, 16] is used throughout the chapter. The problem of a spherically symmetric compression of the ball with micropore in the center is considered (some details see in [17]).

2 Governing Equations

The calculations of the residual stresses close the microdefects are necessary carried out in the finite irreversible strain framework with complicated rheological properties. Further consideration is provided by the framework of finite elastocreep deformations (see details in [14]). The kinematic equation for parts of the Almansi

total strain d_{ij} can be written in the Cartesian system (Eulerian coordinates) in the form

$$\begin{aligned}\frac{De_{ij}}{Dt} &= \varepsilon_{ij} - \gamma_{ij} - \frac{1}{2}\left((\varepsilon_{ik} - \gamma_{ik} + z_{ik})e_{kj} + e_{ik}\left(\gamma_{kj} - \varepsilon_{kj} - z_{kj}\right)\right),\\ \frac{Dp_{ij}}{Dt} &= \gamma_{ij} - p_{ik}\gamma_{kj} - \gamma_{ik}p_{kj},\end{aligned} \tag{1}$$

where $e^e_{ij} = e_{ij} - 0.5e_{ik}e_{kj}$ is the reversible part of the Almansi total strain tensor, p_{ij} is the irreversible part of the Almansi total strain tensor, D/Dt denotes the convective derivative with respect to time, γ_{ij} is the irreversible strain rate tensor, ε_{ij} is the strain rate tensor. The total strain rate tensor can be computed by the equation

$$\varepsilon_{ij} = \frac{1}{2}\left(v_{i,j} + v_{j,i}\right), \tag{2}$$

where v_i are the components of velocity vector, the index after comma denotes partial derivative with respect to the corresponding spatial coordinate.

The convective derivative with respect to time in (1) from an arbitrary tensor n_{ij} reads:

$$\begin{aligned}\frac{Dn_{ij}}{Dt} &= \frac{dn_{ij}}{dt} - r_{ik}n_{kj} + n_{ik}r_{kj},\\ r_{ij} &= w_{ij} + z_{ij}\left(e_{ij}, \varepsilon_{ij}\right), \quad w_{ij} = \frac{1}{2}\left(v_{i,j} - v_{j,i}\right),\end{aligned} \tag{3}$$

wherein w_{ij} is the angular rate tensor and $z_{ij}\left(e_{ij}, \varepsilon_{ij}\right)$ is the nonlinear part of the rotation tensor r_{ij} (see in full in [5]). Thus, the components of the Almansi total strains d_{ij} in terms of its parts e_{ij} and p_{ij} taking account of Eqs. (1) and (3) are presented as follows

$$d_{ij} = e_{ij} + p_{ij} - \frac{1}{2}e_{ik}e_{kj} - e_{ik}p_{kj} - p_{ik}e_{kj} + e_{ik}p_{km}e_{mj}, \tag{4}$$

or to other hand

$$d_{ij} = \frac{1}{2}\left(u_{i,j} + u_{j,i} - u_{i,k}u_{k,j}\right), \tag{5}$$

where u_i are the translational displacements. This assumption allows to derive the constitutive equations like the Murnaghan's constitutive equations well known in the non-linear elasticity [18]:

$$\sigma_{ij} = -p\delta_{ij} + \frac{\partial Q}{\partial e_{ik}}\left(\delta_{kj} - e_{kj}\right), \tag{6}$$

where Q is the strain-energy function, p denotes the hydrostatic pressure function as a Lagrangian multiplier to enforce the incompressibility constraint. For isotropic hyperelastic materials, the strain-energy function can be expressed in terms of the invariants of the reversible strain tensor. Let us expand Q into the Taylor series in the vicinity of the natural state $e_{ij} = 0$, disregarding the terms of higher order than the second one. The following form of the expansion is obtained for isotropic, homogeneous and incompressible body

$$\begin{aligned} Q &= (\alpha - \mu)J_1 + \alpha J_2 + \beta J_1^2 - \kappa J_1 J_2 - \zeta J_1^2, \\ J_1 &= e^e_{jj}, \quad J_2 = e^e_{ij} e^e_{ji}, \end{aligned} \tag{7}$$

wherein $\alpha, \mu, \beta, \kappa, \zeta$ are elastic nonlinear constitutive constants.

During process, anticipating plastic flow, and in the unloading, the irreversible strain rate tensor γ_{ij} is identified by the creep strain rate tensor $\gamma_{ij} = \varepsilon^v_{ij}$. The energy dissipation law is valid for creep stage of deforming. Let accept the dissipation potential in the power form like Norton–Bailey power creep law [19, 20]:

$$\begin{aligned} \varepsilon^v_{ij} &= \frac{\partial V(\Sigma)}{\partial \sigma_{ij}}, \\ V(\Sigma) &= B\Sigma^n(\sigma_{ij}), \\ \Sigma &= \sqrt{\frac{3}{2}((\sigma_1 - \sigma)^2 + (\sigma_2 - \sigma)^2 + (\sigma_3 - \sigma)^2)}. \end{aligned} \tag{8}$$

Here $\sigma_1, \sigma_2, \sigma_3$ are the principal values of Cauchy stress tensor and B, n are the creep constitutive constants.

3 Boundary Value Problem

Let examine the changes in the geometry of a single spherical microdefect (micropore) under hydrostatic compression and stress relaxation process during unloading of the material within the proposed framework are spherically symmetric. We consider the solid ball of the initial radius R_0 with a single spherical defect (micropore) of the initial radius s_0 in the center of the sphere. The loading process is given by the boundary conditions

$$\begin{aligned} \sigma_{rr}|_{r=R(t)} &= -P(t), \\ \sigma_{rr}|_{r=s(t)} &= 0, \end{aligned} \tag{9}$$

where σ_{rr} is the radial component of the stress tensor in the spherical coordinates (r, θ, φ), $R(t) \gg r_0$ is the radius of the spherical surface which is given by the external pressure $P(t)$, $s(t)$ is the current radius of the micropore. Reversible (elastic)

e_{ij} and irreversible (creep) p_{ij} parts of the Almansi total strain tensor (5) are defined by the differential equations of change (transfer) (1). Stresses with reversible deformations are related by Eq. (6). The constraints of the incompressibility in the present case of the spherical symmetry leads to the differential continuity equation

$$\left(1 - u_{r,r}\right) \cdot \left(1 - \tfrac{u_r}{r}\right)^2 = 1, \tag{10}$$

where u_r is the only nonzero displacement. The solution of the Eq. (10) is obtained in form

$$\begin{aligned} u_r &= r - \left(r^3 + \varphi(t)\right)^{\frac{1}{3}}, \\ \varphi(t) &= s_0^3 - s^3(t) = R_0^3 - R^3(t). \end{aligned} \tag{11}$$

Note that the kinematics is specifies with an accuracy of an unknown function $\varphi(t)$.

The equation of motion in considered spherically symmetric case can be deduced in form

$$\sigma_{rr,r} + 2\frac{\sigma_{rr} - \sigma_{\theta\theta}}{r} = -\rho_0\left(\frac{\ddot{\varphi}(t)}{3r^2} + \frac{2}{9}\frac{\dot{\varphi}^2(t)}{r^5}\right), \tag{12}$$

wherein $\sigma_{\theta\theta}$ denotes the angular stress, ρ_0 denotes the mass density.

Equation of motion (12) should be supplemented by equation for components of irreversible strain tensor

$$\begin{aligned} \frac{dp_{rr}}{dt} &= Bn(1 - 2p_{rr})\Phi^{n-1}(e_{rr}, e_{\theta\theta}), \\ p_{\theta\theta} &= \frac{1}{2}\left(1 - \frac{1}{\sqrt{1 - 2p_{rr}}}\right), \end{aligned} \tag{13}$$

wherein Φ is derived by formula

$$\begin{aligned} \Phi(a,b) = {} & 2\mu(a-b) - \lambda_1 a^2 + \lambda_2 b^2 + \lambda_3 a^3 - \lambda_4 b^3 \\ & + \lambda_5\left(\frac{1}{2}ab^2 - ab\right) + \lambda_6\left(a^2 b - \frac{1}{2}a^2 b^2\right) - \lambda_7 a^4 + \lambda_8 b^4 \\ & + \lambda_9\left(a^4 b + 2a^3 b^2 - \frac{1}{2}a^4 b^2 - 4a^3 b\right) + \lambda_{10}\left(\frac{1}{2}a^6 - 3b^5\right), \end{aligned} \tag{14}$$

and the parameters λ_i can be computed by the following equations

$$
\begin{aligned}
\lambda_1 &= \mu + 4\alpha + 4\beta + 2\xi,\\
\lambda_2 &= \mu + 4\alpha + 8\beta + 4\xi,\\
\lambda_3 &= 2(2\alpha + 2\beta + 4\xi + 3\chi),\\
\lambda_4 &= 4(\alpha + 2\beta + 4\xi + 6\chi),\\
\lambda_5 &= 4\beta + 2\xi,\\
\lambda_6 &= 2\beta + 7\xi + 18\chi,\\
\lambda_7 &= \alpha + \beta + \frac{19}{2}\xi + 9\chi,\\
\lambda_8 &= \alpha + 2\beta + 19\xi + 36\chi,\\
\lambda_9 &= \frac{3}{4}(\xi + 3\chi),\\
\lambda_{10} &= \frac{1}{2}(5\xi + 11\chi).
\end{aligned}
\tag{15}
$$

Resulting system of the integro-differential equations after integrating Eq. (12) under condition (9) is transformed into

$$
\begin{aligned}
P(t) &= 2\int_{s(t)}^{R(t)} \frac{\Psi(r, p_{rr}(r,t), \varphi(t))}{r}\,dr - \\
&\quad - \rho_0\left(\frac{\ddot{\varphi}(t)}{3}\left(\frac{1}{R(t)} - \frac{1}{s(t)}\right) + \frac{\dot{\varphi}^2(t)}{18}\left(\frac{1}{R(t)^4} - \frac{1}{s(t)^4}\right)\right),\\
\frac{dp_{rr}}{dt} &= (1 - 2p_{rr})Bn\,\Psi^{n-1}(r, p_{rr}(r,t), \varphi(t)),
\end{aligned}
\tag{16}
$$

wherein

$$\Psi(r, p_{rr}(r,t), \varphi(t)) = \Phi(e_{rr}, e_{\theta\theta}),$$

after substituting $e_{rr}, e_{\theta\theta}$ by the rules

$$
\begin{aligned}
e_{rr} &= 1 - H^{-\frac{2}{3}}(1 - 2p_{rr})^{-\frac{1}{2}},\\
e_{\theta\theta} &= 1 - H^{\frac{1}{3}}(1 - 2p_{rr}),\\
H &= 1 + r^{-3}\varphi(t).
\end{aligned}
\tag{17}
$$

The parameters corresponding to metal alloy are shown in Table 1 were used for calculations.

The system (16) is numerically analyzed by using symbolic computation algebra *Mathematica*.

Table 1 Material constants

Dimensionless formula	Quantity	Value
$\alpha\mu^{-1}$	Nonlinear elastic constitutive constant	0.9
$\beta\mu^{-1}$	Nonlinear elastic constitutive constant	4
$\xi\mu^{-1}$	Nonlinear elastic constitutive constant	20
$\chi\mu^{-1}$	Nonlinear elastic constitutive constant	80
$B_0 = nB\rho_0 R_0 \mu^{n-2}$	Creep constitutive constant	3.5
n	Creep constitutive constant	3
$s_0 R_0^{-1}$	Ratio between internal and external radiuses	0.03
μ	Lame constant (shear modulus)	42.9×10^9 Pa
ρ_0	Mass density	7.8×10^3 kg/m^3

4 Optimization Methods and Results

Let us introduce the functional

$$J(\varphi(\cdot)) = \max_{\varphi(\cdot)} P(t). \tag{18}$$

$J(\varphi(\cdot)) \to inf$ is required to find, given that

$$\varphi(\tau) = 269 \times 10^{-7} \left(1 - \exp\left(\sum_{i=0}^{5} \alpha_i \tau^i\right)^2\right), \quad \alpha_i \in [-2.0; 2.0] \tag{19}$$

that is $\varphi(\tau)$ is searched among the set of polynomials with coefficients $\alpha_i \in [-2.0; 2.0]$.

A certain complexity in the problem at hand creates a rather time-taking process of the objective function computing calculated by numerical methods. These conditions impose restrictions on the choice of optimization method. It is required to use only zero-order optimization methods. Direct search methods are best known as unconstrained optimization techniques that do not explicitly use derivatives. As a first try to solve the optimization problem it was chosen the blind random search method. This approach does not adapt the current sampling strategy to information that has been garnered in the search process. Its relative simplicity is an appealing feature to both practitioners and theoreticians. The advantages include relative ease of coding in software, reasonable computational efficiency, broad applicability to non-trivial loss functions [21].

The algorithm is rather simple and consists just of two steps.

Step 0 Generate a vector of polynomials coefficients as independent values according to the chosen probability distribution. In study we used the uniform distribution.

Step 1 Calculate the objective function and check the minimality.

These steps are repeated a predetermined number of iterations.

The blind search form of the algorithm is unique among all general stochastic optimization algorithms in that it is the only one without any adjustable algorithm coefficients that need to be tuned to the problem at hand. In fact it is the main weakness of the method [22]. Our study showed not too high efficiency and rather low reliability of the convergence. If there is a need to solve the optimization problem effectively this method should not be used. The Fig. 1 shows graphs of convergence of the method at hand.

The optimum dynamics of the micropore surface $s(t)$ is shown on Fig. 2. Figure 3 shows the optimum loading pressure $P(t)$ which determined by the results of the numerical calculations.

The pure random search method, which tried to solve the problem at the beginning of the study showed not too high efficiency and rather low reliability. Therefore, specifically for this optimization problem was developed greatly simplified analog of the classical bees algorithm [23–26]. This method allows to find the near-optimal solution in a reasonable running time (Figs. 2 and 3).

In contrast to the classical version of the algorithm considers only two types of bees (agents), namely scout bees (s_j) and worker bees (w_k) recruited for best sites. So the swarm is the set $SW = \left\{ s_j \cup w_k, j = \overline{1,S}, k = \overline{1,W} \right\}$. Scout bees are researching throughout the whole search space. Workers are engaged in exploitation phase of the algorithm in the neighbourhood of the best sites, that had been found by scouts. Neighborhood size in our case is fixed $Nradius = 0.25$.

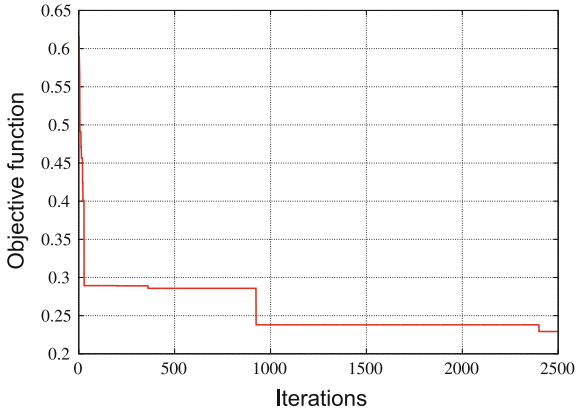

Fig. 1 The algorithm convergence

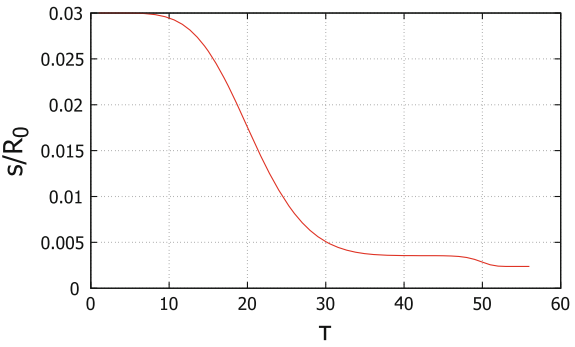

Fig. 2 The optimal micropore surface dynamics

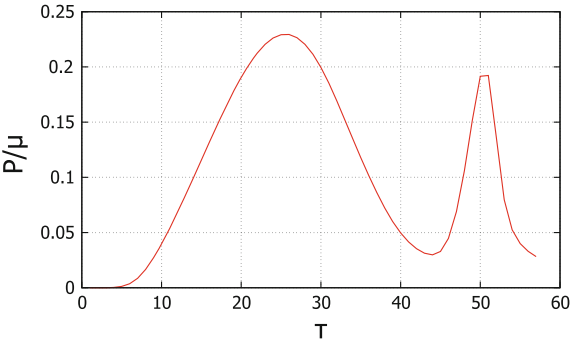

Fig. 3 The optimal loading pressure

Allocates an array ($|SW| \times 5$) for storing values of the polynomials coefficients and the objective function values.

$$array = \begin{pmatrix} s_j^1 & s_j^2 & s_j^3 & s_j^4 & J_j(\phi(\cdot)) \\ & & \cdots & & \\ w_k^1 & w_k^2 & w_k^3 & w_k^4 & J_k(\phi(\cdot)) \\ & & \cdots & & \\ \hat{s}_l^1 & \hat{s}_l^2 & \hat{s}_l^3 & \hat{s}_l^4 & J_l(\phi(\cdot)) \\ & & \cdots & & \\ \hat{w}_m^1 & \hat{w}_m^2 & \hat{w}_m^3 & \hat{w}_m^4 & J_m(\phi(\cdot)) \end{pmatrix}$$

This array is required to find the best sites. In the first part of the array is stored the best values found. The second is used to store checked values. In the initialization phase, the entire array is filled with random values of coordinates (polynomial coefficients) and evaluate the objective function in this points. Then the array is sorted by the value of the objective function in order to find the "best" values that will be used by the worker bees, performing a local search.

The main loop consists of three stages.

Step 1 Generating values from the entire solution space and from the neighbourhood of the fittest solutions ($\hat{s}_l$, $\hat{w}_m$).

Step 2 Calculates the objective function in the generated points $(J_l(\phi(\cdot))$ $J_m(\phi(\cdot)))$.

Step 3 Sorting the updated array.

These steps are repeated so far as the stopping criterion will not be satisfied. In our case used a simple limitation on the number of iterations.

So, the original method of the bees algorithm inspired the authors to develop a rather simple optimization method. There are only three adjustable parameters in concerned algorithm. All parameters are fixed. Due to the sorting procedure at the top of the array at each stage are the best values. Despite a strong simplification of the original algorithm proposed computational process shows good results compared to undirected random search. Thus, the goal is to increase the efficiency of the optimization procedure was achieved.

Through the use of a sorting routine in the beginning of the array are always the best areas that greatly simplifies the implementation of the local search phase procedure.

The Fig. 4 shows graphs of convergence of the bee method at hand.

The optimum dynamics of the micropore surface $s(t)$ is shown on Fig. 5. Figure 6 shows the optimum loading pressure $P(t)$ which determined by the results of the numerical calculations.

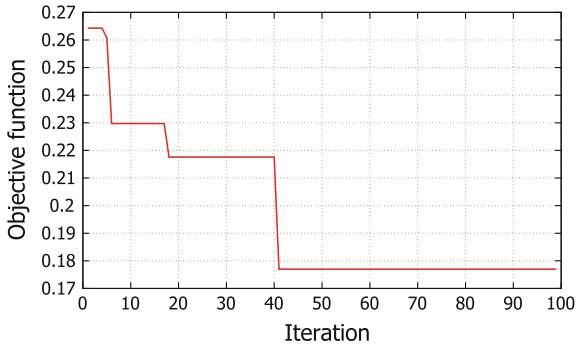

Fig. 4 The algorithm convergence

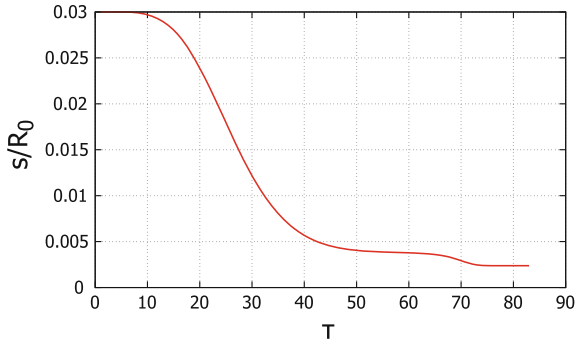

Fig. 5 The optimal micropore surface dynamics

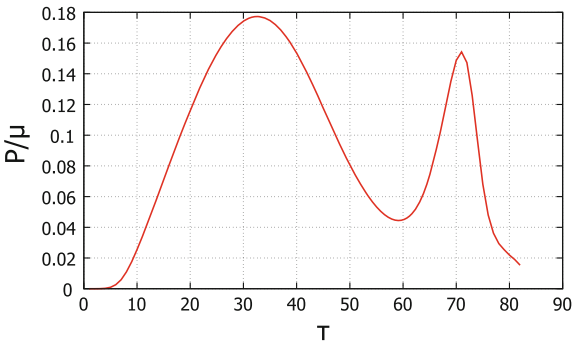

Fig. 6 The optimal loading pressure

5 Conclusions

The boundary value problem of compression of elastic-creep ball with a cavity had been solved. The pressure required to achieve a given strain state had calculated. The optimization problem of hydrostatic compression of elastic-creep ball with a cavity had been solved. The minimal pressure required to achieve a given cavity size had been calculated. The modification of the bees algorithm had been proposed and carried out the comparison with the <<blind>> search method. The significant improvement in the convergence rate had been revealed.

The presented mathematical framework of large elastocreep deformations is based on Eqs. (1), (5), (6), (8) and (12). One can use the presented approach for mechanical design creep fabricated parts from creep-elastic materials determining the strength and the shape of final products. Solved problems for a ball-shaped body with a single spherical defect are consistent with well-known micropore welding process [2]. The proposed method of the loading pressure computing for a given displacements can be used to optimize the treatment metal process under creep conditions. Moreover, on the basis of this mechanical analysis one can work out effective recommendations for improving the technological processes.

Acknowledgement This work was financially supported by the Russian Foundation for Basic Research (Projects 15-31-21111, 16-58-45038).

References

1. Rogachev EE, Polonik MV, Dudko OV, Murashkin EV (2014) Numerical modeling of forming a preform under high temperature creep. Adv Mater Res. doi:10.4028/www.scientific.net/AMR.1040.898
2. Gorelov VI (1984) Effects of high pressures on mechanical characteristics of aluminum alloys. J Appl Mech Tech Phys. doi:10.1007/BF00909392
3. Burenin AA, Kovtanyuk LV, Polonik MV (2000) The possibility of reiterated plastic flow at the overall unloading of an elastoplastic medium. Dokl Phys. doi:10.1134/1.1342452
4. Lee EH (1969) Elastic-plastic deformation at finite strains. J Appl Mech. doi:10.1115/1.3564580

5. Shitikov AV, Bykovtsev GI (1990) Finite deformations in an elastoplastic medium. Dokl Akad Nauk SSSR 311(1):59–62 [Sov Phys Dokl (Engl. Transl.) 35:297 (1980)]
6. Levitas VI (1996) Large deformation of materials with complex rheological properties at normal and high pressure. Nova Science Publishers, New York
7. Jiang C, Liu G, Zhang D, Xu X (2006) Kinematic modeling and error analysis for a 3DOF parallel-link coordinate measuring machine. Mater Sci Forum. doi:10.4028/www.scientific.net/MSF.532-533.313
8. Bruhns OT (2007) A thermodynamically consistent Eulerian description of finite elastoplasticity. Key Eng Mater. doi:10.4028/www.scientific.net/KEM.340-341.787
9. Huang YY, Zheng H, Zhou YH (2011) Simulation analysis of concrete Dam's joints based on elastic-plastic creep model. Appl Mech Mater 137:243–249
10. Chen WL, Zhao FS (2012) Study on non-linear viscous elastic-plastic creep model of mica-quartzose schist. Appl Mech Mater. doi:10.4028/www.scientific.net/AMM.157-158.622
11. Mahmoud FF, El-Shafei AG, Abdelrahman AA, Attia MA (2013) Modeling of nonlinear viscoelastic contact problems with large deformations. Appl Math Model. doi:10.1016/j.apm.2013.02.017
12. Li Wu, Zuo QJ, Lu ZL (2013) Study on the constitutive model of visco-elasticity-plasticity considering the rheology of rock mass. Adv Mater Res 639–640:567–572
13. Murashkin E, Polonik M (2013) Development of approaches to the creep process modeling under large deformations. Appl Mech Mater. doi:10.4028/www.scientific.net/AMM.249-250.833
14. Bazhin AA, Murashkin EV (2012) Creep and stress relaxation in the vicinity of a micropore under the conditions of hydrostatic loading and unloading. Dokl Phys. doi:10.1134/S1028335812080095
15. Shitikov AV (1995) A variational principle for constructing the equations of elastoplasticity for finite deformations. J Appl Math Mech. doi:10.1016/0021-8928(95)00016-I
16. Burenin AA, Kovtanyuk LV, Murashkin EV (2006) On the residual stresses in the vicinity of a cylindrical discontinuity in a viscoelastoplastic material. J Appl Mech Tech Phys. doi:10.1007/s10808-006-0049-5
17. Anop M, Murashkin E, Mikhalichuk V, Polonik M (2015) On optimum pressure computing by prescribed displacements in elastic-creep material: finite deformations. In Proceedings of the World Congress on Engineering, WCE, London, UK, 1–3 July, 2015. Lecture notes in engineering and computer science, vol 2. pp 1243–1246. http://www.iaeng.org/publication/WCE2015/
18. Murnaghan FD (1937) Finite deformations of an elastic solid. Am J Math 59:235–260
19. Norton FH (1929) Creep of steel at high temperatures. McGraw Hill, New York
20. Bailey RW (1929) Creep of steel under simple and compound stresses, and the use of high initial temperature in steam power plants. Trans World Power Conf Tokyo 3:1089
21. Kolda TG, Lewis RM, Torczon V (2003) Optimization by direct search: new perspectives on some classical and modern methods. SIAM Rev. doi:10.1137/S0036144502428893
22. Spall JC (2003) Introduction to stochastic search and optimization: estimation, simulation, and control. Wiley, Hoboken
23. Karaboga D (2005) An idea based on honey bee swarm for numerical optimization. Technical report—TR06, Engineering Faculty, Computer Engineering Department, Erciyes University. http://mf.erciyes.edu.tr/abc/pub/tr06_2005.pdf
24. Karaboga D, Akay B (2009) A survey: algorithms simulating bee swarm intelligence. Artif Intell Rev. doi:10.1007/s10462-009-9127-4
25. Karaboga D, Gorkemli B, Ozturk C, Karaboga N (2014) A comprehensive survey: artificial bee colony (ABC) algorithm and applications. Artif Intell Rev. doi:10.1007/s10462-012-9328-0
26. Pham DT, Ghanbarzadeh A, Koc E, Otri S, Rahim S, Zaidi M (2005) The bees algorithm bees a novel tool for complex optimisation problems. Manufacturing Engineering Centre, Cardiff University, Cardiff

Assessment and Comparison of Machining Performance in Rotary and Stationary Tool EDM for Machining AISI D3 Tool Steel

Anand Prakash Dwivedi and Sounak Kumar Choudhury

Abstract The Electric Discharge Machining (EDM) is a well-established and one of the most primitive unconventional manufacturing processes, that is used worldwide for the machining of geometrically complex or hard and electrically conductive materials which are extremely difficult-to-cut by any other conventional machining process. One of the major flaws of EDM, over all its advantages, is its very slow Material Removal Rate (MRR). In order to enhance this slow machining rate, various researchers have proposed various methods like; providing rotational motion to the tool or workpiece or to both, mixing of conducting additives (such as SiC, Cr, Al, graphite etc.) powders in the dielectric, providing vibrations to the tool or workpiece or to both etc. Present work is a comparative study of Rotary and Stationary Tool EDM, which deals with providing rotational motion to the copper tool for the machining of AISI D3 Tool Steel and the results have been compared with stationary tool EDM. It has been found that the tool rotation substantially increases the average MRR up to 49 %. The average surface finish increases around 9–10 % by using the rotational tool EDM. The average tool wear increment is observed to be around 14 % due to the tool rotation. Apart from this, the present work also focusses on the recast layer analysis, which is being re-deposited on the workpiece surface during the operation. The recast layer thickness is less in the case of rotary tool EDM and more for stationary tool EDM.

Keywords AISI D3 · EDM · MRR · Recast layer · Rotary tool EDM · Stationary tool EDM · Surface roughness · TWR

A.P. Dwivedi (✉) · S.K. Choudhury
Department of Mechanical Engineering,
Indian Institute of Technology Kanpur, Kanpur, India
e-mail: anandprakashdwivedi@gmail.com

S.K. Choudhury
e-mail: choudhry@iitk.ac.in

S.-I. Ao et al. (eds.), *Transactions on Engineering Technologies*,
DOI 10.1007/978-981-10-1088-0_8

1 Introduction

Electric Discharge Machining (EDM) process was originated around 1770 when English Scientist Joseph Priestly discovered the erosive effect of the electric discharges (sparks). In 1930, first attempts were made to machine metals and diamonds using electric discharges, and the process was referred to as "arc machining or spark machining" [1].

In 1943, two Russian Scientists, B.R. Lazarenko and N.I. Lazarenko at the Moscow University did pioneering work on EDM [2]. The destructive effect of an electric discharge was channelized and a controlled process for the machining of materials was developed. The relaxation-capacitance (RC) circuit was introduced in the 1950s, which provided the first consistent dependable control of pulse time and a simple servo system control circuit to automatically sense the required inter-electrode gap between the tool and the workpiece. In the 1980s, the introduction of Computer Numerical Control (CNC) in EDM, brought tremendous advancement in improvising the efficiency of the machining process. Modern EDM machines are so stable these days that these can be operated round the clock under adaptive control system monitoring [3].

1.1 Working Principle

EDM is an electro-thermal non-traditional controlled metal removal process, where electrical energy is utilized to generate an electric spark and due to the thermal energy of the spark, most of the material removal takes place. Here, the spark behaves like a cutting tool to cut the workpiece, in order to produce the finished job to the desired shape. The material removal process is accomplished by the application of a pulsating (on/off) electric charge carrying high-frequency current through the electrode to the workpiece. This causes material removal in the form of tiny particles from the workpiece at a controlled rate. Schematic diagram of EDM process is shown in Fig. 1.

1.2 Process Mechanism

The material erosion mechanism primarily utilizes the electrical energy and converts it into thermal energy, through a series of discontinuous electrical discharges occurring between the tool and the workpiece, submerged in the dielectric fluid [4]. The thermal energy generates a virtual plasma channel between the two electrodes [5] at a temperature in the range of 8000–12,000 °C [6], this temperature can go as high as 20,000 °C [7]. This temperature range causes the material of any hardness to melt at the surface of each pole. When the pulsed DC power supply of around

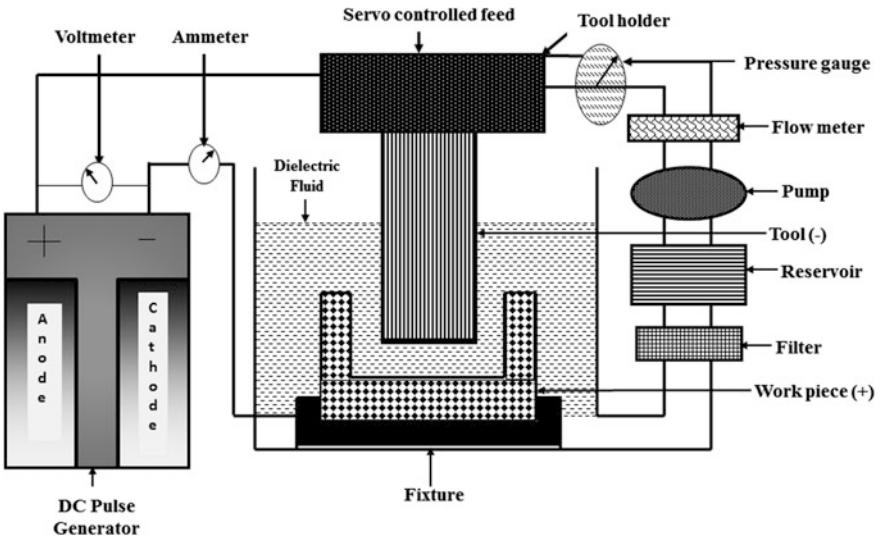

Fig. 1 Schematic diagram of EDM process

20,000–30,000 Hz [8] is turned off, the plasma channel breaks down. This causes an abrupt reduction in temperature at the tool workpiece interface, which allows the circulating dielectric to flush away the molten material from the melt cavity, in the form of microscopic debris [1]. The arc description during the EDM process is shown in Fig. 2.

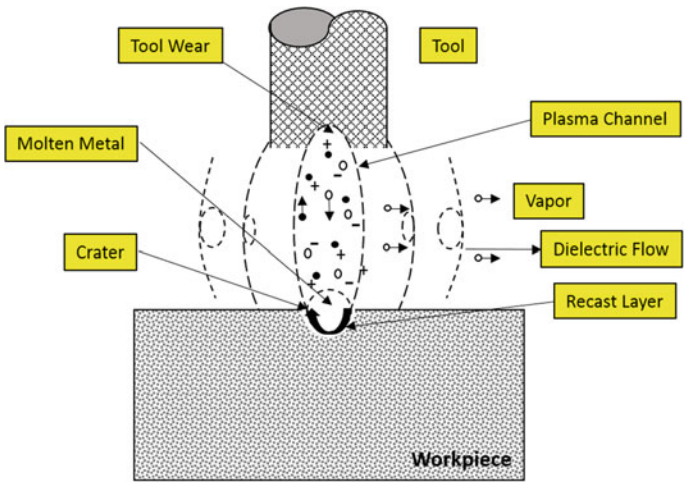

Fig. 2 Arc description in EDM process

The volume of material removed per discharge is approximately in the range of 10^{-6}–10^{-4} mm^3 and the material removal rate (MRR) is typically in between 2 and 400 mm^3/min [1], based on specific applications. As the shaped electrode defines the area wherein the spark erosion would occur, the accuracy of the part produced by EDM is fairly good. After all, electric discharge machining is a reproductive shaping process, in which the form of the tool electrode is mirrored in the workpiece [9].

1.3 Process Characteristics

(i) The process can be used to machine any electrically conductive material, irrespective of its hardness.
(ii) The rate of material removal depends mainly on the thermal properties of the workpiece, rather than its hardness or strength.
(iii) The workpiece and the tool are not in physical contact with each other at any point of time during the machining.
(iv) The tool also needs to be electrically conducting in nature and the tool wear also depends on the thermal properties of the tool material.
(v) The heat affected zone (HAZ) is limited to 2–4 μm of the spark crater.
(vi) The process is burr free.
(vii) There are possibilities of overcut and taper in this process, but these can easily be controlled and compensated by proper tool design and input settings.

2 Experimental Set-up

In order to rotate the tool electrode, a motorized set-up was fabricated and mounted on the Electronics Z-axis Numerical Control (NC) Electric Discharge Machine (Model: ELEKTRA 5535-EZNC). Figure 3 shows the rotating set-up mounted on the EDM.

Electrode rotation helps to solve the flushing difficulty encountered while machining small holes with EDM. In addition to the increase in MRR, the quality of the hole produced is superior to that obtained using a stationary electrode. It produces cavities having very close shape of the electrode. It improves flushing by creating a pumping effect of the dielectric liquid through the gap [10, 11].

Technical features of rotary EDM setup are mentioned in Tables 1 and 2 shows the experimental parameters of the rotary EDM set-up.

Experiments were performed on AISI D3 Tool Steel flats, of thickness 5 mm with a copper rod as tool material having 10 mm diameter. Figure 4 shows the results obtained from six different sets of experiments, each set containing two

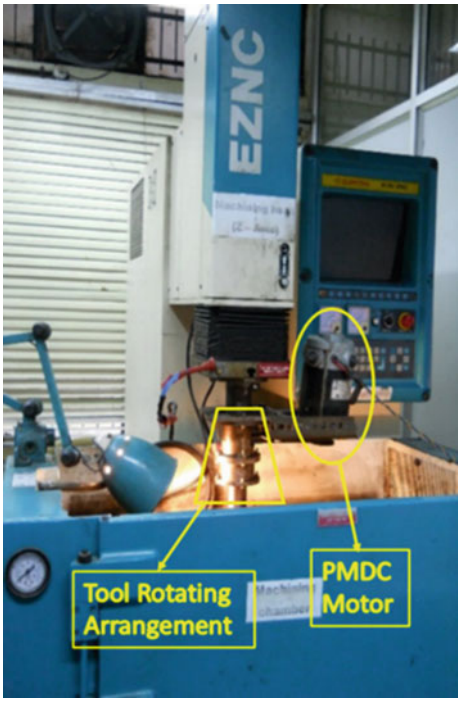

Fig. 3 EDM with rotary tool set-up

Table 1 Technical features of rotary EDM set-up

Motor	PMDC
Voltage	120 V
Current	2 A
Poles	4
Power	240 W
Speed	0–3000 RPM

Table 2 Experimental parameters

Current	5, 10, 15, 20, 25 and 30 A
Voltage	75 V
T_{on}	150 µm
T_{off}	58.33 µm
Polarity	Positive
Tool rotational speed	0–3000 RPM

experiments. The first one (as shown in the 1st row of Fig. 4) was carried out using the stationary EDM and the later one (as shown in the 2nd row of Fig. 4) using the rotary EDM. All the experiments performed using the rotary EDM process have been conducted at a uniform rotational speed of 1000 RPM.

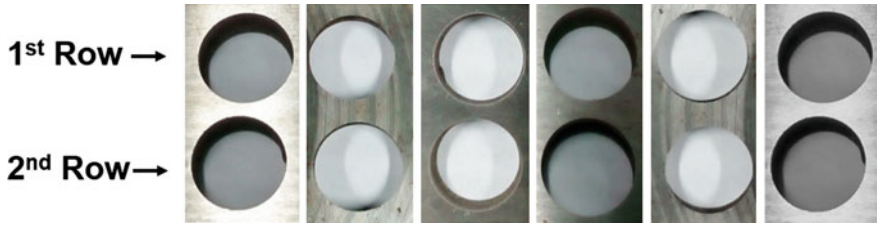

Fig. 4 AISI D3 Tool Steel workpieces after machining

2.1 Tool Details

Copper rods of 10 mm diameter have been used as the tool electrode.
The advantages of using copper as tool are as follows:

(a) High thermal and Electrical Conductivity
(b) Ease of machinability
(c) Ease of availability
(d) Economical.

2.2 Workpiece Details

AISI D3 Tool Steel flat plates of thickness 5 mm have been used as workpiece.
The applications of AISI D3 Tool Steel are as follows:

(a) Blanking, stamping and cold forming dies and punches for long runs
(b) Lamination dies
(c) Bending, forming and seaming rolls
(d) Cold trimmer dies or rolls
(e) Burnishing dies or rolls
(f) Plug gages
(g) Drawing dies for bars or wire
(h) Slitting cutters
(i) Lathe centres that subject to severe wear.

2.3 MRR Analysis

In EDM, the metal is removed from both workpiece and tool electrode. MRR depends on the workpiece material, tool material and the machining variables such as pulse conditions, electrode polarity, and the machining medium. A material of low melting point has a high metal removal rate and hence a rougher surface. Typical material removal rates range from 0.1 to 400 mm^3/min. Experimentally

Table 3 MRR for rotating tool EDM

S. No.	Current (A)	Tool rotation speed (RPM)	MRR (g/min)
1	5	1000	0.0381
2	10	1000	0.0795
3	15	1000	0.1429
4	20	1000	0.2067
5	25	1000	0.2730
6	30	1000	0.3866

Table 4 MRR for stationary tool EDM

S. No.	Current (A)	MRR (g/min)
1	5	0.0189
2	10	0.0401
3	15	0.1029
4	20	0.1837
5	25	0.2436
6	30	0.3141

obtained values of material removal rate for the rotational and stationary tool EDM process are shown in Tables 3 and 4 respectively.

Experimental results, as shown in Fig. 5, indicate that the MRR during the rotary EDM process is always greater than that in the stationary process. This is due to the fact that with the electrode rotation, the molten material from the melt pool is cleared more frequently, as a result of which fresh workpiece surface is exposed to the tool every time the debris is being cleared away. Since the workpiece surface now exposed to the tool surface is fresh and almost free from the leftover molten material, the spark intensity is more, which causes more surrounding material to melt and in

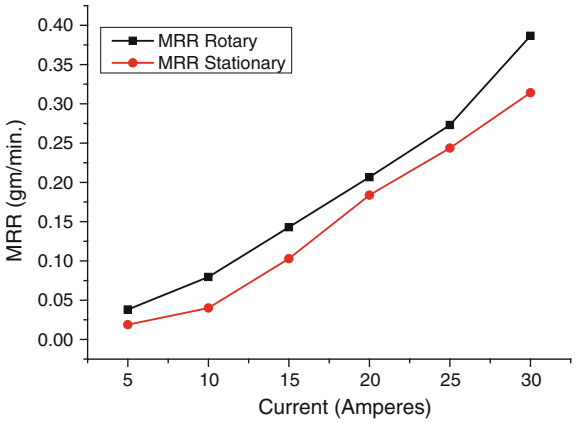

Fig. 5 MRR versus current curve

this way the material in the vicinity of the spark gets melted and flushed away by the flow of the dielectric and electrode rotation, resulting in improved MRR.

2.4 TWR Analysis

Experimentally obtained values of tool wear rate for the rotary and stationary tool EDM process are depicted in Tables 5 and 6 respectively.

Experimental results have been plotted in graphical form and depicted in Fig. 6. It is evident from both, Tables 5 and 6, and the graph in Fig. 6 that the TWR during the rotational process is a bit more than that in the stationary process. With the tool rotation, the molten material from the melt pool is cleared easily and effectively, so fresh materials are exposed after the melt pool is cleared, this causes greater spark intensity which increases the melting of more material in the vicinity of the spark, so the workpiece and the tool material both get incremental sparks which increase both the MRR as well as the TWR. Since the flow of electron is always directed from the negative terminal towards the positive one, more of the workpiece material gets eroded as compared to the tool material. As, a result of which the MRR gets substantially increased by increasing the current and the TWR increases comparatively less, with the increment in the input current [12].

Table 5 TWR for rotating tool EDM

S.No.	Current (A)	Tool rotation speed (RPM)	TWR (gm/min)
1	5	1000	0.0004
2	10	1000	0.0009
3	15	1000	0.0038
4	20	1000	0.0089
5	25	1000	0.0200
6	30	1000	0.0349

Table 6 TWR for stationary tool EDM

S. No.	Current (A)	TWR (g/min)
1	5	0.0003
2	10	0.0007
3	15	0.0029
4	20	0.0075
5	25	0.0162
6	30	0.0349

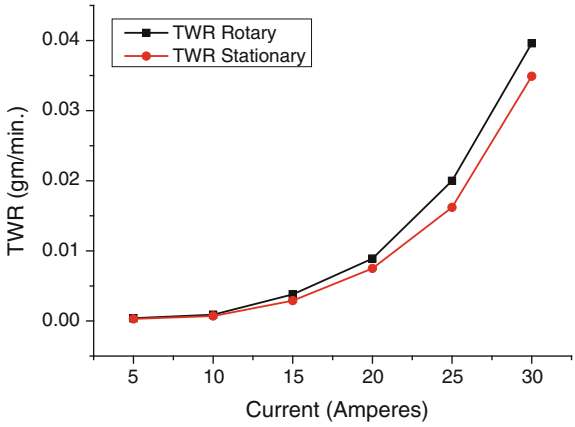

Fig. 6 TWR versus current curve

2.5 *Surface Roughness Analysis*

Average surface roughness is expressed as the 'Ra' value of the material.

Surface texture after EDM process is shown in Fig. 7. Surface roughness analysis was carried out on the workpieces using Bruker GT-KO non-contact type 3-D optical profilometer (Fig. 8).

Tables 7 and 8 show the surface roughness (Ra) values, for the rotary and stationary tool EDM process.

Figures 9 and 10 show the workpiece surface roughness profiles obtained from optical 3-D profilometer, after machining by rotary and stationary tool EDM respectively.

Figure 11 depicts the experimental results plotted in graphical form. It is very evident from both, Tables 7 and 8, and the graph in Fig. 11 that the surface finish during the rotary EDM process is better than that in the stationary EDM process (as Ra for stationary tool EDM is greater than the Ra for rotary tool EDM). This is so, because due to the rotation of the electrode the molten metal does not easily gets deposited on the workpiece surface. With the motion of the electrode, it gets easily

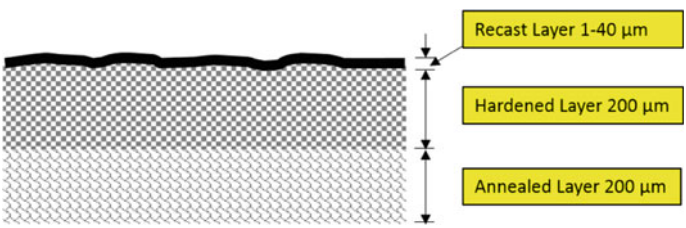

Fig. 7 Various layers on workpiece after EDM process

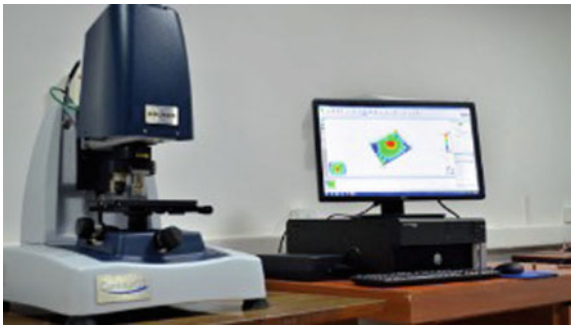

Fig. 8 3-D optical profilometer

Table 7 Ra for rotary tool EDM

S. No.	Current (A)	Tool rotation speed (RPM)	Ra (μm)
1	5	1000	4.91
2	10	1000	5.59
3	15	1000	6.195
4	20	1000	7.02
5	25	1000	7.264
6	30	1000	7.861

Table 8 Ra for stationary tool EDM

S. No.	Current (A)	Ra (μm)
1	5	5.244
2	10	5.889
3	15	6.946
4	20	7.411
5	25	8.394
6	30	9.429

flushed away with the dielectric flow. As a result, the surface produced is more uniform and crack-free as compared with the stationary tool EDM. Figure 11 shows that at every point the Ra value of rotary EDM is less than that of the stationary EDM, i.e., the surface finish of rotary EDM process is better than that of the stationary tool EDM.

2.6 Recast Layer Analysis

Recast layer analysis for the AISI D3 Tool Steel has been carried out by using JEOL JSM-6010LA Scanning Electron Microscope (Fig. 12).

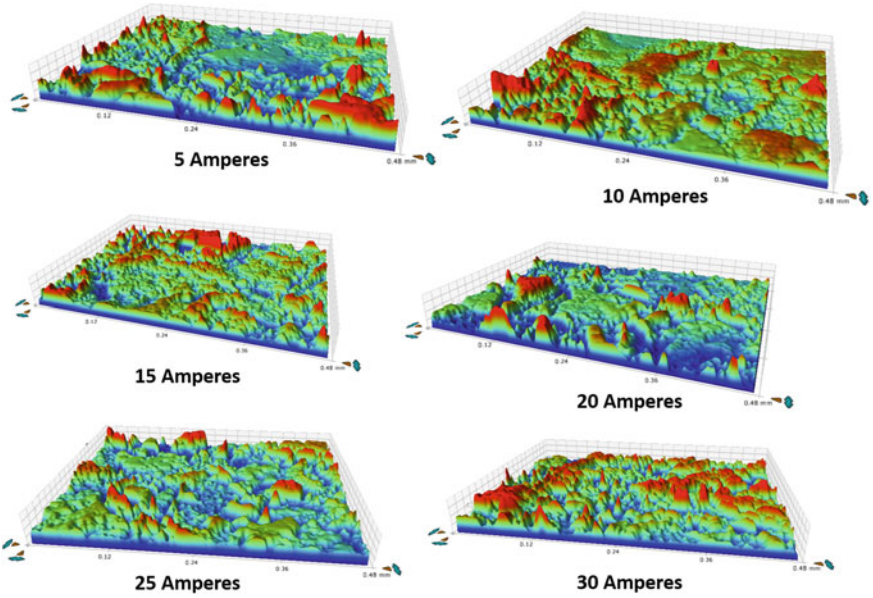

Fig. 9 Surface profiles obtained from 3D optical profilometer for machining AISI D3 Tool Steel using rotary EDM at different values of current

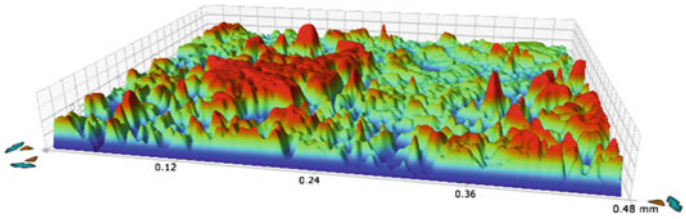

Fig. 10 Surface profile obtained from 3D optical profilometer for machining AISI D3 Tool Steel using stationary EDM at an input current of 5 A

For Rotary EDM

The images obtained by the SEM process show that the recast layer thickness on the AISI D3 Tool Steel machined by the rotary tool EDM is not uniform, it varies from 2–25 µm. Moreover, there are fewer micro-cracks observed on the workpiece surface, as due to the tool rotation almost the entire molten material gets flushed away with the dielectric flow which in the case of stationary EDM remains on the surface and after hardening forms a recast layer with micro-cracks on the workpiece surface.

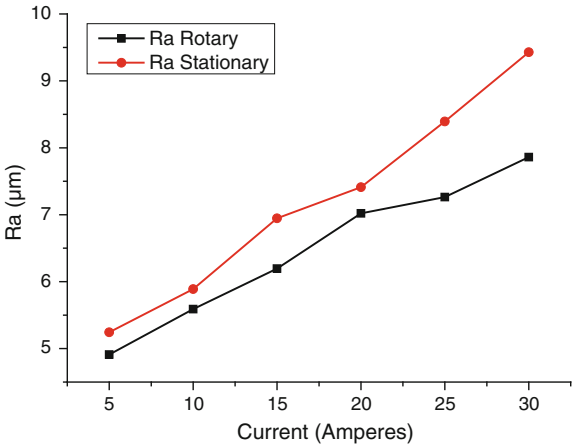

Fig. 11 Ra versus current curve

Fig. 12 Scanning electron microscope

Figure 13 shows the recast layer deposited over the AISI D3 Tool Steel after its machining by rotary EDM process. These layers are formed due to the deposition of molten metal in the machining cavity. This left over material has the constituents of workpiece material, tool material and the decomposed carbon of the dielectric (hydrocarbon oil). When this layer gets hardened, it solidifies over the workpiece surface and it gets some micro-cracks after solidification. As seen in this figure these layers have a thickness in the range of 2–25 μm when observed from the scanning electron microscope, at a magnification level of 500 times the original size at different values of current.

For Stationary EDM

In stationary tool EDM, there are more micro-cracks observed on the workpiece surface as compared to the rotary tool. The thickness of recast layer is almost twice as compared to the rotary EDM process.

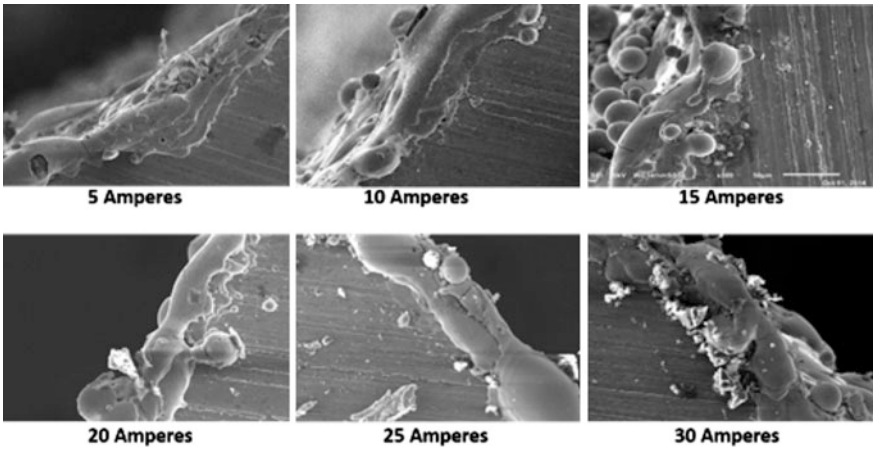

Fig. 13 SEM images of AISI D3 Tool Steel using rotary EDM process at different values of current

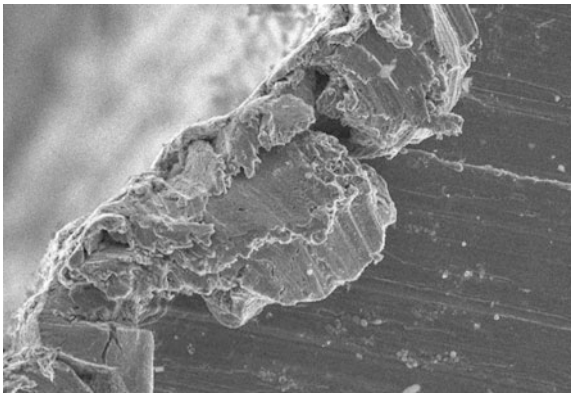

Fig. 14 SEM images of AISI D3 Tool Steel using stationary EDM process at an input current of 5 A

Figure 14 shows the recast layer of thickness 2–40 μm deposited over the AISI D3 Tool Steel after its machining by stationary tool EDM process at an input current of 5 A.

3 Results

The experimental results and analysis of AISI D3 Tool Steel machining using the EDM (Rotary tool and Stationary Tool) process allow us to make the following inferences:

(a) By using the rotary tool EDM, the MRR increases by 49 % as compared to the stationary tool EDM, due to better debris clearance and increased spark intensity.

(b) There is a slight increase in the TWR of around 14 % while using the rotary tool EDM over stationary Tool EDM, since due to increased spark intensity in the case of the rotary tool EDM, both the tool and workpiece experience more erosive action.
(c) The surface finish increases by 9–10 % using the rotary EDM over stationary tool EDM, as the tool rotation enables uniform machining on the workpiece.
(d) The average recast layer during the rotary EDM process is in the range of 2–25 μm while it is 2–40 μm for the stationary tool EDM process. Also, the micro-cracks visible on the machined surface of the workpiece are less in the case of rotary EDM process as compared to the stationary EDM process.

4 Conclusion

From the above research work it can be concluded that the Rotary tool EDM gives a better MRR and surface finish, at the cost of a slightly higher tool wear. Also, the rotary EDM reduces the thickness of recast layer and the surface micro-cracks. The average recast layer thickness increases with the increase in discharge current. Thicker recast layers have more cracking tendency than that of the thinner ones.

References

1. Ho KH, Newman ST (2003) State of the art electrical discharge machining (EDM). Int J Mach Tool Manuf 43:1287–1300
2. Lazarenko BR (1943) To invert the effect of wear on electric power contacts. Dissertation of the All-Union Institute of Electro Technique in Moscow/USSR, Russian
3. Kumar S, Singh R, Singh TP, Sethi BL (2009) Surface modification by electrical discharge machining: a review. J Mater Process Technol 209:3675–3687
4. Tsai HC, Yan BH, Huang FY (2003) EDM Performance of Cr/Cu-based composite electrodes. Int J Mach Tools Manuf 43(3):245–252
5. Shobert EI (1983) What happens in EDM. In: Jameson EC (ed) Electrical discharge machining: tooling, methods and applications. Society of Manufacturing Engineers, Dearbern, Michigan, pp 3–4
6. Boothroyd G, Winston AK (1989) Non-conventional machining processes. In Fundamentals of machining and machine tools. Marcel Dekker, Inc., New York, p 491
7. McGeough JA (1988) Electro discharge machining. Advanced methods of machining. Chapman & Hall, London, p 130
8. Krar SF, Check AF (1997) Electrical discharge machining. Technology of machine tools. Glencoe/McGraw-Hill, New York, p 800
9. Konig W, Dauw DF, Levy G, Panten U (1988) EDM-future steps towards the machining of ceramics. Ann CIRP 37(2):623–631
10. Choudhary SK, Jadoun RS (2014) Current advanced research development of electric discharge machining (EDM): a review. Int J Res Advent Technol 2(3)

11. Jain VK (2002) Electric discharge machining. In: Advanced machining processes. Allied Publishers, India, pp 126–186
12. Dwivedi AP, Choudhury SK (2015) Comparative assessment of MRR, TWR and surface integrity in rotary and stationary tool EDM for machining AISI D3 tool steel. In: Proceedings of the world congress on engineering 2015, WCE 2015, 1–3 July, 2015, London, U.K (Lecture Notes in Engineering and Computer Science), pp 1219–1224

Heat Transfer Performance for an Obliquely Impinging Slot Jet on a Convex Surface

Satyanand Abraham, Abhijeet B. Kakade and R.P. Vedula

Abstract Experimental measurements for the local variation of effectiveness, pressure and Nusselt number for straight and inclined slot jets impinging on a convex cylindrical surface are reported in this study. The curvature ratio, defined as the ratio of slot width to diameter of impingement target surface (b/D) was kept constant at 0.045. Data are reported for Reynolds number, based on the velocity of the jet and width of the slot, equal to 8500 for jets inclined at 0°, 30° and 45° to the jet axis. The non dimensional distances between jet exit and convex surface (H/b) equal to 4, 6, 8 and 10 were studied. The results show that the effectiveness increases on the downhill side but exhibits a rapidly decreasing trend on the uphill side with increase in inclination angle. The maximum pressure coefficient and Nusselt number shifts towards the uphill side for obliquely impinging jets. Detailed distributions of effectiveness and Nusselt number show that the entrainment from the top and bottom edges of the jet after impingement penetrates inwards causing an effectiveness variation along slot height direction at large circumferential distance from impingement point and increases heat transfer at those positions by increasing the turbulence.

Keywords Convex surface · Effectiveness · Heat transfer · Heated jet · Inclined impingement · Pressure variation · Slot jet

Nomenclatures

A_{foil} Area of foil, m^2
b Width of slot, m

S. Abraham (✉) · A.B. Kakade · R.P. Vedula
Department of Mechanical Engineering, Indian Institute of Technology Bombay, Mumbai, India
e-mail: abrahamsatyanand@gmail.com

A.B. Kakade
e-mail: abkakadenec@gmail.com

R.P. Vedula
e-mail: rpv@iitb.ac.in

S.-I. Ao et al. (eds.), *Transactions on Engineering Technologies*,
DOI 10.1007/978-981-10-1088-0_9

Cp	Coefficient of pressure, $(P - P_{amb})/(0.5\rho U^2)$
D	Diameter of convex surface, m
d	Diameter of circular jet tube, m
H	Jet- to-plate distance, m
h	Heat transfer coefficient, W/m^2K
I	Current, A
k	Thermal conductivity of air, W/mK
Nu	Nusselt number, hb/k
P	Pressure, Pa
q	Heat transfer, W
q″	Heat flux, W/m^2
Re	Reynolds number, ρUb/μ
r	Direction along convex surface
T	Temperature, K
U	Average exit velocity of jet, m/s
V	Voltage, V
y	Direction along slot height

Subscripts

amb	Ambient
aw	Adiabatic
j	Jet
loss	Loss
total	Total
w	Wall

Greek

θ	Inclination of impinging surface with jet center line
η	Effectiveness
ρ	Density of air
μ	Dynamic viscosity of air

1 Introduction

Jet impingement heat transfer is characterized by high localized heat transfer coefficients which are useful in cooling or heating of surfaces which experience severe thermal environments. This technique is widely used in food, textile and paper industries. An impinging jet with a temperature equal to the surrounding ambient is typically referred to as an isothermal jet while a jet with a temperature different from the surrounding is referred to as a non-isothermal jet. A non

isothermal jet requires an additional parameter, effectiveness, which characterizes the entrainment of the surrounding fluid by the impinging jet in addition to heat transfer coefficient to characterize the heat transfer performance.

Heat transfer results on a cylindrical convex surface with an isothermal slot jet for various relative curvatures, ratio of jet diameter to diameter of curved surface, b/D, were reported in [1]. At high circumferential distance values, surfaces with lower curvature were reported to experience higher Nusselt number. This was attributed to the reduction in momentum and energy transport by the flow stabilizing behavior of curvature. Heat transfer results on a hemispherical convex surface for a circular jet impinging were reported in [2]. The maximum stagnation Nusselt number was observed at H/d = 6 for lower Reynolds numbers and at H/d = 8 for higher Reynolds numbers. The stagnation Nusselt number was also reported to increase with increasing relative curvature. A secondary maximum at r/d = 2 was reported and the Nusselt number distribution along the circumferential direction was relatively insensitive to curvature ratio after this position. Heat transfer data on a hemispherical convex surface with obliquely impinging circular jet was reported in [3]. Results showed a shift in the maximum Nusselt number from the impinging point to a maximum of 0.67 times the nozzle diameter towards the uphill side. Heat transfer characteristics on a semi-circular convex surface with a slot jet was reported in [4] by using the liquid crystal method. Secondary peaks of Nusselt number were observed because of transition of wall jet from laminar to turbulent and the circumferential position of the peaks were reported to decrease with increase in Reynolds number. The secondary peaks were noticed to diminish for H/b > 8.

Pressure distribution on a cylinder in the presence of slot jets with width varying from 0.06 to 2.5 times the cylinder diameter were reported in [5]. Results showed that the smaller jets gave lesser pressure drop in the wall jet region. Analytical and experimental studies on pressure distribution on a flat plate with obliquely impinging jets were reported in [6]. Results showed that for inclined jets maximum pressure on the impinging surface shifted from the geometric impinging point to the uphill side. This was attributed to the shift in the stagnation point to the uphill side where the velocity becomes zero. Experimental studies on pressure distribution and heat transfer on a flat plate with inclined impinging slot jets were reported in [7]. A shift of the stagnation point and thus the maximum pressure to the uphill side was observed and the maximum Nusselt number was reported to shift to the uphill side.

Experimental data for effectiveness on a flat plate with a circular non-isothermal jet were presented in [8]. The effectiveness was reported to be independent of Reynolds number. The values decrease with increasing H/d and the drop was reported to be very significant for values of distance between the plate and jet greater than the length of the potential core. Analytical calculations of effectiveness were presented in [9] and the match with experimental data for H/d > 5 and x/d > 2 was reported to be satisfactory. A method using linearity in the wall temperature and heat flux variation to extract heat transfer coefficient and effectiveness was reported in [10].

There is a reasonably large volume of work reported for the heat transfer performance of isothermal slot jets impinging on a convex surface. However, studies

for non-isothermal jets are rare available either for normal or inclined impinging slot jets. Effectiveness and Nusselt number data for a non-isothermal slot jet were reported in [11]. However, only circumferential variations at the midway location along the height of slot were reported there. This chapter is a revised version of [11] and additional data on pressure and local distribution of effectiveness and Nusselt number has been included for better understanding of flow behaviour.

2 Experimental Setup and Methodologies

Experimental setup and methodology are similar to that explained in [11] and are reported here for the sake of completeness. A schematic of the experimental setup used in the current study is shown in Fig. 1. Air supplied by a compressor was first stored in a pressure vessel and then routed through a control valve and venturi meter to a plenum chamber. The pressure drop across the venturi meter measured by a water manometer was used to calculate the volume flow rate.

The absolute pressure measured at the throat of the venturi meter was used to estimate the density to calculate the mass flow rate from the measured volume flow rate. A provision for heating the jet to a temperature well above the ambient was included by providing two heaters in series in the flow path after the venturi meter. Air from the heaters was passed into the plenum chamber which had an initial diverging angle of 10° and then subsequently a constant area duct to accomplish uniform flow at the exit section to which the jet plate was connected. The jet plate had an accurately machined slot to which a rectangular section was connected which provided a developing length equal to ten slot widths before the jet emerged. The heaters and the setup downstream of heaters were insulated to minimize heat loss to the ambient. The jet temperature was measured with 8 thermocouples at the exit of the plenum chamber.

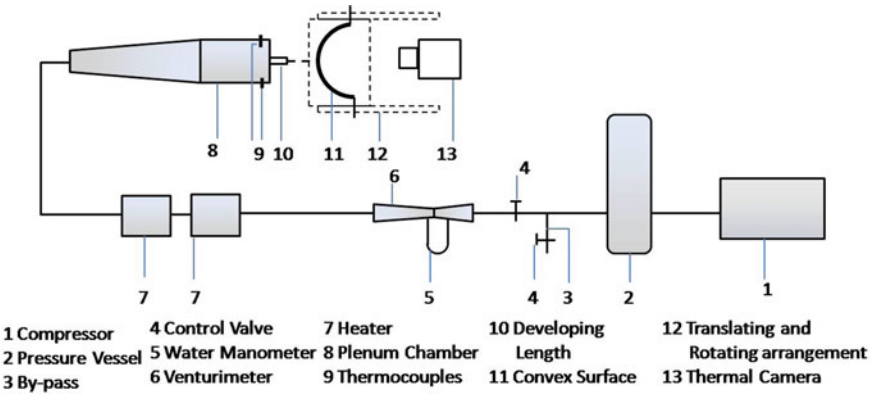

Fig. 1 Schematic of experimental setup

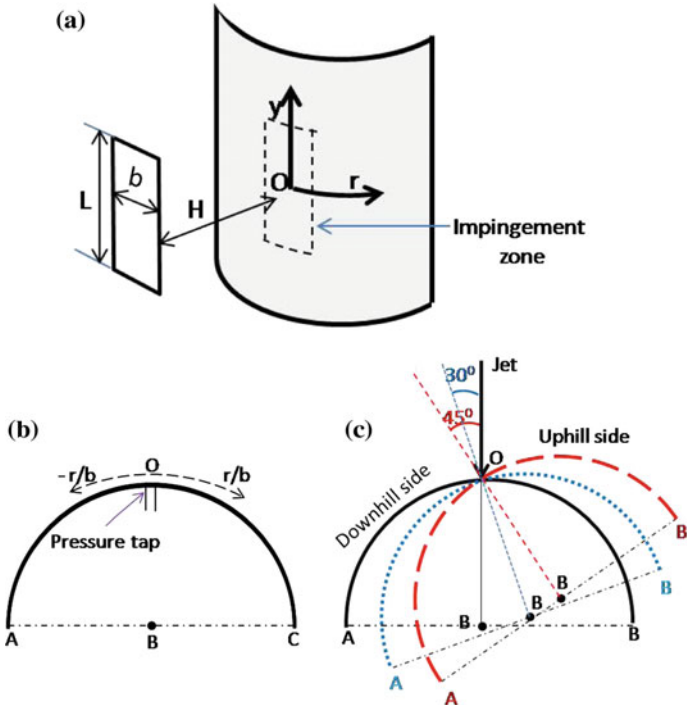

Fig. 2 **a** Co-ordinate system; **b** position of pressure tap; **c** inclination of curved surface

The slot jet height to width ratio was kept constant at 40. A stainless steel foil of thickness 0.11 mm was used for making the cylindrical convex impingement surface for heat transfer measurements. The coordinate system used in the present study is shown in Fig. 2a. The origin of the coordinate system, O, is at the midway location along the height of slot at the impingement point and the normalized distance along the circumference is termed as 'r/b'. The uphill side is on the '+r/b' region and the downhill side on the '−r/b' region. The normalized distance along the height of the slot is termed as 'y/b'. For pressure measurement, a half section of a hollow acrylic pipe was used with a pressure tap at the center as shown in Fig. 2b. The pressure tap was located at the midway location along the height of slot and was connected to an inclined water manometer. Circumferential variation of pressure on the impinging surface was measured by rotating the surface about the point B.

To study the influence of oblique impingement of jet, the impinging surfaces were rotated about the point O instead of inclining the jet as shown in Fig. 2c. The inclination was measured from jet axis with $\theta = 0°$ being the configuration perpendicular to convex surface. The surfaces were attached to a traversing mechanism which was used to change H/b and inclination with respect to the jet. The ratio of the impinging surface distance from the jet to the jet width, H/b, was varied between 4 and 10. The diameter of the impinging surface was chosen such that the

curvature ratio (b/D) was equal to 0.045. Reynolds numbers, based on jet exit velocity and width of slot, equal to 8500 was studied for 0°, 35° and 45° inclination angles. The inclined jet can also be viewed as a normal jet with the geometric impingement point linearly offset from the 0° inclination configuration since the impingement surface is a cylindrical one.

For heat transfer measurements copper bus bars soldered to the ends of the impinging surface were connected to an AC power source and current was passed through the curved surface to heat it to obtain a constant wall flux condition. The jet impinged on the convex surface and the concave side of the impingement plate was painted black and a thermal image of the concave surface was taken with an infrared camera to obtain the wall temperature distribution under steady state conditions. The temperature gradiant across the thickness of foil is very small that the temperature measured on the concave surface can be used for further calculations. The thermal image captured is a planar one and a geometric correction was applied to correctly locate the measured temperature at the corresponding positions on the convex surface. The concave surface experienced a heat loss also since it was exposed to ambient. This heat loss was experimentally measured by insulating the convex surface and supplying heat to the surface such that it reached temperature values encountered in the experiments with impingement. The total heat input to the foil was evaluated as the product of voltage drop across the foil and the current flowing through it. The net heat flux transferred to the jet was calculated as the difference between the total heat flux given and the heat flux lost to surrounding as in Eq. (1).

$$q_{total} = VI \quad q''_w = \frac{q_{total} - q_{loss}}{A_{foil}} \tag{1}$$

In non-isothermal experiments a hot jet was used which entrains the relatively cooler surrounding fluid. The effectiveness which is also required to evaluate the heat transfer performance suggested in [9] is defined as follows.

$$\eta = \frac{T_{aw} - T_{amb}}{T_j - T_{amb}} \tag{2}$$

T_{aw} is the adiabatic wall temperature, i.e. temperature of the wall when no heat transfer happens from the wall. The method for calculating T_{aw} explained in [10] was used in current study and is as follows.

$$q''_w = h(T_w - T_{aw}) = hT_w - hT_{aw} \tag{3}$$

Since 'h' and T_{aw} are constants, the slope of plot of q''_w versus T_w at each location gives 'h' at that location and the T_{aw} is the intercept on the temperature axis. Experiments were conducted with 4 different heat fluxes and it was found that q''_w versus T_w plots were always linear. A typical case with $\theta = 0°$, Re = 8500 and H/b = 4 is shown in Fig. 3.

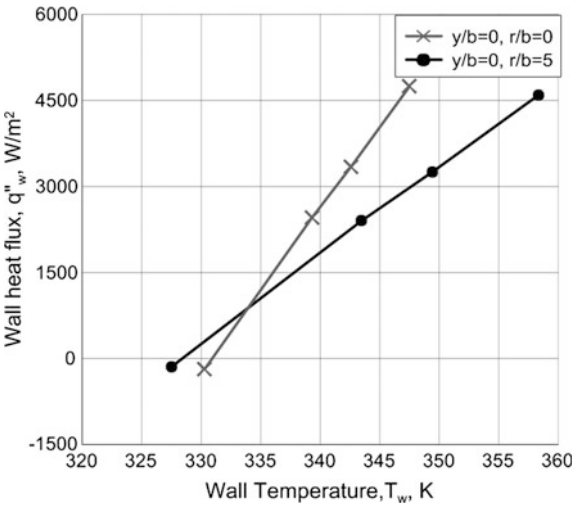

Fig. 3 q''_w versus T_w for calculation of T_{aw}

Nusselt number was calculated from the heat transfer coefficient 'h' with slot width as the characteristic length as follow

$$\mathrm{Nu} = \frac{hb}{k} \tag{4}$$

The difference in pressure between the surface, P and the surrounding ambient, P_{amb} was normalized with the average velocity of the jet at the exit of slot to get the coefficient of pressure as shown in (5).

$$Cp = \frac{(P - P_{amb})}{1/2\,\rho u^2} \tag{5}$$

The thermal camera was calibrated with respect to a calibrated thermocouple that was embedded in an isothermal copper block which was coated with the same black paint as used on the test section. The uncertainty in calibration was determined to be ±1.2 °C with 99.5 % confidence. The error in pressure measurement was equal to 5 Pa. The average uncertainty in effectiveness, coefficient of pressure and Nusselt number calculated using the methodology explained in [12] are 13, 7 and 9.3 % respectively.

3 Results and Discussion

Figure 4 shows a comparison of the Nusselt number in the present study with that reported in [1] and the data are found to be matching reasonably well.

The experimental methodology and data acquisition procedure were confirmed to be accurate for further experimentations.

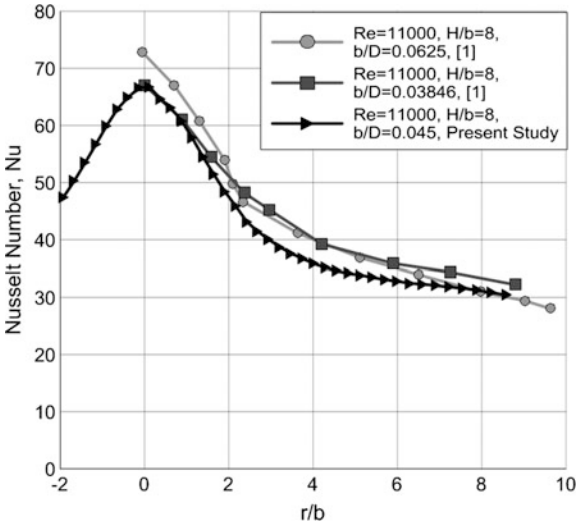

Fig. 4 Comparison of Nusselt number for normal impinging jets

3.1 Effectiveness

Figure 5a shows the detailed distribution of effectiveness for normal impingement of jet on convex surface for H/b = 4. The effectiveness values are constant in the slot height at the geometric impingement zone. The reduction in the effectiveness in the r/b direction is due to the entrainment from the shear layer on top of the impinging surface by wall jet, which is uniform throughout the slot height. The

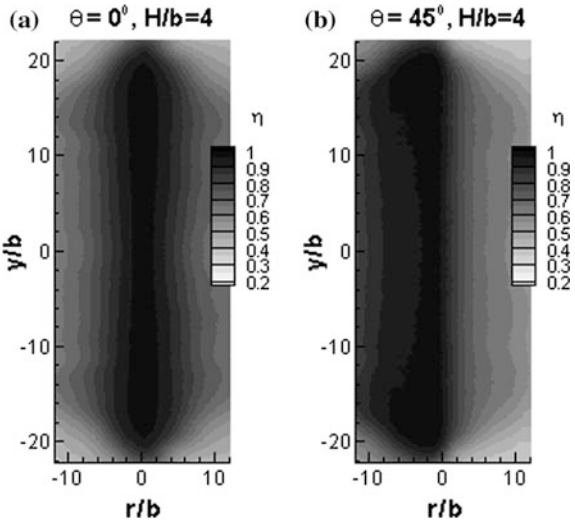

Fig. 5 Detailed distribution of effectiveness **a** θ = 0°, H/b = 4, **b** θ = 45°, H/b = 4

effectiveness values near the top and bottom edges drop much faster than the values near to the center of the slot as r/b increases due to additional entrainment of the ambient to the wall jet from the shear layer formed at the edges. Figure 5b shows the detailed distribution of effectiveness for jet with $\theta = 45°$ at H/b = 4. A high effectiveness persists on the entire downhill side and the values reduce very rapidly on uphill side. Here also contours show that at high ±r/b values the effectiveness variations are not constant along the slot height because of entrainment from the edges, but the variation is less on the downhill side compared to straight jet. It can be noticed that the edge effects do not significantly affect the data for $-15 \leq y/b \leq +15$ and the data at y/b = 0 location can be assumed to be valid in this zone for all inclinations.

Distribution of effectiveness for $\theta = 30°$ is very similar to that of 45° and is not presented here. Also variations for higher H/b are much similar to H/b = 4 to the corresponding inclinations but with lower values.

Figure 6 shows the circumferential variation of effectiveness at y/b = 0 for H/b equal to 4, 6, 8 and 10 and for $\theta = 0°$, 30° and 45°. At $\theta = 0°$ for all jet-to-plate distances, maximum effectiveness is observed at geometric stagnation point. The stagnation point effectiveness is near unity for the lowest H/b value and progressively reduces with increase in jet to impinging surface distance. The rate of reduction in effectiveness in the circumferential direction is higher for smaller H/b. The entrainment of ambient air by the incoming jet is less for lower H/b values

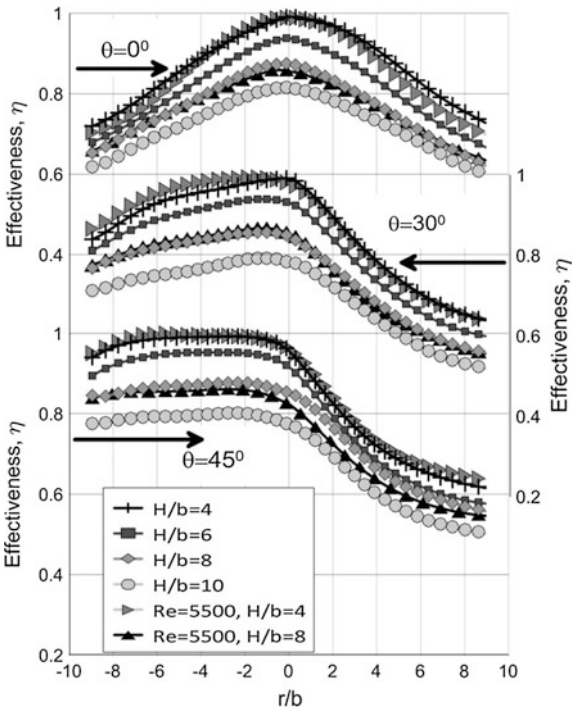

Fig. 6 Circumferential variation of effectiveness

before striking the surface resulting in high effectiveness values at the stagnation point. As the flow moves out in the circumferential direction more fluid gets entrained and effectiveness reduces. As H/b increases, the incoming jet entrains more fluid from the surrounding ambient before impingement thereby reducing the stagnation effectiveness value. At large values of r/b, the entrainment becomes so large that the differences between the different H/b values become small.

The influence of inclination angle can be seen to be very prominent for the effectiveness variations. The variation on downhill side is less, and the high effectiveness values persist to longer lengths downstream of the impinging point. The length of zone where the effectiveness is high on the downhill side increases with increase in inclination angle. This behavior is observed for all the jet to impingement plate distances reported in this study. For inclination of 45° the maximum effectiveness occurs on the downhill side, even though the difference in impinging zone and maximum values are very small. The flow accelerates on the downhill side due to which entrainment is smaller which results in higher effectiveness values. The flow decelerates on the uphill side and the rapidly growing boundary layer entrains larger quantities of surrounding air resulting in reduced effectiveness values.

Effectiveness variations for a Reynolds number equal to 5500 are also included in the figure for all three inclinations at H/b equal to 4 and 8 and noted that the variation of effectiveness with Reynolds number is negligible for all cases. This lack of dependence of effectiveness on Reynolds number has also been reported for jet impinging on a flat surface in with circular jets [8] and is attributed to the absence of the influence of Reynolds number on entrainment of the surrounding fluid by the jet.

3.2 Pressure Coefficient and Nusselt Number

Figure 7 shows the circumferential variation of pressure coefficient at y/b = 0 for H/b equal to 4, 6, 8 and 10 and $\theta = 0°$, 30° and 45°. At $\theta = 0°$ the maximum pressure is noticed to occur at the impinging point since the stagnation point and impinging points are same. For H/b = 4 this maximum value is noticed to be slightly higher than unity because the impinging surface is well within the potential core region and the velocity at the center of the jet is slightly higher than the average velocity at the exit. After the maximum value, pressure coefficient drops rapidly and becomes 0, i.e. the pressure becomes atmospheric at about r/b = ±1. Values continue to decrease to even below atmospheric and reach a minimum value of −0.2 at around r/b = ±2 and then slowly increases to atmospheric pressure. The location till where the pressure drops signifies the region where the velocity accelerates. For inclined jets maximum pressure values shift to uphill side due to shift in stagnation point to uphill side as observed in previous studies, [6, 7], for flat plates. The shift is in the range 0.5–0.7 times the slot width for both inclinations. The stagnation point pressure value decreases with increase in inclination due to

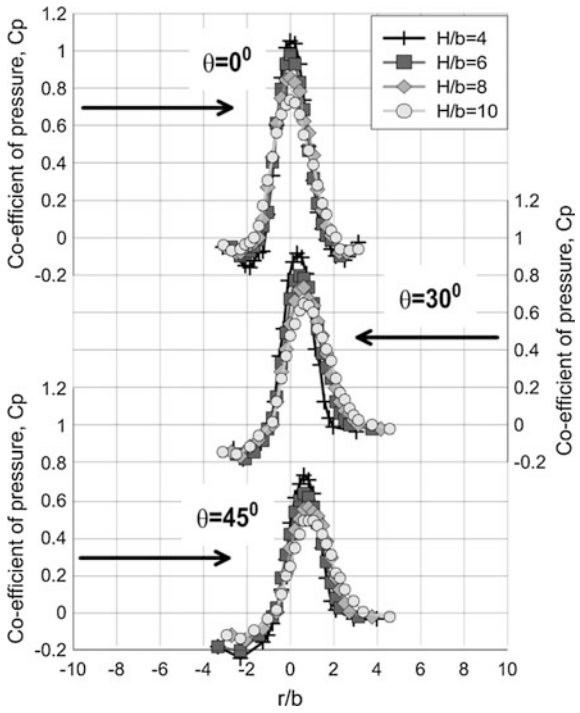

Fig. 7 Circumferential variation of coefficient of pressure

reduction in the momentum change of jet on impingement with inclination. The pressure on the downhill side drops much faster than that on the uphill side after the stagnation value. The values fall below zero on downhill side and an increase in the inclination further reduces the values. However on uphill side the values do not fall below zero and remain close to zero.

Figure 8a shows detailed distribution of Nusselt number at H/b = 4 for θ = 0°. Nusselt number is constant in the slot height at r/b = 0. As r/b increases Nusselt number drops rapidly. It is observed that the drop in Nusselt number with r/b is lowest at the edges. This may attributed to the entrainment of ambient from top and bottom edges and thereby increase in the turbulence, resulting in increased heat transfer. Figure 8b shows detailed distribution of Nusselt number at H/b = 4 for θ = 45°. The peak Nusselt number is observed to have shifted to uphill side. After the peak the Nusselt numbers reduce rapidly on the downhill and the uphill sides. The Nusselt number variation for 30° inclination is similar to the 45° inclination.

Figure 9 show the circumferential variation of Nusselt number for Re = 8500 for inclination angles equal to 0°, 35° and 45° for all jet-to-plate distances studied. The stagnation Nu increases as H/b increases till H/b = 8 and then falls. The highest heat transfer at this H/b value was also reported in [1]. At around r/b = 4 the slope of the Nusselt number variation changes. This may because of transition of wall jet from laminar to turbulent as reported in [4].

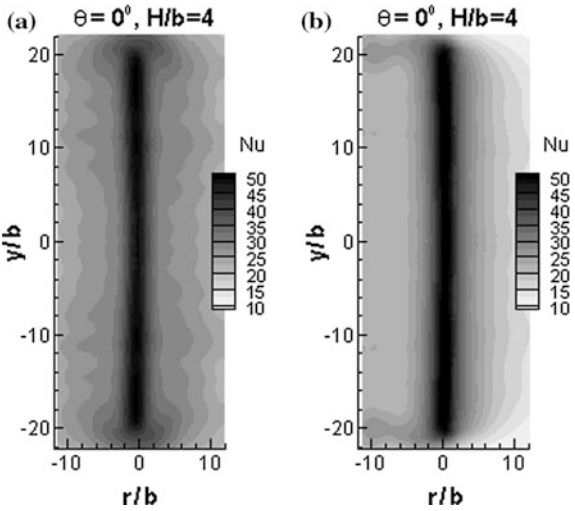

Fig. 8 Detailed distribution of Nusselt number **a** θ = 0°, H/b = 4, **b** θ = 45°, H/b = 4

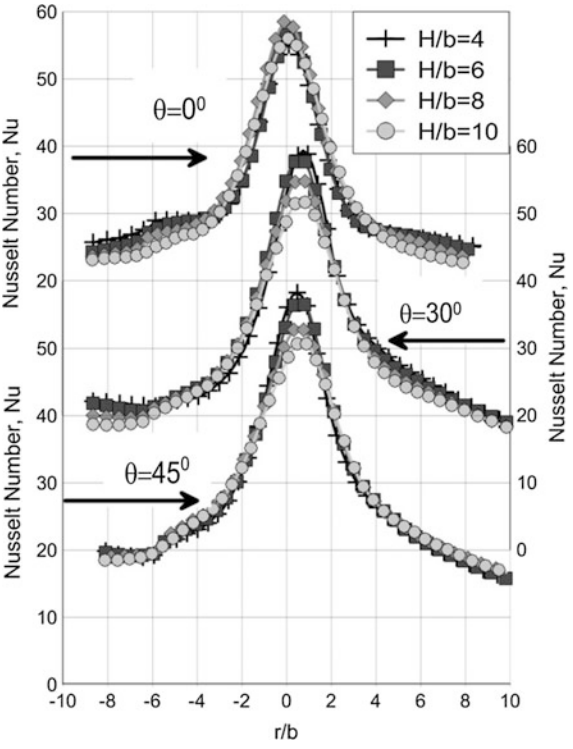

Fig. 9 Circumferential variation of Nusselt number

For inclined jets the shift of the peak Nusselt number towards the uphill side is clearly observed. The shift is maximum for $\theta = 30°$ and equal to 0.7 times the slot width, which is nearly equal to the shift in peak pressure coefficient for inclined impingement as shown in Fig. 7. For both inclinations H/b = 4 shows the maximum Nusselt number. Along the increasing circumferential direction from the peak value zone, Nusselt number decreases both on uphill and downhill sides due to the thickening of the boundary layer. The boundary layer thickens more rapidly due to the adverse pressure gradient on the uphill side resulting in a steeper drop of the Nusselt number values after the peak when compared to the downhill side. The drop is noticed to be higher for the higher inclination angle. After the sudden drop, Nusselt number becomes almost constant in downhill side after r/b = 6. The maximum Nusselt number values for inclined jets decrease as H/b increases and come below the normal impingement jet values since the stagnation zone is much larger in inclined jets due to which the jet momentum is smaller compared to normal jets. However, while the trend with varying H/b is clearly visible, the differences in magnitude of the Nusselt number are within the calculated uncertainty limits.

4 Conclusions

An experimental investigation for impingement of a slot jet on a cylindrical convex surface has been reported here. The inclination affects the effectiveness significantly with higher values observed in the downhill region. The length of zone where the effectiveness is high on the downhill side increases with increase in inclination angle. This behavior is observed for all the jet to impingement plate distances reported in this study. The effectiveness values reduce on the uphill side with increase in inclination angle. The detailed distribution shows that entrainment of ambient from edges reduces effectiveness values at those positions much faster than that at center region.

The presence of obliquely impinging jets causes a shift in the maximum pressure coefficient and Nusselt number towards the uphill side because of shift in stagnation point to this side. Maximum pressure coefficient also decreases with increase in inclination. The highest Nusselt number values are observed at the closest jet to surface spacing for all inclination angles in contrast to the normal impingement case where the Nusselt number first rises and then falls.

References

1. Gau C, Chung CM (1991) Surface curvature effect on slot-air-jet impingement cooling flow and heat transfer process. J Heat Transfer 113:858–864

2. Lee DH, Chung YS, Kim DS (1997) Turbulent flow and heat transfer measurements on a curved surface with a fully developed round impinging jet. Int J Heat Fluid Flow 18:160–169
3. Lim KB, Lee CH, Sung NW, Lee SH (2007) An experimental study on the characteristics of heat transfer on the turbulent round impingement jet according to the inclined angle of convex surface using the liquid crystal transient method. Exp Thermal Fluid Sci 31:711–719
4. Chan TL, Leung CW, Jambunathan K, Ashforth-Forst S, Zhou Y, Liu MH (2002) Heat transfer characteristics of a slot jet impinging on a semi-circular convex surface. Int J Heat Mass Transf 45:993–1006
5. Schuh H, Persson B (1964) Heat transfer on circular cylinders exposed to free jet flow. Int J Heat Mass Transf 7:1257–1271
6. Beltaos S (1976) Oblique impingement of circular turbulent jets. J Hydraul Res 14(1):17–36
7. Akansu YE, Sarioglu M, Kuvvet K, Yavuz T (2008) Flow field and heat transfer characteristics in an oblique slot jet impinging on a flat plate. Int Commun Heat Mass Transf 35:873–880
8. Goldstein RJ, Sobolik KA, Seol WS (1990) Effect of entrainment on the heat transfer to a heated circular air jet impinging on a flat surface. J Heat Transfer 112:608–611
9. Hollworth BR, Wilson SI (1984) Entrainment effects on impingement heat transfer: part I-measurements of heated jet velocity and temperature distributions and recovery temperatures on target surface. J Heat Transfer 106:797–803
10. Fenot M, Vullierme JJ, Dorignac E (2005) A heat transfer measurement of jet impingement with high injection temperature. C. R. Mecanique 333:778–782
11. Abraham S, Kakade AB, Vedula RP (2015) Convex surface heat transfer behaviour in the presence of obliquely impinging non-isothermal slot jets. In: Lecture notes in engineering and computer science: proceedings of the World Congress on Engineering 2015 (WCE 2015), London, UK, pp 1273–1278, 1 July–3 July 2015
12. Coleman HW, Steele WG Jr (1989) Experimentation and uncertainty analysis for engineers. Wiley, New York

Combustion of Coal in Fluidized Bed: Performance Analysis

Abdulkarim Nasir, Shuaibu Ndace Mohammed and Abubakar Mohammed

Abstract Fluidized bed combustion (FBC) technology has the potential to use alternative fuel sources such as coal, wood, or waste and it has the ability to reduce and control the emissions of oxides of nitrogen (NO_x) and sulphur (SO_x). This technology is capable of alleviating the energy problems of the Nigerian nation—a country with billions of tonnes of untapped coal and ironically with gross insufficient electrical energy supply. The aim of this research is to investigate the applicability of this technology to Nigerian low-grade coals (Enugu sub-bituminous coal). To achieve this, a pilot fluidized bed combustor of 3 m tall and 155 mm diameter was fabricated. The experiment was carried out using Enugu sub-bituminous coal of size 850 μm. The effect of coal batch sizes was investigated by feeding the coal over-bed in batches of 0.15, 0.25, 0.35, 0.45 kg/batch. The bed and free-board temperatures were measured using digital thermocouples and the pressure drop was monitored using an orifice meter. The minimum fluidization velocity was obtained to be 1.64 and 1.91 m/s for a coal batch feed of 150 and 450 g respectively.

Keywords Coal · Combustion · Energy · Enugu · Fluidized bed · Sub-bituminous coal

A. Nasir (✉) · S.N. Mohammed · A. Mohammed
Department of Mechanical Engineering, Federal University of Technology, Minna, Nigeria
e-mail: a.nasir@futminna.edu.ng

S.N. Mohammed
e-mail: snm3362@futminna.edu.ng

A. Mohammed
e-mail: a.mohammed@futminna.edu.ng

S.-I. Ao et al. (eds.), *Transactions on Engineering Technologies*,
DOI 10.1007/978-981-10-1088-0_10

1 Introduction

The long periods of availability of cheap liquid and gaseous fuels have favourably influenced industrial and technological development worldwide. At the same time, it has also resulted in an almost complete interruption of research and development of new technologies for coal and other solid fuels combustion [1]. Coal has been increasingly neglected for energy production, especially in thermal energy production for industry. Only countries with extensive coal reserves, traditionally oriented to coal as an energy source continued to rely on coal, at least in large utility electric power systems. A similar orientation was also characteristic of some undeveloped countries rich in coal, which could not afford the use of oil even when it was relatively cheap [1]. It is estimated that 41 % of global electricity generation depends on coal. Its utilization is even higher in countries like South Africa and PR China where it is averaging 93 and 79 % respectively [2]. Fossil fuel combustion is a major energy source in the world. The combustion has been a strong driving force behind the industrial revolution since the 18th century. Lately, the rapid growing use of fossil fuels has been causing severe environmental impact due to pollutant emissions. Acid rain is caused by the emission of nitrogen and sulphur oxides (NO_x, SO_x) which converts to nitric and sulphuric acid in the atmosphere. Particle emissions, especially fine particle, have been found to be a health risk [3], in addition to carbon dioxide concentration in the atmosphere. This is expected to increase the greenhouse effect and hence the average temperature of the earth. Combustion of solid fuel for heat and energy is as old as recorded history. While energy needs are greater and the uses more varied, combustion remains the single leading source of energy production. The energy produced by combustion is no longer used as a direct source for most people. It is used to generate steam for personal and commercial uses such as the generation of electricity. Maximizing the amount of heat extracted from the coal burned is critical for affordable energy production and lessening the impact of this combustion on the environment. It is widely acknowledge that coal, as one of the main energy sources, plays an important role throughout the world. The utilization of low-grade coal in energy is necessary due to increasing cost and decreasing reserves of high-grade fuels. Less work has been reported on combustion of Nigerian coals [4], but since fluidized bed presents a typical problem of non-linearity in operational condition, it becomes difficult to assume existing operational parameters for Nigerian coals. Such non-linearity of coal combustion manifest in heat and mass transfer since these depends on fluid flow conditions.

1.1 Fluidization

The behavior of particles as though it is a fluid is called fluidization. It usually occurs when air is passed through a bed of small particles and setting them in

motion, in the direction of flow. The fluid flow like property acquired will depend on the air inflow rate and the particles size. The smaller the particle sizes the more the fluidized action. At a very low flow rate fluid simply passes through the void spaces between stationary particles without interaction of the particles with the gas flow [5]. As the velocity of flow increases, at first the particles tends to rearrange themselves, to accommodate the flow but with further increase in velocity of flow they are thrown into a state of motion similar to that of boiling liquid because the excess gas flow passes through as a bubble.

1.1.1 Fluidization Regimes

Kuni and Levenspiel [6] have described the fluidization regime and behaviours occurring in fluidized beds. The fluidized state of loose material is effectively the opposite of fixed bed state of loose material. Loose material reposed on a horizontal surface is characterised by immobile particles that lie on one another, touching each other at numerous points of contact, at which they exert frictional and adhesion forces. Gravity force, the weight of the particles and the overall weight of the bed, are transmitted in all directions via the contact points. Normally, the behaviours occurring in fluidized beds are categorized in various ways, including smoothly fluidized, bubbling, slugging, spouting, entrained bed, etc. When a bed of solids is exposed to an increasing upward flow of gas, the pressure drop across the bed increases with increase gas flow. At the point in which the pressure drop just balances the weight of the bed, the bed is fluidized. The velocity at which this occurs is the minimum fluidization velocity. As the velocity is increased further, the bubbles occupy more and more of the bed. The bed operating in the bubbling mode, at velocities below the terminal velocity of most of the bed particles, is normally called a fluidized bubbling bed. Most fluidization processes are operated in this regime. As the velocity to the bed is increased further, the fluidized bed which does not have a distinct surface. At high velocities, which exceed the terminal velocity of all the bed particles, bubbles tend to lose their distinct shape. The bed level disappears and there is a continuous density gradient from the bottom of the vessel to the top. Eventually the fluid bed becomes an entrained bed.

1.1.2 Minimum Fluidization Velocity

Minimum fluidizing velocity is superficial gas velocity at which a bed of particles begins to first exhibit fluid-like properties. The superficial velocity at minimum fluidization, including the bubble rise velocity, bubble fraction, bubble size and the inter phase exchange coefficient, yet it is extremely difficult to predict accurately. If experimental data are available, they naturally should be used. Else, the simplest way of estimating it is to resort to an equation which describes the pressure drop across fixed beds, developed by Ergun [7]. Ergun made his general equation from macro level observations, as a result he did not account for most variables such as

surface roughness. Further experiments conducted alter the pressure after surface roughness was determined [8]. The alternative expression derived by Wen and Yu [9] was achieved through correlation of a wide variety of experimental data and has been shown to be satisfactory for coal [10]. However, significant disagreement was found between predictions of the Wen and Yu's correlation with experimental results for coal at high temperatures [11–13]. Thus further modification of the Wen and Yu correlation has been given by Johnson [11] as shown in Eq. (1) which is suitable for the prediction of minimum fluidizing velocity for coal at high temperature. Though a standard deviation of 30 % existed, further studies also showed that this correlation gives good agreement with the experimental results.

$$U_{mf} = \frac{\mu}{d_p g}\left\{\left(25.25^2 + 0.0651\frac{d_p^3 \rho_f(\rho_p - \rho_f)g}{\mu^2}\right)^{\frac{1}{2}} - 25.25\right\} \quad (1)$$

Where U_{mf} is the minimum fluidization velocity, d_p is the diameter of sand, μ is the viscosity of the fluid, ρ_p is the density of the particles, ρ_f is the density of the fluid, g is the gravitational acceleration constant.

1.1.3 Particle Size

Commercial fluidized bed combustors generally operate with mean particle sizes in the range 0.5–1 mm diameter and mostly comprise non-combustible particles [14, 15]. The smaller particles are subjected to elutriation, while larger particles lead to low heat transfer coefficients due to the gas film between particles size ranges from 5 to 10 mm for small-scale units, up to 30 mm for large-scale units. Broughton and Howard [16] also concluded the inert particle size dominates the fluidized bed characteristics since it comprises of more than 98 % of the bed materials.

1.2 Fluidized Bed Combustion

Fluidized Bed Combustion (FBC) seems to be the most promising technique for use of low-grade solid fuels and to reduce the quantity of atmospheric pollutant such as SO_2 and NO_x released during the combustion. The term fluidized bed describes a finely granulated layer of solid material (referred to as "the mass") that is loosened by fluid flowing through to such an extent that the particles of solid material are free to move to a certain degree. It is called "fluidized" because the solid material takes on properties similar to those of a fluid. The status of any particle-fluid system is limited by two bench marks: the so called minimum fluidization velocity and the entrainment velocity. When a system is operating between these two benchmarks it is known as a bubbling fluidized bed or bubbling AFBC. When a fluidized bed

combustion system is designed to operate above the entrainment velocity it is known as a circulating fluidized bed.

The major advantages of fluidized-bed combustors are uniform temperature distribution, a large solid–gas exchange area, high heat-transfer coefficients, fuel flexibility (various possible sizes and moisture contents, etc.), stable combustion at low temperatures and generally no moving parts [17]. It however, have some disadvantages such as additional required equipment for solid separation or gas purification, erosion of the combustor interior, agglomeration and difficulties operating it at partial load [18, 19]. Despite these drawbacks, FBC is arguably the best clean-coal technology due to its high combustion efficiency and reduced environmental impact [17].

In Nigeria, coal can be found in areas like Enugu, Afuze, Okaba, Lafia and Ogbojoga. Lafia and Enugu coal estimate alone amount to approximately 1000 million tones [5]. Coal was discovered in Nigeria in 1909 and the mining activities began in 1915 at Ogbete in Enugu state, Nigeria [20]. Table 1 shows the coal deposition in Nigeria. The first energy resources to be exploited for rail transport and electricity generation in Nigeria was coal. However, coal remains the smallest contributor to the overall fuel mix and ranks low in worldwide production [21]. Today, the utilization of Nigerian coal is mostly for cement production for use in foundries, brick factories, bakeries and as a domestic cooking fuel. Coal is expected to play a vital role in numerous proposed power generating plants due to the projected increase in global energy demand to between 12 and15 GW by 2025 [22]. Recently, a Chinese consortium signed US$3.7 billion agreement with Nigeria for coal mining and power plant construction with the future goal of generating up to 30 % of Nigerian electricity from coal [23]. The proven coal reserves in Nigeria are estimated to be about 2.5 billion tonnes and lignite constitute 250 million tonnes while the remainder are mainly sub-bituminous [20, 24]. Though Nigerian coals are mainly low rank, its caloric values are comparable with universal figures of the same rank coal. They have also been reported to have good potential for gasification

Table 1 Coal deposits in Nigeria

Location	Indicated reserve (proven)	Inferred reserve
Enugu	54	200
Ezimmo	56	60
Owukpo	57	75
Okaba	73	250
Ogboyoga	107	30
Inyi	20	320
Asaba/Ogwuasi (lignite)	250	30
Lafia Obi (cooking coal)	22	250
Others	–	1360
Total	639	2701

and liquefaction and have fine combustion characteristics [24]. They burn with long flames, which are desirable even though they require large combustion spaces [25].

There are limited literatures in the performance of Enugu sub bituminous in FBC. However, recently, Nasir et al. [26] presented a study on Enugu sub-bituminous. This chapter presents the performance analysis of fluidized bed combustor using coal as fuel.

2 Materials and Method

2.1 Materials

The materials used in this study are Enugu sub bituminous coal and limestone. Sand particle of diameter 850 μm was used as bed material. Propane gas and air was used to fluidize the bed and also raise the bed temperature to 750–900 °C.The sub bituminous coal is dull black and generally contains 20–30 % moisture. The heat content ranges from 16 to 24 million Btu/ton and is used for generating electricity and space heating. Sub bituminous coal is the highest coal in rank after lignite and it is softer than bituminous. The properties of the Enugu sub bituminous coal and Limestone chemical composition are shown in Table 2.

2.2 Sample Preparation

The sample was prepared by fragmenting coal lumps of the Enugu Sub-bituminous into small sizes using a crusher. A sieve size of average particles diameters of 0.85 mm was used. Visual examinations were used to remove any unusual size of particles. Inert bed material was prepared for the 0.85 mm size for experimentation.

Table 2 Properties of Enugu sub-bituminous coal and limestone chemical composition

Enugu sub-bituminous		Limestone	
Properties (%)	Value	Chemicals	Composition (%)
Moisture	7.0	CaO	53.50
Ash (% dry)	3.0	Mg	0.80
Volatile matter	40.3	SO_2	2.00
Calorific value (MJ/kg)	37.5	Al_2O_3	1.50
Carbon	75	Fe_2O_3	1.20
Hydrogen	6.0	SiO_3	0.10
Sulphur	3.0	LOI	42.41
Oxygen	13	Equi $CaCO_3$	96.00
		Equi $MgCO_3$	3.43

The density of the coal particles was measured using mass-volume ratio by pouring a known mass of the coal particles into a container of known volume.

2.3 Apparatus

Atmospheric Fluidized Bed Combustor (AFBC), compressor, laboratory test sieves, stop watch and weighing machine were employed in this study.

2.3.1 Description of Atmospheric Fluidized Bed Combustor

The AFBC was assembled by connecting the inert air/gas pipe to the compressor and gas cylinder. The four thermocouples for bed, freeboard, heat exchanger inlet and outlet temperatures were then fixed and the manometers were placed on the bed and across the orifice plate. The lower part of the vertical mild steel column contained a bed of inert material. The lower end of the cylindrical column (reactor) is the distribution chamber, plenum chamber and a ceramic tile air distributor which supports the bed when de-fluidized. A Red devil 3460 compressor with 160 l capacity and an operating temperature range of 100–1200 °C was used to supply air to the combustor through the ceramic distributor. Above the bed is a secondary airport connected 0.55 m above the bed through a 12.52 mm diameter pipe to the freeboard region. The purpose of the secondary air is to create turbulence in the freeboard region and thereby enhancing the proper mixing of the combustible gases and the volatiles liberated from the bed. The secondary air supplied would ensure the complete combustion of these gases, the volatiles and any un-burnt hydrocarbons released into the freeboard zone. The heat exchanger tube was made of aluminium bronze with an outside diameter of 13.0 mm and exposed area of 0.0245 m^2. The reactor was supported by iron brackets. Four thermocouple probes were installed in the bed, freeboard, inlet and exit of the heat exchanger tubes to measure the temperatures at these points. A pressure probe was also installed in the bed to measure the pressure variation at different flow rates and velocities. An orifice plate was inserted into the 25.4 mm pipe carrying the primary air supply to the plenum chamber so as to measure the air flow rates. A mercury filled manometer was used to measure the differential pressure across the orifice. The fuel was fed into the AFBC using the above-bed feeding method [1] due to its simplicity.

2.3.2 The Fluidized Particles

The fluidized particles are a mixture of sand particles and coarse fuel ash. Ash granules can be removed from the fluidized bed by “bottom”—type extraction or by entrainment with the flue gas once the ash particle have been sufficiently reduced in

size by the eroding action of the fluidized sand. Solid fuel can be fed into the combustor under the fluidized bed, but "over-bed" feeding is possible and easier.

2.3.3 The Combustion Processes

When coal particle enters the FBC, it goes through two distinct combustion processes; volatile combustion and char combustion. For coal, volatile burn rapidly; leaving a slow-burning residual char. Char is normally present in the bed as 1 or 2 % of the bed mass, although the concentrations may be higher or lower, depending on the fuel reactivity. Char particles are porous due to the loss of volatile matter, so combustion can take place either on the external surface, or on the much larger surface. For the coal particle to burn, oxygen must diffuse to the surface, react and products diffuse away from the surface. Thus both mass transfer and kinetic processes come into play and either or both can be rate limiting.

During the combustion process, the combustion heat is recovered via in-bed heat exchangers and adapted standard boiler equipment. Fly ash (and coarse ash) can be recycled for deep combustion with the help of the fuel feeding system. The air required for fluidization and combustion is fed via an air distributor which is commonly a nozzle tray whose design is classified. Freeboard is the section above the bed and its diameter is much larger than the bed diameter in some fluidized bed combustor. The reduced velocity in this region ensures that solid particles entrained in the gas flow return to the bed by gravity. Additional air for post-combustion of gaseous fuel components, known as secondary air, is often introduced into the freeboard region to ensure complete burn-out of the fuel. In theory, at the minimum velocity for fluidization, solid weight is just balanced by upward drag forces. Expansion is the bed reaction to the increase of velocity above the minimum. One of the inherent properties of fluidized bed is the high rate of heat transfer between the bed and the immersed bundles. The heat transfer steps in fluidized beds are generally seen to consist of three contributions: particle convection, gas convection and radiation.

2.4 Experimental Procedure

The combustor column was charged with inert bed material of sand particles with an average diameter of 0.85 mm and a limestone of 1.6 kg mass. The air compressor valve was gradually opened to allow air passed through the ceramic tile air distributor. The air velocity was gradually increased and the corresponding pressure drop across the bed was recorded until a point where further increase in the fluidizing velocity had no effect on the pressure drop across the bed (pressure drop stabilizes). At this point the bed was fully fluidized. The minimum fluidizing velocity was recorded and the bed was left to continue fluidizing for 10 min to ensure proper mixing. The behaviour of the bed was observed through a stainless

steel plate reflector. Butane gas was then introduced and burnt in the bed to raise the temperature of the bed to 750–950 °C. 0.85 mm coal particle diameter was charged into the combustor in batches of 0.15, 0.25, 0.35 and 0.45 kg per batch. The gas supply was cut off as soon as combustion can be sustained by coal alone. The combustion product was collected for analysis. The temperatures across the bed were measured carefully by adjusting the position of the thermocouple probe inserted in the temperature port in the bed. The vibrator was calibrated to continuously feeding coals into the combustor. The following parameters were measured, recorded and analysed; bed temperature, freeboard temperature, inlet and outlet water temperatures from the heat exchanger, pressure drop across bed, pressure drop across the orifice, fluidizing velocity, coal burn out time, ambient temperature, mass flow rate through the heat exchanger, inlet and outlet gas (air) temperatures (Fig. 1).

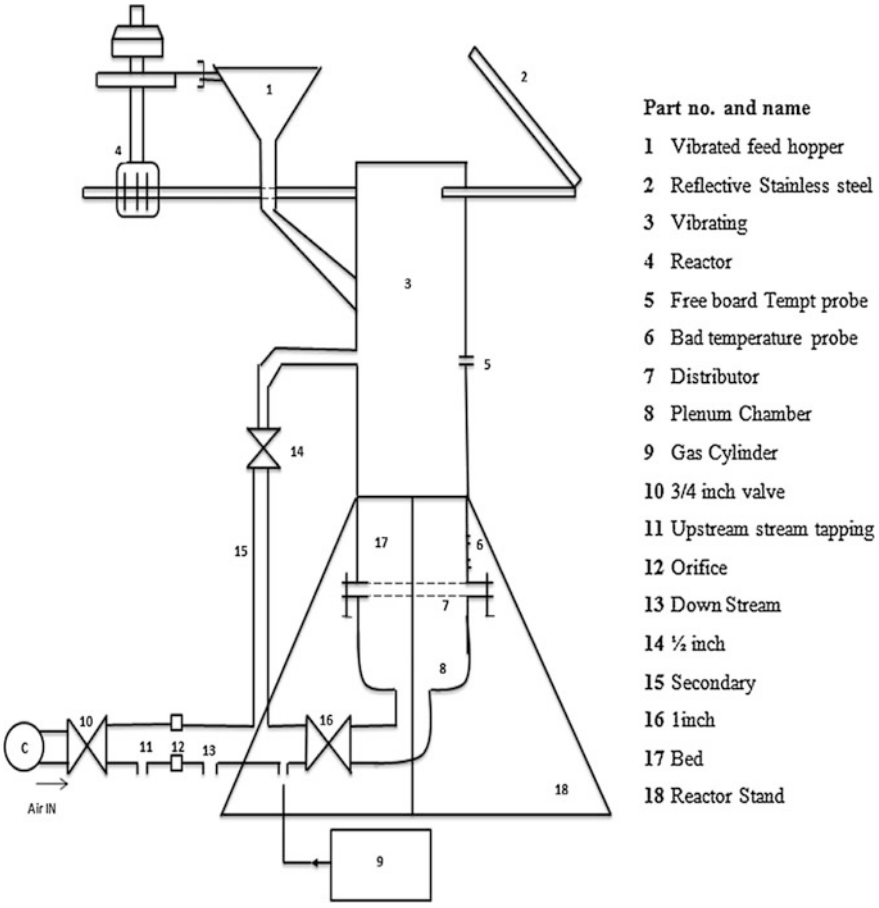

Fig. 1 Fluidized bed combustor

3 Results and Discussion

3.1 Fluidization Velocity and Pressure

As the combustion air passes through the bed, its behaviour was observed through a stainless steel reflector situated at the top of the column. At incipient fluidization, a thick cloud of dust was observed. As soon as the velocity of the compressed air was increased, the bed became fully fluidized. Figure 2 shows that as the superficial velocity increases from 0.5 to 2 m/s, the orifice pressure drop increases from about 260–4000 N/m^2. The increase in the superficial velocity was also accompanied by a corresponding increase in the volumetric flow rate (Fig. 2). Figure 3 shows that the use of batch system of weight 150–450 g with particle diameter of 0.85 mm fed into the fluidize bed increases the minimum fluidization velocity of the bed from

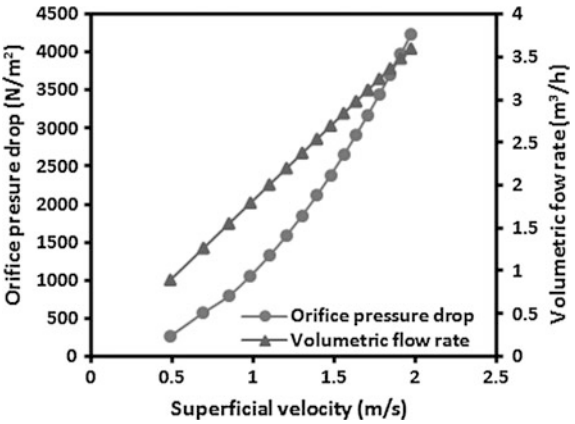

Fig. 2 Pressure drop across the orifice and the volumetric flow rate

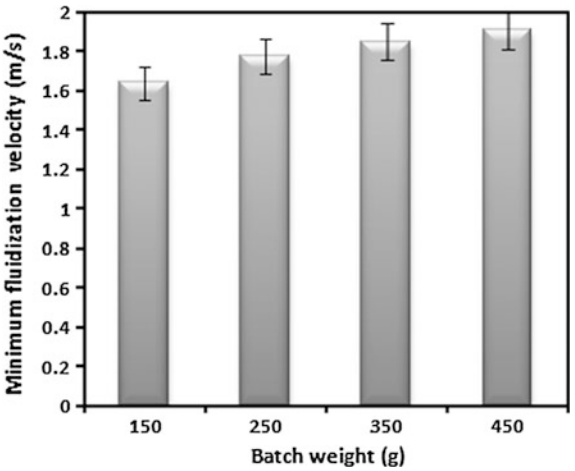

Fig. 3 Minimum fluidization velocity for different batches

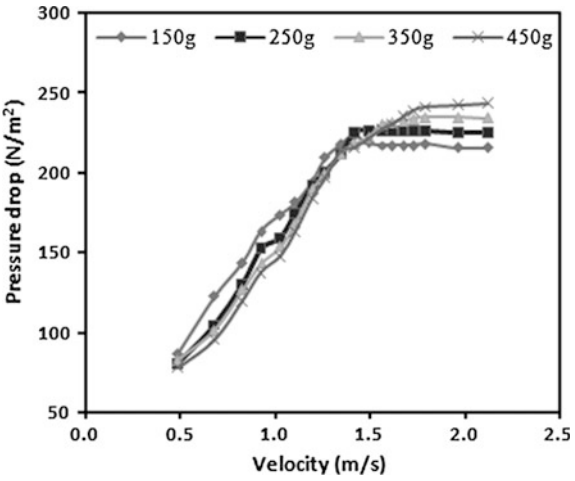

Fig. 4 Pressure drop across bed against superficial velocity

1.64 to 1.91 m/s respectively. The pressure at which the bed attained stable fluidization was lower than the theoretical value. However, the compressor nozzle pressure at which the bed became fluidized was far higher than the bed pressure. This was due to the fact that there was pressure drop along the pipe and within the plenum chamber. From theory, theoretical pressure drop is always greater than the measured and the theoretical value is indicative of the degree of gas misdistribution. Figure 4 shows that as the superficial velocity increases, the bed pressure drop also increases. This increase continues until the fluidization was attained. At fluidization further increase in superficial velocity have no consequence on the bed pressure drop. There was an increase in bed pressure drop as the batch weight increases.

3.2 Freeboard and Bed Temperature

The bed was heated to 850 °C before coal feeding began. Bed temperature reduced to 810 °C as soon as coal was added as some heat was used in heating. This is so because the coal is being heated hot to its ignition temperature. Thereafter there was continuous rise in bed temperature as the combustion process continued. It was however observed that once the temperature of the bed was above 800 °C combustion is sustained by coal and nearly complete. This was as a result of good mixing of inner particles promoted by bubbling action of the bed which allowed particles to receive radiant energy from the flame and corrective heating which helped to maintain bed temperature. The bed temperature rose to the 850 °C and fluctuates between the ranges of 840–950 °C within 2 min of coal feeding as shown in Fig. 5.

The bed temperature was observed to be higher than that in the free board; this should be due to the fact that part of the hot gases that were burnt in the bed

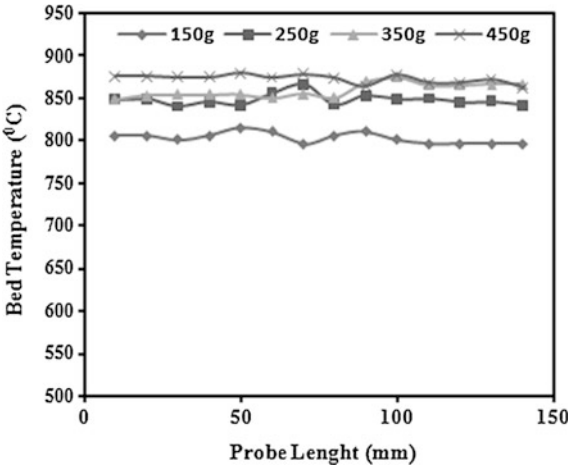

Fig. 5 Bed temperatures across probe length

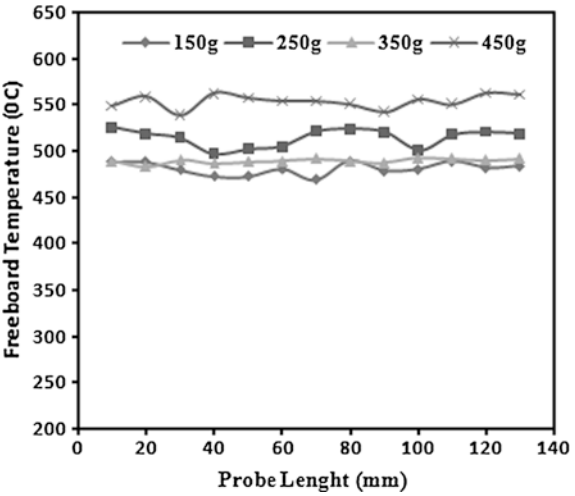

Fig. 6 Freeboard temperatures across probe length

accumulated in it. The introduction of secondary air assisted in the complete combustion within the freeboard region, Fig. 6. As coal was added to hot bed and the secondary air inlet was cut off, there was considerable pyrolytic decomposition of the coal. But as the secondary air was re-introduced, the smoke reduced, volatile matter from the hot bed raised and got burnt in the secondary air region.

Visual observation of the combustion behaviour at the start of the experiment showed that when air flow was too little, not much of the combustible gas was burnt. When it was too much its cooling and diluting effect inhibited combustion. Thus, combustion in the freeboard was only possible over a moderately wide range of secondary air flow.

4 Conclusion

Fluidized bed combustion of coal for energy and the performance and applicability of Nigerian Enugu Sub-bituminous coal in Fluidized Bed Combustor has been presented. The effect of batch feeding of coal into the FBC and the temperature profile during the combustion of the sub-bituminous coal was discussed. The maximum bed temperature of 879 °C was obtained for a batch feed of 450 g and the minimum bed temperature of 796 °C was obtained for 150 g batch feed. The attainment of 879 °C bed temperature in a short time of 2 min confirms the high convective heat transfer coefficient of FBC technology. This is made up of gas and particle convection and it is as a result of intensive gas-particle mixing.

Acknowledgment The authors wish to thank the management of the Federal University of Technology, Minna and the Tertiary Education Trust Fund (TETFund), Nigeria for funding the research.

References

1. Oka SN (2004) Fluidized bed combustion. Mercel Dekker Inc., New York
2. World Coal Association. http://www.worldcoal.org/coal/uses-of-coal/coalelectricity/. Accessed 01 Dec 2015
3. Pope CA, Thun M, Namboodiri M, Dockery D, Evans J, Speizer F, Heath C (1995) Particulate air pollution as a predictor of mortality in a prospective study of U.S. adults. Am J Resp Crit Care Med 151:669–674
4. Adeyinka AJ (1997) Gasification of Nigerian coals in fluidized bed. PhD thesis, Federal University of Technology, Minna, Nigeria
5. Akinbode FO (1985) The potential application of fluidized bed to power generating schemes. Niger Eng 20(2):62–71
6. Kuni D, Levenspiel O (1969) Fluidisation engineering. Willey, New York
7. Ergun S, Orning AA (1952) Fluid flow through packed columns. Chem Eng Prog 48:89–94
8. Kececioglu I, Jiang Y (1994) Flow through porous media of packed spheres saturated with water. Trans ASME 116:164–170
9. Wen CY, Yu YH (1966) A generalized method for predicting the minimum fluidization velocity. AIChE 12:610–612
10. Rajans RR, Wen CY (1980) A comprehensive model for fluidized bed coal combustors. AlChE 26:642–655
11. Johnson JL (1979) Kinetics of coal gasification. The Institute of Gas Technology, Wiley, New York
12. Pillay VL (1987) Analysis of hydrodynamics phenomena and engineering development of a circulation fluidized bed for coal gasification. Master thesis, Natal University, South Africa
13. Saxena SC, Mathur A, Zang ZF (1986) Hydrodynamic characteristics of the gas fluidized beds over a broad temperature range. Powder Technol 47:247–256
14. La Nauze RD (1985) Fundamentals of coal combustion in fluidized beds. Chem Eng Res Des 63:1–30
15. Davidson JF (1992) Proceedings of the seventh engineering foundation conference and fluidisation, pp 1–14
16. Broughton J, Howard JR (1983) Combustion of coal in fluidized beds. In: Howard JR (ed) Fluidized beds. Applied Sciences Publishers, London, pp 37–76

17. Leye M, Amoo L (2015) Computational fluid dynamics simulation of Lafia-Obi bituminous coal in a fluidized-bed chamber for air- and oxy-fuel combustion technologies. Fuel 140:178–191
18. Borodulya VA (2007) Fluidized bed combustion is the universal technology of firing fossil fuels and various types of wastes. Adv Combust Aerotherm Technol 3:103–112
19. Hupa M (2007) Current status and challenges within fluidized bed combustion. Adv Combust Aerotherm Technol 5:87–101
20. Ogunsola OI (1991) Coal production and utilization trends in Nigeria. Fuel Sci Technol Int 9:1211–1222
21. EIA (2009) Country analysis brief-Nigeria, U.S. Energy Information Administration, May 2009. http://www.eia.doe.gov/emeu/cabs/Nigeria/Background.html. Accessed 01 Dec 2015
22. Oji JO, Idusuyi N, Kareem B (2012) Coal power utilization as an energy mix option for Nigeria: a review. AM Acad Sch Res J 4:1–5
23. P.M. News Nigeria. http://www.pmnewsnigeria.com/2013/08/19/nigeriasigns-3-7b-coal-mining-and-power-plant/. Accessed 01 Dec 2015
24. Ezekwe CI, Odukwe AO (1990) Coal in Nigeria. Energy 5:177–182
25. Ogunsola OI, Mikula RJ (1991) A study of spontaneouscombustion characteristics of Nigerian coals. Fuel 70:258–261
26. Nasir A, Mohammed SN, Mohammed A (2015) Performance of Enugu sub-bituminous coal in fluidized bed combustor. In: Lecture notes in engineering and computer science: proceedings of the World Congress on Engineering 2015 (WCE 2015), London, UK, pp 1102–1106, 1–3 July 2015

An Experimental Study of Catalysts and Carrier Gas Transport Through Membranes for Improved Yield of Ester Product

Okon Edidiong, Shehu Habiba, Mohammed Kajama and Gobina Edward

Abstract In this work, an initial study of heterogeneous catalyst activity and carrier gas transport through inorganic ceramic membrane for improved yield of ester product was carried out. Dowex 50W8x, Amberlyst 36, Amberlyst 15 and Amberlyst 16 cation-exchange resins were used as heterogeneous catalysts. The SEM/EDXA (The Zeiss EVO LS10) of the resin catalyst was investigated in order to determine the surface morphology. The EDXA of the catalysts showed the presence of sulphur which confirms the sulfonic acid group in the structure of the polymeric compound. FTIR (Nicolet iS10) was used for the structural analysis of the resins. The permeation properties of inorganic ceramic membrane with the carrier gases were also analysed between the gauge pressures of 0.01–1.00 bar at the temperature of 60 °C (333 K). The carrier gas permeance showed a linear dependence on the inverse square root of the gas molecular weight indicating Knudsen mechanism of transport.

Keywords Cation-exchange resin · Carrier gas diffusion · Characterization · Esterification · Ethyl lactate · Hysteresis · Inorganic membrane

O. Edidiong · S. Habiba · M. Kajama · G. Edward (✉)
Centre for Process Integration and Membrane Technology (CPIMT),
School of Engineering, The Robert Gordon University, Aberdeen AB10 7GJ, UK
e-mail: e.gobina@rgu.ac.uk

O. Edidiong
e-mail: e.p.okon@rgu.ac.uk

S. Habiba
e-mail: h.shehu@rgu.ac.uk

M. Kajama
e-mail: m.n.kajama@rgu.ac.uk

S.-I. Ao et al. (eds.), *Transactions on Engineering Technologies*,
DOI 10.1007/978-981-10-1088-0_11

1 Introduction

The simplest hydroxycarboxylic acid with an asymmetric carbon atom is lactic acid. This acid can be obtained from biomass, petroleum and coal. Copolymers and polymers of lactic acid are known to be eco-friendly and are environmentally compatible due to their biodegradability, which makes them desirable as alternatives to petrochemical polymers [1]. Lactic acid can react with ethanol during esterification process to produce ethyl lactate.

Ethyl lactate is an important organic solvent that can be produced from biomass and is considered to be biodegradable. It can be used as a food additive, agricultural processes (used in cadmium and copper removal from the contaminated soil), solvent, flavour chemicals and perfumery. It can also be used in the pharmaceutical industry as a dispersing/dissolving excipient for several biological compounds without destroying the pharmacological activity of the active ingredient. It serves as a desirable coating for polystyrene and can also act as paint remover. As a solvent it has the ability to dissolve polyurethane resin because of its high solvency properties which has made it an excellent cleaner for the polyurethane industry [2]. Ethyl lactate can replace environmentally damaging solvents including toluene, acetone, N-methyl pyrrolidone and xylene. Membrane-based separation technologies have shown a wide range of application in food, biotechnology, pharmaceutical and in the treatment of other industrial effluents [3].

Membranes can be classified in two groups including inorganic and organic membranes. Inorganic membranes have witnessed increasing application in the separation of gas mixtures at high temperatures. However, one of the most promising use of inorganic membrane is in reactors where product purification by separation and chemical conversion occurs in the same device resulting in process intensification. Moreover, it is possible to obtain important enhancement over the equilibrium conversion by selectively separating one or more reaction products across the membrane wall [4].

In the esterification reaction of lactic acid with ethanol, both heterogeneous and homogeneous catalysts can be used [5, 6]. The function of these catalysts during the esterification of lactic acid is to give a proton (hydrogen) for a chemical reaction between the molecules of the carboxylic acid [7]. Although homogeneous catalysts have shown excellent performance in terms of the rate of reaction, the interest is said to decrease since the recovery and separation of the catalyst are difficult because of the ability of the liquid acid catalyst to mix with the bulk of the reaction [8]. As such, heterogeneous solid catalysts including cation-exchange resin have been suggested for esterification reactions [9]. The use of inorganic ceramic membrane to selectively eliminate water from the reaction product during esterification of lactic acid is yet another important application that has attracted a lot of attention [10]. The function of the membrane during esterification reaction is to selectively remove water from the reaction mixture so as to drive the reaction towards completion [11]. Among the membranes considered, inorganic membrane have been found to be the perfect membrane for the esterification reaction process

because they can allow different catalysts to be deposited easily on the surface of the membrane.

The mechanism of gas transport through porous membranes is generally divided into 5 groups: surface diffusion, capillary condensation, Knudsen diffusion, viscous flow and molecular sieving mechanisms [12]. In Knudsen diffusion mechanism, gas molecules diffuse through the pores of the membrane and then get transported by colliding more frequently with the pore walls. Viscous flow mechanism takes place if the pore radius of the membrane is larger than the mean free path of the permeating gas molecule. Gas separation by molecular sieving mechanism takes place when the pore dimensions of the inorganic ceramic membrane approach those of the permeating gas molecules [13]. However, in capillary condensation mechanism, separation can takes place in the pores of the membrane with mesoporous layer in the presence of condensable gas specie. Surface diffusion mechanism occurs when the adsorption of the permeating gas molecule occurs on the pore surface of the membrane material thereby increasing the gas transport performance [13].

In this work, the experimental study of heterogeneous catalyst behaviour and carrier gas transport through inorganic ceramic membrane for improved yield of ester product will be investigated.

2 Experimental

(a) Membrane preparation

The membrane preparation was carried out based on the patented method by Gobina [14]. The membrane was prepared by dip-coating process. Prior to the permeation test, the support was weighed to determine the actual weight before and after modification. A 545 mL of isopentane (Sigma-Aldrich ≥99 %), was measured into 1000 mL glass cylinder and 50 mL of silicon elastomer (Sigma-Aldrich) was added to the solution together with 5 mL of the curing agent (Sigma-Aldrich). A magnetic stirrer was used to mix the solution and the mixture was allowed to stir for 30 min. After 30 min, the support was dipped into the solution and allowed in the solution for 30 min. After 30 min, the support was carefully withdrawn from the solution and dried in the oven (carbolite oven) for 2 h at a constant temperature of 65 °C. Figure 1 shows the schematic diagram of the dip-coating system for silica membrane preparation.

(b) The permeation cell

The permeation cell consisted of a stainless steel shell with high-temperature resistant. The membrane was centralized in the tube using a graphite seals at either ends. Through the use of various connections and values the cell permits the measurement of the gas flux through the membrane at various feed pressures. A heating tape was wrapped over the stainless steel enables high-temperature studies to be carried out. Prior to permeation experiments, a leak test was carried

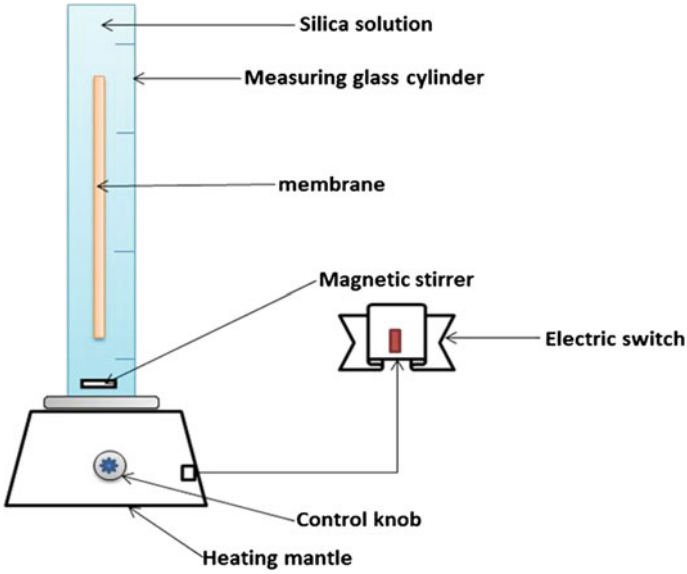

Fig. 1 Schematic diagram of dip-coating system for silica membrane preparation

out by monitoring the downstream pressure increment while the system remained totally closed.

(c) Carrier gas transport through membrane

The transport of the carrier gases through inorganic ceramic membrane was carried out using four different single gases which serve as carrier gases for esterification reaction including argon (Ar), helium (He), carbon dioxide (CO_2) and nitrogen (N_2). The effective length of the support was measured to be 36.6 cm and the inner and outer radius was 7 and 10 mm respectively. The gas transport was carried out at the gauge pressure of between 0.10 and 1.00 bar and temperature of 140 °C (413 K). The different gases were feed into the reactor through the feed gas inlet and the gases penetrate through the membrane and exit through the permeate. The flow rate of the gases was recorded at each gauge pressure. The gases were supplied by BOC, UK. Figure 2 shows the carrier gas permeation setup [15].

(d) Batch process esterification

Aqueous lactic acid (99.9 wt%) and ethanol (99.9 wt%) solutions used for the esterification process were purchased from Sigma-Aldrich, UK and were used as received without further purification. The catalysts used in the experiments were commercial solid cation-exchange resins purchased from Sigma-Aldrich, UK. The deionised water used for the washing of the catalysts was supplied by the Centre for Process Integration and Membrane Technology (CIPMT), Robert Gordon University (RGU), Aberdeen, UK. The 500 mL batch reactor, reflux condenser and

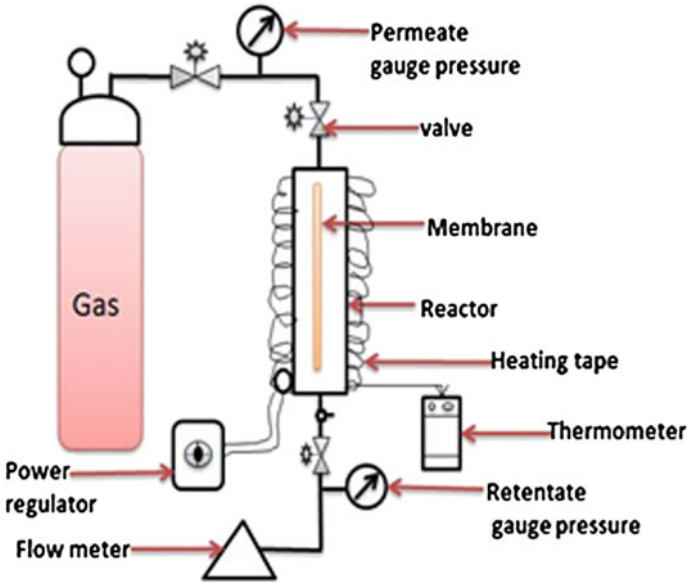

Fig. 2 Schematic diagram of gas permeation setup [18]

the vacuum pump used for the esterification process were all purchased from Sigma Aldrich, UK. Prior to the esterification process, the fresh commercial cation-exchange resin was weighed into a 50 mL beaker and was rinsed with 2 mL of deionised water with 10 mL of ethanol. The catalysts were reweighed and oven dried at 65 °C for 24 h to remove any impurities and moisture completely. After the catalyst cleaning process, 30 mL of lactic acid with 5 g of the resins was charged into the reactor and heated to 60 °C. After attaining the desired temperature, 50 mL of ethanol (which had been previously heated separately) was added to the mixture. The stirring and heating of the reaction mixture was achieved using a magnetic hot plate with a stirrer. The stirrer speed was controlled at the speed of about 400–800 rpm.

(e) Catalyst characterization

The catalysts used in the experiments were commercial solid cation-exchange resins purchased from Sigma-Aldrich, UK. Fourier transform infrared coupled with attenuated total reflection (Nicolet iS10 FTIR-ATR) was used for the structural analysis of the resins. This method was used in order to determine the phenomenon of the component with the strongest absorption strength on the surface of the resin catalysts. The FTIR results interpretation was done using the characteristic library spectra provided by the School of Pharmacy Life Science, Robert Gordon University, UK. Prior to the analysis of the sample, a background spectrum of air (without any solvent) was obtained. Each sample scan was carried out at 32 scans for 5 min before the spectra were generated. The scanning pattern was observed

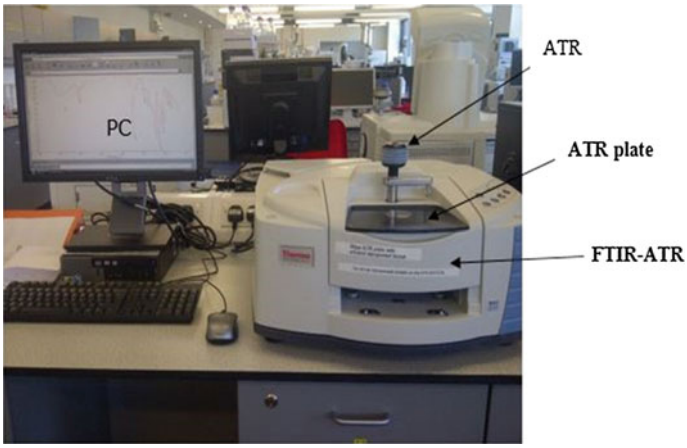

Fig. 3 Pictorial view of the thermo scientific fourier transform infrared coupled with attenuated total reflection (Nicolet iS10), School of Pharmacy Life Science, RGU

within the range of 4000–400 cm^{-1} with the resolution of 4 cm^{-1}. Figure 3 shows the pictorial view of the Fourier Transform infrared coupled with attenuated total reflection (Nicolet iS10). The resin catalysts were also characterized using scanning electron microscopy coupled with energy dispersive X-ray analyser (SEM/EDXA).

3 Results and Discussion

(a) Effect of gauge pressure on carrier gas flowrate

Figure 4 presents the relationship between the gas flow rate (mol s^{-1}) and the gauge pressure (bar). From the result, it can be seen that the gas flow rate increases with increase in gauge pressure. It was also found that He gas with the least molecular

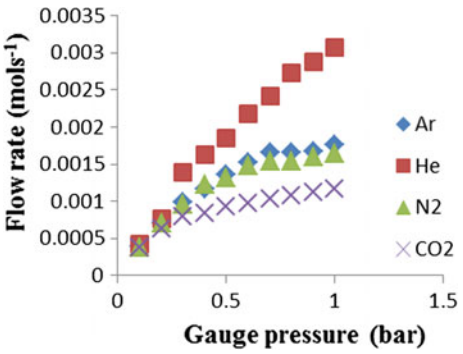

Fig. 4 Flow rate (mol s^{-1}) against gauge pressure (bar)

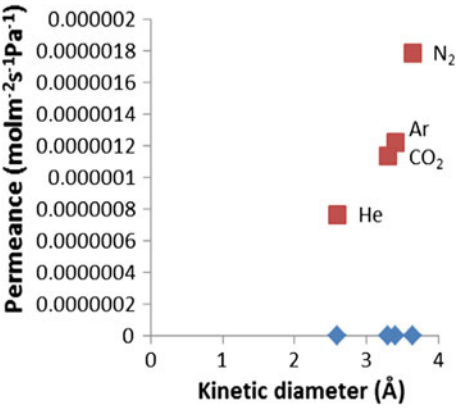

Fig. 5 Permeance (mol m^{-2} s^{-1} Pa^{-1}) against kinetic diameter (Å) at 0.4 bar and at 333 K

weight recorded the highest permeability. Also, above a gauge pressure of 0.50 bar, the flow rate of CO_2, N_2 and Ar were observed to deviate from Darcy's law while Helium continued to obey Darcy's law.

(b) Effect of carrier gas kinetic diameter on permeance

Figure 5 shows the relationship between the gas permeance (mol m^{-2} s^{-1} Pa^{-1}) and the gas kinetic diameter (Å). From the result obtained in Fig. 5, it was found that although the gases followed the order of their kinetic diameter; N_2 (3.64 Å) > Ar (3.43 Å) > CO_2 (3.30 Å) > He (2.60 Å), the gas flow through the silica membrane was not based on the molecular sieving mechanism. For the gas flow to be described by molecular sieving mechanism, N_2 with the highest kinetic diameter would have exhibited a lower permeance in contrast to Ar, CO_2 and He gas. Also the permeability of CO_2 would have been close to Helium rather than Ar since their kinetic diameters are close as shown in Table 1. However, the reverse was the case which implies that the gas flow was controlled by another mechanism of gas transport.

Table 1 describes the respective gases with their kinetic diameter and molecular weight.

(c) Effect of carrier gas molecular weight on flow rate.

Figure 6 presents the relationship between the gas flow rate (mol s^{-1}) and the inverse square root of molecular weight for CO_2, Ar, N_2 and He gases. It was found

Table 1 Gas molecular weight and their respective kinetic diameter

Gases	Molecular weight (g/mol)	Kinetic diameter (Å)
Helium (He)	4	2.60
Argon (Ar)	40	3.43
Nitrogen (N_2)	28	3.64
Carbon dioxide (CO_2)	44	3.30

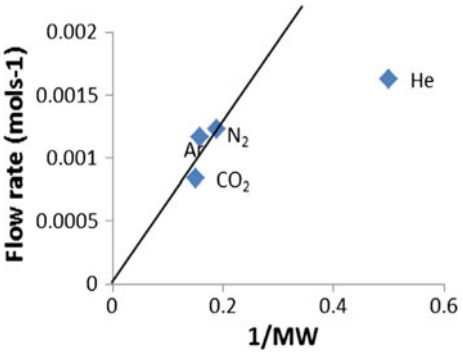

Fig. 6 Flow rate (mol s^{-1}) against inverse square root of molecular weight at 0.4 bar and at 333 K

that the membrane exhibited a linear dependence of flow rate on the inverse square root for CO_2, N_2, and Ar gases as expected for Knudsen flow mechanism of gas transport, whereas He gas was suggested to be controlled by another mechanism of transport.

(d) SEM surface morphology of resin catalysts

The four resin catalysts were analysed using SEM/EDXA at the magnification of 100× and the scale of 100 µm. Figure 7a–d, presents the SEM images of the fresh commercial resin catalysts. The surfaces of Amberlyst 16 (Fig. 7a), Amberlyst 36 (Fig. 7b) and Dowex 50W8x (Fig. 7c) showed a very smooth surface although there was a shiny defect of crack on the surface of amberlyst 15 (Fig. 7d). These results indicate that the resin catalysts were defect-free. A similar result was obtained by Zhang et al. [16].

(e) EDXA elemental composition of resin catalysts

The elemental composition of the resin catalysts was also analysed using EDXA instrument. From Fig. 8, it was found that the EDXA of the resin catalyst consist of the elements such as oxygen, carbon and sulphur. It was also found that sulphur (S) exhibited the highest peak in contrast to other elements and is thought to arise as a result of sulfonic acid group from the structure of the resin catalyst [17]. However, these results will be compared with the images of resins after being used for the esterification experiment.

(f) FTIR of esterification products.

Figures 9 and 10 presents the FTIR spectra for amberlyst 15 and 36 cation-exchange resin catalysts respectively. From Fig. 9, it was observed that the FTIR analysis of the resin catalysts showed the band at 1724 cm^{-1} corresponding to C=O stretching strong adsorption bond, and also the bands at 2986 and 2940 cm^{-1} representing O–H and C–H functional groups which correspond to stretching vibration bond. However, the band at 1211 cm^{-1} was observed to represent =C–O–C–structure. This (=C–O–C–) structure was suggested to originate from the carboxylic acid

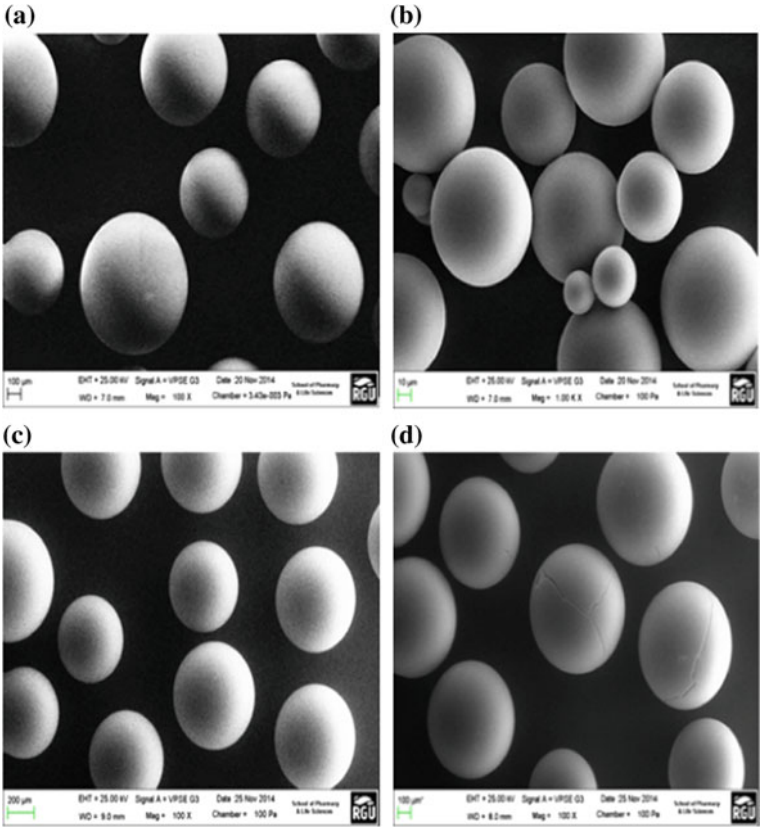

Fig. 7 **a** Amberlyst 16, **b** Dowex 50W8x, **c** Amberlyst 36 and **d** Amberlyst 15: SEM surface morphology of the resin catalyst before esterification

functional group while the O–H are thought to arise from the alcohol functional group. From Fig. 10, it was observed that the highest band at 2978 cm^{-1} correspond to C–H bond corresponding to stretching vibration bond in contrast to Fig. 9. From the repeated structural bonds of C–H, O–H and C–O, it was suggested that the strong adsorption bond of C–O, C–H and O–H, could indicate the fact that ethanol and lactic acid as the adsorption component on the surface of the resin catalysts [18]. Further experiments with other catalysts will be carried out in order to still confirm the absorption components.

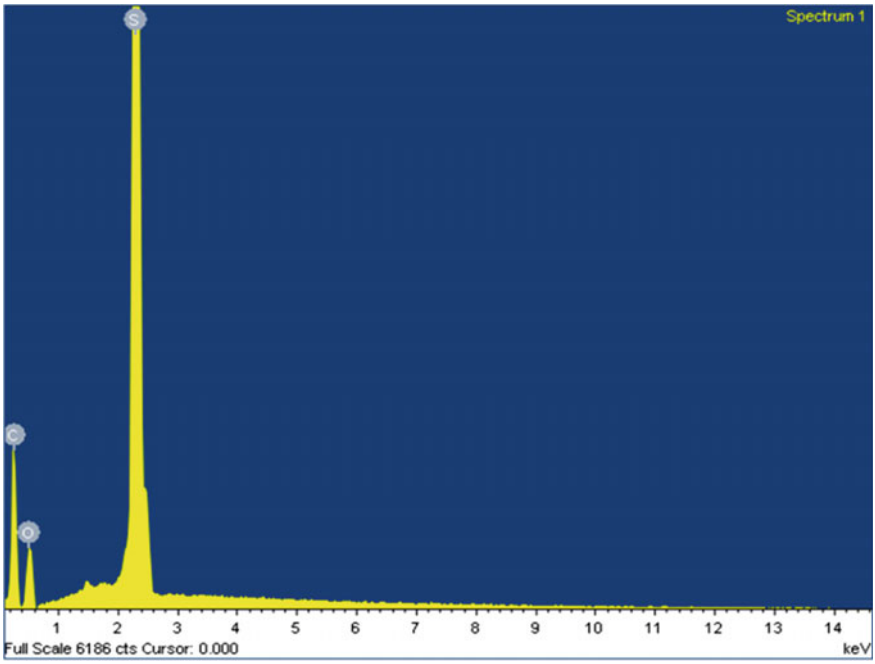

Fig. 8 EDXA of the resin catalyst

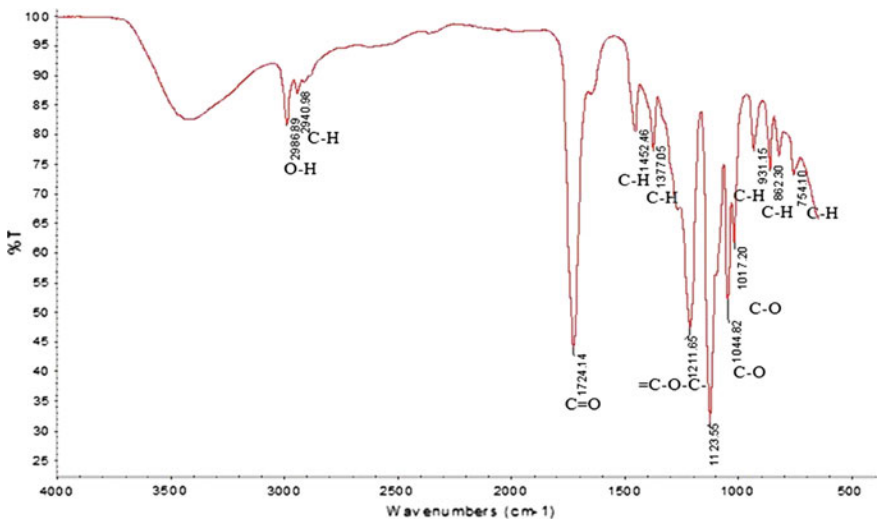

Fig. 9 FTIR spectra of esterification reaction product catalysed by amberlyst 15 at 60 °C and the wavelength region of 500–4000 cm^{-1}

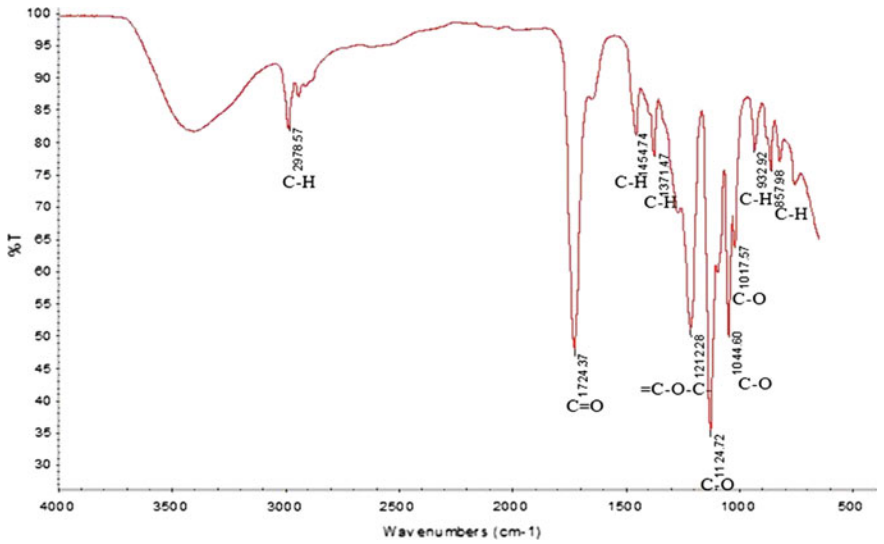

Fig. 10 FTIR spectra of esterification reaction product catalysed by amberlyst 36 at 60 °C and the wavelength region of 500–4000 cm^{-1}

4 Conclusion

The behaviour of carrier gases with inorganic membrane for lactic acid esterification applications was achieved using viscous, Knudsen and molecular sieving mechanisms. It was found that viscous and Knudsen mechanism of transport play a major role with respect to carrier gas transport. However, the membrane exhibited a linear dependence of permeance on the inverse square root of molecular for CO_2, N_2 and Ar indicating Knudsen flow mechanism except for He gas. The EDXA of the catalysts showed the presence of sulphur which confirms the sulfonic acid group in the structure of the polymeric compound. The FTIR of the resin catalysts exhibited different functional groups including C–O, C–H and C=O bonds corresponding to stretching strong vibration and adsorption bonds.

Acknowledgement The conference was sponsored by the Robert Gordon University, Aberdeen, United Kingdom. The Authors acknowledge the Center for Process Integration and Membrane Technology (CPIMT) at RGU for providing the research infrastructure.

References

1. Sanz MT, Murga R, Beltrán S, Cabezas JL, Coca J (2004) Kinetic study for the reactive system of lactic acid esterification with methanol: Methyl lactate hydrolysis reaction. Ind Eng Chem Res 43(9):2049–2053

2. Pereira CS, Silva VM, Rodrigues AE (2009) Fixed bed adsorptive reactor for ethyl lactate synthesis: experiments, modelling, and simulation. Sep Sci Technol 44(12):2721–2749
3. Calvo JI, Bottino A, Capannelli G, Hernández A (2008) Pore size distribution of ceramic UF membranes by liquid–liquid displacement porosimetry. J Membr Sci 310(1):531–538
4. Gobina E, Hou K, Hughes R (1995) Mathematical analysis of ethylbenzene dehydrogenation: comparison of microporous and dense membrane systems. J Membr Sci 105(3):163–176
5. Qu Y, Peng S, Wang S, Zhang Z, Wang J (2009) Kinetic study of esterification of lactic acid with isobutanol and *n*-butanol catalyzed by ion-exchange resins. Chin J Chem Eng 17 (5):773–780
6. Bankole KS, Aurand GA (2014) Kinetic and thermodynamic parameters for uncatalyzed esterification of carboxylic acid. Res J Appl Sci Eng Technol 7(22):4671–4684
7. de la Iglesia Ó, Mallada R, Menéndez M, Coronas J (2007) Continuous zeolite membrane reactor for esterification of ethanol and acetic acid. Chem Eng J 131(1):35–39
8. Ju IB, Lim H, Jeon W, Suh DJ, Park M, Suh Y (2011) Kinetic study of catalytic esterification of butyric acid and n-butanol over Dowex 50W8–400. Chem Eng J 168(1):293–302
9. Nemec D, van Gemert R (2005) Performing esterification reactions by combining heterogeneous catalysis and pervaporation in a batch process. Ind Eng Chem Res 44 (25):9718–9726
10. Asthana N, Kolah A, Vu DT, Lira CT, Miller DJ (2005) A continuous reactive separation process for ethyl lactate formation. Org Process Res Dev 9(5):599–607
11. Jafar JJ, Budd PM, Hughes R (2002) Enhancement of esterification reaction yield using zeolite A vapour permeation membrane. J Membr Sci 199(1):117–123
12. Abedini R, Nezhadmoghadam A (2010) Application of membrane in gas separation processes: its suitability and mechanisms. Pet Coal 52(2):69–80
13. Lee H, Suda H, Haraya K (2005) Gas permeation properties in a composite mesoporous alumina ceramic membrane. Korean J Chem Eng 22(5):721–728
14. Gobina E (2006) Apparatus and method for separating gases. US Patent. Patent No. 7, 048, 778B2. Robert Gordon University, Aberdeen, UK
15. Okon E, Shehu H, Gobina E (2014) Novel application of gas transport properties with ceramic membrane for VOC emission and lactic acid esterification. Eur J Eng Technol 2(2):37–44
16. Zhang Y, Ma L, Yang J (2004) Kinetics of esterification of lactic acid with ethanol catalyzed by cation-exchange resins. React Funct Polym 61(1):101–114
17. Okon E, Gobina E (2015) Initial study of heterogeneous catalysts behaviour and carrier gas permeation with catalytic inorganic ceramic membrane for lactic acid esterification applications. In: Lecture notes in engineering and computer science: proceedings of the World Congress on Engineering 2015 (WCE 2015), London, UK, pp 1287–1291, 1–3 July 2015
18. Sert E, Buluklu AD, Karakuş S, Atalay FS (2013) Kinetic study of catalytic esterification of acrylic acid with butanol catalyzed by different ion exchange resins. Chem Eng Process 73:23–28

A Comparison of Loading on a Single or Double Temporomandibular Joint

Janith Muhandiram, Julia Pierson, Bin Wang and Mahmoud Chizari

Abstract This research is a continuation of our previous study on temporomandibular joint (TMJ). The aim of the research is to investigate the mechanical behaviour of the TMJ, in response to cyclical loading caused through actions of speech and mastication. This study investigates whether a difference exist between the left and right side TMJ simulation and discover a method to reproduce the action of the upper jaw bones on the lower jaw bones as much natural as possible. A set of in vitro experimental tests have been performed on a fresh sheep jaw bone to examine the hypothesis of the study. The study was concluded that the amount of loading is effective on the displacement/elongation of the TMJ.

Keywords Cyclic loading · Double · Mastication · Speech · Single · Temporomandibular joint

J. Muhandiram (✉) · B. Wang
College of Engineering, Design and Physical Sciences, MACE,
Brunel University London, Uxbridge, UK
e-mail: janith.muhandiram@gmail.com

B. Wang
e-mail: bin.wang@brunel.ac.uk

J. Pierson
National Engineering School of Metz (ENIM), Metz, France
e-mail: piersonjulia@gmail.com

M. Chizari
Mechanical Engineering Department, Sharif University of Technology,
Tehran, Iran
e-mail: mahmoudchizari@yahoo.com

M. Chizari
Orthopaedic Research and Learning Centre, College of Engineering,
Design and Physical Sciences, Brunel University London, Uxbridge, UK

S.-I. Ao et al. (eds.), *Transactions on Engineering Technologies*,
DOI 10.1007/978-981-10-1088-0_12

1 Introduction

1.1 TemporoMandibular Joint (TMJ)

The temporomandibular joint is a geometrically complex and extremely mobile joint [1, 2]. The bone of the lower jaw, mandible, is connected by the TMJ to the upper temporal bone of the skull and mediates the regulation of jaw movement. The bi-condylar TMJ contains condyles located at the opposite ends of the mandible which function simultaneously [1]. The condyle is the round upper end of the lower jaw which glides along the articular fossa during opening and closure of the mouth. The condylar movement along the articular fossa is allowed by a disc located between the condyle and the articular fossa functions as a stress absorber [2].

The joint is separated into two compartments by the disc which disperses the stress imposed on the joint through contact of temporomandibular components during jaw movements. A significant feature of the TMJ as a distinguished joint is the fibrocartilage of the disc which covers the articular surfaces of the condyle and the fossa [2].

The temporomandibular joint is the most frequently used joint in the human body. It opens and closes 1500–2000 times per day during its diverse movements, which include: mastication, speech, deglutition, yawning and snoring. The closure of the mouth is enabled by the masseter muscle, one of the strongest muscles in the human body which plays a key role in mastication [2]. A significant number of the human population is affected by the pathologies of the complex temporomandibular joint (TMJ) [3].

The simulation of the TMJ behaviour during diverse movements can be immensely useful to the understanding of this articulation by physicians contributing to the investigation of prevention and treatment techniques of mandibular issues [2].

1.2 TemporoMandibular Disorders (TMD)

Temporomandibular disorder is a generic term used for clinical conditions of the temporomandibular joint and masticatory muscles [4]. It was reported that 20–25 % of the human population exhibit symptoms of TMD [1]. A higher prevalence in women (6.3–15 %) in comparison to men (3.2–10 %) was observed among these patients [5]. Key symptoms of TMD include pain in the jaw, restricted jaw movement, grating and clicking sounds of the temporomandibular joint, earache and headache. Majority of the conditions of patients with TMD are improved with simple therapies; use of mouth guards and preventive measures such as avoiding extreme jaw movements to minimize aggravation of the conditions. At the end-stage of TMD, surgical therapies such as repairment and reconstruction of TMJ are utilized in the treatment of patients [6]. Parafunctional activities such as grinding or clenching the teeth, presence of osteoarthritis or rheumatoid arthritis in the TMJ and trauma may cause TMD as a result of deformation of TMJ and masseter muscles [7].

Fig. 1 The sheep's temporomandibular joint (TMJ)

Varying degrees of force is applied on to the mandible during functions of mastication and speech, and force overload leads to the rise of TMD.

The articular disc, a fibrocartilaginous plate which facilitates the movement between the mandible and the temporal bone, is the main constituent of the TMJ. The articular disc functions as a stress absorber and prevent impairment of the articulating surfaces by distribution of the load over greater area of contact. Hence damage of the articular disc may cause TMD [8].

Due to limited jaw movements, patients with myofascial TMD pain may have impaired masticatory function and the awareness of muscle pain may also obstruct mastication [5] (Fig. 1).

1.3 Jaw Movement in Mastication and Speech

Motor functions such as mastication and speech involve the movement of jaw. Anatomy of muscles and biomechanical properties such as reflex, sensory and motor components are shared to a certain extent between masticatory and speech systems [9]. The measurement of rate and amplitude in speech and the formation of bolus in mastication present a quantitative evaluation of jaw movement. The movement, rate and amplitude of jaw movement were greater in mastication in comparison to that in speech, according to Ostry and Flangan in 1989 [9], as reported in Table 1. The process of mastication is composed of three stages including ingestion of food, bolus formation followed by clearance and swallowing. The key masticatory muscles are masseter, temporalis, digastric, lateral pterygoid and medial pterygoid [1]. The masseter muscle, one of the strongest muscles of the human body is the main muscle of mastication [2]. The muscles ensure the mandible is appended to the skull and pivoted at the condyle at both sides of the jaw through the TMJ [1]. The zygomatic bone (cheek bone) on the skull is attached to the mandible through the masseter muscle which controls the opening and closure of the mouth. The temporalis muscle is attached to the temporal bone and regulates elevation of the mandible [1].

During mastication, the movement of the functional condyle occurs towards the direction in which the condyle compresses on the mandibular fossa than the balancing condyle [9].

Table 1 Kinematics of mandible at mastication and speech [10]

	Normal opening		Normal closing	
	Mastication	Speech	Mastication	Speech
Amplitude, cm	0.63	0.26	0.64	0.26
Duration, ms	318	234	356	267
Acceleration, ms	110	69	99	94
Deceleration, ms	208	163	257	133
*V_{max}, cm/s	6.82	2.93	5.38	2.82
	Fast opening		Fast closing	
	Mastication	Speech	Mastication	Speech
Amplitude, cm	0.45	0.24	0.44	0.24
Duration, ms	132	110	143	342
Acceleration, ms	74	49	145	148
Deceleration, ms	58	61	95	64
*V_{max}, cm/s	7.21	4.06	6.76	4.00

*V_{max} is the maximum instantaneous velocity

A cycle of chewing is comprised of three sectors including the opening, closing, and occlusal phase. In biomechanical applications, mandibular displacement, velocities of jaw opening and closing, and masticatory frequency are key features of mastication [1].

The lateral capsule elongates during the mastication and slowly returns to the original formation once the process is completed. Due to the complexity of the human masticatory system, performance of muscular activity includes balance and coordination of the masticatory muscles on both sides during mastication.

In the field of biomechanics, the masticatory system is classified as static, dynamic and kinematic computational models in order to investigate various aspects. The mandibular deformation under muscle forces or loads and its impact on masticatory functions are studied by static models. Different properties of the masticatory system are investigated by the dynamic models through the analysis of muscle forces and directions. Kinematic models are dedicated to the study of mandibular movement [1].

1.4 Objective of the Study

The aim of this research is to confirm the hypothesis of the previous study carried out by authors of this article [10]. The purpose of this experiment is to compare the displacement of the right side TMJ, left side TMJ and both sides of the TMJ simultaneously and conclude if the correct protocol has been used for the experiment and whether it can be applied on both sides of TMJ. The importance of different factors on speech and mastication on the TMJ has been investigated. In order to do so, the jaw movement during mastication was simulated in the study.

2 Methods

The study was carried out using fresh sheep jaw bones to simulate the mechanical behaviour of the jaw under daily mechanical loading on the TMJ. The study uses the lower jaw which *was harvested from the sheep's head.*

The sheep's head was stored in the freezer for less than a month at a temperature of −20 °C. On the day of the experiment it was defrosted in ambient temperature. The experiment was set by placing the lower jaw on a custom made fixture which was secured with screws and mountable nylon cable ties. A custom made dummy bone model with a density close to the jaw bone specimen (20 pcf) was attached to crosshead to be used as contact points between the machine and the TMJ (Fig. 2, Table 2).

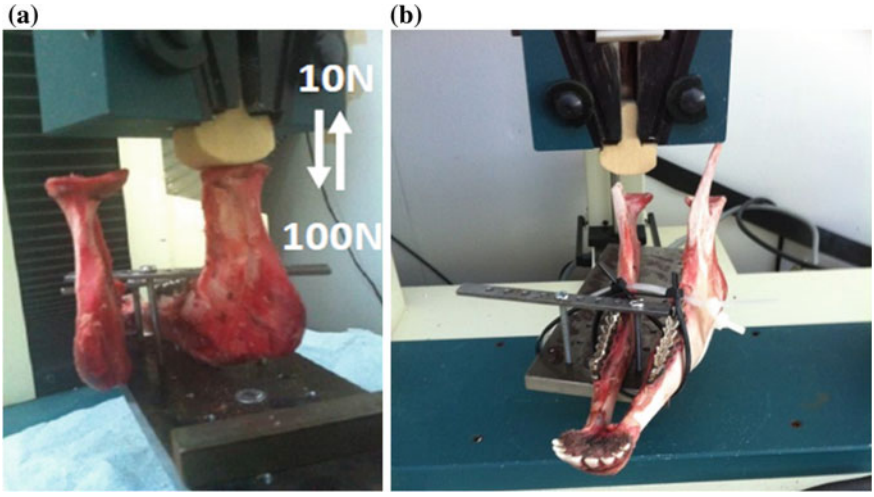

Fig. 2 The sheep jaw bone specimen mounted into the testing machine (**a**); the contact points between the dummy bone model and a single side the TMJ (**b**)

Table 2 Number of sheep's jaw movements per day [4]

Eating	30,008
Ruminating	40,950
Chewing	70,958

Table 3 The data used for the sheep's jaw bones

Amplitude of the mouth	22.4 mm
Amplitude of the TMJ	1.3 mm
Frequency	1.57 Hz
Density	20 pcf

Table 4 Specification of the ten tests

Load range, N	100
Extension range, mm	5
Speed, mm/min	100
Preload, N	5
Number of the cycles	500

Table 5 Results table

	Displacement, mm		Elongation, mm
	1st cycle	500th cycle	
1st test	1.4	1.82	0.42
2nd test	1.82	2.05	0.23
3rd test	1.75	1.82	0.07
4th test	1.65	1.7	0.05
5th test	2.55	3.25	0.7
6th test	2.8	3.25	0.45
7th test	2.4	2.6	0.2
8th test	2.15	2.3	0.15
9th test	2.05	2.25	0.2
10th test	2.05	2.15	0.1
Average of the ten tests	2.062	2.319	0.257

Table 6 Results of the study

Max. displacement	1.6 mm
Min. displacement	1.0 mm
Max. stiffness	880 N/mm at 0 mm
Min. stiffness	25 N/mm at 1.4 mm
Max. stress	0.62 N/mm^2 at 1.2 mm/mm
Min. stress	0.08 N/mm^2 at 0 mm/mm

Table 7 Maximum stiffness, stress, and displacement obtained from the experiment

Load, N	Stiffness, N/mm	Stress, N/mm^2	Displacement, mm
10	875	0.066	0
100	69.4	0.62	2.05

Table 8 Left sides TMJ results

	Displacement, mm		Elongation, mm
	1st cycle	500th cycle	
1st test	2.25	2.9	0.45
2nd test	1.3	1.5	0.2
3rd test	1.45	1.55	0.1
4th test	1.35	1.4	0.05
5th test	1.35	1.4	0.05
6th test	1.35	1.35	0
7th test	1.3	1.35	0.05
8th test	1.25	1.25	0
9th test	1.2	1.2	0
10th test	1.25	1.25	0
Average of the ten tests	1.405	1.515	0.18

A computer drive, Hounsfield hydraulic testing machine (Tinius Olsen, UK), was used to carry out the test. The machine was armed with a 1000 N load-cell on its crosshead. The machine was controlled with the QMat V5.3 software (Tinius Olsen, UK). The software enabled the user to introduce the input data to the testing machine (Table 3).

The study includes 10 tests which utilized polyurethane foam tool (20 pcf) to simulate the action of the temporal bone on the TMJ. The 10 tests were done under the same conditions. A compression-cyclic routine from the QMat database was used to carry on the test (Tables 4, 5, 6, 7, 8, 9 and 10).

Table 9 Right sides TMJ results

	Displacement, mm		Elongation, mm
	1st cycle	500th cycle	
1st test	3.4	4.3	0.9
2nd test	4.7	5.15	0.45
3rd test	2.6	2.8	0.2
4th test	2.5	2.6	0.1
5th test	2.7	2.8	0.1
6th test	3	3.1	0.1
7th test	2.95	3	0.05
8th test	2.9	3	0.1
9th test	2.95	3	0.05
10th test	2.85	2.9	0.05
Average of the ten tests	2.758	3.065	0.21

Table 10 Both sides TMJ results

	Displacement, mm		Elongation, mm
	1st cycle	500th cycle	
1st test	0.85	1.1	0.25
2nd test	1.3	1.35	0.05
3rd test	1.125	1.125	0
4th test	1	1.05	0.05
5th test	1	1	0
6th test	0.9	1	0.1
7th test	0.9	1	0.1
8th test	0.95	1	0.05
9th test	0.95	1	0.05
10th test	1.125	1.125	0
Average of the ten tests	1.01	1.075	0.065

3 Results and Discussion

3.1 Experiment 1: Single Side TMJ

There is no significant difference between the ten tests. The results show that by increasing the load on TMJ, the displacement of the bone would increase. However, the behaviour of the load-displacement curve was not linear. The maximum displacement is 1.6 mm and the average of the displacement is 1.4 mm.

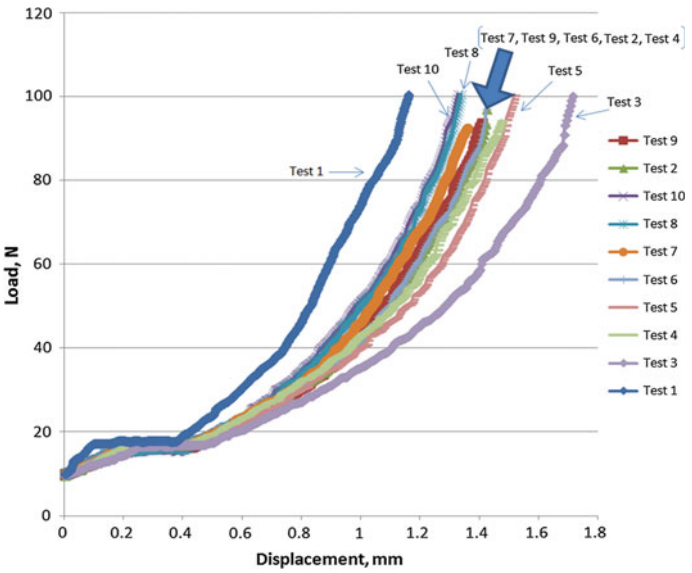

Fig. 3 Load and displacement result of the ten tests applied on a sheep jaw bone sample

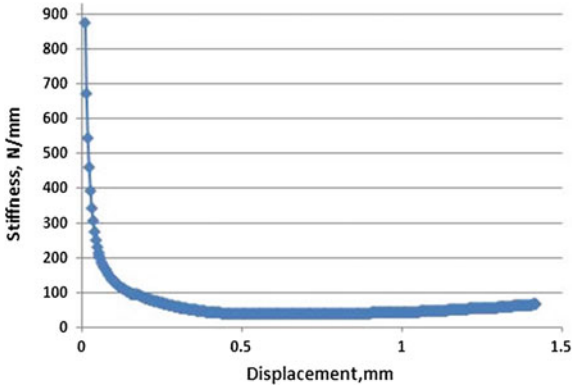

Fig. 4 The stiffness versus displacement obtained from experiment

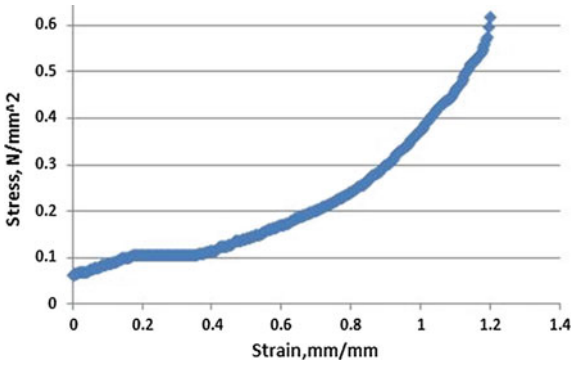

Fig. 5 The stress versus strain results extracted from the experiment

A difficulty was experienced on the fixation of the sheep jaw bone on the testing rig which may have caused a minor movement while the specimen was under loading. This unexpected movement may influence the accuracy of the recorded data. The jaw bone was insufficiently dampened with water and cracked slightly; this may have had an impact on the results (Figs. 3, 4, 5, 6 and 7).

3.2 Experiment 2: Double Side TMJ

Due to the complexity of the human masticatory system, performance of muscular activity includes balance and coordination of the masticatory muscles on both sides during mastication. Therefore, an experimental approach which considered both sides of the TMJ was designed. The purpose of this experiment was to compare the

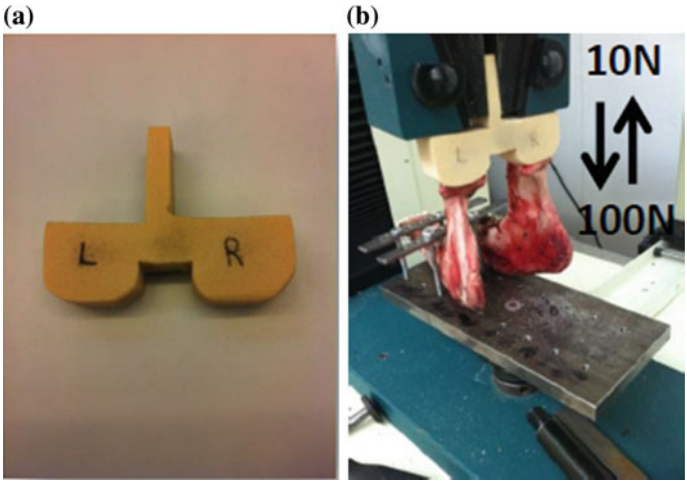

Fig. 6 The dummy bone model used to load both sides TMJ simultaneously (**a**); the experiment performed on both sides TMJ (**b**)

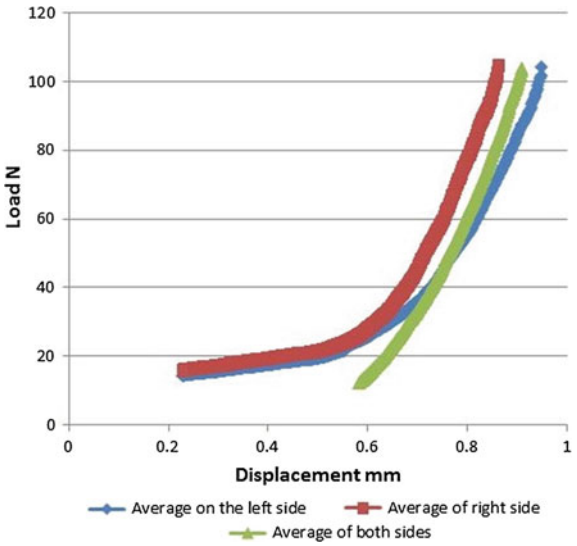

Fig. 7 Results obtained for the three groups of the specimens

displacement of the right side TMJ, left side TMJ and both sides of the TMJ simultaneously and conclude if the protocol we used for experiment 1 was correct and can be applied for both sides of TMJ. Therefore, new sheep's head was required to ensure no tests were previously done on the lower jaw bone. The jaw bones were thoroughly cleaned to remove all the meat, muscles and ligaments and the lower jaw bones were dissociated from the upper jaw bones.

This experiment is composed of 30 tests: 10 tests on the left side TMJ, 10 tests on the right side TMJ and 10 tests on both sides of TMJ were simultaneously carried out. All of the tests have been performed with the same conditions as described in experiment 1. The only difference of conditions, for the tests on both sides TMJ was the new dummy bone model that was designed to enable it to be in contact with both sides of the TMJ simultaneously.

It is observed on the graph below, that there is no significant difference between the left side TMJ and the right side TMJ. It can be remarked that left side TMJ and right side TMJ share one part of the graph; which may be due to the improper fixation of the jaw bones. The steel plate which the jaw bone is fixed, is not optimal. The regular shape is not the ideal as a round shaped steel plate would have been better. Another limitation is the application of some weight in order to maintain the balance and prevent the plate shifting along with the tool.

It can be observed in above tables, that the results of the first two tests are non-consistent with the following tests on each table. Some adjustments were made during the experiment to enhance the other tests.

It can be said that there is no significant difference between the left and the right side TMJ. However, the use of only one side of the TMJ is not realistic. The results of tests carried out on the both sides of TMJ are more interesting as it is observed that there is not much elongation on the TMJ happens when it is under loading. Means the risk of fracture during speech, chewing or mastication is quite low.

4 Conclusion and Future Work

This research focuses on the cyclical loading applied on the temporomandibular joint during speech and mastication. A set of in vitro tests were performed to examine the hypothesis of the study. A fresh sheep jaw bone was used to compare the mechanical properties of single and double TMJ in response to cyclical loading caused through actions of speech and mastication. The study was performed by means of a mechanical method of input loading and further investigated kinematic loading may be effective on the deformation of the TMJ. It was observed that there is no significant difference between the left side TMJ and the right side TMJ. The results of tests carried out on both sides of TMJ show the elongation of the TMJ during the tests is low.

This study is still under investigation and the outcome has not yet been finalized. However, the concept of the study may be used or better understanding of the TMJ problems.

The hypothesis of the study may need further investigation with more jaw bone specimens. The accuracy of the future experiments could be enhanced by adopting an improved testing rig which would correctly support the specimen onto the testing machine.

Finally, the study suggest the use of real TMJ condyles (instead of dummy bone model), firstly because it will provide a better match at TMJ contact zone. Secondly, the property of the TMJ will be closer to the reality.

Acknowledgment The authors would like to thank the Biosurgical Lab at the Brunel University London for providing the animal materials and test facilities. Also would like to thank Niwedhie Muhandiram, Jani Muhandiram and Aloka Jayathilake for proofreading. Special thanks my parents, Jayakody Muhandiram and Nishanthie Muhandiram, for all the support they have given me so far.

References

1. Muhandiram J, Pierson J, Wang B, Chizari M (2015) An investigation on stiffness of the temporomandibular joint under cyclical loading. Lecture notes in engineering and computer science. In: Proceedings of the world congress on engineering 2015, WCE 2015, 1–3 July, 2015, London, UK, pp 582–585
2. Ingawalé S, Goswami T (2009) Temporomandibular joint: disorders, treatments, and biomechanics. Ann Biomed Eng 37(5):976–996. doi:10.1007/s10439-009-9659-4 Epub 2009 Feb 28
3. Villamil MB, Nedel LP, Freitas CM, Macq B (2012) Simulation of the human TMJ behavior based on interdependent joints topology. Comput Method Progr Biomed 105(3):217–232. doi:10.1016/j.cmpb.2011.09.010
4. Jalali AR, Norgaard P, Weisbjerg MR, Nadeau E (2012) Effect of stage of maturity of grass at harvest on intake, chewing activity and distribution of particle size in faeces from pregnant ewes. Animal 6(11):1–10. doi:10.1017/S1751731112000493
5. Shimada A, Baad-Hansen L, Svensson P (2015) Effect of experimental jaw muscle pain on dynamic bite force during mastication. Arch Oral Biol 60(2):256–266. doi:10.1016/j.archoralbio.2014.11.001
6. Singh M, Detamore MS (2009) Biomechanical properties of the mandibular condylar cartilage and their relevance to the TMJ disc. J Biomech 42(4):405–417. doi:10.1016/j.jbiomech.2008.12.012
7. Coleta KED, Wolford LM, Gonc JR, dos Santos Pinto A, Cassano DS, Goncalves DAG (2009) Maxillo-mandibular counter-clockwise rotation and mandibular advancement with TMJ Concepts total joint prostheses, Part III—Pain and dysfunction outcome. Int J Oral Maxillofac Surg 38:228–235. doi:10.1016/j.ijom.2008.11.021
8. Soledad Commisso M, Martínez-Reina J, Ojeda J, Mayo J (2015) Finite element analysis of the human mastication cycle. J Mechan Behav Biomed Mater 41:23–35. doi:10.1016/j.jmbbm.2014.09.022
9. Miyawaki S, Tanimoto Y, Araki Y, Katayama A, Kuboki T, Takano-Yamamoto T (2004) Movement of the lateral and medial poles of the working condyle during mastication in patients with unilateral posterior crossbite. Am J Orthod Dentofacial Orthop 126(5):549–554
10. Muhandiram J, Wang B, Chizari M (2014) Effect of cyclic loading on the temporomandibular joint. Lecture notes in engineering and computer science: proceedings of the world congress on engineering 2014, WCE 2014, July 2–4, 2014, London, UK, pp 655–658
11. Ostry DJ, Flanagan JR (1989) Human jaw movement in mastication and speech. Arch Oral Biol 34(9):685–693. Available: http://www.ncbi.nlm.nih.gov/pubmed/2624559

Catalytic Membrane Reactor for VOC Destruction 1

Mohammed Nasir Kajama, Ngozi Claribelle Nwogu and Edward Gobina

Abstract Platinum-alumina (Pt/γ-Al_2O_3) membrane was prepared using evaporative-crystallization deposition method for volatile organic compounds (VOCs) destruction. SEM-EDXA observation, BET measurement, permeability assessment and the catalytic oxidation of propane, n-butane and propylene representing VOC was obtained. Remarkable propane conversion of VOC with Pt catalyst was achieved at moderate temperature. The temperature at which the catalytic combustion takes place for the VOC is lower than the one obtained from the literature for the same VOC on Pt/γ-Al_2O_3 catalysts. The conversion was achieved by varying the reaction temperature using flow-through catalytic membrane reactor operating in the Knudsen flow regime.

Keywords Flow-through membrane reactor · n-butane conversion · Platinum supported alumina catalysts · Propane conversion · Propylene conversion · Volatile organic compounds (VOCs)

Nomenclatures

Symbols

F Permeation flux (mol m^{-2} s^{-1} Pa^{-1})
K Knudsen permeation flux (mol m^{-2} s^{-1} Pa^{-1})
L Thickness (m)
M Molecular weight of gas (g/mol)
P_{av} Average pressure (Pa)

M.N. Kajama · N.C. Nwogu · E. Gobina (✉)
School of Engineering, Centre for Process Integration and Membrane Technology, Robert Gordon University, Aberdeen, UK
e-mail: e.gobina@rgu.ac.uk

M.N. Kajama
e-mail: m.n.kajama@rgu.ac.uk

N.C. Nwogu
e-mail: n.c.nwogu@rgu.ac.uk

S.-I. Ao et al. (eds.), *Transactions on Engineering Technologies*,
DOI 10.1007/978-981-10-1088-0_13

r Mean pore radius (m)
R Gas constant (8.314 J K^{-1} mol^{-1})
T Temperature (K)

Greek Symbols

β Viscous permeation flux (mol m^{-2} s^{-1} Pa^{-1})
ε Porosity (–)
μ Viscosity (Pa s)
τ Tortuosity (–)

1 Introduction

In recent years enormous environmental and health concerns arising with regards to the pollution being emitted from various industries and automobile exhausts have emerged [1]. These pollutants are mentioned as volatile organic compounds (VOCs), nitrogen oxides (NO_x), sulphide oxides (SO_x) among others. This has prompted the issuance of stringent regulations on the emissions of these pollutants (e.g. VOCs). VOC emissions have been strictly regulated in different countries around the globe. For example, in the air quality standards developed by the United States Environmental Protection Agency (USEPA) the maximum 3-h concentration of 1.6×10^{-4} kg/m^3 (0.24 ppm) hydrocarbon content should not be exceeded for a period of more than a year [2, 3]. However, reduction of VOC emissions that exceed the current national air quality standard for ozone of 0.12 ppm is mandated under Title I of the US Clean Air Act Amendment (USCAAA) of 1990. Also, Title III of the amendments requires 90 % reduction in emissions of 189 toxic pollutants, of which 70 % are VOCs. The recently passed European Community emissions limit is 35 g total organic compounds (TOC) per cubic meter gasoline loaded [2]. Likewise, the Gothenburg protocol states that by 2020 the European Union (EU) should reduce VOC emission levels by 50 % compared to the year 2000.

In African countries, VOC legislation is not a very common practice but VOC regulations can be found for example in North Africa. Morocco has approved a draft decree which sets standards for air quality and the manner of installation of monitoring networks [4]. The decree is similar to the National Ambient Air Quality Standards (NAAQS) in South Africa and includes regulations for benzene [4]. Most sections of the National Environmental Management: Air Quality Act (NEMAQA) in South Africa have been brought into effect. The legislative reform in the form of the National Environmental Management: Air Quality Act (No. 39 of 2004) in 2004 replaced the outdated Atmospheric Pollution Prevention

Act (APPA) from the year 1965 (No. 45 of 1965). The act provides the basis for setting standards for ambient air quality and emissions respectively.

Different techniques are available to control VOCs emissions. These techniques include process and equipment optimizations [2, 5], add-on or end-of-the-pipe control techniques, absorption, adsorption and condensation [2, 5, 6]. These techniques are categorized under either destruction and/or recovery of the pollutants. Contaminants can be destroyed by either oxidation/incineration or by biodegradation. Among the VOC abatement technologies mentioned above, the most widely implemented VOC destruction methods are thermal and catalytic oxidation in which VOCs are combined with oxygen at specific temperatures and yield carbon dioxide (CO_2) and water (H_2O).

Thermal oxidation or thermal incineration is the process of oxidizing combustible materials such as VOCs by increasing their temperature above the auto-ignition point and when combined with oxygen at a high temperature yields carbon dioxide and water. Thermal oxidizers are very popular for VOC combustion [2, 5, 7, 8]. The temperature range used to achieve VOC combustion for thermal oxidation systems is typically between 704 and 982 °C [2, 5]. Some compounds that are difficult to combust or are present at low inlet concentrations will need greater heat input and retention time in the combustion zone. Inlet concentrations above 25 % of the lower explosive limits (LEL) are avoided due to explosion hazards [2, 5, 9]. The disadvantage of thermal oxidizers when operating at temperatures near 982 °C is that they produce higher levels of nitrogen oxides, which is a secondary pollutant that may require further treatment.

Catalytic oxidation or catalytic incineration systems also combust VOCs in a similar way that thermal oxidation does. As its name implies, catalytic oxidation uses a catalyst in order to facilitate the rate of a chemical reaction without itself being consumed. The main difference between thermal and catalytic oxidation is that catalytic oxidation operates at a lower temperature typically between 371 and 482 °C [2, 5]; 260 and 482 °C [6]. They offer many advantages for the appropriate application. The required energy for catalytic oxidation is lower than that for thermal oxidation due to the presence of the catalyst resulting in lower operating and/or capital cost [2, 5, 6]. Destruction efficiencies in excess of 90 % with a higher destruction and removal efficiency of 95 % are common [2, 5, 10]. Catalytic oxidation can be applied to the abatement of VOCs at low concentrations at a higher range of total gas flow rate [11, 12]. Catalytic oxidizers are usually applied to mitigate emissions from VOC sources, including process vents, solvent evaporation processes as well as gasoline bulk-loading operations [13]. Catalytic oxidation can also be used in mobile sources. For example, the automotive exhaust gases formed in gasoline engines contain a lot of environmentally unfriendly compounds as a result of incomplete oxidation, such as hydrocarbons (HCs), carbon monoxide (CO) and NO_x which necessitate the introduction of a catalytic converter in order to treat the exhaust gas [6, 14]. A catalytic converter converts three regulated emissions which are VOCs, CO and NO_x, and known as the *Three Way Catalyst (TWC)* to CO_2, H_2O and N_2. The introduction of the TWCs started in the 1970s [15] and now almost 85 % of the world's cars are fitted with the TWC [6].

Literature discloses that platinum supported on alumina are more superior for the catalytic combustion of VOCs [11, 16–22]. Noble-metal based catalysts are mostly obtained with γ-Al_2O_3 as a support with over 65 % dispersion [11]. Performance of catalysts robustly relies on the method of preparation. This will dictate the degree of metal dispersion on the surface of the support and the metallic nano-particles size. The content of the noble metal should be low due to its high cost. Consequently, particle size and dispersion are among the key parameters ensuing in preparing such catalysts for VOC abatement [11]. This approach was employed in a sequence of work by [23, 24] who used catalytically modified fly-ash filters for alcohol dehydration and for the reduction of nitrogen oxides with ammonia. A step further was taken in previous work by [16] in which toluene combustion was proposed using a Pt/Al_2O_3 catalytic membrane operating in the Knudsen diffusion regime [25].

Gluhoi et al. [22] compared the oxidation of propene and propane over gold-copper oxide (Au/Al_2O_3) and (Pt/Al_2O_3) catalysts. Propene conversion for Au/Al_2O_3 was obtained at nearly 450 °C compared to (Pt/Al_2O_3) below 300 °C. Their findings exhibited that Pt/Al_2O_3 has higher activity than the Au containing catalysts for propene and propane conversion.

Besides the industrialized VOCs abatement processes, destruction of VOC into CO_2 and H_2O have been widely studied using membrane reactors [11, 16–22]. A membrane reactor is a process which combines reaction and separation in a single unit [26]. They can be made from different materials such as metals, ceramics and polymers [27]. Different definitions exist for membrane reactors (MRs). The International Union of Pure and Applied Chemistry (IUPAC) define a membrane reactor as a device for simultaneously carrying out a reaction and membrane-based separation in the same physical enclosure [28]. According to a wider definition, any reactor in which a chemical reaction is performed in the presence of a membrane is called membrane reactor [29]. The application of membrane reactors has received attention over five decades and quite a lot of papers have been published on the subject of catalysis, membrane science and chemical engineering [30–34]. The membrane is used as an active candidate in a chemical conversion for increasing the reaction rate, selectivity and yield [30]. The interest of membrane reactors has been demonstrated on the laboratory scale for dehydrogenation, hydrogenation, decomposition and oxidation reactions among others [30].

In recent years, the concept applied to the combination of membranes and reactors is being proposed. The concept is classified into three groups namely; extractor, distributor and contactor which are related to the role of the membrane in the process [30].

Extractor This type of concept is used to selectively remove the product(s) from the reaction mixture. Extractor mode membrane rectors are applied to enhance conversion if there is limitation due to thermodynamic equilibrium. For example, by enhancing catalytic dehydrogenation of alkanes by selectively extracting the hydrogen being produced [35]. Steam reforming of methane, water gas shift and the decomposition of H_2S have also been demonstrated on the laboratory scale with membrane using the reactor extractor mode [27]. Two main factors controlling the

efficiency of this particular process are the hydrogen permeability of the membrane and its permselectivity. But most extractors feature the removal of hydrogen while some decomposition reactions consider oxygen removal [30].

Gobina and Hughes [36] investigated the catalytic dehydrogenation of n-butane in a membrane reactor. They used palladium and silver (Pd/Ag) membranes with a thickness of 6 μm. The use of inert nitrogen and reactive sweep gases nitrogen/carbon monoxide and nitrogen/oxygen enhanced their conversion of n-butane.

Dehydrogenation of cyclohexane to benzene has been investigated by Tiscarño-Lechuga et al. [37]. A comparison between a pure membrane reactor, a conventional packed bed reactor, and a hybrid membrane reactors consisting of a packed bed reactor segment followed by a membrane reactor segment was carried out. The conversion obtained in a pure membrane reactor was 60–128 % higher than that obtained in a conventional packed bed reactor. However, the increases in the conversion level obtained are not primarily attributed to the selective removal of hydrogen through the membrane but to the reduction of the partial pressures of the reactants in the retentate stream.

Distributor This type of concept is used to control the addition of reactants to the reaction mixture. A distributor mode membrane reactor is the second mode of application for permselective membranes. This mode is typically tailored in partial oxidation or oxydehydrogenation of hydrocarbons [30]. For example, in reacting an alkane with oxygen, a distributor is used to control the supply of oxygen in a fixed bed of catalysts. The supply of the oxygen by-passes the explosive zone in order to optimize the oxygen concentration and maximize the selectivity in the desired product [30, 31]. The oxygen permselectivity of the membrane is a significant factor since air can also be used rather than pure oxygen in the oxygen supply side [30, 31]. However, the main concern in this type of mode is that commercially available oxygen selective membranes being developed have low permeability (e.g. dense oxygen permselective membranes) and can only operate at relatively high temperatures >800 °C. Also, there are issues of long term stability [30]. Due to these constraints, some authors have applied macroporous and mesoporous membranes as oxygen distributors for oxidative reactions at temperatures <700 °C [30, 31].

Coronas et al. [38] used a fixed bed of Li/MgO catalyst deposited on a porous ceramic membrane. Oxygen was permeated through the membrane while ethane was fed axially. They used two different configurations; a homogeneous wall membrane reactor and a mixed system equivalent to a membrane reactor followed by a conventional fixed bed reactor. They obtained high conversions of ethane, while maintaining good selectivity. The yield to ethylene and higher hydrocarbons of up to 57 % was reported.

Finally, Contactor This type of concept is used to intensify the contact between reactants and the catalyst. The active contactor mode membrane reactor involves a forced flow-through membrane reactor, where the membrane acts as a diffusion barrier and is catalytically active [30, 31]. This type of membrane is used to provide

a reaction space where the catalyst is deposited inside the membrane pores. The catalyst-membrane arrangement leads to high catalytic activity [30, 31]. The forced flow-through contactor mode has been widely employed by many researchers in the total oxidation of VOCs [23, 35, 39–45].

Zalamea et al. [43] also developed catalytic membranes operating in a mixed permeation regime i.e. Knudsen and laminar contributions. The membranes prepared had wide pores and presented a low pressure drop. The Pt/γ-Al_2O_3 was active for VOC combustion. They achieved complete n-hexane conversion at 300 °C with 2 wt% γ-Al_2O_3 and 0.15 wt% Pt respectively.

Pina et al. [25] investigated the combustion of VOCs over platinum-based catalytic membranes in a porous catalytic membrane using toluene and methyl ethyl ketone (MEK) as representative VOCs. The Pt loading used was between 0.016 and 0.45 wt% and the membrane operating under the Knudsen diffusion regime. The two methods used were impregnation and chemical vapour deposition (CVD). The membrane performed efficiently allowing total VOC destruction at temperatures below 300 °C.

Saracco and Specchia [46] also investigated VOC abatement with catalytic filters using Pt/γ-Al_2O_3 catalyst by the wet impregnation method. However, they also used naphthalene representing PAH, propylene representing alkenes, propane representing alkanes and methane are well-known refractories to catalytic combustion as VOCs at a temperature of up to 600 °C.

Tahir and Koh [18] extended the development of noble metal catalysts by depositing a low Pt-loading on the external surface of the Al_2O_3 support for the removal of traces of various VOCs. They applied a series of Pt-loadings ranging from 0.05–0.4 wt% for methanol, toluene, n-butyl-amine and n-hexane destruction. The authors observed a 50 % increase of the temperature during toluene conversion from 180 to 263 °C when Pt loading decreased from 0.4 to 0.05 wt%.

The objective of this work is to prepare a platinum-alumina membrane using a simple but effective method for VOC destruction on a low Pt catalyst.

2 Experimental

2.1 Alumina Ceramic Support

The alumina tube supplied by Ceramiques Techniques et Industrielles (CTI SA) France consists of 77 % alumina + 23 % TiO_2 and possessed an internal and outer diameter of 7 and 10 mm respectively. The support consisted of a permeable length of 348 mm and a porosity of 45 %. This membrane was chosen because it possesses good resistance to corrosion and oxidation, as well as chemical and mechanical stability at high temperature, and it is commercially available in different shapes and sizes. The tubular alumina membrane used for this experiment is depicted in Fig. 1.

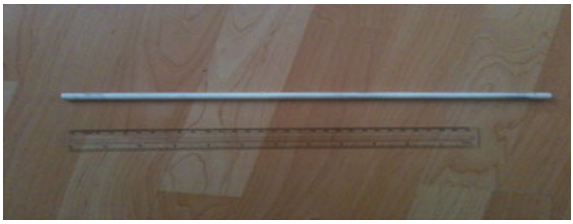

Fig. 1 Pictorial view of commercial tubular ceramic support

2.2 Catalytic Membrane Preparation

Platinum supported on γ-alumina was demonstrated as the most efficient catalytic system for VOC destruction [11, 12, 19, 47] leading to the lowest operating temperature. The Pt/γ-Al_2O_3 membrane was prepared by the repeated dip-coating technique. Chloroplatinic acid solution (H_2PtCl_6) has been used as a platinum precursor. The tubular support was first dried at 65 °C. After weighing, it was dipped for 2 h in deionized water before Pt introduction. The deposition method used was based on evaporation-crystallization steps. This method was based on the so-called "reservoir" method proposed by [48–50]. The tube was dipped in a 10 g/l H_2PtCl_6 precursor solution for 10 h. The sample was then dried at room temperature for 24 h to favor evaporation from the inner side and deposition in the top layer. Metallic platinum was obtained after thermal treatment of the sample under flowing hydrogen at 400 °C for at least 2 h followed by nitrogen flow for 1 h at 400 °C. After the above processes the membrane could be used as a reactor.

2.3 Membrane Characterization and Flow Configuration

Scanning electron microscopy (Zeiss EVO LS10) was used to determine the position of platinum particles inside the porous structure of the ceramic material. Samples for crosswise Pt EDXA were prepared by breaking the tube after depositing a film on the section. SEM and EDXA results (Fig. 2) indicate the presence of Pt. The surface area of the support and Pt/Al_2O_3 was measured using Brunauer-Emmett-Teller (BET) method from nitrogen adsorption-desorption at 77 K using automated gas sorption analyzer (Quantachrome instrument version 3.0) (Table 1). All samples were first degassed at 400 °C for 2 h prior to the nitrogen adsorption analysis. Gas permeation measurements of propylene were performed before and after Pt deposition using a conventional setup [48]. The gas permeate flow was measured [48–51] by a digital flowmeter (Cole-Parmer). The catalytic tests were carried out on a membrane reactor consisting of a stainless steel shell housing the catalytic membrane and operated by means flow-through contactor configuration.

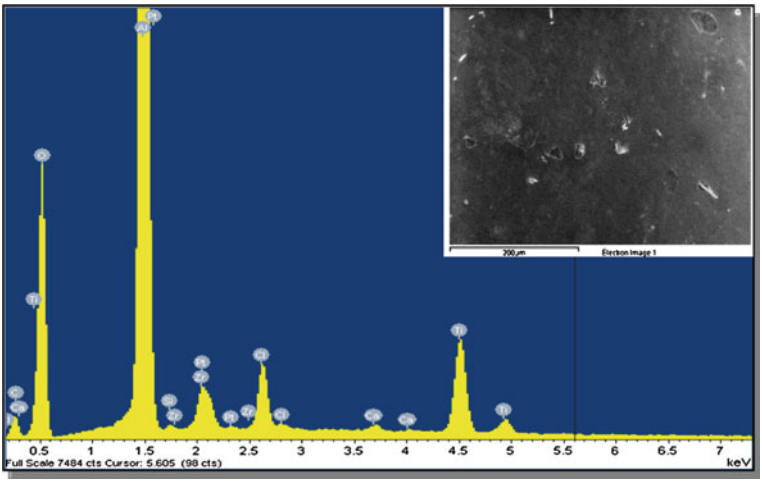

Fig. 2 SEM-EDXA image of the Pt membrane outer surface

Table 1 BET surface area and average pore diameter of the alumina support and Pt membrane

Membrane	BET surface area (m^2/g)	Pore diameter (nm)
Alumina support	0.364	4.17
Pt membrane	0.426	3.70

The VOC reactants mixture was composed of propane/oxygen, n-butane/oxygen and propylene/oxygen. The reaction products were analyzed by CO_2 analyzer (CT2100-Emissions Sensor).

3 Results and Discussion

3.1 Platinum Membrane Characterization

The experimental results of gas permeation and the selected VOCs (propane, n-butane and propylene) destruction on Pt/Al_2O_3 membrane reactor are discussed below.

Permeation experiments were carried out at 25 °C using propylene as the permeating gas in order to quantify the viscous and Knudsen flow contributions. Equation (2) was used to relate the permeation flux and average pressure [16].

$$F = \beta P_{av} + K \tag{1}$$

where β and k equals;

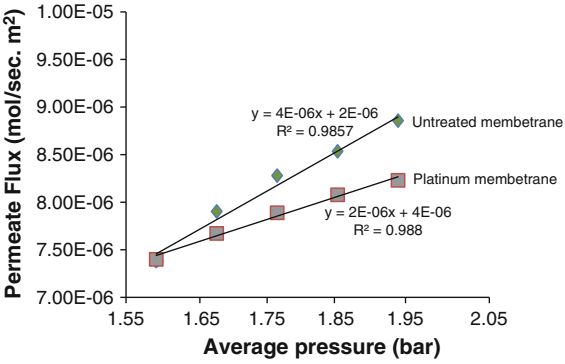

Fig. 3 Permeation flux against average pressure across the membrane for untreated membrane (γ-Al_2O_3) and platinum membrane (Pt/γ-Al_2O_3) membrane at 298 K

$$\beta = 0.125\frac{\varepsilon r^2}{L\tau\mu RT}, \quad \text{and} \quad K = 1.06\frac{\varepsilon r}{L\tau\sqrt{MRT}} \tag{2}$$

where, F is the permeation flux per unit of time and area, ε is the porosity of the membrane, r is the mean pore radius (m), $P_{av} = (p_1 + p_2)/2$ is the average pressure (Pa), μ is the viscosity (Pa s) and L is the thickness of the membrane (m), τ is the tortuosity, M is the molecular weight of the diffusing gas (g/mol), R gas constant (8.314 J K^{-1} mol^{-1}) and T the permeation temperature (K). β and K can be regarded as viscous and Knudsen contributions to the permeation flux.

Figure 3 depicts the permeate flux of the untreated and Pt/Al_2O_3 membranes. From Fig. 3, it can be seen that the slope of the line corresponding to the untreated membrane is high indicating a large viscous flow contribution. On the other hand, after Pt impregnation, a lower slope is obtained which indicates a reduction in the viscous flow contribution. The obtained results almost corroborate the literature [16].

3.2 Propane Conversion

Pt optimization to be deposited on the alumina membrane is the key subject to be addressed in order to achieve a higher conversion of VOC (at minimum precious metal content) to less harmful products inside the catalytic membrane. The application of higher Pt contents would possibly result in a further activity increase [46]. In addition, Pt concentrations higher than 5 wt% are only employed in industrial practice [46, 52].

Figure 4 depicts the propane conversion curve in the tubular membrane reactor as a function of temperature for the 3.52 wt% Pt catalyst at different total flow rates ranging from 180 to 286 ml/min. It can be seen that 72 % propane conversion is achieved at a temperature of 232 °C. Gluhoi et al. [22] obtained 72 % propane conversion at nearly 275 °C on 1-wt% Pt/Al_2O_3. Saracco and Specchia [46] also

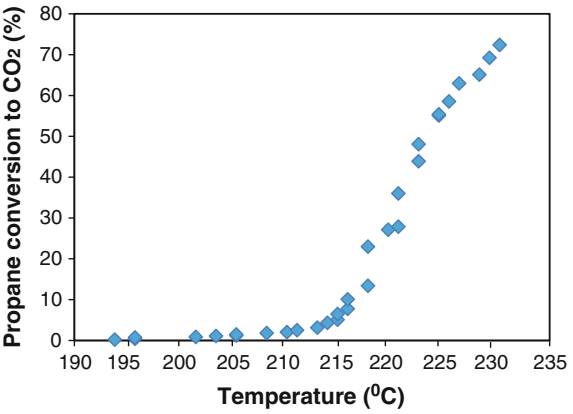

Fig. 4 Propane conversion against reaction temperature

obtained 72 % propane conversion at nearly 365 °C on 5-wt% Pt/γ-Al_2O_3. Therefore, the temperature at which the catalytic combustion takes place for this VOC in this study is lower than those obtained in the literature [22, 46] for the same organic compounds on Pt/γ-Al_2O_3 catalysts.

3.3 n-Butane Conversion

Figure 5 depicts the relationship between the (20 % n-butane and 80 % nitrogen) conversion curve in the tubular membrane reactor as a function of temperature for the 3.52 wt% Pt catalyst at different total flow rates ranging from 271 to 319 ml/min. It can be seen that a 46 % n-butane conversion is achieved at a temperature of 273 °C on Pt/γ-Al_2O_3 catalysts. This result corroborates with the work of Okal and Zawadzki [53] were 46 % n-butane conversion was achieved at

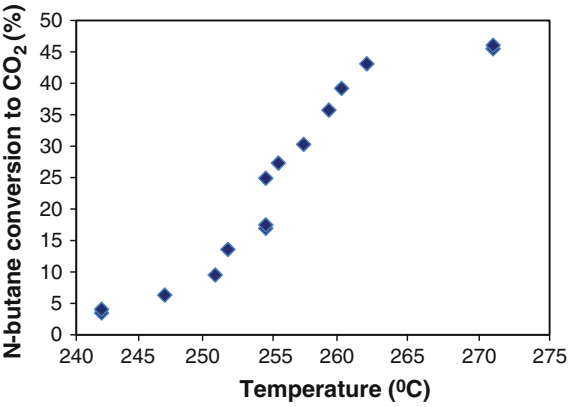

Fig. 5 n-butane conversion against reaction temperature

295 °C using 4.6 % Ru/γ-Al_2O_3 catalyst. This is a clear indication that Pt catalysts are superior to other noble metals for VOC abatement.

3.4 Propylene Conversion

Figure 6 depicts propylene conversion in the tubular membrane reactor as a function of temperature for the 3.52 wt% Pt catalyst at different total flow rates ranging from 148 to 452 ml/min. From Fig. 6, a 68 % propylene conversion is achieved at a temperature of 220 °C on Pt/γ-Al_2O_3 catalyst. Saracco and Specchia [46] also obtained a similar conversion at almost 260 °C with 5-wt% Pt content. In this study, the temperature at which the catalytic combustion takes place for propylene is lower than the one obtained by Saracco and Specchia [46] on similar catalysts.

In general, the experimental VOC conversion occurred because in the Knudsen diffusion regime, the probability of collisions between the molecules and the membranes pore wall is maximized which renders the optimum use of the catalyst on the pores of the membrane [16]. The fact that a high conversion is achieved at moderate temperature is also an indication that the impregnation of the catalyst is uniformly distributed and well dispersed over the surface of the membrane. Otherwise, if there was any crack on the membrane, the preferential permeation through the defected region would probably give rise to decreased conversion. In addition, the membrane used was able to maintain prolonged experiments over 100 h under reaction at approximately 400 °C without any loss of mechanical integrity or catalytic activity.

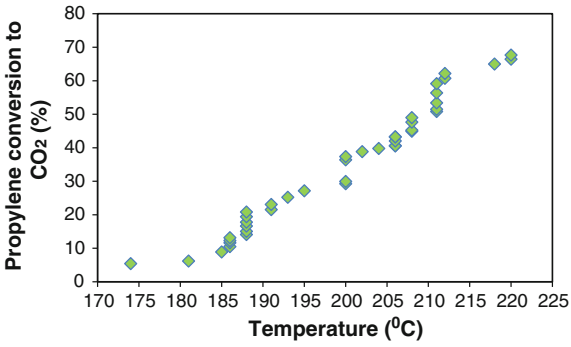

Fig. 6 Propylene conversion against reaction temperature

4 Conclusion and Future Work

This study had demonstrated the attractiveness of tubular membrane reactor for separation and reaction. The membrane reactor designed was operational for high temperature as well as corrosion resistant. Experimental procedure to implement VOCs destruction was developed. Experiments on the catalytic combustion of VOCs were conducted with alumina membrane reactor. VOC conversion was significantly achieved and the product yield permeated through the alumina membrane which is monitored using CO_2 analyzer. The conversion enhancements over Pt catalyst were obtained at lowest reactant flow rates and moderate temperatures. Also, the maximum conversion obtained by the membrane reactor was comparable with some literature.

The result of the selected VOC conversion confirms that the flow-through membrane reactor operation is a promising alternative using this simple but effective "reservoir technique". The reservoir method combined with proper selection of the support resulted in high conversion and reduced precious metal content. This will reduce cost and enhance commercialization.

The experimental study was to develop an understanding of some important factors that contribute to the influence of alumina membrane reactor for catalytic membrane reactor/separator. This demonstrates that the use of a membrane reactor enhanced reactant conversion as well as product yield. The use of simulation study is recommended for future study in order to accurately assess and validate the performance of this experimental design.

Acknowledgment The authors gratefully acknowledge Petroleum Technology Development Fund (PTDF) Nigeria for funding this research, and School of Pharmacy and Life Sciences RGU Aberdeen for the SEM and EDXA results.

References

1. Choudhary T, Banerjee S, Choudhary V (2002) Catalysts for combustion of methane and lower alkanes. Appl Catal A 234(1):1–23
2. Khan FI, Ghoshal AK (2000) Removal of volatile organic compounds from polluted air. J Loss Prev Process Ind 13(6):527–545
3. Tamaddoni M, Sotudeh-Gharebagh R, Nario S, Hajihosseinzadeh M, Mostoufi N (2014) Experimental study of the VOC emitted from crude oil tankers. Process Saf Environ Prot 92 (6):929–937
4. Ojala S, Pitkäaho S, Laitinen T, Koivikko NN, Brahmi R, Gaálová J et al (2011) Catalysis in VOC abatement. Top Catal 54(16–18):1224–1256
5. Ruddy EN, Carroll LA (1993) Select the best VOC control strategy. Chem Eng Progr (USA) 89(7)
6. Rusu AO, Dumitriu E (2003) Destruction of volatile organic compounds by catalytic oxidation. Environ Eng Manage J 2(4):273–302

7. Marks J, Rhoads T (1991) Planning saves time and money, when installing VOC controls. Chem Process 5:42
8. William JC, Lead PE (1997) VOC control strategies in plant design. In: William JC, Lead PE (Eds). Chemical Processing: Project Engineering Annual. Chicago, IL: Putman, Fall, p 44
9. Mukhopadhyay N, Moretti EC, Nilson T (1993) Current and potential future industrial practices for reducing and controlling volatile organic compounds. Center for Waste Reduction Technologies, American Institute of Chemical Engineers
10. Patkar A, Laznow J (1992) Hazardous air pollutant control technologies. Hazmat World 2:78
11. Benard S, Ousmane M, Retailleau L, Boreave A, Vernoux P, Giroir-Fendler A (2009) Catalytic removal of propene and toluene in air over noble metal catalyst This article is one of a selection of papers published in this special issue on biological air treatment. Can J Civil Eng 36(12):1935–1945
12. Liotta L, Ousmane M, Di Carlo G, Pantaleo G, Deganello G, Boreave A et al (2009) Catalytic removal of toluene over Co_3O_4–CeO_2 mixed oxide catalysts: comparison with Pt/Al2O3. Catal Lett 127(3–4):270–276
13. Moretti EC (2002) Reduce VOC and HAP emissions. Chem Eng Prog 98(6):30–40
14. Nice K, Bryant CW (2000) How catalytic converters work. http://www.howstuffworks.com/HowStuffWorks. Accessed 10 Mar 2004
15. Heck RM, Farrauto R, Gulati S (2010) Catalytic air pollution control: commercial technology. Platin Met Rev 54(3):180–183
16. Pina M, Menéndez M, Santamaria J (1996) The Knudsen-diffusion catalytic membrane reactor: an efficient contactor for the combustion of volatile organic compounds. Appl Catal B 11(1):L19–L27
17. Paulis M, Gandıa L, Gil A, Sambeth J, Odriozola J, Montes M (2000) Influence of the surface adsorption–desorption processes on the ignition curves of volatile organic compounds (VOCs) complete oxidation over supported catalysts. Appl Catal B 26(1):37–46
18. Tahir SF, Koh CA (1999) Catalytic destruction of volatile organic compound emissions by platinum based catalyst. Chemosphere 38(9):2109–2116
19. Paulis M, Peyrard H, Montes M (2001) Influence of chlorine on the activity and stability of Pt/Al_2O_3 catalysts in the complete oxidation of toluene. J Catal 199(1):30–40
20. Radic N, Grbic B, Terlecki-Baricevic A (2004) Kinetics of deep oxidation of n-hexane and toluene over Pt/Al_2O_3 catalysts: platinum crystallite size effect. Appl Catal B 50(3):153–159
21. Kim DH, Kung MC, Kozlova A, Yuan S, Kung HH (2004) Synergism between Pt/Al_2O_3 and Au/TiO_2 in the low temperature oxidation of propene. Catal Lett 98(1):11–15
22. Gluhoi AC, Bogdanchikova N, Nieuwenhuys BE (2006) Total oxidation of propene and propane over gold–copper oxide on alumina catalysts: comparison with Pt/Al_2O_3. Catal Today 113(3):178–181
23. Saracco G, Specchia V (1995) Catalytic ceramic filters for flue gas cleaning. 2. Catalytic performance and modeling thereof. Ind Eng Chem Res 34(4):1480–1487
24. Saracco G, Specchia S, Specchia V (1996) Catalytically modified fly-ash filters for NOx reduction with NH_3. Chem Eng Sci 51(24):5289–5297
25. Pina M, Irusta S, Menéndez M, Santamaria J, Hughes R, Boag N (1997) Combustion of volatile organic compounds over platinum-based catalytic membranes. Ind Eng Chem Res 36 (11):4557–4566
26. Sanchez Marcano J, Tsotsis T (2002) Catalytic membrane reactors and membrane reactors
27. Westermann T, Melin T (2009) Flow-through catalytic membrane reactors—principles and applications. Chem Eng Process 48(1):17–28
28. Koros W, Ma Y, Shimidzu T (1996) Terminology for membranes and membrane processes (IUPAC Recommendations 1996). Pure Appl Chem 68(7):1479–1489
29. Saracco G, Specchia V (1994) Catalytic inorganic-membrane reactors: present experience and future opportunities. Catal Rev Sci Eng 36(2):305–384

30. Julbe A, Farrusseng D, Guizard C (2001) Porous ceramic membranes for catalytic reactors—overview and new ideas. J Membr Sci 181(1):3–20
31. Coronas J, Santamarıa J (1999) Catalytic reactors based on porous ceramic membranes. Catal Today 51(3):377–389
32. Hwang S (2001) Inorganic membranes and membrane reactors. Korean J Chem Eng 18 (6):775–787
33. Lu G, da Costa JD, Duke M, Giessler S, Socolow R, Williams R et al (2007) Inorganic membranes for hydrogen production and purification: a critical review and perspective. J Colloid Interface Sci 314(2):589–603
34. Uemiya S (2004) Brief review of steam reforming using a metal membrane reactor. Top Catal 29(1–2):79–84
35. Dittmeyer R, Höllein V, Daub K (2001) Membrane reactors for hydrogenation and dehydrogenation processes based on supported palladium. J Mol Catal A: Chem 173 (1):135–184
36. Gobina E, Hughes R (1996) Reaction coupling in catalytic membrane reactors. Chem Eng Sci 51(11):3045–3050
37. Tiscarño-Lechuga F, Hill C, Anderson M (1996) Effect of dilution in the experimental dehydrogenation of cyclohexane in hybrid membrane reactors. J Membr Sci 118(1):85–92
38. Coronas J, Menendez M, Santamaria J (1995) Use of a ceramic membrane reactor for the oxidative dehydrogenation of ethane to ethylene and higher hydrocarbons. Ind Eng Chem Res 34(12):4229–4234
39. Irusta S, Pina M, Menendez M, Santamaria J (1998) Development and application of perovskite-based catalytic membrane reactors. Catal Lett 54(1–2):69–78
40. Lange C, Storck S, Tesche B, Maier W (1998) Selective hydrogenation reactions with a microporous membrane catalyst, prepared by sol–gel dip coating. J Catal 175(2):280–293
41. Yamada M, Fugii K, Haru H, Itabashi K (1988) Preparation and catalytic properties of special alumina membrane formed by anodic oxidation of aluminum. The Light Metal Educational Foundation, Inc., Report of the research group for functionalizing of aluminum and its surface films, pp 175–182
42. Splinter A, Stürmann J, Bartels O, Benecke W (2002) Micro membrane reactor: a flow-through membrane for gas pre-combustion. Sens Actuators B: Chem 83(1):169–174
43. Zalamea S, Pina M, Villellas A, Menéndez M, Santamaría J (1999) Combustion of volatile organic compounds over mixed-regime catalytic membranes. React Kinet Catal Lett 67(1): 13–19
44. Maira AJ, Lau WN, Lee CY, Yue PL, Chan CK, Yeung KL (2003) Performance of a membrane-catalyst for photocatalytic oxidation of volatile organic compounds. Chem Eng Sci 58(3):959–962
45. Tsuru T, Kan-no T, Yoshioka T, Asaeda M (2003) A photocatalytic membrane reactor for gas-phase reactions using porous titanium oxide membranes. Catal Today 82(1):41–48
46. Saracco G, Specchia V (2000) Catalytic filters for the abatement of volatile organic compounds. Chem Eng Sci 55(5):897–908
47. Marécot P, Fakche A, Kellali B, Mabilon G, Prigent P, Barbier J (1994) Propane and propene oxidation over platinum and palladium on alumina: effects of chloride and water. Appl Catal B 3(4):283–294
48. Uzio D, Miachon S, Dalmon J (2003) Controlled Pt deposition in membrane mesoporous top layers. Catal Today 82(1):67–74
49. Iojoiu E, Walmsley J, Raeder H, Bredesen R, Miachon S, Dalmon J (2003) Comparison of different support types for the preparation of nanostructured catalytic membranes. Rev Adv Mater Sci 5(3):160–165
50. Kajama M, Nwogu N, Gobina E (2015) Propylene oxidation using pt-alumina impregnated catalytic membrane reactor. Lecture notes in engineering and computer science: proceedings of the world congress on engineering 2015, WCE 2015, 1–3 July 2015, London, UK, pp 900–903

51. Bénard S, Giroir-Fendler A, Vernoux P, Guilhaume N, Fiaty K (2010) Comparing monolithic and membrane reactors in catalytic oxidation of propene and toluene in excess of oxygen. Catal Today 156(3):301–305
52. Jackson S, Willis J, McLellan G, Webb G, Keegan M, Moyes R et al (1993) Supported metal catalysts: preparation, characterization, and function: I. Preparation and physical characterization of platinum catalysts. J Catal 139(1):191–206
53. Okal J, Zawadzki M (2009) Catalytic combustion of butane on Ru/γ-Al_2O_3 catalysts. Appl Catal B 89(1):22–32

Characterization of an Alumina Membrane Using Single Gas Permeation

Ifeyinwa Orakwe, Ngozi Nwogu and Edward Gobina

Abstract This paper discusses the results of initial experiments carried out using a commercially available alumina membrane. The paper also reveals the important features of ceramic membranes as well as the different transport mechanisms that could take place through these membranes. The experimental results were based on single gas permeation method involving He, O_2, CO_2 and N_2. The effect of trans-membrane pressure drop, gas molecular mass, kinetic diameter, permselectivity, temperature and permeance were studied and discussed. Helium showed a faster flowrate through the membrane and the order of flow was He > O_2 > N_2 > CO_2.

Keywords Alumina membrane · Gauge pressure · Kinetic diameter · Molecular mass · Permeance · Permselectivity · Temperature

Nomenclatures

α	Knudsen separation factor
a	Gas of interest
A	Surface area of the membrane (m^2)
b	Other gas (es)
F	Flowrate (mol s^{-1})
Fi	Flowrate of gas i (mol s^{-1})
F_k	Flowrate due to Knudsen diffusion (mol s^{-1})
i	Gas of interest

I. Orakwe · N. Nwogu · E. Gobina (✉)
School of Engineering, Centre for Process Integration and Membrane Technology (CPIMT), The Robert Gordon University, Aberdeen AB10 7GJ, UK
e-mail: e.gobina@rgu.ac.uk

I. Orakwe
e-mail: i.r.orakwe@rgu.ac.uk

N. Nwogu
e-mail: n.c.nwogu@rgu.ac.uk

S.-I. Ao et al. (eds.), *Transactions on Engineering Technologies*,
DOI 10.1007/978-981-10-1088-0_14

MW_a Molecular weight of gas a
MW_b Molecular weight of gas b
ΔPi Pressure difference of gas i across the membrane (Pa)
Qi Permeance of gas i (mol s^{-1} m^{-2} Pa^{-1})

1 Introduction

A membrane can be defined as a semi-permeable barrier or an interphase between two phases [1, 2].

Membrane technology has drawn so much attention in recent years from both research and industrial sectors including oil and gas, chemical processing, waste water treatment, metal processing and environmental processes. This interest in membrane technology is as a result of their diverse useful and important applications [3].

Ceramic membranes play a part in quite a number of separation processes; either solely or in combination with other separation processes and these can be carried out in both mild and adverse conditions [2]. The membrane technology may involve the separation of individual gases or liquids from a mixture or processes involving separation of gas or vapour mixtures [4, 5].

Figure 1 shows a schematic diagram of a membrane separation process.

The measurement of transport through the membrane is a very vital process that helps in the exploration of the flow characteristics of various gas molecules through a membrane [6]. The performance of a ceramic membrane depends on two major factors which are the selectivity and the flowrate through the membrane [2].

Different types of gas transport mechanisms come into play during gas permeation. The pressure difference across the membrane is used as the driving force for

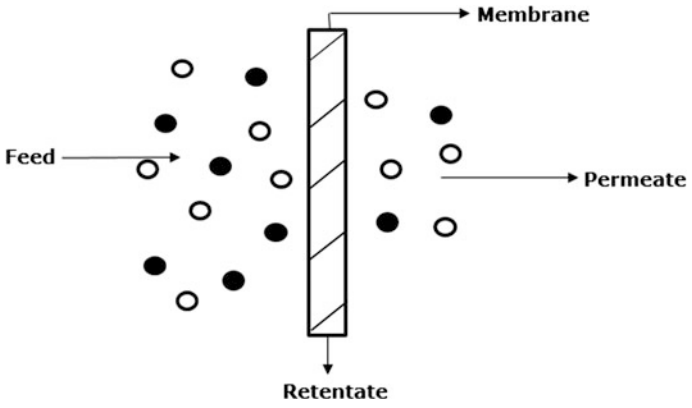

Fig. 1 Schematic diagram of a membrane separation process between two phases [2]

transport [7]. The gas transport is based on the assumption that the pores in a membrane are made up of capillary tubes, and these capillary tubes serve as a passage for gas from the feed to the permeate/retentate side. The transport mechanisms governing this gas transfer has been explained in various forms: viscous flow, Knudsen diffusion, molecular sieving, surface diffusion, multi-layered diffusion and solution diffusion [3]. There are also different factors that may determine the transport mechanism. These factors could be due to the molecular weight of the gases, kinetic diameter which is the size of the molecules, temperature, the gas concentration, or the affinity of the gas for the membrane [7].

Figure 2 shows a diagram of the different transport mechanisms that can take place through a membrane. In Fig. 2, porous and dense systems were being described as well as the pore sizes of the membranes that could exist.

The various transport mechanism shown in Fig. 2 are explained below.

The viscous flow mechanism describes a transport where molecule-molecule gas collision is more predominant than the gas molecule-pore wall collision. This occurs when the mean free path is smaller than the pore size of the diffusing molecule [3].

Knudsen flow mechanism explains the gas transport in a membrane in which the collision between molecules and pore wall is more frequent than molecule-molecule collision. If the molecule-pore collision is greater than the molecule-molecule collision, Knudsen flow occurs [3].

Surface diffusion explains the behaviour of permeant as they flow through a membrane at high pressure or at a low temperature. The membrane surface tends to attract the permeants thereby absorbing them into the pore walls of the membrane [3]. This attraction also makes it possible for the absorbed gases to diffuse on the

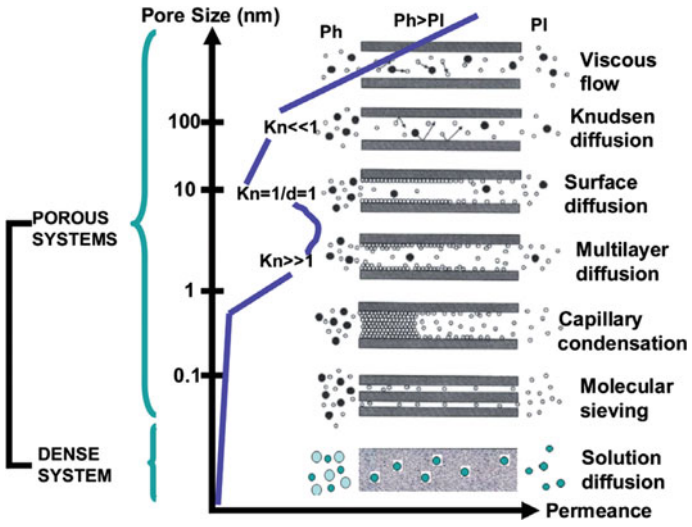

Fig. 2 Diagram of the different types of separation mechanism [6]

surface. The properties of the membrane material are assumed to play a major part in surface diffusion [8].

Multi-layer type of gas transport describes the permeating species being adsorbed at different layers as they flow through the membrane [6].

In capillary condensation, some molecules in the permeating species condense into a liquid form [9]. This happens in a case where there exist a condensable and a non-condensable gas. The condensable gases flow through the membrane as liquids thereby preventing the flow of the non-condensable gases. The capillary condensation type of gas transfer greatly depends on the nature of separation as well as the chemical composition of the membrane in question [4].

Molecular sieving type of gas transport is based on the membrane pore size and the gas molecular size. For a gas separation to occur, the membrane's pore diameter has to fall within the molecular sizes of the gases to be separated [9].

Solution diffusion mechanism is predominant in the dense type of membrane. It occurs when the permeating species dissolves in the membrane itself and this then pass through the membrane due to a concentration gradient [9]. It is presumed to be a three stage process: the first stage occurs at the upstream where the membrane surface absorbs the gas molecules, this is then followed by diffusion of the gas molecules through the membrane material and lastly at the downstream end where the gas molecule evaporates [10].

In this study, the gas transport characteristics through the membrane has been critically evaluated. Transport mechanisms have been deduced from the results [8].

Equation 1 can be used to calculate the membrane's selectivity factor α of two or more gases [8].

$$\propto_{a/b} = \frac{F_a}{F_b} \tag{1}$$

where

α Knudsen separation factor
F Flowrate through the membrane (mol/s)
a Gas of interest
b Other gas (es)

In the case of Knudsen flow, Eq. (1) can be written as

$$\alpha_{a/b} = \frac{F_{k^a}}{F_{k^b}} = \sqrt{\frac{MW_b}{MW_a}} \tag{2}$$

where

F_k Flowrate due to Knudsen diffusion (mol/s)
MW_a Molecular weight of gas a
MW_b Molecular weight of gas b

2 Experimental

The membrane used was supplied by Ceramiques Techniques et industrielles (CTI SA) France. It is a commercially made ceramic membrane tube of permeable length of 31.8 cm. The inner and outer diameters were 0.07 and 0.1 cm respectively. The single gases used for the permeation analysis were helium (He), oxygen (O_2), nitrogen (N_2) and carbondioxide (CO_2). Figure 3 shows a picture of the ceramic membrane.

Figure 4 shows the experimental setup for the permeation test. The setup consists of the delivery system for the different gases, the membrane reactor, pressure gauge and flow meter. The membrane was sealed inside the membrane reactor prior to the analysis. This was done to ensure that there is no leakage during the gas permeation. This is shown in Fig. 5. Gas flowrates were maintained with the control valve located before the gauge pressure. Digital gauges measured the pressure at which the gases flowed into the membrane reactor. The flowmeter connected to the permeate port measured the flow rate of the permeate gas. The permeate was maintained at atmospheric pressure. The permeation tests were carried at various temperature of 298–470 K. For the permeation at different temperatures, the reactor was wrapped with a heating jacket with series of thermocouples located at strategic positions along the reactor length to allow monitoring of the membrane temperature. This method was adopted from Gobina [11].

Fig. 3 Ceramic alumina membrane

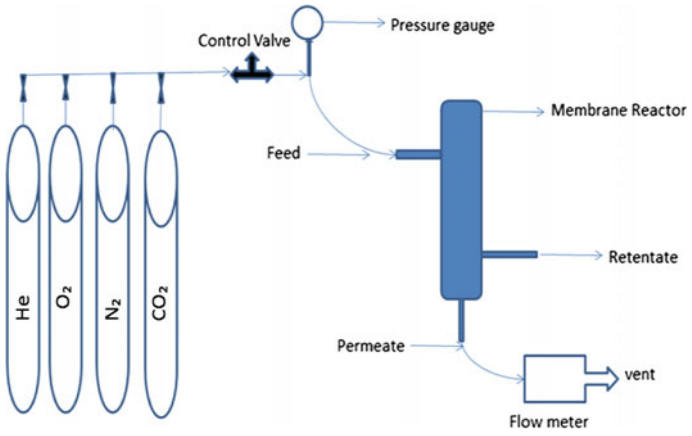

Fig. 4 Schematic diagram of the experimental setup

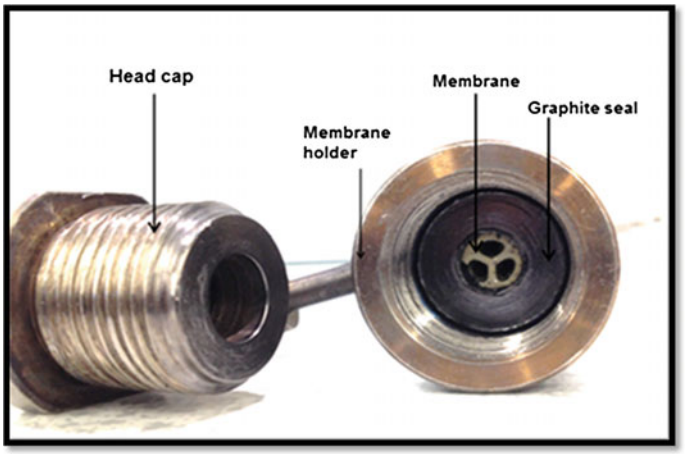

Fig. 5 Picture of the membrane reactor showing the membrane seal

The permeance of the gas is obtained from the mathematical expression in Eq. (3) [12, 13].

$$Q_i = \frac{F_i}{A\Delta P_i} \tag{3}$$

where

Q_i Permeance of gas i (mol s^{-1} m^{-2} Pa^{-1})
F_i Flowrate of gas i (mol s^{-1})
A Surface area of the membrane (m^2)
ΔP_i Pressure difference of gas i across the membrane (Pa)

3 Results and Discussion

Figure 6 shows the effect of increasing the gauge pressure on the flowrates of helium (He), oxygen (O_2), nitrogen (N_2) and carbon dioxide (CO_2). It was observed that there was a proportional rise in flowrate as the pressure increased. For gauge pressure of up to and less than 0.6 bar, it was observed that for O_2, N_2 and CO_2, there was a proportional relationship between pressure and flowrate, i.e., as pressure increased, the flowrate increased. However, for these three gases, above 0.6 bar, the flowrate witnessed a more or less constant value as pressure was increased. Therefore below 0.6 bar, Darcy flow was observed while non-Darcy flow occurred above 0.6 bar. For Helium (He) however, there was no non-Darcy region and the flow increased monotonically with pressure. Helium gas showed the highest flow

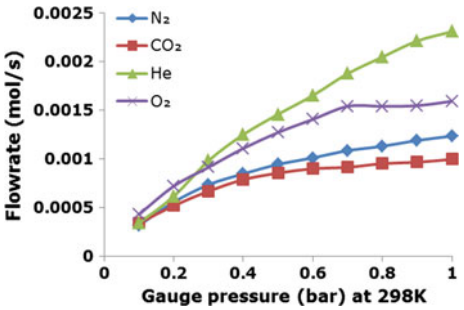

Fig. 6 Flowrates of He, N_2, O_2 and CO_2 against gauge pressure

Table 1 Molecular weight and kinetic diameter of gases

Gases	Molecular mass	Kinetic diameter
He	4	2.6
O_2	32	3.0
N_2	28	3.64
CO_2	44	3.30

rate with respect to the other gases, while the rate of flow of CO_2 was the slowest. This results indicated that the permeation of the gases is dependant on their molecular weight. Table 1 shows the molecular weights of the gases. CO_2 is heavier than Helium.

It was also observed from Fig. 6, two distinct flow regions were observed for N_2, CO_2 and O_2 and above 0.6 bar for these gases there was a gradual increase in flowrate as the pressure was increased. For He gas a higher increase of flowrate as the pressure was increased was observed. He gas showed a Darcy type of gas transport while the other gases displayed an initial Darcy flow followed by non-Darcy flow.

Figure 7 shows the effect of kinetic diameter on the rate of flow of gases through the membrane at a pressure of 0.45 bar. In Table 1, it is seen that O_2 has a smaller kinetic diameter than that of N_2. This means that, though O_2 is heavier than

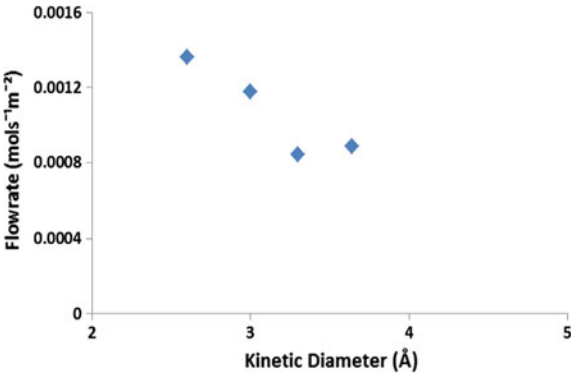

Fig. 7 A graph of flowrates of He, N_2, O_2 and CO_2 against kinetic diameter (Å)

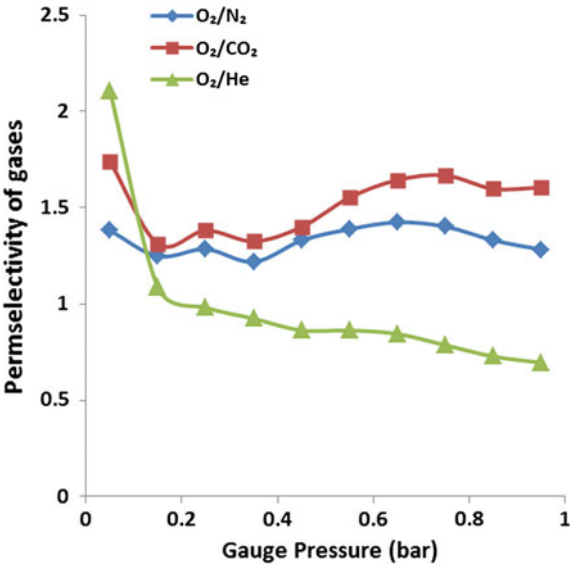

Fig. 8 Permselectivity of gases against gauge pressure (bar)

nitrogen, it is actually smaller in molecular size and tend to diffuse through the membrane faster than nitrogen [14]. The rate of flow of O_2 is determined by this lower kinetic size.

The nature of the flowrate of the gases also showed that the gas flow was not only dependant on the molecular weight but also on the kinetic diameter of the gases. Based on molecular weight, it is expected that N_2 should flow faster than O_2, but the reverse was the case, O_2 showed a higher flow rate than N_2.

Figure 8 shows the permselectivity for O_2 plotted against N_2, CO_2 and He plotted against the gauge pressure.

The results of Fig. 8 is discussed in Tables 2 and 3. Table 2 shows the permeabilities of the gases at 0.95 bar gauge pressure and Table 3 shows the experimental and the theoretical selectivities obtained. From the results, the experimental values were greater than the theoretical values and this implies the selectivity of the gases is Knudsen type.

Table 2 Permeability (mol s^{-1} m^{-2} Pa^{-1}) at 0.95 bar gauge feed pressure

Gauge pressure (bar)	O_2	N_2	CO_2	He
0.95	2.632e−3	2.055e−3	1.642e−3	3.784e−3

Table 3 Experimental and theoretical selectivities at 0.95 bar gauge feed pressure

Experimental selectivity			Knudsen theoretical selectivity		
O_2/N_2	O_2/CO_2	O_2/He	α_{O_2/N_2}	α_{O_2/CO_2}	$\alpha_{O_2/He}$
1.280	1.60	0.695	0.707	1.25	0.378

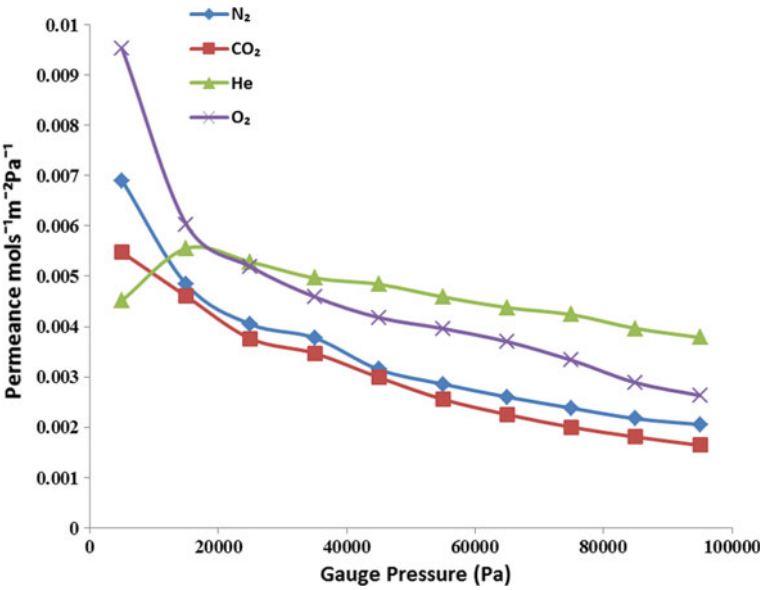

Fig. 9 A graph of permeance against gauge pressure (Pa)

In Fig. 9, the gas permeance was plotted against the gauge pressure at room temperature of 298 K. From the results obtained, as the gauge pressure was increased, there occurred an initial steep drop for O_2, N_2 and CO_2 followed by a more gradual drop in permeability signifying Knudsen diffusion predominant over the viscous flow. He gas however, witnessed an initial permeance rise followed by a gradual drop in permeance.

Figure 10 shows the gas transport behaviour of the gases at different temperatures at 0.5 bar pressure. Results obtained from the plots showed an order in the rate

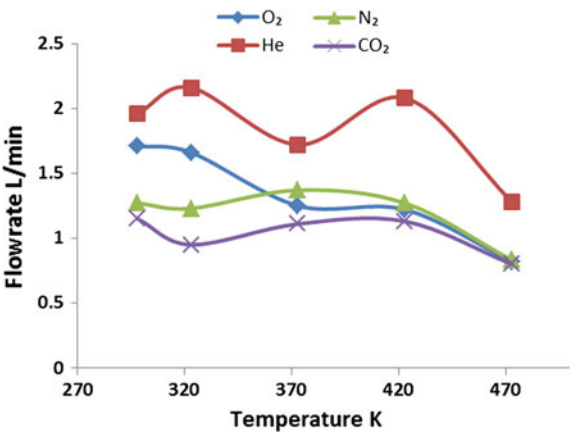

Fig. 10 Flowrate L/min of gases against temperature K

of flow of the gases through the membrane. At 298 K and 323 K, for example, the flow rate increased in the order He > O_2 > N_2 > CO_2. As the temperature was increased to 373 K, 423 K and 473 K, the order of increase in flow rate then switched to He > N_2 > O_2 > CO_2.

4 Conclusion and Future Work

Gas permeation experiments have been carried out using an alumina ceramic membrane. Gas permeation test is actually an interesting way of characterizing a membrane to obtain valuable information which can be used in understanding membrane's performance. From the gas transport study, it was observed that both Darcy and non-Darcy flow occurred for O_2, N_2 and CO_2 below 0.6 bar. For He gas however, little non-Darcy flow occurred.

The experimental selectivity of O_2/CO_2 showed the highest values in comparison to that for O_2/He and O_2/N_2. From the permselectivity calculations,, the experimental selectivity was greater than the theoretical value and this can be interpreted to mean that the molecules collide more with the membrane walls than among themselves. All experimental selectivity values obtained were higher than theoretical Knudsen selectivity indicating promising selectivity features for O_2.

The transport of the oxygen and nitrogen gases showed a molecular sieving type of gas transport where the permeation was dependant on the molecular size. Also higher temperature favoured the permeation of N_2 over O_2. This feature is very important for industrial separation of air and oxygen enrichment.

In conclusion, the transport mechanisms present are a combination of molecular sieving and the Knudsen mode of gas transport.

Further work will continue in identifying and developing catalytic membranes which should demonstrate higher permeation and separation properties.

Acknowledgment This research has been supported by the Center for Process Integration and Membrane Technology, School of Engineering, Robert Gordon University, Aberdeen.

References

1. Li K (2007) Ceramic membranes for separation and reaction. Wiley, Hoboken
2. Mulder M (1996) Basic Principles of Membrane Technology. Second edition, Kluwer Academic Publishers, London
3. Li H, Schygulla U, Hoffmann J, Niehoff P, Haas-Santo K, Dittmeyer R (2014) Experimental and modeling study of gas transport through composite ceramic membranes. Chem Eng Sci 108:94–102
4. Fain DE (1994) Membrane gas separation principles. MRS Bull 19(04):40–43
5. Tan X, Liu S, Li K (2001) Preparation and characterization of inorganic hollow fiber membranes. J Membr Sci 188(1):87–95

6. Ohwoka A, Ogbuke I, Gobina E (2012) Performance of pure and mixed gas transport in reconfigured hybrid inorganic membranes Pt.2. Membr Technol 2012(7):7–9
7. Melish K, Keller P, Kancewick J, Jones M. Graphene membrane for gas separation. Available: http://research.che.tamu.edu/groups/Seminario/nanotechnology/Pshort_U3_Graphene%20membrane%20for%20Gas%20Separation_v1.pptx
8. Carlos Finol JC (1999) Permeation of gases in asymmetric ceramic membranes. Chem Eng Educ 33:58–60
9. Pandey P, Chauhan R (2001) Membranes for gas separation. Prog Polym Sci 26(6):853–893
10. Javaid A (2005) Membranes for solubility-based gas separation applications. Chem Eng J 112 (1–3):219–226
11. Gobina E (inventor) (2006) Anonymous apparatus and method for separating gases. US Patent and Trademark Office 7,048,778, Washington, DC
12. Orakwe IR, Nwogu NC, Kajama M, Shehu H, Edidiong Okon, Edward Gobina (2015) An initial study of single gas permeation using a commercial alumina membrane. Lecture notes in engineering and computer science: proceedings of the world congress on engineering 2015, 1–3 July, 2015, London, UK, pp 737–739
13. Lee D, Zhang L, Oyama ST, Niu S, Saraf RF (2004) Synthesis, characterization, and gas permeation properties of a hydrogen permeable silica membrane supported on porous alumina. J Membr Sci 231(1–2):117–126
14. Murphy K, Are nitrogen molecules really larger than oxygen molecules? Available: www.getnitrogen.org/pdf/graham.pdf

A Motorized Yam Pounding Machine Developed to Improve Living Standard of Average Nigeria for Sustainable Economic Growth

Austin Ikechukwu Gbasouzor and Muncho Josephine Mbunwe

Abstract The aim of this research work is based on the design and development of a motorized yam pounder for pounding yam, this research was considered because of the importance of pounded yam in Africa particularly in Nigeria and because of the time and energy wasted using the traditional mortar and pestle method of yam pounding. The research work aimed at eliminating the labour involved in traditional method of pounding. Through this improvement the possibility of food contamination by sweating while pounding will be control. This project work sought to design a yam pounder that pounds yam right from the peeled cooked stage in a pounding bowl with the help of an electric motor that transmits power through rotary motion together with the help of shaft. The pounding blades functions as the pestle. The machine is to be operated by electricity and it consists of shaft, electric motor, yam beaters or pounding blades, bowl and the frame. Low cost materials were used so as to make the machine affordable for average Nigerian homes, thereby improving the standard of living. In order to avoid food contamination stainless material were also incorporated for smooth and clean pounding before consumption.

Keywords Contamination · Eliminating · Mortar · Peeled · Pestle · Pounding blades · Rotary motion · Stainless material · Yam tuber

A.I. Gbasouzor (✉)
Department of Mechanical Engineering, Chukwuemeka Odumegwu Ojukwu University, Uli, Anambra State, Nigeria
e-mail: unconditionaldivineventure@yahoo.com

M.J. Mbunwe
Department of Electrical Engineering, University of Nigeria, Nsukka, Nigeria
e-mail: mamajoesix@gmail.com

S.-I. Ao et al. (eds.), *Transactions on Engineering Technologies*,
DOI 10.1007/978-981-10-1088-0_15

1 Introduction

Yam is another crop cultivated across Nigeria. It is a seasonal crop and very difficult to preserve as it tends to rot. Nearly all Nigerians consume yam on regular basis and in large quantities particularity the Yoruba tribe in Nigeria.

Nature allows yam to form a bond when it is pounded or beaten in a mortar, it is then consumed as a meal with a choice soup. Pounded yam is a staple food consumed by all. The indigenous process of pounding yam is very laborious. It requires physical pounding by one or more people depending on the quantity in the mortar.

In a bid to reduce the labor involved in yam pounding came the manufacturing of Habert mixer, the Kenwood mixer and Hammer mill in early 1975. These intended yam pounders failed due to some limitations in their operational functions. The Habert and Kenwood mixers had almost the same operational principle and they had been identified for poor pounding due to the flapping (moving up and down) of their stirrer or mixer which is keyed to the electric rotating shaft.

In addition to the poor pounding of both pounders, the Habert mixer was found to heat excessively and as a result, the machine has to be stopped intermittently for cooling purpose.

This cooling time takes up to ten minutes and this makes the machine inefficient since the pounding temperature has to be constant throughout the pounding process in order to obtain a fine textured pounded yam.

1.1 Background

It should be noted that the method employed in preparing food determines in the long run its level of acceptance by the people. For example, our European counterparts have difficulties in accepting our local food simply because they consider the method of preparation to be cruel and unhygienic. Secondly, women liberation and involvement in the work force has completely displaced the concept of full time housewife thereby making it imperative for a mechanized and modernized method of food preparation; hence, this present study and research.

1.2 Aims and Objectives

Yam is cooked and pounded to ensure easy swallowing and digestion, hence the purpose of this study and the design of this project. This design is aimed at replacing the old, laborious, and cruel method of pounding yam to a more hygienic and mechanized means. This does not only reduce the labor involved in pounding yam but also reduces the time of pounding and ensures cleanliness, efficiency and

safety. Many engineers are developing the fabrication of this machine and different operational principle has been employed. While some are employing complex design, others are using very expensive material thereby making the finished product expensive for avenge home. That is to say, that in this research, we consider seriously one of the major factors in selection of materials (cost) thereby employing low cost materials without compromising standard, reliability, safety and durability.

Another purpose for the design was to eliminate the noise and vibrations associated with the traditional method of pounding (pounding with mortar and pestle).

1.3 Scope of Research

The design and fabrication is considered with only a working model (prototype) commercialization and market feed back is not inclusive in the study. Problem definition is covered in order to realize the purpose of the research. Literature review of past work on this research work was also examined in order to understand the areas that need improvement.

1.4 Limitations

One of the outstanding limitations of this work is its inability to pound all varieties of yam. It can only pound two varieties namely:

- white yam (Discorea rotandata)
- water yam (Diascorea alata)

There is also the problem of finance, time and electricity problem. The machine can only pound yam for maximum of six persons for consumption, while before pounding the yam it must be sliced, cooked, until it becomes soft.

2 The Economic Importance of Yam Pounding Machine

Yam (Dioscorea spp) is common throughout the world tropical areas; they are staple food throughout Africa but are particularly important in West Africa where they are used as fufu and other fufu-like staples, the Yorubas further process yam into flour for “elubo” (Local yam flour) this flour is highly cherished especially in Ekiti, Ondo, Oyo and Ogun State of Nigeria. Dioscorea rotundata is usually preferred to other species for mass flour production which may be due to its moisture content being lower than others and better colour of the flour after processing. Oleniyi [1] and Onyekere [2].

They come in different varieties—the white yam (dioscorea rotundata), yellow yam (dioscorea cayenesis), water yam (dioscorea alata), Chinese yam (dioscorea esculenta), sweet yam (dioscorea batatas) African bitter yam (dioscorea dunetorum) aerial yam (dioscorea bulbifera) Onwueme [3] and Asiedu [4, 5] etc. The yam most cultivated in Africa is believed to have come from Asia, Latin America in the first century A.D. It is also believed that the name yam was given by an African slave on North America who used the West African word (nana) which later became yam in English. Although there is a controversy as to whether yam is a monocotyledonous plant or not, it is still classified as a monocot crop.

Yam is a seasonal crop and at present a very difficult to preserve as it tends to rot. It is consumed by both the middle and upper class and nearly all Nigerians consume it on a large scale during harvest season. It can be prepared in many ways for consumption, but the commonest way of preparing it is to pound it into a sticky lump free mesh and after that it can be eaten with soup.

In Africa, the pounding is done traditionally with a wooden mortar and pestle. The mortar is designed in a cuplike shape. The yam is feed into the mortar and then pounded with the pestle (Figs 1 and 2).

The above technologies are for different applications except for the traditional pounding method using mortar and pestle, which uses human energy, it is slow and labour intensive. The development of a motorized Yam Pounding Machine will

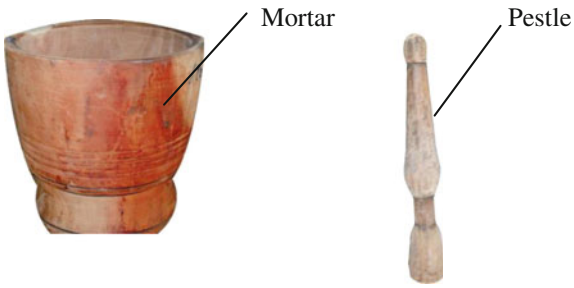

Fig. 1 Traditional pounding mortar and pestle

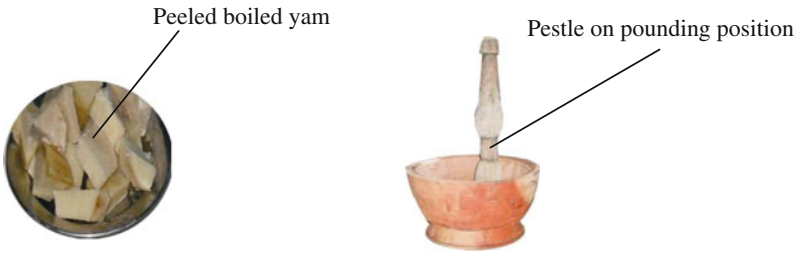

Fig. 2 Traditional pounding mortar in action to pound the peeled boiled yam

provide a relief of human labour, speed up pounding and produce uniform/ smoothness of a better end product [6].

Pounding yam with the traditional method pounding that is (pounding with mortal and pestle) is laborious, process, it generate noise and vibrations, it is only hygienic because of human sweat droping into the food your are pounding, while yam pounding machine replace the old, labourious, and cruel method with a more hygienic and mechanized means. This does not only reduce labour involved in pounding yam but also reduces the time of pounding and ensures cleanliness, efficiency and safety.

Furthermore, in most part of Asia, pounding is done with stone and the yam is rolled with a wooden roller on a flat stone until a sticky mesh is obtained. This method is also laborious and unhygienic method of pounding.

In some parts of east and West Africa., yam is pounded by beating and stirring the already boiled yam with a wooden spoon until it is completely smooth. This also is laborious process and might take time unnecessarily as it will need one person to hold the bowl and one person to stir. The pounded yam is shaped into balls known as fufu and served with a choice soup.

However, over the years, the idea of mechanical engineers has been to design a modern or mechanized yam pounder, but this idea suffered a lot of setbacks, basically because of the cultural significance attached to yam. Yam was seen as the king of crops in Africa and it stood for manliness. One who could feed his family on yam from one harvest season to another was considered to be a very great man.

Another setback was that many housewives saw the yam pounding machine as a western culture innovation, accepted that their husbands preferred the traditional way of pounding.

Also, the advert of Cadbury dried yam product popularly called poundo which did not require pounding with mortar and pestle gained much patronage though the fufu made from poundo was not as fresh as pounded yam and it used to be brownish in color.

Yam provides a more sustained form of energy and gives better protection against obesity and diabetes. Traditional ceremonies still accompany yam production, indicating the high status given to it.

In order to facilitate the processing of yam for consumption, a yam pounding machine was designed and developed to hygienically process yam and it was designed to pound from kilograms to kilograms weight of cooked yams for both domestic and commercial uses. The machine entirely eliminated the laborious process of traditional pounding.

2.1 Material Selection and Components Used

The selection of material for any engineering design depends on the following factors among others: Availability, strength, Fabric ability, Appearance, Stainless material.

2.2 Pounding Chamber Materials

The pounding pot is made of stainless steel to avoid contamination of food (food poisoning) that may occur due to rusting. In addition, the pounding blade is made of coated corrosion resistant mild steel to avoid contamination too.

2.3 Body Materials

The body is made of two particular metals:

- The frame work: this is made using a square hollow mild steel pipe because of its rigidity and ability to radiate heat from the system.
- The cover: the cover is a galvanized mild steel to give a better shape and look.

It is worthy to note that the body was thoroughly painted using very good rust resistance paint (Aluminum Paint) (Table 1).

Table 1 Sequences used in construction

S/N	Operation	Procedure	Tool and equipment
1.	Measurement of the materials and making out	Measure the material needed at every point and mark out clearly	Steel ruler and scriber
2.	Cutting frame metal	Hold the steel firmly on a vice and cut effectively at the marked point	Hack saw, steel ruler and bench vice
3.	Welding of the frame	Attach the electrode to the welding torch, switch on the welding machine. Ignite the electrode and put it into contact with the material and weld firmly.	Welding machine, bench vice, steel ruler, and electrode e.t.c.
4.	Forming of the galvanized steel into shape	Measure the area punched and form into shape	Centre punch, hammer and anvil scriber
5.	Welding and riveting of the galvanized steel	Weld the steel into the frame and rivet if need be	Welding machine and bench vice
6.	Fixing of components	Fix the pounding pot, capacitor, electric motor and the rotating blade. Switch at the appropriate positions.	Spanner, pliers, screw driver and screws
7.	Electric wiring	Wire and connect the cables to the component switches	Screw driver and cello tape
8.	Testing	Connect the plug to the power source and switch on the pounder. Also test the rotor/shaft rotation	

3 Methodology

Design of Yam Pounding Machine
In the design of yam pound many things were considered when analyzing the system.

3.1 Parts Design and Material Selection

Jain R. K [7], described manufacturing processes as the processes involved in using various construction methods in producing the extracting machine. In manufacturing, the principal common characteristic is that something physical is being produced or created i.e. output consists of goods or machine, which differs physically.

Manufacturing therefore requires some physical transformation or a change in utility of resources. The parts are different components that when assembled make up the unit in such processes care precision should be the top most priority when carrying out the construction. As far as the selection of material for the construction of machine component and parts is a vital aspect of design.

Various manufacturing processes were carried out during the fabrication, production and assembling of the components parts of this machine in order to be producing the required or particular goods.

The processes involves in producing the machine are as follows:

- Marking out operations or procedures
- Cutting operations or procedures
- Assembling operations
- Welding operation
- Machining operation.

3.2 Marketing Out Operations/Procedures

This is done to get the required shape and size of the design according to our dimensions in order to meet out expectation or aim. It is done or carried out by using tapes, marker, squares, vernier caliper etc.

3.3 Cutting Operations/Procedures

- Power saw: for cutting of thick pipes and circular bars.
- Hacksaw: for cutting of rectangular plates and circular bars.

- Emery cloth: for smoothing and polishing of rough edges of wood.
- Chisel and hammer: for cutting of casing of the yam pounder.
- Guillotine machine: for cutting of mark out shit of stainless steel and mild steel into the required dimension or measurement.

3.4 Assembling Operations/Procedures

This aspect is bringing together of all required part components to form a unit or a complete machine.

3.5 Welding Operations/Procedures

This process is the system of using electric welding and electrode to join the art material into shape.

3.6 The Design Description

The yam pounder consists of various components and its detailed description illustrated below.

3.7 Stainless Pot

This houses the pounding vanes and contains the yam to be pounded.

3.8 One Horse Power Geared Electric Motor

This impacts the momentum force to the pounding vanes.

3.9 Pounding Vanes/Blades

This does the actual pounding. The blades are twisted at an angle of 45° to each other and the space between them on the rotating shaft is 90°.

3.10 Switch

is the component that regulates the electric support.

3.11 The Frame

It gives the entire system support.

3.12 Capacitor

An electrical device that have the ability to charge when a potential difference is maintained between two conductors.

3.13 Electric Components

Figure 3.

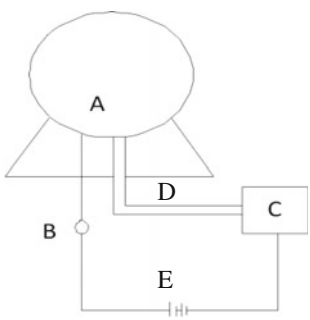

Fig. 3 Machine components **a** electric motor, **b** switches, **c** capacitors, **d** cable wires, **e** power source

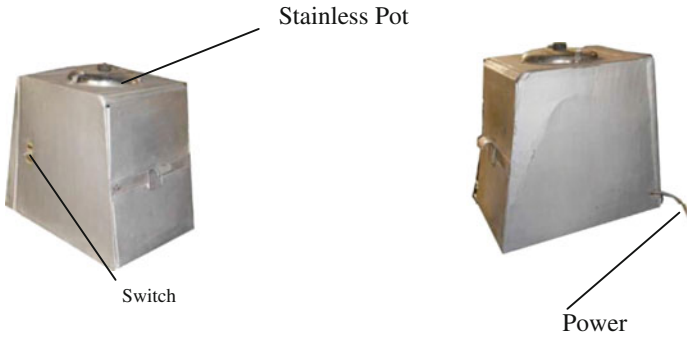

Fig. 4 The designed yam pounding machine showing front and side views

Fig. 5 Pounding Vanes/Blades with boiled yam specimen

Fig. 6 Interior description of the yam pounding machine

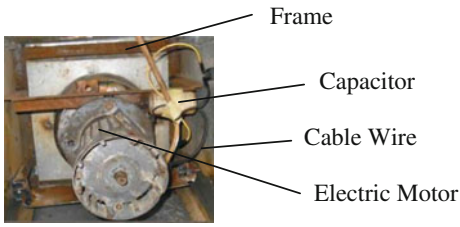

3.14 Brief Description of the Principle Operation

When the yam is cooked and transferred into the pounding pot and the electric motor is switched on, the shaft rotates which carries the blades that pound the yam. At the first rotation, the shorter blade cut the yam into smaller pieces and redirects the yam particles to the longer arm that does most of the actual pounding (Figs. 4, 5 and 6).

3.15 Assembly

The work on its construction had the various materials put in place in its various stipulated places. The hollow metal used for the frame work, the pot, the electric motor, the galvanized metal sheets used for covering the frame work were all assembled in their various ways and positions.

1. Hollow metal: This is used for its frame work because of its strength and weld ability.
2. Pounding pot: This is made of stainless steel that is ragged to accommodate the heating effect.
3. Rotor: This rotates the blades/vanes.
4. Wires: materials that conducts electricity into the motor for the functioning of the machine.
5. Switch: the controls the on and off of the machine.

3.16 Safety Considerations

The safety considerations in this work stem up from the fact that as an electromechanical device, injuries and damages are bound to occur.

Thus the safety precautions are as follows:

1. Ensure that all the electric components are thoroughly earthed.
2. Avoid hand contact with the pounding blade
3. Avoid opening the pounding chamber when the machine is on.

4 Fundamental Mathematical Analysis of the Design

We made use of one horsepower electric motor. 1 hp- = T (Nm) × N (r.p.m)/3600 where the theories of Gupta J.K, Khurmi R.S [8], stated that

$$\mathrm{T} = \text{torque in Newton/meters.} \tag{1}$$

N = speed in revolution per minute. h_p, = horse power.

Therefore: $H_p = T \times N/3600$

T = hp × 3600/N

But one horsepower (hp) = 745.7 w Speed (N) = 1000 r.p.m T = 745.7 × 3600/1000 = 2684.52 Nm

4.1 Maximum Volume of Yam to Be Pounded

The volume of yam to be pounded depends on the following:

1. The volume of the pot.
2. Thickness of the blades/vanes.
3. Nature of the yam.
4. Power rating of the shaft.

From the design dimensions, we have the following measurements:
Diameter of the pot (d) = 210 mm = 0.21 m.
Height of pounding pot
(h =) 100 mm = 0.1 m
Length of blade (L) = 115.5 mm = 0.1155 m
Thickness of the blade (t) = 2:5 mm 0:0025 m
Therefore, Volume of pot

$$(V_p) = \pi d^2 h/4 \tag{2}$$

Vp = π × 0.21 × 0.1/4
Vp = 0.003463605 m^3

4.2 Volume of the Blade

$$Vb = \pi d^2 L \tag{3}$$

Whereby π x $(0.0025)^2$ x 0.1155 = 0.000002267 m^3
For four blades Vb = 4 x 0.000002267 = 0.000009071 m^3
The net volume of the pounding pot.
Vnet = Vp−Vb = 0.003463605−0.000002267
Vnet = 0.003454534 m^3
Therefore, if average yam tuber is about 200 mm (0.2 m) long and has a mean diameter of about 70 mm (0.07 m^2).
Then the volume

$$V = d^2 L/4 \tag{4}$$

V = π × $(0.07)^2$ × 0.2/4
V = 0.0007696 m^3
Thus, this can only hold for $1^{1/3}$ tubers of yam allowing about 10 % increase in volume of the already cooked yam (that is after cooking).

Table 2 Theoretical load of coefficient

Material	Dry	Lubrication
Wood on wool	0.25–0.5	0.02–0.1
Metal on wood	0.2–0.6	0.02–0.08
Metal on metal	0.2–0.3	0.04–0.08
Leather on metal	0.3–0.40	0.1–0.25

4.3 Frictional Effect Analyses

Velocity ratio (VR) = Speed of driver/Speed of the driven. Efficiency of machine = Actual load/Theoretical load Coefficient of friction for different materials at average pressure and low speed is given below: (Table 2).

Coefficient of friction = Effect of friction/Pressure between surfaces. Effect of friction = Coefficient of fiction × Pressure between surfaces.

But pressure between wall and yam = F/A and F = T/D Where F = Force T = torque.

A = Area of the pot D = Pot diameter Therefore, F = 26845.21 0.07 = 383502 N/m.

Area of pot (A) = $\pi D^2 = \pi \times (0.21)^2 = 0.13854^2$.

Pressure between wall and yam = 383502/0.13854 = 2.768 Nm.

Effect of friction = 0.04 × 2.768 = 0.11072 N/m minimum Or = 0.08 × 2.678 = 0.22144 N/m minimum.

In the effect of friction, the yam serves as a lubricant between the pounding vanes and the pot. Hence friction is assumed to have effect on metal to metal (pot and blade).

4.4 Testing and Analysis

After fabrication, the system (work) was tested by operating it with electricity and the result was satisfactory. The pounded yam was firm and smooth in texture, compact with adequate hardness. The yam used was cut into small sizes.

4.5 Evaluation

The machine (yam pounder) was well evaluated to suit its usage. That is, the components parts.

The make up of the machine was duly selected to carrying out its purpose and making it easily operational to the users. The factor considered and evaluated are as follows:

- Weight of motor.
- Weight of metallic base.

- Thickness of pot and blade.
- Total weight of the machine.

4.6 Repair/Maintenance Schedule

Repairs are affected when a machine fails to function effectively and efficiently as required. The machine parts likely to fail which could have a great effect on this machine are electric motor, electric switches, shaft and blades.

The machine is economically fabricated to aid replacement of damaged parts as well as periodic inspection. The maintenance system or process includes

- Cleaning of the pots before and after operation.
- Greasing of motor bearings.
- Storing the machine in a cool and dry place.
- General inspection and cleaning of the worn out parts.

As a matter of fact, the maintenance requirements are categorized into:

1. Breakdown maintenance.
2. Overhaul maintenance.
3. Planned preventive maintenance/Corrective maintenance

5 Conclusion

This research work has successfully presented a functional and highly efficient low cost yam pounding machine by minimizing traditional technique of pounding and health condition of individual, and avoids inconveniency of neighbor hood through noise and vibration of pounding with mortar and pestle. This machine is design for home and restaurant usage, in other to improve a healthy and hygienic condition of an individual. It is expected that an average home in Nigeria can afford the machine.

From this research, we recommend that some chemical analysis of the end product should be carried out to determine the degree of contamination of the pounded yam by the material employed in the machine construction.

Also, there is room for improvement in the efficiency and physical outlook of the machine. We also recommend that this write up in design and fabrication of this project should serve as a stepping stone for further and well defined fabrication.

Acknowledgement I wish to acknowledge the immerse support given to me by the Tertiary Trust Fund (TetFund), The Vice Chancellor in person of Prof. Okafor Fidelis Uzochukwu for their financial support, encouragement of staff to be attending conferences and presenting papers thereby boosting the image of the University through its output in research, thus, making our academic activities Robust and Excellent diverse field.

References

1. Oleniyi AO (1973) Tropical Tubers: yam, cassava, and cocoyam published by John Wiley and son's Inc. Chichester
2. Onyekwere OO (1987) The processing of root and tuber in the theme. The role of food science and technology in operation feeding the nation conference Nigeria Institution food Science and Technology, pp 10, 5th May 1977
3. Onwueme IC (1978) The tropical tuber crops: yam, cassava, sweet Potato and cocoyam's published by John Wiley and Sons Inc. Chichester ISBN 10: 0471996067, ISBN 13: 978047199
4. Asiedu JJ (1992) Processing of tropical corps technological approach. Macmillan publishing Co, Inc. London, pp 249–261
5. Asiedu JJ (1992) Processing of tropical corps, 1st edn. Vikas publishing house limited, Noida
6. Gbasouzor AI, Mbunwe MJ (2015) Development of a motorized Yam pounding machine design to improve standard of living for sustainable economic development in Nigeria. In: Proceedings book of the World Congress on Engineering (WCE 2015), London, UK, pp 984–988, 1–3 July 2015
7. Jain RK (2007) Production Technology 16th Ed. Published by Romesh Chander Khanna for Khanna Publishers, Delhi
8. Khurmi RS, Gupta JK (2008) Theory of machines 14th Ed. Eurasia publishing House (PVT) Ltd Ram Nagar, New Delhi

Lean Six Sigma Project for Productivity Enhancement

Valter Rocha Morais, Sérgio Dinis Teixeira de Sousa and Isabel da Silva Lopes

Abstract The competitive market that companies are facing nowadays leads them to introduce frequently new products and, therefore, producing small series. This dynamic environment requires frequent changes in production lines and requires flexibility in the processes, which can cause reductions in the level of quality and productivity. This paper presents a Lean Six Sigma improvement project performed in a production line of the machining sector of a company from the motorcycles components branch. The project aims to eliminate losses that cause low productivity, affecting the fulfilment of the production plan, customer satisfaction and the increase of costs. The use of Lean methodology following the DMAIC phases allowed analyzing the factors that influence the line productivity losses. The major problems and causes that contribute to a reduction of productivity in the studied sector are the lack of standardization in the setup activities and the excessive stoppages for adjustment of the processes that caused an increase of defects. Quality tools such as control charts, Pareto analysis and cause-and-effect diagrams were used to analyze the problem. On the improvement phase of the DMAIC methodology, the reconfiguration of the line layout as well as the modernization of the process were the solutions chosen since their benefits justify their cost. The defective product units were reduced by 84 % and an increase of 29 % of line capacity was noticed.

Keywords Case study · DMAIC · Industrial projects · Lean · Quality improvement · Six sigma

V.R. Morais
SUFRAMA, Avenida Ministro Mário Andreazza, No 1424,
Distrito Industrial - CEP, Manaus 69075-830, Brazil
e-mail: megavalter@hotmail.com

S.D.T. de Sousa (✉) · I. da Silva Lopes
ALGORITMI Research Centre, University of Minho, Campus de Gualtar,
Braga 4710-057, Portugal
e-mail: sds@dps.uminho.pt

I. da Silva Lopes
e-mail: ilopes@dps.uminho.pt

S.-I. Ao et al. (eds.), *Transactions on Engineering Technologies*,
DOI 10.1007/978-981-10-1088-0_16

1 Introduction

The Lean Six Sigma (LSS) method promotes, in organizations, the continuous improvement of products (and/or services) and processes that aligns with the business strategy to maximize the value of products [1]. The LSS can be defined as a work philosophy adopted by companies using methods and tools to reduce the variability of processes to eliminate waste and improve the quality perceived by the customer. This philosophy is aligned with the strategic planning of the company, providing greater opportunities in the market. It offers unique features combining multiple tools, serving to support the development of business strategies. It also assists in the breakdown of steps in improvement projects and in the achievement of planned results [2].

Strategic planning has an important role in running a business and allows foreseeing future implications of present decisions and prepare for the changes that occur in the political environment, economic, social and technological, seizing opportunities and meeting the unique threats of these environments [3]. Making organizations more efficient requires continuous planning and may require investments to adapt processes to the company's strategy. These actions may not bring immediate results, but differentiate them from competitors over time [4].

Standardization is an important factor to reduce variation and increase the efficiency of processes [5]. For Harrington [6], statistical process control is a source of information for the manager and assists in the continuous improvement of operations performance and processes in a sustainable manner. Organizations need to adapt to market needs and to identify opportunities in order to maximize three factors:

- Efficiency: producing with fewer resources;
- Effectiveness: achieving the desired results;
- Flexibility: Adapting to the market needs to meet customer expectations.

The Six Sigma methodology is the basis for the development of improvement project, starting by defining what the Defect is. The goal of the project will be the reduction of its occurrence, increasing the sigma level. The methodology has a set of steps, namely, Define, Measure, Improve and Control (DMAIC) and tools that contribute to the success of a project.

The justification to combine Lean and Six Sigma can be explained by its complementary advantages. According to Werkema [7], Lean philosophy does not have associated tools to carry out statistics analysis or a structured method to solve processes' variability problems. Six Sigma does not emphasize speed improvement of processes and the reduction of lead time. Therefore, using the best outcome of each methodology allows obtaining a method for process improvement by reducing variation and lead time while improving quality and speed of processes [8].

The work presented in this paper focuses on reducing problems that cause unscheduled downtimes, and therefore productivity reduction, in machining operations line. Three issues considered relevant were studied in its development:

1. The factors that influence the performance of operations on the production line;
2. How these different factors affect the performance (efficiency) of the production line;
3. How to define and implement a solution to improve line efficiency aligned with strategic planning, and considering existing restrictions.

The chapter is organized as follows. Section 2 brings some details about the problem to be addressed. In Sect. 3, the different phases of the project are exposed and last section draws the conclusions.

This chapter is an extended version of the paper presented at the World Congress on Engineering 2015 [9].

2 Problem Identification

The project focused a production line that manufactures in pairs (left and right) shock absorbers to two main customers: Moto Honda and Yamaha. The study aimed to characterize, following the DMAIC methodology, the operation of the production line and evaluate the root cause of the problem of low productivity. To carry out the project, a team was constituted to address this problem over five months.

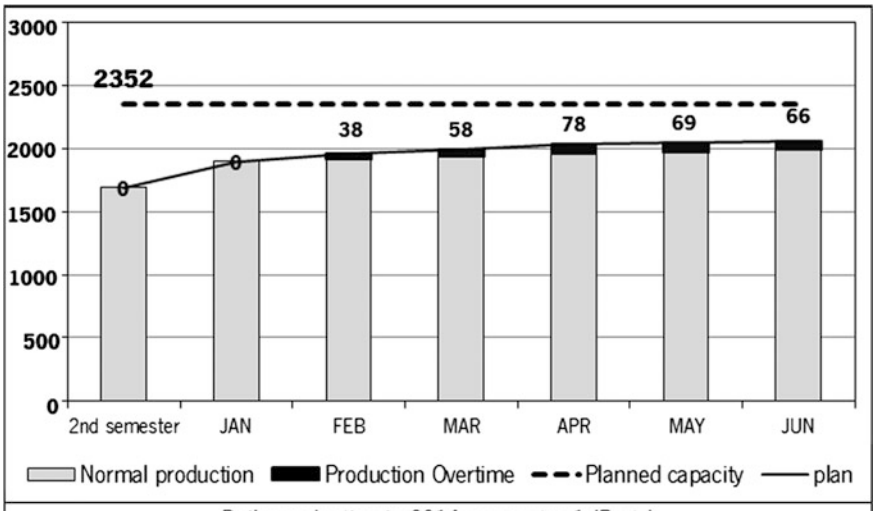

Daily production in 2014 semenstre 1 (Parts)							
month	2nd semester	JAN	FEB	MAR	APR	MAY	JUN
plan	1693	1900	1957	1996	2035	2045	2061
Normal production	1693	1900	1957	1938	1957	1976	1994
Production Overtime	0	0	**38**	**58**	**78**	**69**	**66**

Fig. 1 Graph with the production plan and line production capacity

A SIPOC diagram was developed by the project team to characterize the manufacturing process of the production line.

To better understand the problem, data were collected about production in regular and overtime hours from the second half of 2013 to the first half of 2014, as shown in Fig. 1.

The line used overtime in the production schedule to meet deliveries, during the first half of 2014. Despite the line has used overtime to fulfil the production plan, its capacity would allow meeting the production plan in regular hours. The study aims to identify the root cause of this problem.

3 Dmaic Phases

3.1 Define

The definition and quantification of the analyzed problem could be made by different metrics. However, in terms of the customers who require these parts (shock absorbers), the relevant information which is directly associated with the problem is "planned unit not produced". Therefore, the team decided that this would be the "defect definition" for this project, according to the Six Sigma methodology.

In the production process of the machining lines performance indicators are used regularly such as: Scrap (not usable material for the line), setup time and process efficiency. The latter is a time index established by the engineering sector which measures the availability of the line and the production losses.

To identify the root cause of the problem, the capacity of the production line was analyzed using this index.

The efficiency index is the relation between the time actually used to produce, which is the available time after subtracting planned and unplanned stoppages, and the available time. The unplanned stops are due to: equipment failures; settings; lack of material; quality issues; other (special meetings, lack of energy, etc.).

The collection of information for the determination of this indicator allows a detailed description of factors that cause production interruption.

3.2 Measure

For the analyzed period of time, the available time per day was 21 h a day and the efficiency index calculated by the company was 77.78 %.

Considering the efficiency index and a product cycle time of 25 s, the production line capacity is 2352 units/day, since the available time is 75,600 s (21 * 60 * 60) and the time actually used to produce is therefore 58,802 s (75 600 * 0.7778).

Currently the daily production is approximately 2200 pieces. When comparing the 2200 units' production plan with the production capacity, it was found that it

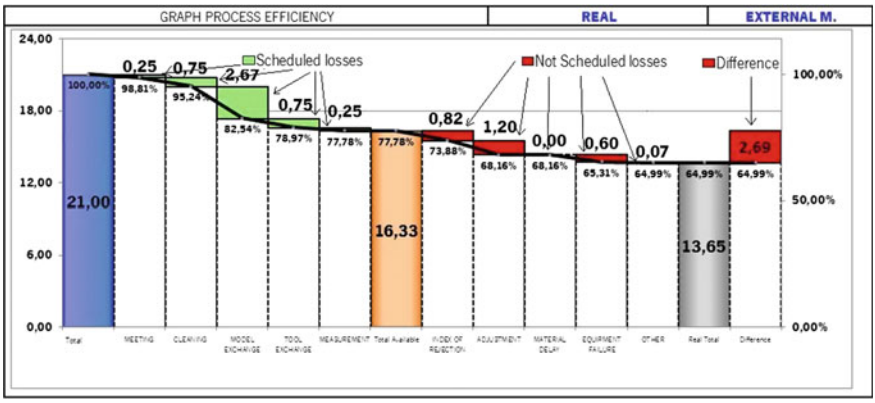

Fig. 2 Graph of the production line efficiency

meets production needs, and the use of overtime to meet demand is not substantiated.

However, it was observed that only planned stoppage and few losses were considered in the efficiency index. Therefore, the identification has focused on finding the losses that reduce the productive capacity. The planning of stratification on collecting data for evaluating the production line efficiency allowed the analysis of different categories of losses and its causes.

The collection of data was performed during 6 months. Information was collected about: quality, adjustments, damage, material delays, others.

The project team developed the line efficiency chart, as shown in Fig. 2.

With the characterization of the losses, the graph shows the difference between the planned production time and the actually production time. The problems/failures encountered are related to production unplanned stoppages, contributing to a situation that compromises the efficiency of processes, reducing the line capacity. The failures or unplanned stoppages are shown in red, totalling 2.69 h/day.

3.2.1 Evaluation of Operations with the Greatest Losses

After the evaluation of losses in the line operations, the team identified the operation that has the highest number of adjustments using a Pareto diagram, as shown in Fig. 3.

Based on the graph, it was concluded that the largest losses of productive capacity arose in the drilling and tapping (BTA) operations.

After verification of the losses, the productive capacity was recalculated based on an efficiency index of 64.99 %. Considering the efficiency index and a product cycle time of 25 s, the production capacity obtained was 1965 units/day. This production capacity justifies the need of overtime to fulfil the 2200 units/day plan.

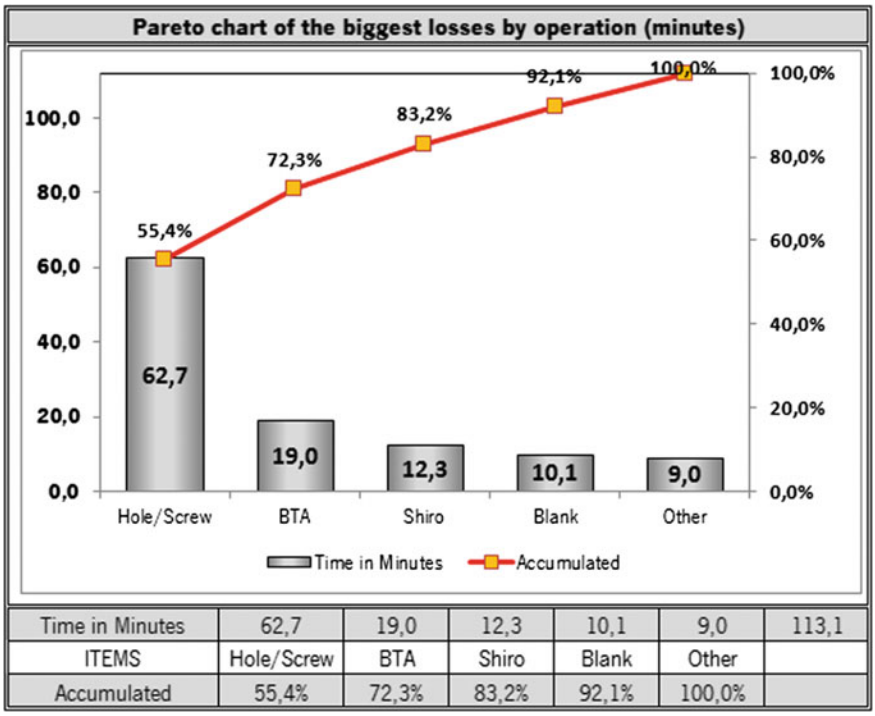

Time in Minutes	62,7	19,0	12,3	10,1	9,0	113,1
ITEMS	Hole/Screw	BTA	Shiro	Blank	Other	
Accumulated	55,4%	72,3%	83,2%	92,1%	100,0%	

Fig. 3 Pareto chart of the losses by operation

To analyze how much of the production is "being lost" (units not produced), the initial planned daily capacity of 2352 units is compared with the actual daily production capacity (1965 units) giving a total of units not produced in the line of 387 units/day, representing approximately 16.44 % of the total capacity. Considering the first half of 2014, the total number of units not produced was 54,917.

To clarify the impact of these losses, the value associated with this waste was calculated. Considering 6€ the cost of not producing a planned unit, the total monetary losses relating to non-produced units in the first half of 2014 is 329 499€.

3.2.2 Calculation of the Current Sigma Level and Target

The sigma level is based on the ratio between the number of non-produced units (387 units) and the total production or number of opportunities (2352 units). The sigma level calculation, for continuous variables following a normal distribution, considers that the process mean can shift 1.5 standard deviations towards one specification limit. The sigma level is therefore 2.48.

3.3 Analyze

In the previous phase, categories that impact the efficiency of processes were identified: quality, adjustments, failures and other stoppages. To identify the root causes of the problem, a brainstorming was performed with professionals whose functions are directly linked to the production line (operators, leaders and the sector head).

The method used to list the causes was the cause-and-effect diagram, since it facilitates the ordering of categories, divided into six groups (Machine, Method, Measure, Environment, Materials and Manpower). Table 1 presents the problems observed on adjustments realization.

Table 2 presents the analysis of the causes of quality problems and Table 3 presents the causes of equipment failures.

After identifying the factors that influence the process, the team developed a Cause-and-effect matrix to characterize the potential impacts of improvement actions on the effects, which, in this case, is the excessive stoppage for adjustments.

Table 1 Causes of adjustment problems

Items	Adjustments problems
Machine	Lack of flexibility High setup times Device fixation difficult to perform
Manpower	Low precision in regulating devices Fatigue (overtime)
Method	Adjustments method cause physical wear of operators Missing pattern in the set of activities
Materials	Many materials lost in parameter settings
Measure	Delay in the measurement of parts for machine settings

Table 2 Causes of quality problems

Items	Quality problems
Machine	Setup excess causes many losses in dimensional test Settings is performed using parts (technology characteristic) Heavy devices hinder accuracy in settings
Manpower	Adjustments incorrectly made Much effort of the operator on the device positioning Operator makes the device adjustments manually
Method	The accumulation of material causes finishing flaws Adjustments precision dependent of operators' effort Transportation using metal carts
Materials	Handling excess causes failure on the parts Accumulation of material causes finishing flaws
Measure	Adjustments are low when they require three-dimensional measurement
Environment	Layout does not allow moving the product on carts

Table 3 Causes of equipment failure

Item	Equipment failure
Machine	Too many changes in the machine parameters Technology keeps values parameters Natural wear of the devices due to excessive adjustments
Manpower	Adjustments incorrectly made by operators Low motivation
Method	Failure to observe the changes in parameters before setup Adjustments on processes without verification of machine condition
Measure	Long time between stoppage and registration
Environment	Long distance from maintenance to the line

Cause-and-effect matrix						
ranges from 0 to 5		Y1	Y2	Y3	Total	Prioritization
Item	X's	Severity	Need	Benefits		
X1	Lack of Flexibility	4	5	5	100	1º
X2	High Setup Times	4	4	5	80	2º
X3	Faults and Breaks Equipment	4	4	4	64	3º
X4	Accuracy in trade models operator dependent	4	3	4	48	4º
X5	Excessive wear devices	3	3	5	45	5º
X6	Layout provides movement between posts	3	3	5	45	6º
X7	Space for storing WIP	3	2	4	24	7º
X8	Setup method that causes physical wear the operator	3	2	3	18	8º
X9	Inadequate method of fixing devices	3	2	3	18	9º
X10	Lack of standardization in the setup activities	3	2	3	18	10º

Fig. 4 Cause-effect matrix

The critical points will be the focus of study in the next phase, the improvement phase. The matrix in Fig. 4 was performed following the criteria:

- Items: The causes identified in the cause and effect diagram that are more likely to influence the process outcome;
- Rating variables: severity, need and benefits;
- Score: The score of each variable ranges from 0 to 5 (five is the most important). The total score is the product of the variables' scores.

3.4 Improve

Traditionally the improvement phase of DMAIC methodology relies on creativity of the project team to things better, cheaper or faster [10], evaluating the data collected in the process. It is not provided guidance on observing the performance

of other opportunities outside the studied context such as new technological developments. In this case study the project team looked outside the studied process, to find potential solutions and by analyzing their impact on the performance of operations and alignment with strategic planning.

3.4.1 Analysis of the Characteristics of Bottlenecks Operations

As shown by the data collected in the measurement phase, the main source of the problems encountered is related to the drilling and tapping operations. An analysis to understand the technical characteristics and working patterns of such equipment was performed. The relevant points associated with drilling and tapping operations and respective equipment are:

- Machines whose main function is to do holes, using a high-revving engine with one or more bits, removing the desired material;
- Machines are used for various operations such as drilling, tapping and slotting, involving the replacement of tools;
- Performing the setups is difficult, requiring a variable time for adjusting the repositioning after exchanging some product model.

Due to the recent increase in the number of the line models, there is an increase in time spent on these activities, reducing the availability of the work machines and dependency on the human factor and on its accuracy. Therefore, the process needs to be more flexible to perform frequent model changes.

3.4.2 Comparison of Improvement Opportunities

Two improvements were proposed and compared:

- The application of single minute exchange of die (SMED) methodology—SMED is used to reduce setup times, working in machine preparation activities, before turning off the machine, reducing the total time. However, it is limited since it only reduces a percentage of the time and does not act in machinery start-up waste;
- Exchange of technology—model exchange is performed only by exchanging software programs. The new computer controlled machine performs the tasks with greater productivity and lower setup times.

3.4.3 Results

As a result from assessment of the two alternatives (Table 4), the new technology is the one that best meets the project requirements, since it not only allows reducing

Table 4 Comparison of improvement opportunities

Items	SMED	CNC technology
Advantages	Reduce setup times Standardizes activities No investment	Reduce setup times Reduces the rejection indices Reduces the duration of processes Offers greater operating range Allows grouping processes
Disadvantages	Only act on setup Devices changeover conditions not changed Condition of the other lines problems not changed	High investment Hand labour training is required

the time used in the setup, but reduces also other activities that the customer does not pay, such as adjustments, failure to execute operations and movements.

The main impacts of the proposal on the system are: the faster exchange of models, better working environment, elimination of the physical efforts of operators in the regulations of the devices, greater precision in machining operations, reduction of quality defects and grouping operations, reduction of the number of devices on the line.

3.4.4 Planning the Implementation of the Selected Improvements

The project team sought not only using the new technology, but also standardizing the activities of processes. The implementation was carried out according to the following sequence:

1. Grouping operations: design a new layout for the machining process.
2. Redo the line balancing and provide training to employees.
3. Assess the new line capacity and performance.

3.4.5 Grouping of Operations

Without the need to group processes by families, it became possible to group processes by operations. Thus, the operations defined for equipment were hole and screw. Grouping is made to assure that all holes and screws are made in new equipment, as shown in Fig. 5.

3.4.6 Line Balancing and New Job Positions

The minimum number of equipment that ensures productivity consists of three pieces of equipment. However, if four pieces of equipment is used, it enables to

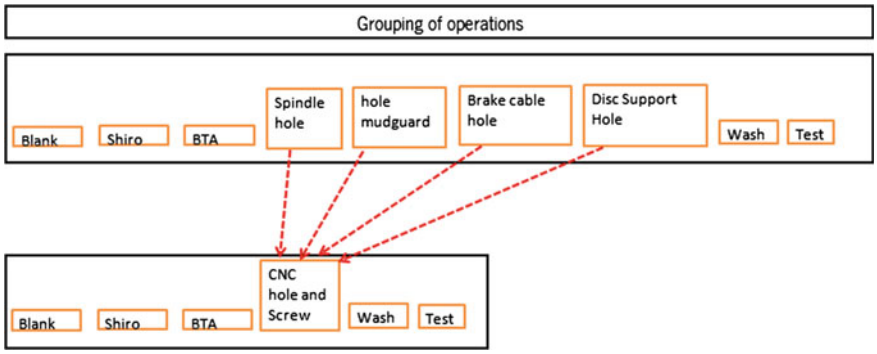

Fig. 5 Grouping of operations at CNC

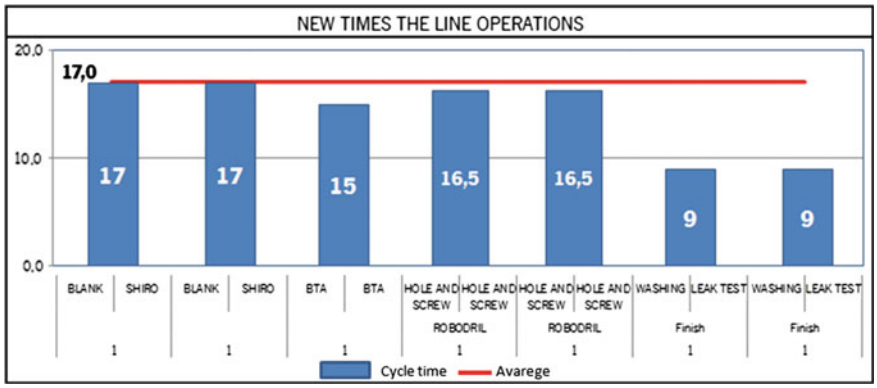

Fig. 6 Grouping of operations at CNC

expand the capacity of these operations and form two production lines, significantly increasing productivity. Figure 6 illustrates the new distribution line.

The new times redefined the productive capacity, for now the line presents another bottleneck. The Blank and Shiro are the largest operating time with 34 s on the job. However, two lines are now realizing production. With the new balance, the cycle time of the line decreases from 25 to 17 s.

3.4.7 Performance After Improvement

A reduction in the settings from 72 min to 12 min was achieved. The rejection decreases from 3.9 to 1.9 %. Figure 7 shows the new values of process efficiency.

There is a significant reduction in losses due to unscheduled stops with increased availability of operation and consequently an increase in the line efficiency,

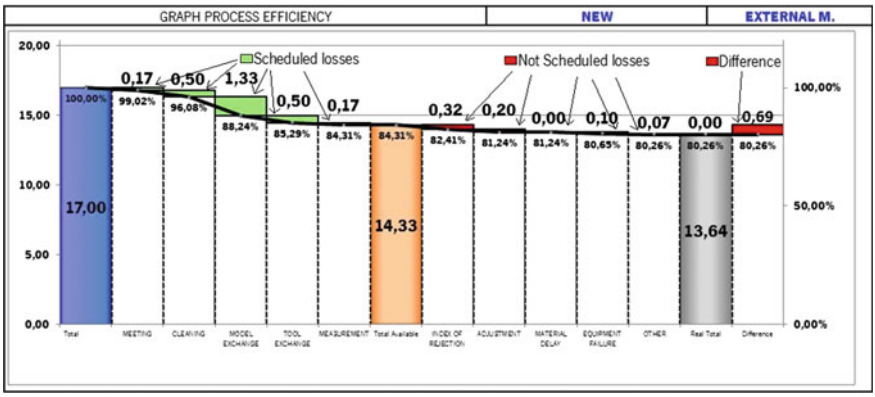

Fig. 7 New line efficiency

Table 5 Results after improvement

Items	Initial	New	Unit
Work in progress	190	84	Parts
Hand labour	21	16	Operator
Capacity	2352	3035	Parts/day
Productivity	112	190	Parts/operator
Lead time	418.5	226.5	Seconds

allowing the sector to comply with delivery deadlines. With the new balancing of 17 s and 84.31 % efficiency, the new production capacity is 3035 units/day.

With the new capacity of 3035 units/day, in two shifts, the demand of 2200 units was fulfilled. This has eliminated the need of the third shift, also reducing the total number of employees in the line from 21 to 16. Although the capacity is higher than current needs, the company's strategic plan had the goal of increasing production volume, to meet an increase in demand of approximately 9 % every year for the last four years.

Other positive results were also achieved, as shown in Table 5.

3.5 Control

3.5.1 Impact and Effectiveness of Improvements

The implementation phase ended in June 2014. The number of non-produced parts reduced from 387 in 2352 opportunities to 78 in 3035 opportunities. This corresponds to a new sigma level of 3.45.

This represents a reduction on DPMO from 164,429 to 25,581 representing a reduction on defects (units not produced) of 84.4 % (from its original value). This

Table 6 Cost savings achieved with improvements

Description	Values
Loss reduction	€ 325 259
Hand labour reduction	€ 40 645
Reduction in devices maintenance	€ 0
Total	€ 365 904

Table 7 Return on Investment

Description	Values
Investment	€ 419 355
Return	€ 365 904
Return time (year)	1.15

was achieved together with an increase in line capacity of 29 %, from 2352 units/day to 3035 units/day and a reduction in the number of defective products from 3.9 % to 1.9 %.

3.5.2 Process Monitoring

For the monitoring of the new operations times and confirmation of stabilization, graphs were established. A registration system for faults and errors of procedures performed by operators was also implemented.

3.5.3 Return on Investment

To demonstrate the monetary results achieved with improvements, it is necessary to measure the cost savings, increased productivity and improved performance. This study will be based on three factors: hand labour, number of devices used and reduction of stoppages. Table 6 shows the costs saving of € 365 904/year.

The team calculated the potential payback of the investment in new equipment. Table 7 shows the return time of the investment (ROI). The ROI is 1.15 years or about 14 months. The project proved to be viable, with significant gains to the company.

4 Conclusion and Future Work

A LSS project was done to improve the performance of a machining line that produces shock absorbers for motorcycles. The Defect definition was “units planned but not produced”. The defect definition is not related to a defective part, as it is usual in LSS project, but as a negative process outcome. Other works [11, 12] have

also reported metric definitions not related directly to product quality or product defect.

Some relevant performance indicators were used to analyze the problem. The analysis revealed excessive stops for adjustments in operations, reducing the efficiency of processes and compromising the delivery. Improvement actions were carried out in order to correct these problems, standardizing the setup of activities, increasing the availability of equipment and improving the productivity of the line.

The changes implemented in the production line consisted in a reconfiguration of the production system, modernizing operations that cause major losses of productivity. To perform the actions the project team developed a new layout, improving the provision of equipment and facilitating the flow of materials.

The implementation of actions brought positive impacts: the reduction of settings stops from 72 for 12 min, the reduction of defective units by approximately 50 % (from 3.9 to 1.9 %). The new working conditions led to a reduction in the number of operators from 21 in three shifts to 16 in two commercial shifts, also contributing to the increase in production capacity of 2352 to 3035 units/day and the system productivity increased from 98 to 152 units per operator a day. Overall the sigma level increased from 2.48 to 3.45. The investment on new equipment was also studied. The ROI is 14 months despite its contribution to other company's strategic objectives.

It can be concluded that the development of the project contributed to the achievement of sector goals and improved the company's competitiveness in the market.

This work reports a Six Sigma project that allows justifying investment in new technology. The acquisition of a new technology was chosen instead of implementing improvements in the use of existing equipment since its impact is reduced.

Future works could test, through different cases, the usefulness of Six Sigma projects to justify investment in new equipment.

Acknowledgment This work has been supported by FCT—Fundação para a Ciência e Tecnologia within the Project Scope: PEst2015-2020 UID/CEC/00319/2013.

References

1. George ML (2002) Lean six sigma—combining six sigma quality with lean speed. McGraw-Hill Professional, USA
2. George ML (2005) The lean six sigma pocket toolbook: a quick reference guide to nearly 100 Tools for improving process quality, speed, and complexity. McGraw-Hill Professional, USA
3. Drucker PF (1992) Administrando para o futuro, 4th edn. Pioneira, São Paulo
4. Porter ME (1996) What is strategy? Harvard Business Review, Boston 74(6):61–78
5. Hopp WJ, Spearman ML (2004) To pull or not to pull: what is the question? M&SOM Manuf Serv Oper Manage 6(2):133–148
6. Harrington HJ (1997) Business process improvement workbook: documentation, analysis, design and management of business process improvement. McGraw-Hill, New York

7. Werkema MC (2008) Integração Lean & Seis Sigma: muito barulho por nada? Banas Qualidade. São Paulo, ano XVII, n 192, pp 48–54
8. Ferguson D (2007) Lean and six sigma: the same or different? Manage Serv J Inst Manage Serv 12–13 (01 out)
9. Morais V, Sousa S, Lopes I (2015) Implementation of a lean six sigma project in a production line, lecture notes in engineering and computer science. In: Proceedings of the World Congress on Engineering (WCE 2015), London, UK, pp 847–852, 1–3 July 2015
10. Pyzdek T (2003) The six sigma handbook—revised and expanded. McGraw-Hill, New York
11. Abreu P, Sousa SD, Lopes I (2012) Using six sigma to improve complaints handling, lecture notes in engineering and computer science. In: Proceedings of the World Congress on Engineering 2012 (WCE 2012), London, UK, pp 1363–1368, 4–6 July 2012
12. Sousa SD, Nunes EP, Antunes D (2014) Lean six sigma in internal logistics: a case study. In: Ao Alan SI, Chan HS, Katagiri H, Xu L (eds) IAENG transactions on engineering sciences special issue of the international multiconference of engineers and computer scientists 2013 and world congress on engineering 2013. CRC Press, Boca Raton, pp 161–170

A Method for Mechanical Design of AM Fabricated Viscoelastic Parts

Alexander V. Manzhirov

Abstract Mechanical design of additive manufacturing (AM) fabricated viscoelastic parts under consideration. Such a design is of great importance for obtaining final products with desired shape and strength which are determined by their stress–strain state. Mathematical model of model of viscoelastic solid which grows due to the process of additive manufacturing is proposed. Complete system of boundary value problem equations is obtained. A method for solving formulated boundary value problem is developed. Qualitative conclusions concerning the behavior of growing solids are presented.

Keywords Additive manufacturing technologies · Growing solid · Shape · Residual stresses · Strength · Viscoelastic parts

1 Introduction

Additive manufacturing technologies include stereolithography, electrolytic deposition, laser and thermal 3D printing, production of 3D integrated circuits and a number of other technologies. Actually, there is a real boom in the development of

A.V. Manzhirov (✉)
Institute for Problems in Mechanics of the Russian Academy of Sciences,
Vernadsky Ave 101 Bldg 1, Moscow 119526, Russia
e-mail: manzh@inbox.ru

A.V. Manzhirov
Bauman Moscow State Technical University, 2nd Baumanskaya Str 5/1,
Moscow 105005, Russia

A.V. Manzhirov
National Research Nuclear University MEPhI (Moscow Engineering Physics Institute),
Kashirskoye shosse 31, Moscow 115409, Russia

A.V. Manzhirov
Moscow Technological University, Vernadsky Ave 78, Moscow 119454, Russia

S.-I. Ao et al. (eds.), *Transactions on Engineering Technologies*,
DOI 10.1007/978-981-10-1088-0_17

AM technologies since they allow to reproduce a 3D object of arbitrarily complicated shape (in theory from any material) with high accuracy and low expenses in a short time. However, problems of deformation and strength of products fabricated using such technologies remain still unsolved. Mathematical models and methods developed in the paper allow one to study the stress–strain state of parts of devices, machines, and mechanisms created in AM processes from viscoelastic materials. This gives an opportunity to estimate their shape distortion, strength, stability and life time. This problem is of general interest for the modern technologies in engineering, medicine, electronics industry, aerospace industry, and other fields.

2 Characteristic Features of AM Fabricated Solids

The process of accretion or deposition of new material to a solid is studied in the fundamental scientific area called Growing Solids Mechanics. This area deals with all sorts of solid materials including elastic, viscoelastic, plastic, composite and graded materials. Currently a great number of AM fabricated part are made from viscoelastic materials with complex properties so we consider just such materials.

By a (piecewise) continuously growing solid we mean a solid whose composition, mass or volume varies as a result of a (piecewise) continuous addition of material to its surface. The process of adding new material to the solid is called accretion or growth. For piecewise-continuous accretion the following basic stages of its deformation are strictly followed: before accretion, during the continuous growth, and after the accretion has ceased and growth has stopped. Each of these stages is characterized by the times when it starts and ends. The first is characterized by the time of application of a load to the solid and the time when growth starts. The second by the time when growth starts and the time when it ends. Conversely, the third is characterized by the time when growth ends and the time when it starts. The process under investigation is usually concluded by the third stage, for which the time when the next stage begins is taken to be as long as desired. The solid on whose surface new material is deposited starting from the time when accretion starts is called the basic or original solid. The solid consisting of the material pieces added to the basic solid over the time interval from the beginning of accretion up to a given instant of time is called the additional solid. The additional solid can have a complex structure and consist of a collection of solids formed over different time intervals of continuous accretion. We call them sub-solids. The additional solid is obviously the union of sub-solids. The domains occupied by the former and latter can be disconnected. The union of the basic and the additional solids will be called the accreted or growing solid. Note that accretion can also occur without the basic solid, starting from an infinitesimal material element. The part of the surface where infinitesimal pieces of the material are deposited at the actual instant is called the accretion or growth surface. The growth surface may be disconnected, in general. In particular, it can be the whole surface of the solid. Finally, the part of the surface of the original or the growing solid that coincides with the growth surface at the time

when growth starts will be called the base surface. The base surface is clearly the part of the surface of the solid on which material is to be deposited during the next stage of continuous accretion. At different stages it coincides, as a rule, with the surface between the basic solid and the additional solid as well as with the surfaces between the sub-solids.

We assume that the basic solid, which is made from a viscoelastic ageing material, occupies a domain Ω_0 with the surface S_0 and is free of stresses up to the time τ_0 of application of the load. From τ_0 up to the time τ_1 when accretion starts the classical boundary conditions are given on S_0, the specific form of which is stated below. At τ_1 the continuous accretion of a solid begins due to the addition of material particles to the accretion surface $S^*(t)$. As it grows, the solid occupies a domain $\Omega(t)$ with surface $S(t)$. It is obvious that $S^*(t) \subseteq S(t)$. The time when a particle characterized by a position vector x is deposited on the solid will be denoted by $\tau^*(\mathbf{x})$ and called the time of deposition of the particle on the growing solid. The configuration of the accreted solid is completely defined by the function $\tau^*(\mathbf{x})$ depending on the spatial coordinates. Boundedness and piecewise-continuity are the general conditions usually imposed on $\tau^*(\mathbf{x})$.

We denote by $\tau_1^*(\mathbf{x})$ the time when an element of the growing solid is formed and by $\tau_0(\mathbf{x})$ the time when a load is applied to it. Naturally, $\tau_1^*(\mathbf{x}) \leq \tau_0(\mathbf{x}) = \tau_0$ for the elements of the basic solid ($\mathbf{x} \in \Omega_0$).

To simplify the problem we consider the case of small deformations and zero volumetric force.

The vector equilibrium equation is obviously satisfied in the domain occupied by the growing solid at each instant of time. For quasistatic processes it has the form

$$\mathbf{x} \in \Omega(t) : \nabla \cdot \mathbf{T} = \mathbf{O}, \tag{1}$$

where T is the stress tensor, and ∇ is the Hamilton operator (here and henceforth we use the conventional notation of tensor calculus).

The Cauchy conditions and the compatibility equations for deformations are always satisfied in the domain occupied by the basic solid

$$\mathbf{x} \in \Omega_0 : \mathbf{E} = \frac{1}{2}\left[\nabla \mathbf{u} + (\nabla \mathbf{u})^T\right], \quad \nabla \times (\nabla \times \mathbf{E})^T = \mathbf{O}, \tag{2}$$

where $\mathbf{E}$ is the strain tensor and $\mathbf{u}$ is the displacement vector. But in the domain $\Omega^*(t)$ occupied by the additional solid ($\Omega^*(t) = \Omega(t)/\Omega_0$) only their analogues involving the rates of change of the corresponding variables are satisfied

$$\mathbf{x} \in \Omega^*(t) : \quad \mathbf{D} = \frac{1}{2}[\nabla \mathbf{v} + (\nabla \mathbf{v})^T], \quad \nabla \times (\nabla \times \mathbf{D})^T = \mathbf{O},$$
$$\mathbf{D} = \frac{\partial \mathbf{E}}{\partial t}, \quad \mathbf{v} = \frac{\partial \mathbf{u}}{\partial t},$$

i.e. the strains are incompatible, in general.

The latter reflects the fact that deposited elements may be subject to deforming actions prior to the time of deposition on a basic solid independently of the processes taking place in the solid itself.

To study the stress strain state (SSS) of a growing solid one must know the laws of deformation of the basic solid from the instant τ_0 when the load is applied up to the instant τ_1 when accretion starts and of the deposited material from the instant $\tau_0(\mathbf{x})$ when a load is applied to this material up to the instant $\tau^*(\mathbf{x})$ of their deposition on the growing solid. The state of the original solid is determined from the solution of the problem with fixed boundary. The initial state of new elements which represent deposited surfaces as well as the boundary condition on the moving surface of a growing body can be determined by solving an additional contact problem of interaction between a solid and a surface.

Furthermore, we observe that

$$\tau^*(\mathbf{x}) = t \tag{3}$$

is the equation of the growth surface and, by (4)

$$s_n = |\nabla \tau^*(\mathbf{x})|^{-1} \tag{4}$$

is the velocity of motion of the surface $S^*(t)$ in the normal direction.

The traditional boundary conditions for the displacement vector and the vector of surface forces are given on the stationary sections of the surface of the growing solid.

To describe the behavior of the material of the growing solid we use the constitutive equations for an nonuniform ageing solid. Extending the definition of $\tau_0(x)$ by a constant τ_0 to the domain occupied by the original solid, we write

$$dev\mathbf{E}(\mathbf{x},t) = \frac{dev\mathbf{T}(\mathbf{x},t)}{2G(t-\tau_1^*(\mathbf{x}),\mathbf{x})} - \int\limits_{\tau_0(\mathbf{x})}^{t} \frac{dev\mathbf{T}(\mathbf{x},\tau)}{2G(\tau-\tau_1^*(\mathbf{x}),\mathbf{x})} \times K_1(t-\tau_1^*(\mathbf{x}),\tau-\tau_1^*(\mathbf{x}),\mathbf{x})\,d\tau, \tag{5}$$

$$I_1[\mathbf{E}(\mathbf{x},t)] = \frac{I_1[\mathbf{T}(\mathbf{x},t)]}{E^*(t-\tau_1^*(\mathbf{x}),\mathbf{x})} - \int\limits_{\tau_0(\mathbf{x})}^{t} \frac{I_1[\mathbf{T}(\mathbf{x},\tau)]}{E^*(\tau-\tau_1^*(\mathbf{x}),\mathbf{x})} \times K_2(t-\tau_1^*(\mathbf{x}),\tau-\tau_1^*(\mathbf{x}),\mathbf{x})d\tau, \tag{6}$$

where $G(t)$, $E^*(t)$ and $K_1(t,\mathbf{x})$, $K_2(t,\mathbf{x})$ are the instantaneous elastic strain moduli and creep functions for pure shear and uniform compression, respectively, $I_1(\mathbf{K})$ denotes the first invariant of a tensor $\mathbf{K}$, and $dev\mathbf{K}$ is the deviator of $\mathbf{K}$.

The description of the process of continuous accretion of a viscoelastic ageing solid involves three characteristic instants: the instant $\tau_1^*(\mathbf{x})$ when the element with coordinate $\mathbf{x}$ is formed, the instant $\tau_0(\mathbf{x})$ when a load is applied to this element, and the instant $\tau^*(\mathbf{x})$ when the element is deposited on the growing solid. These three instants are different, in general.

The deposition process is largely determined by specifying these three instants. If the processes of continuous concrete casting, ice formation, crystal growth, etc. are studied, then $\tau_1^*(\mathbf{x}) = \tau_0(\mathbf{x}) = \tau^*(\mathbf{x})$, i.e. the elements are deposited at the same instant as they are formed and a load is applied to them. If spray deposition or erection of a structure from a large number of blocks is modelled by a continuous growth process, then, as a rule, $\tau_0(\mathbf{x}) = \tau^*(\mathbf{x})$ and the instant $\tau_1^*(\mathbf{x})$ when the elements are formed is arbitrary. If the deformation of elements begins as soon as they are formed and they are being added to the basic solid only over some time interval, then $\tau_1^*(\mathbf{x}) = \tau_0(\mathbf{x}) \neq \tau^*(\mathbf{x})$ and so on.

Before formulating the problem considered in the present paper, we emphasize that the problem of the growth of a solid differs in a major way from that involving the removal of material. The latter is characterized solely by the fact that the domain occupied by the solid is reduced, subject to the standard equations and boundary conditions.

Suppose that a homogeneous viscoelastic ageing solid occupying a domain Ω_0 with surface S_0 ($\mathbf{x} \in \Omega_0$) is formed at instant $\tau_1^*(\mathbf{x}) = 0$ and is free of stresses up to the instant $\tau_0 \geq 0$ when a load is applied. Starting from the latter instant, we consider two kinds of boundary conditions on the surface of the solid (surface forces on $S_1(t)$ and displacements on $S_2(t)$).

The sections of the surface on which different boundary conditions are given do not intersect one another and cover the whole surface of the solid. The dependence of S_i on t enables us to take into account the possible evolution of the system of loads, punches, etc. on S_0, and is assumed to be piecewise constant. Unless the solid surface is closed, the behaviour of stresses or strains at infinity is prescribed.

Continuous deposition of material formed simultaneously with the solid ($\tau_1^*(\mathbf{x}) = 0$) starts at $\tau_1 \geq \tau_0$. The solid occupies a domain $\Omega(t)$ with surface $S(t)$ during its growth. The growth surface $S^*(t)$ ($S^*(\tau_1) \subset S_0$) moves in space. The sections $S_i(t)$ ($i = 1, 2$) on which the common boundary conditions are given can vary because of the loading of the stationary surface of the additional solid. We assume that the growing surface is always free of outer loads and new deposited surfaces are loaded at the instant of their deposition.

At the instant $\tau_2 > \tau_1$ the accretion of the solid ceases, and starting from this instant four kinds of boundary conditions are given on the sections $S_i(t)$ of the surface $S_1 = S(\tau_2)$ of the solid occupying the domain $\Omega_1 = \Omega(\tau_2)$.

After some time, at the instant $\tau_3 > \tau_2$ the solid accretion may start again. An accretion surface may appear which is not related in any way to the previous one. Then the accretion may stop at instant τ_4, and so on, leading to the problem of piecewise-continuous accretion of a solid with n instants at which the growth starts and, respectively, n instants when it stops.

Proceeding to the study of the basic stages of the process of piecewise-continuous accretion of a viscoelastic solid, we note that fairly slow processes will be considered everywhere below, so that the inertial terms can be neglected in the equilibrium equations.

3 Mathematical Model of a Solid Prior to the Growth Process

We consider the SSS of a viscoelastic ageing solid Ω_0 in the time interval $[\tau_0, \tau_1]$. We write the equilibrium equation in the form (1)

$$\nabla \cdot \mathbf{T} = \mathbf{O}. \tag{7}$$

We represent the boundary conditions described above as follows

$$\begin{aligned} &\mathbf{x} \in S_1(t): \quad \mathbf{n} \cdot \mathbf{T} = \mathbf{p}_0, \\ &\mathbf{x} \in S_2(t): \quad \mathbf{u} = \mathbf{u}_0, \end{aligned} \tag{8}$$

where $\mathbf{p}_0$ and $\mathbf{u}_0$ are given vectors of surface forces and strains and $\mathbf{n}$ is the unit vector normal to the solid surface. The Cauchy conditions are written as follows (see (2))

$$\mathbf{E} = \frac{1}{2}\left[\nabla \mathbf{u} + (\nabla \mathbf{u})^T\right]. \tag{9}$$

We take the constitutive equations in the form (6) and (7), assuming that the transverse contraction (Poisson's) ratio of the instantaneous elastic strain and the creep strain of the ageing material are identical and are equal to v. Then we have (see [1, 2])

$$\mathbf{T} = G(\mathbf{I} + \mathbf{N}(\tau_0, t))[2\mathbf{E} + (K-1)I_1(\mathbf{E})\mathbf{1}], \tag{10}$$

where

$$\begin{aligned} (\mathbf{I} + \mathbf{N}(\tau_0, t))^{-1} &= (\mathbf{I} - \mathbf{L}(\tau_0, t)), \\ 2G &= E(1+v)^{-1}, \quad K = (1-2v)^{-1}, \\ \mathbf{L}(\tau_0, t)f(t) &= \int_{\tau_0}^{t} f(\tau)K(t,\tau)d\tau, \\ \omega(t,\tau) &= 2C(t,\tau)(1+v), \\ K(t,\tau) &= E(\tau)\frac{\partial}{\partial \tau}\left[E^{-1}(\tau) + C(t,\tau)\right] \\ &= K_1(t,\tau) = G(\tau)\frac{\partial}{\partial \tau}\left[G^{-1}(\tau) + \omega(t,\tau)\right], \end{aligned}$$

where $E = E(t)$ and $G = G(t)$ are the elastic moduli under tension and shear, $C(t,\tau)$ and $\omega(t,\tau)$ are the creep measures under tension and shear, $K(t,\tau)$ is the

creep function under tension, and **1** is the unit tensor. The arguments are omitted in a number of obvious cases above. They will also be omitted in what follows and will be used only in those cases when their absence may be misleading.

Thus (8)–(11) constitute the boundary-value problem (BVP) of the linear theory of elasticity for a homogeneous ageing basic solid, the SSS of which can be described by the solution of the system for $t \in [\tau_0, \tau_1]$.

We transform the BVP for the basic solid. Let us introduce the notation

$$\begin{aligned} \mathbf{N}^0 &= \mathbf{H}(\tau_0, t)\mathbf{N}G^{-1}, \quad \mathbf{a}^0 = \mathbf{H}(\tau_0, t)\mathbf{a}G^{-1}, \\ \mathbf{H}(\psi, t) &= (\mathbf{I} - \mathbf{L}(\psi, t)), \end{aligned} \tag{11}$$

where **N** and **a** are an arbitrary tensor and arbitrary vector, respectively. We apply the operator $\mathbf{H}(\tau_0, t)$ to the relations in (8)–(11) containing **T** after dividing them by G. Then, since $\mathbf{H}(\tau_0, t)$ commutes with the Hamilton operator, we obtain the following BVP using (12) ($\tau_0 \le t \le \tau_1$)

$$\begin{aligned} \nabla \cdot \mathbf{T}^0 &= \mathbf{O}, \\ \mathbf{x} \in S_1(t): &\quad \mathbf{n} \cdot \mathbf{T}^0 = \mathbf{p}_0^0, \\ \mathbf{x} \in S_2(t): &\quad \mathbf{u} = \mathbf{u}_0, \\ \mathbf{E} &= \frac{1}{2}\left[\nabla \mathbf{u} + (\nabla \mathbf{u})^T\right], \\ \mathbf{T}^0 &= 2\mathbf{E} + (K - 1)I_1(\mathbf{E})\mathbf{1}. \end{aligned} \tag{12}$$

Unlike (8)–(11), time occurs in the BVP (13) as a parameter. The latter is mathematically equivalent to the BVP of the theory of elasticity with a parameter t. All analytic and numerical methods of the theory of elasticity can be used when constructing the solution of such a problem, which undoubtedly lends itself better to investigation than the problem (10)–(13) of the theory of viscoelasticity.

In order that **T**, **E**, and **u** be a solution of the BVP (8)–(11) it is necessary and sufficient that $\mathbf{T}^0$, **E**, and **u** form a solution of the BVP (13) and the relation

$$\mathbf{T}(\mathbf{x}, t) = G(t)\left[\mathbf{T}^0(\mathbf{x}, t) + \int_{\tau_0}^{t} \mathbf{T}^0(\mathbf{x}, \tau)R(t, \tau)\, d\tau\right] \tag{13}$$

be satisfied ($\tau_0 \le t \le \tau_1$). Here $R(t, \tau)$ is the resolvent of the kernel $K(t, \tau)$.

Therefore, solving the BVP (12) with t as a parameter, one can reconstruct the true characteristics of the SSS of the original viscoelastic ageing solid (10)–(13) from using (14).

4 Mathematical Model of a Continuously Growing Solid

We now consider the process of continuous accretion of a solid ($\tau_1 \le t \le \tau_2$). For a growing solid we have:

the equilibrium equation

$$\nabla \cdot \mathbf{T} = \mathbf{O}, \tag{14}$$

the boundary conditions on the stationary part of the surface

$$\begin{aligned} &\mathbf{x} \in S_1(t): \quad \mathbf{n} \cdot \mathbf{T} = \mathbf{p}_0, \\ &\mathbf{x} \in S_2(t): \quad \mathbf{u} = \mathbf{u}_0, \end{aligned} \tag{15}$$

the condition on the growing surface which can be obtained from the solution of a contact problem for solid and surface provided that they interact without friction (smooth contact)

$$\begin{aligned} &\mathbf{x} \in S^*: \mathbf{n} \cdot \frac{\partial \mathbf{HT}}{\partial t} = p\,\mathbf{n}, \quad p = -\frac{s_n}{G}(\mathcal{T}_s : \mathbf{L}), \\ &\mathbf{v} = \frac{\partial \mathbf{u}}{\partial t}, \quad s_n = \mathbf{n} \cdot \mathbf{v}, \quad (t = \tau^*(\mathbf{x})), \end{aligned} \tag{16}$$

where $\mathcal{T}_s$ is the 2D tensor of the deposited elastic surface tension, $\mathbf{L}$ is the 2D tensor of this surface curvature, the relation between the rates of strain and displacement

$$\mathbf{D} = \frac{1}{2}\left[\nabla \mathbf{v} + (\nabla \mathbf{v})^T\right], \tag{17}$$

and the constitutive equation in the form

$$\begin{aligned} \mathbf{T} &= G(\mathbf{I} + \mathbf{N}(\tau_0(\mathbf{x}), t))[2\mathbf{E} + (K-1)I_1(\mathbf{E})\mathbf{1}], \\ \tau_0(\mathbf{x}) &= \begin{cases} \tau_0, & \mathbf{x} \in \Omega_0, \\ \tau^*(\mathbf{x}), & \mathbf{x} \in \Omega^*(t). \end{cases} \end{aligned} \tag{18}$$

Relations (15)–(19) form a general non-inertial initial BVP (IVBP) for a continuous growing solid, where the operator $(\mathbf{I} - \mathbf{L}(\tau_0(\mathbf{x}), t)) = \mathbf{H}(\tau_0(\mathbf{x}), t))$ and its inverse $(\mathbf{I} + \mathbf{N}(\tau_0(\mathbf{x}), t))$ can be determined from (11) and (12) with τ_0 replaced by $\tau_0(\mathbf{x})$. We observe that the process of continuous deposition of new elements on the basic solid under investigation leads, in general, to governing relations containing discontinuities on the interface between the original and the additional solids.

Let us transform the IBVP for a continuously accreted viscoelastic ageing solid into a problem with the time parameter that has the same form as the BVP of the

theory of elasticity. We omit technical details and obtain the final result in the form of BVP as follows

$$\begin{aligned}
&\nabla \cdot \mathbf{S} = \mathbf{O}, \\
&\mathbf{x} \in S_1(t): \quad \mathbf{n} \cdot \mathbf{S} = \mathbf{R}\mathbf{p}_0, \\
&\mathbf{x} \in S_2(t): \quad \mathbf{v} = \mathbf{v}_0, \\
&\mathbf{x} \in S^*(t): \quad \mathbf{n} \cdot \mathbf{S} = p\mathbf{n}(t = \tau^*(\mathbf{x})), \\
&\mathbf{D} = \frac{1}{2}\left[\nabla \mathbf{v} + (\nabla \mathbf{v})^T\right], \\
&\mathbf{S} = 2\mathbf{D} + (K-1)I_1(\mathbf{D})\mathbf{1},
\end{aligned} \tag{19}$$

where $\mathbf{R}$ acts on an arbitrary vector $\mathbf{a}(\mathbf{x}, t)$ by the rule

$$\begin{aligned}
\mathbf{R}\mathbf{a}(\mathbf{x}, t) = &\frac{1}{G(t)}\frac{\partial \mathbf{a}(\mathbf{x}, t)}{\partial t} + \int\limits_{\tau_0(\mathbf{x})}^{t} \frac{\partial \mathbf{a}(\mathbf{x}, \tau)}{\partial \tau}\frac{\partial \omega(t, \tau)}{\partial t} d\tau \\
&+ \mathbf{a}(\mathbf{x}, \tau_0(\mathbf{x}))\frac{\partial \omega(t, \tau_0(\mathbf{x}))}{\partial t}, \quad \mathbf{S} = \frac{\partial(\mathbf{HT})}{\partial t},
\end{aligned} \tag{20}$$

Note that the conditions on $S_1(t)$ and $S^*(t)$ are identical.

Relations (20) supplemented with the initial conditions for the basic solid at $t = \tau_1$ form an BVP with t as a parameter.

For $\mathbf{T}$, $\mathbf{E}$, and $\mathbf{u}$ to be solutions of IBVP (15)–(19) it is necessary and sufficient that $\mathbf{S}$, $\mathbf{D}$, and $\mathbf{v}$ form the solution of (20) and that the following relations be satisfied

$$\begin{aligned}
\mathbf{T}(\mathbf{x}, t) = G(t)\Bigg\{&\frac{\mathbf{T}(\mathbf{x}, \tau_0(\mathbf{x}))}{G(\tau_0(\mathbf{x}))}\left[1 + \int\limits_{\tau_0(\mathbf{x})}^{t} R(t, \tau)\, d\tau\right] \\
&+ \int\limits_{\tau_0(\mathbf{x})}^{t}\left[\mathbf{S}(\mathbf{x}, \tau) + \int\limits_{\tau_0(\mathbf{x})}^{\tau} \mathbf{S}(\mathbf{x}, \zeta)\, d\zeta R(t, \tau)\right] d\tau\Bigg\}, \\
\mathbf{u}(\mathbf{x}, t) = \mathbf{u}(\mathbf{x}, \tau_0(\mathbf{x})) + &\int\limits_{\tau_0(\mathbf{x})}^{t} \mathbf{v}(\mathbf{x}, \tau) d\tau.
\end{aligned} \tag{21}$$

Hence, the solution of the problem of the accretion of a viscoelastic ageing solid can be obtained by the solution of the mathematically identical problems with a parameter t, which have the same form as the BVP of the classical theory of elasticity. Then the true stresses and displacements in the growing solid can be reconstructed using (22).

Relations (22) indicate that the SSS for a growing viscoelastic solid depends on the whole history of loading and accretion of the solid. The initial values of the displacements $\mathbf{u}(\mathbf{x}, \tau^*(\mathbf{x}))$ of the deposited elements in (22) are usually set to be zero (since the SSS of the growing solid does not depend on them).

5 Mathematical Model of a Solid After the Growth Stop

Suppose that the solid ceases to grow at instant τ_2. At this instant it occupies a domain Ω_1 with surface S_1, on which two kinds of boundary conditions are specified, as in the case of the problem for the basic solid. Moreover $S^*(\tau_2) = S_1^* \subseteq \cup_i S_i(t)$ $(i = 1, 2)$. In this case the problem for the invariable solid occupying Ω_1 is similar to (15)–(19) without the initial-boundary condition on $S^*(t)$

$$\begin{aligned}
&\nabla \cdot \mathbf{T} + \mathbf{f} = \mathbf{O}, \\
&\mathbf{x} \in S_1(t) : \mathbf{n} \cdot \mathbf{T} = \mathbf{p}_0, \quad \mathbf{x} \in S_2(t) : \mathbf{u} = \mathbf{u}_0, \\
&\mathbf{D} = \frac{1}{2}\left[\nabla \mathbf{v} + (\nabla \mathbf{v})^T\right], \\
&\mathbf{T} = G(\mathbf{I} + \mathbf{N}(\tau_0(\mathbf{x}), t))[2\mathbf{E} + (K-1)I_1(\mathbf{E})\mathbf{1}],
\end{aligned} \tag{22}$$

with $\tau^*(\mathbf{x}) = \tau_2$ for $\mathbf{x} \in S_1^*$. The stresses, strains and displacements at $t = \tau_2$ found by solving the growth problem at the previous step serve as the initial conditions.

One can obtain the following BVP (see (20))

$$\begin{aligned}
&\nabla \cdot \mathbf{S} = \mathbf{O}, \\
&\mathbf{x} \in S_1(t) : \mathbf{n} \cdot \mathbf{S} = \mathbf{R}\mathbf{p}_0, \quad \mathbf{x} \in S_2(t) : \mathbf{v} = \mathbf{v}_0, \\
&\mathbf{D} = \frac{1}{2}[\nabla \mathbf{v} + (\nabla \mathbf{v})^T], \\
&\mathbf{S} = 2\mathbf{D} + (K-1)I_1(\mathbf{D})\mathbf{1},
\end{aligned} \tag{23}$$

where the initial conditions remain as before.

For $\mathbf{T}$, $\mathbf{E}$, and $\mathbf{u}$ to be solutions of the IBVP (23) it is necessary and sufficient that $\mathbf{S}$, $\mathbf{D}$, and $\mathbf{v}$ form a solution of BVP (24) and that relations (22) be satisfied.

Thus, to construct the solution of the problem over the time interval $[\tau_0, \tau_3]$ one has to construct the solutions of the following tree identical problems (having the same form as the BVP of the theory of elasticity with a parameter t): problem (13) for $t = \tau_0$ as well as problems (20), and (24). The SSS of the growing solid can then be reconstructed for any $t \in [\tau_0, \tau_3]$ from (14) and (22).

6 Mathematical Model of a Piecewise-Continuously Growing Solid

Suppose that the growth process restarts at instant τ_3 and deposition of new elements begin on the surface S_1 of the solid (or part of it) occupying the domain Ω_1. Then, by analogy with Sect. 3, one can obtain a problem in the form (20) describing the behaviour of the growing viscoelastic solid up to the instant τ_4 when the accretion stops again. Naturally, the new growth surface may not be related in any way to the previous one, the functions and parameters in (20) may take new values. Once the problem is solved, the SSS of the growing solid can be determined using (22).

For $t \geq \tau_4$, when the solid does not grow, the problem can be reduced in the same way to the form (23) and then (22) can be used.

The following step-wise scheme can be used to solve the problem of arbitrary piecewise-continuous accretion. First (13) is solved. Then solutions of (20) and (24) are constructed at each stage involving either continuous accretion or, respectively, no growth at all. The final results can be obtained using (22).

Hence it follows that the process of piecewise-continuous accretion of a viscoelastic ageing solid with any finite number of instants when the growth starts and stops can be considered using the method proposed. The problem with n instants when growth starts (and, naturally, n instants when it stops) can be reduced to the study of $2n + 1$ problems of one type, which have the same form as the BVP of the theory of elasticity containing t as a parameter. Once these $2n + 1$ problems are solved, the SSS of the viscoelastic ageing solid under consideration can be easily reconstructed for any time from the above formulas.

The one-to-one correspondence between the solutions of the problem of piecewise continuous accretion of a viscoelastic ageing solid and the BVP of the theory of elasticity established in the present section enables us to conclude that a unique solution of the IBVP exists that describes the piecewise continuous accretion of a viscoelastic solid because a unique solution of the BVP of the theory of elasticity exists.

7 Conclusions

One can obtain a number of interesting results from (13), (20), (24), (14) and (22) using the property of limited creep of a viscoelastic material (see also [3–15]). If one assumes that only the surface of the basic solid is subject to a load, the actions are stationary, and accretion does not involve pretension, then the interaction between newly deposited particles and the solid already formed can be neglected starting from some instant t^0. In other words, starting from t^0 the growth process has little effect on the state of the part of the solid formed prior to to and the part formed for $t > t^0$ is practically stress-free. In particular, if the instant when a stationary load

is applied to the basic solid is much earlier than the instant when the accretion starts, all other conditions being equal, then the effect of accretion on the state of the basic solid will be quite small and practically the whole additional solid will be strain-free. Similar conclusions can be drawn when considering a load regime of the original solid under which the actions remain constant for a prolonged period of time prior to the beginning of growth, irrespective of their variation at earlier times.

The effects considered have a clear mechanical meaning. Indeed, the deformation of a viscoelastic solid will practically cease after a period of time under limited creep conditions and stationary actions. Subsequent deposition of stress-free elements leads to a situation when the interaction between the parts of the solid already formed and those being created during the growth process is negligible.

Relations (13), (20), (24), (14) and (22) also enable us to predict such phenomena inherent in growing solids as the presence of residual stresses after the loads are removed, the presence of surfaces of stress discontinuity in the growing solid, and the dependence of the SSS of a viscoelastic solid on the growth rate (only the order of the acts of deposition and loading matters in the elastic case).

Finally, we discuss one more important aspect of the problem of accretion of a solid. It is concerned with the correspondence between the solution of the accretion IBVP and the viscoelasticity BVP for a variable boundary. The question is as follows: when will the solution of the non-classical accretion problem be the same as that of the classical problem of solid mechanics in a domain which varies with time? It turns out that the solutions are the same only when the strains in the growing solid and the deposited elements can be made compatible. Being a degenerate case of the IBVP describing the accretion of a solid, such an accretion regime clearly cannot be realized in practice.

Unlike the degenerate case when the strains in the whole solid are compatible during the accretion process in the case of stress-free elements being deposited on the solid which is a completely relevant version of the accretion process the problem will fail to become much simpler. It provides a brilliant demonstration of the effects related to accretion in model examples and is often encountered in applications. Here we have a situation when some inhomogeneous condition, rather than the homogeneous one, is trivial in a certain sense, unlike the traditional formulation of the BVP in solid mechanics.

Thus, using the presented approach for mechanical design of AM fabricated parts from viscoelastic materials one can determine the strength and the shape of final products. Moreover, on the basis of this mechanical analysis one can work out effective recommendations for improving the technological process.

Acknowledgment This work was financially supported by the Russian Science Foundation under Grant 14-19-01280.

References

1. Manzhirov AV (2015) Mechanical design of viscoelastic parts fabricated using additive manufacturing technologies. In: Lecture notes in engineering and computer science: proceedings of the World Congress on Engineering, WCE, London, pp 710–714
2. Manzhirov AV (1995) The general non-inertial initial-boundary value problem for a viscoelastic ageing solid with piecewise-continuous accretion. J Appl Math Mech 59(5):805–816
3. Manzhirov AV (2013) Mechanics of growing solids and phase transitions. Key Eng Mater 535–536:89–93
4. Manzhirov AV, Lychev SA, Gupta NK (2013) Nonlinear models of growing solids. Proc Indian Natl Sci Acad 79(4):529–545
5. Manzhirov AV (2014) Mechanics of growing solids: new track in mechanical engineering. In: Proceedings of ASME 2014 international mechanical engineering congress & exposition, IMECE 2014, Montreal, Canada, 10p
6. Manzhirov AV, Lychev SA (2014) Mathematical modeling of additive manufacturing technologies. In: Lecture notes in engineering and computer science: World Congress on Engineering, WCE, London, pp 1404–1409
7. Lychev SA, Manzhirov AV (2014) Discrete and continuous growth of hollow cylinder: finite deformations. In: Lecture notes in engineering and computer science: World Congress on Engineering, WCE, London, pp 1327–1332
8. Manzhirov AV, Lychev SA (2015) An approach to modeling of additive manufacturing technologies. In: Transactions on engineering technologies: World Congress on Engineering. Springer, Netherlands, pp 99–115
9. Lychev SA, Manzhirov AV, Bychkov PS (2015) Discrete and continuous growth of deformable cylinder. In: Transactions on engineering technologies: World Congress on Engineering. Springer, Netherlands, pp 239–254
10. Manzhirov AV, Parshin DA (2015) Arch structure erection by an additive manufacturing technology under the action of the gravity force. Mech Solids 50(5):559–570
11. Manzhirov AV, Parshin DA (2015) The influence of the erection mode on the stress state of a viscoelastic arch structure which is built up using an additive manufacturing technology under the action of the gravity force. Mech Solids 50(6)
12. Manzhirov A, Gupta N (2015) Fundamentals of continuous growth processes in technology and nature. In: IUTAM symposium on growing solids. Symposium materials. Institute for Problems in Mechanics RAS, Moscow, pp 73–76
13. Lychev S, Manzhirov A, Shatalov M, Fedotov I (2015) Transient temperature fields in growing bodies subject to discrete and continuous growth regimes. In: IUTAM symposium on growing solids. Symposium materials. Institute for Problems in Mechanics RAS, Moscow, pp 68–71
14. Kazakov K, Kurdina S, Manzhirov A (2015) Multibody contact problems for discretely growing systems. In: IUTAM symposium on growing solids. Symposium materials. Institute for Problems in Mechanics RAS, Moscow, pp 39–42
15. Manzhirov AV (2015) Problems of growing solids mechanics in modern industrial technologies. In: Topical problems of continuum mechanics: proceedings of the IV international conference. National University of Architecture and Civil Engineering, Yerevan, pp 471–475

Lean Manufacturing Implementation in Intermittent Environments: A Framework

Tiago Ferreira, Amilcar A. Baptista, Susana Garrido Azevedo and F. Charrua Santos

Abstract This chapter suggests a framework for the implementation of Lean Manufacturing in intermittent production environments—Job shop. The environment faced by organizations request the adoption of more efficient management models and practices in order to increase their competitiveness. In this context, Lean philosophy, in particular Lean Manufacturing has proven to be an extremely powerful management paradigm. However, the Lean philosophy when is applied incorrectly may turn out to be a failure for the organizations. In this sense there are several factors that can hamper the correct development of Lean Manufacturing within organizations such as (i) lack of commitment by top management; (ii) lack of qualified and graduates employees without know how on this paradigm; (iii) lack of guidelines on the application of tools and methodology of Lean Manufacturing. This research shows that over the past few years, tools have been developed within

T. Ferreira
OGMA, Lisbon, Portugal
e-mail: tiagoferreira19713@gmail.com

T. Ferreira
University of Beira Interior, Covilhã, Portugal

A.A. Baptista (✉)
C-MAST Center for Mechanical and Aerospace Sciences and Technologies, University of Beira Interior, Calçada Fonte do Lameiro, Ed. I das Eng, Elect. Dept., 6200-001 Covilhã, Portugal
e-mail: amilcarb@ubi.pt

S.G. Azevedo
Department of Management and Economics, CEFAGE-UBI—Center for Advanced Studies in Management and Economics, University of Beira Interior, Estrada do Sineiro, 6200-209 Covilhã, Portugal
e-mail: sazevedo@ubi.pt

F.C. Santos
Electromechanical Department, C-MAST Center for Mechanical and Aerospace Sciences and Technologies, University of Beira Interior, Calçada Fonte do Lameiro, Ed. I das Eng, Elect. Dept., 6200-001 Covilhã, Portugal
e-mail: bigares@ubi.pt

S.-I. Ao et al. (eds.), *Transactions on Engineering Technologies*,
DOI 10.1007/978-981-10-1088-0_18

Lean Manufacturing relating it to different types of industrial environments. However, guidelines for implementing this paradigm "step-by-step" is missing.

Keywords Automotive industry · Case study · Framework · Job shop · Lean manufacturing · Lean philosophy

1 Introduction

Organizations with complex production processes, such as intermittent or job shop process, report an increased difficulty in the implementation of Lean Manufacturing (LM). One barrier observed in different job shop industries is the lack of a guiding tool with the objective of implementing the lean manufacturing in this kind of environment. One of the barriers faced was the difficulty to identify where to apply a policy of continuous improvement and the other the kind of LM' tools that should be used. Obviously in this environment, as in the others, a strategy is needed to implement the lean philosophy as well as a training plan to promote the involvement of collaborators. As a result, this chapter shows the need for a new framework to guide the implementation of the LM [1].

Organizations are encouraged to produce with higher added value. However these job shop processes are characterized by a big multiplicity of demanded products and companies are often faced with the incapability to meet the increased requirements, because they do not have the right organization to answer this need. To get over these difficulties it is necessary rethinking and restructuring processes, eliminate waste and activities that don't add value to products or services. Companies aims meet the needs of this markets with a high internal stability [1, 2]. Also the companies are confronted with the need to high flexibility to respond to an increasing fragmented demand, and at the same time improve the productivity through reduction of waste.

One example is the automotive industry, which is considered a reference as it is conciliate high production levels, quality and flexibility through innovative designs organization models. The measures taken by this industry, particularly by component suppliers have come to meet the cost reduction maintaining the high quality. Some of these measures have gone through the analysis product by reducing costs but simultaneously improving performance in terms of quality. Currently the quality of the components has as a reference 20–30 low quality Parts Per Million, (PPM), while a decade ago the goal was from 1000 to 2000 PPM [3]. Also in the automotive industry the reduce of lot size resulting from the variation in demand and increased customization of products was felt significantly. To reply to this reality innovative management models were adopted, such as just-in-time (JIT) which has the intention of making the production more flexible and increase quality levels, without rupture because in this industry there are significant economic penalties for suppliers delays [3].

The globalization, in addition to changes in market behavior, also conditioned other significant factor the price. While a few decades ago the price was imposed by the producer it is now imposed by the market. As a result, in order to maintain margins that allow it to survive, companies force themselves to reduce the cost of production, to create added value as a result of improvement of quality and responsibility to customers. In resume, the global market has forced companies to produce more quality diversifying its offer, which led to smaller production batches, in the limit of piece by piece production, with the delivery times shorter and shorter. In this context, the aim of this chapter is to propose a framework for the implementation of lean manufacturing in intermittent production environment or Job shop (JS).

2 Classification of Production Systems

The classification of production systems is not easy as a result of the big number of different processes. However some classifications have prevailed: (i) by type of production; (ii) by product characteristics; (iii) by production environment; (iv) by characteristics of the production flow.

In this work the classification by characteristics of the production flow was adopted.

It is now usually accepted that the discrete manufacturing systems can be classified according to the characteristics of production flows of the components in the following categories [4–6]: (i) Intermittent (job shop), (ii) lots (batch), (iii) line, this case can be divided into two sub categories: mass and continuous production (Flow shop, shop process).

Production of small batches of a variety of products, especially when these have a different sequence of processes have the Anglo-Saxon designation of Job Shop (JS). In this environment, the equipment is arranged, habitually in work centers according to their characteristics.

The job shop environment, JS, is characterized by the production of different orders in different flows. Each work order consists in a set of tasks or jobs that are processed only one time in each machine. There are many constraints in the operations and machinery level, namely: (i) the sequence which operations are processed can vary; (ii) operations after begin cannot be interrupted and each machine can operate only one task at a time; (iii) each task is processed in only one machine at a time.

The batch process, Batch Shop, differ from job shop process essentially by the way it processes the sequence of operations. In the Batch Shop the sequence is the same for all products.

Assembly Line, differs from Batch Shop essentially by the size of the batch, bigger in this case.

As mentioned above, different factors have been forcing the diversification and fragmentation of production which accentuates the tendency of companies to develop more complex processes as the job shop and simultaneous more flexible.

3 Lean Manufacturing

The Production System developed by Toyota within the automobile production in Japan, Toyota Production System (TPS) is, among the known models, one of the most efficient in the elimination of waste and production flexibility [7]. This philosophy is today a case study as an organizational model. Their success around the world, results in a methodology that would be called "lean production" or the Lean Manufacturing [8]. The principles of lean manufacturing have become state-of-the-art in modern production design and its implementation has become a vital pre-requisite in global competition [9].

LM is a manufacturing strategy that aims to achieve a smooth production flow by eliminating waste and by increasing the activities value. The basic principle of lean manufacturing is eliminating waste, reducing production costs and instituting employee empowerment. The different types of wastes generally found in a manufacturing environment include overproduction, waiting, transporting, inventory, unnecessary/excess motion, defects and rework, along with other forms of wastes including equipment downtime due to job setups [10]. If industrial organizations ignore the LM strategy, they would not be able to stand a chance against the current global competition for higher quality, faster delivery and lower costs [11, 12]. The cost savings have been achieved using tools derived from lean thinking [13], in particular "value stream mapping" (VSM) [14], "spaghetti chart or diagram" and the activity worksheet.

The main features associated to LM include: one unit at a time production; non-value added time eliminated; production in the work content time only [15].

Some studies have been developed in order to optimize the application of LM, in particular by establishing guiding tools in the application of this paradigm in different industrial environments. Though the lean manufacturing principles have been adopted globally over years, most of the organisations have started implementing lean tools currently [16, 17]. These tools are a guidance to solve the deficiency skills sometimes responsible from the failures in the application of LM.

Abdulmalek et al. [18] in order to orientate the implementation of LM, suggests a classification that sets the processes according to their suitability for the implementation of the LM. However this classification identifies few processes. Subsequently, Rathi and Farris [19], have continued the classification developed by Abdulmalek, building a more complete classification with more variables by adding features of interest, resulting in a clearer and complete classification model, see Table 1. The application of LM varies with the industrial environment. This classification simplifies the processes differentiation. The processes are characterized by different variables, as can be seen in Table 1.

Table 1 Type of production processes

	Mass production	Batch production	Job shop production
Demand	Deterministic and stable	Deterministic or stochastic, stable	Deterministic or stochastic variable
Lot size	Big	Medium low	Very low
Production	Standard to stock	Standard or flexible By lots	Flexible
Number of raw material	Low	Moderate	High
Number of finish goods	Low	Moderate	High
Equipment's	Specialized/Dedicated	Dedicated	Flexible
Layout	Layout by product	Layout mix	Layout by process
Materials flow	Continuous	Continuous to intermittent	Intermittent
Process flexibility	Low	Medium	High
Example	Oil refinery	Textile industry	Metalworking

As result are identified different approaches to the application of LM. However, this analysis needs more intensive studies in some types of production like the Job shop environment. Anand and Kodali (2010) presented a study about the LM implementation in different types of industry. We can see that the LM has been implemented in many different industrial environments in the last years [20]. The literature also shows that the number of studies about LM implementation is more representative in the automobile industry since it continues to be a reference in the application of LM [21].

The authors report that none of the studies provides a "step by step" or a guidance tool to the application of LM methodology. The approach to implement the LM is different from an industrial unit to another, from one production system to another, so it is important to have guiding tools early in the process of implementation and some indicators about the major or minor appetence to implement. Though, there are some studies that relate the Lean tools with different waste [20].

4 Proposal of a Framework for the Application of LM in Job Shop Environment

Considering the above mentioned, it is pertinent the development of a methodology for the application of LM in intermittent environments that go beyond the results shown.

It seems clear that it is necessary to develop a framework for LM application in intermittent environments, particularly in the initial phase of its implementation. The Lean philosophy includes tools aimed to the improvement and waste

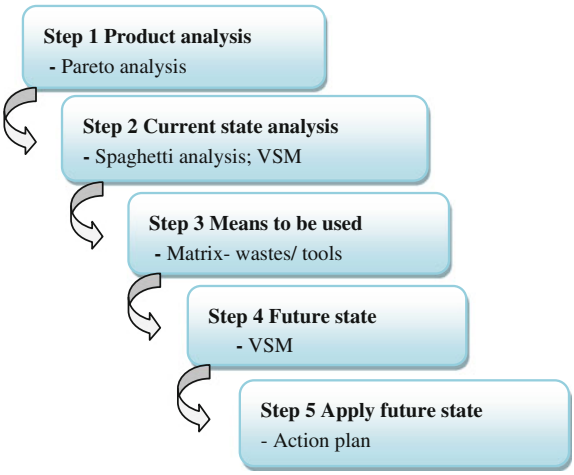

Fig. 1 Framework proposal for LM implementation in intermittent environments

elimination such as the Value Stream Mapping (VSM). The VSM is a powerful diagnostic tool, but in more complex production scenarios the difficulties justifying a more detailed analysis.

According to Achanga et al. [22] the success of LM implementation depends on the following factors: leadership and management; finance; skills and expertise; and supportive organizational culture of the organization. Some researchers also suggested that applying the full set of lean principles and tools also contribute to the successful LM transformation [23].

The framework proposed in this work aims to improve the third point, the lack of guidance on the application of LM, especially in industries with intermittent production processes. In Fig. 1 the five phases of the proposed framework are identified.

4.1 Step 1—Product Analysis

In intermittent environments is more difficult to identify where to begin the implementation of Lean practices, the existence of many products and complex flows make it difficult to focus, so it is inevitable that make a careful analysis. This analysis aims to identify the most significant products, most representatives in sales volume and the volume of the business.

Organizations that produce a large number of products can't assign the same importance to all of them, because the costs associated with this control would be high. In this case it is customary to utilize the Pareto analysis to identify the most significant products. Pareto analysis can also be used to identify the products and flows most significant in applying the LM.

This tool has been used in numerous industries, and is one of the seven basic tools of quality [24]. The Pareto analysis follows the rule of 80:20, where 20 % of

the articles typically represent 80 % of total sales [25]. Using the Pareto analysis in the current study should be made as follows: (i) quantify all products manufactured and record them in a table; (ii) quantify the products in sales volume; presenting the percentage of each product in relation to the total; prepare the cumulative percentage. The objective of this analysis is to identify the most representative product and analyze it in a perspective of LM philosophy. The application of LM for all production turns impossible its implementation. The Pareto analysis in this case is the beginning of the LM implementation. The Pareto analysis ranks the products. The choice must be based on the best-selling. This decision will take into account the company's strategy, for example, the product life cycle. The application of the LM to the product with more sales may have very positive results for the company, since it identifies and order the changes to make.

The selection of a product or family of products for implementing the Lean philosophy in intermittent environment not against the principle of LM based on continuous improvement. What has been examining throughout this work is the methodology to be followed to start the implementation of LM in intermittent production environment.

After the product analysis phase using the Pareto analysis is initiated the second phase.

4.2 Step 2—Current State Analysis

Identified the product, will be studying the value chain of this product. The aim is to quantify the activities without added value and waste.

The first step is to study the flow of materials in a visual way, to understand its complexity. The use of a spaghetti diagram is a possible method to visualize these movements (Fig. 2). The preparation of a spaghetti diagram is made in a simple and intuitive way: the flow and the direction of the raw material is represented superimposed on plant equipment implementation [26].

The spaghetti diagram alone is not sufficient to proceed with analyzing the actual added value. The spaghetti diagram represents only the materials flow throughout the process. The spaghetti chart or diagram is a visual way to trace the flow of a product, a patient, or a document through processes in a diagrammatic form [27]. A spaghetti flow is a simple way of showing what happens to this virtual "spaghetti" while the patient moves through each process, department, ward or building. It is called a spaghetti chart because the result typically looks like a dish of spaghetti [28].

To continue it is required to analyze other important data for the characterization and quantification of the actual value added using other tools. The lean tool for this purpose, is the value stream mapping (VSM) (Fig. 3). VSM has become a popular implementation method for lean manufacturing in recent years. It is considered one of the most important lean production techniques for mapping processes [13]. VSM helps identify wastes that exists in business processes being considered as an

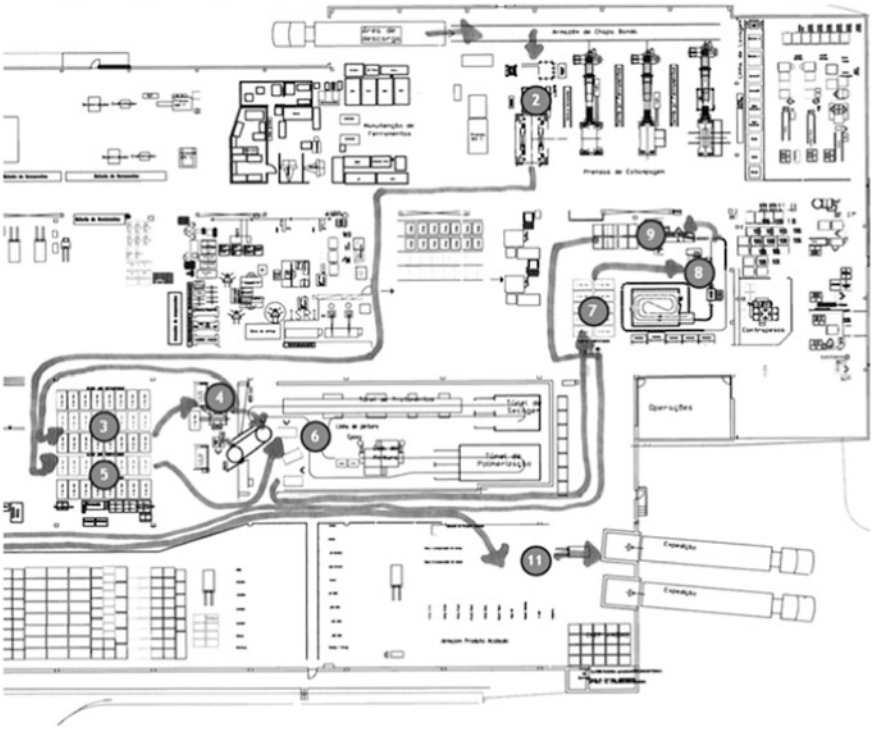

Fig. 2 Example of the spaghetti diagram

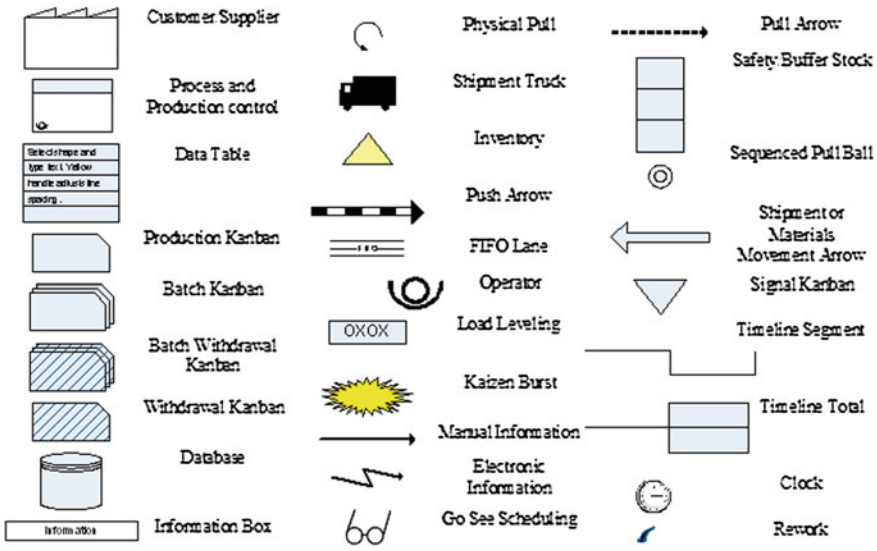

Fig. 3 Common VSM icons (adopted from [31])

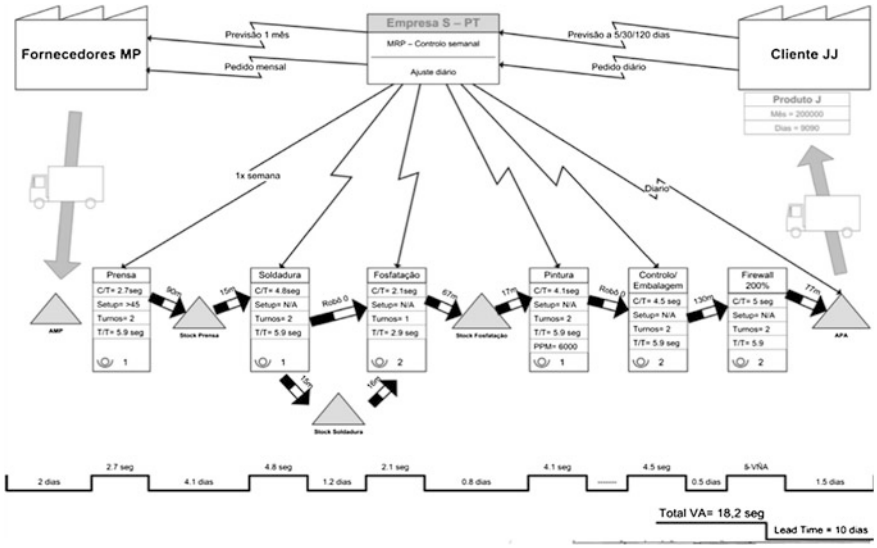

Fig. 4 Example of value stream map

activity [29] or behaviour [30] that adds cost but does not add value. The VSM is a process of direct observation of the information and material flows, by drawing them. VSM uses codified icons, such as process/activity box, in which important data concerning cycle time (C/T) and changeover time (C/O) are entered. Other important icons are triangles, which represent inventories, and arrows, which represent material transportations [27] (Fig. 3).

This tool helps the value chain visualization, highlighting the inefficiency of processes, and guiding to improve them. The VSM helps to visualize more than one process, it allows the visualization of the entire flow, allows also to relate the flow of information with the flow of materials associated [32].

The VSM is an essential part of the methodology presented by its characteristics at diagnosis, being an indispensable tool for the implementation of Lean [8] (Fig. 4).

This tool allows two views, the first, the current state, and the second of the future state, a situation for which you want to walk. At this stage, with the development of the current VSM, it is possible identify waste and its location. In step III will analyze the tools to use to eliminate waste found, aiming an optimized future state.

4.3 Step 3—Tools to Be Used

With the current VSM prepared and analyzed, it is necessary to find solutions to eliminate or reduce the different identified waste. As discussed throughout this

Table 2 Lean' tools according to the area of decision making

	5's	SMED	*Kanban*	*Heijunka*	TPM	SW	*Poka yoke*	Cellular work
Stocks		1	3	3				2
Movements	2					2		3
Transport	1							3
Quality defects			1		2	2	3	
Overprocessing						2	3	
Overproduction		1	3	3				
Setup time	2	3			1	2		

paper, the LM has many tools that can be useful. Rathi and Farris [19] have a matrix that relates the waste found in Job Order production system Lean tools. Table 2 aims to provide a support base the decision on the selection of the lean tools to be applied. This matrix cannot be seen in an inflexible way, because there are factors that vary from organization to organization. To designate the degree of relationship it is used a 3 point-likert scale as follows: 1 = some relationship; 2 = moderate relationship; 3 = high relationship.

4.4 Step 4—Future State

The future state aims to eliminate all sources of waste, linking all processes to the customer through a continuous and pulled flow. The aim is to produce only what is needed and when it is needed, eliminating all intermediate activities that not add value to the product to the customer's point of view.

For the preparation of the future state map has to take into account the tack time (TT), which processes can be integrated creating a continuous flow, which Pacemaker process used to pull production and set the pace, that supermarkets use, which processes need improvement [32]. In resume, the VSM future should show graphically how will the process be after the application of the tools described in the previous step.

4.5 Step 5—Apply Future State

The future status is the result of effective implementation of the previous steps. To the future state becomes real it's necessary put in practice the lean tools. This implementation must observe a detailed action plan. The fulfillment of this plan will depend on the success of the application.

5 Conclusion

The adoption of Lean philosophy as a management model for organizations requires a strong synergy of methodologies and tools with the culture in which the organization operates. It also has a strong commitment from management, clarifying business objectives of the application of lean. If there is no commitment of management potential gains from the implementation of this paradigm are lost or don't even truly be started. The focus of the work was directed to developing a tool with the purpose of optimizing the application of the LM in intermittent production environments.

The developed solution passed through the creation of a tool that gathers and organizes the tools already known within the LM as: VSM, spaghetti diagram and Pareto analysis. This collection of tools was made with the aim of defining what to do in each step of this process. The developed tool proposes a methodology, following a sequence of steps. These steps culminate in the implementation of the future state. This methodology aims to help implement the lean philosophy in intermittent environments.

This work opens the way to new research. It would be interesting to develop a tool for application in different industrial environments.

Acknowledgments The authors wish to thank University of Beira Interior and C-MAST—Center for Mechanical and Aerospace Science and Technologies, for giving us all support that was needed. The authors are also pleased to acknowledge financial support from Fundação para a Ciência e a Tecnologia and FEDER/COMPETE (grant UID/ECO/04007/2013).

References

1. Ferreira T, Baptista AA, Azevedo S, Charrua-Santos F (2015) Tool development for support lean manufacturing implementation in intermittent production environment. In: Lecture notes in engineering and computer science: proceedings of the World congress on engineering, WCE 2015, vol 2, London, UK, 1–3 July 2015, pp 972–977
2. Van Hoek R (2001) The rediscovery of postponement a literature review and directions for research. J Oper Manage 19:161–184
3. Barnes J, Morris M (2008) Staying alive in the global automotive industry: what can developing economies learn from South Africa about linking into global automotive value chains? Eur J Dev Res 20:31–55
4. Chase RB, Aquilano NJ, Jacobs FR (2006) Operations management for competitive advantage. McGraw-Hill/Irwin, New York
5. Reid RD, Sanders RN (2010) Operations management, 4 edn. Wiley, New York
6. Abduelmula A, MacIsaac R, ElMekkawy TY (2005) Lean manufacturing implementation to a robotic-press line. AG Simpson Automotive Systems, Toronto, pp 19–22
7. Russell RS, Taylor BW (2011) Operations management: creating value along the supply chain. Wiley, New York
8. Chen L, Meng B (2010) The application of value stream mapping based lean production system. Int J Bus Manage 5:203

9. Matt DT (2008) Template based production system design. J Manufact Technol Manage 19:783–797
10. Hobbs DP (2004) Lean manufacturing implementation: a complete execution manual for any size manufacturer. J. Ross Publishing, Boca Raton
11. Flott LW (2002) Industry in transition. Metal finishing 77–82
12. Srinivasaraghavan J, Allada V (2006) Application of mahalanobis distance as a lean assessment metric. Int J Adv Manuf Technol 29:1159–1168
13. Womack JP, Jones DT, Ross D (1991) The machine that changed the World: the story of lean production. Harper Collins, New York
14. Rother M, Shook J (1998) Learning to see. The Lean Enterprise Institute, Brookline
15. Pattanaik LN, Sharma BP (2009) Implementing lean manufacturing with cellular layout: a case study. Int J Adv Manuf Technol 42(7/8):772–779
16. Anand G, Kodali R (2009) Selection of lean manufacturing systems using the analytic network process—a case study. J Manuf Technol Manage 20(2):258–289
17. Chen JC, Li Y, Shady BD (2010) From value stream mapping toward a lean/sigma continuous improvement process: an industrial case study. Int J Prod Res 48:1069–1086
18. Abdulmalek FA, Rajgopal J, Needy K (2006) A classification scheme for the process industry to guide the implementation of lean. Eng Manage J 18:15
19. Rathi N, Farris J (2009) A framework for the implementation of lean techniques in process industries. Texas Tech University, Lubbock
20. Anand G, Kodali R (2010) Development of a framework for implementation of lean manufacturing systems. Int J Manage Pract 4:95–116
21. Kasul RA, Motwani JG (1997) Successful implementation of TPS in a manufacturing setting: a case study. Ind Manage Data Syst 274–279
22. Achanga P, Shehab E, Roy R, Nelder G (2006) Critical success factors for lean implementation within SMEs. J Manuf Technol Manage 17:460–471
23. James T (2006) Wholeness as well leanness. IET Manuf Eng 14–17
24. Ishikawa K, Lu DJ (1985) What is total quality control? the Japanese way, Prentice-Hall, Englewood cliffs
25. Courtois A, Martin-Bonnefous C, Pillet M (2006) Gestão da produção, 6 edn. LIDEL, Lisbon
26. Bicheno J (2004) The new lean toolbox: towards fast, flexible flow. PICSIE Books, Johannesburg, p 212
27. Chiarini A (2013) Waste savings in patient transportation inside large hospitals using lean thinking tools and logistics solutions. Leadersh Health Serv 26(4):356–367
28. Labach EJ (2010) Using standard work tools for process improvement. J Bus Case Stud 6:39–47
29. Ohno T (1988) Toyota production system. Productivity Press, Portland
30. Emiliani ML (1998) Lean behaviors. Manage Decis 36(9):615–31
31. Manos A, Sattler M, Alukal G (2006) Make healthcare lean. Qual Progr 24–30
32. Rother M, Shook J (2003) Learning to see: value stream mapping to create value and eliminate mud. Productivity Press, Portland

Using Owas in Automotive Subsidiary Sector: A Case Study

Hatice Esen, Tuğçen Hatipoğlu and Nilgün Fiğlali

Abstract Musculoskeletal Disorders (MSDs) that lead to important health problems and the depletion of social resources are the most common drawbacks affecting the working population. MSDs that are at the top of the list showing the expenditures for all disorders, and affecting the job efficiency, life quality and physical and social functions of a worker in a negative way, is generally due to the poor working postures. There are several methods to identify the poor working postures that cause Musculoskeletal Disorders (MSDs) and financial burdens to the economies along with serious health problems for workers. OWAS (Ovako Working Posture Analysing System), one of these methods, depends on the observational analysis of work movements especially in physically demanding works. In this study, the working postures in tire raw materials production process are analyzed with OWAS method and some suggestions are made about the possible improvements to eliminate the poor working postures.

Keywords Automotive subsidiary industry · Engineering applications · Ergonomics · Musculoskeletal disorders · Working posture analysis · OWAS

H. Esen (✉) · T. Hatipoğlu
Faculty of Engineering, Industrial Engineering Department Umuttepe Campus,
Kocaeli University, 41380 Kocaeli, Turkey
e-mail: hatice.eris@kocaeli.edu.tr

T. Hatipoğlu
e-mail: tugcen.hatipoglu@kocaeli.edu.tr

N. Fiğlali
Faculty of Management, Industrial Engineering Department Umuttepe Campus,
Kocaeli University, 41380 Kocaeli, Turkey
e-mail: figlalin@kocaeli.edu.tr

S.-I. Ao et al. (eds.), *Transactions on Engineering Technologies*,
DOI 10.1007/978-981-10-1088-0_19

1 Introduction

Due to the rapid increase of frequency and cost of work-based MSDs in developed countries, studies of risk factors, loss of working days, and its cost have come to the forefront in recent years. Great difficulties are experienced in diagnosing whether MSDs are work-based while the prevalence of heavy and unergonomic working conditions, trauma, and overload are known in developing countries [1].

Musculoskeletal Disorders (MSDs), as defined by ICOH (International Commission on Occupational Health), are illnesses or disorders in musculoskeletal system due to the work conditions [2]. MSDs cause serious health problems in workers and also bring financial burdens to countries' economies. 30 % of MSDs identified in the world are due to the work conditions. MSDs represent 34 % of work losses resulting from occupational illnesses, and work accidents [3]. In Germany, the lost days due to MSDs represent 30 % of all lost days due to illnesses whereas this rate is 46 % in Holland. In England, each year 10 million work days are lost due to MSDs and among these, 50 % is due to back pains, 30 % due to neck and arm pains and 20 % is due to leg problems [4].

Musculoskeletal Disorders (MSDs) that lead to important health problems and the depletion of social resources are the most common drawbacks affecting the working population. MSDs that are at the top of the list showing the expenditures for all disorders, and affecting the job efficiency, life quality and physical and social functions of a worker in a negative way, is generally due to the poor working postures.

There are also numerous methods in the literature to be able to detect inappropriate working postures that lead to MSDs and their risk levels, and to shed light on improvement and development plans to be made on these problems. These methods can be categorized into three classes: Load lifting-related methods (Snook's Table, Revised NIOSH Lifting Equation, Putting Down, Pushing, Pulling and the Carrying model and so forth), observation or survey-based methods (OWAS—Ovako Working Posture Analyzing System, RULA—Rapid Upper Limb Assessment, REBA—Rapid Entire Body Assessment, Job Strain Index, Quick Exposure Check and etc.) and ergonomic checklists (ACGIH-Hand/arm Vibration Threshold Limit Value, Risk Factor Checklist and etc.) [5].

In this study, OWAS methodology is used which has many applications in the literature and is used to analyze the problems in musculoskeletal systems at standing and dynamic working postures on physically demanding works. By using this method, working postures in tire raw materials production are analyzed. At the end of the study, some suggestions are made to improve the poor working postures.

In the second part of the study, the methodology, OWAS, is explained. The details of application are presented in the third section. Finally the conclusion is drawn in Sect. 4.

2 Ovako Working Posture Analysing System

OWAS is a working postures analysis method based on observation to identify the poor working postures which causes musculoskeletal disorders. OWAS method, designed to help the work analysts, is a work sampling method based on the analysis of working postures examples collected in certain time periods [5]. The method which was first used in steel industry is now in use in many sectors [6]. Although, the first applications of the method were made by using special printed forms and hand calculations, half-computerized systems are developed for its applications now [7]. Nowadays, during the recording step of the working postures, video-camera can be used and images can be analyzed in different time intervals in different works [8].

In the analysis, the working postures of workers are standardized as 'OWAS working postures'. Back, arm and leg postures and load weight classified by using OWAS method are shown below [1]:

Back
1 = straight
2 = bent forward, backward
3 = twisted or bent sideways
4 = bent and twisted or bent forward and sideways.

Arms
1 = both arms are below shoulder level
2 = one arm is at or above shoulder level
3 = both arms are at or above shoulder level.

Legs
1 = sitting
2 = standing with both legs straight
3 = standing with the weight on one straight leg
4 = standing or squatting with both knees bent
5 = standing or squatting with one knee bent
6 = kneeling on one or both knees
7 = walking or moving.

Load
1 = weight is 10 kg or less
2 = weight exceeds 10 kg but is less than 20 kg
3 = weight exceeds 20 kg.

OWAS method helps to identify the poor postures and actions, to determine how much the repeating system forces a worker and to find the optimum work methods. Besides, it allows to evaluate the work place in terms of efficiency, comfort and occupational health and to examine the human machine segment systematically. The postures are classified according to the method and systematic improvements are

suggested through the design of work place to eliminate the uncomfortable factors for workers [5].

OWAS method, applied successfully in different industrial areas, is used for [8];

- Evaluation of postural weight ergonomically and decrease the loading in musculoskeletal system,
- Improvement and planning of working environment, methods, machines and equipment,
- Occupational health investigations,
- Ensuring the security and efficiency.

In this method, the analyst makes a qualitative analysis of worker movements during working processes by evaluating the working postures of back, arms, legs and the loaded weight. The body postures of workers are classified according to the power consumption during the work. Because OWAS method is conducted by direct observations, it can be time consuming sometimes [9].

We get 252 standard postures and weight combinations considering 4 back, 3 arm, 7 leg and 3 different weight levels by using OWAS method. During the analysis step of the method, the time spent for each work and the frequency of postures are evaluated [7]. During the application of that method, the postures are stored according to the 4 digit coding (arm, back, leg, load) system. A large cod number represents an undesired working posture [10].

The observed posture combinations are classified according to the 4 risk categories. This classification depends on the health risks of each working postures and posture combinations on the musculoskeletal system predicted by professionals. The risk categories that determine the priority of risky postures are mentioned below and details may be also found in Ref. [11].

Category 1: working postures don't have any harmful effect on musculoskeletal system. There is no need of ergonomic regulations for these postures.
Category 2: There are some harmful effects of working postures on the musculoskeletal system. Necessary ergonomic regulations should be planned in the future.
Category 3: Working postures have some harmful effects on the musculoskeletal system. Necessary ergonomic regulations should be planned as soon as possible.
Category 4: Working postures have very harmful effects on the musculoskeletal system. Necessary ergonomic regulations should be implemented urgently [8].

One of the several methods aiming to analyze the working postures in the literature, OWAS, is a successful methodology that considers the postures at all parts of a body. In the literature, there are many successful examples of OWAS application in very different sectors. These applications range from construction sector to automotive sector, from maintenance works to household works, from health services to livestock sector. OWAS method is applied to a tire production factory working for automotive subsidiary industry.

3 An Application of Working Posture Analysing

Due to the nature of the works in tire production factories, poor working postures and overloading to body are encountered quite often. This study is conducted in a tire production factory working for automotive subsidiary industry in Kocaeli. All physical works in the considered department are done in standing posture. Many workers on the department take breaks and medical reports due to musculoskeletal disorders. To identify and improve the working postures that cause these problems, the working postures of tire raw materials preparation job are analyzed with OWAS.

Tire raw materials preperation job has production prescriptions for each different type of tire. Worker gets the materials written in the prescription from the corresponding stands, carries them to the mixing boiler, and unload them after weighting. The related data is also entered by worker into the computer at control pane. After that, worker makes the loading of the prepared boiler into the machine. The boiler that contains mixed raw material is carried manually from the machine to the related storage areas by worker. Worker also does the cleaning of mixture preparing machine manually if it is necessary.

A worker is recorded for 45 min to be able to make OWAS analysis. 45 min include 8 job cycles which is found to be enough to represent the whole job. The postures recorded with video are stopped for each second and the working posture at that time is coded according to OWAS method. The observation period is taken

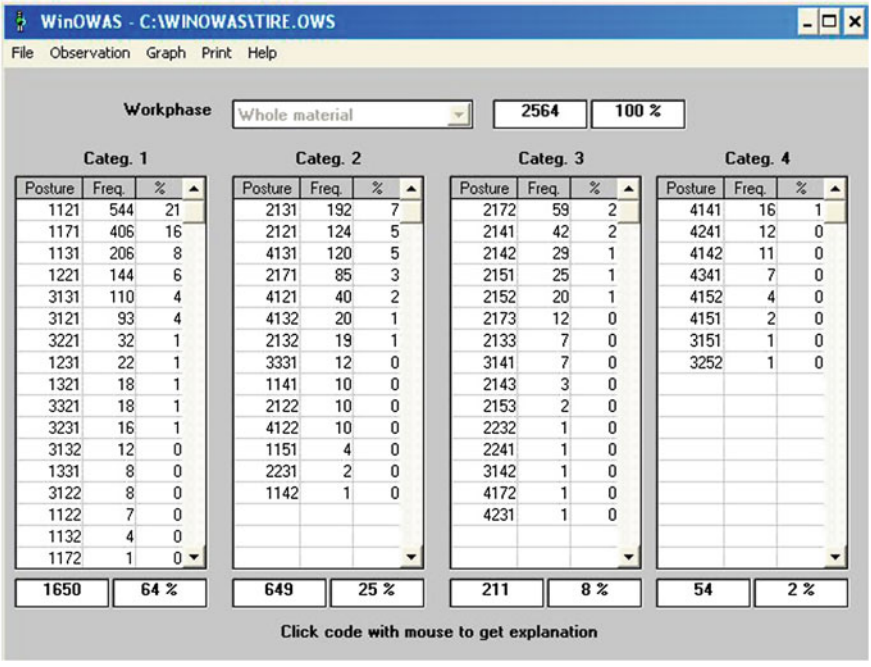

Fig. 1 OWAS results in tire raw materials preparation job

as 1 s to increase the observational sensitivity. WinOwas package software is used during the analysis of the postures. 2564 working postures are collected and the risk categories of these postures are shown in Fig. 1.

The distribution of working postures in risk categories and the frequency of each posture within the whole work can be found with WinOwas software. As it can be seen from Fig. 1, 10 % of working postures fall in 3. and 4. risk categories. The postures in 3 and 4 categories urgently need modifications from an ergonomic perspective. When we consider whole working postures, 10 % of them create a danger for musculoskeletal system.

When we analyze the working postures in 3. and 4. categories, we see that they generally occur in processes of carrying full boiler, cleaning the machine and taking the packages from the stands. These working postures can be eliminated by making some changes in the working process and work place.

Even though the boiler has wheels under it, worker has to work in poor postures due to the load in the boiler. If the carriage of filled boiler is done with another carrier like a forklift, then these poor postures can be eliminated. Worker does the cleaning of mixer machine manually with a brush. During that process, s/he has to work by bent and twisted postures. That is why these postures fall under 4th risk category. If the cleaning is done with mechanical cleaning system instead of a brush, then these working postures can be eliminated. The other postures in 3rd and 4th categories occur during taking of the materials in the prescription from the corresponding stands. During taking materials from the ground shelf of a two shelves stand, workers bend and twist. Raising up these stands by considering the average waist height of workers would resolve these poor postures. Also designing a new stand system with multiple shelves that will prevent the overlapping of materials would be convenient.

In the improvement of working postures, the trainings of workers are important. Workers should be informed about the importance of moving in line with work flow. This is because workers generally work with some steps that are not actually in work flow due to the habituation and the purpose of making it easier for themselves. Additionally, giving necessary trainings to workers about the right usage of their bodies and equipment will make the ergonomic improvements less required.

The suggestions made to the company managers according to the results of the analysis are evaluated as implementable suggestions and required improvements studies are started. After the suggestions are implemented, a further study for the same worker and job can prove how the suggestions improved the situation.

4 Conclusion

Investigating working postures with scientific methods, analyzing and performing necessary improvements and adjustments provide important contributions to the subjects of effectively controlling job performance and decreasing MSDs. Among the methods such as OWAS, RULA, Rapid Exposure Assessment and etc. that are situated in the literature and aim at analyzing working postures, OWAS is a method

with high success that can be applied to very diverse areas and assesses postures in every body part. But, albeit the success of OWAS method in revealing risky situations by analyzing working postures in many different areas in the literature, its need for an expert analyst during analysis and its coding being time-consuming and demanding prevent its frequent use in practice.

Identification of overloading into the workers due to working postures has an important role in building of a health and successful work life. Repetitions of inappropriate and poor body postures and movements result in musculoskeletal disorders and financial losses both for government and employer. The working postures in industry can be best evaluated by doing observations. In this study, working postures of tire raw materials preparation job are analyzed by using OWAS method, an analysis system for working postures that allows for identification of poor working postures and overloading in musculoskeletal system of workers. At the end of the analysis, some suggestions are made to eliminate the working postures that are identified as poor. In addition to the implementation of these suggestions, with a more comprehensive anthropometric study, work place design and/or ergonomic equipment design can also be made.

References

1. Fığlalı N, Cihan A, Esen H, Fığlalı A, Çesmeci D, Güllü MK, Yılmaz MK (2015) Image processing-aided working posture analysis: I-OWAS. Comput Ind Eng 85:384–394
2. Cohen AL, Gjessing CC, Fine LJ, Bernard BP, McGlothin JD (1997) Elements of ergonomics: a primer based on workplace evaluations of musculoskeletal disorders. OH: DHHS (NIOSH) Publication, pp 97–117
3. Leigh J, Macaskill P, Kuosma E, Mandryk J (1999) Global burden of disease and injury due to occupational factors. Epidemiology 10(5):626–630
4. OSHA (2007, Aug) Introductıon to muscoskeletal disorders about work. Available: http://osha.europa.eu/fop/turkey/tr/publications/oshayayin/cv_fs_71.pdf
5. Eriş H, Can GF, Fığlalı N (2009) Working postures and musculoskeletal disorders. J Ind Manag Eng-Chamb Mech Eng 129:8–14
6. Akay D, Dağdeviren M, Kurt M (2003) Ergonomic analysis of working postures. J Fac Eng Arch Gazi Univ 18(3):73–84
7. Loupajarvi T (1990) Ergonomic analysis of workplace and postural load. In: Bullock MI (ed) Ergonomics. Longman Publishers, UK, pp 51–78
8. Pinzke S, Kopp L (2001) Marker-less systems for tracking working postures–results from two experiments. App Ergon 32:461–471
9. Mattila M, Karwowski W, Vilkki M (1993) Analysis of working postures in hammering tasks on building construction sites using the computerized OWAS method. Appl Ergon 24(6):405–412
10. Jin K, Lei L, Sorock G, Courtney TK, Ge L, Liang Y (2002) Postural assessment with revised OWAS system. In: the third international cyberspace conference on ergonomics
11. Hoy J, Mubarak N, Nelson S, de Sweerts Landas M, Magnusson M, Okunribido O, Pope M (2005) Whole body vibration and posture as risk factors for low back pain among forklift truck drivers. J Sound Vib 284(3–5):933–946
12. Esen H, Hatipoğlu T, Fığlalı N (2015) Analysis of working postures in tire production sector by OWAS method. In: Proceedings of the world congress on engineering, WCE 2015, 1–3 July, 2015, London. Lecture notes in engineering and computer science, pp 726–730

Manufacturing Flexibility as a Strategy to Deal with Uncertainty

Özlen Erkal Sönmez and Tufan Vehbi Koç

Abstract In uncertain environments, increased flexibility is necessary to facilitate the development of fast adaptation capability that lead to an effective environmental response. Manufacturing companies generally have some problems about coping with the uncertainty in their industries and they tend to increase the flexibility level of their manufacturing system. Measurement of flexibility is required for this purpose. This paper intends to develop an entropy based model to measure flexibility. The model proposed includes manufacturing characteristics such as type of machinery, number and type of operations, routing for each product as well as time spend for operations, machine set up activities and material handling. An application of the model is performed in a job shop. Flexibility level is measured and the association between the total entropy value and flexibility level is discussed.

Keywords Entropy · Flexibility level · Flexibility measurement · Job shop · Manufacturing flexibility · Manufacturing activities

1 Introduction

Competitiveness is the ability to get customers to choose products or services over competing alternatives on a sustainable basis [1]. While companies in a variety of industries strive to be competitive they started to face a more dynamic and demanding environment that is represented by unexpected changes in market requirement, unpredictability of economic conditions etc. that altogether contribute

Ö. Erkal Sönmez (✉)
Faculty of Engineering, Department of Industrial Engineering, Istanbul University, Avcılar Campus, 34320 Avcılar-Istanbul, Turkey
e-mail: ozlenerkal@istanbul.edu.tr

T.V. Koç
Faculty of Management, Department of Industrial Engineering, Istanbul Technical University, Maçka Campus, 4367 Maçka-Istanbul, Turkey
e-mail: koctu@itu.edu.tr

S.-I. Ao et al. (eds.), *Transactions on Engineering Technologies*,
DOI 10.1007/978-981-10-1088-0_20

to uncertainty. Therefore to be competitive, companies should develop capabilities that enable them to adapt to fast and unexpectedly changing conditions. In parallel with this, Ref. [2] claims that static environments are giving way to continuously changing, dynamic environments and firms' capabilities to anticipate and assess environmental demands in order to cope with these pressures and mobilize for change are becoming crucial. On the other hand under high uncertainty, accurately predicting environmental needs may not be possible. In an uncertain environment firms may not take correct decisions and take effective actions against competitors since they can not respond properly to change in the conditions of industry.

To be competitive in the targeted market, companies form competitive strategy that has traditionally been based on the four basic competitive priorities of cost, quality, delivery and flexibility [3]. Considerable evidence indicates that when faced with an uncertain environment, firms invest in manufacturing flexibility (e.g. [4, 5]). Reference [6] states that flexibility is a strategic imperative that enables firms to cope with uncertainties. Reference [7] claims that market changes reflect unpredictable customer needs for an increasing variety of products, whereas technological changes reflect continual advances that occur with the introduction of new products. In such industries, firms that possess the manufacturing flexibility to introduce modified or new products at minimal cost and lead time will gain a competitive advantage over others. In literature there is a large body of research that examines manufacturing flexibility but they are mostly empirical studies investigating the relationships among environmental uncertainty, manufacturing flexibility and performance rather than the measurement of flexibility. The studies that focus on the measurement of flexibility are scarce in literature. Since manufacturing flexibility is a complex and multidimensional subject, it encourages researchers to limit their studies with few dimensions of flexibility. This paper intent to contribute to this perspective of the field and aims to propose a model that is designed to measure the overall manufacturing flexibility.

2 Manufacturing Flexibility

Manufacturing flexibility involves multiple factors. That's because most of the concepts concerning flexibility are merely related to particular situations.

In literature, a variety of flexibility types are studied. For instance; adaptation, assembly system, application, dispatch, job, material, state, design, demand and machining system flexibilities are mentioned in [8]. Reference [7] refers to changeover, rerouting and sequence flexibilities. Reference [9] notices operation and expansion flexibilities. Process, program, product and production flexibilities are studied by [10]. Reference [11] distinctly addresses new product, labor and modification flexibilities. When the classification and relevant definitions of flexibility are examined, it can be seen that studies in literature usually consider a limited number of components of overall flexibility of a manufacturing system.

Some authors divide flexibility into its sub-elements. In Zhang's model proposed in [6] the "*Flexible manufacturing competences*" are determined as machine flexibility, labor flexibility, material handling flexibility and routing flexibility. These elements altogether result in "*Flexible manufacturing capabilities*" which are volume flexibility and mix flexibility that play an important role for customer satisfaction to be provided. In parallel with this definition, Ref. [12] claims that focusing on volume and mix flexibility as the main capabilities of flexible manufacturing is not intended to ignore the other components of manufacturing.

2.1 Flexible Manufacturing Competences

2.1.1 Machine Flexibility

Machine flexibility enables the machine process for different operations to keep a low machine idle time [13]. It defines the ability of a machine to be set up quickly and to handle product variety [12]. Among various types of manufacturing flexibility that have been addressed in literature, machine flexibility is regarded as one the most important and fundamental flexibility types that other types of flexibility generally depend on [14].

Machining time, inefficient idle time, setup time, and repair time determine the general machine status. Among these, the machining activity is the only activity that adds value to the parts produced and other activities are in fact no needed for manufacturing [15].

2.1.2 Labor Flexibility

It shows the ability of a worker to handle various types of jobs and the easy adaptation for the transitions among several tasks. The level of flexibility may be affected by the physical conditions of workers as well as the degree of their capabilities, experiences and personal tendencies.

2.1.3 Material Handling Flexibility

Material handling flexibility is the ability of the material handling system to transport and locate workpieces of different types and sizes. The larger material handling flexibility is, the better the machines can be supplied with workpieces. Thus, flexibility of the machines is not hindered by the limitations of material handling system. Technical design and the layout of transportation paths can influence material handling flexibility [9].

2.1.4 Routing Flexibility

Routing flexibility enhances a system easier scheduling of parts by better balancing the machine loads and allows the system to produce a given set of part types or part families without interruption [16]. It applies when a workpiece with a given process plan can follow different routes through the system. Several identical machines can be alternatively used for performing an operation [9]. The flexibility of system routing reduces the possibility of bringing a production line to a halt when unexpected events occur [16]. A system with alternative production routes can maintain a high production performance when one of the machines is broken down or under maintenance.

In job shop environment which is characterised by large variety of components and functionally grouped general-purpose machines; the routing flexibility would especially be more important. The parts are routed around in small lots to various machines and the products are diverse so as to provide customer satisfaction.

2.2 Flexible Manufacturing Capabilities

2.2.1 Volume Flexibility

Volume flexibility is defined as the ability of a production system to adjust amount of output for demand fluctuations [12]. It is also described as the ability of the system to work economically at different output levels.

Changing production volume for some products requires to use production equipment for different additional tasks and have the ability to change output rates of machines and work cells [10]. Therefore, volume flexibility can be defined as a property of the system as a whole [9].

2.2.2 Mix Flexibility

The uncertainty as to which products will be accepted by customers creates a need for the mix flexibility. It includes changeover and modification flexibilities together. Changeover flexibility deals with the uncertainty as to the length of product life cycles and modification flexibility is directly about the uncertainty as to which particular attributes customers would desire [7].

3 Entropy as a Measure of Flexibility

Methods used for measuring manufacturing flexibility diverse according to the conceptual approach adopted. Flexibility classification directly affects the input parameters of the method. Some metrics in literature are based on easily definable consequences of any altering factor. For instance, reduction in production volume due to disturbances such as machine breakdowns or demand fluctuations may lead to some economic losses which can be used for measuring flexibility. Besides such economic consequences; various performance criteria may also be used for the evaluation [17]. Measures such as the number of units produced per downtime hour may be used for machine flexibility. A plant-wide ratio of set-up times to cycle times can be used for operation flexibility. The number of design changes per year in a model to be assembled is proposed as versatility index (V_p) of an assembly process while versatility index of an assembly system (V_s) is defined as the number of times per year that the system to be reconfigured to assemble a new model. Assembly system selection would occur by matching (V_p) and (V_s) [18].

Measurements for manufacturing flexibility may be made partially or in a holistic view, as well. However, partial measures are more common in literature.

An obvious first partial measure is the range over which the system remains profitable. Volume flexibility may be measured how small the volumes can be for all part types with the system still being run profitably. Break-even point for production of single product is defined as the quantity for which the Average Total Cost is equal to Marginal Revenue; that is when the profit is zero. Volume flexibility (VF) can be calculated as in Eq. (1); while V_R is profitability range, C_{max} is the maximum capacity of the system, a is the number of capacity units required per part produced, N_B is the lower limit of profitable production.

$$VF = \frac{V_R}{C_{max}} = \frac{C_{max} - aN_B}{C_{max}} \tag{1}$$

This measure has a theoretical range from 0 to 1; where zero means there is absolutely no scope for demand fluctuation and 1 means that there is scope for demand changes across the entire capacity range. This definition is useful for one type of product scenarios only. To extrapolate, break-even analysis must be substituted for many products [19].

Routing flexibility is evaluated in Ref. [20] for a flexible manufacturing system (FMS) with dynamic arrival of part types. A simulation model is developed for the quantification. Routing flexibility (RF) is calculated via Eq. (2) while routing efficiency (E), routing versatility (R) and routing variety (D) in the equation below. k shows number of the part types.

$$RF = \frac{1}{k}\sum_{j=1}^{k} E_j R_j D_j \tag{2}$$

An another partial measurement example may be given for the expansion flexibility. Value of flexibility in decision analysis may be measured by the difference between the Expected Monetary Values (EMVs). It is assumed this information is gained by delaying a decision. The difference between EMF for flexible and conventional options results in expansion flexibility measure as below. In Eq. (3) EF shows expansion flexibility while EMV_F is Flexible Expected Monetary Values and EMV_C is Conventional Flexible Expected Monetary Values [19].

$$EF = EMV_F - EMV_C \tag{3}$$

Decision and information theories are useful for measuring flexibility [17]. Discounted cash flow (DCF) techniques can be used for quantifying manufacturing flexibility [18]. Fuzzy based decision methods also exist in literature. Reference [21] measures the overall flexibility as a combined effect of nine types of partial flexibilities. IF and THEN rules are used to model the functional dependencies between chosen operational characteristics. Similarly, Ref. [22] performs a fuzzy flexibility quantification approach stating the absence of an effective crisp method for the synthesis of functional parameters affecting each type of flexibility. Fuzzy present worth analysis is performed in economic aspect.

Reference [18] develops a probabilistic approach to measure flexibility. Product, operation and capacity flexibilities are all together shown in a metric called POC. POC is calculated by the Eq. (4); while D is the number of potential changes, X_i is the ith potential change, $Pn(X_i)$ is te penalty for X_i and $Pr(X_i)$ is the probability for X_i.

$$POC = \sum_{i=1}^{D} Pn(X_i)Pr(X_i) \tag{4}$$

The lower POC means higher level of flexibility. In that approach, the system is considered to be inflexible when a high penalty is faced with to adapt the changes.

Petri-nets may be also used for the measurement of flexibility. Simulation of Petri-nets can provide estimates of the times required for a system to adapt to various random disturbances which may be used for the flexibility measurement. A more mathematical way in information theory is based on the premise that flexibility should be a function of the number of available options and relative freedom with which these options can be selected [18]. References [10, 23, 24] focus on entropic measurement of manufacturing flexibility in this context.

Entropy is a thermodynamic property which is a measure of energy that is not available for work in thermodynamic processes. It is defined by the second law of thermodynamics and expresses the disorder, randomness or complexity in the system. The close relationship between uncertainty and flexibility suggests the use of entropy to measure flexibility. Entropy simply measures the degree to which energy is mixed up inside a system that is spread or shared among the components [25].

The static complexity of the manufacturing system may be assessed through the Shannon entropy [26]. Entropy is a logarithmic measure of number of states. The general equation for Shannon entropy is given in Eq. (5). Relevant parameters of the equation are as follows.

S Total entropy value
k_B Boltzzman's constant
P_i Relative share of ith outcome in an experiment (Probability of being at ith state)
n Number of possible outcomes in an experiment (Number of possible states)

$$S = -k_B \sum_{i}^{n} P_i \ln P_i \tag{5}$$

Through the mathematical inference, S attains the maximum value in the equiprobable case, when $p_i = 1/N$ for all i values.

Conversely, S vanishes in the case that some $p_j = 1$ (and thus, $p_j = 0$ if $i \neq j$) [27].

S is a function of n choices and of the freedom of these choices represented by fractions. The maximum value of S should monotonically increase with number of possible options (n). When equal freedom is observed for every event, there would be a more flexible manufacturing environment because of the existence of more possible choices [23].

4 Application

In this research, assessment of overall manufacturing flexibility is performed for a job-shop. In order to reach a single numeric value to represent the overall flexibility level, input parameters of the study are selected from manufacturing competences. According to Zhang's model (2003), the competences may be listed as machine, labor, material handling and routing flexibilities.

Because of the fact that the concept 'time' is an integrating indicator for the characteristically different types of flexibility elements; the attributes corresponding to the machine, labor, material handling and routing are included to the model in a time-based view. Manufacturing flexibility is calculated according to the type and operational sequence of machinery, number and type of operations and routing for each product as well as time spend for operations, machine set up activities and material handling.

The job shop examined has the capability of producing 10 different products via 10 machines located in a certain layout plan. The machines in the job shop are encoded as T035, T043, F30, F31, F32, M6, PL6, BS2, BA1 and PAH. In the job

Table 1 Transportation time matrix

	T035	T043	PL6	M6	BA1	BS2	PAH	F30	F31	F32
T035										
T043	10									
PL6	60	60								
M6	40	40	20							
BA1	100	100	40	60						
BS2	80	80	20	40	20					
PAH	120	120	60	80	20	20				
F30	20	20	40	20	80	60	100			
F31	20	20	40	20	80	60	100	10		
F32	20	20	40	20	80	60	100	10	10	

shop; there are two turning machines (T035 and T043), one planer (PL6), one drilling machine (M6), one vertical slotting machine (BA1), one broaching machine (BS2), two hobbing machines (F31 and F30), one deburring machine (PAH) and one milling machine (F32).

Any product to be processed is transported to the any required *first* machine (according to its operational sequence) in 60 s. According to the layout plan, transportation of products between the machines is performed as shown in the time table in Table 1. The values for the transportation time between two machines are given in seconds, which have to be converted into minutes in the calculation phase. Matrix given below is symmetrical across the diagonal.

In the job shop, some products are produced through several operation steps whereas some are completed in only one operation [28]. The operational data including operational sequences for each product type are given in Table 2. Application details may be also found in Ref. [29].

Each worker has different working speed from one another. However, the speed value assumed to remain same for each operator. The time losses are determined under another assumption of longer lasting operational activity on its specific machine, necessitates a higher level of qualified worker.

In order to capture the dynamic aspect of machine and routing flexibilities, elements such as the probability of assigning an operation to a machine and the probability of assigning and transferring an operation from one machine to another can be considered [6]. In this study, relative shares are used to determine the contribution of each operation to the total entropy value. With this aim, the operations are considered separately and products are transferred as production planning requires.

To observe the overall operating pattern in sequence for each machine, a sample manufacturing plan is firstly prepared to have a general point of view. In this plan, according to product type (x) and related operational sequence (m), the operation

Table 2 Operational data

Product type	Operational sequence	Machinery sequence	Operation time (in min)	Machine setup time (in min)
P1	1	TO35	180	45
	2	TO43	60	25
	3	PL6	60	5
	4	M6	130	5
	5	BA1	120	25
P2	1	TO43	166	23
	2	TO35	158	43
	3	PL6	60	15
	4	M6	90	3
	5	BA1	64	23
P3	1	BA1	37	37
P4	1	BA1	37	37
P5	1	BA1	26	37
P6	1	BA1	37	37
P7	1	BS2	12	23
	2	F31	40	43
	3	PAH	10	5
	4	F32	32	43
P8	1	F30	20	25
P9	1	F30	32	25
P10	1	F31	100	43
	2	F32	60	43
	3	PL6	64	5

process sequences are named as (xm)—with a two digit indicator. (e.g. The indicator 73 shows the 3rd phase of product 7). It is accepted that, the process goes through continually until the last operation is accomplished and there is no interruption in producing the products requiring multi-processes as long as the machines are available for the next operation. Each machine is used immediately after the last process is finished. The sequence priorities are also considered within the operation phases of a product but there is no priority between producing different products. The uncertainty is about which set of products to be produced or which products to be desired by the customers. Therefore an uncertainty also exists about which products to produce and how much time that it is allocated in total time.

For the analysis, data is grouped in machine based approach at onset. Time values corresponding to process, machine set up time and downtime originated from labor and transportation are separately analysed according to the product type that each machine performs. Table 3 shows the product types and relevant machines.

Table 3 Product types and relevant machines

Machines	Products
T035	P1-P2
T043	P1-P2
PL6	P1-P2-P10
M6	P1-P2
BA1	P1-P2-P3-P4-P5-P6
BS2	P7
PAH	P7
F30	P8-P9
F31	P7-P10
F32	P7-P10

Each product is treated for different period of times in different operational sequences and on different machines in order to gain its last form. The time passed to produce one type of product through different phases on different machines can be seen in Table 3. The period of time defined as the manufacturing time of the job shop is the sum of the all periods of time that are allocated for given products.

From the system view, overall flexibility is the sum of the flexibilities of the system's functions [7]. Therefore, the total entropy value can be calculated as the sum of the portions of the entropy belongs to each machine in the system.

The input parameters of the model proposed are as follows:

t_o Machine operation time
t_s Machine set up time
t_t Transportation time between subsequent machines
t_l Downtime originated from labor
n Indicator for machine type
m Indicator for operation sequence in the production steps on machine n
t_{total} Total time for production of all products in job shop
S Entropy value
k Constant for entropy calculation
p Relative share

$$t_{total} = \sum_{n=1}^{10} \sum_{m=1}^{10} (t_{o_{nm}} + t_{s_{nm}} + t_{t_{nm}} + t_{l_{nm}}) \tag{6}$$

The relative share p is calculated via Eq. (7) by a proportion of total time spend for all manufacturing activities on a machine to the total time spend for all machines.

For each machine subject to $n = [1, 10]$;

$$p_n = \frac{(to_n + ts_n + tt_n + tl_n)}{T_{total}} \tag{7}$$

Then the entropy value on a specific machine can be calculated by means of Shannon formula as in Eq. (8).

$$S_n = -(p_n \ln p_n) \tag{8}$$

The total entropy which is also an indicator for the flexibility degree of the manufacturing unit can be calculated as in Eq. (9).

$$S_{total} = -\sum p_n \ln p_n \tag{9}$$

The graphical distribution of relative shares and related entropy values of each machine may be observed in Fig. 1. It can be seen that both parameters show similar characteristics at different numeric value levels. Higher values for each machine represent the entropic variation while lower values indicate relative shares.

The entropy shares calculated through Shannon formula for job shop and the results on processing time, set-up time, transportation time and downtime caused by operators are grouped based on relevant machines and the results are calculated accordingly. The total entropy value of the operations on the manufacturing unit is calculated as 2.05615. This is not a standard value in a universal scale; therefore it should not be compared with other manufacturing systems. It is a suitable indicator for comparing the pre or post results of the same manufacturing unit. Based on this indicator, different factors such as new machines, labour, factory layout etc. that would decrease the time loss and their effects on flexibility level can be investigated.

Relative share is the hidden indicator of entropic evaluations. Any change in time does not only change the relevant time variable but also affects the total time value. Therefore, the relative share change does not have a regular or predictable form.

Machines	p_n	$-p_n \ln p_n$
(T035)	0,19038	0,31579
(T043)	0,12274	0,25747
(PL6)	0,095742	0,22462
(M6)	0,102492	0,23347
(BA1)	0,234951	0,3403
(BS2)	0,016389	0,06738
(F31)	0,102047	0,2329
(PAH)	0,007783	0,03779
(F32)	0,080607	0,20298
(F30)	0,046867	0,14343
Total Entropy		2,05615

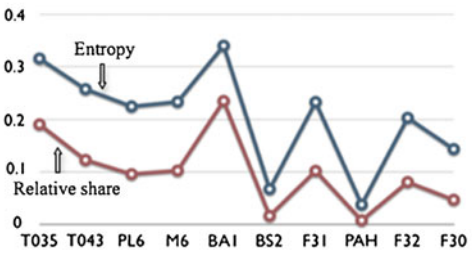

Fig. 1 Distribution of relative shares and entropy

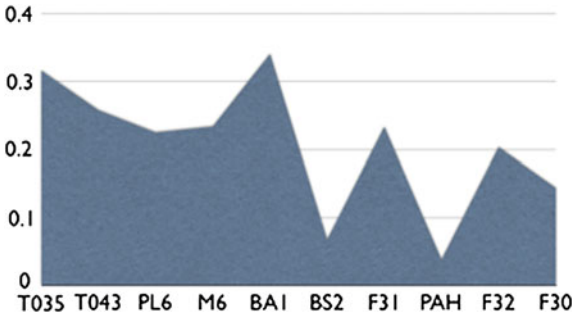

Fig. 2 Total entropy values for each machine

As it can be seen in Fig. 2 total entropy values are different for each machine. The maximum value belongs to the machine BA1 while the lowest values belong to PAH and BS2. That is directly related to the number of part types that these machines can perform. The machines that are able to process various kinds of parts have a higher impact on both entropy value and overall flexibility.

Entropy values are analyzed by means of the time that are allocated for process, set up, transportation and labor operation for each product type. The relative shares of each machine is separately calculated as in Eqs. (10)–(13).

Process (10)	Machine set-up (11)	Transportation (12)	Labor (13)
$p_p = \frac{t_p}{\sum_{i=1}^{10} t_{p_i}}$	$p_s = \frac{t_s}{\sum_{i=1}^{10} t_{s_i}}$	$p_t = \frac{t_t}{\sum_{i=1}^{10} t_{t_t}}$	$p_l = \frac{t_l}{\sum_{i=1}^{10} t_{l_i}}$

Entropy values for each manufacturing activity may be observed from Table 4. Time losses for the work to be performed on specific machine entropies are equal to "0". That means the p values (relative share) is equal to "1" since $\ln 1 = 0$. The basic difference of these "0" entropy value machines from the others are the number of their operation steps. During the manufacturing period, the PAH and BS2 machines have only one process step for this production. Therefore we can claim that these machines as inflexible. In other words, if the relevant product is taken out of product mix; the machine would not perform any operation within that manufacturing unit. Analyzing the maximum entropy values of all belong to BA1 machine operation has the maximum operation steps of "6". The operations performed for the production of relevant products on this machine is the most flexible one among various operations grouped.

Table 4 Entropy values for each manufacturing activity

Operations	Entropy of the time spent	Operations	Entropy of the time spent
Process TO35	0.6910274	Process BS2	0
Set up TO35	0.6928889	Set up BS2	0
Transport TO35	0.4011899	Transport BS2	0
Labour TO35	0.6931472	Labour BS2	0
Process TO43	0.578718	Process F31	0.5982696
Set up TO43	0.6922789	Set up F31	0.6931472
Transport TO43	0.4011899	Transport F31	0.6931472
Labour TO43	0.6931472	Labour F31	0.6931472
Proccss PL6	1,098,143	Process PAH	0
Set up PL6	0.9502705	Set up PAH	0
Transport PL6	0.9936232	Transport PAH	0
Labour PL6	10,986,123	Labour PAH	0
Proccss M6	0.676526	Process F32	0.6460905
Set up M6	0.6615632	Set up F32	0 6931472
Transport M6	0.6931472	Transport F32	0.2974804
Labour M6	0.6931472	Labour F32	0.6931472
Proccss BA1	16,400,083	Process F30	0.6662784
Set up BA1	17,729,916	Set up F30	0.6931472
Transport BA1	17,917,595	Transport F30	0.6931472
Labour BA1	17,917,595	Labour F30	0.6931472

5 Conclusion

The majority of literature agrees that flexibility is a competitive key to cope effectively with environmental uncertainty. However, investing in flexibility is costly since it requires high skill labor, machinery etc. Mistakes in decisions regarding the flexibility improvement may lead to dramatic results such as losing competitive position. In addition to this, in literature measurement problem is mentioned as one of the main factors of failures of flexibility improvement efforts for many companies. In order to improve flexibility the flexibility level of manufacturing system should be measured. When companies find out that their flexibility level is lower than required from the environment they can prioritize investments in the flexibility improvement of their manufacturing system.

This study focuses on the measurement of flexibility that is scarce in literature and proposes a methodology to measure the flexibility level of manufacturing system. In the model proposed, manufacturing characteristics such as type of machinery, number and type of operations and routing for each part as well as time spend for operations, machine set up activities and material handling are considered

to calculate flexibility level of the manufacturing unit. An application of the model to a job shop is performed to analyze whether or not a time based flexibility measure can adapt to entropy based evaluation method for flexibility including the total time loss in every step of the manufacturing. When the parameters are defined in same scale by using a common indicator, the relative shares of the elements would give a clue for the distribution of entropy and flexibility levels. The overall entropy is calculated as the sum of the partial entropies of machines in the job shop. The machines that perform work on more products have higher relative share and thus, have the higher entropy value. It is accepted in literature that higher entropy value indicates a higher level of manufacturing flexibility. The machines that are able to process various kinds of parts are shown to have a higher impact on overall flexibility. Entropy based evaluation for manufacturing flexibility may be regarded as a consistent measurement method for manufacturing systems.

There are also some limitations of this study. Firstly the entropy value of a manufacturing system is not a standard value, therefore can not be used for comparison of flexibility levels. It can rather be used for comparing the results of the same manufacturing system over different time periods to investigate changes in the layout plan, implementing new machinery or balancing the workforce in job shop. Secondly, it does not measure the operational flexibility that includes design, purchasing, distribution, marketing, services, etc. Therefore it does not represent the overall company flexibility. This limitation suggests a further study to measure company flexibility in that all other organizational factors are represented. In addition, a computer simulation can be used to test the measure through a number of different scenarios using a discrete-event stochastic simulator to evaluate the performance of the measurement system with various possible values of relevant parameters.

References

1. Schlie TW (1995) Advanced manufacturing and new directions for competitive strategy. J Bus Res 33:103–114
2. Pettigrew A, Whipp R (1991) Managing change for competitive success. Blackwell, Oxford
3. Hayes RH, Wheelwright SC (1984) Restoring our competitive edge: competing through manufacturing. Wiley, New York
4. Boyer KK (1999) Evolutionary patterns of flexible automation and performance: a longitudinal study. Manage Sci 45(6):824–842
5. Patel P, Terjesen S, Li D (2012) Enhancing effects of manufacturing flexibility through operational absorptive capacity and operational ambidexterity. J Oper Manage 30(3):201–220
6. Zhang Q, Vonderembse MA, Lim J (2003) Manufacturing flexibility: defining and analyzing relationships among competence, capability, and customer satisfaction. J Oper Manage 21 (2):173–191
7. Beach R, Muhlemann AP, Price DHR, Paterson A, Sharp JA (2000) A review of manufacturing flexibility. Eur J Oper Res 122:41–57
8. Swamidass PM (2002) Innovations in competitive manufacturing. AMACOM Div Am Manage Assoc 4–5:119–120

9. Tempelmeier H, Kuln H (1993) Flexible manufacturing systems: decision support for design and operation. John Wiley & Sons
10. Shuiabi E, Thomson V, Bhuiyan N (2005) Entropy as a measure of operational flexibility. Eur J Oper Res 165:696–707
11. Koste LL, Malhotra MK, Sharma S (2004) Measuring dimensions of manufacturing flexibility. J Oper Manage
12. Schneeweiss C, Schneider H (1999) Measuring and designing flexibility as a generalized service degree. Eur J Oper Res 108:76–82
13. Nagarur N, Azeem A (1999) Impact of commonality and flexibility on manufacturing performance: a simulation study. Int J Prod Econ, pp 110–121
14. Wahab MIM, Wu D, Lee CG (2008) A generic approach to measuring the machine flexibility of manufacturing systems. Eur J Oper Res 186:137–149
15. Choi SH, Kim JS (1998) Study on the measurement of comprehensive flexibility in manufacturing systems. Comput Ind Eng 34:103–118
16. Chang AY (2007) On the measurement of routing flexibility: a multiple attribute approach. Int J Prod Econ 109:122–136
17. Gupta YP, Goyal S (1989) Flexibility of manufacturing systems: Concepts and measurements. Eur J Oper Res 43:119–135
18. Chryssolouris G (1996) Flexibility and its measurement. Ann CIRP 45(2):581–587
19. Parker RP, Wirth A (1999) Manufacturing flexibility: measures and relationships. Eur J Oper Res 118:429–449
20. Joseph OA, Shidharan R (2011) Evaluation of routing flexibility of a flexible manufacturing system using simulation modelling and analysis. Int J Manuf Technol 56:273–289
21. Tsorveloudis NC, Phillis YA (1998) Manufacturing flexibility measurement: a fuzzy logic framework. IEEE Trans Robot Autom 14:513–524
22. Kahraman C, Beskese A, Ruan D (2004) Measuring flexibility of computer integrated manufacturing systems using fuzzy cash flow analysis. Inf Sci 168:77–94
23. Kumar V (1987) Entropic measures of manufacturing flexibility. Int J Prod Res 25:957–966
24. Chang AY, Whitehouse DJ, Chang SL, Hsieh YC (2001) An approach to measurement of single machine flexibility. Int J Prod Res 39:1589–1601
25. Timings RL (2004) Basic manufacturing, 3rd edn. Newnes Elsevier, Great Britain, pp 1–33
26. Trujillo MJ (2007) Determining the value of volume and process flexibility in market driven manufacturing operations. Master of Science thesis in engineering systems, Massachusetts Institute of Technology
27. Wahab MIM, Stoyan SJ (2008) A dynamic approach to measure machine and routing flexibilities of manufacturing systems. Int J Prod Econ 13:895–913
28. Koç T (1992) İleri Teknolojili İmalat Sistemleri İçin Yatırım Değerlendirme Modeli, Doctoral Dissertation I.T.U Industrial Engineering Department, pp 106–108
29. Erkal Sönmez Ö, Koç T (2015) On quantifying manufacturing flexibility: an entropy based approach. In: Lecture notes in engineering and computer science: proceedings of the world congress on engineering 2015, WCE 2015, 1–3 July, 2015, London, UK, pp 961–966

Ore Processing by PGM Concentration Process and Assessment of CO_2 Equivalent Emissions and Environmental Damage Directly Involved

Junior Mabiza-ma-Mabiza and Charles Mbohwa

Abstract Platinum group metals are more and more pointed out as key players to contribute to addressing the making headway issues of environmental damage impacts through technological innovations. Of immediate past, interest in hydrogen has grown rapidly resulting to the development of the concept of hydrogen economy to address two growingly noticed challenges namely climate change impacts due to GHG emissions and the need for clean energy, security and sustainability supply. The recognitions to PGM are of without a doubt, but goings-on around PGM recovery process are reported with environmental concerns; the best known are identified as land transformation, livestock and wildlife affected by use of chemicals and other non-renewable resources. Life cycle assessment analysis of ore-concentration was developed and equivalent carbon dioxide emissions quantified. One tonne of Ore-based PGM Concentrates, a total amount of equivalent carbon dioxide of about 1.574,96 kg CO_2-eq was associated with this process. In an annual initiative, the concentrator can process up to 36,547 million metric tons of ore milled accounting for 57.5 million kg CO_2-eq. Important emissions in this phase are waterborne and emissions to soil.

Keywords Bushveld complex · Direct environmental damages · Equivalent carbon dioxide emissions · Life cycle inventory assessment · Ore-based platinum metals concentration process · Platinum group metals

J. Mabiza-ma-Mabiza (✉)
Faculty of Engineering and the Built Environment, Department of Quality and Operations Management, University of Johannesburg, C Green 6, Bunting Road Campus, Auckland Park, Johannesburg, Gauteng Province 2092, South Africa
e-mail: jmabiza@uj.ac.za; jmabiza2008@hotmail.fr

C. Mbohwa
Faculty of Engineering and the Built Environment, University of Johannesburg, C Green 5, Bunting Road Campus, Auckland Park, Johannesburg, Gauteng Province 2092, South Africa
e-mail: cmbohwa@uj.ac.za

S.-I. Ao et al. (eds.), *Transactions on Engineering Technologies*,
DOI 10.1007/978-981-10-1088-0_21

1 Introduction

Energy is the life force driving our modern civilization and its dimensions, being economy and development, work, spare time, social and physical welfare all is influenced by the supply of a sufficient and uninterrupted energy. However the challenge of the demand for energy worldwide has been growing at significant rate and of recent clean energy supply is a new restriction.

Of immediate past, interest in hydrogen has grown rapidly resulting to the development of the concept of hydrogen economy. The primary reason for this awakening is that hydrogen economy may be an answer to two major challenges already faced by the world, which are growingly noticed nowadays. The first challenge is a severe series of environmental impacts resulting to climate change which is caused by greenhouse gas emissions (GGEs) formed by carbon dioxide (CO_2) and equivalent carbon dioxide (CO_2-eq) emissions. CO_2-eq emissions being other pollutants such as NO_x, SF_x, and SO_x; they result both with CO_2 emissions mainly by burning fossil fuels, coal and natural gas. The second challenge, not the least, is the need for security of energy and sustainability supply.

Hydrogen economy may be a major key answer to strip off CO_2 calamities and contribute to sustain energy security supply. Hydrogen economy is defined as the free CO_2/CO_2-eq emissions built-up system, in which one of the universal energy carriers is hydrogen, the other electricity. In hydrogen economy the two energy carriers will coexist with possibility to generate one another to provide, convey and store energy [1].

Hydrogen satisfies to the requirements of an energy carrier which, in the long run, might meet all energy needs together with electricity. Such energy system would be independent of energy sources since both electricity and hydrogen can be produced from the most available primary energy sources and added to the energy supply mix [2].

Hydrogen produced from water by electrolysis process is the most environmentally friendly but with prerequisites to be met for efficient and effective activity. The process involves platinum group metals (PGM) as catalyst to increase the efficiency through the use of solid polymer electrolyzer (SPE) currently experimented as the best electrolyzer high output volume of hydrogen. However the engineering recovery process of PGM suffers criticisms as reported by many scholars of real concerns of emissions to the immediate environment affecting local communities and seen as future threats to the regional biodiversity, contributing to climate change globally as well.

South Africa is the largest world PGM economy accounting about 75 % of the global reserves. The country's PGM's wealth has been seen as a significant competitive advantage for the global HFCT development initiatives in view of the abundant platinum metals deposits in the country in terms alternative solutions through clean and renewable energy supply, mitigation of GHG emissions, new types of business ventures, etc. [3].

Table 1 PGMs reserves and production by country [4]

Country	Production			Reserves[b]	Reserve base[b]
	t Pt	t Pd	t PGMs	t PGMs	t PGMs
South Africa	165.83	86.46	310.92	63,000	70,000
Russia	27.00	96.80	138.30	6200	6600
Canada	6.20	10.50	20.20	310	390
Zimbabwe	5.30	4.20	11.00	–	–
United States	3.86	12.80	–	900	2000
Columbia	1.40	–	–	–	–
Australia	~0.90[a]	~0.73[a]	–	–	–
World	212	219	509	71,000	80,000

[a]Assuming Australia is credited with PGMs extracted from ores and concentrates exported to Japan

[b]They are broadly similar to reserves and resources as used in South Africa, Canada, Australia, and elsewhere. With t = tonne metric, Pt = platinum, Pd = palladium

The global supply of PGM (Table 1) is largely dominated by South Africa due to its large economic reserves in the stratiform deposits built with Precambrian mafic to ultramafic layered intrusions known as the Bushveld Complex. South African PGM reserves are estimated to be 71,000 tonnes whilst the global reserves are estimated to be 80,000 tonnes [4].

Dominant PGM producers are progressively raising a capital reserve of platinum metals for the global hydrogen fuel cell technology (HFCT) industry. According to [5], it is significant to recognize that resource issues such as ore grade declination, increase of more energy and water consumption and environmental issues are possible constraints on future PGM production. The rate of PGM production growth may also be constrained by demand which is foreseen. South Africa, for instance, prepares to make reserves available to supply 25 % of the global catalyst demand for the HFCT industry by 2020 [6].

The South African miner, Anglo Platinum Limited is the largest producer of platinum group metals in the world. It owns varied mines and operates three smelters of which Waterval (Rustenburg) where precious metals are refined and Mortimer (Limpopo) both located on the western limb of the Bushveld complex. The third smelter, Polokwane (Polokwane), is located on the eastern limb of the Bushveld complex (Fig. 1) [7]. The Bushveld Complex is the world's largest PGM reserve that has led the global production of PGM since 1971. Bushveld Complex abounds also in Chromium and Vanadium with the world's largest reserves [8]. Due to the Bushveld Complex location in South Africa, the country covers the largest potential economic of PGM resources ever discovered in the world, which is estimated about 80 % of the global reserves.

Operational sites of the Anglo American Platinum.

Anglo American Platinum operates in the Western limbs of the Bushveld Complex exploiting the world's largest known igneous complex that extends over 65,000 km^2 and reaches a depth of about 7 km.

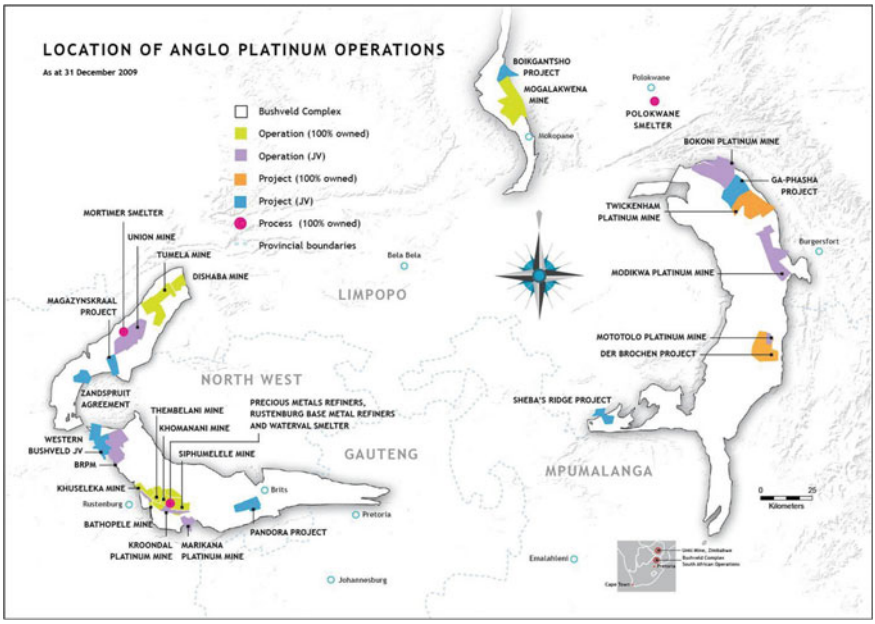

Fig. 1 Location of Anglo Platinum operations in the Bushveld complex. *Source* [7] (color figure online)

An average concentration of PGM of about five grams (5 g) can be found in one metric ton (1000 kg) of mined ore which can be sent directly to the Precious Metals Refinery (PMR) unit. The rest of the mined ore undergoes ore concentration operations. Precious metals are completely recovered from the mined ore [8].

2 Ore Concentration Unit

Ore mined is received at the ore concentration unit mainly for the separation of valuable contents to rocks and sand. Ores undergo crushing, milling, and wet-screening to obtain pumpable slurry bearing the precious metals. Separation occurs in flotation cells where the reagents (chemicals) are added to aerate slugs carrying high-grade collected PGM [9].

Operations of ore concentration are accountable for large amounts of water use with possibly large emissions to water and soil. An approximate composition of a metric ton received at the ore concentration unit of Waterval is given in Table 2.

Table 2 Analysis of concentrates at the Waterval concentration unit [15]

	Al_2O_3 (%)	CaO (%)	Co (%)	Cr_2O_3 (%)	Cu (%)	FeO (%)	MgO (%)	Ni (%)	S (%)	SiO_2 (%)	PGM (g/t)	Total (%)
Anglo-plat Waterval	3.2	4.7	0.08	0.80	2.1	20	15	3.6	9	34	143	92

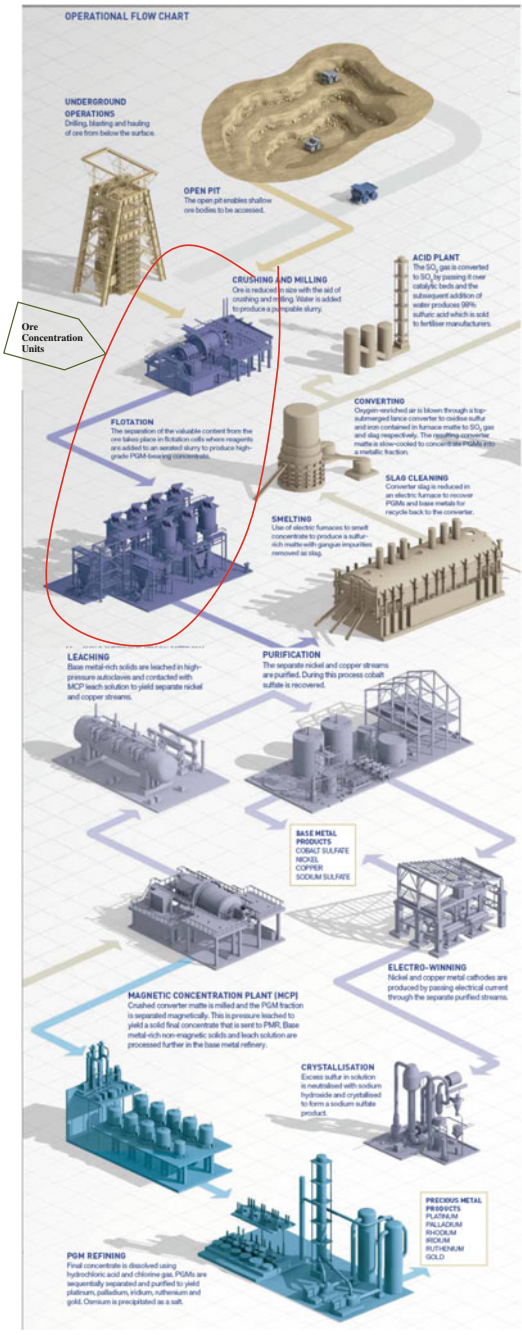

Fig. 2 Operational sites of the Anglo American Platinum [14]

This is a typical composition of a layer of the western Bushveld complex predominated with sulfur and iron [10].

Schematic Recovery Process of the PGM at Anglo American (Fig. 2).

In general ore concentration process results in land transformation, livestock, fauna, and flora affected by use of chemicals and other non-renewable resources. Important and varied wastes are generated which interact with local communities. Airborne emissions affect and put under stress local communities and the immediate environment such as underground water, livestock, fauna, and flora. In return, mining companies put in place appropriate management systems tailored to ISO 14001:2004 standards to track legal compliance in an effort to prevent pollution [9].

3 Methods of Assessment and Instruments

Life-Cycle Assessment: *Definition, Goal and Scope* (ISO 14040)
The life-cycle assessment, also known as ISO 14040, is a method in which raw material and energy consumption, types of emissions and other major factors related to a specific product are being measured and analyzed over the entire product life cycle from an environmental point of view [11].

Life Cycle Inventory Analysis (ISO 14041)
The inventory analysis, for such specific products or techniques, consists of developing a process tree, also called flow-material chart, in which all processes from the raw materials extraction and input materials through operation, to final product, waste recycle, disposal treatment, and emissions are mapped out and connected, and mass and energy balances are closed [11]. The Life Cycle Inventory Analysis (LCIA) of a single or a simple set of unit processes (Fig. 3) may be established using a simple input/output balance sheet analysis. In the case of a more complex LCIA processes however, LCIA analysis can be achieved through specific and appropriate LCA tools such as 'Umberto for carbon footprint software package'. Umberto for carbon footprint package is introduced in the following sub-headings. Equivalent carbon dioxide can be quantified at the inventory analysis stage of LCA development.

Sketch of Input/output single stage or unit process in a flow chart.

Umberto for Carbon Footprint Software Package:
Umberto is a helpful tool which is used by LCA professionals, scientists and manufacturing companies. Umberto trademark comprises a number of product packages which are specifically designated for different approaches in the LCA analysis [12].

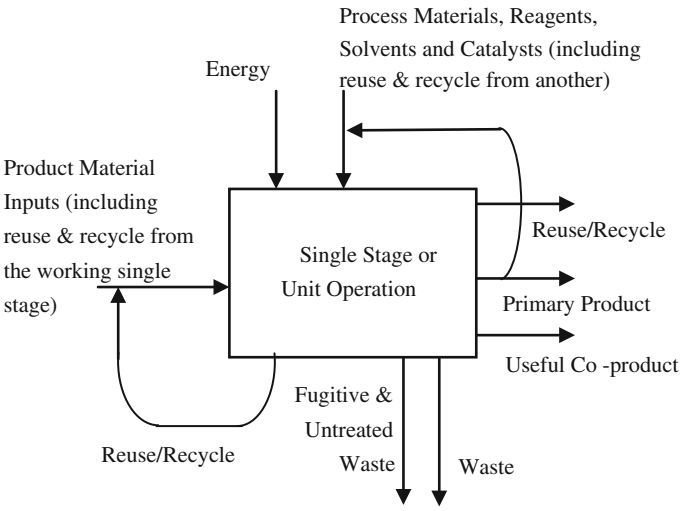

Fig. 3 Input/output of single stage or unit operation or unit process in a flow chart. *Source* [10]

The concept of Equivalent Carbon Dioxide Emission:
'Equivalent Carbon Dioxide' refers to an amount of emissions describing, for a given mixture, an equivalent amount of CO_2 that would have the same global warning potential measured over a timescale generally of 100 years [13].

4 Inventory Assessment of Flow-Material in the Concentration Phase of PGM Recovery

The concentration phase of PGM recovery accounts for significant solid and liquid emissions ending at tailings dams dug in the surroundings. Because of the of soil permeability, liquid residues end up expanding to neighboring environment. Acid mine drainage is one of the residues that affects and contaminates the groundwater sources and identified as one of the most important issues with the concentrates phase of platinum recovery process.

The Inventory Flow-Chart: 400 g of PGM per tonne of Concentrates (Fig. 4).

Concentration phase uses large quantities of water; and this calls for on-site recycling wastewater, which in turn causes direct and indirect emissions due to the use of a certain amount of energy from emitting resources in CO_2 and the use of chemicals. It is to be noted that South Africa is 88 % based coal burning plant power generation.

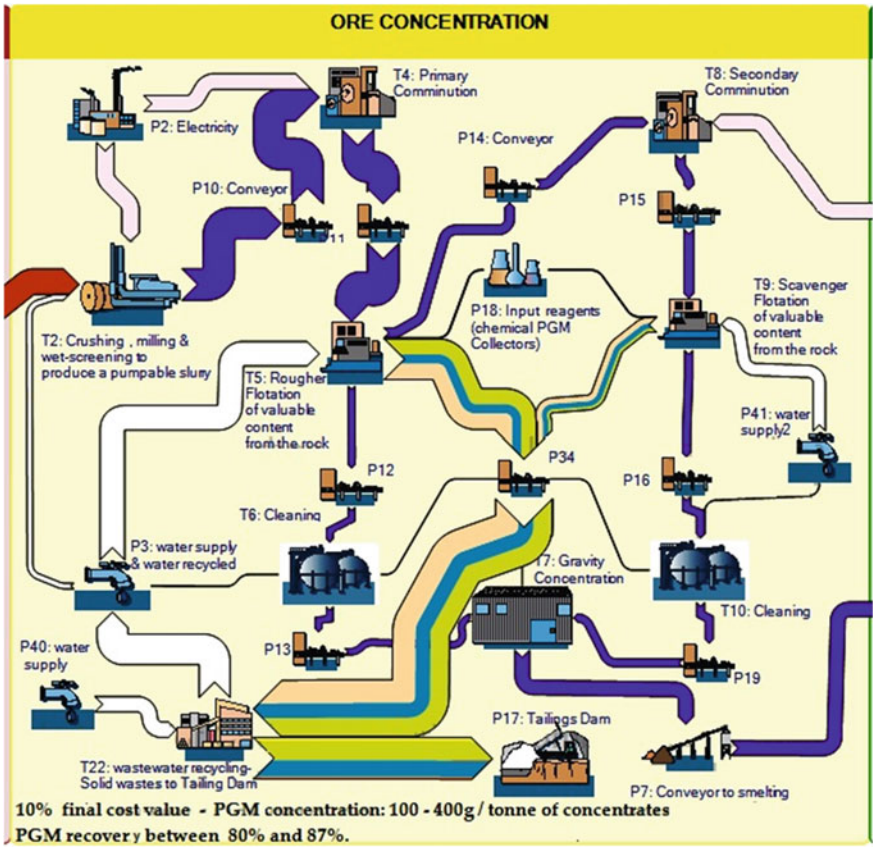

Fig. 4 Flow-material in the concentration phase of PGM recovery process [8]

5 Individuals and Overall Equivalent Carbon Dioxide (CO_2-eq) Emissions

The following Table 3 shows a total amount of carbon equivalent of 1574.96 kg CO_2-eq to process one metric ton of ore by concentration. The masses displayed in the column "product" together with the designated constituents, are apparent weights which are in relation to the molecular masses of these constituents.

They are the total masses of the constituents in the entire life cycle analysis (mining-off-gas. The column "share", however depicts, by a length, the amount of CO_2-eq emissions emitted by each constituent in the phase.

Table 3 Equivalent carbon dioxide emissions in the concentration phase [8]

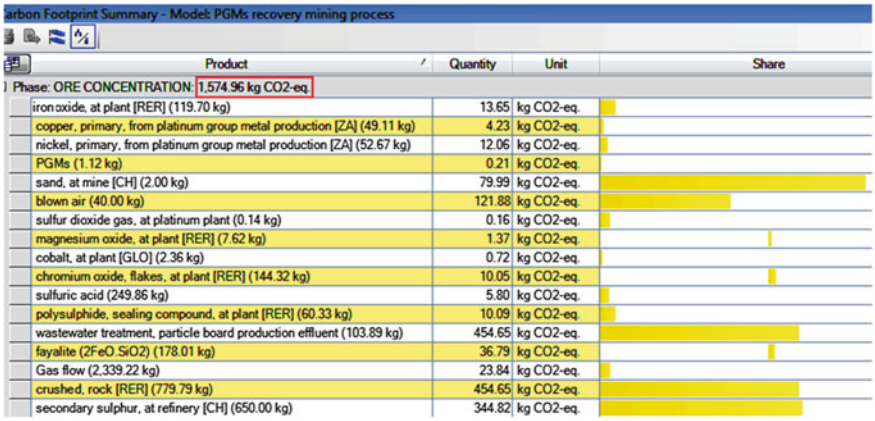

arbon Footprint Summary - Model: PGMs recovery mining process

Product	Quantity	Unit	Share
Phase: ORE CONCENTRATION: 1,574.96 kg CO2-eq.			
iron oxide, at plant [RER] (119.70 kg)	13.65	kg CO2-eq.	
copper, primary, from platinum group metal production [ZA] (49.11 kg)	4.23	kg CO2-eq.	
nickel, primary, from platinum group metal production [ZA] (52.67 kg)	12.06	kg CO2-eq.	
PGMs (1.12 kg)	0.21	kg CO2-eq.	
sand, at mine [CH] (2.00 kg)	79.99	kg CO2-eq.	
blown air (40.00 kg)	121.88	kg CO2-eq.	
sulfur dioxide gas, at platinum plant (0.14 kg)	0.16	kg CO2-eq.	
magnesium oxide, at plant [RER] (7.62 kg)	1.37	kg CO2-eq.	
cobalt, at plant [GLO] (2.36 kg)	0.72	kg CO2-eq.	
chromium oxide, flakes, at plant [RER] (144.32 kg)	10.05	kg CO2-eq.	
sulfuric acid (249.86 kg)	5.80	kg CO2-eq.	
polysulphide, sealing compound, at plant [RER] (60.33 kg)	10.09	kg CO2-eq.	
wastewater treatment, particle board production effluent (103.89 kg)	454.65	kg CO2-eq.	
fayalite (2FeO.SiO2) (178.01 kg)	36.79	kg CO2-eq.	
Gas flow (2,339.22 kg)	23.84	kg CO2-eq.	
crushed, rock [RER] (779.79 kg)	454.65	kg CO2-eq.	
secondary sulphur, at refinery [CH] (650.00 kg)	344.82	kg CO2-eq.	

6 Results

The most significant CO_2-eq emissions in the concentration process of PGM recovery, as referred in Table 3, are, in the order of magnitude, attributed to wastewater treatment (454.65 kg CO_2-eq), crushed rocks (454.65 kg CO_2-eq), Sulphur (344.82 kg CO_2-eq), blown air (121.88 kg CO_2-eq) and the sand (121.88 kg CO_2-eq). Blown air represents indirect CO_2-eq due to the energy used to pump slurry from milling to comminution. Comminution consists of grinding the slurry ore to powder (Fig. 3). It is also important to observe that wastewater treatment can likely transfer reagents (PGM collectors) to the tailings dam, with the unfortunate occurrence acid mine drainage.

7 Conclusion

South African PGM producers have set up appropriate management systems tailored to ISO 14001 standards. These also track legal compliance and prevent pollution [9]. Nevertheless real damage to environment are very much involved in the production of the platinum precious metals with tangible adverse emissions to the surroundings of processing plants which respond to disturbances namely, air pollution with volatile organic compounds and dust emission, noise pollution, acid mine drainage containing chemicals interacting with local populations, affecting human health, underground water, livestock, fauna, flora and forcing countryside exodus.

Table 4 Recapitulation of CO_2-eq emissions in processing a metric ton of ore from mining to off-gas handling phase [8]

Product	Relative mass (kg)	CO_2-eq (kg)					
		Mining	Ore concentration	Smelting	Converting	Off-gas handling	Total
Blown air	40.00	42.65	121.88	115.49	34.38	1.43E−15	314.40
Chromium oxide. Flakes	144.32	3.52	10.05	121.41	75.33	−5.16E−15	210.31
Cobalt	2.36	0.25	0.72	8.70	90.60	6.33E−16	100.27
Copper	49.11	1.48	4.23	51.07	314.37	1.74E−14	371.15
Crushed rocks	779.79	138.29	454.65				592.94
Dust	0.20	1.26					1.26
Fayalite	178.01	12.87	36.79	467.46	355.30	−1.02E−13	872.42
Gas flow/particles	2339.22	8.34	23.84	287.95	94.38	401.01	815.52
Iron oxide	119.70	4.78	13.65	164.89	118.18	6.43E−14	301.50
Limestone				177.36			177.36
Magnesium oxide. Flakes	7.62	0.48	1.37	16.50	44.59	−4.36E−15	62.94
Nickel	52.67	4.22	12.06	145.65	355.22	3.58E−14	517.15
PGM	1.12	0.07	0.21	2.57	83.34	1.90E−16	86.19
Polysulphide. Sealing compound	60.33	3.53	10.09	144.94	60.81		219.37
Sand	2.00	17.43	79.99	4.39			101.81
Secondary sulphur	650.00	102.35	344.82	126.96			574.13
Sulphuric acid	249.86	2.03	5.80	70.09	23.03	107.80	208.75
Sulphur dioxide	0.14	0.06	0.16	1.92	0.63	2.71	5.48
Wastewater treatment. Particle board production effluent	103.89	138.29	454.65	177.36			770.30
Total equivalent carbon dioxide (kg CO_2-eq)		481.90	1574.96	2084.71	1650.16	511.52	6303.25

8 Recapitulation of CO_2-eq Emissions in Processing One Metric Ton of Ore for the Recovery of PGM

See Table 4.

References

1. Pennel SS (2006) Steps towards the hydrogen economy. Energy 31(1):33–43
2. Barbir F (2005) PEM electrolysis for production of hydrogen from renewable energy sources. Sol Energy 78(66):1–9
3. DST (2007) Innovation towards a knowledge-based economy: ten-year plan for South Africa (2008–2018). Department of Science and Technology, Pretoria
4. Mudd GM, Glaister BJ (2010) The environmental costs of platinum—PGM mining and sustainability: Is the glass half-full or half-empty? Miner Eng 23(5):438–450
5. Mudd GM (2009) The sustainability of mining in Australia: key production trends and environmental implications. Research report 5 (revised ed.), Department of Civil Engineering, Monash University and Mineral Policy Institute, Melbourne, Australia (Online). Accessed on Apr 2009 http://civil.eng.monash.edu.au/about/staff/muddpersonal/rr5/
6. Mange S (2007) National hydrogen and fuel cell technologies research: development and innovation strategy. Draft document. Department of Science and Technology, Pretoria
7. Groot D, Pistorius PC (2007) Can we decrease the ecological footprint of base metal production by recycling? In: Conference proceedings of the 4th Southern African conference on base metals. Southern African Institute of Mining and Metallurgy (SAIMM), Namibia
8. Mabiza MJ, Mbohwa C (2015) Quantifying CO_2-eq emissions of ore-based pgm concentration process in South Africa and identifying the immediate environmental impacts related. In: Lecture notes in engineering and computer science: proceedings of the world congress on engineering 2015, WCE 2015, 1–3 July, 2015, London, U.K., pp 863–865
9. Anglo Platinum Limited (2009) Platinum: a precious metal for a precious planet: annual report on financial, social and environmental performance (online). Available www.angloplatinum.investoreports.com/angloplat_arpdf_2009/
10. Anglo Platinum Limited (2003) Operations review: flow chart: annual business report (online). Available www.angloplatinum.com/investors/reports/ar_03/b_rprt/financials/appendix_1.htm
11. Bras B, Roman F (2006) An introduction to life cycle analysis/assessment (LCA). Systems Realization Laboratory, Georgia Institute of Technology, Atlanta
12. Ifu Hamburg (2011) Umberto: Carbon footprint software (online). Available at http://www.carbonfootprint-software.com/en/
13. Pertsova CC (2007) Ecological economics research trends. Nova Science Publishers Inc.
14. Mabiza MJ (2013) Energy potential and sustainability management of platinum catalyzed fuel cell technology in South Africa (Master's thesis). Retrieved from dissertations and theses. Available at https://ujdigispace.uj.ac.za/handle/10210/8672
15. Jones RT (1999) Platinum smelting in South Africa. S Afr J Sci 95:525–534. Available at Nov/Dec 1999 http://www.pyrometallurgy.co.za/Mintek/Platinum/Platinum.htm

Optimal Policies of Condition-Based Maintenance Under Multiple Imperfect Inspections

Ahmed Raza and Vladimir Ulansky

Abstract This study provides analytical modeling of condition-based maintenance with periodic imperfect inspections for a stochastically deteriorating system. In addition to the critical threshold, for each time point of inspection a replacement threshold is introduced. An inspection consists of checking the system state parameter against the replacement threshold in the upcoming time intervals. A new decision rule is proposed for inspecting the system condition, which is based on the comparison of the time of inspection with the estimated remainder of the time to failure. Based on this decision rule, general expressions are derived for calculating the probabilities of correct and incorrect decisions with considering the results of previous inspections. For the first time it is shown that even in case of perfect inspections the probabilities of incorrect decisions are nonzero when checking system suitability. To determine the optimal replacement threshold at each time of inspection, different criteria are proposed to use such as maximum net income, minimum Bayes risk, and minimum total error probability. The proposed approach is illustrated by deriving the probabilities of correct and incorrect decisions for a linear stochastic deterioration process model. A numerical example is given.

Keywords Condition-based maintenance · Corrective replacement · Decision rule · False failure · Imperfect inspection · Optimal replacement threshold · Preventive replacement · Total error probability · Undetected failure

A. Raza
Department of the President's Affairs, Overseas Projects and Maintenance,
P.O. Box 372, Abu Dhabi, United Arab Emirates
e-mail: ahmed_awan@hotmail.com

V. Ulansky (✉)
Department of Electronics, National Aviation University, prosp. Kosmonavta,
Komarova 1, Kiev 03058, Ukraine
e-mail: vulanskyi@yahoo.com

S.-I. Ao et al. (eds.), *Transactions on Engineering Technologies*,
DOI 10.1007/978-981-10-1088-0_22

1 Introduction

Currently condition-based maintenance (CBM) is considered to be a perspective approach to improve the operational reliability and reduce the operating costs of many military and civil engineering systems. The basic maintenance operation of this type is condition monitoring, which can be continuous or periodic. Continuous monitoring is impractical in some cases. It can be more practical to monitor the system periodically, for example, due to the cost reasons. Evidently, condition monitoring is preferred among other maintenance techniques in those cases where system deterioration can be measured, and wherein the system enters the failed state when the state parameter deteriorates beyond the threshold of functional failure. The growing interest about CBM is evident from the large number of studies related to various mathematical models and optimization techniques. Most of the existing mathematical models of CBM with inspections at discrete times can be classified into two groups: models of CBM with perfect inspections and models of CBM with imperfect inspections. The latter is the subject of this study.

Maintenance models with imperfect inspections usually consider two types of errors: "false positives" (false alarms) with probability α and "false negatives" (i.e. non-detecting of failure) with probability β; for example [1]. Such models are not CBM models because in reality the error probabilities are not constant coefficients but depend on time, parameters of the deterioration process and results of previous multiple inspections. Therefore, we analyze only those studies in which the probabilistic indicators of the inspection errors depend on the deterioration process parameters. In [2], CBM policies with imperfect operability checks are analyzed. The probabilities of four possible correct and incorrect decisions when checking system operability are considered. The proposed expressions depend on the deterioration process parameters and the results of previous inspections. In [3], a non-repairable deteriorating system subject to imperfect checks is considered. The probabilities of correct and incorrect decisions are determined with considering the results of previous multiple checks. In [4], the result of a measurement includes the original deterioration process along with a normally distributed measurement error. Based on this model, a decision rule was analyzed and optimal monitoring policies were found. The same approach was used in [5] to include measurement error in a Wiener diffusion process-based degradation model. A similar approach was used in [6] to find the likelihood for more than one inspection. A simple extension to the Bayesian updating model was proposed, such that the model can incorporate the results of inaccurate measurements. In [7], the threshold-type policy introduced for the maintenance action. If the system deterioration stage is less than the minimal threshold, no maintenance is conducted; if the system deterioration stage is found to be between the minimal threshold and the major threshold, than minimal maintenance is carried out; and major maintenance is performed if the system deterioration stage is larger than the major maintenance threshold. The model is based on a stochastic Petri net. In [8], an optimal replacement policy is considered when the state of system is unknown but can be estimated based on the observed condition.

A proportional hazards model is used to represent the system's degradation. The optimization of the optimal maintenance policy is formulated as a partially observed Markov decision process, and the problem is solved using dynamic programming. In [9], the analytical model is developed for condition-based imperfect inspections of a stochastically deteriorating single-unit system. The analytical expressions for the probabilities of correct and incorrect decisions are derived considering the measurement errors. However, the proposed model ignores the results of previous inspections.

This paper presents a more general CBM model with imperfect inspections, which assumes that the monitoring data are mixed with measurement errors or noise and that incorrect decisions can occur when checking the system suitability in the coming interval of operation. The probabilities of correct and incorrect decisions are determined based on such a concept as measurement error of time to failure and considering the results of previous inspections.

2 Imperfect Inspections

2.1 Decision Rule

In this study, a deteriorating system subject to random failure is considered. It is assumed that the state of a system is completely identified by the value of one parameter $X(t)$, which is a nonstationary stochastic process with continuous time. A system should be inspected at successive times t_k ($k = 1, 2,\ldots$), where $t_0 = 0$. When the system state parameter exceeds its functional failure threshold FF, the system passes into the failed state. In the presence of measurement error in the inspection of the system state parameter, let $Z(t_k)$ be the measured value of $X(t_k)$ and relate to $X(t_k)$ by the following equation:

$$Z(t_k) = X(t_k) + Y(t_k) \tag{1}$$

where $Y(t_k)$ is the measurement error of the state parameter at time t_k.

A typical realization of the stochastic process $X(t)$ measured at time t_k ($k = 1, 2, \ldots, j$) is shown in Fig. 1.

We introduce the following decision rule when inspecting the system condition at time t_k.

If $z(t_k) < PF_k$, the system is said to be suitable over the interval (t_k, t_{k+1}), where PF_k ($PF_k < FF$) is the replacement threshold at time t_k. If $z(t_k) \geq PF_k$, the system is said to be unsuitable, and it should not be used in the interval (t_k, t_{k+1}). Thus, this decision rule is aimed toward the rejection of systems that are unsuitable for use in the next operation interval.

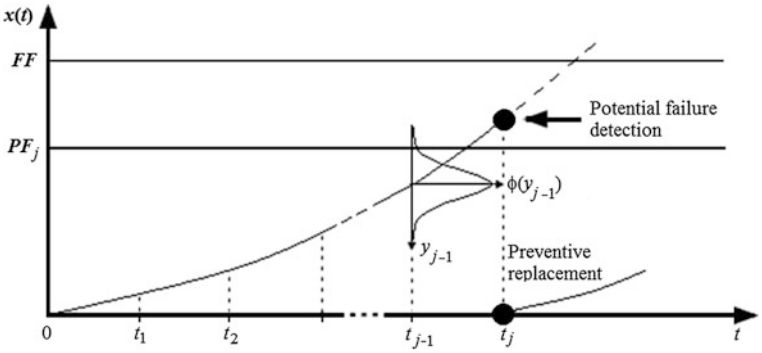

Fig. 1 Realization $x(t)$ of the stochastic process $X(t)$ measured at time point t_k ($k = 1, 2, \ldots, j$) with error y_k having the probability density function $\varphi(y_k)$

2.2 Maintenance Policies

Based on the introduced decision rule two maintenance policies are possible. If $PF_k \leq Z(t_k) < FF$, the preventive replacement or repair is conducted at time t_k. If $Z(t_k) \geq FF$, the corrective replacement or repair is performed at time t_k. Any type of replacement or repair leads to a complete renewal of the system, i.e. after replacement the system becomes as good as new.

2.3 Space of Events

From the perspective of the system suitability for use in the interval (t_k, t_{k+1}) when checking the parameter $X(t)$ at time $t = t_k$, one of the following mutually exclusive events may appear:

$$H_1(\overline{t_1, t_k}; t_{k+1}) = \left\{ X(t_{k+1}) < FF \bigcap \left[\bigcap_{i=1}^{k} Z(t_i) < PF_i \right] \right\} \tag{2}$$

$$H_2(\overline{t_1, t_k}; t_{k+1}) = \left\{ X(t_{k+1}) < FF \bigcap Z(t_k) \geq PF_k \bigcap \left[\bigcap_{i=1}^{k-1} Z(t_i) < PF_i \right] \right\} \tag{3}$$

$$H_3(\overline{t_1, t_k}; t_{k+1}) = \left\{ X(t_k) < FF \bigcap X(t_{k+1}) \geq FF \bigcap \left[\bigcap_{i=1}^{k} Z(t_i) < PF_i \right] \right\} \tag{4}$$

$$H_4(\overline{t_1, t_k}; t_{k+1}) = \left\{ X(t_k) < FF \bigcap X(t_{k+1}) \geq FF \bigcap Z(t_k) \geq PF_k \bigcap \left[\bigcap_{i=1}^{k-1} Z(t_i) < PF_i \right] \right\} \tag{5}$$

$$H_5(\overline{t_1, t_k}; t_{k+1}) = \left\{ X(t_k) \geq FF \bigcap \left[\bigcap_{i=1}^{k} Z(t_i) < PF_i \right] \right\} \tag{6}$$

$$H_6(\overline{t_1, t_k}; t_{k+1}) = \left\{ X(t_k) \geq FF \bigcap Z(t_k) \geq PF_k \bigcap \left[\bigcap_{i=1}^{k-1} Z(t_i) < PF_i \right] \right\} \tag{7}$$

where $H_1(\overline{t_1, t_k}; t_{k+1})$ is the joint occurrence of the following events: the system is suitable for use over the interval (t_k, t_{k+1}) and judged to be suitable when checking at time points $t_1, \ldots, t_k$; $H_2(\overline{t_1, t_k}; t_{k+1})$ is the joint occurrence of the following events: the system is suitable for use over the interval (t_k, t_{k+1}), judged as suitable at time points $t_1,\ldots, t_{k-1}$ and judged as unsuitable when checking at time point t_k; $H_3(\overline{t_1, t_k}; t_{k+1})$ is the joint occurrence of the following events: the operable at time t_k system fails until the time t_{k+1} and when checking the system at time points $t_1,\ldots, t_k$ it is judged as suitable; $H_4(\overline{t_1, t_k}; t_{k+1})$ is the joint occurrence of the following events: the operable at time t_k system fails until the time t_{k+1}; when checking the system at time points $t_1,\ldots, t_{k-1}$ it is judged as suitable and at time point t_k the system is judged as unsuitable; $H_5(\overline{t_1, t_k}; t_{k+1})$ is the joint occurrence of the following events: at time point t_k the system is inoperable and judged as suitable when checking suitability at time points $t_1,\ldots, t_k$; $H_6(\overline{t_1, t_k}; t_{k+1})$ is the joint occurrence of the following events: at time point t_k the system is inoperable; when checking suitability at time points $t_1,\ldots, t_{k-1}$ the system is judged as suitable and at time point t_k the system is judged as unsuitable.

Let us to find the probabilities of events (2)–(7). Suppose that a random variable Ξ ($\Xi \geq 0$) denotes the failure time of a system with failure density function $\omega(\xi)$. We introduce two new random variables associated with the replacement threshold PF_k. Let $\Xi_{0,k}$ denote a random time of the system operation until it exceeds the replacement threshold PF_k by the parameter $X(t)$, and let Ξ_k denote a random assessment of $\Xi_{0,k}$ based on the results of inspection at time t_k.

The random variables Ξ, $\Xi_{0,k}$ and Ξ_k are determined as the smallest roots of the following stochastic equations:

$$X(t) - FF = 0 \tag{8}$$

$$X(t) - PF_k = 0 \tag{9}$$

$$Z(t_k) - PF_k = 0 \tag{10}$$

From the definition of the random variable Ξ_k, it follows that

$$\Xi_k = \left\{ \begin{array}{l} t_k, \text{if } Z(t_k) \geq PF_k \quad (k = 1, 2, \ldots) \\ > t_k, \text{if } Z(t_k) < PF_k \end{array} \right\} \tag{11}$$

Based on Eq. (11), the previously introduced decision rule can be converted to the following form: the system is judged to be suitable at time point t_k if $\xi_k > t_k$; otherwise (i.e., if $\xi_k \leq t_k$), the system is judged to be unsuitable, where ξ_k is the realization of Ξ_k for the system under inspection.

From Eq. (10), it follows that Ξ_k is a function of random variables Ξ and $Y(t_k)$. The presence of $Y(t_k)$ in Eq. (10) leads to a random measurement error with respect to time to failure at time t_k, which is defined as follows:

$$\Lambda_k = \Xi_k - \Xi, \quad k = 1, 2, \ldots \tag{12}$$

The additive relationship between random variables Ξ ($0 < \Xi < \infty$) and Λ_k ($-\infty < \Lambda_k < \infty$) leads to $-\infty < \Xi_k < \infty$. Mismatch between the solutions of Eqs. (8) and (10) results in the appearance of one of the following mutually exclusive events when inspecting system suitability at time t_k:

$$H_1(\overline{t_1, t_k}; t_{k+1}) = \left\{ \Xi > t_{k+1} \bigcap \left(\bigcap_{i=1}^{k} \Xi_i > t_i \right) \right\} \tag{13}$$

$$H_2(\overline{t_1, t_k}; t_{k+1}) = \left\{ \Xi > t_{k+1} \bigcap \Xi_k \leq t_k \bigcap \left(\bigcap_{i=1}^{k-1} \Xi_i > t_i \right) \right\} \tag{14}$$

$$H_3(\overline{t_1, t_k}; t_{k+1}) = \left\{ t_k < \Xi \leq t_{k+1} \bigcap \left(\bigcap_{i=1}^{k} \Xi_i > t_i \right) \right\} \tag{15}$$

$$H_4(\overline{t_1, t_k}; t_{k+1}) = \left\{ t_k < \Xi \leq t_{k+1} \bigcap \Xi_k \leq t_k \bigcap \left(\bigcap_{i=1}^{k-1} \Xi_i > t_i \right) \right\} \tag{16}$$

$$H_5(\overline{t_1, t_k}; t_{k+1}) = \left\{ \Xi \leq t_k \bigcap \left(\bigcap_{i=1}^{k} \Xi_i > t_i \right) \right\} \tag{17}$$

$$H_6(\overline{t_1, t_k}; t_{k+1}) = \left\{ \Xi \leq t_k \bigcap \Xi_k \leq t_k \bigcap \left(\bigcap_{i=1}^{k-1} \Xi_i > t_i \right) \right\} \tag{18}$$

From Eqs. (15) and (16), we see that in terms of system suitability over the interval (t_k, t_{k+1}), the event $H_3(\cdot)$ corresponds to the incorrect decision, and the event $H_4(\cdot)$ corresponds to the correct decision. When the event $H_3(\cdot)$ occurs, the unsuitable system is mistakenly allowed to be used over the time interval (t_k, t_{k+1}).

From the system operability checking standpoint, the event $H_3(\cdot)$ corresponds to the correct decision, and the event $H_4(\cdot)$ corresponds to the incorrect decision.

The event $H_2(\cdot)$ is further called a 'false failure', and events $H_3(\cdot)$ and $H_5(\cdot)$ are called 'undetected failure 1' and 'undetected failure 2', respectively. Events $H_1(\cdot)$, $H_4(\cdot)$ and $H_6(\cdot)$ correspond to the correct decisions pertaining to system suitability and unsuitability.

Note that even when $Y(t_k) = 0$ ($k = 1, 2,\ldots$), incorrect decisions are possible when checking system suitability. Indeed, if $Y(t_k) = 0$, Eqs. (13)–(18) are converted to the following form:

$$H_1(\overline{t_1, t_k}; t_{k+1}) = \left\{ \Xi > t_{k+1} \bigcap \left(\bigcap_{i=1}^{k} \Xi_{0,i} > t_i \right) \right\} \tag{19}$$

$$H_2(\overline{t_1, t_k}; t_{k+1}) = \left\{ \Xi > t_{k+1} \bigcap \Xi_{0,k} \le t_k \bigcap \left(\bigcap_{i=1}^{k-1} \Xi_{0,i} > t_i \right) \right\} \tag{20}$$

$$H_3(\overline{t_1, t_k}; t_{k+1}) = \left\{ t_k < \Xi \le t_{k+1} \bigcap \left(\bigcap_{i=1}^{k} \Xi_{0,i} > t_i \right) \right\} \tag{21}$$

$$H_4(\overline{t_1, t_k}; t_{k+1}) = \left\{ t_k < \Xi \le t_{k+1} \bigcap \Xi_{0,k} \le t_k \bigcap \left(\bigcap_{i=1}^{k-1} \Xi_{0,i} > t_i \right) \right\} \tag{22}$$

$$H_5(\overline{t_1, t_k}; t_{k+1}) = \emptyset \tag{23}$$

$$H_6(\overline{t_1, t_k}; t_{k+1}) = \left\{ \Xi \le t_k \bigcap \Xi_{0,k} \le t_k \bigcap \left(\bigcap_{i=1}^{k-1} \Xi_{0,i} > t_i \right) \right\} \tag{24}$$

where Ø denotes the impossible event.

The errors arising at $Y(t_k) = 0$ are methodological in nature and non-removable with the decision rule used herein.

3 Probabilities of Correct and Incorrect Decisions

Determination of probabilities (13)–(18) is based on the use of the well-known formula for calculating the probability of hitting a random point $\{\Xi, \Xi_1,\ldots, \Xi_k\}$ to the known area. Denoting the joint probability density function (PDF) of random variables $\{\Xi, \Xi_1,\ldots, \Xi_k\}$ as $\omega_0(\xi, \xi_1,\ldots, \xi_k)$, it is easy to find that

$$P[H_1(\overline{t_1,t_k};t_{k+1})] = \int_{t_{k+1}}^{\infty}\int_{t_k}^{\infty}\cdots\int_{t_1}^{\infty}\omega_0(\vartheta,\overline{u_1,u_k})\overline{du_1du_k}d\vartheta \tag{25}$$

$$P[H_2(\overline{t_1,t_k};t_{k+1})] = \int_{t_{k+1}}^{\infty}\int_{-\infty}^{t_k}\int_{t_{k-1}}^{\infty}\cdots\int_{t_1}^{\infty}\omega_0(\vartheta,\overline{u_1,u_k})\overline{du_1du_k}d\vartheta \tag{26}$$

$$P[H_3(\overline{t_1,t_k};t_{k+1})] = \int_{t_k}^{t_{k+1}}\int_{t_k}^{\infty}\cdots\int_{t_1}^{\infty}\omega_0(\vartheta,\overline{u_1,u_k})\overline{du_1du_k}d\vartheta \tag{27}$$

$$P[H_4(\overline{t_1,t_k};t_{k+1})] = \int_{t_k}^{t_{k+1}}\int_{-\infty}^{t_k}\int_{t_{k-1}}^{\infty}\cdots\int_{t_1}^{\infty}\omega_0(\vartheta,\overline{u_1,u_k})\overline{du_1du_k}d\vartheta \tag{28}$$

$$P[H_5(\overline{t_1,t_k};t_{k+1})] = \int_{0}^{t_k}\int_{t_k}^{\infty}\cdots\int_{t_1}^{\infty}\omega_0(\vartheta,\overline{u_1,u_k})\overline{du_1du_k}d\vartheta \tag{29}$$

$$P[H_6(\overline{t_1,t_k};t_{k+1})] = \int_{0}^{t_k}\int_{-\infty}^{t_k}\int_{t_{k-1}}^{\infty}\cdots\int_{t_1}^{\infty}\omega_0(\vartheta,\overline{u_1,u_k})\overline{du_1du_k}d\vartheta \tag{30}$$

As seen from Eqs. (25)–(30), to find the probabilities of correct and incorrect decisions we need to know the joint PDF ω_0 (ξ, ξ_1,…, ξ_k). We denote the conditional PDF of random variables Λ_1, …, Λ_k as f_0 (λ_1, …, $\lambda_k|\xi$) under the condition that $\Xi = \xi$. We use the following equation to express PDF ω_0 (ξ, ξ_1,…, ξ_k) through the PDFs $\omega(\xi)$ and f_0 (λ_1, …, $\lambda_k|\xi$) [10]:

$$\omega_0\left(\xi,\overline{\xi_1,\xi_k}\right) = \omega(\xi)f_0\left[\overline{(\xi_1-\xi),(\xi_k-\xi)}|\xi\right] \tag{31}$$

The substitution of Eq. (31) to Eq. (25) gives

$$P[H_1(\overline{t_1,t_k};t_{k+1})] = \int_{t_{k+1}}^{\infty}\omega(\vartheta)\int_{t_k}^{\infty}\cdots\int_{t_1}^{\infty}f_0\left(\overline{u_1-\vartheta,u_k-\vartheta}|\vartheta\right)\overline{du_1du_k}d\vartheta \tag{32}$$

Assuming that $g_i = u_i - \vartheta$ (i = 1, …, k) in Eq. (32), we have

$$P[H_1(\overline{t_1,t_k};t_{k+1})] = \int_{t_{k+1}}^{\infty}\omega(\vartheta)\int_{t_k-\vartheta}^{\infty}\cdots\int_{t_1-\vartheta}^{\infty}f_0(\overline{g_1,g_k}|\vartheta)\overline{dg_1dg_k}d\vartheta \tag{33}$$

Carrying out a similar change of variables in Eqs. (26)–(30), we obtain

$$P[H_2(\overline{t_1,t_k};t_{k+1})] = \int_{t_{k+1}}^{\infty} \omega(\vartheta) \int_{-\infty}^{t_k-\vartheta} \int_{t_{k-1}-\vartheta}^{\infty} \cdots \int_{t_1-\vartheta}^{\infty} f_0(\overline{g_1,g_k}|\vartheta)\overline{dg_1 dg_k}d\vartheta \quad (34)$$

$$P[H_3(\overline{t_1,t_k};t_{k+1})] = \int_{t_k}^{t_{k+1}} \omega(\vartheta) \int_{t_k-\vartheta}^{\infty} \cdots \int_{t_1-\vartheta}^{\infty} f_0(\overline{g_1,g_k}|\vartheta)\overline{dg_1 dg_k}d\vartheta \quad (35)$$

$$P[H_4(\overline{t_1,t_k};t_{k+1})] = \int_{t_k}^{t_{k+1}} \omega(\vartheta) \int_{-\infty}^{t_k-\vartheta} \int_{t_{k-1}-\vartheta}^{\infty} \cdots \int_{t_1-\vartheta}^{\infty} f_0(\overline{g_1,g_k}|\vartheta)\overline{dg_1 dg_k}d\vartheta \quad (36)$$

$$P[H_5(\overline{t_1,t_k};t_{k+1})] = \int_{0}^{t_k} \omega(\vartheta) \int_{t_k-\vartheta}^{\infty} \cdots \int_{t_1-\vartheta}^{\infty} f_0(\overline{g_1,g_k}|\vartheta)\overline{dg_1 dg_k}d\vartheta \quad (37)$$

$$P[H_6(\overline{t_1,t_k};t_{k+1})] = \int_{0}^{t_k} \omega(\vartheta) \int_{-\infty}^{t_k-\vartheta} \int_{t_{k-1}-\vartheta}^{\infty} \cdots \int_{t_1-\vartheta}^{\infty} f_0(\overline{g_1,g_k}|\vartheta)\overline{dg_1 dg_k}d\vartheta \quad (38)$$

As seen from Eqs. (33)–(38), to calculate the probabilities of correct and incorrect decisions we need to know the PDFs $\omega(\xi)$ and $f_0(\lambda_1, \ldots, \lambda_k|\xi)$. It should also be noted that Eqs. (33)–(38) are general, i.e., can be used with any type of a random process $X(t)$.

4 Deterioration Process Modeling

Let us consider a deteriorating system in which its degradation behavior is assumed to be described by the following monotonic stochastic function:

$$X(t) = a_0 + A_1 t \quad (39)$$

where a_0 is the initial parameter value and A_1 is the random rate of parameter deterioration defined in the interval from 0 to ∞.

It should be noted that a linear model of stochastic deterioration process was used in many previous studies for describing real physical deterioration processes. For example, a linear model was used in [6] for representing a corrosion state function and a linear regressive model studied in [11] describes a change in radar supply voltage with time.

Assume that $Y(t_1)$,…, $Y(t_k)$ and Ξ are independent random variables and the system deterioration process is described by Eq. (39), then conditional PDF f_0 (λ_1, …, $\lambda_k|\xi$) is given by [10]

$$f_0\left(\overline{\lambda_1,\lambda_k}|\xi\right)=\left(\frac{FF-a_0}{\xi}\right)^k\prod_{i=1}^{k}\varphi\left[\frac{(a_0-FF)\lambda_i}{\xi}+PF-FF\right] \tag{40}$$

where $\varphi(y_i)$ is the PDF of the random variable $Y(t_i)$ at time point t_i.

To find the probabilities of correct and incorrect decisions, we substitute PDF (40) into Eqs. (33)–(38); after long mathematical manipulations we obtain

$$P[H_1(\overline{t_1,t_k};t_{k+1})]=\int_{t_{k+1}}^{\infty}\omega(\vartheta)\left[\prod_{i=1}^{k}\int_{-\infty}^{\frac{(a_o-FF)(t_i-\vartheta)}{\vartheta}+PF_i-FF}\varphi(y_i)dy_i\right]d\vartheta \tag{41}$$

$$\begin{aligned}P[H_2(\overline{t_1,t_k};t_{k+1})]=&\int_{t_{k+1}}^{\infty}\omega(\vartheta)\left[\prod_{i=1}^{k-1}\int_{-\infty}^{\frac{(a_o-FF)(t_i-\vartheta)}{\vartheta}+PF_i-FF}\varphi(y_i)dy_i\right]\\&\times\int_{\frac{(a_o-FF)(t_k-\vartheta)}{\vartheta}+PF_k-FF}^{\infty}\varphi(y_k)dy_k d\vartheta\end{aligned} \tag{42}$$

$$P[H_3(\overline{t_1,t_k};t_{k+1})]=\int_{t_k}^{t_{k+1}}\omega(\vartheta)\left[\prod_{i=1}^{k}\int_{-\infty}^{\frac{(a_o-FF)(t_i-\vartheta)}{\vartheta}+PF_i-FF}\varphi(y_i)dy_i\right]d\vartheta \tag{43}$$

$$\begin{aligned}P[H_4(\overline{t_1,t_k};t_{k+1})]=&\int_{t_k}^{t_{k+1}}\omega(\vartheta)\left[\prod_{i=1}^{k-1}\int_{-\infty}^{\frac{(a_o-FF)(t_i-\vartheta)}{\vartheta}+PF_i-FF}\varphi(y_i)dy_i\right]\\&\times\int_{\frac{(a_o-FF)(t_k-\vartheta)}{\vartheta}+PF_k-FF}^{\infty}\varphi(y_k)dy_k d\vartheta\end{aligned} \tag{44}$$

$$P[H_5(\overline{t_1,t_k};t_{k+1})]=\int_{0}^{t_k}\omega(\vartheta)\left[\prod_{i=1}^{k}\int_{-\infty}^{\frac{(a_o-FF)(t_i-\vartheta)}{\vartheta}+PF_i-FF}\varphi(y_i)dy_i\right]d\vartheta \tag{45}$$

$$P[H_6(\overline{t_1,t_k};t_{k+1})] = \int_0^{t_k} \omega(\vartheta)\left[\prod_{i=1}^{k-1}\int_{-\infty}^{\frac{(a_o-FF)(t_i-\vartheta)}{\vartheta}+PF_i-FF}\varphi(y_i)dy_i\right] \times \int_{\frac{(a_o-FF)(t_k-\vartheta)}{\vartheta}+PF_k-FF}^{\infty}\varphi(y_k)dy_k d\vartheta \tag{46}$$

It is easily seen that the sum of probabilities (41)–(46) is equal to 1.

5 Optimal Replacement Threshold

The problem of determining the optimal replacement threshold $PF_{k,opt}$ at time t_k (k = 1, 2,…) depends on the selected optimization criterion. Let us consider some optimization criteria.

The criterion of maximum net income is formulated as

$$\begin{aligned} PF_{k,opt} \Rightarrow \min_{PF_k}\big\{ & C_{profit}(t_{k+1}-t_k)P[H_1(\overline{t_1,t_k};t_{k+1})] - C_{pr}P[H_4(\overline{t_1,t_k};t_{k+1})] \\ & - \big(C_{pr}+C_{sp}\big)P[H_2(\overline{t_1,t_k};t_{k+1})] - C_{cr}P[H_6(\overline{t_1,t_k};t_{k+1})] \\ & - C_{uf}\{P[H_3(\overline{t_1,t_k};t_{k+1})] + P[H_5(\overline{t_1,t_k};t_{k+1})]\}\big\} \end{aligned} \tag{47}$$

where C_{profit} is the average profit per unit of time from operation of the system, C_{pr} is the average cost of preventive replacement (repair) of the system, C_{sp} is the average cost of additional spare parts due to the premature preventive replacement (repair) of the system, C_{cr} is the average cost of corrective replacement (repair) of the system, and C_{uf} is the average loss due to the 'undetected failure'.

The minimum Bayes risk criterion can be formulated as follows:

$$\begin{aligned} PF_{k,opt} \Rightarrow \min_{PF_k}\big\{ & \big(C_{pr}+C_{sp}\big)P[H_2(\overline{t_1,t_k};t_{k+1})] \\ & + C_{uf}\{P[H_3(\overline{t_1,t_k};t_{k+1})] + P[H_5(\overline{t_1,t_k};t_{k+1})]\}\big\} \end{aligned} \tag{48}$$

The criterion of minimum total error probability is represented as

$$PF_{k,opt} \Rightarrow \min_{PF_k}\{P[H_2(\overline{t_1,t_k};t_{k+1})] + P[H_3(\overline{t_1,t_k};t_{k+1})] + P[H_5(\overline{t_1,t_k};t_{k+1})]\} \tag{49}$$

6 Numerical Example

Radar transmitter is the most expensive part in a radar system. In practice, it is very important to provide failure prediction of radar transmitter using CBM. According to [11], if the output voltage of a certain radar transmitter exceeds the threshold FF = 25 kV, a corrective maintenance is required. Let us determine the optimal value of the replacement threshold PF_k (k = 1, 2,…), which minimizes the total error probability. Assume that the output voltage of radar transmitter is described by Eq. (39) and A_1 is a normal random variable. In this case, the PDF of the random variable Ξ is determined as [12]

$$\omega(t) = \frac{m_1\sigma_1^2 t^2 + \sigma_1^2 t(FF - a_0 - m_1 t)}{\sqrt{2\pi}\sigma_1^3 t^3} \exp\left\{-\frac{(FF - a_0 - m_1 t)^2}{2\sigma_1^2 t^2}\right\} \tag{50}$$

where $m_1 = E[A_1]$ and $\mathrm{var}[A_1] = \sigma_1^2$.

When calculating probabilities (41)–(46) we use some initial data given in [11]. The data are: a_0 = 19.645 kV; m_1 = 0.025 kV/h; and σ_1 = 0.012 kV/h. Assume that A_1 and Y are normal random variables. Moreover, $E[Y] = 0$ and $\sigma[Y]$ = 0.1 kV.

Let us determine the optimal thresholds PF_k (k = 1, 2,…) for time points $t_k = k\tau$, where τ = 100 h, by the criterion of minimum total error probability. Assuming k = 1, t_1 = 100 h and t_2 = 200 h, the plot of the total error probability versus threshold PF_1 is shown in Fig. 2. As seen, the optimal threshold value is 22.33 kV and minimum value of the total error probability is 0.025. Note that if $PF_1 = FF$ = 25 kV, the total error probability is 0.43. Thus, the use of the optimal replacement threshold PF_1 significantly reduces the total error probability.

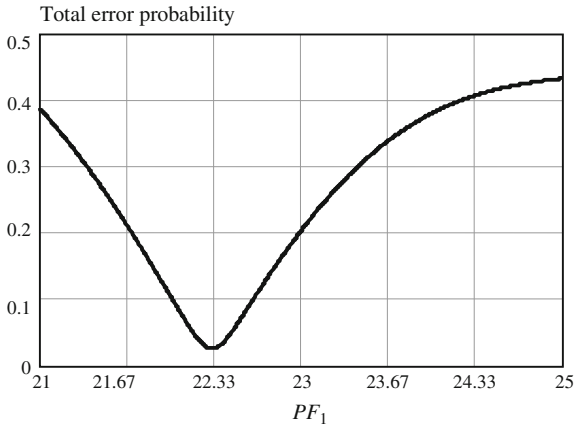

Fig. 2 Total error probability versus threshold PF_1 when t_1 = 100 h and t_2 = 200 h

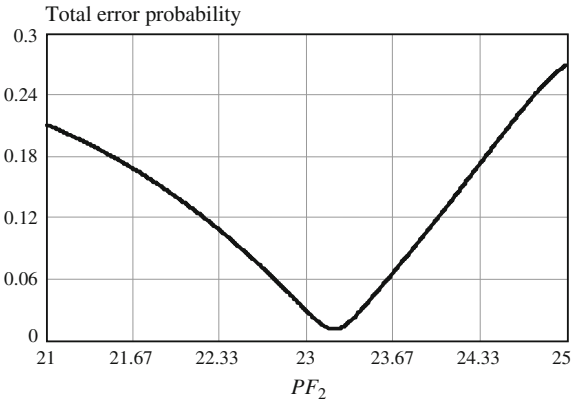

Fig. 3 Total error probability versus threshold PF_2 when t_2 = 200 h, t_3 = 300 h and PF_1 = 22.33 kV

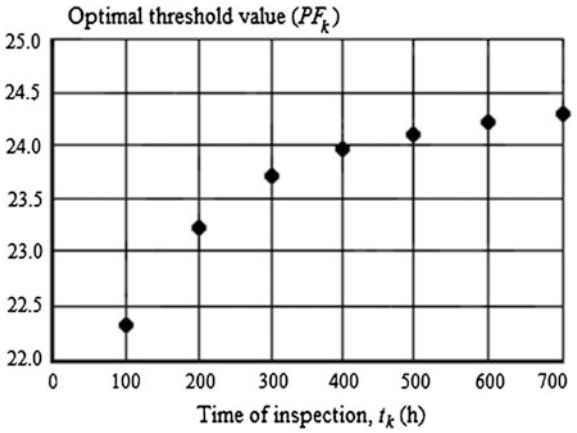

Fig. 4 Optimal threshold value versus time point of inspection t_k (k = 1,…, 7)

The plot of the total error probability versus threshold PF_2 when k = 2, t_2 = 200 h, t_3 = 300 h and PF_1 = 22.33 kV is shown Fig. 3. As can be seen in Fig. 3, the optimal replacement threshold value is 23.21 kV, which is greater by 0.88 kV the value of PF_1. Thus, we can conclude that optimal replacement threshold increases toward the threshold FF with an increase of system operating time.

The dependence of the optimal replacement threshold value versus the time point of inspection t_k (k = 1,…, 7) is shown in Fig. 4.

As seen from Fig. 4, the optimal threshold value increases with increasing the time point of inspection, which is explained by the increase of mathematical expectation of the random process (39) with time.

7 Conclusion and Future Work

In this study, we have derived the equations for the probabilities of correct and incorrect decisions when checking suitability of a stochastically deteriorating system, which is periodically inspected by imperfect measuring equipment. Proposed expressions also consider the decisions taken at the previous inspections. It has been shown that even in case of perfect inspections the probabilities of incorrect decisions are nonzero when checking system suitability. Such errors are methodological in nature and unrecoverable with the decision rule used herein. The proposed general expressions for the probabilities of correct and incorrect decisions have been illustrated by the derivation of the corresponding probabilities for a monotonically increasing linear stochastic deterioration process. The problems have been formulated for determining the optimal replacement thresholds by the criteria of maxim net income, minimum Bayes risk and minimum total error probability. In the numerical example, the effectiveness of the proposed approach to the determination of the optimal replacement thresholds has been illustrated. Our future work will involve consideration of various models to describe the real processes of degradation and determination for these models the probabilities of correct and incorrect decisions when checking suitability of a system.

References

1. Berrade M, Cavalcante A, Scarf P (2012) Maintenance scheduling of a protection system subject to imperfect inspection and replacement. Eur J Oper Res 218:716–725
2. Ulansky V (1987) Optimal maintenance policies for electronic systems on the basis of diagnosing. In: Collection of proceedings: issues of technical diagnostics, Rostov-on-Don. RISI Press, pp 137–143 (in Russian)
3. Ulansky V (1992) Trustworthiness of multiple-monitoring the operability of non-repairable electronic systems. In: Collection of proceedings: saving technologies and avionics maintenance of Civil Aviation Aircraft, Kiev. KIIGA Press, pp 14–25 (in Russian)
4. Newby M, Dagg R (2002) Optimal inspection policies in the presence of covariates. In: Proceedings of the european safety and reliability conference ESREL'02, 19–21 Mar 2002, Lyon, pp 131–138
5. Whitmore G (1995) Estimating degradation by a Wiener diffusion process subject to measurement error. Lifetime Data Anal 1:307–319
6. Kallen M, Noortwijk J (2005) Optimal maintenance decisions under imperfect inspection. Reliab Eng Syst Saf 90(2–3):177–185
7. Hosseini M, Kerr R, Randall R (2000) An inspection model with minimal and major maintenance for a system with deterioration and Poisson failures. IEEE Trans Reliab 49 (1):88–98
8. Ghasemia A, Yacouta S, Oualia M (2007) Optimal condition based maintenance with imperfect information and the proportional hazards model. Int J Prod Res 45(4):989–1012
9. Raza A, Ulansky V (2015) A probabilistic model of periodic condition monitoring with imperfect inspections. Lecture notes in engineering and computer science: proceedings of the world congress on engineering 2015, WCE 2015, 1–3 July 2015, London, UK, pp 999–1004

10. Raza A, Ulansky V (2015) Modelling condition monitoring inspection intervals. In: Electronics and electrical engineering: proceedings of the 2014 Asia-Pacific electronics and electrical engineering conference (EEEC 2014), 27–28 Dec 2014, Shanghai, China. CRC Press, Francis & Taylor Group, London, pp 45–52
11. Ma C, Shao Y, Ma R (2013) Analysis of equipment fault prediction based on metabolism combined model. J Mach Manuf Autom 2(3):58–62
12. Ignatov VA, Ulansky VV, Taisir T (1981) Prediction of optimal maintenance of technical systems. Znanie, Kiev (in Russian)

Identifying Maintenance Actions Using Portable Lubrication Analytical Instrumentation for Maintenance Application

Adrian Chaplin, Frances Hardiman and Daragh Naughton

Abstract Machine efficiency can be enhanced by adapting maintenance practices. Organisations have adapted a proactive approach to maintenance by incorporating predictive maintenance and condition monitoring techniques. Machinery and equipment are required to operate non-stop for organisations to achieve maximum capabilities. Recent advanced analytical instrumentation for the maintenance of machinery has become more compact and portable and has been developed to maintain the harsh continuous cycling of machinery. This research explores if one of these latest and sophisticated analytical instruments developed, namely, a portable *Fourier Transform Infrared* (FTIR) oil analysis instrument, can be successfully incorporated into a predictive maintenance program. The research examines if maintenance personnel can use the results from such analysis to successfully identify maintenance actions within a maintenance program. A case study on how maintenance personnel perform when analyzing used engine oils was carried out. Post training interviews established that experienced maintenance personnel struggled to identify a maintenance action from the results of the portable instrument. Hence, further training was created and performed to overcome these difficulties. Therefore, this research has shown there is a deficiency in maintenance training regimes.

Keywords Condition monitoring · FTIR oil analysis · Lubrication · Maintenance · Oil analysis · Production optimization

A. Chaplin (✉) · D. Naughton
Department of Mechanical and Automobile Engineering, ACORN Research Centre, Limerick Institute of Technology, Moylish, Limerick, Ireland
e-mail: Adrian.chaplin@lit.ie

D. Naughton
e-mail: daragh.naughton@lit.ie

F. Hardiman
Department of Electrical and Electronic Engineering, ACORN Research Centre, Limerick Institute of Technology, Moylish, Limerick, Ireland
e-mail: frances.hardiman@lit.ie

S.-I. Ao et al. (eds.), *Transactions on Engineering Technologies*,
DOI 10.1007/978-981-10-1088-0_23

1 Introduction

This chapter contains a revised and extended study to the research completed by Chaplin et al. [1] that was published and presented at the *World Congress for Engineering* (WCE) in London 2015.

This research is concerned with analyzing used oils from machinery and equipment by using a portable FTIR spectrophotometric analytical instrument. The work compared the results of analyzing used oils with the portable instrument to the traditional bench mounted instrument used in commercial laboratories by scientists. It was found that the same results were achieved by both instruments, hence, the portable instrument can achieve accurate results. However, on-site analysis using portable instrumentation has many benefits over laboratorial analysis. This research also identified other modern, portable, analytical instrumentation for lubrication analysis and analysed their operating principles, benefits, limitations and applications to achieve a complete on-site analysis of lubricating oils.

The drive towards increasing operational capabilities and lowering production costs is forcing organisations to improve maintenance practices. An effective maintenance program will increase production, deliver high quality products and increase profits [2]. Asset life can be increased by monitoring the lubricating substances that provide invaluable protection. Lubrication is essential for equipment efficiency. It provides a barrier for components in motion, shields from thermal effects, protects against oxidation and contamination, limits deterioration and removes unwanted particles from the system [3]. There are many places oil is used as a lubricant and oil will inevitably degrade over time, thereby reducing its effectiveness as it is exposed to internal and external contaminants that reduce the oils life-span [4]. Viscosity of a lubricating substance is a measure of the oils ability to resist flow and an effective lubricating substance requires a certain specified viscosity [5, 6].

In the manufacturing and production industries, machines are high value assets and routine oil analysis protects their value while avoiding expensive repairs [7]. Oil analysis is used to positively influence a maintenance program, to avoid failures and to increase plant availability [6]. The increasing complexity of fluids requires a large number of analytical procedures for a complete analysis. These techniques may include the analysis of wear particles, chemical degradation, viscosity, contamination and additive depletion [8].

Wear particle testing involves extracting a sample of the lubricant from the machine or engine and studying the particle content of the oil. It provides invaluable information about component particle displacement caused by the erosion of surfaces in contact from which the reason for failure can be identified [9]. The analysis also involves studying the particles contour, structure, magnitude and quantity. A comprehensive analysis using spectroscopy, microscopy and ferrography examines the debris and can provide a detailed analysis of the oil sample. Wear debris analysis can be an effective method of identifying component failure at an early stage [10].

Oil analysis by FTIR spectrometry can identify Total Base Number (TBN), Total Acid Number (TAN), contamination in the oil, chemical degradation in the oil and additive depletion in the oil [4].

Procedures are traditionally carried out by a scientist in commercial laboratories using large bench mounted instruments. These procedures can delay the response time for maintenance personnel. However, recent developments of portable analytical instrumentation have created the scenario whereby maintenance personnel are conducting on-site analysis. The portable instrumentation is required to be robust and accurate.

These intelligent tools have provided the means to increase production and reliability, eliminating detrimental plant failures [3]. In this study, experienced maintenance personnel from industry are trained to perform oil analysis using a portable FTIR instrument. The maintenance personnel tested four different oil types, namely, gear oil, hydraulic oil, turbine oil and engine oil. Different parameters are measured in each oil sample and this depends on their chemical composition. The parameters the instrument is capable of measuring are oxidation, water and glycol levels, TAN levels, TBN, additive depletion, nitration, soot, and sulphur.

Oxidation (abs/mm^2) is measured by the concentration of infrared light absorbed per 0.1 mm thickness of the oil (path length). This measurement directly relates to the peak intensities measured from the difference in spectrum of the virgin oil to the used oil. This results in the oil thickening and creating a varnish formation on the surfaces of moving components and increases the acidity of the oil, which can lead to corrosion. Additives are present in the oil to prevent oxidation occurring. When these additives are fully depleted the oxidation process escalates. The use of FTIR oil analysis can identify when the additive is nearing depletion, hence indicating a need for an oil change before components begin to corrode [11]. Engine oil over time will deteriorate and operational time and exposure to high temperatures causes the oil to become oxidized. Oxidization occurs when the oil at high temperature reacts with the oxygen in the air. This affects the usefulness of the oil by reducing its viscosity and restricting its ability to reduce engine wear. Effective management of the engines condition is achieved by reducing the corrosive effects of acids in the process [12].

Water and glycol (ppm) found in oil is identified by parts per million and 1000 ppm is 0.1 % of water in the oil. Water contamination requires urgent attention and signals that a large problem has been identified. Water found in an oil sample can be a result of condensation, which can assist machine wear and significantly reduces the life of the oil. Regular monitoring of the oil is required to detect the presence of water in the oil and prolongs the life of the oil [13].

TAN (mg KOH/g) is a measurement of the remaining life of the oil. It is determined by the amount of potassium hydroxide (KOH) base required to neutralize the acid in one gram of an oil sample and the standard unit of measure is mg KOH/g. A direct comparison of the acidic level of the used oil to an unused sample will indicate its suitability for additional use and the increasing presence of acids in oil will advance the corrosion rate of metallic parts. Unused oil has suitable levels

of antioxidant and a low TAN value. During operation the oil degrades reducing the antioxidant capabilities and increasing the Tan value [14].

TBN (mg KOH/g) is a measure of the amount of base in the oil and is measured by the amount of Potassium Hydroxide (KOH) in milligrams it takes to neutralise the base reserve (additive in the oil to neutralise any acids forming) in 1 g of oil. If the oil is to be subjected to large amounts of acidic compounds during operation, then there is a requirement for the oil to have a high TBN value [12]. The measurement of TBN provides vital information that can be used to reduce wear or failures while increasing the mechanical integrity of the equipment.

Additive depletion (%), additives are incorporated in oil to help the oil withstand a wide range of harsh environments and the chosen additives for oil depend on the oils application. Common additives are anti-oxidant, anti-wear, friction modifier, anti-foam and pour point depressant additives [15]. During an engine's use these additives deplete over time. Monitoring the depletion of additives can be an early indication of a forthcoming oil failure. Anti-wear additives are most commonly used to prevent the wear of components that are in contact and also in motion [4].

Nitration (abs/mm^2) occurs from the reaction of the oil to nitrogen oxides produced from the oxidation of atmospheric nitrogen during the combustion process. It is measured by the concentration of infrared light absorbed per 0.1 mm thickness of the oil (path length). This measurement directly relates to the peak intensities measured from the difference in spectrums between the virgin and used oil. Nitration is similar to oxidation, it also causes the oil to thicken and produce a varnish formation on the surface of the components in the engine. High levels of nitration can indicate an incorrect air to fuel mix in the combustion process, incorrect timing of spark plugs, excessive loads and low operating temperatures [16].

Soot (wt%) found in engine oil is a by-product of a partial combustion process of the engine and oil has the ability to tolerate large amounts of soot. The amount of fuel soot detected is reported as % weight. By monitoring oil samples over time it is possible to identify a large increase in soot in the oil. An increased level of soot may indicate an incorrect mix of the ratio of fuel to air in the engine. This could be caused by clogged air filters reducing the flow of air to the combustion chamber. A high level of soot may also signal that the oil has not been changed in a long time and the oil change is overdue [17].

Sulphur (abs/mm^2) in lubricating oil develops when by-products of the combustion process enter the crank case where the lubricating oil is located. Acidic levels in the oil increase and escalates corrosion. This is measured by the concentration of infrared light absorbed per 0.1 mm thickness of the oil (path length).

Research has shown that a complete portable oil analysis program can be incorporated into a maintenance program [18]. However, the results displayed from these instruments are displayed in very scientific terms and are difficult to decipher for maintenance personnel to identify specific maintenance actions. Chaplin et al. [19] has described a knowledge deficit in maintenance training regimes. The course of this research aims to identify if knowledgeable and qualified maintenance

personnel possess the skillset to use a portable analytical instrument and then to accurately identify specific maintenance actions for these results.

The outcomes of this study can assist maintenance training bodies improve their courses. The next section describes how it was determined if maintenance personnel possess these skills.

2 Case Study

Oil samples were supplied by industry for testing. This section outlines what facilities provided the oil samples, what industries the maintenance personnel that carried out the testing are from, the instrument used for testing, how the pre-defined alarm limits are set for lubricants and the SOP followed during the testing is also outlined.

2.1 Oil Sampling

Oil samples were provided by local industries from machines and engines. The industrial partners were a Bauxite processing facility in Limerick, Ireland, a maintenance repair facility that overhauls large jet-transport aircrafts in Shannon, Co. Clare, Ireland and a car servicing facility based in Limerick, Ireland. The oil samples varied between 50 and 100 ml and were extracted onsite using an in-line vacuum pump. This method eliminates any dust particles from the surrounding environment from entering the sampling bottle. A polyurethane tube is placed in a position where there is a turbulent flow of oil. This means the oil sample that is extracted is from a position where the oil is operational and not at the bottom of a sump or reservoir where contaminants are prevalent.

2.2 Portable Oil Analysis

A FluidScan Q1000 portable oil analyser as presented in Fig. 1 was used for testing the used oils. The portable instrument uses mathematical algorithms to process the data from a graph of the analysis to produce quantitative results that can be used to identify any contaminants in the oil [4, 20]. The portable instrument delivers an instant fluid condition assessment based on ASTM Standard E2412 (Standard Practice for Condition Monitoring of In-Service Lubricants by Trend Analysis Using FTIR Spectrometry). The results produced are in text format and this removes the skills of deciphering complex graphs of absorbance against wavenumbers that bench mounted instruments produce. A sample of one of the results for engine oil obtained during testing is shown in Table 1.

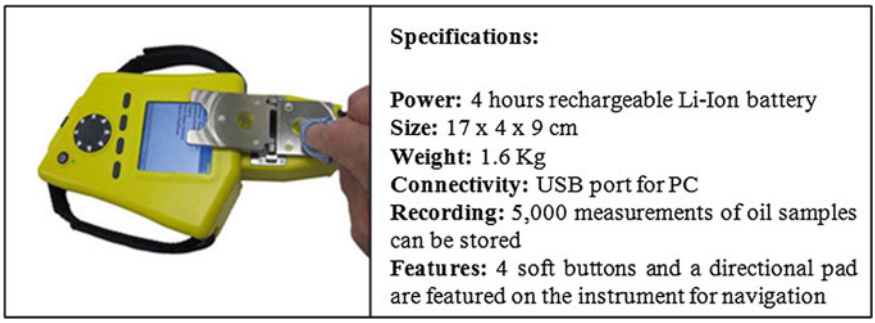

Fig. 1 Portable oil analysis instrument used for testing

2.3 *Alarm Limits for Each Parameter on the Portable Instrument*

Each lubricant selected for the testing process has set pre-defined alarm limits that are obtained from the lubricants technical specifications, *Owner Equipment Manuals* (OEM) and are tested in accordance to *American Society of Testing and Materials* (ASTM) test methods. These predefined alarm limits consist of a warning limit and a maximum limit and have a colored traffic light system. These alarm limits are presented in Table 1. If the parameter is highlighted in bold, it has exceeded the warning alarm limit and indicates the oil is nearing it the end of its useful life. If the parameter is highlighted in italic it indicates the oil has exceeded its useful life and that a particular parameter exceeds the maximum limit. When the parameter is highlighted in italic, the oil must be replaced. Equipment will eventually fail if it is continued to be used without the oil being replaced. This practice can lead to expensive maintenance correction and long periods of downtime.

The recording of oil analysis results for the same engine or machine over time can be beneficial to a maintenance program. This historical trending can provide graphical representations identifying parameters creeping towards a specified alarm limit. This practice can identify potential failures at an early stage.

2.4 *Performing the Oil Analysis Using the SOP*

During the testing a SOP was followed to ensure each participant analyses the oils in the same way for repeatable results. The standard operating sequence followed by the maintenance personnel for analysing used oil is outlined using an eighteen step procedure. This SOP was developed during testing and is specific to the "FluidScan" Q1100 model, portable FTIR used oil analyser for analyzing engine oil.

Table 1 Pre-defined alarm limits for engine oil

Parameters								
	Anti-wear additive (%)	Glycol (%)	Nitration (abs/mm^2)	Oxidation (abs/mm^2)	Soot (wt%)	Sulfation (abs/mm^2)	TBN (mg KOH/g)	Water (ppm)
Lower limit	40	0	0	0	0	0	8.5	0
Lower warn limit	60	0	0	0	0	0	9.5	0
Upper warn limit	0	2	0	30	2	35	0	2000
Upper limit	0	3	30	40	3	45	0	3000
Actual result	**56**	***0.3***	***14.4***	***24.8***	***0.08***	***27.9***	*0*	**2419**

2.4.1 Standard Operating Procedure

1. Select "Take Measurement" by pressing the select button from the main menu.
2. Select measure fluid by using the up/down button to highlight the required function, and then press the select button when "measure fluid" is highlighted.
3. As the unit has just been powered up, a background measurement must be performed. Press "OK".
4. The instrument will then check if the cell is dirty, as it has been powered up, it assumes the cell is dirty and you must open the cell and clean it. Close the cell and press OK.
5. The instrument knows you have cleaned the cell and it will initiate a background measurement.
6. When the background measurement is complete, press OK.
7. Highlight the fluid family the oil to be tested is in (e.g. Petroleum Gear) by using the up/down cursor and press "next".
8. Highlight the oil that you are testing and select "next" (e.g. Castrol Alpha SP 150).
9. Put in a sample ID for tracking use only (e.g. #3) by selecting "edit" and using the keyboard display on the instrument, press "select" for the desired characters when they are highlighted and press "done" when the sample ID has been complete.
10. Press next to continue the testing.
11. The instrument will then ask you to "Place sample in cell". Open the cell, place 1 ml of used oil on the cell, do a visual inspection of the sample after closing the cell and ensure there are no bubbles present.
12. Press ok to begin the measurement of the sample (takes about 90 s).
13. On screen you will see "Please wait, analysing results".
14. The results for the measurement of the sample will be displayed on the screen. If the measured parameter is bold italic, it is inside the pre-defined alarm limits and the oil is OK to be continued to be used. If the parameter is bold, this signals a warning that the parameter is nearing the pre-defined limit for use; it

signals that the oil should be monitored more closely and is nearing the end of its useful life. If the parameter is italic, then the parameter has exceeded the pre-defined alarm limit and the oil should be changed.
15. Press save to store the results for further use.
16. "Save is complete, Click OK to continue" will appear, press "OK".
17. This will end the measurement of the current sample and the instrument is now ready for the next measurement.
18. If this is the end of testing, the cell must be thoroughly cleaned before pressing the power button to turn off the instrument.

The selected maintenance personnel required further training as they struggled to use the results from the testing to identify maintenance actions.

Therefore, a training specification was developed and it included a training aim, training objectives, training duration, training approach, record system, assessment system and a review of process post training activities. The training specification outlined that one full training day was required. From the training specification a training schedule and its contents were developed. This included a PowerPoint presentation detailing an introduction and safety for analysing used oils, a background on the practice of oil analysis and its benefits, the technical specifications for the analytical instrumentation, spectrometry, lubricant composition, oil sampling, lubricant application and lubricant degradation.

A comprehensive document was then created titled "*Procedure for interpreting oil analysis results for identifying maintenance actions in a maintenance program*". This document included instructions for maintenance personnel on how to select maintenance actions for exceeded parameters from the oil analysis and it also detailed the effects of using degraded lubricants. These instructions can be seen in Tables 2 and 3 for engine oil.

During this training the participants were exposed to a practical demonstration on how to use the instrument and interpret the results. Each participant then performed an oil analysis using the instrument and the procedure to interpret the results. The participants were assessed post training. When the training session was complete, the training was evaluated by means of interviewing the participants.

2.5 Selecting Maintenance Personnel from Industry

Experienced maintenance personnel were selected from industry to establish if the current knowledge for maintenance technicians could successfully perform an oil analysis using the instrument and from the results identify maintenance actions. Nine maintenance personnel from various industries participated in the research. These industries include an organization that builds bespoke electro-pneumatic automated machinery, companies involved in the overhaul of jet engines, a car servicing facility and production facilities in the medical devices sector. The maintenance personnel all work in a maintenance department, carrying out any

Table 2 Maintenance actions for exceeded parameters in engine oil

Measured parameter	Maintenance actions for exceeded parameters
Oxidation	– Check the engine for overheating as this causes oxidation – Check the condition of the oil pump as oxidation produces sludge in the oil that is hard to pump – Check engine for high pressures as this leads to oxidation – Check the engine oil for wear debris as this could cause agitation and promote oxidation – Check the engine for coolant leaks as coolant in the oil accelerates oxidation
Anti-wear additive	– Check engine for overheating and an increase in pressure – Check engine for wear – Check the combustion process
Soot	– Check the combustion process – Check the mix of the ratio of fuel to air in the combustion process – Check if the air filters are clogged – Check if the oil change is overdue – Check has the engine low operating revolutions – Check if there is a restriction in the intake and exhaust systems – Check the functionality of the turbochargers
Nitration	– Check the mix of the ratio of fuel to air in the combustion process – Check the timing of the spark plugs – Check the engine for excessive loads – Check for abnormal "blow by" past the compression rings – Check the engine for overheating, this may cause thermal breakdown in the oil – Check the engine for air leaks that may cause excessive aeration
Water	– Check the engine for condensation – Check the engine for a leak in the coolant system
Sulfation	– Check the engine for a leak in the coolant system
Glycol	– Check the combustion process – Check the mix of the ratio of fuel to air in the combustion process
Total base number (TBN)	– Additive depletion reduces the amount of base material in the oil

required maintenance operations. The personnel have a range of qualifications such as vocational and undergraduate engineering training. Oil analysis was performed on 5 samples by the maintenance personnel. These results are presented in Table 4.

The results of testing the used oils for four different types of oil were obtained during the testing. However, this study only displays the results for testing engine oil. Each oil sample that was tested has a color coded result for each parameter as described earlier in this section. Table 2 presents a list of maintenance actions for the results from the engine oil analysis and Table 3 presents the effects of using the contaminated engine oil for prolonged periods.

Table 3 The effects of degraded engine oil in a system

Measured parameter	Effects when alarm limits are exceeded
Oxidation (abs/mm^2)	– Increased oil viscosity – Filters can be clogged – Engine overheats – Engine performance is effected – Metal parts corrode – Sludge deposits form – Increased wear
AW additive (%)	– Operating temperature increase – Increased engine wear – Varnish formation – Soot build up on components – Corrosion – Poor lubrication
Soot (0.05 wt%)	– Increased viscosity – High operating temperature – Loss of engine performance – Soot build-up on components – Excessive emissions
Nitration (abs/mm^2)	– Cylinders can start sticking – Carbon deposit build-up – Increases wear metal corrosion – Increased viscosity of oil
Water (ppm)	– Loss of engine power – Metal corrosion – High levels of wear metals – Coolant loss in engine – Lubricant can appear milky in colour – Engine overheating
Sulfation (abs/mm^2)	– Deposits are formed from corrosion – Sludge and varnish forms on the components in the engine – Lubricant rapidly degrades – Corrosion
Glycol (%)	– Engine failure – High viscosity – Poor lubrication – Corrosion – Engine overheating – Acid formation – Reduced additive effectiveness
TBN (mg KOH/g)	– Corrosion – Additive depletion in oil – Oil life is reduced – Engine performance is effected

3 Discussion

As presented in Table 4, four oil samples tested parameters show an abnormality. All participants were asked to identify a maintenance action for each parameter if it had exceeded its pre-defined alarm limit and hence has displayed a red light. During this initial phase of testing with the qualified and experienced maintenance personnel, it was found that none of the participants could successfully use the results from the testing to successfully identify a maintenance action. Therefore a framework was created to help identify specific maintenance actions depending on the parameter exceeded for each oil type. The potential causes and effects of exceeded parameters are tabled in this section and were achieved through both primary and secondary research methods. These tables identify how the results of analysing used oil with a portable FTIR instrument can be used to identify maintenance actions. Expert and experienced machinery lubricant analysts in a commercial laboratory that was visited during the research provided information on how to use the results obtained from FTIR analysis for a maintenance program. The researcher also obtained knowledge for the development of the tables during the training attended to become a certified machinery lubricant analyst. Furthermore, the research conducted during the literature review helped towards the development of the tables. The type of oil that was tested must be known for correct interpretation of the results from the oil analysis. After each participant completed the training, a training evaluation was performed by means of interviews. It was found that by using the Tables 2 and 3 during the training each participant could successfully identify a specific maintenance action for the results of the oil analysis. These results are discussed in the next section.

Portable instrumentation for maintenance application provides an opportunity for on-site analysis of assets in real time. Quick and reliable maintenance decisions can enhance a maintenance program. Recent research by Chaplin et al. has identified that the traditional practice of analyzing lubricants in a commercial laboratory by scientists can be achieved on-site using portable instrumentation. This practice is currently being performed by maintenance personnel such as fitters and maintenance engineers.

Table 4 Oil analysis results for engine oil

Parameters								
No.	Anti-wear additive (%)	Glycol (%)	Nitration (abs/mm^2)	Oxidation (abs/mm^2)	Soot (wt%)	Sulfation (abs/mm^2)	TBN (mg KOH/g)	Water (ppm)
1	**56**	***0.3***	***14.4***	***24.8***	***0.08***	***27.9***	*0*	**2419**
2	***35***	***0.6***	***12.2***	*42.1*	***1.1***	***15.6***	***6.0***	***1232***
3	***23***	**2.1**	***9.4***	***18.4***	***1.4***	***12.9***	***5.4***	***1344***
4	***11***	***0.1***	***18.0***	***24.5***	***0.05***	***33.7***	***8.1***	***988***
5	*66*	***0.3***	***4.2***	***30.3***	***0.08***	***8.9***	***7.9***	***448***

Suitable, experienced and qualified maintenance personnel were selected from industry to carry out testing using one such portable instrument for analyzing lubricants, namely, a FTIR oil analyser. It was found that the participants during testing could successfully follow the SOP that was developed to get the results of analyzing the lubricant. However, this study has found that maintenance personnel struggled to identify any maintenance actions from the results of the testing to enhance a maintenance program. Therefore, anecdotal evidence suggests that maintenance personnel receive inadequate training to support the effective use of modern instrumentation for maintenance application. A deficiency has been identified in the training of maintenance personnel, current maintenance training regimes will need to be reviewed to ensure modern technological advancements are included to equip maintenance personnel with the necessary skills for current maintenance application.

The participants found using the instrument was relatively easy, therefore the training for using the instrument could be at vocational training level. The participants found interpretation of the results very difficult without adequate training. Specific training was then provided including topics such as spectrometry, lubricant composition, oil sampling, lubricant application, lubricant degradation, maintenance actions for specific exceeded parameters and the effects of using degraded lubricants. The participants were then successfully able to identify specific maintenance actions using Tables 2 and 3. Therefore, this advanced level of training could be implemented at undergraduate level in maintenance engineering training regimes. This course of research has concentrated on one portable analytical instrument, recent literature published by Chaplin et al. describes how more and more traditional laboratory practices are becoming portable. Future work can investigate the growth of portable instrumentation in terms of technology, reliability and maintenance effectiveness to identify where these practices lie within maintenance training regimes.

Tables 2 and 3 identify specific maintenance actions and effects when a measured parameter has exceeded a pre-defined alarm limit and this can benefit a maintenance department by having a controlled sequence of maintenance actions when an abnormality is identified. The maintenance activities can be carried out in an efficient and timely way to ensure the availability and reliability of plant is achieved. Staff turnovers can be problematic as knowledge is often lost. By adhering to the framework created during this study, this problem is minimised as the appropriate maintenance and actions are listed. The associated costs and plant downtime with errors made by new staff is therefore minimised. As trending of used oils in industry is achieved, the Tables can be adjusted to correlate with the data acquired. Prioritisation of maintenance actions can also be achieved.

4 Conclusion and Further Work

4.1 Conclusion

Manufactures of analytical instrumentation have provided the markets with a range of portable instruments for a complete on-site oil analysis program within a maintenance program. While laboratory measurements of oils are mature and robust, there can be several delays involved in getting the oil sample to the laboratory. Often, plant, equipment and machines can be located in remote and harsh environments. Breakdowns and equipment failures can be very costly. Portable instrumentation has many benefits when compared to laboratorial practices including quicker decision making and associated economic cost saving benefits. Traditionally the analysis in commercial laboratories is performed by highly skilled and knowledgeable scientists. The portability of these instruments results in maintenance personnel conducting the analysis with little or no training to support such practices. It was found during this study that the current knowledge set for qualified and experience maintenance personnel is inadequate for the practice of using modern, portable analytical instrumentation.

This study has provided maintenance personnel with adequate training to successfully use a portable instrument for maintenance application and to successfully use the results from the testing to enhance a maintenance program. Comprehensive training is required for maintenance personnel to support the effective use of portable instrumentation. An absence of good maintenance practices and not maintenance itself increases revenue expenditure. Good maintenance practices require adequate levels of training. If current maintenance training regimes are not reviewed, the deficit between adequate maintenance activities and plant efficiency will continue to widen as levels of technological advancement increase. This information can positively impact a maintenance department and assist in protecting organisations valuable assets. The deficits can be improved, but instant action is required to reduce the widening gap of what industry requires and what education produces.

4.2 Further Work

Further research is proposed to investigate the development and growth in portable instrumentation, techniques and onsite analysis in terms of technology, reliability and maintenance effectiveness. This can be achieved by conducting industrial case studies to further address the application of portable oil analysis techniques in modern maintenance programmes. Furthermore, it proposes to use these case studies to examine the limitations that exist both within industry and in the training of maintenance technicians. It also proposes to develop a framework to address these limitations.

Further work also recommends investigating current maintenance practices in Ireland and abroad in terms of the use or lack of use of portable instrumentation for on-site analysis across a variety of industries. This investigation can identify what industries are most suited to the use of portable instrumentation. Furthermore, research to develop and assess a training framework can be carried out to effectively to allow for portable oil analysis techniques and instrumentation to be successfully deployed by technicians as part of a predictive maintenance programme. A review of the impact of the trained engineers has on a predictive maintenance program will then been carried out. This work is important for the training of future maintenance engineers to attain all the necessary knowledge for the field within they are submerged. The results of this research can be used by academic bodies for revising current training courses.

Acknowledgments The author wishes to express gratitude to the Industry partners that assisted the research by providing used oil samples for testing and to the ACORN research Centre for providing analytical instrumentation for the research. The author also wishes to express gratitude to the Limerick Institute of Technology for funding this research through its Graduate Office Bursary (GRO) bursary.

References

1. Chaplin A, Hardiman F, Naughton D (2015) Portable lubrication analytical instrumentation for maintenance application. In: Lecture notes in engineering and computer science: proceedings of the world congress on engineering 2015, WCE 2015, 1–3 July 2015, London, UK, pp 746–751
2. Al-Najjar B (2007) The lack of maintenance and not maintenance which costs: a model to describe and quantify the impact of vibration-based maintenance on company's business. Int J Prod Econ 107(1):260–273
3. Mobley RK (2002) Plant engineering: an introduction to predictive maintenance, 2nd edn. Butterworth-Heinemann, Burlington
4. PerkinElmer (2011) Raising the bar in FT-IR: getting the most out of on-site oil condition monitoring. Lube Magazine
5. Zięba-Palus J, Kościelniak P (1999) Differentiation of motor oils by infrared spectroscopy and elemental analysis for criminalistic purposes. J Mol Struct 482–483:533–538
6. Kahandawala MSP, Graham JL, Sidhu SS (2004) Impact of lubricating oil on particulates formed during combustion of diesel fuel—a shock tube study. Fuel 83(13):1829–1835
7. PerkinElmer (2002) The JOAP method for oil condition monitoring. Available from http://shop.perkinelmer.com/content/applicationnotes/app_oilexpress-joap-method.pdf
8. Kim Y et al (2013) Classification and individualization of used engine oils using elemental composition and discriminant analysis. Forensic Sci Int 230(1):58–67
9. Pouzar M, Černohorský T, Krejčová A (2001) Determination of metals in lubricating oils by X-ray fluorescence spectrometry. Talanta 54(5):829–835
10. Macián V et al (2003) Analytical approach to wear rate determination for internal combustion engine condition monitoring based on oil analysis. Tribol Int 36(10):771–776
11. Guan L et al (2011) Application of dielectric spectroscopy for engine lubricating oil degradation monitoring. Sens Actuators, A 168(1):22–29
12. Lakshminarayanan PA, Nayak NS (2011) Critical component wear in heavy duty engines. Wiley, Hoboken

13. Ng E-P, Mintova S (2011) Quantitative moisture measurements in lubricating oils by FTIR spectroscopy combined with solvent extraction approach. Microchem J 98(2):177–185
14. Adams MJ, Romeo MJ, Rawson P (2007) FTIR analysis and monitoring of synthetic aviation engine oils. Talanta 73(4):629–634
15. Nassar AM et al (2016) Synthesis and utilization of non-metallic detergent/dispersant and antioxidant additives for lubricating engine oil. Tribol Int 93(Part A):297–305
16. Kral J Jr et al (2014) Degradation and chemical change of long life oils following intensive use in automobile engines. Measurement 50(34–42):34–42
17. Spikes H (2001) Tribology research in the twenty-first century. Tribol Int 34(12):789–799
18. Toms A, Toms L (2010) Oil analysis and condition monitoring, in chemistry and technology of lubricants. In: Mortier RM, Fox MF, Orszulik ST (eds) Springer, The Netherlands, pp 459–495
19. Chaplin A, Hardiman F, Naughton D (2014) A critical analysis of maintenance training regimes for an industrialised economy. Int J Eng Manage Econ 4(3/4):249–266
20. Kaur H (2009) Spectroscopy. Pragati Prakashan, Meerut

A Mathematical Model of Integrated Production-Inventory-Distribution System for Billet Steel Manufacturing

Parwadi Moengin

Abstract A significant phase of billet steel manufacturing is the cooling process. This phase may be completed in the finished goods warehouse and it must meet both production optimization and customer needs. The fluctuation of customer demand and production process in this phase may cause some problems of production schedule and inventory of billet steel. The decreasing of customer demand can increase the inventory level in finished goods warehouse. Therefore, the company need to consider a production planning that gives an optimum decision of billet steel production schedule. In this paper, a mathematical model of integrated production-inventory-distribution system of billet steel will be proposed. The model is used to find the optimal production schedule of billet steel, based on the relevant parameters of the productive system, such as: set-up time, processing times, and demand profile. The study is completed by a case study to investigate the proposed model.

Keywords Billet steel production · Integrated system · Linear programming · Mathematical model · Production-inventory-distribution system · Scheduling

1 Introduction

This paper discusses the optimal method of production scheduling in billet steel products ordered by consumers considering the limitations of space in the warehouse. Fluctuations in consumer demand can be considered as one of the causes of some problems in the production and supply company. Increased demand led to problems concerning storage capacity cooling billet steel products and raw material supply of iron ore. Decline in demand cause overproduction and excessive accumulation of finished goods. This poses particular problems in the cooling

P. Moengin (✉)
Faculty of Industrial Technology, Department of Industrial Engineering,
Trisakti University, Jl. Kyai Tapa No. 1, Jakarta 11440, Indonesia
e-mail: parwadi@trisakti.ac.id

S.-I. Ao et al. (eds.), *Transactions on Engineering Technologies*,
DOI 10.1007/978-981-10-1088-0_24

warehouse capacity of billet steel products. Observing this, companies need to consider the production planning so that activities are carried out more optimal production to meet market demand. Production planning concerns the tactical planning provides optimum decisions based on the availability of time and the capacity of the company's inventory to overcome problems related to the production process.

Utilization of mathematical model for the optimization of production, especially the production of billet steels has been done by many researchers, including Chen and Wang [1] which uses linear programming models for production planning and distribution of steel, Kapusinski and Tayur [3] model the production system limited to periodic demand and Kalagnanam et al. [2] addressed the issue of excess inventory in the process industry.

Several other authors such as Lally et al. [4] have made a model of sequencing a continuous casting operation in order to minimize costs, Mohanty and Singh [6] using a hierarchical approach to planning system steel manufacturing, Tang et al. [7] using a mathematical programming model for scheduling the production of continuous casting of steel and Tang et al. [8, 9] have discussed the problem of production planning and scheduling using Lagrange relaxation. Zanoni and Zavanella [11] discuss the optimization of the production system of billet steel products.

According to Tang et al. [8], the following approaches have been adopted to build a production plan in steel:

- Operational Research/OR;
- Artificial Intelligence/AI:
  - Expert Systems;
  - Intelligent search methods, such as Genetic Algorithm/GA, SA (Simulated Annealing) and TS (Tabu Search);
  - Constraint satisfaction;
- Human–machine coordination methods;
- Multi Agent methods.

In general, the billet steel production process starting from (1) the process of melting and cooking through the stages: filling and blending sponge iron, iron and hot scrap bracket iron in the bucket; smelting in the Electric Arc Furnace; Oxidation processes Refining and Electric Arc Furnace; (2) Ladle Refining Furnace process on, and ends with (3) a process in Continuous Casting Machine.

Schematic representation of billet steel manufacturing shown in the following Fig. 1.

This paper is structured as follows. Writing begins from the introduction that discusses the optimization of production associated with distribution, scheduling and inventory that has been done by some previous authors; followed by the proposal of a model of integer linear programming for integrated production-inventory-distribution systems of billet steel products. A case study in PT. XYZ is used to apply the proposed model.

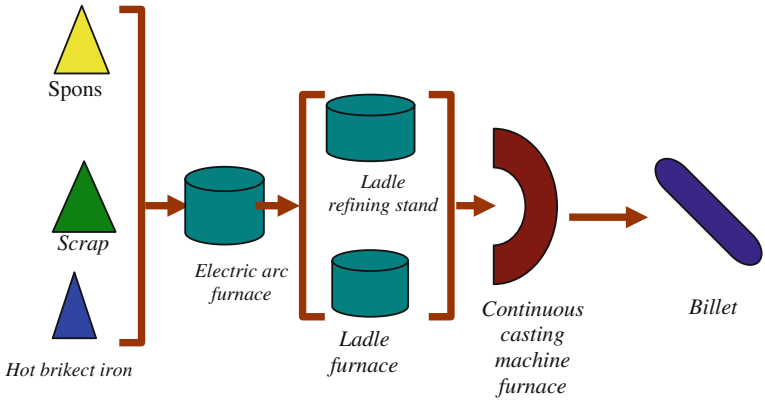

Fig. 1 Billet steel production process [10]

2 Model Formulation for Integrated Production-Inventory-Distribution System

The model is formulated to focus on the optimization of production planning, i.e. the amount of production in the planning horizon. The mathematical model is focused on sustainable production, where finished goods warehouse capacity becomes an important part in the production cycle. To solve this problem, an integer linear programming models is introduced by taking into account the capacity of finished goods warehouse in continuous production planning.

In continuous production, initially satisfied the market demand of finished goods inventory in the warehouse, then just do the next planning to meet the rest of the reservation. In this case the integer linear programming models are used, has a goal to maximize profits at the end of the sale of products incorporating the costs saved in the finished goods warehouse, and also pay attention to the cost penalty as the costs incurred because the manufacturer cannot meet the market reservations on time.

Basically the integer linear programming model of this paper, consider three kinds of costs, namely:

- Saving costs, these costs directly affect the final profit of the company, according to the duration of storage of finished products in the finished goods warehouse.
- Production costs (which is one of its components is a set up cost)
- Penalty cost, as ‘fine’ company being unable to meet market reservations on time.

Model of integrated production-inventory-distribution systems is formulated with respect to some constraints, i.e. the production time, the quantity of products in the warehouse, production planning period, the suitability of the products sold by the products ordered in the planning, the quantity of product sales, and warehouse capacity. Decision variables of the model is the number of products to be produced, the number of products available in the warehouse, the number of products are delivered to consumers each period, as well as the decision whether or not to produce billet steel in the planned time period.

The following are the parameters of the mathematical model of integer linear programming for continuous production planning [5]:

n the number of product type
m planning time period (in months/weeks/days)
i index of product ($i = 1,\ldots, n$)
j index of time ($j = 1,\ldots, m$)
h production planning in the future (12 months)
s_i surface area product type i
NBC_i maximum production capacity of product type i
Pt required production time
$\mathrm{H_d}$ available production time (=28 days/month for 12 months/year)
$\mathrm{I_c}$ holding cost per print products per day
$\mathrm{P_r}$ average profit per mold products
St average *set up* time at machine EAF
O_{ij} demand quantity of product i in period j
L_{Inv} length of warehouse
$\mathrm{I_{O}}i$ initial inventory in the warehouse of product i
M large numbers (been greater than the amount of product that can be produced per period)
aux_i auxiliary variable that represents how much space is required to store the products i
C_s penalty cost per unit for late delivery in quarter s ($s = 1, 2, 3, 4$)
P_{ij} decision variables, the number of product i produced in the period j
I_{ij} decision variables, the number of products available in the cooling warehouse during the period j
S_{ij} decision variables, the number of products i are delivered to customers in the period j
y_{ij} binary decision variable (set up machine EAF to produce billet tiper i in period j)

$$y_{ij} = \begin{cases} 1, & \text{if produce product } i \text{ at period } j \\ 0, & \text{otherwise} \end{cases}$$

The following is the formulation of the model for production-inventory-distribution system:

Maximize:

$$Z = \Bigg[\sum_{i=1}^{n} \sum_{j=1}^{m} (P_r.S_{ij} - I_{ij}.I_c.H_d) - C_1. \sum_{i=1}^{n} \sum_{j=1}^{\frac{h}{4}} \left(O_{ij} - S_{ij}\right) - C_2. \sum_{i=1}^{n} \sum_{j=\frac{h}{4}+1}^{\frac{h}{2}} \left(O_{ij} - S_{ij}\right) - C_3. \sum_{i=1}^{n} \sum_{j=\frac{h}{2}+1}^{\frac{3h}{4}} \left(O_{ij} - S_{ij}\right) - C_4. \sum_{i=1}^{n} \sum_{j=\frac{3h}{4}+1}^{h} \left(O_{ij} - S_{ij}\right) \Bigg]$$

subject to:

$$\sum_{i=1}^{n} \left[\mathrm{Pt}.P_{ij} + \mathrm{St.y_{ij}} \right] \leq \mathrm{Hd}, \quad \forall j = 1, \ldots, m \tag{1}$$

$$I_{i1} = \mathrm{Io}_i + P_{i1} - S_{i1}, \quad \forall i = 1, \ldots, n \tag{2}$$

$$I_{ij} = I_{i,j-1} + P_{ij} - S_{ij}, \quad \forall i = 1, \ldots, n, \quad j = 2, \ldots, m \tag{3}$$

$$\sum_{j=1}^{h} P_{ij} = \sum_{j=1}^{h} \left(O_{ij} - \mathrm{Io}_i\right), \quad \forall i = 1, \ldots, n \tag{4}$$

$$\sum_{j=1}^{h} S_{ij} = \sum_{j=1}^{h} O_{ij}, \quad \forall i = 1, \ldots, n \tag{5}$$

$$\sum_{d=1}^{j-1} S_{id} \leq \sum_{d=1}^{j-1} O_{id}, \quad \forall i = 1, \ldots, n, \quad j = 2, \ldots, m \tag{6}$$

$$P_{ij} \leq M y_{ij}, \quad \forall i = 1, \ldots, n, \quad j = 1, \ldots m \tag{7}$$

$$\sum_{i=1}^{n} I_{ij}.s_i.\mathrm{NBC}_i.\mathrm{aux}_i \leq L_{Inv}, \quad \forall_j = 1, \ldots, m \tag{8}$$

$$P_{ij}, I_{ij}, S_{ij} \geq 0 \,\text{integer}, \quad y_{ij} \in \{0, 1\} \tag{9}$$

This model involves one goal and nine constraints. The objective function is to maximize the profit from the selling of billet steel by taking into account the inventory cost, production cost and penalty cost. In the models, the average profit per mold product (P_r) represents the difference between the selling price per unit of the product with the production cost. In the objective function is assumed also that the number of delivered product shall not exceed the amount of the requested product, so that $O_{ij} - S_{ij} \geq 0$. The nine constraints considered in the model are (1) describe the available production time of each month (the sum of the set-up time and the time of production must be less than one month), (2) and (3) the quantity of products in the warehouse based on the type and month, (4) the amount of production in the planning period (the difference between the amount of demand for products in the same period the number of initial inventory of products in the warehouse), (5) demonstrate the suitability of the products sold by the products ordered in the planning, (6) guarantee the quantity of products sold up to a period of months-d (d = 1,…, H) less than or equal to the quantity to be delivered, (7) ensure that the model is linear binary variable y_{ij} allocated, as well as barrier (8) the capacity of the warehouse, where the products are stored for refrigerated warehouse cannot exceed available capacity. Constraint (9) is limiting for the decision variables.

3 Solution of the Model

In the specific industrial case considered, the linear model proposed (Sect. 2) requires 144 variables and 159 constraints. It was implemented and solved by Excel Solver. The output gives:

1. The number of product *i* produced in the period *j*
2. The number of products available in the cooling warehouse during the period *j*
3. The number of products *i* are delivered to customers in the period *j*
4. Set up machine EAF to produce billet tiper *i* in period *j*.

The planning horizon (12 months) may be easily modified. As usual, computational time is a strategic parameter to be considered in evaluating the performance of the model. Simple cases are solved in a few seconds. On the other hand, if the set of orders uses up most of the available capacity, the solution procedure may find difficulty in quickly identifying a feasible solution, thus the computational effort may take several hours.

It should be emphasized that the number of stack layers (indirectly, the cooling time of stacks) should be a decisional variable. Such a formulation adds to the model complexity and the consequent computational time. The result of various experiments are presented to show the behavior of the model and to introduce an efficient solving heuristic.

4 Case Study

Here is presented a case study on PT. XYZ to implement the proposed model. PT. XYZ is an integrated steel industry in Indonesia with a production capacity of 2.5 million tons of crude steel per year. PT. XYZ produces various kinds of products according to customer demand. The resulting product is a sponge iron, steel slab, billet steel, hot rolled coils, cold rolled steel, and wire rod. In this paper focused on the production of billet steels which consists of three types, namely billet steel 110, billet steels 120 and billet steel 130. This paper presents an attempt to optimize the production planning process cooling products ranging from billet steel to billet steel product deliveries to customers by taking into account the limited capacity of finished goods warehouse. The data needed is a billet of steel product sales data for the two previous years are used to forecast the demand for billet steel products in the coming year, the data amount of the initial inventory of finished goods in the warehouse, inventory cost data, the cost penalty, the average profit per year, wide warehouse, set up time and production capacity.

Here is a Table 1 summarizing the results of forecasting demand by using three types of forecasting methods for billet steel products:

The objective of case study conducted in PT. XYZ is maximize profits from the sale of billet steels. The model is formulated involving 144 binary decision variables and 159 constraints. Therefore, the completion of the model is done with the help of software Microsoft Excel Solver. Initial inventory for all three types of billet steels each is 505 sheets, 457 sheets and 139 sheets, respectively. Table 2 is the result of the calculation of the optimal production quantities.

Table 1 The results of all three types of demand for billet steel products

Month	Type of product (sheet)		
	Steel billet 110	Steel billet 120	Steel billet 130
January	1.837	2.448	15.597
February	1.763	2.350	14.969
March	1.696	2.260	14.401
April	1.641	2.187	13.931
May	1.601	2.133	13.591
June	1.579	2.104	13.404
July	1.577	2.101	13.383
August	1.594	2.124	13.529
September	1.630	2.171	13.833
October	1.681	2.240	14.274
November	1.746	2.326	14.821
December	1.818	2.423	15.438
Total	20.163	26.867	171.171

Table 2 Optimal production of billet steel

Month	Type of product (sheet)		
	Steel billet 110	Steel billet 120	Steel billet 130
January	0	1.991	15.458
February	3.379	0	14.969
March	0	4.739	1.124
April	3.053	0	16.627
May	1.885	4.320	12.995
June	0	0	19.680
July	0	4.076	15.604
August	3.180	124	16.136
September	3.200	4.300	11.940
October	1.475	2.111	15.854
November	1.907	2.326	15.207
December	1.579	2.423	15.438
Total	19.658	26.410	171.032

Table 3 Production plan of billet steel

Month	Type of product (sheet)		
	Steel billet 110	Steel billet 120	Steel billet 130
January	0.677	0.902	5.744
February	2.255	3.005	19.146
March	1.236	1.627	10.493
April	3.340	4.451	28.366
May	1.635	2.179	13.887
June	3.147	4.193	26.724
July	2.308	3.076	19.600
August	2.595	3.458	22.035
September	1.341	1.787	11.389
October	1.514	2.017	12.853
November	2.554	3.404	21.692
December	1.994	2.657	16.929
Total	24.596	32.776	208.858

From the data of the production plan in next year, we compare the results obtained by calculating the optimal production of the model. The production plan of the next year in PT. XYZ is as follows (Table 3):

Here is a graph illustrating the comparison between planned production and the optimal production is for all three types of steel. The graph in Figs. 2, 3 and 4 shows that the production plans of billet steel PT. XYZ is generally greater than the results of the calculation of the mathematical integer programming model production. The possibility of excess production would lead to a buildup of inventories

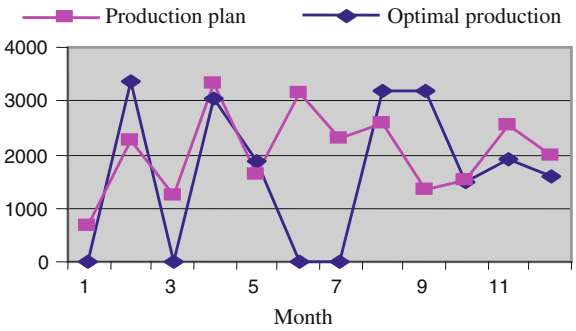

Fig. 2 Production plan and optimal production of billet steel 110

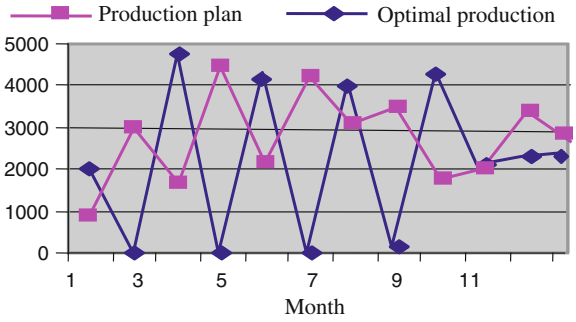

Fig. 3 Production plan and optimal production of billet steel 120

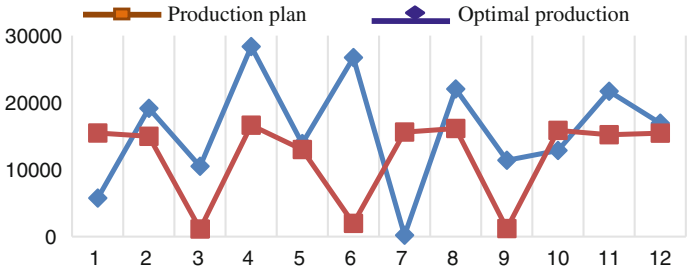

Fig. 4 Production plan and optimal production of billet steel 130

of finished goods in the warehouse cooling. This will cause expenses, which increased storage costs, because of the possibility that the number of products shipped to consumers with unbalanced output, in which the amount of production is greater than the market demand.

Table 4 The optimal inventory of billet steel in warehouse

Month	Type of product (sheet)		
	Steel billet 110	Steel billet 120	Steel billet 130
January	0	0	0
February	284	0	0
March	284	129	22
April	0	0	0
May	284	129	0
June	284	129	22
July	0	0	0
August	0	0	0
September	284	129	22
October	78	0	0
November	237	0	0
December	0	0	0

The optimal inventory of each type of billet steel products are presented in Table 4. The results of these calculations, obtained the following results.

Table 5 describes the number of billet steel products for any type that is sent to the consumer. In January there were 505 pieces of billet delivery in the 110 even though there is no production, because there is still a beginning inventory that exceeds consumer demand.

The total number of billet steel products are shipped within one year for each species (Table 5) exactly the same as the number of products demanded by consumers (Table 1); this case shows that the model has been valid. From Table 5 also

Table 5 The number of product to be delivered

Month	Type of product		
	Steel billet 110	Steel billet 120	Steel billet 130
January	0.505	2.448	15.597
February	3.095	0	14.969
March	0	4.610	1.102
April	3.337	0.129	16.649
May	1.601	4.191	12.995
June	0	0	19.658
July	0.284	4.205	15.626
August	3.180	0.124	16.136
September	2.916	4.171	11.918
October	1.681	2.240	15.876
November	1.748	2.326	15.207
December	1.816	2.423	15.438
Total	20.163	26.867	171.171

Table 6 Decision whether or not to set up the machine EAF in each month

Month	Decision					
	Steel billet 110		Steel billet 120		Steel billet 130	
	Result	Notes	Result	Notes	Result	Notes
January	0	No set-up	1	Set-up	1	Set-up
February	1	Set-up	0	No set-up	1	Set-up
March	0	No set-up	1	Set-up	1	Set-up
April	1	Set-up	0	No set-up	1	Set-up
May	1	Set-up	1	Set-up	1	Set-up
June	0	No set-up	0	No set-up	1	Set-up
July	0	No set-up	1	Set-up	1	Set-up
August	1	Set-up	1	Set-up	1	Set-up
September	1	Set-up	1	Set-up	1	Set-up
October	1	Set-up	1	Set-up	1	Set-up
November	1	Set-up	1	Set-up	1	Set-up
December	1	Set-up	1	Set-up	1	Set-up

shows that the delivery of billet steel 110 and 120, respectively do not have to be done every month,

From the calculation, it is known that in January, March, June, and July do not need to be set-up machine EAF to produce billet steel 110, which is in line with the production of billet steel 110, which in the fourth month, do not do production for billet steel 110 in February, April, and June did not do the set-up machine EAF to produce billet steel 120, for the three months was not done for the production of billet steel 120. Based on the results over the planning horizon of twelve months, the obtained gains production of billet steel for one year is $ 113.5 million.

Table 6 describes whether or not to set up the machine EAF in each month. In January there were 505 pieces of billet 110 deliveries for the month although there is no production, because there are initial inventory that exceeds consumer demand.

Table 6 are in accordance with Table 2, which describes when performed sets up the machine EAF to produce steel billets per month. The total amount of billet steel products shipped in one year for each type (Table 5) exactly the same as the number of products demanded by consumers (Table 1); this indicates that the model was valid. From Table 5 also shows that the delivery of steel billet 110 and 120 do not have to be done every month.

5 Conclusion

In this paper we propose a mathematical model for production planning in the process of making billet steels. Starting from the case of billet steel industry, the proposed model considers the amount of billet steels available in the previous

month, consumer demand in the current month and billet cooling area in the warehouse as an integrated part of the system of billet steel production. Microsoft Excel Solver software developed to optimize the production schedule.

For that reason in producing billet steel production should be done at every period, so that the company can optimize the use of warehouse/finished goods warehouse for the cooling process to the delivery of billet steel products to consumers. Thus, companies can minimize the expenditure in terms of cost savings and cost penalties. Future studies directed to involve patterns of raw material supply in a model system of production-inventory-distribution.

References

1. Chen M, Wang W (1997) A linear programming model for integrated steel production and distribution planning. Int J Oper Prod Manage 17(6):592–610
2. Kalagnanam JR, Dawande MW, Trumbo M, Lee HS (2000) The surplus inventory matching problem in the process industry. Oper Res 48(4):505–516
3. Kapusinski R, Tayur S (1998) A capacitated production inventory model with periodic demand. Oper Res 46(6):899–911
4. Lally B, Biegler L, Henein H (1997) A model for sequencing a continuous casting operation to minimize costs. Iron Steelmaker 10:63–70
5. Moengin P, Fitriana R (2015) Model of integrated production-inventory-distribution system: the case of billet steel manufacturing. In: Lecture notes in engineering and computer science: proceedings of the world congress on engineering 2015, WCE 2015, 1–3 July 2015, London, UK, pp 791–795
6. Mohanty RP, Singh R (1998) A hierarchical production planning approach for a steel manufacturing system. Int J Oper Prod Manage 12(5):69–78
7. Tang L, Liu J, Rong A, Yang Z (2000) A mathematical programming model for scheduling steelmaking continuous casting production. Eur J Oper Res 120(2):423–435
8. Tang L, Liu J, Rong A, Yang Z (2001) A review of planning and scheduling systems and methods for integrated steel production. Eur J Oper Res 133(10):1–20
9. Tang L, Luh PB, Liu J, Fang L (2002) Steel-making process scheduling using Lagrangian relaxation. Int J Prod Res 40(1):55–70
10. Widjaja AM (2006) Aplikasi model integer programming dalam sistem produksi-persediaan-distribusi terpadu produk baja billet pada PT. Krakatau Steel. Tugas Akhir. Jurusan Teknik Industri Universitas Trisakti Jakarta
11. Zanoni S, Zavanella L (2005) Model and analysis of integrated production-inventory system: the case of steel production. Int J Prod Econ 93–94:197–205

Novel Study of Catalysts and Membrane in Esterification Reaction

Okon Edidiong, Shehu Habiba and Gobina Edward

Abstract In this work, the characterisation of resin catalysts and performance of silica membrane with single carrier gases was analysed to determine the flow mechanism of the gases at the gauge pressure range of 0.01–1.00 bar and a temperature of 140 °C. The resin catalyst used for the characterisation process was amberlyst 16 resin. The gas permeance was found to decrease with respect to the gauge pressure in the order $N_2 > Ar > He > CO_2$ confirming non-Knudsen mechanism. FTIR-ATR was used for the structural identification of the component with the strongest adsorption strength on the surface of the resin catalysts. The resin catalysts used for esterification process was also characterized using liquid N_2 adsorption measured at 77 K using an automated adsorption instrument. The BET (16.994 m^2/g) results of the N_2 adsorption isotherm for the resin catalysts showed a type IV adsorption isotherm with hysteresis. The result of the FTIR analysis of the resin catalysts showed that the band at 1728 cm^{-1} correspond to C–O stretching with strong adsorption bond while the band at 2986 cm^{-1} representing O–H corresponds to stretching vibration bond suggesting ethanol and lactic acid as the adsorption components on the surface of the resin catalysts.

Keywords Adsorption isotherm · Cation-exchange resin · Characterization · Esterification · Ethyl lactate · Gas flux · Inorganic membrane · Permeability

O. Edidiong · S. Habiba · G. Edward (✉)
School of Engineering, Centre for Process Integration and Membrane Technology (CPIMT), The Robert Gordon University, Aberdeen AB10 7GJ, UK
e-mail: e.gobina@rgu.ac.uk

O. Edidiong
e-mail: e.p.okon@rgu.ac.uk

S. Habiba
e-mail: h.shehu@rgu.ac.uk

S.-I. Ao et al. (eds.), *Transactions on Engineering Technologies*,
DOI 10.1007/978-981-10-1088-0_25

Nomenclatures

Symbols

A Surface area of the membrane (m^2)
J Flux (mol s^{-1} m^{-2})
Q_i Permeance (mol m^{-2} s^{-1} Pa^{-1})
M Gas molecular weight (g/mol)
Q Gas flow rate (mol s^{-1})
T Temperature (Kelvin)
ΔP Transmembrane pressure drop (bar)

Greek Symbols

Å Angstrom
μ Viscosity (Pa^{-1} s)

1 Introduction

Solvents play a major role in all stages of industrial manufacturing sector. The environmental and toxicological effects of solvents have become important in chemical processes. Because environmental problems have threatened the natural order including climate change and global warming, a lot of research is being carried out to find environmentally safe chemicals and processes [1]. Lactic acid is the simplest hydroxyl carboxylic acid with an asymmetric carbon atom. It can be obtained from feedstock, petroleum or natural gas liquid and coal. Copolymers and polymers of lactic acid are known to be eco-friendly and compatible. Due to their biodegradability, they can be used as alternatives to petrochemical polymers [2]. Ethyl lactate esterification can be carried out in liquid-phase reversible reaction between lactic acid and ethanol in the presence of an acid catalyst. It can be used as food additives, agricultural processes (used in cadmium and copper removal from the contaminated soil), solvent, flavour chemicals and perfumery. As a solvent, it has the ability to dissolve numerous polyurethane resins because of its high solvency properties which has made it an excellent cleaner for the polyurethane industry [2]. Ethyl lactate can therefore replace environmentally damaging solvents including toluene, acetone, N-methyl pyrrolidone and xylene.

The use of inorganic ceramic membrane to selectively eliminate water from the reaction product during esterification of lactic acid is yet another important application that has attracted a lot of attention [3]. Materials such as zirconia, zeolite, metals, alumina and carbon are used as commercially available porous inorganic membrane. Other materials used for the manufacture of inorganic membrane include titania, tinoxide, cordierite and silicon nitride. Although inorganic membranes are generally expensive in contrast to their organic polymeric counterparts, they have a lot of advantages in gas separation including well defined stable pore

structure, chemical inertness and wear resistance [4]. The function of the membrane during esterification reaction is to selectively remove water from the reaction mixture which will result in an equilibrium shift thus, driving the reaction towards completion [5, 6]. Gas separation is a membrane process whereby a pressurized gas mixture interacts with the membrane on one side (high pressure side) with the other side kept under vacuum or at low pressure using a vacuum pump or an inert sweep gas. The driving force (i.e. partial or total) is a pressure difference through the membrane [7]. The transport mechanism through porous membrane can be explained using various transport mechanisms based on the membrane material and the average pore size. The different mechanisms of gas transport through porous membranes include Knudsen diffusion, Poiseuille or viscous flow, capillary condensation, surface diffusion and molecular sieving [7].

Knudsen mechanism takes place when the mean free path of the diffusing gas molecules is greater than the pore size of the membrane [8]. In this mechanism, random collision occurs between the molecules of the gas and the pore wall than between each permeating gas molecules. In the capillary condensation mechanism of transport, partial condensation within the pores occurs as a result of low vapour pressure. The condensed feed component diffuses through the pores of the membrane blocking other components resulting in separation [9]. Poiseuille flow also known as viscous flow occurs if the pore radius of the membrane is larger than the mean-free-path of the permeating gas molecule [10]. In this case more collision will take place between the permeating gas molecules (molecule–molecule collision) than between the molecule and the pore wall of the membrane. In surface diffusion, the adsorption of gas molecules are considered to be adsorbed on the surface of the pore wall and move on the surface by jumping between the minimum potential energy generated on the membrane pore surface. For molecular sieving to occur, the membrane must have pore diameters which are roughly the same as those of the gas molecules for separation to take place [11].

2 Experimental

2.1 Gas Transport Test

The permeability of the single gases with inorganic ceramic membrane was carried out using four different gases which serve as carrier gases for esterification reaction including argon (Ar), helium (He), carbon dioxide (CO_2) and nitrogen (N_2). The effective length of the support was measured to be 36.6 cm and the inner and outer radius was 7 and 10 mm respectively. The permeability experiment was carried out at the gauge pressure of between 0.10 and 1.00 bar and temperature of 140 °C (413 K). The flow rate of the gases was obtained at each gauge pressure. The gases were supplied by BOC, UK.

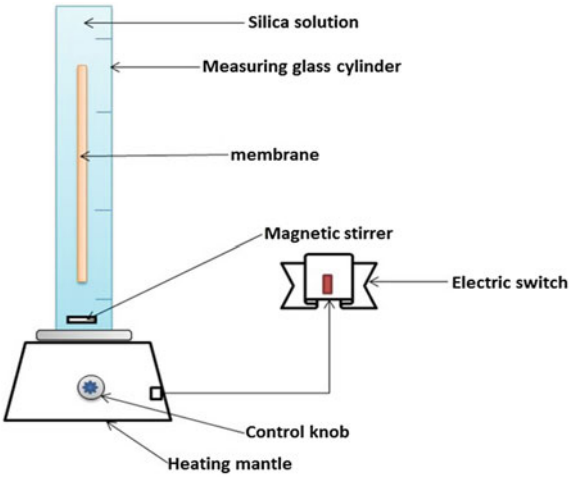

Fig. 1 Schematic diagram of gas permeation setup

2.2 *Membrane Preparation*

The membrane preparation was carried out based on the patented method by Gobina [12]. The membrane was prepared by dip-coating process. Prior to the permeation test, the support was weighed to determine the actual weight before and after modification. A 545 mL of isopentane (Sigma Aldrich ≥ 99 %), was measured into 1000 mL glass cylinder and 50 mL of silicon elastomer was added to the solution together with 5 mL of the curing agent. A magnetic stirrer was used to mix the three solutions and the mixture was allowed to stir for 30 min. After 30 min, the support was dipped into the solution and allowed in the solution for 30 min. After 30 min, the support was taken out from the solution and dried in the oven for 2 h at a constant temperature of 65 °C. Figure 1 shows the schematic diagram of the dip-coating process. Figure 2 shows the gas permeation setup.

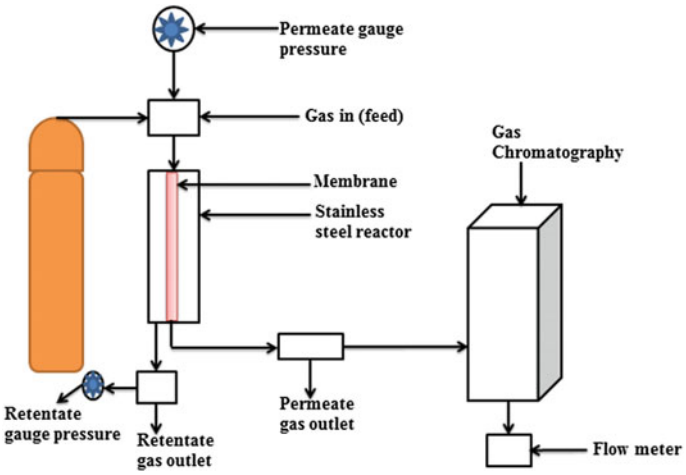

Fig. 2 Schematic diagram of gas permeation setup [13]

2.3 Catalyst Characterization

Aqueous lactic acid (99.9 wt%) and ethanol (99.9 wt%) solutions used for the esterification process were purchased from Sigma-Aldrich, UK and were used as received without further purification. The catalysts used in the experiments were commercial solid cation-exchange resins purchased from Sigma-Aldrich, UK. The characterization of the resin catalysts was also carried out to using FTIR to determine the component with the strongest adsorption strength on the surface of the resin catalysts. Amberlyst 16, was used as the resin catalysts. The deionised water used for the washing of the catalysts was supplied by the Centre for Process Integration and Membrane Technology (CIPMT), Robert Gordon University (RGU), Aberdeen, UK. The 500 mL batch reactor, reflux condenser and the vacuum pump used for the esterification process were all purchased from Sigma Aldrich, UK.

2.4 Catalyst Cleaning

Prior to the esterification process, the fresh commercial cation-exchange resin was weighed into a 50 mL beaker and was rinsed with 2 mL of deionised water with 10 mL of ethanol. The catalysts were reweighed and oven dried at 65 °C for 24 h to remove any impurities and moisture completely. The catalysts cleaning process was carried out based on a similar method by Jogunola et al. [14].

2.5 Batch Process Esterification

After the catalyst cleaning process, 30 mL of lactic acid with 5 g of the resins was charged into the reactor and heated to 60 °C. After the desired temperature was reached, 50 mL of ethanol which has been heated separately using the heating mantle was added to the mixture. The stirring and heating of the reaction mixture was achieved using a magnetic hot plate with a stirrer. The stirrer speed was controlled at the speed of about 400–800 rpm. Figure 3 shows the batch process esterification reaction set-up.

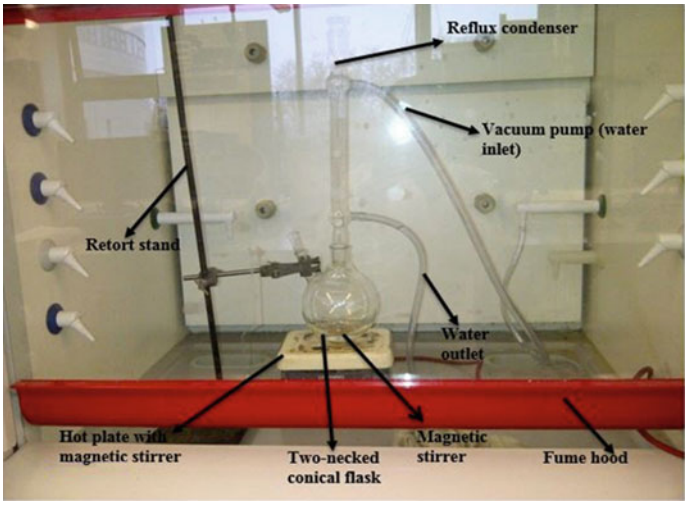

Fig. 3 Batch process esterification process set-up

3 Results and Discussion

The graph of the permeance ratio against the gauge pressure drop was plotted for argon, helium, nitrogen and carbon dioxide gases. From Fig. 4, the experimental selectivity of the gases were found to be higher than the Knudsen selectivity at 0.10–1.00 bar and 413 K.

Figure 5 shows the graph of the gas flux (mol m^{-2} s^{-1}) against the gauge pressure at 413 K. From Fig. 5, it was observed that the flux of the four gases increases with respect to the gauge pressure. Nitrogen and helium gases with the

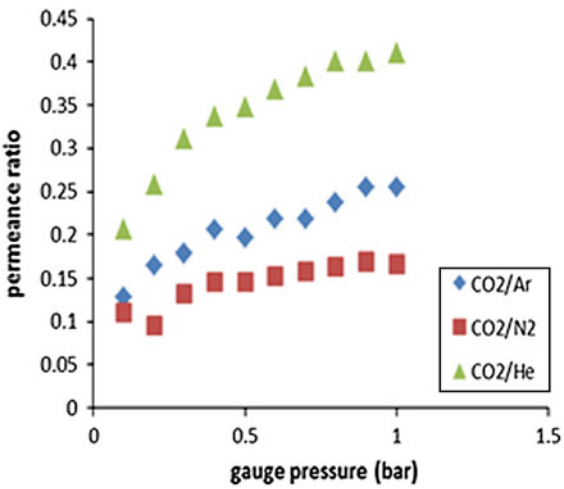

Fig. 4 Permeance ratio against gauge pressure (bar) at 413 K (color figure online)

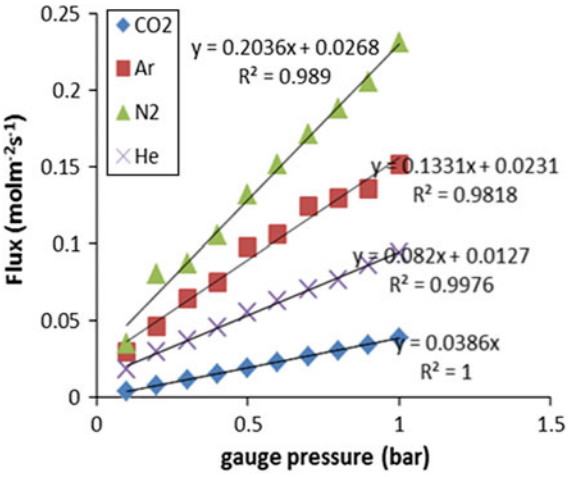

Fig. 5 Gas flux (mol m^{-2} s^{-1}) against gauge pressure drop (bar) at 413 K (color figure online)

Table 1 Molecular weight, viscosity and kinetic diameter of N_2, Ar, He and CO_2

Gases	Molecular weight (mol/kg)	Gas viscosity (Pa s^{-1})	Kinetic diameter (Å)
Nitrogen	28	15	3.64
Argon	40	17.81	3.4
Helium	4	20	2.9
Carbon dioxide	44	22.7	3.3

molecular weight of 28 and 4 g/mol respectively showed a higher flux in contrast to CO_2 gas with higher molecular weight of 44 g/mol as shown in Table 1. The correlation coefficient (R^2) value indicates a good fit of the experimental data. Although CO_2 gas seems to show the least permeance among other gases as shown in Fig. 5, the R^2 value was higher than other gases. It was also suggested that there could be another mechanism of transport responsible for the flow of CO_2 gas. The order of the gas flux was observed to be $CO_2 < He < N_2 < Ar$.

A linear equation was obtained for all the gases with the gradient of the graph being less than 1. R^2 values indicating good fit of data were obtained for the gases. The gas flux was calculated using the following equation:

$$J = \frac{Q}{A} \tag{1}$$

where J = flux (mol m^{-2} s^{-1}), Q = flow rate of the gases (mol s^{-1}), A = membrane surface area (m^2). The permeance is then obtained from the flux using the equation:

$$Q_i = \frac{J}{\Delta P} \tag{2}$$

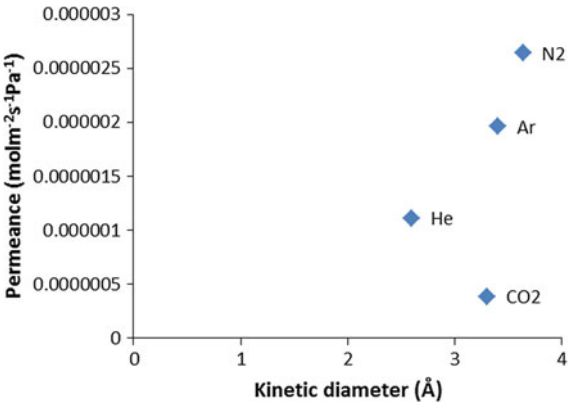

Fig. 6 Gas permeance (mol m^{-2} s^{-1} Pa^{-1}) against kinetic diameter at 0.5 bar and 413 K

where ΔP is the transmembrane pressure drop (bar), J = flux (mol m^{-2} s^{-1}) and Q_i is the permeance (mol m^{-2} s^{-1} Pa^{-1}).

Figure 6 shows the plot of the permeance (mol m^{-2} s^{-1} Pa^{-1}) against the kinetic diameter (Å) of N_2, CO_2, He and Ar gas at the gauge pressure of 0.5 bar and 413 K. From the result obtained in Fig. 6, it observed that the gas transport was not based on molecular sieving mechanism since the gas flow did not follow the order of the kinetic diameter. N_2 and Ar gases with a close kinetic diameter (as shown in Table 1) showed permeance flow which did not support that of a molecular sieving mechanism.

The order of the gas kinetic diameter from the highest was given as N_2 > Ar > CO_2 > He. In the case of molecular sieving mechanism, He and CO_2 gases with the lowest kinetic diameter should have been close to each other with a higher permeance value while N_2 and Ar with a higher kinetic diameter would have been close to each other with a lower permeance. It was suggested that there could been another mechanism of transport that was responsible for the flow of the gases at 0.5 bar and 413 K.

Table 1 shows the molecular weight (g/mol), viscosity (Pa s^{-1}) and Kinetic diameter (Å) of the four gases.

The relationship between the gas permeance and the inverse of the gas viscosity was also plotted at the gauge pressure drop of 0.7 bar and 413 K. From Fig. 7, it was observed that gases with highest viscosity value showed the least permeance which suggests that the gas flow through the silica membrane was based on viscous mechanism.

The relationship between the gas permeance and the gauge pressure drop was also obtained as shown in Fig. 8. From the results obtained in Fig. 8, it was found that the gas permeance decreases with respect to gauge pressure indicating gas-phase mass transfer limitation. It was found that N_2 showed an initial increase at 0.2 bar before decreasing while He, CO_2 and Ar did not follow the trend. This was attributed to the low molecular weight of N_2 gas contrast to CO_2 and Ar. The

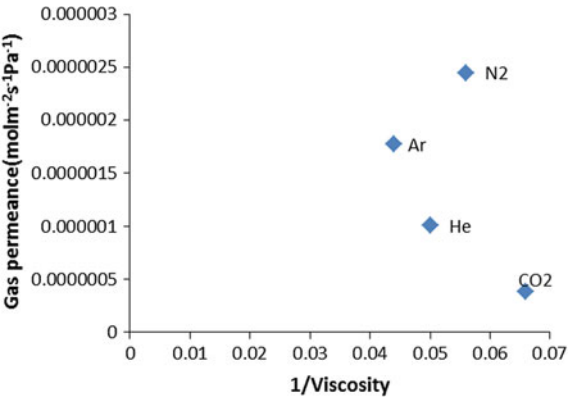

Fig. 7 Gas permeance (mol m^{-2} s^{-1} Pa^{-1}) against 1/viscosity (Pa s^{-1}) at 0.7 bar and 413 K

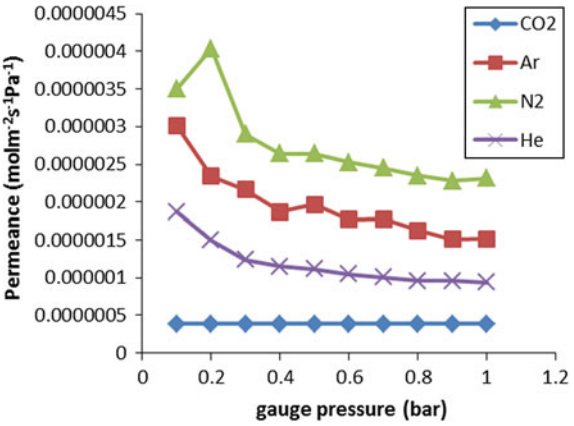

Fig. 8 Gas permeance (mol m^{-2} s^{-1} Pa^{-1}) against gauge pressure (bar) at 413 K (color figure online)

order of the gas permeance with respect to the gauge pressure drop was $N_2 > Ar > He > CO_2$.

Figure 9 presents the relationship between the gas flow rate (mol s^{-1}) and the inverse square root of the gas molecular weight for the four gases. For a gas transport to be described by Knudsen flow mechanism, the membrane would have to exhibited a linear dependence of flow rate on the inverse square root of the molecular weight McCool et al. [15]. However, from Fig. 9, it was found that there was no linear dependence between the flow rate and the inverse square root of the gas molecular weight as expected for gas transport that is dominated by Knudsen mechanism indicating that the gas flow was based on another mechanism of transport [16].

Figure 10 present the FTIR-ATR spectrum of the percentage transmittance (%) against the wavelength (cm^{-1}) for the esterification product catalysed by the different cation-exchange resin catalysts at 60 °C. From the results obtained in Fig. 10 it was found that reactant solvent possess different functional group on the spectra which was

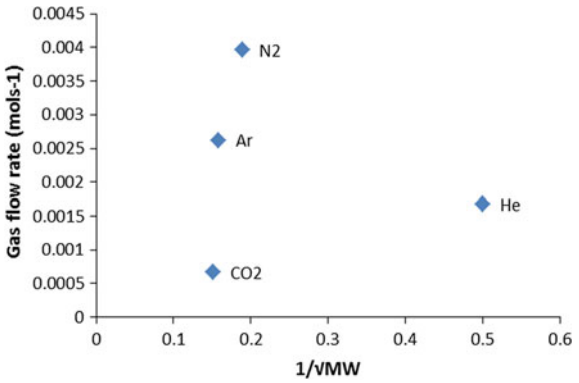

Fig. 9 Gas flow rate (mol s^{-1}) against inverse square root of the gas molecular weight at 0.9 bar and at 413 K

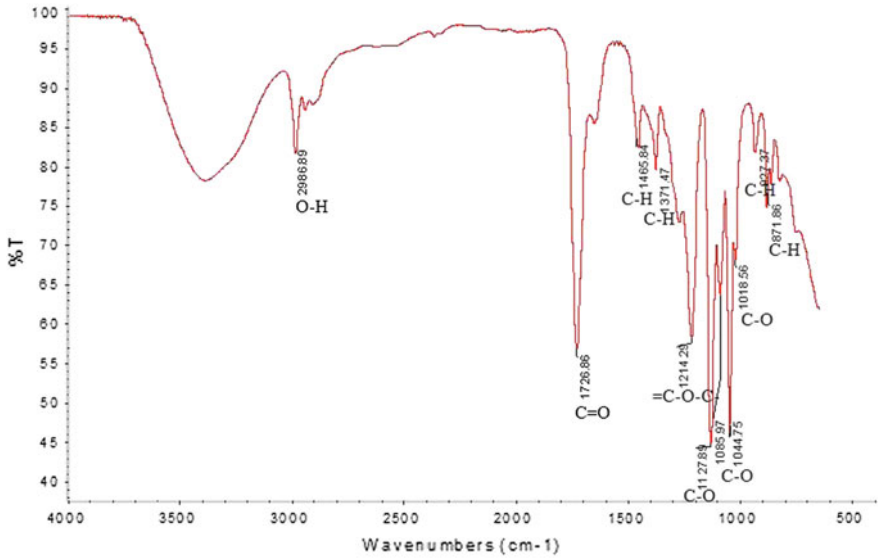

Fig. 10 FTIR spectra of esterification reaction product catalysed by amberlyst 16 at 60 °C and the wavelength region of 500–4000 cm^{-1}

used to evaluate the component that absorbed most on the surface of the resin catalysts. The overall wavelength was set in the scale range of 400–4000 cm^{-1}.

It was observed that the resin exhibited a wavelength in the range of 2986.89 cm^{-1} which was attributed to symmetric and asymmetric stretching vibration of O–H groups. This O–H was suggested to have resulted from water adsorption on the surface of the resin catalyst. It was also observed that the peak intensity increases between the wavelengths of 1728–1018 cm^{-1} with a decrease

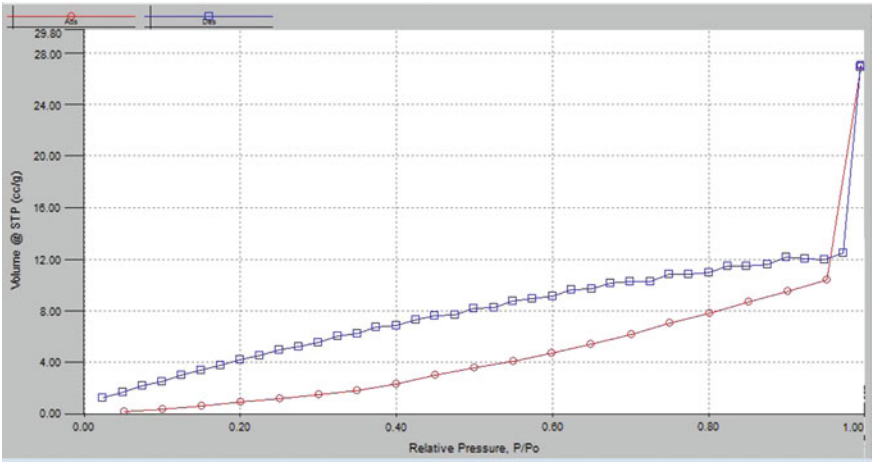

Fig. 11 BET isotherm for amberlyst 16 at 77 K

after that. This was attributed to the stretching vibration of C=O functional group. From the reoccurrence of C–O from ethanol and C–H and C=O from the structure of lactic acid reactant. It was suggested that it could be ethanol and lactic acid that adsorbed on the surface of the resin catalyst.

Figure 11 depicts the BET surface area for amberlyst 16 cation-exchange resin at the liquid nitrogen temperature of 77 K. From Fig. 11, it was found that the BET result for amberlyst 16 resin catalysts showed a higher surface area (16.994 m^2/g) which confirmed catalytic activity of amberlyst 16 catalysts for esterification. However a positive slope and intercept was also obtained for the catalysts. The BET isotherm of the resin catalyst exhibited a type IV isotherm with hysteresis loop on the curve indicating a mesoporous material in the range of 2–5 nm.

4 Conclusion

Carrier gas permeation performance in mesoporous silica membrane for use in lactic acid and ethanol esterification at the 413 K and 0.10–1.00 bar pressure drop was determined. The gas transport was tested using Knudsen, viscous and molecular sieving mechanisms. The best fit was found to be based on viscous flow. However, the theoretical Knudsen selectivity was found to be higher than the experimental selectivity indicating that some Knudsen flow was also occurring. The order of the gas permeance with respect to the gauge pressure drop was found to be $N_2 > Ar > He > CO_2$. The BET surface area of the resin catalyst exhibited a higher surface area with a positive slope and intercept. The FTIR result of the esterification product catalysed with the resin catalyst confirmed ethanol and lactic acid as the most adsorbed components on the surface of the resin catalyst.

Acknowledgements The conference was sponsored by IDEAS Research Institute, The Robert Gordon University, Aberdeen, United Kingdom. The Aurthors of this paper acknowledge the Center for Process Integration and Membrane Technology at RGU for providing the research infrastructure.

References

1. Nigiz FU, Hilmioglu ND (2015) Green solvent synthesis from biomass based source by biocatalytic membrane reactor. Int J Energy Res
2. Engin A, Haluk H, Gurkan K (2003) Production of lactic acid esters catalyzed by heteropoly acid supported over ion-exchange resins. Green Chem 5(4):460–466
3. Pereira CS, Silva VM, Rodrigues AE (2011) Ethyl lactate as a solvent: properties, applications and production processes—a review. Green Chem 13(10):2658–2671
4. Pereira CS, Silva VM, Rodrigues AE (2009) Fixed bed adsorptive reactor for ethyl lactate synthesis: experiments, modelling, and simulation. Sep Sci Technol 44(12):2721–2749
5. Zhang Y, Ma L, Yang J (2004) Kinetics of esterification of lactic acid with ethanol catalyzed by cation-exchange resins. React Funct Polym 61(1):101–114
6. Dassy S, Wiame H, Thyrion FC (1994) Kinetics of the liquid phase synthesis and hydrolysis of butyl lactate catalysed by cation exchange resin. J Chem Technol Biotechnol 59(2):149–156
7. Delgado P, Sanz MT, Beltrán S (2007) Isobaric vapor–liquid equilibria for the quaternary reactive system: ethanol water ethyl lactate lactic acid at 101.33 kPa. Fluid Phase Equilib 255(1):17–23
8. Calvo JI, Bottino A, Capannelli G, Hernández A (2008) Pore size distribution of ceramic UF membranes by liquid–liquid displacement porosimetry. J Membr Sci 310(1):531–538
9. Gobina E, Hou K, Hughes R (1995) Mathematical analysis of ethylbenzene dehydrogenation: comparison of microporous and dense membrane systems. J Membr Sci 105(3):163–176
10. Li H, Schygulla U, Hoffmann J, Niehoff P, Haas-Santo K, Dittmeyer R (2014) Experimental and modeling study of gas transport through composite ceramic membranes. Chem Eng Sci 108:94–102
11. Mulder M (1996) Basic principles of membrane technology, 2nd edn. Kluwer Academic Publishers, Berlin
12. Gobina E (2006) Apparatus and method for separating gases. US patent. Patent No. US 7,048,778 B2. Robert Gordon University, Aberdeen, UK
13. Okon E, Shehu H, Kajama M, Nwogu N, Orakwe I, Gobina E (2015) Int J Eng Res Technol 4(4):465–469
14. Jogunola O, Salmi T, Wärnå J, Mikkola JP (2012) Kinetic and diffusion study of acid-catalyzed liquid-phase alkyl formates hydrolysis. Chem Eng Sci 69(1):201–210
15. McCool BA, Hill N, DiCarlo J, DeSisto WJ (2003) Synthesis and characterization of mesoporous silica membranes via dip-coating and hydrothermal deposition techniques. J Membr Sci 218(1–2):55–67
16. Okon E, Shehu H, Kajama M, Adesola O, Nwogu N, Orakwe I, Gobina E (2015) Hydrodynamic performance in mesoporous silica membrane for lactic acid and ethanol esterification. In: Lecture notes in engineering and computer science: proceedings of the world congress on engineering 2015, WCE 2015, 1–3 July 2015, London, UK, pp 781–784

Maintenance Practice in a Sand Casting Foundry

Ignatio Madanhire and Charles Mbohwa

Abstract The chapter gives an in-depth review of challenges as well as strengths and weaknesses that characterize maintenance practices in a sand casting manufacturing company. The study was done for a ferrous foundry which was producing mainly grey and white iron. A number of suggestions put across were on appropriate practices which could be taken on board and areas of possible improvement in that specific plant. The generated recommendations could find wide application in similar foundries to enhance plant operations through high maintenance efficiency as a way to save finite input resources and improve operational bottom line.

Keywords Efficiency · Foundry · Maintenance · Manufacturing · Plant · Preventive · Sand casting

1 Introduction

As global manufacturing and trading industry continues to evolve, most businesses are now faced with an ever increasing need to rapidly adapt to these changes. The changes include areas like market demand, product design, product life cycle, changes in production and manufacturing technologies [1]. As markets gradually shift from mass markets into niche markets, it is becoming imperative that manufacturing

I. Madanhire (✉)
Faculty of Engineering and the Built Environment, School of Engineering Management, University of Johannesburg, Auckland Park 2006, South Africa
e-mail: imadanhire@eng.uz.ac.zw

I. Madanhire
Department of Mechanical Engineering, University of Zimbabwe, P.O. Box MP167, Mount Pleasant, Harare, Zimbabwe

C. Mbohwa
Faculty of Engineering and the Built Environment, Department of Engineering Management, University of Johannesburg, Auckland Park 2006, South Africa
e-mail: cmbohwa@uj.ac.za

S.-I. Ao et al. (eds.), *Transactions on Engineering Technologies*,
DOI 10.1007/978-981-10-1088-0_26

entities respond with proactive strategies to ensure not only their continued survival but also facilitate for growth in the prevailing competitive environment. Any organization needs to focus on quality of products, the cost of products, timely delivery of products and the flexibility of their internal business process to adapt to rapid changes [2]. The aspect of flexibility becomes very critical especially when an organization is trying to capture an immediate intermittent demand of a product.

A study was carried out in Zimbabwe, a developing country which had a declining manufacturing production capacity due to a number of constraints. Manufacturing companies were grappling with challenges such as obsolete equipment, skills flight and depressed market activity. Most of the raw material was procured as imports. The resulting set-back was the inability to supply products at the right time, in the right quantities, at the right level of quality and at a competitive price in the region and globally. This paved the way the way for casting foundries to face stiff competition even on the local market from Asian suppliers [1].

Upgrading of manufacturing system to quickly respond to rapid market demand changes and other issues such as the scarcity of financial resources and material resources was required. High breakdown frequency, non- reliability in terms of products with consistent quality and reduced productivity militated against the supposed system efficiency. Hence total productive maintenance (TPM) philosophy advocates for a holistic approach to manufacturing whereby each activity in the production system is analyzed and improvements made that would ensure that efficiency is achieved under such industrial adversities just mentioned [2, 3].

2 Ferrous Foundry Processes

2.1 Casting Process

The sand casting process is the main production activity, where most of the molding is done by machinery. Pipe production is done using a centrifugal casting method and the equipment is referred to as “The Pipe Spinning Plant”, while melting is done at the Cupola furnaces [4]. This study is based on the main foundry. Production plans were derived from sales orders and no production was done for products without orders. Thus planning was done by balancing the product requirements, and molding machine and furnace capacities.

2.2 Melting Operations

The metal charges are melted in the Cupola furnace, and coke is the fuel used in this cold blast process. The rate of metal tapping is 3.2 tons per hour. Production targets normally range from 18 tons per hour for grey iron and 20 tons per day for white iron [1].

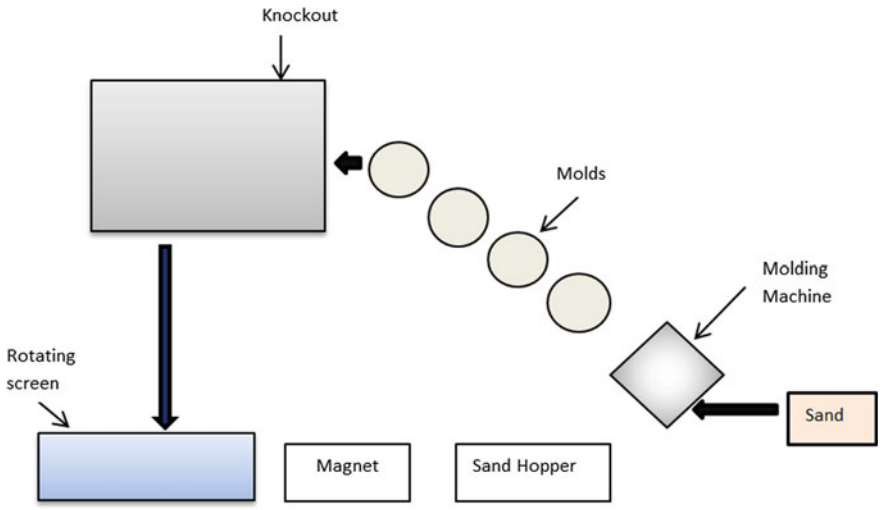

Fig. 1 Sand preparation and handling system

2.3 Sand Preparation

The sand from the sand mill is compacted on a metal pattern on the molding machines through the action of the machine or through the action of a hand held sand rammer. The molds are inspected and closed and placed on a gravity roller conveyor or on the powered mold conveyor line of the foundry. After casting the molds are placed on the knockout machine where the product is separated from the mold. The hot sand is taken by the conveyor through a rotating screen, where lumps, metal particles, slag and non-metallic particles are removed. The sand then passes through a magnet which removes magnetic particles from the sand. The sand is then deposited in hoppers where it is allowed to cool as shown by Fig. 1. The sand then goes through where it mixed, crushed and aerated. In the sand mill new sand, coral bentonite, coal dust and water are added to the sand after the sand batches are tested. The sand is then ready for molding and the cycle repeats [4].

2.4 Molding, Casting and Product Knockout

Two types of molding machines used are the straight draw molding and the turn-over machines. The turnover machines are used in association with the straight draw molding machines. The turnover machine has the advantage over the straight draw in its ability to automatically turn over the drag after compaction. Production rates of up to 30 full molds per hour are obtainable from these machine pairs. The

cores and mold halves are inspected after molding and any irregularities are corrected before closing the mold halves. For larger molds, e.g., for the size 20–30 pots and bath tubs, the mold is dried using a commercial mold cote spray mixed with ethanol which is used to bake the mold and cores by burning it [5].

Casting of the mold is then done using hand held shanks. Two men carry the shank ladle whilst the third man skims off the dross and impurities on the melt. Pouring is then done with the molding box on a gravity roller conveyor or on a pallet conveyor.

On solidification, the molding box is either lifted onto the knockout machine with overhead cranes or pushed onto the shakeout machine by a box pusher (air actuated cylinder). The product is separated from the runners and gates. The molding sand drops into the on a conveyor beneath the knockout machines for recycling. The product is then inspected for defects whilst the runners and gates are re-melted at the cupola furnace. Some defective products are also taken for recycling whilst others with correctable defects are passed on to fettling with the good products [6].

2.5 Fettling and Product Finishing

The product from the knockout is carted to the shot blast machine for cleaning. The castings are then taken through a series of grinding operations depending on the type of product. In the case of enamelware products two further shot blast operations are done before the product is ready for enameling. Products that have a paint finish will then be drilled and assembled before spray painting. Pipes, pipe fittings and man-hole covers and frames are dipped into bitumen paint. Inspections done in the fettling shop results in some products being scrapped whilst others may be repaired by welding or filling with adhesives [7].

The enamelware products are initially ground coated and then baked in the enameling furnaces at 900 °C for 3 min before being sprayed with enameling powder. The product is then taken into the furnace to melt the enamel powder. If the quality is less satisfactory a decision is made to scrap or to send the product back for re-blasting. It may be necessary to anneal the products in the enameling furnaces before grinding and drilling if the castings are too hard [8].

3 Case Study Organizational Operations

3.1 Organizational Structure

The study was done at Casting Co. Ltd. and the organizational chart is shown by Fig. 2.

The maintenance function was under the jurisdiction of the Factory Manager. Its main functions were to maintain existing equipment and buildings, install new

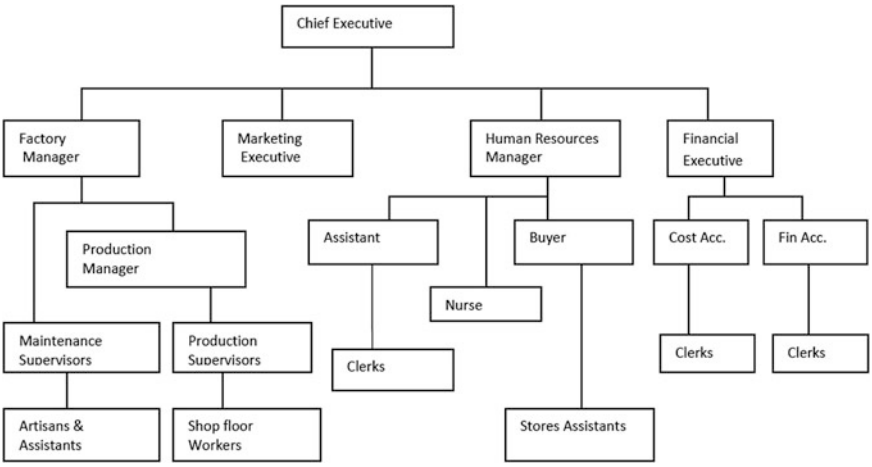

Fig. 2 Organizational chart

equipment, ensure safe operation of the equipment and attain plant availability in excess of 80 % within budgetary confines.

3.2 Maintenance System Assessment

A Fixed Time Maintenance (FTM) system was in place and documented as part of the ISO 9001 procedures, and it involved only daily inspections carried out by the tradesman. Figure 3 depicts the FTM system.

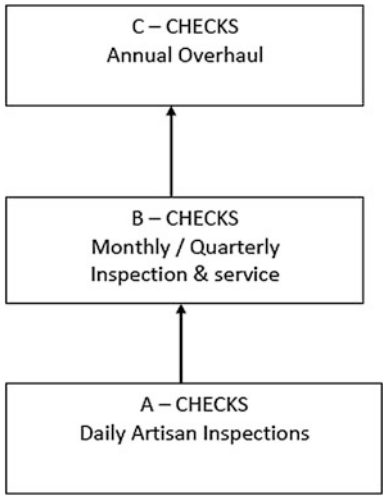

Fig. 3 Hierachy of the FTM system

The A—Checks are the walk around inspections that are done by the artisans daily to determine oil levels and top it up if necessary, discern any abnormal sounds, vibrations, smells, oil leaks, loose bolts and excessive heat. The A—checks are done when the equipment is operational. Depending on the Annual Plans B—Checks are more rigorous than the first level checks involving oil changes minor corrective work. Maintenance windows are required to perform B—Checks. The C—Checks are complete overhauls done annual during the shutdown period. Spares requirements have to be met before embarking on either the B or C—Checks. B and C checks are derived from an annual plan, which is broken into weeks. The weekly/daily plan cascaded from this plan. The preparation of these plans was the responsibility of the Maintenance manager in consultation with the Production Manager. Figure 4 illustrates this maintenance planning structure.

The plans were communicated to the artisans through the Job Request Card and if the job was done the plant record and history cards were updated. In situations where the job was not done, agreement with the Production Manager would be sought. Information from breakdowns and checklists was communicated to maintenance supervisor and assessments done to find out and procure the resource requirements. The information from work generated from breakdowns and inspections was similarly processed.

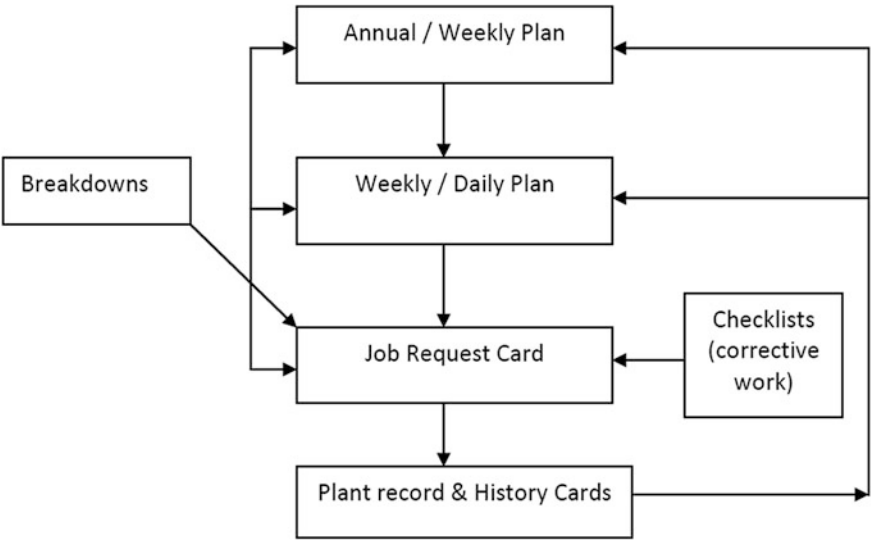

Fig. 4 Maintenance planning structure

3.3 Maintenance Management Practice

The plant history and plant record cards were not being updated. The annual plans were not in place and the overhauls were not being adequately done, for example the pallet conveyor and the sand mill was not serviced during the previous shutdown and as a result by February 2014 had failed. The ring gear of the sand mill which failed was to be replaced at a cost of USD 52,000.

The plant availability was not known and as a result the overall equipment efficiency (OEE) was also not known. As a result it was found that:

- 67.5 h were lost due to breakdowns;
- 37.4 h due molten metal shortage; and
- 4.5 h were lost as a result of sand shortage, bringing the total downtime to 109.4 h in February 2014. This meant that the plant availability was 65.5 %.

Lubricants being used on the industrial gearboxes were of an automotive grade type, SAE 80w90 oil instead of an industrial ISO VG grade. Production personnel were responsible for lubricating molding machines and gear boxes, whilst a maintenance operative lubricated knockout machines, cupola fan and sand mills. Sometimes production personnel kept topping up the oil without realizing that there were leaks. Maintenance personnel sometimes did not keep to the lubrication schedule. No oil analysis was done and the oil changes were not done on time.

The interface between production and maintenance personnel was limited to reporting and resolution of breakdowns.

3.4 Quality Practices

Quality Assurance existed in form of laboratory personnel to man the metallurgical laboratory where spectrographic analysis and hardness testing was done. As well as the sand testing laboratory for molding sand [9].

Inputs into the cupola such as foundry coke, cast iron scrap, steel scrap, pig iron ingots, dolomite, ferrosilicon and ferromanganese were inspected by quality inspectors who would write on a prescribed form that the inputs comply with the specifications. The cupola furnace charge was then determined and depended on the various input metal proportions. This would also determine the amount of ferroalloy additions into the charge. Some of the molten metal was then cast into test moulds for spectrographic analysis and chill testing. Periodic analysis of the samples was done on an hourly basis. Any deviation from specification was corrected by a change in the metal charge or amount of ferroalloy addition. Hardness tests were also done. Sand testing was done on hourly intervals, and if there were any deviations from specifications correction was done promptly.

Castings were visually inspected before they proceeded to the next process. Pipes were leak tested with water. In the case of pots water was left to settle in the

pots to detect any leaks. Go and no-go gauges were used to check on the internal diameter of the tubes.

33.08 tons of grey iron products and 24.7 tons of mill balls were defective in February 2014. This represented scrap rates of 17.1 % for grey iron and 4.8 % of white iron products respectively.

3.5 Environmental Management

Effluents from the foundry entailed waste water, solid waste and gaseous emissions. Combustion waste products from the cupola were gases, particle emissions, slag and heat losses. The gases and particle emissions were emitted to the environment, although there was grit arrestors on the cupolas, there were no air cleaners. There was also no waste heat recovery equipment on the cupolas. Slag was deposed of at municipal landfills. Cooling water, used when purging slag and when cooling the furnace for re-patching, was discharged into the municipal drainage system.

There were no dust extraction equipment in the main foundry at knockouts save for the underground dust extraction fan. The dust extraction units at the shot blast were not very effective. There was only one fume extractor at the painting booth for pots. There were no other extractors for the pipe and pot painting areas. Some dust extraction fans in the enameling shop were not operational and there was no air cleaning equipment before the air was discharged into the atmosphere.

Energy consumption per month averages 211,000 kWh, with an off peak usage of 7550 kWh and on peak usage of 135,000 kWh. The power factor ranged from 0.96 to 0.99 and the load factor was around 0.34.

3.6 Summary of Study Findings

Observed concerns that needed to be addressed in order to improve the efficiency of the plant were mostly to do with equipment upkeep for the plant parameter levels given in Table 1, which had to be improved.

These results amply indicated that there was room for improving maintenance practice at the case study organization with respect to possible maintenance productivity level based on the World Class benchmarking.

Table 1 Operating efficiency parameters

Parameter	Percentage level (%)
Quality rate	90.5
Performance rate	75.4
Plant availability	65.5
OEE	44.7

4 Analysis of Maintenance System

4.1 World Class Maintenance (WCM) Model

WCM involves waste minimization technologies. Central to these strategies will be the need to have safe and reliable equipment and teamwork. Realization of WCM and the competitiveness thereof hinges on total preventive maintenance (TPM). Figure 5 depicts the proposed idealization of WCM model [4].

The model is a universal set of all manufactures and their customers.

$$\xi = \{M; C\}$$

The set of manufactures consists of those organizations that do not have continuous improvement (Kaizen) techniques and are viewed as traditional organizations TM.

$$TM = (TEI \cup EMS \cup TPM \cup TQM)'$$

Some organizations have different levels of adoption and integration of TPM, TQM, TEI and EMS. Those organizations that have harmoniously integrated these four Kaizen techniques are the World-Class Manufacturers.

$$WCM = TPM \cup TQM \cup TEI \cup EMS$$

However both the World-Class Manufactures and the Traditional Manufacturers are both subsets of the set of manufacturers.

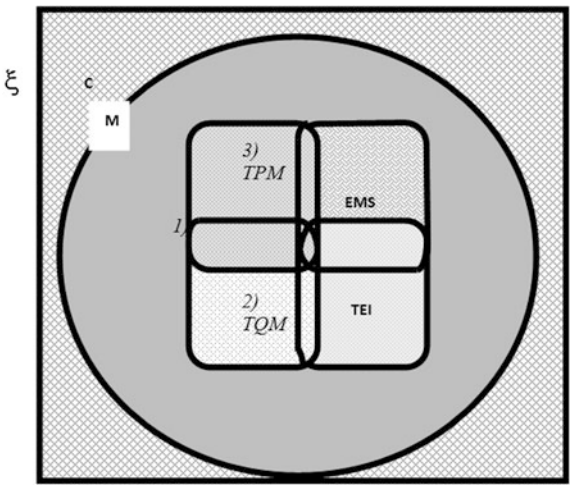

Fig. 5 The proposed WCM model. *Key* ξ = Universal set, M = set of all manufacturers, C = set of customers, TPM = set of organizations using TPM, TEI = set of organizations using the EI principle, TQM = set of organizations using TQM, EMS = Set of organizations using EMS, (where *TPM* total productive maintenance, *TEI* total employee involvement, *TQM* total quality management, *EMS* environmental management system)

$$Common\ Elements = TPM \cap TQM \cap EMS \cap TEI$$

where TPM, TQM, EMS and TEI, refer to implementation requirements and techniques; it is worth noting that the proposed model advocates for simultaneous implementation of all four WCM facets. TPM, EMS and TQM are all continuous improvement principles that involve employee participation thus TEI is naturally enshrined in their implementation. The full realization of TPM, TQM, TEI and EMS will impart the organization with WCM competitiveness. Shop level participation by top level management could be enhanced in the case study foundry through directed small group activities, which form part of the formal structure to achieve world class maintenance for high productivity [1].

4.2 Total Employee Involvement (TEI)

There was need to form quality circles and open formal employee suggestion structures, as well as formalizing job specifications and job descriptions to enable measurement of deviation of performance and thereby correct the causes of such deviations [2]. A concerted effort could be made through cross fertilization of skills within the maintenance department to attain a high level of multi-skilled personnel. There was need for basic equipment maintenance skills training for production personnel and maintenance personnel to be trained in specialist maintenance skills in electronics, pneumatics and hydraulics.

4.3 Molding, Casting and Product Knockout Sections

Deliberate efforts could be made to increase the machine productivity through institution of these recommended measures. Due to delays in import spare parts lead time, effort may be made to seek increasing the local content of the spares, as is the case for leather seals and oil seals.

Multi-skilling of the entire maintenance team and machine operators could be implemented to avoid reliance on a core of workers in maintenance alone. Operator training may include basics of machine maintenance.

Regular and scheduled maintenance with correct lubricants may go a long way in reducing break downs and increase plant availability. Both operators and maintenance personnel training on the inspection and service of the machines is critical.

Crane failures can be avoided through training operators in correct lifting and operation techniques. Also regular maintenance and statutory inspections and services have to be religiously followed to guard against disruptive incidents.

4.4 Fettling and Product Finishing Sections

A thorough study of shot blast wheel bearing failure frequencies and running times will help determine the overhaul times and frequency. Adequate seals could also be used to eliminate the likelihood of contamination of the bearings for both or all shot blasts. There was need to enhance the fettling plant capacity through use of pedestal grinders and extra pneumatic hand grinders. Such improvements in the process plant before casting would result in elimination of product defects.

4.5 Maintenance Strategy

A radical shift could be made from the current crisis maintenance strategy to TPM. This would enable the maintenance team to take more control of the reliability of the plant as they would concentrate on predictive rather than crisis maintenance, less rigorous duties such as daily walk-around (A) checks will then be delegated to production personnel with the concomitant effect of empowering the operators.

4.6 Maintenance Management Practice

Maintenance supervisor could be trained that they get to know and be able to calculate the quality rates, performance rate, availability and OEE. As well as being in a position to explain the meaning of these to their charge-hands and production personnel.

Lubricating oils such as ‘Shell Tellus 320’ or ‘Mobil Gear Oil 632’ should be used for industrial gearboxes, instead of automotive gear oils. Training on lubrication could be done and lubrication schedules must be adhered to and control measurers put in place to verify the adherence to such a schedule. Arrangements with lubricant suppliers for oil analysis must be arranged, and quite a number of lube suppliers readily offer oil analysis to their customers for free.

To avoid uncontrolled maintenance expenditure, more impetus has to be put on preventive measures, such that at least 50 % of the plant maintenance budget could be dedicated to TPM implementation and save in the long run.

4.7 Energy Costs

Poor maintenance practices had a direct adverse effect on high energy consumption. In this regard, proper insulation of enameling furnaces could reduce heat losses to the environment. Also eliminating the need for remedial work, such as re-annealing,

re-melting, re-blasting and welding of castings would mean less energy bills as all products just go a single cycle, and save on energy and time.

Use of high-energy efficient equipment would be required to avoid unnecessary rewinding of electric motors (as re-wounded motors are less efficient). Although the power factor is close to unit, the load factor of 0.34 is lower than the general value for industrial operations and there need to structure the load for improvement in this regard. Operating 24 h a day, with three shifts, which are as long as the present shifts, could attain higher load factors. Around the clock operation is only possible if the equipment reliability is high.

5 Conclusion and Future Work

Systematic inspection of all plant machinery and equipment at regular intervals ensures that the plant availability would be guaranteed at all times. After completion of service, quality of work needs to be inspected by the Engineer before machine could be handed over to user department. The need to have improved plant availability could be enhanced through reliability systems put in place as well as intelligent condition monitoring to assist the operations of the foundry. Systems and procedures could be revisited with the view to expose the components which require urgent attention in terms of replacement and repairs with minimum interruption of the required production targets. In the foundry industry, plant availability is critical as export orders have to be timely processed on time for delivery to the customer to survive the competitive market in the region.

In as much as the good scheduling of maintenance work is good work practice, studies have shown that basic maintenance has to be transferred to machine operators to mind their own machines through doing basic maintenance work as well as trained to be multi-skilled for positive results. Therefore further investigation could be done to investigate maintenance impact in terms of human resource leverage to excel in plant availability.

References

1. Madanhire I, Mbohwa C, Enhancing maintenance practices at a casting foundry: case study. Lecture Notes and computer science: proceedings of the world congress on engineering 2015, vol II, WCE 2015, 1–3 July 2015, London, UK, pp 763–768
2. Madanhire I, Mbohwa C, Implementing successful total productive maintenance (TPM) in a manufacturing plant. In: Proceedings of the world congress on engineering 2015, vol II, WCE 2015, 1–3 July 2015, London, UK, pp 796–801
3. Madanhire I, Mbohwa C, Maintenance technology tools to improve availability for dairy industry: case study. In: Proceedings of the world congress on engineering 2015, vol II, WCE 2015, 1–3 July 2015, London, UK, pp 933–938

4. Mugwindiri K, Madanhire I, Mhlanga G (2013) Enhancing maintenance at casting foundry manufacturing company. Int J Innovation Technol Res (IJITR) 1(2):142–154
5. Copeland T, Koler T, Murrin J (2000) Valuation measuring and managing the value of companies, 3rd edn. Wiley, New York
6. Bloom N (2006) Reliability centered maintenance. McGraw Hill, New York
7. Sun Y (2007) Effects of preventive maintenance on the reliability of production lines. Available at: http://eprints.qut.edu.au/
8. Mobley KR (2002) An introduction to predictive maintenance, 2nd edn. Butter-worth Heinemann, Amserdam
9. Adam E (2004) Productivity and quality: measurement as a basis for improvement. http://hiattengineeringltd.com/home

A Hybrid Knowledge-Based Lean Six Sigma Maintenance System for Sustainable Buildings

Jasim Saleh Aldairi, Mohammed Khurshid Khan and J. Eduardo Munive-Hernandez

Abstract The complexity of sustainable building maintenance environment enforces organizations to develop a standardized maintenance quality management system that can be applied in all concerned departments. This Chapter presents a novel conceptual model of a hybrid Knowledge-Based Lean Six Sigma Sustainable Building Maintenance System (Lean6-SBM). The KB model seeks to apply the Lean Six Sigma philosophy to support implementation of an ideal building maintenance system. The conceptual KB model also integrates GAP technique to support benchmarking and decision making. The proposed conceptual model is presented to show the fundamental components of the Lean6-SBM.

Keywords Benchmarking · Building maintenance · GAP · Knowledge base (KB) · Lean Six Sigma (LSS) · Sustainability

1 Introduction

As part of facility management processes, building maintenance plays an important role since it deals with uncertain factors affecting the performance of the organization. According to Dhillon [1], maintenance is costing 60–75 % of the large system's or product's life cycle costs. This automatically creates a challenge to maintenance managements in validating asset performance and allocating the required funds. One of the main reasons behind weaknesses in maintenance management systems is the lack of experience which results in imprecise information obtained for the decision making and hence, losing the control of priorities. On the

J.S. Aldairi (✉) · M.K. Khan (✉) · J.E. Munive-Hernandez (✉)
University of Bradford, Bradford BD7 1DP, UK
e-mail: jawareh8@hotmail.com

M.K. Khan
e-mail: m.k.khan@bradford.ac.uk

J.E. Munive-Hernandez
e-mail: j.e.munive@bradford.ac.uk

S.-I. Ao et al. (eds.), *Transactions on Engineering Technologies*,
DOI 10.1007/978-981-10-1088-0_27

other hand, the dramatic population increase with the simultaneous increase in living standard requirements have increased the energy demand. The priority in the search for new energy sources has been shifted towards applying new methods that can reduce energy consumption. Therefore, one of the best currently emerging techniques is the transformation into constructing green or sustainable buildings [2]. These give a reason to develop a Knowledge-Based (KB) management system that can integrate Lean Six Sigma (LSS) as an advance quality philosophy for sustainable building maintenance based on international best practice. The system will be embedded with Gauge Absence Prerequisites (GAP) analyzes technique to support benchmarking and decision making process.

1.1 Maintenance

Maintenance is defined by British Standard BSI Publication [3] as "*the combination of all technical and associated administrative actions intended to retain an item in, or restore it to, a state in which it can perform its required function*".

Zawawi et al. [4] insist that the performance in maintenance operations management have to be analysed and reviewed continuously in order to achieve high service quality. Ding [5] has specified that sustainability is built on assessment tools that apply quantitative performance indicators of a building and rating tools which determine the performance level of that specific building. However, the traditional maintenance approach to achieving a high consistent performance leads to over exhaustion of resources. Thus there is a need for a newer approach to these problems.

1.2 Lean Six Sigma (LSS)

LSS is a quality philosophy that utilizes Lean management technique to speed up the process while applying Six Sigma (SS). This is performed by eliminating the non-value added elements from the process. In fact, the whole process will be leaned to the minimum requirement of SS tools and techniques. Therefore, Lean and SS are complementary to each other. LSS is recognized as "*a business strategy and methodology that increases process performance resulting in enhanced customer satisfaction and improved bottom line results*" [6]. In addition to eliminating the non-value added elements, Lean improves speed and efficiency, whereas Six Sigma promotes effectiveness by removing variants from the process. According to Zhang et al. [7], LSS utilizes Lean and Six Sigma tools and techniques to form a powerful remedial action that can eliminate the problems behind implementing each one of these approaches.

Laureani and Antony [8] stated that LSS entered an implementation era in late 1999. However, there is no central certification authority, as with other quality

principles, and thus most of the practitioners are being assessed internally by their own organizations or external quality bodies [e.g., American Society for Quality (ASQ), International Quality Federation (IQF), and the British Quality Foundation (BQF)]. They have explored the current LSS best practices in different industries. Their study indicates that the high variation in the certification standard has caused difficulty in evaluating and measuring actual competencies and implementation success.

1.3 GAP Technique

Gauge Absence Prerequisite (GAP) is a benchmarking tool that will be used in KB Lean6-SBM. It will assess the existing company situation with the desired situation (i.e.; the Benchmark) in order to find out the gap between them. The development of a conceptual model for KB Lean6-SBM will be supported by the published articles on KB and GAP. All factors that are critical to develop the new Lean6-SBM model will be revised and analyzed using GAP technique. There is no evidence in the literature that a combination of KB, and GAP has been utilized as an approach in the field of managing LSS in SBM.

It has been proven from literature review that the GAP is a powerful benchmarking technique. For examples, it has been integrated with hybrid KB Systems as a benchmarking tool in some areas, like lean manufacturing [9], and Maintenance Strategy and Operation [10]. Therefore, this research will extend the use of GAP to the area of sustainable building maintenance.

The following sections are designed to give a brief research background, followed by defining the main attributes of the proposed KB Lean6-SBM conceptual model.

2 Research Background

There is evidence in the literature [4] that the implementation of current maintenance management systems has not achieved the expected level of success (e.g.; maintenance schedules are not implemented on time and priorities are difficult to identify). This is due to lack of maintenance management skills and execution experience which lead to poor impact and crucial negative effects on facility performance. In fact, failure to perform maintenance strategies results in dramatic waste of resources and resulting in poor quality. Milana et al. [10] have described this waste in maintenance area by saying that unnecessary repair or inspection will definitely lead to increase in maintenance budget commitments and drop in quality performance. These give indication that maintenance processes have non-value adding steps which need continuous improvement. In parallel to this, the complexity of sustainable building maintenance environment requires managers to define and implement appropriate standardized quality management system suitable for this function.

The significant of this research is to advance the use of a hybrid KB/GAP system to develop a Lean6-SBM. This approach is very new and will assist in identifying quality perspectives while implementing different maintenance strategies in sustainable building context. It will go further to suggest optimum and semi-optimum solutions based on experts' opinions and functional priorities. Thus, the research will deliver an affective decision support system that will assist top management in addition to quality/maintenance managers and practitioners in sustainable building maintenance sector to prioritize and monitor their performance and hence, increase the productivity. In addition, the system will integrate LSS and a readiness evaluation framework to facilitate the implementation of this system.

3 The Conceptual Model

This Chapter focuses on proposing a novel generic model for KB Lean6-SBM as currently no existing model that can examine the implementation of LSS in Sustainable Building Maintenance with the support of KB capabilities exists. The following subsections will detail the proposed conceptual model that has been derived based on extensive literature review and field experience. The conceptual model is divided into three main stages: Planning, Designing, and Implementation. The Planning and Designing Stages formulate the strategic level, while the operational level is represented by the Implementation Stage.

3.1 Planning Stage (Identification)

As it can be seen in Fig. 1, the Planning Stage includes the strategic level, which contains the organization business, environment, and resources perspectives, in addition to the change management readiness assessment framework. In this stage, general information of the organization will be requested in order to assess its strategic capabilities and readiness to change into the new LSS (green) environment. Due to its criticality, this stage can be described as a filtration chamber, in which it can ascertain whether the organization can proceed further with LSS implementation or it will be in need of major changes.

3.1.1 Organization Environment and Business Perspectives

In order to achieve a comprehensive assessment for a building maintenance environment, there must be an investigation to the organization objectives, market share, and financial analyzes. For the business perspectives, a general information of company/organization environment, market analyzes, and financial analyzes is required to identify a manufacturing business [11]. The organization statement

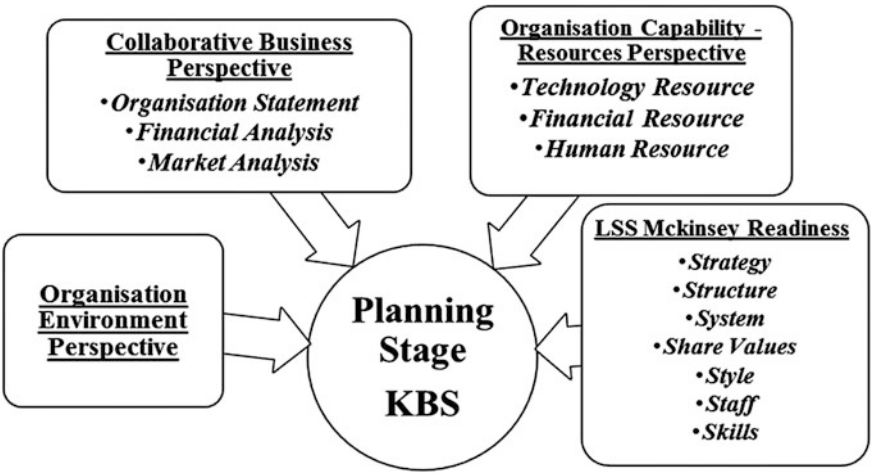

Fig. 1 Conceptual model (planning)

represents the gate of the initial identification. It specifies vision, mission, and business objectives that describe the bold guidelines of the business operation. In addition to that, the organization environment will capture the current situation of the SBM organization, including general information about the age of the organization, number of employees, suppliers, customers, and number of competitors, which can be used to determine the size of the firm [9]. On the other hand, it is obvious that market place highlights the area where the maintenance service is applied, whether it is restricted area, local or global. This might influence the service lead-time. Therefore, it is necessary to analyze the market performance and evaluate how well the organization in attracting the customers through its services. Mohamed and Khan [12] stated that market share reflects the percentage of how much business received from customers. In parallel with market share, the financial analyzes has a critical importance in deriving the actual organization financial statement, impacting on how well it will be able to deliver its KPIs. According to Stefan and Paul [13], Return on Investment (ROI), Return on Equity (ROE), and Return on Asset (ROA) are the key financial indicators that can give a clear financial analyzes based on Lean6-SBM model. These operating returns ratios [14] are captured from the organization balance sheet, cash flow, and income statement.

3.1.2 Resources Perspectives

Albliwi et al. [15] described the lack of resources as one of the main critical failure factors in implementing LSS. Therefore, this stage will identify the organization resources capability that determine technology, financial, and human aspects [16]. Nawawi et al. [9] and Mohamed and Khan [12] have tested these organization resources capabilities in manufacturing sector. However, this research has listed

similar resources which can be applied to building maintenance organization. The functional purpose is to gauge the existing organization capability in terms of the availability of enough resources to carry out the required implementation. These can be categorized as: first, the human resource which will trigger employees' development, the associated culture, and benefits (e.g.; rewards, and salaries). Secondly, the technology resource which deals with managing technologies (e.g.; maintenance systems like Enterprise Resource Planning or CMMS). Finally, the financial resource will take place in regard to annual budget allocated for employees, technical aspects and technology development in the field of sustainable building maintenance.

3.1.3 LSS McKinsey Framework

As part of the strategic level, the organization is in need to prove the readiness to change. Despite the different culture, pressure, and reasons of change in organizations, change management frameworks play an important role in minimising the distractions and impacts by keeping any change effort under control [17]. The literature indicates that in more than 90 % of surveys about Lean, SS, and LSS projects there is a degree of resistance to change, and lack of management commitment. These are the main impediments against successful project implementation [15, 18]. In spite of having built-in change management awareness process in DMAIC model, there is a need to enhance this approach with a comprehensive plan that should analyze and assess the organization readiness to tackle such obstacles. For that reason, a readiness evaluation framework is necessary to be integrated into the system. This will be based on the McKinsey 7S framework, which is widely used in the field of Information Technology. The organization readiness has to be tested prior to LSS implementation in order to highlight the degree of human resource gap points. Hanafizadeh and Ravasan [19] indicate that McKinsey's 7S framework can be categorized into soft S's and hard S's. Soft S's are difficult to implement and contain Staff, Skills, Style, and Share values, whereas hard S's are easy to identify and contain Systems, Structure, and Strategy.

3.2 Designing Stage

This Designing Stage is identified as the second stage. It will study the core business of the organization by assessing the capability of integrating LSS to support relevant know-how of sustainable building maintenance based on the applied taxonomy structure. For both, SBM and LSS, it is very necessary to consider sustainability metrics. These must integrate social, environmental, and economic impacts within the selected SBM and LSS performance measures. Accordingly, the conceptual design will consider the most suitable LSS elements with respect to SBM in order to generate Lean6-SBM. Next, Lean6-SBM has to be

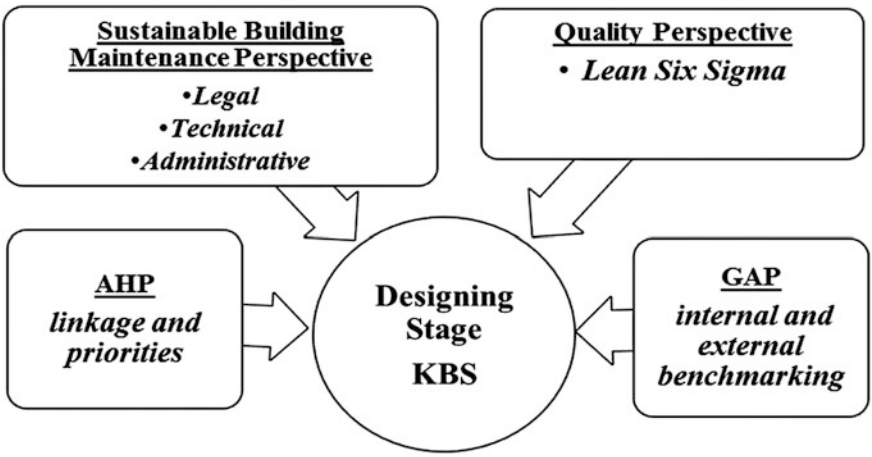

Fig. 2 Conceptual model (designing)

supported by a decision making process to finalize the application conceptual design.

This requires to have a powerful methodology that can trigger two deliverables in KB Lean6-SBM: the benchmarks between the existing practice and the desired ones, and listing the recommended solutions based on priorities (*AHP is not included in this chapter*). In this stage, the Lean6-SBM model will proceed with benchmarking through integrating GAP analyzes technique (see Fig. 2). The outcome of the stage will reflect how far the organization or the maintenance department is from the desired best practice (Benchmark).

3.2.1 Lean Six Sigma (LSS)

Due to the nature and complexity of this philosophy, there is a need to narrow down the selective tools and techniques, which are going to be included in the KB system in later stage. Setijono et al. [18] stated in their findings of the survey done in 101 manufacturing and service companies some critical success factors which might affect the LSS implementation. The majority of respondents highlighted the importance of "leadership styles", "organizational culture", "management commitment", and "linking LSS to business strategy". This study has been enhanced by Albliwi et al. [15], where they show that around 34 factors affect LSS implementation. The top factors are related to lack of top management attitude, lack of training, poor project selection, and lack of resources.

According to Al-Aomar [20], there are seven types of wastes in production and construction environment: these are delays, defects, excessive people movement, excessive transport, over inventory, over production, and long delivery of equipment and materials which will definitely affect the lead-time in building

maintenance process. On the other hand, Bhatia and Drew [21] defined the need of customer focus where all of the activities must be tested to ensure their efficient and they are adding value to the buyer.

3.2.2 Sustainable Building Maintenance Taxonomy

From the researcher's experience, and close investigation in maintenance practices of sustainable buildings, it is found that sustainable maintenance taxonomy and strategies are not independent of the traditional maintenance processes and practices. Motawa and Almarshad [22] have designed their Building Maintenance (BM) taxonomy based on existing BM contracts of public sector. This scheme has been verified by professionals to suit with the specified work environment. The research will extend the use of this taxonomy with a provision of verification and refinement in later stage. It will be presented as the main sustainable building maintenance taxonomy structure that will be integrated into the KB Lean6-SBM system. The taxonomy is consisted of three categories: Legal, Technical, and Administrative.

Virtually, this taxonomy will help to assess the organization in terms of how it is committed to the maintenance contract conditions, bidding regulations, health, and safety [23]. The second part of the assessment is technical. Alnaser [24] elucidated the need to check the compliance of the organization in terms of sustainability metrics, which include energy efficiency, natural resource conservation, indoor air quality, and social responsibility. The next step is to analyze the lead time of the maintenance work orders and how they fulfil the desired specifications and standards [25]. The final checkpoint will acquire the answers to be given for some questions regarding administrative aspects. This includes availability of the documented business process [26], budget compliance in conjunction with financial resources, and human resource management based on the organization's human resource assessment [25].

3.3 Implementation Stage

SS is widely implemented through Define, Measure, Analyze, Improve, and Control (DMAIC) cycle. According to De Mast and Lokkerbol [27] this method is developed in practice from engineering industries, and that DMAIC is suitable for solving complex problem tasks if and only if it is required to expose all problem components (i.e.; define, diagnose, and design of solutions).

On the other hand, they declare that it is not suitable for unstructured or subjective problems. Therefore, the DMAIC methodology for the proposed KB system can be described as: *Define* the sustainable building maintenance values, and results along with customer needs for a particular area, department, or a project. *Measure* and validate data which helps in setting priorities and criteria, *Analyze* to find out root causes and well understanding of the process and problem, *Improve* by

developing solutions and refining goal statements, and finally *Control* and monitor the changes by developing a tracking process.

3.4 Knowledge-Based System

An Expert System or a KB System is one of the Artificial Intelligence concepts and methodologies. The terms ES and KBS are having the same meaning and therefore, most of the scholars use them synonymously. In fact, when ESs were developed, they contained considerable knowledge regardless if it was not matching with the performance of human experts, and therefore they were called KB system. This KB contains rules, facts, and the acquired knowledge from human experts [9].

Currently, there is a dramatic increase in using KB systems in various disciplines. The reason is basically to reduce the high expenditures of hiring experts and to get ease of knowledge transfer within the organization, and consequently improving the productivity.

4 Generation of KB Rules

The created model has been verified through J. AlDairi et al. [28] and converted into a framework in order to develop the conceptual design of the KB Lean6-SBM system. The framework is structured in 6 Levels where they form the system modules: Level 0 Organization Environment, Level 1 Collaborative Business Perspective, Level 2 Organization Capability—Resources Perspective, Level 3 LSS Mckinsey Readiness, Level 4 Sustainable Building Maintenance Perspective, and Level 5 LSS Perspective. Each Level in the framework will demonstrate relevant critical Key Performance Indicators (KPIs). This Chapter will highlight three examples of rule sets taken from the sub-module technical of the SBM perspective module. These include the dimensions of sustainability metrics, work orders, specifications and standards as part of the operational decision Level 4 (Fig. 3).

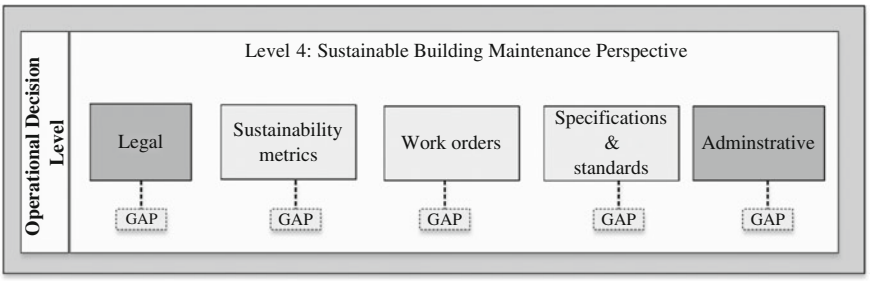

Fig. 3 The system structure of SBM perspective module

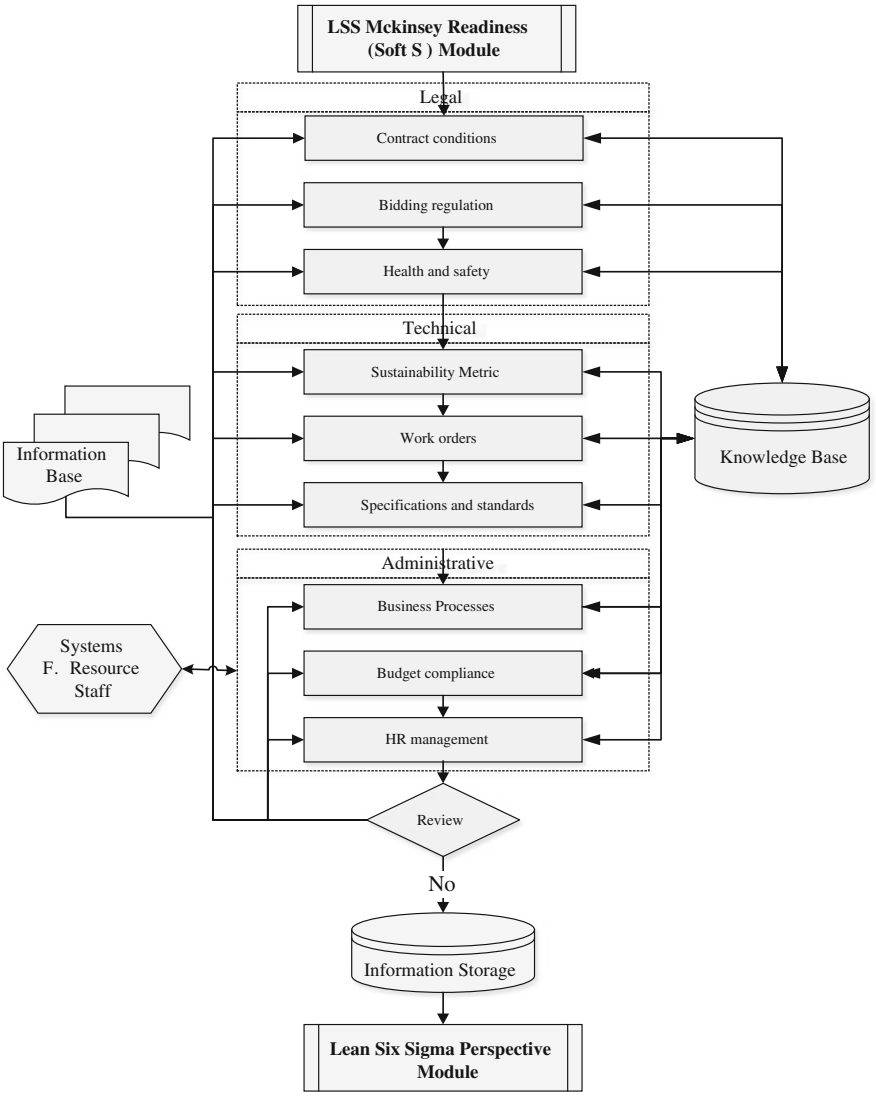

Fig. 4 Process flowchart of SBM module

The KB Lean6-SBM rule sets for this module can be generated using the flowchart in Fig. 4. It can be noticed that some KPIs in this module are influenced by other KPIs (e.g., KPIs of organizational resource capabilities and LSS McKinsey Readiness); and hence, this issue will be addressed by creating some action rules in a cross-functional manner. Each KPI is linked with an information base as a data acquisition platform and benchmarked with the existing knowledge of best practises. Lastly, user feedback must be reviewed and verified at the end of the process.

Generally, The KB rule sets are designed to interact with different level of users by driving a serious of questions related to each module in a sequential order. These are integrated with GAP analyzes based on degree of severity obtained from experts, books, manuals, and practical field experience.

4.1 Sustainability Metrics

As it has been mentioned above, the sustainability metrics will evaluate the measures towards energy efficiency, natural resource conservation, indoor air quality and social responsibility. The following brief example illustrates one of the KB rule sets in this dimension:

IF	*the organization has implemented the HSE regulations in the work flow* (**Yes**: GP; **No**: BP-**PC-1**)
AND	*the Mean Time to Recovery (MTTR) is within the specified contract scope* (**Yes**: GP; **No**: BP-**PC-1**)
AND	*the materials used in maintenance are environmentally compatible and meet specifications* (**Yes**: GP; **No**: BP-**PC-1**)
AND	*the maintenance work process has done as per the standard procedure* (**Yes**: GP; **No**: BP-**PC-3**)
AND	*there is no overspend within the allocated budget* (**Yes**: GP; **No**: BP-**PC-3**)
AND	*the customer satisfaction is high with respect to work execution* (**Yes**: GP; **No**: BP-**PC-2**)
THEN	*the organization has achieved the main objectives of Sustainability in Maintenance.*
OR	*the organization status is below the standard and has not achieved Sustainability in Maintenance*

4.2 Work Orders

In this stage, the organization will be assessed in fulfilling the information needed in a work order template (e.g., location, task, instructions, and maintenance checklist), the percentage of work orders completed against deferred or pending within the planned preventive maintenance schedule. The following example explores one of the KB rule sets in the dimension of work orders:

IF	*the Lean6-SBM organization has identified a standard process/form/template of creating work orders* (**Yes**: GP; **No**: BP, **PC-1**)
AND	*the Lean6-SBM organization has set effective policy of receiving and distributing work orders between all departments* (**Yes**: GP; **No**: BP, **PC-1**)

(continued)

(continued)

AND	*the Lean6-SBM organization has effective work order follow-up and traceability system* (**Yes**: GP; **No**: BP, **PC-1**)
AND	*the Lean6-SBM organization has maintained a maintenance history records* (**Yes**: GP; **No**: BP, **PC-1**)
AND	*the Lean6-SBM organization has records of work orders statistical analyzes for maintenance improvement* (**Yes**: GP; **No**: BP, **PC-2**)
AND	*the Lean6-SBM organization has developed a job completion signature step within the work order process* (**Yes**: GP; **No**: BP, **PC-1**)
AND	*the Lean6-SBM organization has developed a customer feedback step within the work order process* (**Yes**: GP; **No**: BP, **PC-2**)
THEN	*the Lean6-SBM organization is good in work order handling process*
OR	*the Lean6-SBM organization needs to focus on rectifying the internal process of handling work orders*

4.3 Specifications and Standards

This dimension will be triggered by the lead time of the maintenance work orders and how they fulfil the desired specifications and standards to meet the excellence maintenance of the targeted asset (e.g., identifying hazardous, selecting the right parts, and applying the recommended process from manufacturer O&M manuals), as an example:

IF	*the Lean6-SBM organization has developed a proper replenishment system and storage facility for the critical and hazardous materials at the work place* (**Yes**: GP; **No**: BP, **PC-1**)
AND	*the Lean6-SBM organization has developed a comprehensive safety training to the pertinent technicians for the use of these materials* (**Yes**: GP; **No**: BP, **PC-1**)
AND	*the Lean6-SBM organization has a quality assurance system that test the personnel use of safety protective equipment* (**Yes**: GP; **No**: BP, **PC-2**)
AND	*the material safety data sheet (MSDS) is used and implemented* (**Yes**: GP; **No**: BP, **PC-1**)
AND	*the Lean6-SBM organization has set a proper transportation safety procedures for these materials* (**Yes**: GP; **No**: BP, **PC-3**)
AND	*there is a proper disposal system of the hazardous materials* (**Yes**: GP; **No**: BP, **PC-3**)
THEN	*the Lean6-SBM organization has implemented the basic regulations of hazardous materials*
OR	*the Lean6-SBM organization has to focus on implementing a proper safety precaution system*

From the above selected KB Lean6-SBM rule sets, it is obvious that the organization is going to be evaluated from different dimensions within the main three sub-modules of the SBM. The KB rules includes GAP analyzes where Good Points (GP) reflect the availability of prerequisites to the Lean6-SBM organization, and Bad Points (BP) are representing the areas that need further improvements. These BPs are categorized in severity order from PC-1 to PC-9 where PC-1 is the most severe and critical issue that need to be addressed immediately according to Mohamed and Khan [12].

5 Results and Analyzes of Technical Sub-module

In order to optimize and find-out the GAPs within the system, the created KB rule sets will be fired based on a KB Lean6-SBM built-in questionnaire. The output will identify how far the organization is from the desired practice. For a simulation purpose, the typical results/output of SBM module is shown in Table 1. A total number of 235 questions have been asked. As a result, 117 have been answered as GPs whereas 113 have been answered as BPs. These BPs are categorized as 40 PC-1, 18 PC-2, 13 PC-3, 6 PC-4, 10 PC-5, 1 PC-6, 9 PC-8, and 18 PC-9 which indicate the weak points in SBM module that need to be improved.

With regard to technical sub-module, it can be noticed that sustainability metrics has the highest number of BPs (58 %) followed by 56 % for standards and specifications and 33 % for the work orders in respect to the number of questions asked. The drawback in sustainability (7 PC-1) seems to be more due to the lack of awareness in applying green/sustainable maintenance. This includes but limited to proper cleaning practice and replacement of parts to analyzing the efficiency of water and energy saving techniques. Furthermore, the importance of specification and standards might be detected from declaring that all BPs of this dimension fall under major problem categories (PC-1 to PC-4).

Table 1 Level 4—SBM perspective

Sub-module	Dimension	Number of questions	Good points (GP)	Bad points (BP)	Bad point problem category (PC)								
					1	2	3	4	5	6	7	8	9
Legal	Sub total	67	38	24	0	6	6	0	0	0	0	1	4
Technical	Sustainability metrics	43	18	25	7	3	3	2	4	1	0	2	3
	Work orders	30	20	10	3	1	0	0	1	0	0	2	3
	Specifications and standards	25	11	14	5	2	3	4	0	0	0	0	0
	Sub total	98	49	49	15	6	6	6	5	1	0	4	6
Administrative	Sub total	70	30	40	16	6	1	0	5	0	0	4	8
Grand total		235	117	113	40	18	13	6	10	1	0	9	18

6 Conclusion and Future Work

This Chapter has presented the conceptual model of a KB system to support the application of LSS principles in building maintenance with a focus on sustainability. The maintenance function can have a strong impact on organizational performance. This is also relevant in the context of sustainable building maintenance. The LSS philosophy seeks to achieve continuous improvement of the maintenance function. The novelty of this approach consists of the integration of LSS with SBM using GAP analyzes for benchmarking in order to support decision making within a hybrid KB system. The Mckinsey 7S framework is applied to assess organizations for readiness.

The method of creating KB rule sets has been described with three examples from SBM perspective. Relatively, 235 KB rule sets were developed and the results are presented and discussed. The Benchmark are achieved by identifying the key problems (GAPs) which need further improvements. Therefore, this approach is valid in promoting a powerful Benchmarks for the sustainability of Building Maintenance.

Future research will consider further development of the conceptual model into a practical KB system.

Acknowledgments This work was supported by the Ministry of Defense Engineering Services (MoDES—Sultanate of Oman) and the University of Bradford (United Kingdom).

References

1. Dhillon BS (2006) Maintainability, maintenance, and reliability for engineers. CRC Press, Boca Raton
2. Oxley R (2011) Breeam code for sustainable homes information pack. http://www.hrsservices.co.uk/downloads/breeam_info_pack.pdf. Accessed 26 Dec 2014
3. BSI Standards Publication (2010) Maintenance terminology. In: BS EN 13306:2010. BSI, United Kingdom
4. Zawawi EMA, Kamaruzzaman SN, Ithnin Z, Zulkarnain SH (2011) A conceptual framework for describing CSF of building maintenance management. Procedia Eng 20:110–117
5. Ding GKC (2008) Sustainable construction—the role of environmental assessment tools. J Environ Manage 86:451–464
6. Snee RD (2010) Lean Six Sigma-getting better all the time. Int J Lean Six Sigma 1:9–29
7. Zhang Q, Irfan M, Khattak MAO, Zhu X, Hassan M (2012) Lean Six Sigma: a literature review. Interdiscip J Contemp Res Bus 3:599–605
8. Laureani A, Antony J (2011) Standards for Lean Six Sigma certification. Int J Prod Performance Manage 61:110–120
9. Nawawi M, Khan M, Hussain K (2008) Knowledge-based collaborative lean manufacturing management (KBCLMM) system. J KONBiN 8:145–156
10. Milana Khan MK, Munive-Hernandez JE (2014) A framework of knowledge based system for integrated maintenance strategy and operation. Trans Tech Publication, Stafa-Zurich, pp 619–624

11. Zulkifli-Udin M, Khan MK, Zairi M, Giaglis GM (2006) A collaborative supply chain management framework: part 1-planning stage. Bus Process Manage J 12:361–376
12. Mohamed NMZN, Khan MK (2012) The development of a hybrid knowledge-based system for the design of a low volume automotive manufacturing (LVAM) system. Int J Intell Syst Technol Appl 11:17–35
13. Stefan A, Paul L (2008) Does it pay to be green? A systematic overview. Acad Manage Perspect 22:45–62
14. Berk J, DeMarzo P (2014) Corporate finance: the core, global edition, 3rd edn. Pearson Education
15. Albliwi S, Antony J, Abdul Halim Lim S, van der Wiele Ton (2014) Critical failure factors of Lean Six Sigma: a systematic literature review. Int J Qual Reliab Manage 31:1012–1030
16. Waldeck NE (2000) Advanced manufacturing technologies and workforce development. Garland Publishing
17. Kotter J (2011) Change management vs. change leadership—what's the difference? Forbes. http://www.forbes.com/sites/johnkotter/2011/07/12/change-management-vs-change-leadership-whats-the-difference/. Accessed 21 Sept 2015
18. Setijono D, Laureani A, Antony J (2012) Critical success factors for the effective implementation of Lean Sigma: results from an empirical study and agenda for future research. Int J Lean Six Sigma 3:274–283
19. Hanafizadeh P, Ravasan AZ (2011) A Mckinsey 7S model-based framework for ERP readiness assessment. Int J Enterp Inf Syst (IJEIS) 7:23–63
20. Al-Aomar Raid (2012) A lean construction framework with Six Sigma rating. Int J Lean Six Sigma 3:299–314
21. Bhatia N, Drew J (2006) Applying lean production to the public sector. McKinsey Q 3:97–98
22. Motawa I, Almarshad A (2013) A knowledge-based BIM system for building maintenance. Autom Constr 29:173–182
23. Hon CKH, Chan APC, Yam MCH (2014) Relationships between safety climate and safety performance of building repair, maintenance, minor alteration, and addition (RMAA) works. Saf Sci 65:10–19
24. Alnaser NW (2008) Towards sustainable buildings in Bahrain, Kuwait and United Arab Emirates. Open Constr Build Technol J 2:30–45
25. Stopwaste.org (2013) A guide to green maintenance and operations. http://www.stopwaste.org
26. Frank OL, Omer SA, Riffat SB, Mempouo B (2015) The indispensability of good operation & maintenance (O & M) manuals in the operation and maintenance of low carbon buildings. Sustain Cities Soc 14:e1–e9
27. De Mast J, Lokkerbol J (2012) An analysis of the Six Sigma DMAIC method from the perspective of problem solving. Int J Prod Econ 139:604–614
28. AlDairi J, Khan MK, Munive JE (2015) A conceptual model for a hybrid knowledge-based Lean Six Sigma maintenance system for sustainable buildings. Lecture notes in engineering and computer science: proceedings of the world congress on engineering 2015, WCE 2015, 1–3 July 2015, London, UK, pp 939–944

Strategic Leadership Practices for Sustainable Competitive Advantage in the Global Market

Nelson Sizwe Madonsela, Paulin Mbecke and Charles Mbohwa

Abstract The global economy is currently facing challenges in relation to the poor performance of economies globally from both developed and developing countries. It is noted that the global market environment has become complex and difficult to predict. At the national level, countries are investing in various aspects like advanced technologies and talent to strengthen their global position within the global economy and enhance economic growth, yet, the global market environment is still volatile. Therefore this chapter highlights the nature of the global market environment, which requires a knowledge integration perspective in order to sustain the competitive advantage of the 21st century. It provides strategic leadership practices approach to address the challenges associated with the global market environment drivers such as technologies and globalization of manufacturing, to name but few. Furthermore, the chapter emphasizes on strategic leadership practices through knowledge integration perspective for sustainable competitive

N.S. Madonsela (✉)
Faculty of Engineering and the Built Environment (FEBE), Department of Quality and Operations Management, University of Johannesburg (UJ), Johannesburg, South Africa
e-mail: nel_madon@yahoo.com

P. Mbecke
Faculties of Political, Administrative and Social Sciences and Economic and Management Sciences, Department of Community Development, University du Moyen Lualaba (UML), Kalima, Democratic Republic of Congo
e-mail: pmbecke@gmail.com

P. Mbecke
Department of Public Administration and Management, College of Economic and Management Sciences, University of South Africa (UNISA), Pretoria, South Africa

C. Mbohwa
Faculty of Engineering and the Built Environment (FEBE), Department of Quality and Operations Management, FEBE's School of Mechanical and Industrial Engineering, University of Johannesburg (UJ), Johannesburg, South Africa
e-mail: cmbohwa@uj.ac.za

S.-I. Ao et al. (eds.), *Transactions on Engineering Technologies*,
DOI 10.1007/978-981-10-1088-0_28

advantage. Finally, the chapter proposes strategic leadership practices that are applicable at national and organizational levels to sustain competitive advantage.

Keywords Global market environment · Global competitive advantage · Knowledge acquisition and application · Knowledge integration · Strategic leadership practices · Sustainable competitive advantage · Competitiveness

1 Introduction

The global economy is currently facing challenges in relation to the poor performance of economies globally from both developed and developing countries. Economic theorists such as [1] believe that the global market environment has become complex and difficult to predict. Most economies of developing and developed countries face multiple challenges to face the current nature of the global market. Ireland and Hitt [1] maintain that the global market forces firms to "compete simultaneously on a variety of competitive priorities in order to respond quickly to market opportunities and treats". The critical point is that the global market environment requires a broader understanding of its dynamics and adequate knowledge acquisition and application [2].

Economies and their firms need to align strategic leadership practices toward the global environment through extensive knowledge integration in order to sustain competitive advantage. Ireland and Hitt [1] defines strategic leadership "as a person's ability to anticipate, envision, maintain flexibility, think strategically, and work with other to initiate changes that will create a viable future for the organization". The success of any country or firm lies on the leader's ability to integrate these key. This chapter highlights the current global market environment's drivers with their constraints. It proposes strategies to address the challenges associated with the drivers.

2 Current Global Market Environment

Global market environment have been studied for centuries, thus far, it's erratic. In the 21st century it has become more complex and drawn attention from economies. Nations have invested in Research and Development (R&D) institution to acquire in-depth understanding of the current global markets environment behavior [2]. Also in Information and Communication Technologies (ICT), infrastructural, transportation, and talent [3, 4]. Regrettably, both developed and developing countries still find it difficult to sustain competitive advantage within the global market.

The current global market environment has been influencing by many drivers, which also were noted by the World Economic Forum in 2011 [5]. Therefore, it is

fundamental that economies and firms identify these drivers to establish how they impact the global market to be able to encapsulate its nature.

It is certain that the current global market environment is difficult to predict as well as to describe in a simple form since it is inconsistent. Regardless, the approach in understanding the global market environment should based on articulating the dynamics of the global market. Bahl and Shaw [6] defines market dynamics as the "interrelation of market structure (actors and products), actions (financing, innovation, and transparency), and outcomes (price, supply, quality, and sustainability)". Correspondingly, these elements are complementary to the drivers as they facilitate the execution of the global market drivers. Sustain competitive advantage does not depend on the nation's economic strength or whether is a developed, or developing country.

In the global market environment context, depends on mastering the main drivers. Studies have shown that the global leading manufacturing economies like China's success lies on advancement of technology in trading systems, revised policies and affordable labor [3]. This implies knowledge acquisition and application approach, clearly it shows that such nation understood the nature of globalization in order to incorporate these drivers to sustain competitive advantage [2]. The notion is that the current global market environment's main drivers are the advancement of technology, globalization of manufacturing, and knowledge integration perspective.

2.1 Advancement of Technology

The advancement of technology has made it possible for the global village to function around the globe [7]. Today we see customers conducting business transactions anywhere, anytime in the world thanks to the advancement of technology. Bitner et al. [8] observed that one of the elements in the global market is that the influence of technological change has created self-service beyond our imagination. These authors also noted that service offerings has been altered by technology through facilitation of automated services, for example the internet-based services, smart meters. It means that customers can interact with a nation or firms remote and access services without human contact.

Equally, employees can share organizational resources and collaborate with other organization thanks to the advancement of technology. Dahlman [3] argues that "technology is an increasingly important element of globalization and of competitiveness and that the acceleration in the rate of technological change and the prerequisites necessary to participate effectively in globalization are making it more difficult for many developing nations to compete". While it is true that technologies has enabled the global market environment to be integrated in such way that any economies or firms that wants to enter must indeed adopt them.

Although, it does not guarantee success because there are other key elements that need to be taken to consideration like the ICT infrastructure, higher skilled

workforce which is encompasses higher labor cost and changing dynamics in the global labor market. Actually, these technologies are also so complex and require special expertise, and talent. As a result, the global market environment has been experiencing geographical shift of talent or employment globally [5, 9]. Meaning that puts more pressure to economies and firms to formulate retention strategies. It cannot be argued that advancement of technologies is becoming the main driver of the constant changing global market environment.

Therefore, an economies and firms need to adopt a strategic leadership practices that ensures such knowledge is integrated in decision-making, failure to do so it might hinder a nation's or firm's ability to compete successfully in the global market. As an illustration, developing economies like South Africa experienced challenges of engineers leaving the country due to lack of strategic leadership practices, as well as the inability to revise its ICT policy to enable the country's firms to invest in ICT.

A nation that seeks to gain competitive advantage in the global market environment should be willing to formulate an adequate strategic leadership practices that integrates knowledge. Hence technological capability can allow economies and firms to accelerate the penetration of global market [3]. In addition, technologies are key enabling infrastructure that creates access to vital information, supply chain, competitors, global market networks and customers. Although are complementary to technical expertise. Therefore, the adoption of technologies ought to pay serious attention not only on infrastructure, but also acquiring the necessary technical skills and innovation to address any encountered obstacles. The assumption is that the economies and firms that acquire such capabilities stand a good chance of succeeding on sustaining competitive advantage.

2.2 Globalization of Manufacturing

The globalization manufacturing sector has strengthened economies' economic growth and attracted foreigner investors. Furthermore, globalization has created equal opportunities for developed and developing economies access to the global market to acquire raw materials, technologies and talent, what is more, to trade. Notwithstanding, there are barriers that preventing some economies to take advantage of the global market, such policies, cultural, higher-skilled workforce, infrastructural and lack of attracting foreign investors. This heavily lies on strategic leadership practices of a nation's government to create enabling environment that addresses all these barriers. Reference [10] argues that "understanding global market dynamics requires global network reach"; moreover, he is of the opinion that developing and sustaining competitive advantage can be attained through gaining insight into socio-economic behavior through the lens of global markets. His case study emphasizes that competitiveness and innovation depend on information accessibility; and that "social and economic sciences play a vital role in improving knowledge management and decision-making in business strategy and

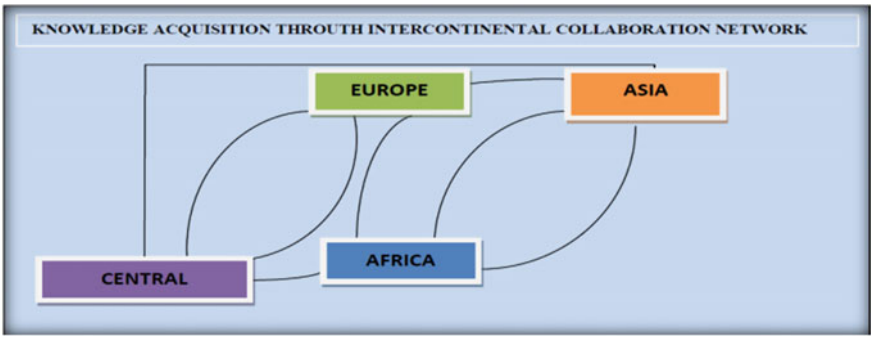

Fig. 1 Intercontinental collaboration network. *Source* Authors

government policy" [10]. Figure 1 shows an example of the global network reach perspective lens for knowledge acquisition through intercontinental collaboration.

The above diagram depicts the intercontinental grid technology that allows economies and firms to have access to acquire knowledge, which we have observed economies signing inter-relational or intercontinental agreement in relation to trading systems and knowledge sharing. Globalization has created a boundless world that forces economies to collaborate. Interestingly, the globalizations of manufacturing have few constraints that need serious attention, namely:

2.2.1 Policy Constraints

Globalization has been putting pressure on economies to revise their policies in order to enter the global marketplace [3]. Meanwhile other economies and researchers perceive as a strategy of disaggregating between developed and developing economies [11].

Mintzberg [11] in 2010 questioned the purpose of globalization through his study entitled: Developing leaders? Developing Countries? Hence some economies' policies are among the barriers that depriving them to benefit from the global marketplace. In developed countries like America we've noted firms relocating to China due to labour policy that could not be changed, which means China's policies (like cheap labour) are favourable to attract foreign invest within the global market [3].

Equally, in developing within Africa specifically South Africa, there have been some policies issues surrounding the National Development Plan 2030 implementation, to be more precisely, the ICT policy [12]. Yet, economies such as China and India are flourishing within the global marketplace due to revised policies to sustain competitive advantage. It is certain that China government acquired knowledge about the global market environment through Research and Development (R&D) institutions in order to align its strategic leadership. This has been illustrated by the

revised policies of trading systems and labour (cost and supplying engineers). Today, China is the leading trader in the world. Thus, it is imperative that leaders pay serious attention to the global market environment, what is more, the policy marker should acquire global perspective rather than national perspective if these economies need to survive the turbulent market.

2.2.2 Cultural Constraints

It has been argued that what is working in developed economies is not bound to working in developing economies. Likewise, culture is complex across countries; in fact, it is a challenge even within the individual economies. Therefore, trading in a different country challenges economies and firms to establish that country's culture, which some time might be difficult. So economies are invested in R&D to address this national cultural barrier, however, some economies due to lack of such infrastructure it might be detrimental to trade in a nation that they have no understating of its culture.

To take a case in point, in 2008 [13] maintain that the largest retailer Wal-Mart failed to penetrate the Germany market as a result of cultural barrier. The authors are of the opinion that Wal-Mart did to acquire knowledge with regard to the Germany's culture. Wal-Mart based its decision-making on the successful strategy that was working well in Unites States of America to expand to German and South Korea.

Meanwhile the Germans found it unfavorable; moreover the stores were managed by American managers [13]. Consequently, Wal-Mart has to surrender 85 stores to the Germans losing 1 billion of revenue. The global market requires adequate strategic leadership practices that have a sense of knowledge integration from economies and firms. There is a possibility that firms believe having resource guarantees success within the global market and also that creates an opportunity to expand.

Success in the global market depends on knowledge acquisition and application through scanning the global market environment. Knowledge acquisition depends on leadership strategy and the capability of a nation or company to establish the necessary techniques and institutions. Recently we have noted that many nations and companies are investing in Research and Development (R&D) and advanced technology. In addition, there has been a strong competition for talent, which has become the main driver. It seems that Americans [4] agrees when they concedes, "one core principle of an effective national strategy for advanced manufacturing is to take a cohesive approach to research, development, and deployment".

Larose [14] however believes that there is a challenge in relation to data transformation, since there is lack of adequate human analytical skills. The authors' perspective is that even though advanced technology can be applied, there is still a need for human expertise to establish or deepen the understanding of the dynamics of the global market. Equally, this will successfully address the changing dynamic

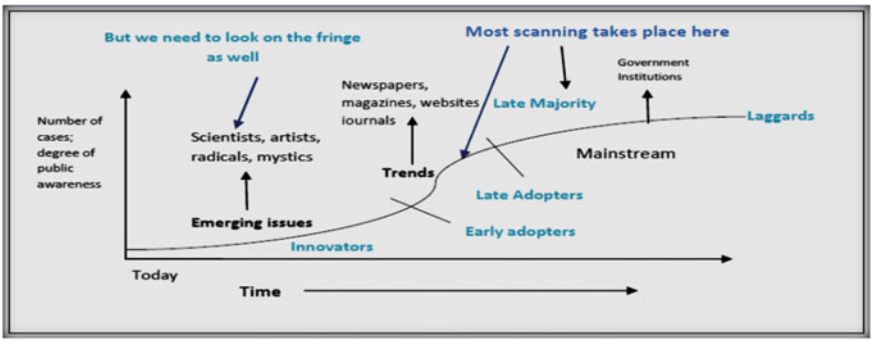

Fig. 2 Life cycle of a trend. *Source* Thinking Futures [10]

of the global market. In doing so, it means a nation or company needs to scan the global market environment to identify the emerging trends and issues. This implies the application of best business practice, innovation and a high skilled workforce, which will be able to interpret the data into information [15]. Indicated early that by gaining insight into social-economic behavior through the lens of global markets, a nation or company can develop and sustain competitive advantage.

The understanding of the global market lies in scanning the environment to identify the emerging issues and trends in order to have a broader awareness of its dynamics as illustrated in Fig. 2. Collaboration between different functionalities is the key fundamental element in enhancing a company's competitiveness, and it encourages the needs of knowledge acquisition and application that is extracted from data mining. Larose [14] defines data mining as "the process of discovering meaningful new correlations, patterns, and trends by technologies as well as statistical and mathematical techniques." Successful manufacturing firms have a strong sense of data mining and continuous innovation which allows them to respond rapidly to customer demands and adapt easily to the constantly changing global market. This is evident in the giant companies such as Wal-Mart [10]. This implies that companies and nations are required to collaborate to share knowledge, more importantly global knowledge, as well as education and training. The fact that some companies and nations might not have access to the global network reach or information can be detrimental for them. Larose [14] shares an insight that as "the practice of data mining becomes more widespread, companies that do not apply these techniques are in danger of falling behind and losing market share, because their competitors are using data mining and are thereby gaining the competitive edge".

In summary, all institutions, whether academic, business, or government, cannot afford to overlook the significance of the current global market trends. The 21st century we are living in is a boundless world in which we are linked in almost all aspects of life in both developed and developing nations. The issue of social and human sustainable development, sustainable economic growth, and the shortfall in a

higher-skilled workforce is impacting on all nations. Accordingly, to be responsive to these issues requires an understanding of the dynamics of the global market environment. This can be attained through acquisition and application of global knowledge of all the vital mentioned elements. Companies and nations can apply these elements through a continuous systematically approach such as Research and Development departments and Service Design techniques. Thereafter, the successfully execution of the obtained knowledge relies on an appropriate execution

2.2.3 Infrastructural Constraints

The infrastructure is the key enabler for economies to operate effectively local and international. Interestingly, in manufacturing industries for both developing and developing economies lack of infrastructure such as ICT and transportation (roads, railroads, airport, and seaports) has been reported hindrance to competitiveness [3]. Along the same line, firms become affected too since their success lies on the enabling infrastructure to function adequate. Recent studies shows that developing economies are able to produce competitive products, yet, the transportation cost is extremely high and in some areas there is a lack transportation infrastructure [3]. It is certain that some economies still facing challenges in relation to the development of infrastructure even some of the developed economies.

The World Economic Forum report stated that "investing in effective infrastructure has been essential for emerging nations to be included as a potential location by multinationals and thus participate in the benefits derived from the globalization of manufacturing". It is of importance that economies develop enable infrastructural in order to support the firms to gain access within the global market.

2.2.4 Higher Cost Labour

The higher cost labor is still challenging all economies and firms, in particularly those who are interested on entering the global market. This barrier is interesting hence it has been experienced in developed countries with the implications of not attracting foreigner investors. While the South African experience has been detrimental within the manufacturing sector in particular the mine industry. There have been several strikes related to demand of higher wages and other labor issues. This affected the manufacturing sector's output, equally, the South African economic growth [16]. In addition, there were assumptions that some foreigner investors are treating to put out their business from the country. Unfortunately, the higher labor costs are linked to the economies labor policies, which cannot be amended easily. Progressively, the economies can revise these policies as a strategic alignment to be responsive to the global market needs and expectations. This forces firms to consider location strategies to avoid higher cost labor.

2.2.5 Higher-Skilled Workforce and Talent

The unpredictable global market has been influencing by the need of talent and higher-skilled workforce. Economies and firms around the globe are seeking talent to become and remain competitive. This implies that a nation or firm with adequate strategic leadership practices will know how to scout talent and higher-skilled workforce and moreover, to develop retention strategies. In 2012 the South African manufacturing industry observed that most the country's engineers and artisans are seeking green pasture in neighboring countries [9]. Interestingly, even developed economies like America noted shortage of higher-skilled workforce, which can be said that this might have been attributed to the loss of 110 years leading global manufacturing competitiveness [17].

The Australian government also became aware of the shortage of higher-skilled workforce in 2008 specifically within the manufacturing sector. Fortunately the latter was that "manufacturers need to engage new thinking, technologies and practices to meet the new challenges" such as "international standards, addressing the sustainability skill and ensure that the present and future skill and workforce needs of enterprises are being met" [18]. The authors subscribe to this approach because it is associated with strategic leadership practices. Equally, the Americans government also had the same perspective, therefore, they developed "a national strategic plan for advanced of manufacturing" that incorporate an action plan to strengthening workforce skills [4]. This was influenced by the findings that the country was facing shortages of higher-skilled workforce. There is no doubt the demand of higher-skilled workforce is facing both developed and developing economies. In brief, the global market environment demands extensive and broader knowledge acquisition from economies and firms in order to align the future strategic planning. Along the same line, such aspect embodies the knowledge integration element of understanding the challenges and articulates what is needed to be done to address them.

2.3 A Knowledge Integration Perspective

Gartner Group [19] "knowledge integration focus specifically on knowledge about how to get work done" and "is practical and action-based". These authors are of the opinion that "when knowledge is successfully integrated within an organization:

- Everyone has a clear understanding of how the unique work of the organization get done.
- Management's understanding of roles, responsibilities and methods match worker's understanding.
- It is easy to identify and remedy barriers to success and best practices are rapidly identified and implemented".

Knowledge integration also lies on the strategic leadership practices that create enabling environment that ensures the knowledge is transferred to the workers level, especially tacit knowledge. Lapin [20] maintains that knowledge can be attained through the scanning of external environment by

- "Detecting scientific, technical, economic, social, and political interactions and other elements important to the organization.
- Defining the potential threats or opportunities and the potential changes for the organization caused by those events.
- Promoting a futures orientation in management and staff.
- Alerting management and staff to trends that are converging, diverging, speed up, slowing down, or interacting".

Equally this gained knowledge needs to transfer to the entire firm with the assumption that it will used adequate to sustain competitive advantage.

3 Recommendations

Ireland and Hitt [1] calls for strategic leadership to address the changing environment of the economy and knowledge with the belief that this approach will assist with interpretation of the dynamics of the global market. Global marketing strategy is vital to develop a foundation to execute the knowledge gained for addressing the challenges of the constantly changing global market. Reijiers and Mansar [21] suggest the following as best practices at the firm level, namely:

- "*Customer*, which focus on improving contacts with customers.
- *Business process operation*, which focus on how to implement the workflow.
- *Business process behavior,* which focus on when the workflow executed.
- *Organization,* which considers both the structure of the organization (mostly the allocation of resources) and the resources involved (types and number).
- *Information,* which describes best practices related to the information the business process uses, creates, may use or may create.
- *Technology,* which describes best practices related to the technology process uses, creates, may use or may create.
- *External environment,* which try to improve upon the collaboration and communication with the third parties."

This perspective concedes with our standpoint that firms needs to intensify the quest of knowledge acquisition and application to survive the complexity of global market. At the national level, we have noted the emerging trends such as the development of R&D institution, investment in ICT infrastructure, policy revision, skills and talent development and political shift. Clearly, the flourishing economies are advancing in these practices (for example China, India, United State of America and South Korea). Leaders at all level need to adopt [22] strategy, which derive

from service design perspective that integrates different aspects of expertise such marketing, research, design and management. These aspects integrate [21] best practices, moreover, concede with our view that competitive advantage in the global market lies on strategic leadership practices. Thus, it is imperative that both developed and developing economies and firms create an enabling environment that incorporates best practices in order become or sustain competitive advantage.

4 Conclusion

The chapter provided in-depth understanding of the global market environment's complexity. It highlighted the current global market environment's main drives that are affecting both developed and developing economies, and the firms. It have been articulated that economies and firms need gain insight into the dynamics of the global market environment through knowledge acquisition and application. The main drivers were adequate explained how they influence the global market environment and the underpinned key elements such as cultural, higher skilled workforce, infrastructural were indicated. Although we subscribe to the advancement of technologies, it is not sufficient to sustain competitive edge.

It has been singled out that successful nations in the global market such as china embraced globalization a long time ago, and as a result, they acquired the necessary technologies and talent to lead the global market. Thus it is vital to understand the dynamics and main drivers of the global market for both economies and firms in order to develop a strategic leadership practices that aligned with the global market environment. Herewith, we recommended strategic leadership practices that aligned with the global market environment with believe that these practices can allow economies to sustain competitive advantage.

References

1. Ireland RD, Hitt MA (2005) Achieving and maintaining strategic competitiveness in the 21st century: the role of strategic leadership. Acad Manage Executive 19(4):63
2. Madonsela NS, Mbecke P, Mbohwa C (2015) The dynamics of global market: a knowledge acquisition and application approach. In: Proceeding of the world congress on engineering 2015, WCE 2015, 1–3 July 2015, London, UK. Lecture Notes in Engineering and Computer Science. pp 330–307
3. Dahlman C (2007) Technology, globalisation, and international competitiveness: challenges for developing countries. Industrial development for the 21st century. Available: http://www.ruralfinance.org/fileadmin/templates/rflc/documents/1_2.pdf
4. National Science and Technology Council (2012) A national strategic plan for advanced manufacturing. United States of America
5. World Economic Forum (2012) The future of manufacturing: opportunities to drive economic growth

6. Bahl K, Shaw P (2012) Expanding access to LLINs: a global market dynamics approach. Results for Development Institute, Washington, DC. Available: http://www.resultsfordevelopment.org/sites/resultsfordevelopment.org/files/resources/R4D_LLIN%20report_24Apr_Final.pdf
7. Madonsela NS, Mbecke P, Mbohwa C (2013) Improving the South African manufacturing sector's competitiveness through the adequate use of ICT. In: International conference on information technology and computer systems engineering, pp 69–73
8. Bitner MJ, Zeithaml VA, Gremler DD (2010) Technology's impact on the gaps model of service quality. Available: http://www.gremler.net/personal/research/2010_Technology_in_Services_in_IBM_Handbook.pdf
9. Manufacturing Bulletin (2012) Manufacturing circle: quarterly review first quarter. Available: http://www.manufacturingcircle.co.za/docs/manufacturing_bulletin_q1_2012.pdf
10. Thinking Futures (2009) Environment scanning: what it is, how to do it? Available: http://thinkingfutures.net/wp-content/uploads/2010/10/ES-Guide-April-09.pdf
11. Mintzberg H (2010) Developing leaders? Developing countries? Oxf Leadersh J 1(2)
12. National Development Plan 2030 (2010) Vision for 2030. Available: http://www.npconline.co.za/medialib/downloads/home/NPC%20National%20Development%20Plan%20Vision%202030%20-lo-res
13. Robbins ST, DeCenzo DA (2008) Fundamentals of management: essential concepts and applications. Prentice Hall, Upper Saddle River
14. Larose DT (2005) Discovering knowledge in data. An introduction to data mining. Wiley, New Jersey
15. Lloyd V (2013) Case study: understanding global market dynamics requires global network reach. Available: https://www.google.co.za/?gws_rd=ssl#q=lloyd+ashley%2C+case+study:+understanding+global+market+dyanmics
16. Bhorat H, Goga S, Stanwix B (2013) Changing dynamics in the global labour market: evidence from South Africa. In: International symposium for employees on the future of work
17. Swezey D, McConaghy R (2011) Manufacturing growth: advanced manufacturing and the future of the American economy: the Schwartz initiative on American economic policy, 26 Oct 2011
18. Manufacturing Skills Australia (2008) Sustainable manufacturing for sustainability report
19. Gartner Group (2008) Knowledge integration: the secret to efficient, agile, highly-productive organizations
20. Lapin JD (2004) Using external environmental scanning and forecasting to improve strategic planning. J Appl Res Commun Coll 11(2):105–113
21. Reijiers HA, Mansar SL (2005) Best practices in business process redesign: an overview and qualitative evaluation of successful redesign heuristics. J Manage Sci 33:283–306
22. Moritz S (2012) Service design: practical access to an evolving field. Available: http://stefan-moritz.com/_files/Practical%20Access%20to%20Service%20Design.pdf

Reinventing the Energy Bill in Smart Cities with NoSQL Technologies

Carlos Costa and Maribel Yasmina Santos

Abstract With the increasing use of electrical devices, cities consume more energy to sustain their daily activities, facing more challenges associated with energy control and distribution. This chapter revisits a previously proposed architecture to extract, load, transform, mine and forecast Big Data within a Smart City context, in order to discuss the adequacy of NoSQL databases to deliver a Smart City service that reinvents the traditional energy bill, using web and mobile applications. Citizens will benefit from a new form of self-monitoring their electricity and gas consumption, by comparing themselves to others within their cluster or region and by forecasting future energy consumptions. Moreover, the service also delivers to energy providers and cities a smarter overview of the energy landscape. The technological architecture was previously validated using simulated data from the United States of America (USA), due to its open availability, and revealed very satisfactory results concerning the performance of clustering and time series forecasting models. This chapter extends the previously proposed technological architecture, by providing real-time concurrent web and mobile access to citizens, while presenting a broad review of several NoSQL benchmarks available in the scientific community, knowledge that is essential in the adoption of a specific database to support these web and mobile applications.

Keywords Big data · Clustering · Energy consumption · Forecasting · NoSQL · NoSQL benchmark · Smart cities

C. Costa (✉) · M.Y. Santos (✉)
ALGORITMI Research Centre, University of Minho, Campus de Azurém,
4800-058 Guimarães, Portugal
e-mail: id6011@alunos.uminho.pt

M.Y. Santos
e-mail: maribel@dsi.uminho.pt

S.-I. Ao et al. (eds.), *Transactions on Engineering Technologies*,
DOI 10.1007/978-981-10-1088-0_29

1 Introduction

Urban centres are growing and they seem to be the first choice for modern living, based on the fact that more than half of the population is living in urban environments [1]. With this phenomenon, various problems arise and cities need to adapt themselves to this trend, leading to a new concept, the concept of Smart Cities. Governments are facing more costs on labour, transportation, infrastructures, energy, and many other basic needs. Furthermore, citizens are behaving like natural consumers of government's services and are now demanding more, regardless of the existing constraints [2]. Here is where Big Data comes along. Cities and their citizens generate vast amounts of data, with multiple degrees of complexity, at different velocities, from various sources, that do not conform with traditional technologies, characteristics that lead us to the general definition of Big Data [3–5].

The emerging need to make cities smarter, associated with the relatively recent concept of Big Data and the possibilities it brings, constituted the motivational basis for the development of a Big Data analytics architecture [6]. The previously proposed architecture demonstrated its adequacy to process Big Data about energy consumption and to provide intelligent services through the use of data mining techniques, such as clustering and time series forecasting [7]. Clustering was used to identify groups of homogeneous homes, with similar patterns in terms of energy consumption, enabling comparison and ranking, while time series forecasting was used to foresee future consumptions. The data used to validate the architecture was the "EPLUS TMY2 residential base" dataset [8], containing 237 files, where each file represented one year of electricity and gas hourly consumption, from a simulated home in a certain city in USA. Although the dataset did not refer to a single city, but to multiple cities in USA, it was adequate to validate the clustering and forecasting of energy consumptions.

This chapter delivers a broad review of several scientific benchmarks of NoSQL databases, in order to justify the choice of a particular one to support a Smart City service, in this case a service where citizens can smartly monitor and foresee their energy consumption and compare themselves with other citizens, through the use of web and mobile applications. The architecture proposed in [6] is also revisited, in order to accommodate the applications' needs of real-time concurrent access by thousands of citizens, and it is also described how the interaction between the citizen and the service occurs.

This chapter is structured as follows: Sect. 2 summarizes related work and describes the ways in which this work contributes to the state-of-the-art in this field; Sect. 3 presents the review of several scientific NoSQL benchmarks; Sect. 4 revisits the architecture proposed in [6], to support real-time concurrent access to data, through web and mobile applications, and also details the service that can be delivered to citizens within a Smart City context; finally, Sect. 5 concludes with some remarks about the undertaken work and some guidelines of future work.

2 Related Work

Within the scientific community there are already available some approaches to forecast energy consumption. Some of the works are mainly related with the energy price [9–11], while others address the research around energy loads [12, 13]. Other related works already describe the smart meter data as Big Data, presenting some methods to visualize information and extract knowledge [14, 15]. Apart from that, there are some works being developed in order to study the relevance of the storage and processing infrastructure [15–17], highlighting non-relational databases and Hadoop.

In [6] we aim to demonstrate how the extracted energy data can be processed through a Big Data analytics technological architecture, using clustering and time series forecasting techniques, not only to select the adequate forecasting models (Linear Regression, Neural Network, Support Vector Machines or Decision Tree) for each cluster, but also to enrich the visual analysis and final smart service, delivering a reinvented energy bill to citizens and a new form of monitoring and targeting energy consumption to governments and energy providers.

This chapter extends the approach in [6], by focusing on the revision of several NoSQL benchmarks from the scientific community, in order to demonstrate which are the most popular databases and how well they perform under intensive workloads. This justifies the adoption of HBase in [6] and contributes to a better understanding of what are the advantages and disadvantages of each database. To the best of our knowledge, no other work aims to review such a variety of benchmarks of NoSQL databases, making available a significant amount of observations regarding these databases. In the present chapter, the architecture proposed in [6] is also revisited to support real-time concurrent access for web and mobile applications, enhancing the direct interaction of citizens within a Smart City.

3 Reviewing NoSQL Benchmarks

NoSQL databases play a relevant role in the storage and processing of Big Data. Although they are known as databases that can assure significant speed in data reading and writing, by distributing data and operations across a cluster of machines, their use must be planned according to the capabilities they bring to certain types of data workloads. There are multiple NoSQL databases already developed and in order to choose one that fits a project's goal, their performance for certain workloads should be considered, along with the flexibility of its schema, considering the nature of the data being processed.

When it comes to the types of NoSQL databases, the usual classification is the following [18–21]: *Key-value*, where a certain value is indexed by a key, in what is also commonly referred as hash table; *Column-oriented*, where related data is saved within rows and columns, where columns are frequently grouped according

to the relationship between them; *Document-based*, where data is organized as a collection of documents; *Graph*, where data is stored according to relationships between nodes.

Each of these types of NoSQL databases represent a pattern in the data's storage model, different from the traditional way of storing data, the relational and structured model. To better understand how several NoSQL databases behave when storing data and performing read/write operations, this chapter reviews a variety of comparisons and benchmarks (after 2010, due to the temporal dependency of technology), in order to conclude about the adequacy of certain databases. Cassandra, HBase and MongoDB seem to be frequently benchmarked among the scientific community, as can be seen in Table 1. Taking that into consideration and adding the fact that the set of NoSQL engines is too broad to be studied in a reasonable amount of time, this study will proceed within the scope of the three databases mentioned above, although some relevant facts about the other databases could be mentioned, when interesting results are shown. This study is also focused on open source/free NoSQL databases.

The following comparisons are not directly related to each other and the conclusions of each author may depend on several factors, for example, cluster configuration or type of benchmark. So, the presented results are meant to be analysed independently, in order to better understand the characteristics and performance of Cassandra, HBase and MongoDB in different situations.

In the work of [21], citing results from [22] prior to their scientific publication [23], refer the original laboratory benchmark using Yahoo! Cloud Serving Benchmark (YCSB), over 120 million records, totalling 0.12 TB, running on six nodes. The authors demonstrate two different scenarios: a write-intensive environment (number of writes are equal to the number of reads), wherein Cassandra's read performance is superior to HBase's. However, the write performance in HBase seems to be superior when compared to Cassandra's. It is important to mention that these differences are not substantial, due to the fact that for a throughput of 5000 operations/second the difference in read or write latencies is below 10 ms, for example; the second scenario is a read-intensive environment, wherein the results

Table 1 Databases mentioned within benchmarks conducted by the scientific community

Database	[21]	[18]	[24]	[25]	[26]	[27]	[23]	[28]	[29]
Cassandra	x	x	x	x	x		x		
Sherpa/PNUTS	x						x		
HBase	x	x	x	x	x		x	x	
MongoDB		x	x	x		x		x	x
OrientDB		x							x
Redis		x			x				x
Voldemort					x				
VoltDB					x				
MySQL Shard	x				x		x		
Elasticsearch									x

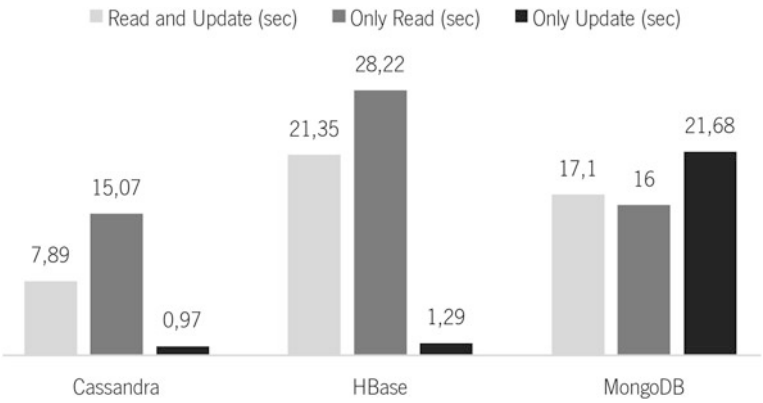

Fig. 1 NoSQL benchmark. Based on [18]

show similar behaviour, despite being a different workload. The work of [24] also agrees with [21], mentioning Cassandra's low read latencies and HBase's low update latencies.

Abramova et al. [18] also used the YCSB benchmark, with 3 main workloads: 50 % reads/50 % updates; only reads; only updates. The authors generated 600,000 rows, each one with 10 fields. The workloads consisted in the execution of 1000 operations, on a single virtual machine, thus not making use of the distributed capabilities present in these databases. Figure 1 shows the obtained results for each workload and database. Regarding the three databases mentioned in Fig. 1, Cassandra performed best in every workload. HBase performed the worst in workloads where only read operations were included. Finally, MongoDB came in a close second in the only read workload, despite being last in the only update workload. In general, Cassandra strikes a great balance between read and update operations, with regard to HBase, which results only show good performance in the only update workload. MongoDB shows good read performance, but falls in the updating department. Although Redis' results are not present in the figure, it is worth mentioning that its in-memory (RAM) nature assures the best results of the benchmark, either for reading or for updating, which is expectable. So, Redis could be the adequate choice for unmatchable performance, at the expense of managing a volatile memory environment. It needs to be considered that this benchmark presents numbers that result from a single virtual machine implementation and some of these databases may not perform well under these circumstances, which is the case for HBase that can present performance constraints on clusters with less than 3 nodes [23].

The work of [25] compared Cassandra, HBase and MongoDB, using a custom developed benchmark, written in Java. This benchmark presents results in terms of elasticity, scalability and performance, which results in an extensive comparison between the three databases. To conduct the study, [25] used Amazon's EC2 and Rackspace's Cloud Servers, in order to process 10 million Wikipedia articles, taking 28 GB of disk space. The designed workload consisted in 80 % of read

requests. Regarding the elasticity measure, including the time for stabilization after new nodes were added to the cluster and the impact on performance, HBase presents the best results, mainly due to the fact that HBase's Master does not have to move all the stored data to disks, but instead only has to tell new nodes (Region Servers) which are the regions they are serving and route new requests to these nodes. Cassandra bootstrapping process reveals a significant impact on performance. However, MongoDB emerges as the database that suffers the most from the bootstrapping process, given the elasticity score. Overall, the results show that HBase takes minutes to stabilize, unlike the other two databases that may take hours. When it comes to scalability, Cassandra and HBase manage to keep nearly constant performance, when the authors [25] increased the number of nodes from 6 to 12 and the number of operations from 10,000 to 20,000. MongoDB revealed inferior scalability, because performance decreased 78 %. Dede et al. [27] also discuss the fact that a large number of connections causes a more significant bottleneck than the total data volume in MongoDB. When the authors increased the number of nodes to 24, Cassandra revealed an unexplainable linear increase in performance, while HBase's performance decreased. The authors could not explain Cassandra's fascinating behaviour, but pointed out the possible adequacy of algorithms for larger cluster sizes. Kashyap et al. [24] also commented Cassandra's good scalability. HBase's performance loss was due to the fact that one of the 24 region servers was serving most of the requests, a fact that the authors could not find explanation for, even after some attempts to solve HBase behaviour. Finally, in terms of pure performance, HBase and MongoDB showed the fastest performance for a cluster size of 6 nodes. However, for a cluster of 12 nodes, HBase continues to be the fastest, but MongoDB's performance drops and it ties with Cassandra, due to MongoDB's poor scalability. Due to Cassandra's great scalability and HBase's bad request partitioning, Cassandra emerges as the fastest when operating with 24 nodes. Table 2 shows the summarized results, taking into consideration that there

Table 2 Benchmark results. Based on [25]

Measure	Indicator (lower is better)	Nodes	Cassandra	HBase	MongoDB
Elasticity	Stabilization time (min)	6–12	141	12.3	183
		12–24	201	17.2	352
		24–48	88	45	–
	Elasticity score	6–12	1735	646	4626
		12–24	1044	70	4009
		24–48	3757	73	–
Scalability	Scalability score	6–12	−0.06	0.05	0.78
		12–24	−0.28	1.68	–
Performance	Execution time (s)	6	99.33	43.30	50.46
		12	93.48	44.30	90.05
		24	67.54	118.75	–

are no values for MongoDB after 12 nodes, due to technical problems with MongoDB in the insertion phase.

Rabl et al. [26] conducted a study using the already mentioned YCSB benchmark, running on two locally deployed clusters: the most used cluster stored 10 million records (700 MB) on each node and the other cluster stored 150 million records (10.5 GB). The authors discuss the results for multiple workloads, based on read, write and scan operations, and also take into consideration factors such as disk usage. On the conducted tests, Cassandra outperforms HBase in throughput and read latency, while HBase's write latency reveals to be better. These results are consistent across write or read-intensive workloads, which corroborates the results presented by [21], in terms of latency. However, when the authors tested different throughputs rather than the maximum one, most of the time Cassandra assumed its position of a write-oriented database, while HBase showed its read-oriented nature, contradicting the latency results for maximum throughput [26]. Cassandra also demonstrated a more adequate disk usage than HBase.

To conclude, the results in the original YCSB paper are presented by [23]. Since most of the conclusions presented in this review are derived from YCSB workloads, it can be relevant reasoning on the results presented in the original work from its authors. Reference [23] confirm that, in a write-oriented workload, Cassandra assures the best throughput and the lowest read latency, when compared to HBase that assures the lowest update latency. In a read-oriented workload the differences in throughput are not very significant, with a slightly advantage to HBase, and Cassandra continues to assure the lowest read latency, while HBase maintains the lowest update latency. Cooper et al. [23] also corroborate [24] and [25], regarding Cassandra's good scalability. The authors point out a relevant factor concerning HBase's inadequate performance for clusters with less than three nodes. Finally, the authors agree with [25] on the elasticity capabilities of HBase and on the impact that the bootstrapping process brings to Cassandra's performance.

After the analysis of the state-of-the-art benchmarks, regarding the comparison of NoSQL databases, the main findings are as follows:

- *Cassandra*
  - Can assure low read latencies on write or read-intensive environments [21, 23, 24, 26]. However, [26] demonstrate that most of the time, when throughput is not maximum, Cassandra has a lower write latency than HBase;
  - Strikes a great balance between read and update execution times, being the first to finish all workloads [18];
  - The process of adding new nodes to the cluster impacts performance significantly [23, 25];
  - Good Scalability, 100 % linear scalability (sometimes even better) [23–25];
  - High throughput in write or read-intensive workloads [26];
  - Good results concerning disk usage [26].

- *HBase*
  - Can assure low write latencies on write or read-intensive environments [21, 23, 24, 26]. However, [26] demonstrate that most of the time, when throughput is not maximum, HBase has a lower read latency than Cassandra;
  - Assures a low execution time in the update only workload, but high execution time in read only and 50-50 workloads [18];
  - Good elasticity, with reduced time to achieve stabilization after adding new nodes [23, 25];
  - Good scalability, despite the incomprehensible loss of performance after increasing the number of nodes to 24 [25];
  - Some performance concerns in cluster with less than 3 nodes [23].
- *MongoDB*
  - Shows good execution times in the read only workload (almost the same as Cassandra), but falls short in the update only and 50-50 workloads [18];
  - Takes a significant amount of time to achieve stabilization after adding new nodes to the cluster [25];
  - Inferior scalability [25] when compared with Cassandra and HBase. A large number of connections seems to create more bottleneck problems than the total data volume does [27].

Concerning the NoSQL databases, taking into consideration the results from the several analysed benchmarks, Cassandra or HBase seem the more adequate databases in terms of pure performance. Choosing between the two is a matter of considering: Cassandra's low read latency or HBase's low write latency on intensive workloads; Cassandra's good scalability or HBase's good elasticity; Cassandra's good disk usage and adequate performance even in small clusters. In the proposed architecture, HBase was chosen. However, it could also be possible to adopt Cassandra as the NoSQL database, since they are both adequate choices and the difference in overall performance between them is not that significant for most of the cases.

4 A New Energy Bill for Smart Cities

In [6], an architecture to extract, load, transform, mine and forecast Big Data related to energy consumptions was presented. This technological architecture made use of a dataset containing electricity and gas consumption of homes distributed within multiple USA's cities and states, due to the open availability of this dataset. The main purpose of the work in [6] consisted in delivering to citizens a new form of self-monitoring their electricity and gas consumption, by comparing their homes to other homes within their cluster or region and by forecasting future energy consumptions. Moreover, the architecture also delivered to the city's management and

energy providers a smarter overview of the energy landscape. The proposed technological architecture showed that it is possible to identify accurate clusters of homes based on their energy consumption and that is also possible to forecast future electricity consumptions with a small margin of error.

The main advantages of the proposed approach are that citizens can periodically monitor their energy consumption, comparing themselves with others in the same cluster or region and foreseeing how much energy they will spend if they keep their consumption trend. Cities' government and energy providers can also adopt this approach, in order to manage more efficiently the energy consumption of the city, to use the processed data in green marketing initiatives and to predict energy needs, for example.

This section aims to extend the approach in [6], by revisiting the proposed architecture, in order to deliver a Smart City service based on web and mobile applications, which also makes use of HBase as the NoSQL database, but changes its role to ensure real-time concurrent access to data.

4.1 Big Data Architecture Supporting Web and Mobile Applications

In this chapter, the NoSQL database also supports the web and mobile applications, as opposed to [6], which only uses HBase as the staging area, for data processing tasks. Figure 2 presents the extended proposed architecture.

The architecture makes use of multiple Hadoop components, such as: Hadoop Distributed File System (HDFS) to store raw files; PIG to process scripts in order to aggregate data; HBase to not only serve as a staging area, but also to store the results to be visualized in web and mobile applications for citizens; HIVE to act as a data warehouse, to serve data visualization purposes for government and energy providers. Talend Open Studio for Big Data is responsible for all the data flow processes, directing data from HDFS and HBase to the local file storage where WEKA runs. Then, WEKA is used to build clustering and forecasting models. Talend Open Studio for Big Data uses the WEKA's Java library to integrate the models "on the fly" and store the results on HDFS (which will then be used by HIVE) and HBase. Finally, we are able to perform visual data analytics, using Tableau, and to serve the web and mobile applications, using HBase.

4.2 A Citizen-Oriented Smart City Service

Since the developed system is capable of processing energy consumption data and it is also capable of clustering and forecasting it [6], new perspectives on how to give feedback to citizens can emerge. Figure 3 shows a visual data analysis for a home in New York City.

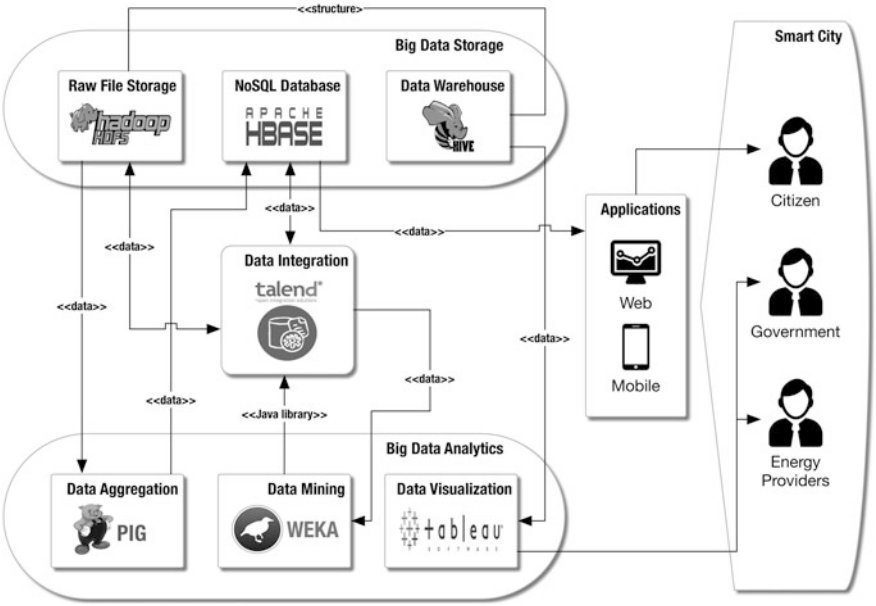

Fig. 2 Technological architecture overview

Although the analysis in Fig. 3 is developed using Tableau, it represents the information that can be contained in the web and mobile applications, once they are developed. The analysis begins by comparing the New York home against the cluster in which it is inserted, presenting the average energy consumptions. Then, the line chart overlaps the home's electricity consumption with the cluster's consumption, containing not only historical data but also predicted values, obtained from the application of the time series forecasting model. Besides that, it is also possible to rank homes by their energy consumption, comparing a certain home to others within its cluster. That ranking can be illustrated in a geographical map. The last chart in Fig. 3 shows a heat map, with the aim of comparing the home's weekly consumption in New York with other homes in the same USA's state.

The analysis described above exemplifies how innovative and intelligent Smart Cities services can be, and in this particular case, how clustering and time series forecasting can be joined to form a visual analysis that contributes significantly for citizens to have a more controlled consumption experience, monitoring historical and predicted data and comparing their home with others in their cluster or region. Figure 4 describes an example of the experience associated with the proposed Smart City service, based on Fig. 3 demonstration data.

Traditional energy bills do not give a clear overview of energy consumption. They, of course, demonstrate how much energy is spent in a certain period, but if we want to make our cities smarter and put architectures like this in real world applications, the energy bill could: tell how our home compares to our cluster

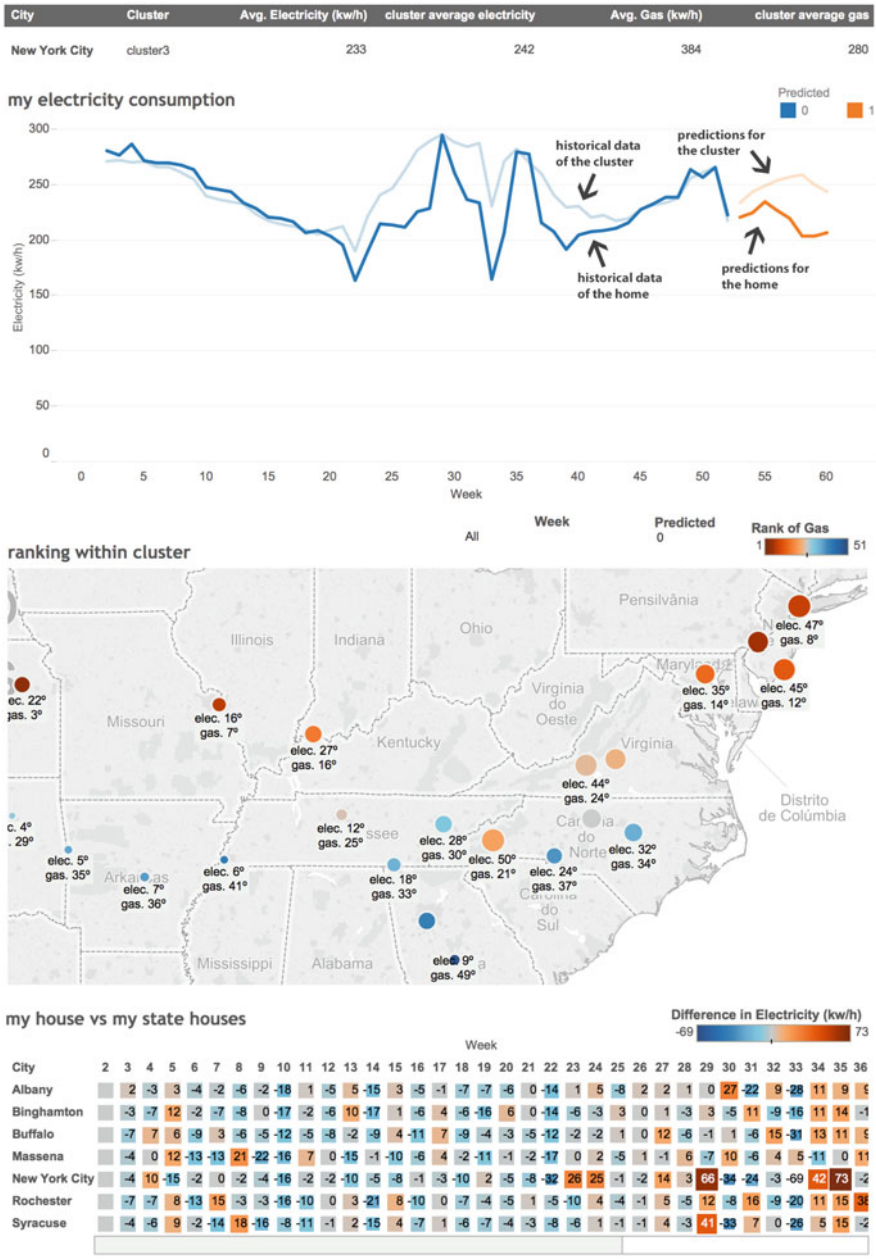

Fig. 3 Reinvented energy bill. Extracted from [6] (Colour figure online)

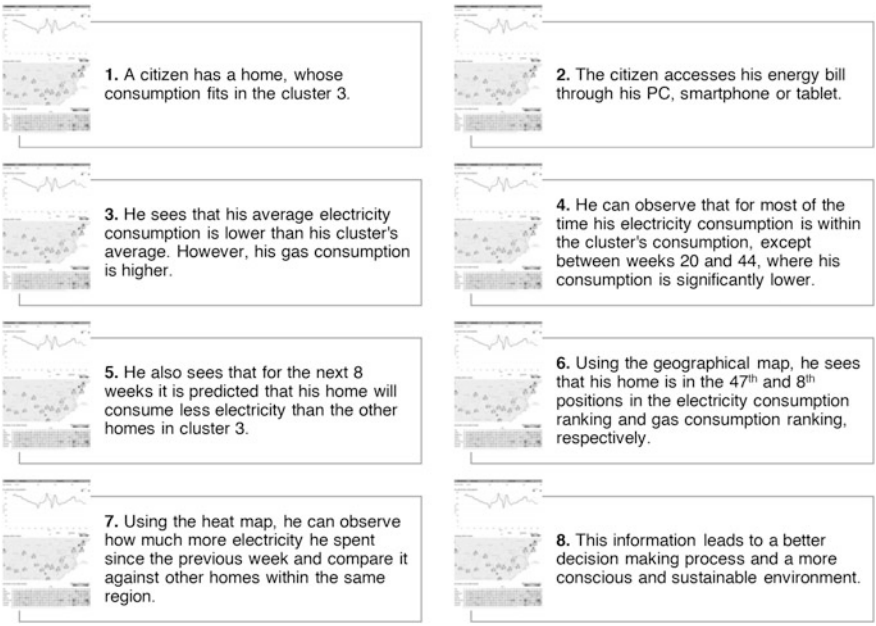

Fig. 4 The reinvented energy bill service

average, and how it will compare in the future if we keep spending energy the way we did; illustrate in a geographical map what is our home's energy ranking, using historical or predicted data; show us how we compare to others in the same region, on a weekly basis. These are only some of the possible examples. The other perspective that can be provided to government and energy providers is already fully described in [6].

5 Conclusion and Future Work

This chapter presented a review of several NoSQL benchmarks conducted by the scientific community and discussed the role of HBase in a Smart City service to deliver a reinvented energy bill to citizens.

The review consisted in the analysis of 9 benchmarks, observing the most frequently mentioned databases and focusing the observations on them. The results showed that Cassandra and HBase are commonly recognized as good overall performers and can be adopted without many concerns. Briefly summarizing the results, Cassandra consistently revealed superior read performance and scalability, while HBase consistently revealed superior write performance and elasticity. Choosing between the two is a matter of consider the expected workload and

constraints of a certain application, since most of the time differences in performance are not noticeable (measured in few milliseconds).

The architecture presented in this chapter extended the one proposed in [6], which was already validated to extract, load, transform, mine and forecast Big Data within a Smart City context, revealing adequacy to support the storage, processing and mining of all data. The architecture proposed in this chapter, where NoSQL now plays a relevant role to serve web and mobile applications, represents a step forward to solve one of the aspects of future work identified in [6], by showing new ways of serving data for other applications, like the ones in web and mobile environments. In this chapter, it is also described how the interaction between the citizen and the service can occur. Citizens can now use their devices to see how their home's energy consumption compares with others in the same cluster or region and foresee future consumptions, just to mention some examples.

For future work, the seasonality of the consumption should be integrated. To accomplish that, a dataset with multiple years of consumption needs to be used. Besides, Open Data, cluster management and security concerns can be further explored.

Acknowledgments This work was supported by *FCT—Fundação para a Ciência e Tecnologia*, within the Project Scope: UID/CEC/00319/2013 and funded by the SusCity project, MITP-TB/CS/0026/2013.

References

1. Vilajosana I, Llosa J, Martinez B, Domingo-Prieto M, Angles A, Vilajosana X (2013) Bootstrapping smart cities through a self-sustainable model based on big data flows. IEEE Commun Mag 51(6):128–134
2. Hedlund J (2013) The smart city: using IT to make cities more livable
3. Chen M, Mao S, Liu Y (2014) Big data: a survey. Mob Netw Appl 19(2):171–209
4. Krishnan K (2013) data warehousing in the age of big data, 1st edn. Morgan Kaufmann Publishers Inc., San Francisco
5. Zikopoulos P, Eaton C (2011) Understanding big data: analytics for enterprise class hadoop and streaming data, 1st edn. McGraw-Hill Osborne Media, New York
6. Costa C, Santos MY (2015) Improving cities sustainability through the use of data mining in a context of big city data. In: Proceedings of The World Congress on Engineering 2015, London, U.K., (Lecture Notes in Engineering and Computer Science) pp 320–325
7. Gama J (2010) Knowledge discovery from data streams. Taylor & Francis Group, Boca Raton
8. Commercial and Residential Reference Building Models (2013) Commercial and residential hourly load profiles for all TMY3 locations in the United States', Catalog, 2013 [Online]. Available: http://en.openei.org/doe-opendata/dataset/commercial-and-residential-hourly-load-profiles-for-all-tmy3-locations-in-the-united-states. Accessed 01 Dec 2014
9. Xie Y, Zheng H, Zhang L-Z (2007) Electricity price forecasting by clustering-LSSVM. In: International power engineering conference, IPEC 2007, pp 697–702
10. Zhou H, Wu XH, Li XG (2011) An ANFIS model of electricity price forecasting based on subtractive clustering. In: 2011 IEEE power and energy society general meeting, pp 1–5

11. Azevedo F, Vale ZA (2006) Forecasting electricity prices with historical statistical information using neural networks and clustering techniques. In: Power systems conference and exposition, 2006. PSCE '06. 2006 IEEE PES, pp 44–50
12. Alzate C, Sinn M (2013) Improved electricity load forecasting via Kernel Spectral clustering of smart meters. In: 2013 IEEE 13th international conference on data mining (ICDM), pp 943–948
13. Gu Y-D, Cheng J-Z, Wang Z-Y (2011) An fuzzy forecasting algorithm for short term electricity loads based on partial clustering. In: 2011 international conference on machine learning and cybernetics (ICMLC), 2011, vol 4, pp 1560–1565
14. Alahakoon D, Yu X (2013) Advanced analytics for harnessing the power of smart meter big data. In: 2013 IEEE international workshop on intelligent energy systems (IWIES), pp 40–45
15. Simmhan Y, Aman S, Kumbhare A, Liu R, Stevens S, Zhou Q, Prasanna V (2013) Cloud-based software platform for big data analytics in smart grids. Comput Sci Eng 15 (4):38–47
16. Arenas-Martínez M, Herrero-Lopez S, Sanchez A, Williams JR, Roth P, Hofmann P, Zeier A (2010) A comparative study of data storage and processing architectures for the smart grid. In: 2010 first IEEE international conference on smart grid communications (SmartGridComm), pp 285–290
17. Mayilvaganan M, Sabitha M (2013) A cloud-based architecture for big-data analytics in smart grid: a proposal. In: 2013 IEEE international conference on computational intelligence and computing research (ICCIC), pp 1–4
18. Abramova V, Bernardino J, Furtado P (2014) Which NoSQL database? A performance overview. Open J. Databases 1(2):17–24
19. Leavitt N (2010) Will NoSQL databases live up to their promise? Computer 43(2):12–14
20. Tiwari S (2011) Professional NoSQL. Wiley, New York
21. Tudorica BG, Bucur C (2011) A comparison between several NoSQL databases with comments and notes. In: 2011 10th Roedunet international conference (RoEduNet), pp 1–5
22. Cooper BF (2015) Yahoo! cloud serving benchmark, 31 Mar 2010 [Online]. Available: https://s.yimg.com/ge/labs/v1/files/ycsb-v4.pdf. Accessed 11 Mar 2015
23. Cooper BF, Silberstein A, Tam E, Ramakrishnan R, Sears R (2010) Benchmarking cloud serving systems with YCSB. In: Proceedings of the 1st ACM symposium on cloud computing, New York, NY, USA, pp 143–154
24. Kashyap S, Zamwar S, Bhavsar T, Singh S (2013) Benchmarking and analysis of NoSQL technologies. Int J Emerg Technol Adv Eng 3(9):422–426
25. Dory T, Mejías B, Van Roy P, Tran N-L (2011) Comparative elasticity and scalability measurements of cloud databases. In: Proceedigs of the 2nd ACM symposium on cloud computing (SoCC), vol 11
26. Rabl T, Gómez-Villamor S, Sadoghi M, Muntés-Mulero V, Jacobsen H-A, Mankovskii S (2012) Solving big data challenges for enterprise application performance management. Proc VLDB Endow 5(12):1724–1735
27. Dede E, Govindaraju M, Gunter D, Canon RS, Ramakrishnan L (2013) Performance evaluation of a mongodb and hadoop platform for scientific data analysis. In: Proceedings of the 4th ACM workshop on scientific cloud computing, pp 13–20
28. Chevalier M, El Malki M, Kopliku A, Teste O, Tournier R (2015) Benchmark for OLAP on NoSQL technologies comparing NoSQL multidimensional data warehousing solutions. In: 2015 IEEE 9th international conference on research challenges in information science (RCIS), pp 480–485
29. Abubakar Y, Adeyi TS, Auta IG (2014) Performance evaluation of NoSQL systems using YCSB in a resource austere environment. Perform Eval 7(8)

Using Hurst Exponent and Machine Learning to Build a Predictive Model for the Jamaica Frontier Market

Sherrene Bogle and Walter Potter

Abstract The Jamaica Stock Exchange (JSE) has been defined by Standard and Poor's as a frontier market. It has undergone periods where trading gains exceeded that of major markets such as the London Stock Exchange. The randomness of the JSE was investigated over the period 2001–2014, using statistical tests and the Hurst exponent to reveal periods when the JSE did not follow a random walk. This chapter focuses on machine learning algorithms including decision trees, neural networks and support vector machines used to predict the JSE. Selected algorithms were applied to trading data over a 22 month period for price and trend forecasting and a 12-year period for volume forecasts. Experimental results show 90 % accuracy in the movement prediction with mean absolute error of 0.4 and 0.95 correlation coefficient for price prediction. Volume predictions were enhanced by a discretization method and support vector machine to yield over 70 % accuracy.

Keywords Hurst exponent · Jamaica · Machine learning · Pre-processing · Random walk · Stock prediction

1 Introduction

Historically, stocks have been perceived as the most attractive and yet the least understood among financial markets. Prior to the 1990s it was believed that it was easy for individual investors to apply simple rules and make substantial returns. However, the scientific literature suggests otherwise [1]. Although time series analysis methods are used to predict the stock market, they are not a panacea for

S. Bogle (✉)
University of Technology Jamaica, 237 Old Hope Road, Kingston, Jamaica
e-mail: sbogle@utech.edu.jm

W. Potter
Department of Computer Science, University of Georgia, GSRC 415,
Brooks Drive Athens, Athens, GA 30602-7404, USA
e-mail: potter@uga.edu

S.-I. Ao et al. (eds.), *Transactions on Engineering Technologies*,
DOI 10.1007/978-981-10-1088-0_30

gaining a fortune in the short or even long term. Reference [2] highlights the unpredictability of the stock market by citing Mark Twain's 1984 aphorism of the January stock calendar effect. Twain said

> *October. This is one of the peculiarly dangerous months to speculate stocks…The others are July, January, September, April, November, May, March, June December August and February* (p 1)

Similarly, Burton suggested that a blindfolded monkey throwing darts at a newspaper's financial pages was just as effective in selecting a portfolio as the experts [3]. While historical data can improve prediction accuracy, the stock market remains difficult to predict and while patterns may be detected with the aid of statistical and computing tools, interpretation of the patterns is a challenging task even with economic, financial and scientific forecasting and time series experts.

A range of statistical and machine learning approaches has been used to successfully predict various stock exchanges worldwide. ARIMA is the most dominantly used statistical approach. While several machine learning methods have been used, ranging from artificial neural networks (ANNs) to support vector machines (SVMs), neural networks have been most popular due to noise tolerance and ability to handle the complicated data that is chaotic in nature. Neural networks and genetic algorithms have gained over 80 % accuracy in predicting the Singapore and Korean indices [4, 5]. Prediction of movement has generally had a high level of accuracy due to its binary output.

This study analyzed 14 years of historical data and used selected periods to predict movement, price and volume of selected indices on the Jamaica Stock Exchange (JSE). Two hypotheses below were tested:

1. JSE main index follows a random walk.
2. Machine learning approaches are superior to statistical approaches for forecasting JSE data.

This study assumes that the market is weak form, based on the efficient market hypothesis.

2 Contribution

Although the JSE is a frontier market, there have been periods when it has outperformed the London and New York markets such as 1981–1985 [6]. Previous studies on the JSE have only used statistical approaches to test the efficiency of the JSE in relation to the efficient market hypothesis (EMH). Reference [7] used the serial correlation of stock returns to test efficiency of the JSE while [6] gave a historical analysis of the market between 1969 and 1985 focusing on returns with associated risk as per beta coefficient in comparison with the US and UK markets. Reference [8] tested for randomness of returns in the earlier years. Section three

identifies periods of randomness between 2001 and 2014 for which no previous studies were found.

The experimental results in this study, detailed in Section four, have far exceeded those of the statistical models used in previous works which did not focus on prediction accuracy. This study builds on the first published work on applying machine learning approaches to the JSE data [9]. It shows that supervised learning algorithms such as SVM and ANN are more accurate than generic statistical models such as regression and presents a more accurate stock prediction model on the JSE dataset [10].

3 Random Walk Test

This section uses the Hurst exponent to identify periods of predictability and performs random walk test on a 14 year dataset. It also outlines the results of experiments which tested *hypothesis one* using similar methods to [11] and [12]. The dataset consisted of 2001–2014 with two subset periods of

- 2001–2010
- 2010–2014

The distinction is made in the split of the dataset because of two debt exchanges that occurred in early 2010 and 2013 when successive governments sought public compromise to reduce the contractual interest on bonds.

Reference [13] tested for randomness of returns in the earlier years, using the runs test. It was found that the JSE did not follow a random walk between the periods 1969–1986 and 1969–1976. However, the random walk hypotheses could not be rejected for the sub-period 1977–1986.

3.1 Tests of Randomness

A variety of tests for randomness of time series exist. These range from a mere visual examination of time series plot to a runs test [14]. Reference [11] proposed statistical tests such as the runs test to determine whether stock returns conform to the random walk model. Reference [12] used the Hurst exponent, calculated by the rescaled range analysis, to determine periods of predictability. To ascertain whether the time series of stock prices for the selected blue chip companies on the JSE follows a random walk a visual test and a runs test were performed and the Hurst exponent was also calculated.

3.1.1 Visual Test

For the visual test, a scatter plot of the closing prices for the time period was plotted. The difference was also calculated for the time series and plotted. The standard deviation of the closing prices and differences were compared. A random walk was indicated by a meandering of the closing price plot, differences that follow a random process and the standard deviation of the closing prices being larger than the standard deviation of the differences.

3.1.2 Runs Test

The runs test is a statistical non-parametric test based on runs of observations. A run is defined where an observed value is greater than or less than an average value, and is recorded for the duration of the time series. The average can be the median or mean. This method may ascertain short term correlation. Under the null hypothesis of randomness, the expected number of runs are compared with the recorded number of runs [14]. For this study, a significance value of less than 0.05 accepts the null hypothesis of randomness i.e. the stock is assumed to follow the random walk model. For a significance value greater than 0.05, it rejects the hypothesis of randomness.

3.1.3 Hurst Exponent

Reference [12] describes an algorithm for estimating the Hurst exponent of a time series using rescaled range analysis. The Hurst exponent ranges between zero and one. A Hurst value of 0.5 indicates randomness and values closer to one indicate greater predictability since the period would reject the random walk model. A Hurst value closer to one indicates a persistent series, whereas a Hurst value less than 0.5 indicates an anti-persistent series. An anti-persistent series is often described as "mean-reverting", which values alternate above and below the mean consistently. A macro was developed to calculate the Hurst exponent from the rescaled range time series using the algorithm outlined by [12, p 2].

3.2 Results

The closing prices of ten blue chip stocks were tested for randomness over the period January 1, 2001 to June 30, 2014. This included 3392 trading days. The results are shown below for each of the two periods:

(i) 1st January 2001–31st December 2009 (Period I: 2263 days)
(ii) 1st January 2010–30th June 2014 (Period II: 1129 days)

The ten blue chip stocks were selected from those used by a local stock broker, who also trades on the JSE. They are CAR, CCC, DG, GK, GLNR, JBG, JMMB, JP, LIME and NCBJ. LIME is the rebranded trading name for CWJ.

3.2.1 Period I: 2001–2009

Figure 1 shows the closing prices for the CAR stock meanders. The differences plot, though not illustrated here, also seem to follow a random process. This is confirmed by the standard deviation of the closing prices (14.13) being larger than the standard deviation of the differences (1.21); and further validated by significance value of the runs test being less than 0.05, shown in Table 1.

Both the visual test and runs test were performed for the remaining stocks: CCC, DG, GK, GLNR, JBG, JMMB, JP, LIME and NCBJ. The closing prices for the remaining stocks also displayed a meandering pattern and their differences plot also seemed to follow a random process. This is confirmed by the standard deviation of the closing prices being larger than the standard deviation of the differences shown in Table 2; and further validated by significance value of the runs test being less than 0.05 for each stock.

3.2.2 Period II: 2010–2014

Since the visual test and runs test yielded the same results for Period I, only the runs tests was performed for the ten stocks in period II. All had a significance value less than 0.05 and therefore conformed to the random walk model. Table 3 shows the result for DG which had the highest number of runs.

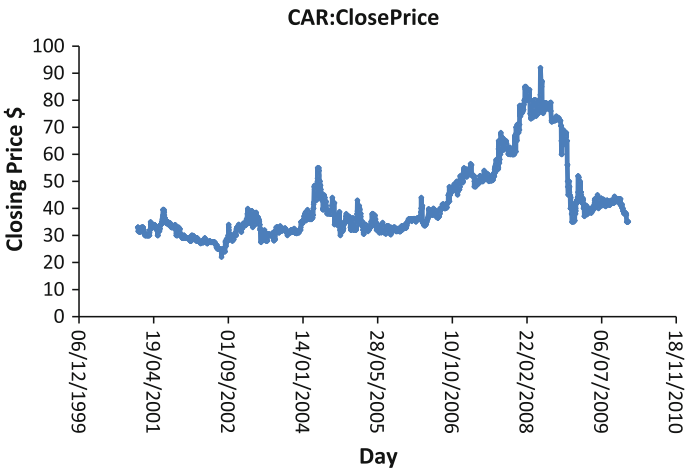

Fig. 1 Scatter plot of CAR closing prices

Table 1 Runs test for CAR stock prices 2001–2009 performed on **a** median **b** mean

Statistic	ClosePrice
Runs test (a) median	
Test value (a)	37
Cases < test value	1131
Cases ≥ test value	1132
Total cases	2263
Number of runs	57
Z	−45.227
Asymp. Sig. (2-tailed)	0.000
Runs test (b) mean	
Test value (a)	41.67
Cases < test value	1501
Cases ≥ test value	762
Total cases	2263
Number of runs	41
Z	−45.701
Asymp. Sig. (2-tailed)	0.000

Table 2 Standard deviation of stocks closing prices versus differences

Stock	ClosePrice	Differences
CCC	3.83	0.25
DG	1.65	0.20
GK	28.32	1.33
GLNR	0.61	0.09
JBG	1.38	0.12
JMMB	4.23	0.34
JP	3.83	0.25
LIME	0.44	0.04
NCBJ	6.86	0.43

3.3 Hurst Exponent and Periods of Predictability

This section uses the aforementioned Hurst exponent to identify periods of predictability over the period 2001–2014. The Hurst exponent ranges between zero and one. Sample Periods of 250 trading days, approximately one year, were randomly chosen from periods I and II and the Hurst exponent computed to determine predictability.

3.3.1 NCB

Figure 2 shows the Hurst exponent of NCB closing prices for 2008 with a trend line attached. As indicated by the Hurst exponent below 0.5 for most of the year, prices

Table 3 Runs test results for DG stock prices 2010–14 performed on **a** median **b** mean

Statistic	ClosePrice
Runs test (a) median	
Test value (a)	4.20
Cases < test value	564
Cases ≥ test value	579
Total cases	1143
Number of runs	40
Z	−31.515
Asymp. Sig. (2-tailed)	0.000
Runs test (b) mean	
Test value (a)	4.1986
Cases < test value	564
Cases ≥ test value	579
Total cases	1143
Number of runs	40
Z	−31.515
Asymp. Sig. (2-tailed)	0.000

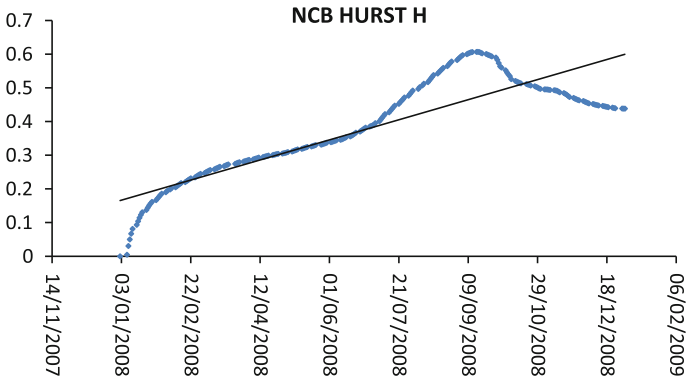

Fig. 2 Hurst exponent of NCB closing prices for 2008

were generally predictable as they were in the limited range of $20–25, thus rejecting the random walk model. Between February and July the trend line for the Hurst exponent was also consistent.

3.3.2 LIME

Figure 3 shows the LIME Hurst values for 2002. The LIME Hurst values were generally between 0.65 and 0.8 for the period 2001–3. In 2004, the predictability declined to a low of almost 0.58, but was still above 0.5; the threshold which indicates a perfectly random model.

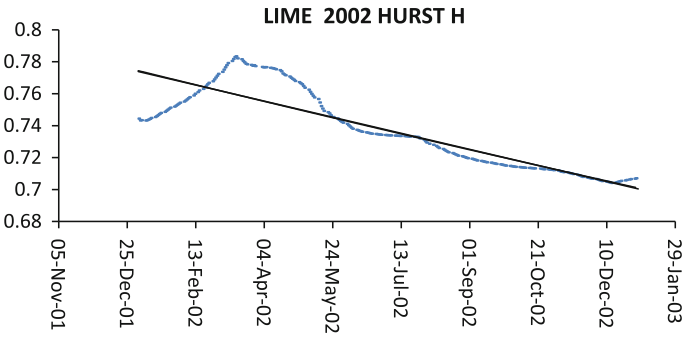

Fig. 3 Hurst exponent of LIME closing prices for 2002

3.3.3 CAR

An examination of the Hurst exponent rejected the random walk hypothesis for the sub-period 2001–2004 within Period I.

The CAR visual test and runs test for the sub-period failed to reject the random walk hypothesis. As [13] indicated, a runs test *may* indicate correlation of prices. Hence, the Hurst was computed for the same sub-period. Thus Fig. 4 shows the Hurst exponent of the CAR stock on closing prices for 2002 was above 0.5. Here, the visual test and runs tests failed to identify the predictability of the stock. In 2003, the second half of the year Hurst exceeded 0.58. In 2004, the Hurst ranged from 0.52 to 0.63.

3.3.4 GLNR

Figure 5 shows Hurst Exponent on close prices for the GLNR stock in 2002.

The stock exhibited characteristics of an anti-persistent or mean-reverting series, indicated by an exponent below 0.5 for the entire year.

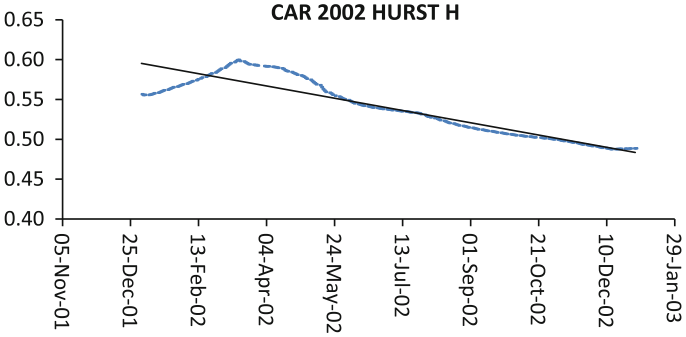

Fig. 4 Hurst exponent of CAR closing prices for 2002

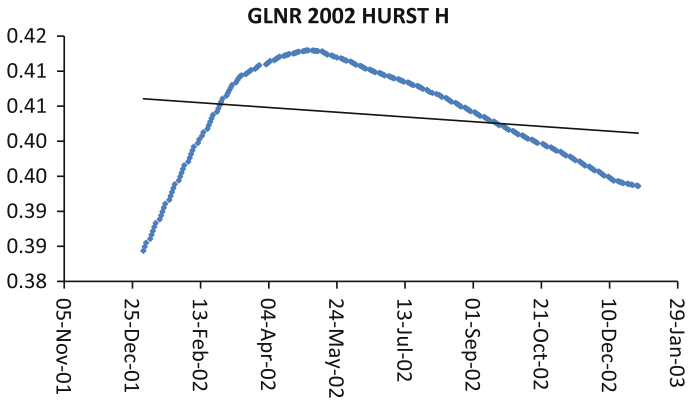

Fig. 5 Hurst exponent on close prices for the GLNR stock in 2002

3.4 Summary

In this section we compared the runs test, visual test and the Hurst exponent to determine whether to accept or reject the random walk hypothesis. The statistical runs and visual test proved to be less accurate than the Hurst exponent. In the sub-period 2001–4, CAR and GLNR did not exhibit random walk. This is evidenced by the Hurst exponent being above and below 0.5 respectively. Identifying periods of predictability by Hurst exponent was found to be more effective than the statistical tests. The anti-persistence of the GLNR stock may account for the runs tests failing to reject the random walk model.

Over longer time periods the JSE was found to exhibit random walk. This was confirmed by both the runs test and visual test comparing the standard deviation of close prices and their differences. Also, Hurst exponent was close to 0.5 for both periods I and II for all stocks. However, small to medium periods were found to reject the random walk theory as confirmed by the Hurst exponent computed for CAR and GLNR 2001–2004, NCB February to July 2008, and LIME several months between 2001 and 2003.

4 Prediction Results -Statistical Versus Machine Learning Methods

4.1 Introduction

This section describes machine learning approaches such as Naive Bayes (NB), artificial neural networks (ANN), decision trees (DT) and support vector machines (SVM) used to predict indices of the Jamaica Stock Exchange (JSE). The

Table 4 Price Prediction of Various Companies on the JSE

Statistical Parameters	Linear Regression	Multilayer Perceptron
Correlation coefficient	0.9284	0.9502
Mean absolute error	7.1556	7.5095
Root mean squared error	20.0838	17.6571
Relative absolute error	25.5137 %	26.7758 %
Root relative squared error	37.1844 %	32.6916 %

predictions include trend of the seven indices, volume and prices of blue chip stocks trading on the JSE.

Only one previous work, [14], describes neural network approaches used to predict the Jamaican financial market which focused on forecasting core inflation rate from oil prices, treasury bills, exchange rate and base money. The use of neural nets as a successful financial predictor has been suggested by [15]. Stocks were not included in that study.

Machine learning approaches used in the JSE predictions include neural networks, support vector machines and linear regression for continuous data prediction as well as decision trees, neural networks and Naïve Bayes for binary predictions and multiclass discrete data. Trading data over the 22 month period from January 2010 to November 2011 was formatted to do three types of predictions: prices, movement and volume.

(i) Closing ask *prices* of companies and their respective shares- This dataset includes 44 companies that trade 59 instruments on the JSE. Some companies trade up to 4 securities. The trading period is from January 10, 2010 to November 11, 2011 totaling 10,158 instances. The predictions were done using linear regression and neural networks. The results are shown in Table 4. Test mode was split 66.0 % train, remainder test; as given the time series nature of the dataset, cross fold validations were not used in the experiments here.

(ii) *Movement* of seven indices. This binary prediction was done using decision trees, neural networks and Naïve Bayes. This is shown in Tables 5 and 6.

(iii) *Volume* of ten blue chip stocks: Eight of the stocks were selected for volume predictions: CAR, CCC, CWJ (later traded as LIME), DG, GK, GLNR, JMMB and JP. The results are shown in Tables 7 and 8.

4.2 Results

In order to avoid over fitting, neural network experiments unless otherwise stated had the following parameters: learning rate: 0.3, momentum: 0.2, training time: 2500, and validation threshold: 20.

Table 5 Movement prediction of various indices of all and main JSE index

Index	Scheme	MAE	N	Accuracy (%)
All[a]	DT	0	880	**100**
All[a]	ANN	0.44	880	35
All[a]	NB	0.13	880	85
1	DT	0	162	100
1	ANN	0.13	162	89
1	NB	0.25	162	77

Key
[a]All refers to all seven indices
N—number of Instances

Table 6 Movement prediction of JSE select (2), all jamaican composite (3), cross listed index (4), junior market index (5), combined index (6) and US equities index (7)

Index	Scheme	Instances	Mean absolute error	Correctly classified instances (%)
2	NB	162	0.1175	90
2	DT	162	0	**100**
2	ANN	162	0.04	95
3	NB	162	0.1663	91
3	DT	162	0	**100**
3	ANN	162	0.0817	93
4	NB	162	0.0409	93
4	DT	162	0	**100**
4	ANN	162	0.0476	93
5	NB	162	0.1475	77
5	DT	162	0.	**100**
5	ANN	162	0.1219	84
6	NB	55	0.1081	91
6	DT	55	0.0364	**96**
6	ANN	55	0.1125	89
7	NB	16	0.1587	81.2
7	DT	16	0	**100**
7	ANN	16	0.193	75

A. *Price prediction:* Table 4 shows the results of the closing ask price prediction of the companies that trade on the JSE for the period January 2010 to November 2011. The data set includes the following nine attributes: Stock-Code, Value-Date, Last-Price, Previous-Price, Price-Change, Percentage-Change, Volume-Traded, Year-High and Year-Low.
B. *Movement prediction*: The seven indices on the JSE are: (1) JSE Market Index, (2) JSE Select Index, (3) JSE All Jamaican Composite, (4) JSE Cross Listed Index, (5) JSE Junior Market Index, (6) JSE Combined Index and (7) JSE US Equities Index. For each of the indices the following 12 attributes were used:

Value-Date, Value, Value-Change, Percentage-Change, Volume-Traded, Year-High, Year-Low, YearToDate, QuarterToDate, MonthToDate, WeekToDate and Movement.

Table 5 shows the results of the movement prediction of companies on all seven indices as well as the main index. Table 6 shows Movement on all remaining indices. Two hidden layers and a training time of 1500 were used for the neural network experiments in Tables 5 and 6.

C. *Predicting Company Volume*: The volume was predicted for eight blue chip stocks on the JSE. Since the prediction accuracy was a mere 13 % on the continuous data, discretization was used to gain an improvement on the prediction accuracy [9]. It was also found that support vector machine (SVM) had a higher accuracy and lower MAE than neural networks. Hence, SVM was used for experiments in Table 8. As shown in the literature, feature discretization uses thresholds to convert continuous values to discrete ones. There were 261 instances and 6 attributes: Date, LastPrice, ClosePrice, Change dollar value, ChangePercent, VolumeDisc (Discretized volume derived from [7]). The results are shown in Table 8.

4.3 Analysis of Results

In this study, the decision trees were found to have 100 % accuracy in predicting movements of all seven indices. Naïve Bayes' accuracy ranged from 77 to 93 %. Neural networks outperformed linear regression in predicting prices, whereas decision trees were more accurate in the binary movement prediction. SVM combined with discretization proved the most effective method for volume prediction.

A. *Price Prediction*: In price prediction, neural network had a higher correlation coefficient (0.97) than linear regression and a lower mean absolute error, as shown in Table 4.

B. *Movement Prediction*: Decision trees have 100 % accuracy on predicting movement on all seven indices except the combined index where the accuracy was 96 %. Naïve Bayes had 77–93 % accuracy on index two to seven and 85 % on the main index. Tables 5 and 6 indicate that while neural networks had lower prediction accuracy on the movement of the combined and US indices, the mean absolute error was also higher making it a slighter weaker predictor than Naïve Bayes and decision tree. The 35 % accuracy obtained on neural networks prediction on all seven indices is odd, but can be favorably countered. Since movement is a binary prediction, and the historical accuracy is known to be low, one could simply assume the opposite trend and 65 % accuracy would be achieved. Reference [16] conducted an empirical study comparing decision trees, artificial neural networks, and linear regression methods based on the number and types of independent variables and sample size. It concluded that

Table 7 Results of eight blue chip company volume predictions using neural networks

Company	Hidden layers	MAE	Correctly classified instances (%)
CAR	2	0.0054	13
CCC	2	0.0063	26
CWJ	2	0.0051	17
DG	2	0.0069	33
GLNR	2	0.0071	37
GK	2	0.0051	15
JMMB	2	0.01	20
JP	2	0.0073	52

Table 8 Volume predictions of blue chip companies using SMO SVM Polykernel

	Kernel evaluations	Accuracy (%)	Precision	Recall	MAE
CAR	55	60	0.734	0.6	0.19
CCC	1225	70	0.744	0.695	0.19
CWJ	210	41	0.397	0.413	0.20
DG	45	72	0.697	0.719	0.18
GLNR	231	66	0.696	0.665	0.17
GK	28	52	0.531	0.525	0.18
JMMB	55	51	0.657	0.419	0.18
JP	55	73	0.657	0.517	0.19

for continuous and categorical independent variables, linear regression was best when the number of categorical variables was one, while the artificial neural network was superior when the number of categorical variables was two or more. Also, the artificial neural network performance improved faster than that of the other methods as the number of classes of categorical variable increased. This supports the theory that ANNs perform better on multiclass predictions (three or more classes) than binary predictions, as evidenced by these results.

C. *Volume Prediction*: Table 7 reveals that of the eight blue chip companies analyzed with neural networks, only Jamaica Producers had an accuracy above 50 %. This experiment was performed using continuous data of actual volume traded. The volume data was discretized using categories of volume indices outlined in [9], and then SVM used to perform the predictions shown in Table 8 where seven out of eight companies had accuracy above 50 %.

Among the blue chip companies, only CWJ had an accuracy of less than 50 %. The 41 % accuracy for the CWJ (LIME) stock could be attributed to competition faced by CWJ after the government lifted the decades old monopoly for telecommunications which they previously enjoyed.

5 Review of Hypotheses

Hypothesis 1 *JSE main index follows a random walk.*

As explained in section three, blue chip companies that trade on the JSE main index were found to follow a random walk for the periods 2001–2009 and 2010–2014. However, this hypothesis was rejected for CAR, GLR and LIME for the sub-period 2001–2004.

Hypothesis 2 *Machine learning approaches are superior to statistical approaches for forecasting JSE data.*

This hypotheses proved to be true in all cases. In section four, it was demonstrated that the ML approaches have a greater accuracy at predicting movement, prices and volume as well as a lower error rate.

6 Summary

Stock prediction is by no means an exact science and many pundits believe it is virtually impossible to accurately predict stocks because they follow a random walk. Also, based on the efficient market hypothesis, the market is designed to correct itself over time so any periods of predictability are usually short lived. Against this background, this study achieved the contributions outlined below:

(i) Using the JSE dataset that covers the period 1st January 2001–30th June 30 2014, the entire period was tested for random walk using a trio of methods.

- It was proven that periods of predictability exist within the stock market; even where the main index is deemed to follow a random walk we used sub-periods and gained high predictability. Specifically, CAR & GLNR failed to accept the null hypothesis of randomness for the sub-period 2001 to 2004. LIME prices also proved predictable for the same sub-period with an average Hurst exponent of 0.7, and topping 0.8 for some trading days in 2001.

(ii) Experimental results show 90 % accuracy in the movement prediction and 0.95 correlation coefficient for price prediction. Volume predictions were enhanced by a discretization method and support vector machine to yield over 70 % accuracy for all but one of the stocks.

(iii) The high accuracy in ML predictions can be justified by the Hurst exponent indicators which proved more effective than statistical tests in identifying periods of random walk.

In a related work [17], the authors developed SentAMaL architecture for accepting qualitative input in the form of tweets from social media and analyzing these tweets as input to complement relevant historical stock data. The architecture considered tweets based on a January 2015 legislation to make predictions for

companies of the JSE that were most likely to be impacted by the legalization of medical marijuana. Experimental results show 87 % accuracy in the movement prediction and 0.99 correlation coefficient for price prediction with a mean absolute error of 0.5. Experimental results indicate that as a hybrid SentAMaL's accuracy was close to its non sentiment based counterpart. However it had a lower mean absolute error on the dataset used.

References

1. Lorie JH, Dodd P, Kimpton MH (1985) The stock market. Irwin
2. Kovalerchuk B, Vityaev E (2000) Data mining in finance: advances in relational and hybrid methods. Springer, New York
3. Kuepper J (2011) Using genetic algorithms to forecast financial markets. Retrieved on 9 June 2012 from http://www.investopedia.com/articles/financial-theory/11/using-genetic-algorithms-forecast-financial-markets.asp
4. Phua P, Ming D, Lin W (2001) Neural network with genetically evolved algorithms for stocks prediction. Asia-Pac J Oper Res 18:103–107
5. Kim K, Han I (2000) Genetic algorithms approach to feature discretization in artificial neural networks for the prediction of stock price index. Expert Syst Appl 19(2):125–132
6. Kitchen R (1986) The role of the Jamaican stock exchange in the capital market. Caribb Finan Manage 2(2):1–23
7. Agbeyegbe TD (1994) Some stylised facts about the Jamaica stock market. Social Econ Stud 143–156
8. Koot R, Miles J, Heitmann G (1989) Security risk and market efficiency in the jamaican stock exchange. Caribb Finan Manage 5(2):18–33
9. Bogle SA, Potter WD (2015) A machine learning predictive model for the Jamaica frontier market. Lecture notes in engineering and computer science. In: Proceedings of the world congress on engineering 2015, London, UK, pp 291–296, 1–3 July 2015
10. JSE (2011) Jamaica stock exchange. Retrieved 05 Dec 2012 from http://www.jamstockex.com/controller.php?action=about_exchange
11. Robinson J (2005) Stock price behavior in emerging markets: tests for weak form market efficiency on the Jamaica stock exchange. Soc Econ Stud 54(2):51–69
12. Qian B, Rasheed K (2004) Hurst exponent and financial market predictability. In: Proceedings of the 2nd IASTED international conference on financial engineering and applications, pp 203–209
13. Chatfield C (2004) The analysis of time series: an introduction. CRC Press Chapman & Hall, USA
14. Serju P (2000) Monetary conditions and core inflation: an application of neural networks, Bank of Jamaica Working Paper. Retrieved on 25 Oct 2013 from http://www.boj.org.jm/uploads/pdf/papers_pamphlets/papers_pamphlets_monetary_conditions_and_core_inflation__an_applicationof_neutral_networks.pdf
15. Chakraborty S, Sharma SK (2007) Prediction of corporate financial health by artificial neural network. Int J Electron Finan 1(4):442–459 (Inderscience)
16. Kim YS (2008) Comparison of the decision tree, artificial neural network, and linear regression methods based on the number and types of independent variables and sample size. Expert Syst Appl 34(2):1227–1234
17. Bogle SA, Potter WD (2015) SentAMaL- a sentiment analysis machine learning stock predictive model. In: Proceedings of the 17th international conference on artificial intelligence. CSREA Press, UK. ISBN: 1-60132-405-7, 1-60132-406-5

A New Secure Framework in MCC Using Homomorphic Signature: Application in Banking Data

Karim Zkik, Maha Tebaa and Said El Hajji

Abstract Mobile Cloud computing is a new concept, which is gaining more and more popularity, allowing users to use the services of Cloud computing by using their mobile device. Unfortunately, and despite of its various benefits, MCC faces several challenges due to resource limitations of mobile devices and several security problems. Because of these problems related to security and privacy, MCC still very limited, particularly for storing and downloading sensitive data. We propose a secure framework using homomorphic encryption to forge a robust digital signature and to encrypt data, which allows mobile users to download data from a remote private cloud server while ensuring authentication, integrity, confidentiality and privacy. Our security system is primarily dedicated to companies and organizations that use the Cloud Computing services to storage of their sensitive data and their customer's personal data in order to have more storage space, to obtain more resources, and to increase their services quality. It is proposed thereafter a security analysis and an implementation of our platform in banking data, which simulate secure banking operations. The simulation results demonstrate the efficiency and the robustness of our framework, and that it offers a high level of data security.

Keywords Authentication · Banking data · Confidentiality · Homomorphic digital signature · Homomorphic encryption · Mobile cloud computing

K. Zkik (✉) · M. Tebaa · S. El Hajji
Laboratory of Mathematics, Computing and Applications,
Faculty of Sciences, University of Mohammed V-Rabat, Rabat, Morocco
e-mail: karim.zkik@gmail.com

M. Tebaa
e-mail: maha.tebaa@gmail.com

S. El Hajji
e-mail: elhajji@fsr.ac.ma

S.-I. Ao et al. (eds.), *Transactions on Engineering Technologies*,
DOI 10.1007/978-981-10-1088-0_31

1 Introduction

Mobile Cloud Computing (MCC) [1] is a concept, where applications and mobile data are downloaded, stored and hosted using cloud computing technology [2, 3]. MCC allows users to have on-demand resource and software and allows retrieving data anywhere and anytime by use of Internet, but its implementation poses more challenges given and storage resources and CPU limitation in mobile.

Security threats and risks related to security and user privacy are the main obstacles to adaptability and rapid expansion of storage services use in the MCC [4–6], and more than 74 % of IT Executives are not interested by the implementation of Cloud computing services because all this security's problems [7].

Kamara and Lauter [8] have describe some security architectures using the cryptographic function for storing data in the mobile cloud. Its structure ensures the confidentiality of shared data between mobile users and cloud server. Hsueh et al. [9] proposed a scheme to ensure security and integrity of mobile users files stored in the cloud, and introduced an authentication mechanism to authenticate the owner of the file downloaded from the cloud server. Wang et al. [10] defines a new homomorphic signature for identity management in mobile cloud computing to compute a homomorphic signature on all users sensitive personal data in MCC.

The goal of our platform is to offer to customers, especially mobile users, the ability to access and download their data using Mobile cloud computing services safely, while ensuring their integrity and privacy. So, we will construct a new secured homomorphic platform for a secure downloading and authentication in the MCC. This platform will firstly allow mobile users to authenticate to a central server safely, and to ensure their data integrity by using a homomorphic signature, and then download and consult safely their personal data stored in the corresponding private cloud server.

The rest of the paper is organized as follows. In Sect. 2, we present some preliminaries. In Sect. 3, we discuss the problematic and the different challenges in our work and we present the global structure of our model. In Sects. 4 and 5, we present in details our proposed model and we describe the authentication and the downloading scheme. In Sect. 6, we analyze the security of our solution and we provide a performance evaluation results, we present an implementation of our framework in banking Data and we provide the different results of our simulation. Finally, in Sect. 7, we conclude the paper.

2 Preliminaries

In this part we will present some cryptographic concepts that we used in designing of our model, including the homomorphic encryption and security requirements in MCC, and we will present the main threats and attacks in a MCC environment.

2.1 Homomorphic Encryption

The homomorphic encryption is a concept that allows making calculations on cipher text without decrypting it, which offer enormous possibilities for users who want to outsource their data and make calculations on remote servers while keeping the confidentialities of their data. Several cryptosystem are homomorphic, for example RSA and Pailler, but it's only for addition or multiplication. Some studies try to find algorithms completely hommomophe [11, 12].

2.2 Challenge and Security Requirements in MCC

The Mobile Cloud Computing is in full expansion and its offers many advantages to users because it offers processing resources and storage space on demand.

Despites the expansion of MCC, its use is limited especially with regard to businesses, because of several constraints:

- Limit in processing power
- Small storage space
- Security issues
- High energy consumption

Several researches have defined the challenges and problems hindering the deployment of Cloud computing, and they have concluded that security is the biggest challenge for users and companies who want to adopt solutions and services of MCC.

2.3 Attacks in MCC

The use of mobile cloud computing offers many benefits to mobile users such outsourcing their personal data and using the different cloud services anywhere and anytime. Therefore, several attackers try through these networks to recover the personal data of those users for dishonest purposes used. So, several attacks have been developed, which primarily target the mobile cloud computing services as forgery attack, unauthorized server attack, brute force attack and replay attack.

3 Problematic and Architecture Description

3.1 Problematic

The goal of our work is to develop an architecture that ensures connection between mobile users and the cloud server in such a way that mobile users can download and interpret their personal data safely. To develop our security structure we need first to respond to security issues:

- The aim of our work is to allow mobile users to connect securely to the remote cloud server. The server-client communications are often subject of attacks through listening or poisoning of these communication channels. So, the connection between mobile user and server must be secure and must be able to ensure his data integrity and safety.
- In our model user's data are initially generated from a local server, which outsources the data and stores them in the cloud. As shown in Fig. 1, Data stored in cloud server is encrypted with the public key PK_{SC} of local server following a homomorphic encryption scheme. Mobile user will be unable to interpret data sent from cloud server.

To avoid these problems, we will develop an authentication system that will allow users to authenticate securely in local server, and then we will develop a downloading system that will allow them to download safely and interpret their sensitive data from the private cloud computing server.

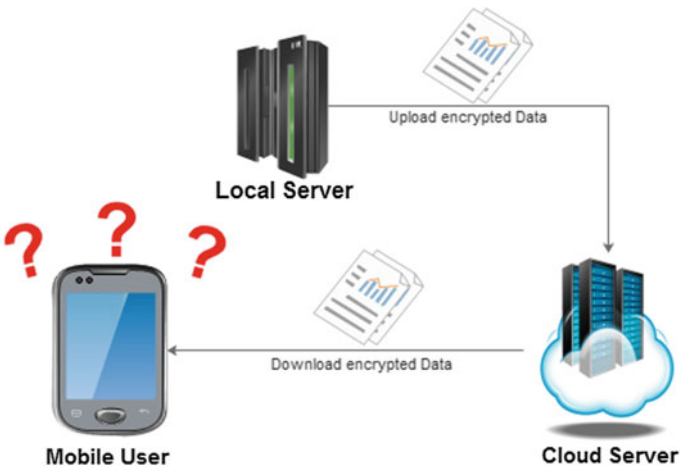

Fig. 1 Data flow in the network

3.2 *Proposed Model*

We will propose a new framework which allows mobile users to access their data stored in the private cloud computing server.

Our basic scheme as shown in Fig. 2 contains four main entities: The mobile device (DM), the central server (SC), a mobile unit (MU), and the private cloud computing server (PCS). The mobile device is responsible for downloading data from the cloud server.

Our security scheme is divided into two parts:

- The first part concerns mobile users authentication.
- The second part concerns data downloading from our private cloud computing server.

It is assumed that our central server can store and download data safely from the private cloud server; data is encrypted and decrypted using the secret key SK_{CS} and the public key SK_{SC} of our central server.

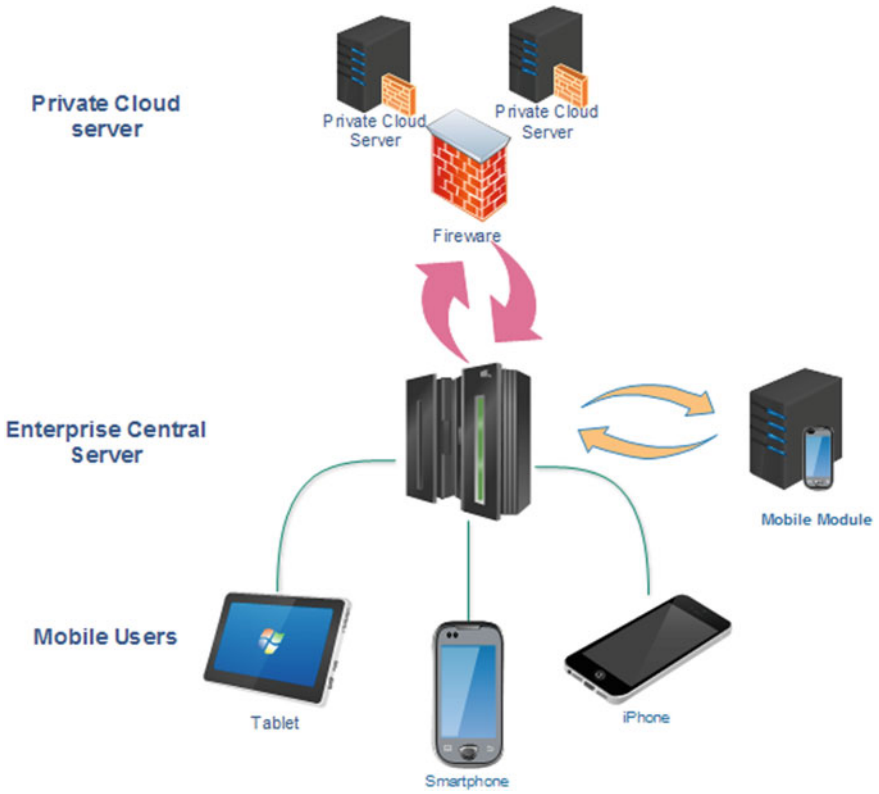

Fig. 2 Basic scheme of our proposed model

4 Authentication Scheme

We will present in this part a mechanism to authenticate the owners of files downloaded in the private cloud computing server.

The authentication scheme ensures the authenticity of the mobile users and the integrity of requests and communications between the mobile and the server.

The mobile device forges a homomorphic signature to ensure the integrity of requests and data on the basis of the algorithm Wang et al. [10], and then it sends an authentication request to the central server. The central server asks its responsible mobile unit to check validity of authentication requests issued by mobile user.

4.1 Homomorphic Signature Scheme

Some attacks aim to forge valid signatures in order to impersonate mobile users, and recover their sensitive data stored in the cloud. The goal of our scheme is to construct homomorphic signatures impossible to forge by attackers [13].

Every mobile user should have an ID for authentication, account number (AN) to access personal data stored in the cloud server and mobile device number (DN). Mobile users create their own signatures from their personal data (PDM) as: PDM = (AN, ID, DN).

Mobile device generates a public key PK_{DM}, and a private key SK_{DM}. For forging our signatures homomorphic, we proceed as:

1. Mobile connect to the server using his login and his password
2. Mobile generate a private key SK_{UM} and a public key PK_{UM}
3. We will choose t as a period of validity and we will compute T = H(t), as H is a hash function
4. We choose a random elements $v = \{v_1, \ldots, v_n\}, r = \{r_1, \ldots, r_n\}$ and u
5. We divide every elements of PDM into several part Pi as P = {P1, …, Pn), and we compute for every parts:

$$S_i = ((r_i)^{P_i} \times u^{v_i})^{1/T} (\mathrm{mod} N) \tag{1}$$

6. The full signature is:

$$Sig = (Sig_1, \ldots, Sig_n) \text{ as } Sig_i = (S_i, v_i, T) \tag{2}$$

7. The mobile device send the full signature to the central server, and our central server redirect the full signature to his mobile unite
8. The mobile unite Compute a new vector $e = (e_1, \ldots, e_n)$ corresponding to an identity ID of the user

9. Compute a new vector N:

$$N = (N_1, \ldots, N_n), \text{where } N_i = e_i \text{ if } e_i = 1, \text{ otherwise } N_i = T'. \quad (3)$$

T' is the current time stamp

10. Output a partial signature on ID S′:

$$S'_i = \prod_{i=1}^{n} S_i^{N_i} \quad (4)$$

11. Compute x

$$x = \prod_{i=1}^{n} r_i^{P_i} \times u^{v'} \text{ as } v' = \sum_{i=1}^{n} N_i \times v_i \quad (5)$$

12. Verify the Signature:

$$if\ Sig^T = x(\text{mod}N)\ output\ 1, otherwise\ output\ 0. \quad (6)$$

The homomorphic Signature Scheme will allow us to ensure the validity of data transmitted between the different entities of our network and to ensure the identity of users, and it will enhance the robustness of our model.

4.2 Mechanism of Authentication

Each mobile user must authenticate in the mobile unit to receive a password (PWD), which will allow him to access and view his personal data in the cloud server. To do so, we will develop a secure authentication scheme. The proposed secure scheme works in four steps. The algorithm of authentication is as follows:

1. First each user sends an authentication request to the central server, this application is defined as:

$$MD \mapsto CS : E_{PK_{UM}}(NC, ID, DN), Sig \quad (7)$$

2. Then the central server redirects the request to his mobile unit

$$CS \mapsto UM : E_{PK_{UM}}(NC, ID, DN), Sig \quad (8)$$

3. Mobile Unit checks the validity of the request, and the authenticity of the homomorphic signature, before generate a password (PWD) which will allow the mobile user to access to the cloud server. The mobile unit sends the PWD to the central server.

$$UM \mapsto CS : E_{PK_{MD}}(NC, ID, DN, E_{PK_{MD}}(PWD)) \tag{9}$$

4. Finally the central server redirects the PWD to the Mobile User

$$CS \mapsto MD : E_{PK_{MD}}(NC, ID, DN, E_{PK_{MD}}(PWD)) \tag{10}$$

Our authentication scheme allows users to connect securely to our central server and retrieve a session key to connect later the Cloud server. Our scheme uses a homomorphic signature to ensure the integrity, queries between different entities are encrypted which ensures confidentiality and for each connection, the user needs to retrieve a new session key which allows to secure user accounts and prevent replays attacks.

5 Downloading Scheme

After authentication, we will propose in this section an architecture that allows mobile users to view and download their sensitive data safely. In our model we assume the data stored in the private cloud server are encrypted with the public key PK_{SC} of our central server. Our basic scheme as shows in Fig. 3 contains three main

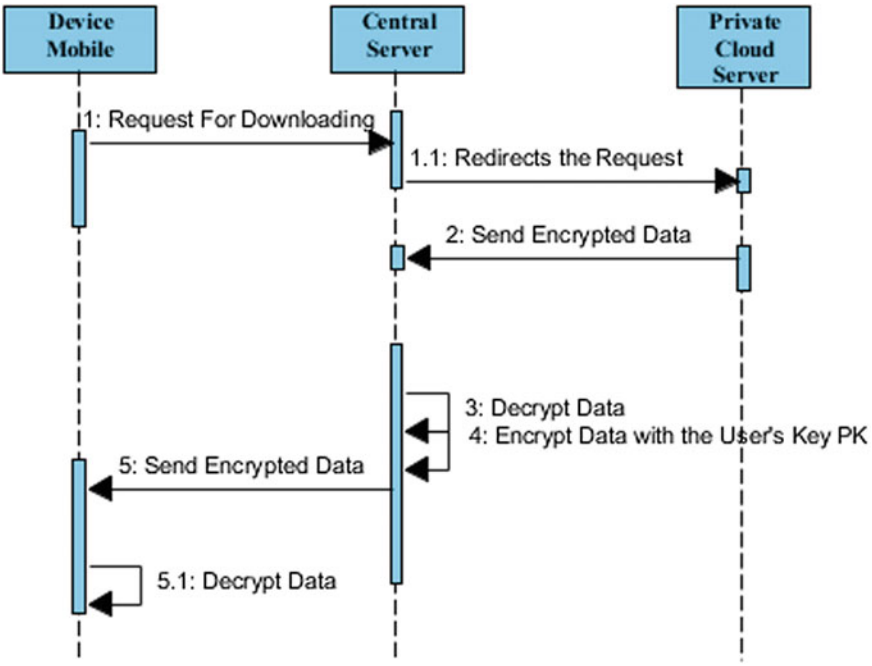

Fig. 3 Downloading scheme

entities: The mobile device (DM), the central server (SC), and the private cloud computing server (PCS).

The downloading algorithm is as follows:

1. For downloading his personal data from the private cloud server, the mobile user sends a request to the central server.

$$MD \mapsto SC : E_{PK_{CS}}(NC, ID, PWD, Ri), Sig \tag{11}$$

   $R = (R_1, \ldots, R_n)$ *such that each* R_i *is a type of request*
2. The central server verify the validity of the signature and then redirect the request to the private cloud server.

$$SC \mapsto PCS : E_{PK_{PCS}}(NC, ID, PWD, Ri), Sig \tag{12}$$

3. Cloud server consults his database before sending the encrypted data to our central server.

$$PCS \rightarrow SC : E_{PK_{SC}}(DATA), Sig \tag{13}$$

4. The server decrypts the data with his secret key SK_{SC}, and re-encrypted with the public key of the mobile user PK_{MD}, and then redirects data to the mobile device.

$$PCS \rightarrow SC : E_{PK_{MD}}(DATA), Sig \tag{14}$$

Our downloading scheme ensures confidentiality and data integrity; it also allows privacy of users because the data stored in the cloud is encrypted. Our scheme uses the services of a private cloud server [14] which increases the level of security and reduces the risk of data loss. The mobile users may be interpreted the received data because they were re-encrypted using the appropriate encryption key for each mobile device.

6 Security Analysis

We will proceed in the following to a security analysis which will allow us to evaluate our security framework compared to vulnerabilities and security threats. We will prove that our structure can tackle all these security issues very efficiently, and offer to mobile users an interface that will allow them to upload and view safely their sensitive personal data stored in the cloud server.

- *Data protection*: Our security framework aims primarily to ensure data security and mobile users privacy. So, all communications between different entities of our structure are encrypted.
- *Authentication and Integrity*: In many cases, it is not very easy to identify users, which can cause security problems. To fix this problem we have developed an authentication scheme that enables users to authenticate in order to receive and view their data safely.
- *Loss of user identity and password*: The Loss of mobile user ID can be very dangerous. But in our structure, it is imperative to make an authentication request to receive a password PWD and then access the data which is located in the distant cloud server. This procedure will prevent mobile users from losing their data even in the case of their ID loss.

7 Simulation and Experiment

7.1 Simulation Process

We propose in this part an implementation of our model for banking data. We chose to work on banking data because they are very sensitive and contain confidential information of the bank and these customers, and because they are generally small in their size, which allow us to fully utilize the homomorphic encryption properties without worrying about treatment time duration. The bank's customers can access to their data stored in the cloud by using a mobile application designed for this purpose. This application is linked directly to the central server of the bank that is connected to the remote cloud servers.

As shown in Fig. 4, the progress of our implementation is as follows: The bank's customers will be able to register in the network from their mobile in order to log into the system and view their data stored in the cloud safely.

We described in this part the different steps that we followed during our implementation, and the different reasons and motivation that led us to choose to work on banking data rather than others, and we also define a manual for our model to ease its use. We should also specify that our model is highly scalable because it allows the addition of multiple features and it may use several crypto systems as needed. It is clear that the banking sector fully illustrates the utility and the robustness of our model but it is also applicable to any other area and any other usage mode.

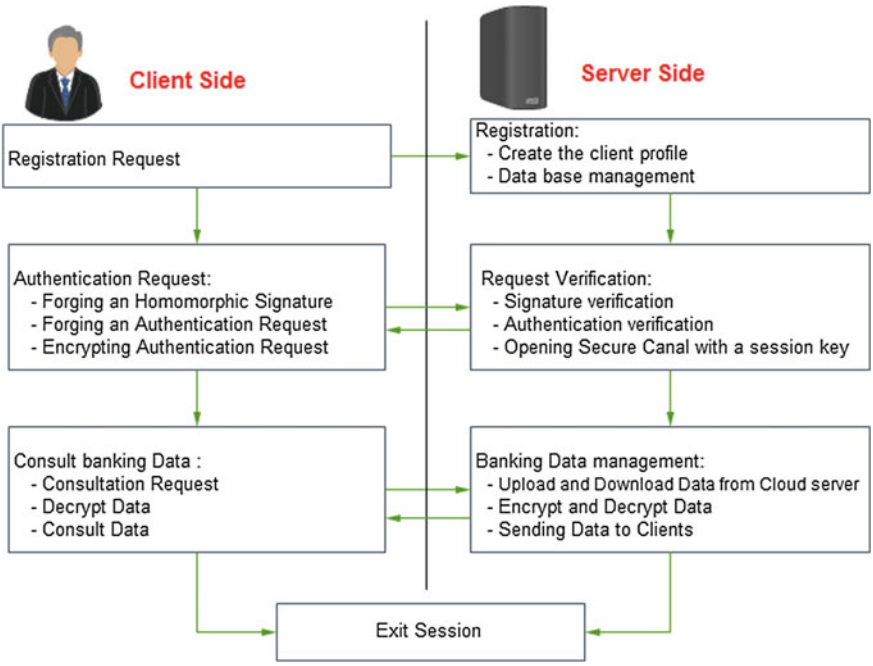

Fig. 4 Simulation process

7.2 Experimental Results

In this part we will propose an implementation of our model. We will develop an application which allows mobile users to access their banking information and consult them safely.

7.2.1 Registration and Authentication Scheme

Each bank customer has an ID and password, which allows him to register in the mobile application. Once connected, he sends a request to the Bank's local server to access his personal data. The local server sends a new password PWD to mobile user, allowing him to securely access his personal data. In Table 1, there is a description of our application use test results.

In what follows we will prove the efficiency of our model compared to the CPU consumption and to the treatment time duration. Figure 5 shows the time required to generate cipher and check the validity of the authentication request according to the key size.

Table 1 Test of use of our registration and authentication platform

Registration: (mobile device)	
Login	Karim.zkik
Password	110251032
Forging a signature from the personal data of user: (mobile device)	
Account number	185156753212
ID	110251032
Phone number	0615318287
N = p * q	193105375012785175488407837176022112881
Time digest	1ff1de774005f8da13f42943881c655f
Number of blocs n	10
signature1_1	718560756192253…130286919974899
signature1_2	635197852275421…200563432254935
signature1_3	244061552333593…961636800483234
signature1_4	847324068849953…124788710851252
signature2_1	365986028155682…896650598164824
signature2_2	621354567605975…532201405198811
signature2_3	101337780267101…986217241841814
signature3_1	763184105730929…644641230225807
signature3_2	438412718836446…987828789067592
signature3_3	836478842306245…472924981807224
Signature	7185607561922532505420421…646721675227 035378472924981807224
Authentication request	1851567532121102510320615318287
Encrypted authentication request PKSC (NC, ID, NP)	8201377451433300020081165456502…525506 255786269622560066270006503758707351
Received data from the mobile user: (central server)	
Encrypted authentication request	8201377451433300020081165456502..5255306 255786269622560066270006503758707351
Signature	7185607561922532505420421… 64672167522703537847292498180722 4
Forging a new signature from the user ID: (central server)	
Time digest	1ff1de774005f8da13f42943881c655f
ID	110251032
Part of signature 1	36598602815568241…2439896650598164824
Part of signature 2	62135456760597578…9053532201405198811
Part of signature 3	10133778026710118…6816986217241841814
Part of signature on ID	230449297454183799081414456 3… 90937462690663996425400824974896
Checking the validity of the signature: (central server)	
Computes x from the user's signature sent by the user	230449297454183799081414456 3… 90937462690663996425400824974896
Final verification	1
Session key	7F45D0E56331A1

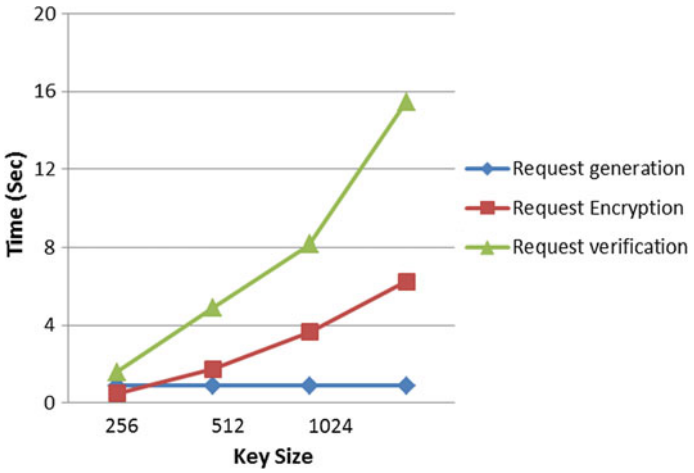

Fig. 5 Request treatment (Colour figure online)

Figure 6 shows the computing power and CPU consumption used to generate and verify the validity of the signature and the authentication request according to key size.

We have detailed the different results obtained, during the generation and verification of homomorphic signature, and during the generation and verification of authentication request, which allowed us to obtain a session key to connect to the cloud server.

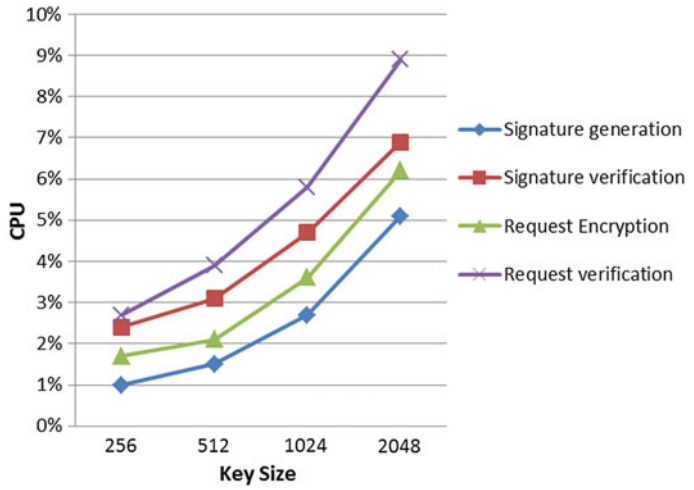

Fig. 6 CPU consumption (Colour figure online)

Table 2 Test of use of our security platform

Send a request to view our bank balance: (mobile device)	
Request to view our bank balance	7F45D0E56331A1, R1 (R1 is the request to see balance)
Receive data from the cloud server: (central server)	
Encrypted data received from the cloud	81753113457405706155871447425455627000641714190010128239010389759581879620235898131436934844921769947876772301833772329937479150552685101725
Decrypt data with the central server's secret key	1000 $
Encrypt data with the user's public key	352778882925008839512541055137779122266772031942505739406487102223896716431643652785
Send encrypted data to mobile user: (mobile device)	
Encrypt data with the user's public key	352778882925008839512541055137779122266772031942505739406487102223896716431643652785
Decrypt data with the user's secret key	1000 $

7.2.2 Downloading Scheme

The mobile user will send a request to see his balance, for example, using the session key. Cloud server will send the required data to the central server, which redirects to the mobile after being decrypted and re-encrypted in such a way that the mobile user is the only one who can interpret them. In Table 2, there is a description of our application use test results:

Our implementation allows mobile users to recover safely their data stored in the cloud, including information on their bank accounts and their balances. We have also demonstrated the efficiency and robustness of our model while describing the results of the various steps of its use.

8 Conclusion and Future Work

Our security structure offers the possibility to fully use the mobile cloud computing services because it allows avoiding the problems related to security. We have demonstrated in our evaluation that our structure ensures the authenticity of users and data protection, and the use of a homomorphic signature allows, on another hand, ensuring the integrity of data and preventing attacks that aim to forge valid electronic signatures. Our structure also allows mobile users to interpret the encrypted data stored in the cloud, even if the data is initially encrypted with the key of the company's central server. We have developed an implementation of our architecture; and we have chosen as an example a Bank that offers online services to

its clients, like viewing their balance. This implementation shows that our structure permits secure downloading of data and user privacy.

It is expected in future work to make an implementation of our application to secure various types of data, including very large data and add data management protocols to manage the big data and facilitated research on encrypted data. Given the resource constraints of mobile devices, we project also in the near future to make our application more efficient, and more flexible to use, and we plan to develop a homomorphic encryption mechanism that will be able to do calculations on received data before returning them to the distant cloud server.

References

1. Dharmale PN, Ramteke PL (2013) Mobile cloud computing. Int J Sci Res (IJSR) 2319–7064
2. Fernando N, Loke SW, Rahayu W (2013) Mobile cloud computing: a survey. Future Gener Comput Syst 29:84–106
3. Shahzad A, Hussain M (2013) Security issues and challenges of mobile cloud computing. Int J Grid Distrib Comput 6(6):37–50
4. Hoang T, Dinh C, Lee D, Niyato, Wang P (2013) A survey of mobile cloud computing: architecture, applications, and approaches. Wirel Commun Mob Comput 13(18):1587–1611
5. Khan AN, Kiah MLM, Khan SU, Madani SA (2013) Towards secure mobile cloud computing: a survey. Future Gener Comput Syst 29:1278–1299
6. Ryan MD (2013) Cloud computing security: the scientific challenge, and a survey of solutions. J Syst Softw 86:2263–2268
7. Zissis D, Lekkas D (2012) Addressing cloud computing security issues. Future Gener Comput Syst 28(3):583–592
8. Kamara S, Lauter K (2010) Cryptographic cloud storage. In: 14th international conference on financial cryptography and data security (IFCA), LNCS. Springer, Berlin, pp 136–149
9. Hsueh SC, Lin JY, Lin MY (2011) Secure cloud storage for conventional data archive of smart phones. In: Proceedings of 15th IEEE international symposium on consumer electronics, ISCE'11, Singapore
10. Wang Z, Sun G, Chen D (2014) A new definition of homomorphic signature for identity management in mobile cloud computing. J Comput Syst Sci 80:546–553
11. Tebaa M, Zkik K, El Hajji S (2015) Hybrid homomorphic encryption method for protecting the privacy of banking data in the cloud. Int J Secur Its Appl 9(6):61–70
12. M. Van Dijk, C. Gentry, S. Halevi and V. Vaikuntanathan (2010) Fully homomorphic encryption over the integers. In: Advances in cryptology-EUROCRYPT 2010. Lecture Notes in Computer Science, vol 6110. Springer, Berlin, pp 24–43
13. Zkik K, Tebaa M, El Hajji S (2015) New homomorphic platform for authentication and downloading data in MCC. In: Proceedings of the world congress on engineering 2015, WCE 2015, 1–3 July, 2015, London, U.K. Lecture Notes in Engineering and Computer Science, pp 508–514
14. Private cloud (internal cloud or corporate cloud). Available: http://www.interoute.com/cloud-article/what-private-cloud

Security Issues in Content Modification Processes

William R. Simpson and Kevin Foltz

Abstract Entities that change the content at some point in the transmission process present assurance problems. These entities include optimizers, accelerators, and target display adapters, among others. Maintaining security when using these entities depends in detail on what the content-changing entity does, and the general problem has not been solved. By way of illustration, we have chosen to examine the assurance issues for a wide area network (WAN) Accelerator. Bandwidth continues to be a problem for the active enterprise, and one solution is the WAN Accelerator. The accelerator works by tokenizing blocks of information that are sent multiple times in network traffic. Because many such communications include previously transmitted material, the accelerator traffic quickly damps out to transmissions that include tokens instead of the original content. The tokens are reconstituted before delivery, and the receiver has a seamless connection and is unaware of the process. The acceleration is not without its drawbacks. The process does not work on encrypted traffic due to the random nature of encryption. For high assurance systems using an end-to-end paradigm, there are two main areas of concern. The first is how to handle confidentiality during the decryption and re-encryption process. The second is how to maintain end-to-end integrity with tokenization and de-tokenization. This chapter discusses the current approach to WAN acceleration and the changes that are required by a high assurance end-to-end approach.

Keywords Content modification · End-to-end security · Encryption · Integrity · IT security · Key management · Network acceleration appliance · Protection · Wide area network

W.R. Simpson (✉) · K. Foltz
Institute for Defense Analyses, 4850 Mark Center Drive,
Alexandria, VA 22311, USA
e-mail: rsimpson@ida.org

K. Foltz
e-mail: kfoltz@ida.org

S.-I. Ao et al. (eds.), *Transactions on Engineering Technologies*,
DOI 10.1007/978-981-10-1088-0_32

1 Introduction

This paper is based in part on a paper published by WCE [1]. Content-changing appliances were considered late in the development of the enterprise architecture and presented quite a dilemma. Even the use of server handler chains cannot solve this problem directly. The class includes web accelerators, re-formatters, and wide area network (WAN) accelerators, among others. The general solution to this is not available, and we continue to handle these entities on a case-by-case basis. For the high assurance environment, we are primarily concerned with four security principles.

- Know the Players—this is done by enforcing bi-lateral end-to-end authentication Fig. 1.
  In Enterprise Level Security the identity certificate is an X.509 PKI certificate [2]. PKI certificates are verified and validated. Ownership is verified by a holder-of-key check.
- Maintaining Confidentiality—this entails end-to-end unbroken encryption Fig. 2.
  Enterprise Level Security establishes end-to-end Transport Layer Security (TLS) [3], encryption (never give away private keys which belong uniquely to

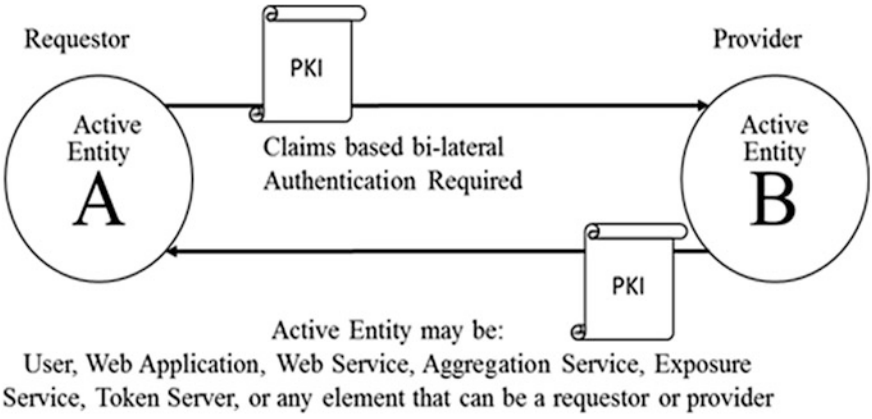

Fig. 1 Bi-lateral authentication

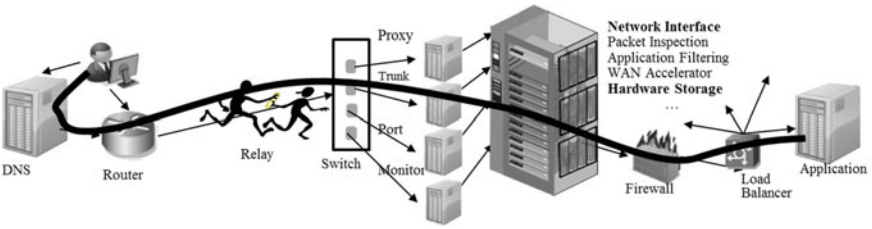

Fig. 2 End-to-end encryption

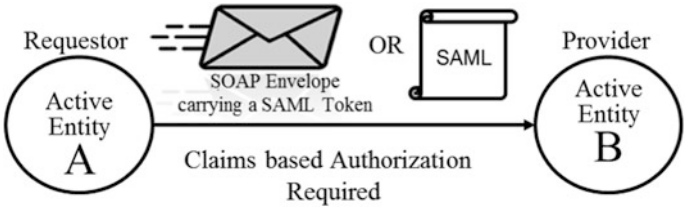

Fig. 3 Claims-based authorization

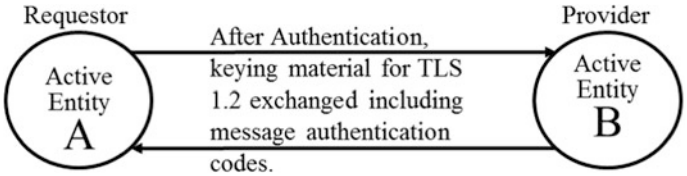

Fig. 4 MAC and other integrity measures

the certificate holder). Message authentication codes are enforced (but they are only valid when the encryption remains unbroken to the end point).

- Enforce Access Control—this is done by an authorization credential Fig. 3.
  In Enterprise Level Security the certificate is the Security Assertion Markup Language (SAML) [4]. SAMLs are signed, and the signatures are verified and validated. The credentials of the signers are verified and validated.
- Maintain Integrity—know that you received exactly what was sent—know that content has not been modified Fig. 4.
  In Enterprise Level Security this is implemented by End-to-End TLS encryption with message authentication codes (MAC). Packages (like SAML tokens) are signed and signatures are verified and validated [5].

In this chapter we use the WAN accelerator as an example of the difficulties that these entities present to secure systems. Bandwidth continues to be a problem for the active enterprise. Accelerators, prepositioning of data, and integrated solutions that use caches of commonly used data are expanding at an alarming rate. The major problem is maintaining the security principles of high assurance.

A WAN accelerator [6] is an appliance that optimizes bandwidth to improve the end user's experience on a WAN. The appliance, which can be a physical hardware component, a software program, or an appliance running in a virtualized environment, speeds up the time it takes for information to flow back and forth across the WAN by using compression and data deduplication techniques to reduce the amount of data that needs to be transmitted. An accelerator works by caching duplicate files or parts of files so they can be referenced instead of having to be sent across the WAN again. Many of the products have evolved beyond the core acceleration techniques. The WAN optimization controllers (WOC) further optimize the WAN link by accounting for known problems with common network

protocols. Protocol optimization cleans up chatty protocols used in common enterprise standards such as Common Internet File System (CIFS), Microsoft Exchange, and even TCP/IP to eliminate the typical overhead found in these communication protocols. These optimizations require a deeper understanding of the protocols and can be accomplished only through significant collaboration with application vendors or reverse engineering by the WAN accelerator vendor.

WAN optimization encompasses [7]:

- Traffic shaping, in which traffic is prioritized and bandwidth is allotted accordingly.
- Data deduplication, which reduces the data that must be sent across a WAN for remote backups, replication, and disaster recovery.
- Compression, which shrinks the size of data to limit bandwidth use.
- Data caching, in which frequently used data are hosted locally or on a local server for faster access.
- Monitoring the network to detect non-essential traffic.
- Creating and enforcing rules about downloads and Internet use.
- Protocol spoofing—a method of bundling chatty protocols so they are, in effect, a single protocol.

WAN optimization vendors include Blue Coat Systems, Cisco, Expand Networks, F5 Networks, Juniper, and Riverbed Technology. Further discussion of WAN optimization is contained in [8–17].

2 Current WAN Accelerator Approaches

Acceleration of unencrypted traffic is not of interest in the high assurance end-to-end paradigm, so we will concentrate on the steps involved in handling encrypted traffic. Initially, there is a need to decrypt the traffic since tokenization is ineffective

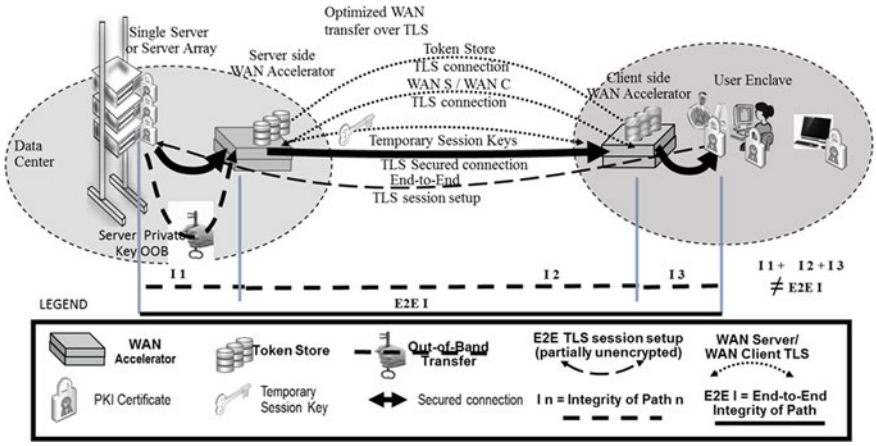

Fig. 5 WAN accelerator current process server to user

for encrypted traffic. This is due to the randomization of bit streams that are a property of encryption. This is normally done by passing the private key of the server to the server-side WAN accelerator appliance, as shown in Fig. 5.

As shown in Fig. 6, the Transport Layer Security (TLS) keys are computed and then passed between the accelerator units. The premaster secret keying material that is passed is protected by the private key of the server. The sharing of the server's private key allows the server-side appliance to extract the premaster secret and compute the session's master secret, just as the endpoints compute it. This is used to generate the encryption keys and Message Authentication Code (MAC) secrets for each TLS connection within this session. As shown in Fig. 5, the session keys and MAC secrets are then transmitted to the client-side WAN accelerator.

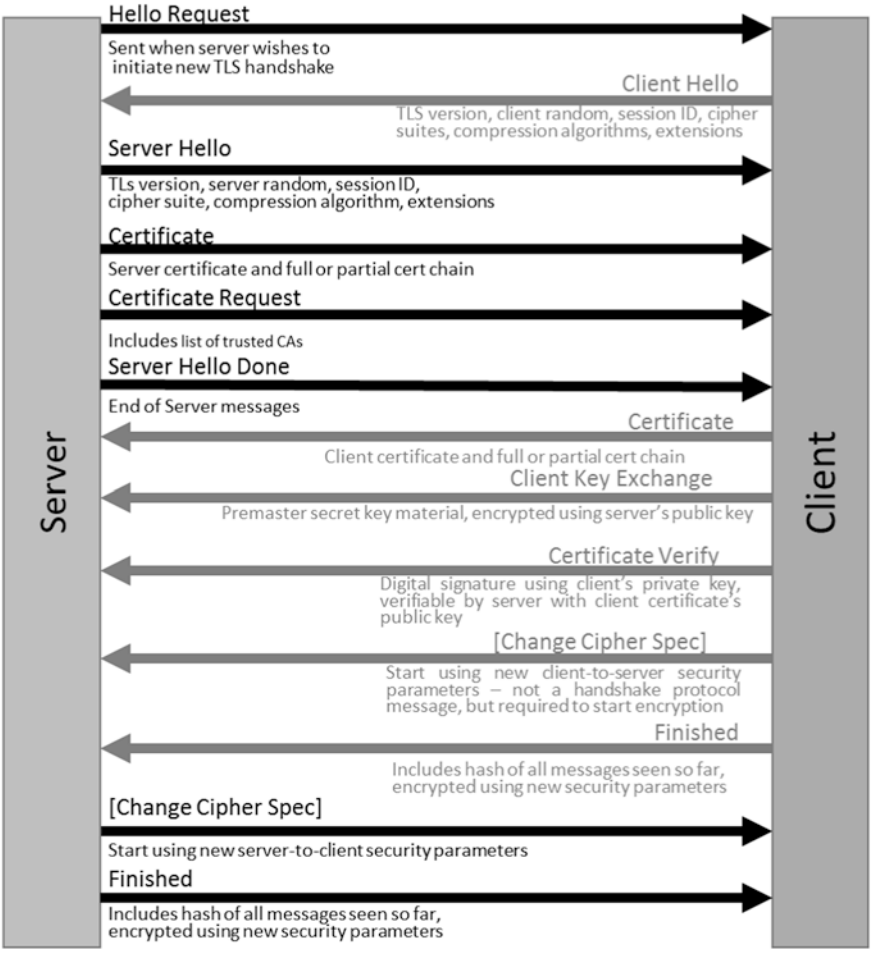

Fig. 6 TLS handshake

While sharing of private keys is an easy way to provide the appliances with visibility to the content, it is a singularly bad idea from a security standpoint. First, in high assurance systems, the private keys are locked in a Hardware Storage Module (HSM) and are not shareable. Second, loss of a private key will compromise identity, break integrity and confidentiality of all TLS traffic to the server (past, present, and future), allow an adversary to impersonate the entity on an existing connection, and allow the adversary to impersonate the entity on new connections initiated by the adversary. In contrast, loss of a session key will entail a loss of only confidentiality for a single connection within a TLS session, with no risks for identity impersonation.

Figure 5 shows the basic flows. This includes the logical end-to-end client-to-server TLS connection and its three secure component connections to, between, and from the WAN accelerators. It also includes TLS sessions to provide the session keys to the client-side accelerator, to transmit the tokenized packets to the client-side accelerator, and optionally to keep the tokenization stores synchronized. Although shown as separate TLS connections between the same endpoints, these may instead be implemented as separate logical flows within a single TLS connection. Aside from key management issues, the difference is not important.

Figure 5 also shows the concern of integrity. The piecewise integrity of the component connections (I1, I2, and I3) does not amount to overall end-to-end integrity (E2E I).

$$\mathrm{I1} + \mathrm{I2} + \mathrm{I3} \neq \mathrm{E2EI} \tag{1}$$

In an end-to-end security paradigm, the goal is for the receiver to verify that the message sent from the server is identical to the message received at the client. Even when TLS MACs are included in all component connections, the integrity of the end-to-end transmission is not preserved unless we undertake some extraordinary measures.

When a component connection retransmits data with a new MAC value, any changes made by that component to the original data will go undetected. In order to avoid explicit trust of the WAN processes, the TLS reconstruction of the server traffic by the client-side WAN accelerator must be modified. To understand this, we must examine the way in which TLS messages are formed.

3 An Alternative to Private Key Passing

For most interactions using enterprise level security approaches, traffic content does not need to be inspected. Firewall functionality will still be available using the headers that are not encrypted. However, certain functions, including WAN acceleration, require content inspection. For these conditions, we recommend an alternative to sharing private keys as follows:

1. Web application shares only the TLS session keys that are needed for each appliance to function.

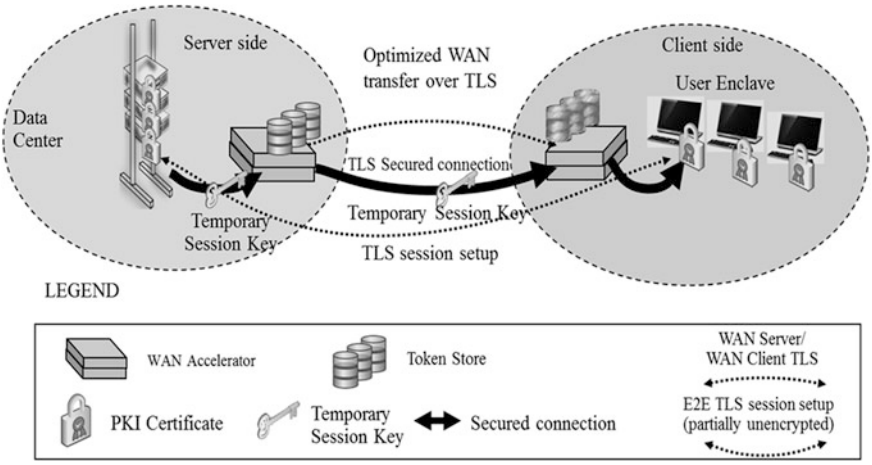

Fig. 7 Alternative encrypted web server communications

2. No shared private keys—each active entity has its own unique public/private key pair.
3. Web application is endpoint for browser requests.

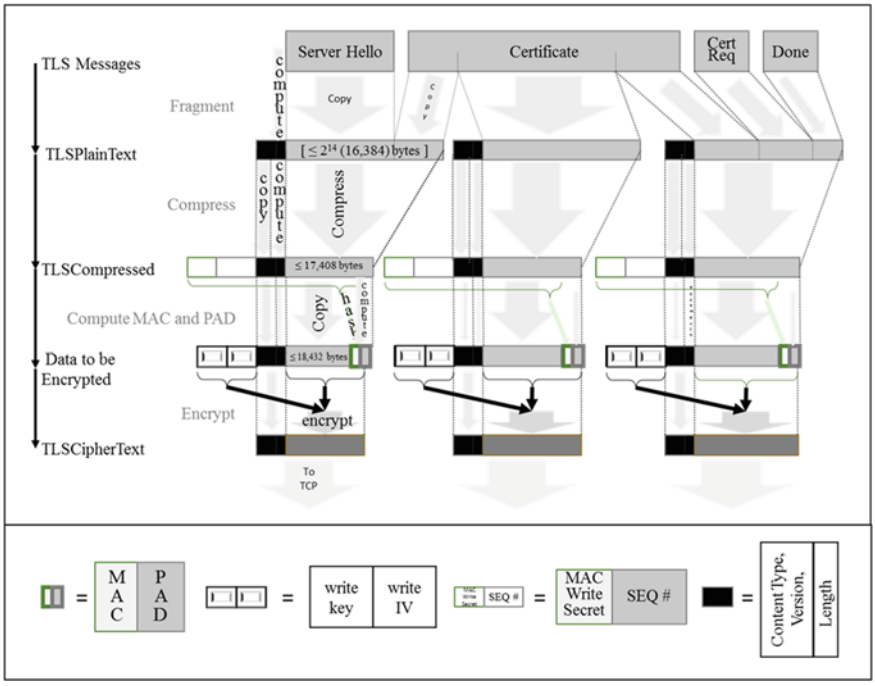

Fig. 8 TLS transmission steps (Color figure online)

Figure 7 shows the alternative recommendation. HTTP traffic is encrypted using TLS from browser to web application. The WAN Accelerator uses the provided session keys to decrypt TLS traffic. The balance of the transaction works in the same way, with the exception of the integrity problem. For this we must examine the TLS package development process.

The message breakdown and TLS packet construction [18, 19] are shown in Fig. 8. The figure includes fragmentation of messages, addition of headers, compression, addition of the MAC and padding, and encryption. The MAC secret and values that depend on it are indicated in white at the beginning of the block "TLSCompressed". The encryption keys and IVs, and values that depend on them, are indicated in white on the beginning of blocks in the row "[data to be encrypted]". The ciphertext has both black and dark gray, since it relies on both the MAC secret and the encryption keys and IVs.

Figure 9 shows the reverse process, where the receiver decrypts, validates the received MAC, decompresses, extracts content, and defragments into the original messages.

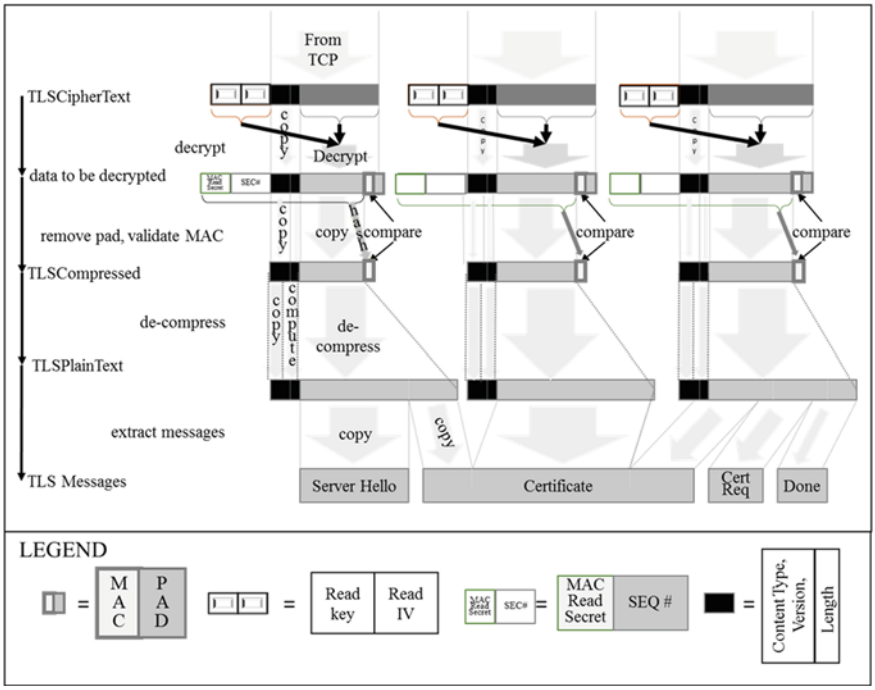

Fig. 9 TLS reception steps

4 Integrity in a TLS Session

One important feature of TLS is that the encryption key/IV and MAC secret are separate values with separate functions. With only the encryption key and IV, an intermediate node can view the content but not modify it. It cannot compute a valid MAC for the modified content without the MAC secret. Also relevant is that the fragmentation boundaries of the original messages are important for MAC computation. Identical messages that are fragmented differently will have different MACs since the MACs depend on the fragments to which they are appended.

5 Flows in a High Integrity System

The overall recommended flows for the high assurance WAN Accelerator on the server-side are provided in Fig. 10. The TLS session keys are passed to the server-side WAN accelerator as shown in Fig. 7 and subsequently passed on to the client-side accelerator through the WAN Server/ WAN Client TLS. The primary addition is the transmission of the original message fragmentation, padding, and MACs. These are needed to make an identical reconstruction of the original message. The original MACs can be added to the reconstructed message, for which the targeted end-point has the MAC key.

The original TLS MAC digests, paddings, and fragmentation are used to construct TLS packets in lieu of the values that would normally be computed by the

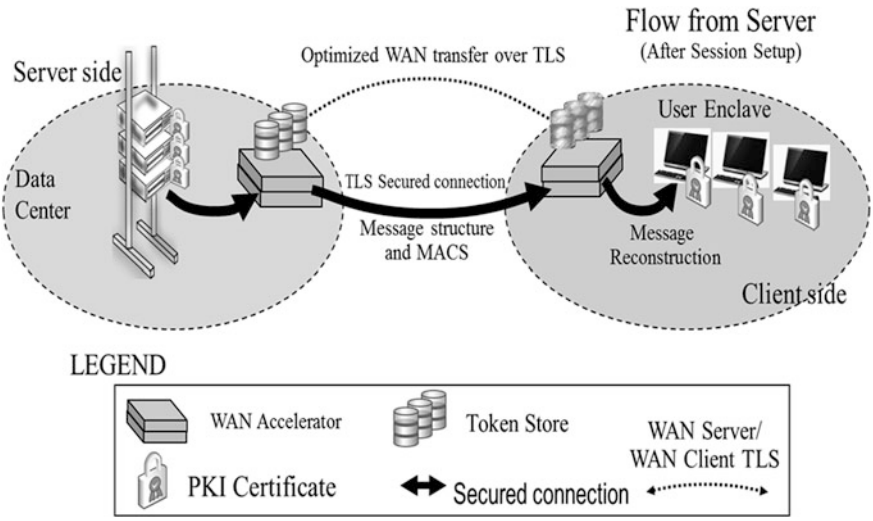

Fig. 10 Flow from the server side

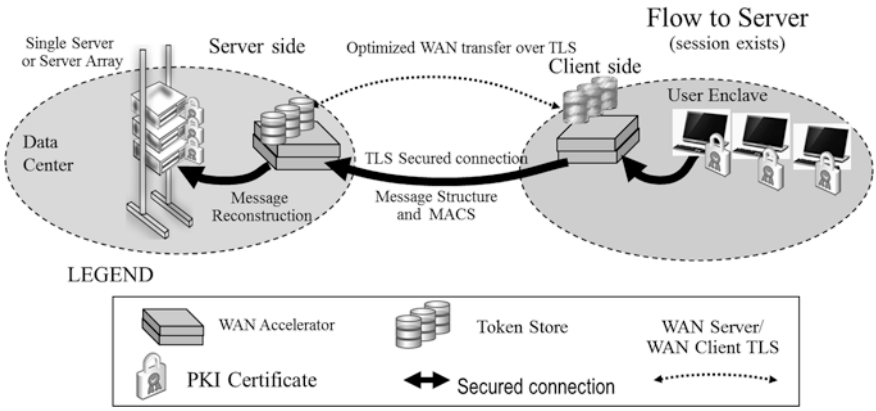

Fig. 11 Flow from the client side

TLS protocol. The client-side flows are given in Fig. 11 and show the same transmission of the fragmentation, paddings, and MACS for the reconstruction of the message on the server-side.

To ensure end-to-end integrity it is necessary that the MAC secret not be available to the WAN accelerator. The receiving WAN accelerator node uses the original content, as received and reconstructed from the WAN connection, the original TLS fragmentation information, and the associated MAC and padding values to construct valid TLS messages to the receiving endpoint. Because only the sending endpoint has the MAC secret, the receiving endpoint has an end-to-end integrity guarantee.

6 Summary

We have reviewed the basic approaches to WAN Acceleration security when dealing with encrypted traffic. These have been found lacking in the specific areas of key protection and message integrity. Key protection is lacking in that out-of-band passing of the private keys of the servers violate specific security tenants. Message integrity is lacking in that piecewise integrity is substituted for overall end-to-end integrity. We have also described the high assurance architectures and protection elements they provide. In order to preserve the high assurance key security and integrity elements, changes to the basic flows must be made. Key security can be maintained by passing only the session key, which provides a lower risk than passing the private key of the server and maintains the unique identity of the server. Overall message integrity can be maintained by conspicuously reconstructing the original messages, including the message authentication codes. The development of WAN accelerator mechanisms does not require distribution of a private key, which is often done with today's appliances. The distribution of private

keys is a fundamental violation of a high assurance model. What remains is the need for high reliability and secure code for passing of session keys, as well as secure means of transporting TLS plans and MACs for the establishment of service interfaces on the appliances. Pilots are in the process of being undertaken, and we expect some modifications as we learn more about how these devices work.

The issue of sharing private keys with appliances has not yet been solved. The network system security is broken, malicious activity is pervasive, and greater resources are being allocated to chase the hope of identifying and mitigating the security threats that are corrupting this system security. The network has such high functionality that it cannot be abandoned. However, the current approach of sharing private keys so that every packet and every transaction can be inspected, even when we do not know what we are looking for, violates primary security properties, and the hunt for solutions is absolutely necessary.

This research is part of a body of work for high assurance enterprise computing using web services. Elements of this work include bi-lateral end-to-end authentication using PKI credentials for all person and non-person entities, a separate SAML credential for claims-based authorization, fully encrypted at the transport layer and a defined federation process. Many of the elements of this work are described in [20–33].

References

1. Foltz K, Simpson WR (2015) Wide area network acceleration in a high assurance enterprise. In: Proceedings world congress on engineering 2015, WCE 2015, 1–3 July, London, UK. Lecture Notes in Engineering and Computer Science. pp 502–507
2. Internet Engineering Task Force (IETF) (1999) RFC 2459, internet X.509 public key infrastructure
3. Request for Comments (2008) The transport layer security (TLS) protocol version 1.2. http://tools.ietf.org/html/rfc5246
4. Mishra P et al (2005) Conformance requirements for the OASIS security assertion markup language (SAML) V2.0. OASIS Standard, March 2005
5. List W, Melville R (1994) IFIP working group 11.5, integrity in information. Comput Secur 13(4):295–301. doi:10.1016/0167-4048(94)90018-3
6. Rouse, M (2009) WAN accelerator. In: Network management and monitoring: the evolution of network control. http://searchenterprisewan.techtarget.com/definition/WAN-accelerator
7. Rouse M (2010) WAN optimization (WAN acceleration). http://searchenterprisewan.techtarget.com/definition/WAN-optimization
8. Cardwell N, Savage S, Anderson T (2011) Modeling TCP latency. INFOCOM 2000. In: Nineteenth annual joint conference of the IEEE computer and communications societies, proceedings of IEEE. Department of Computer Science and Engineering, Washington University, Seattle, WA, IEEE.org. Retrieved 20 July 2011
9. Jacobson V (2011) TCP extensions for long-delay paths. Request for comments: 1072, internet engineering task force (IETF). Retrieved 19 July 2011

10. Floyd S (2011) HighSpeed TCP for large congestion windows. Request for comments: 3649, internet engineering task force (IETF). Retrieved 19 July 2011
11. Paris C (2011) Latency and colocation. Retrieved 20 July 2011
12. Mark R, Igor G (2009) CIFS acceleration techniques. In: Storage developer conference, SNIA, Santa Clara
13. Conway R (2004) Code hacking: a developer's guide to network security. Charles River Media, Hingham, Massachusetts, p 281 (ISBN 1-58450-314-9)
14. Chang R (2002) Defending against flooding-based distributed denial-of-service attacks: a tutorial. IEEE Commun Mag 40(10):42–43
15. Altinel M, Bornhövd C, Krishnamurthy S, Mohan C, Pirahesh H, Reinwald B (2003) Cache tables: paving the way for an adaptive database cache. In: Proceedings of the 29th international conference on very large data bases, Sept 09–12, 2003, Berlin, Germany, pp 718–729
16. Amiri K, Tewari R, Park S, Padmanabhan S (2002) On space management in a dynamic edge cache. In: Proceedings of the fifth international workshop on the web and databases (WebDB 2002) (Madison, Wisc). ACM, New York, pp 37–42
17. Anton J, Jacobs L, Liu X, Parker J, Zeng Z, Zhong T (2002) Web caching for database applications with oracle web cache. In: Proceedings of the 2002 ACM SIGMOD international conference on management of data, 03–06 June, 2002, Madison, Wisconsin. doi:10.1145/564691.564762
18. Request for Comments: 3749 (2004) Transport layer security protocol compression methods. http://tools.ietf.org/html/rfc3749
19. Request for Comments (2006) Transport layer security (TLS) extensions. http://tools.ietf.org/html/rfc4366
20. Simpson WR, Chandersekaran C, Trice A (2008) A persona-based framework for flexible delegation and least privilege. In: Electronic digest of the 2008 system and software technology conference, Las Vegas, Nevada, May 2008
21. Simpson WR, Chandersekaran C, Trice A (2008) Cross-domain solutions in an era of information sharing. In: The 1st international multi-conference on engineering and technological innovation: IMET2008, Orlando, FL, June 2008, vol I, pp 313–318
22. Chandersekaran C, Simpson WR (2008) The case for bi-lateral end-to-end strong authentication. In: World wide web consortium (W3C) workshop on security models for device APIs, London, England, Dec 2008, 4 pp
23. Simpson WR, Chandersekaran C (2009) Information sharing and federation. In: The 2nd international multi-conference on engineering and technological innovation: IMETI2009, Orlando, FL, July 2009, vol I, pp 300–305
24. Chandersekaran C, Simpson WR (2010) A SAML framework for delegation, attribution and least privilege. In: The 3rd international multi-conference on engineering and technological innovation: IMETI2010, Orlando, FL, July 2010, vol 2, pp 303–308
25. Simpson WR, Chandersekaran C (2010) Use case based access control. In: The 3rd international multi-conference on engineering and technological innovation: IMETI2010, Orlando, FL, July 2010, vol 2, pp 297–302
26. Chandersekaran C, Simpson WR (2011) A model for delegation based on authentication and authorization. In: The first international conference on computer science and information technology (CCSIT-2011). Lecture Notes in Computer Science. Springer, Berlin, 20 pp
27. Simpson WR, Chandersekaran C (2011) An agent based monitoring system for web services. In: The 16th international command and control research and technology symposium: CCT2011, Orlando, FL, Apr 2011, vol II, pp 84–89
28. Simpson WR, Chandersekaran C (2011) An agent-based web-services monitoring system. Int J Comput Technol Appl (IJCTA) 2(9):675–685
29. Simpson WR, Chandersekaran C, Wagner R (2011) High assurance challenges for cloud computing. In: Proceedings world congress on engineering and computer science 2011,

WCECS 2011, San Francisco, USA, 19–21 Oct 2011. Lecture Notes in Engineering and Computer Science, pp 61–66
30. Chandersekaran C, Simpson WR (2012) Claims-based enterprise-wide access control. In: Proceedings world congress on engineering 2012, WCE 2012, London, UK, 4–6 July 2012. Lecture Notes in Engineering and Computer Science, pp 524–529
31. Simpson WR, Chandersekaran C (2012) Assured content delivery in the enterprise. In: Proceedings world congress on engineering 2012, WCE 2012, London, UK, 4–6 July 2012. Lecture Notes in Engineering and Computer Science, pp 555–560
32. Simpson WR, Chandersekaran C (2012) Enterprise high assurance scale-up. In: Proceedings world congress on engineering and computer science 2012, WCECS 2012, San Francisco, USA, 24–26 Oct 2012. Lecture Notes in Engineering and Computer Science, pp 54–59
33. Chandersekaran C, Simpson WR (2012) A uniform claims-based access control for the enterprise. Int J Sci Comput 6(2):1–23 (ISSN: 0973-578X)

Capacity and Range Analysis of a Proposed 5G Wireless Network Solution

Hilary Frank

Abstract There have been four generations of wireless networks. Since its inception in the early 1980s, mobile communication has evolved with each succeeding generation emerging approximately every 10 years and introducing additional services to users. Demand for bandwidth capacity has grown with every generation. Available spectrum is being increasingly limited by competing demands, while the primary device for internet connection is steadily becoming wireless. The present mobile generation is gradually reaching its capacity limits, necessitating rigorous studies to find ways of providing greater capacity beyond the current 4G. This paper aims at proposing a 5G solution and analyzing its capacity and range.

Keywords 5G · Bandwidth · Beyond 4G · Data rate · HetNet · Massive MIMO · Spectrum

1 Introduction

There have been four generations of wireless networks. Since its inception in the early 1980s, mobile communication has evolved with each succeeding generation emerging approximately every 10 years and introducing additional services to users. Advances in technology have also enhanced the mobile capability and device types. This has propelled the popularity and growth of wireless communication.

As more devices get connected with diverse mobile applications, the resultant increase in traffic places a huge burden on the network, necessitating demands for higher system capacity. Demand for bandwidth capacity has been growing exponentially. Such growth has been consistent with the evolution of the various generations of wireless networks up to the present 4th generation. This is due to the

H. Frank (✉)
Department of Computer Science, Ken Saro-Wiwa Polytechnic,
P.M.B 20, Bori,
Rivers State, Nigeria
e-mail: hilaryfrank@yahoo.com

S.-I. Ao et al. (eds.), *Transactions on Engineering Technologies*,
DOI 10.1007/978-981-10-1088-0_33

Table 1 Cellular network evolution

Period	Mobile generation	Access technology	Service
1980s	1G—NMT	AMPS	Analogue voice
1990s	2G—GSM, GPRS, EDGE	CDMA/TDMA	Digital voice, higher data rates
2000s	3G—UMTS	WCDMA	Digital voice, data, video and internet
2010–Date	4G—WiMAX, LTE, LTE-ADVANCED	OFDM/SC-FDMA	Enhanced 3G/interoperability, IP based

thirst for an ever greater data rate by users of wireless technologies, which has also been on an exponential trajectory [1]. This can be linked to the reality of Moore's Law, which suggests that the number of transistors on a chip will double approximately every two years [2]. Since the postulation of this Law in 1965, higher density transistors on a circuit have continually led to more processing speed and faster digital electronics. This trend demonstrates that as electronic systems attain higher capacity, usage progresses exponentially which places higher demand on system capacity. With enhanced processing speed, a multiplicity of wireless devices—smart phones, tablets and laptops, compete for access to the internet via the limited spectrum available at the preferred frequencies (Table 1).

The term '5G' as used in this report would mean the 5th Generation wireless networks. The appellation does not represent any defined specification yet. The tag '5G' is only applied in research papers and other reports to signify wireless networks beyond the current 4G. However, the definition of the next generation of wireless networks, here referred to as 5G, is currently been discussed by relevant stakeholders [3].

2 Scope of Paper

This paper is aimed at proposing a 5G solution and analyzing its capacity and range. The work is done within the context of the anticipated challenge of future mobile networks. The focus will be to achieve the following objectives:

1. Identification of requirements of next generation mobile networks (5G)
2. Identification of techniques and technologies for 5G
3. Identification of Applications and Services for 5G
4. Propose a 5G system solution and
5. Analyze the capacity and range of the propose solution.

Some technology solution requirements for a 5G network include higher capacity and data rate. New traffic types, a multiplicity of emerging applications and services such as Internet of Things, among others are driving these solutions. This

report will review a selection of what it considers the main technology solutions that would propel 5G. They are as follows:

1. Heterogeneous Networks (HetNet)
2. Spectrum
3. Massive Multiple Input Multiple Output (MIMO)
4. Interference Management.

3 Heterogeneous Network

One of the techniques for 5G capacity increase is to use Heterogeneous Networks (HetNets). HetNet refers to a wireless network with an integration of multi-layer radio Access Technologies (RAT) such as Wi-Fi, 4G and other future RAT like Millimeter wave (mm-W). The multi-RAT would consist of nodes with varying transmission powers and coverage sizes such as Pico, Femto, and Relay Node (RN) and Remote Radio Heads (RRH) [4]. Figure 1 shows a simplified HetNet structure with multi-cells within the macrocell. HetNet was originally standardized by 4G but the architecture was not designed to fully support it. However, the next generation of wireless networks would require modifications of HetNet to attain much higher capacity and coverage [5].

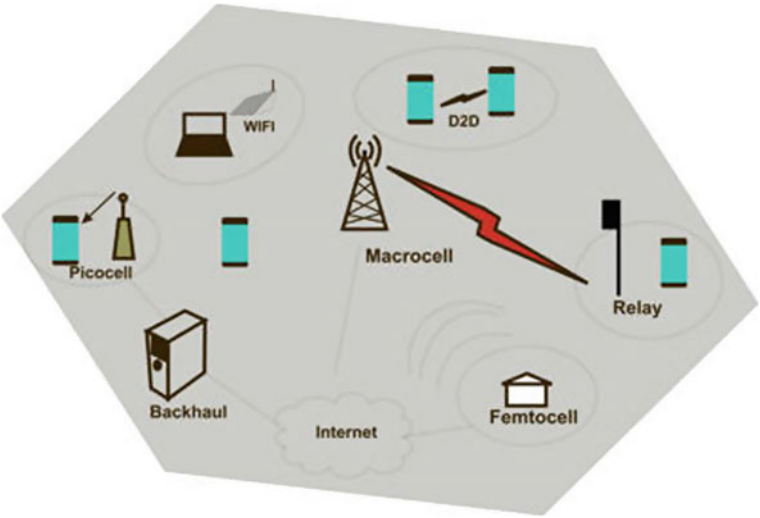

Fig. 1 Heterogeneous architecture with various layers of networks within the macro cell

4 Spectrum

Extra spectrum is another way of attaining the higher data rates in a 5G system. The millimeter wave spectrum range (10 GHz up to 300 GHz) is being proposed for 5G small-cells. The macro-cell layer will consist of microwave frequencies as currently employed while the small-cells will deploy the higher frequencies bands. Spectrum utilization has grown with the evolution of wireless networks. Succeeding cellular generations require higher channel bandwidth.

5 Massive Multi-input Multi-output (MIMO)

MIMO is now widely recognized as an essential technology solution for reaching the ambitious data rate target of the next generation wireless networks. Advanced antenna solutions with a large number (tens to hundreds) of antenna elements can be deployed to boost 5G system capacity by mitigating the impact of RF propagation limitations and manage interference cases within the network [6].

Using massive MIMO, beam-forming gains becomes quite large as to significantly reduce both inter-cell and inter-stream interference. With the use of massive MIMO, high value Spectral efficiency such as 100 b/s/Hz has been attained [7]. If new services such as Device-to-Device (D2D) and machine-type communications are deployed for 5G as projected, a more robust link can be exploited with the use of a larger number of antennas.

6 Interference Management

When transmitted signals interfere with each other by overlapping across the borders of neighbouring cells, throughput is impacted negatively. Advanced interference management schemes are needed to enable the high rates expected of the next generation cellular networks. To realize frequency reuse this paper will consider the benefits of joint scheduling at the network-side interference mitigation while using advanced receivers that has capability of joint detection and decoding for the User Equipment side. When signals from adjoining BSs interfere, joint scheduling process can dynamically synchronize the transmission of signals between the transmitting stations where the signals interfere and coordinate a joint processing of the received signals. The effect of this is that UE located at the interfering region (cell edge) can be jointly served by multiple BSs thereby increasing cell throughput as Fig. 2 illustrates.

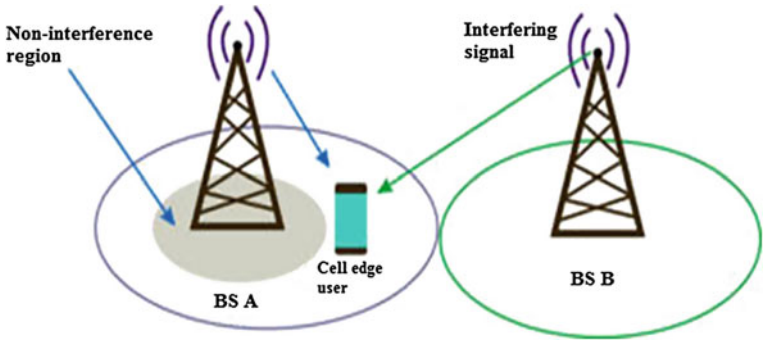

Fig. 2 Signals from an aggressor cell B interferes with the signal performance of a victim cell A. ICIC coordinates the interference between both cells [19]

Table 2 Requirements for 5G [19]

No.	5G network	Requirements
1	System capacity (volume)	1000 × 4G capacity
2	Peak data rate	10 Gb/s (10 × 4G rate)
3	Spectral efficiency	30 bps/Hz/cell (10 × 4G rate)
4	Energy efficiency	10 × 4G rate
5	Cell throughput	7.5 Gbps (25 × 4G rate)
6	Latency	5 × reduction in current latency

7 Requirements for a 5G Network

In order to attain the targets of the next generation mobile networks, wireless systems will have to become more powerful, in terms of higher capabilities. 5G system capacity requirements need to take into consideration the growth in user demand and the increase in the number of users. These conditions can be defined in terms of capacity for supporting connectivity and devices, data rates to sustain new applications, better cell coverage, higher throughput, energy and spectral efficiencies. Based on the various reviews of 5G research papers, this report considers the following as shown in Table 2 as appropriate key requirements for B4G networks.

8 System Requirements

8.1 System Capacity

There are several propositions arising from recent studies which suggest a broadband capacity growth reaching a factor of 1000 by the year 2020 [8]. This supposes

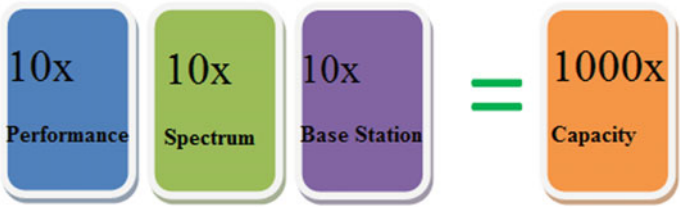

Fig. 3 BS density × spectrum × performance efficiency = 1000 × 4G system capacity

a tenfold rise in broadband subscribers and up to 100 times higher traffic per user per day [9]. 5G capacity therefore would require 1000 times the 4G system capacity. In order to reach this 1000 times capacity gain, spectral efficiency, BS and spectrum will contribute gains of up to 10 times current capacity as Fig. 3 shows.

8.2 Data Rates

The familiar ways to boost data rate are to make available additional bandwidth, extra MIMO branches and utilization of higher modulation order [9, 10]. Also overhead reduction via scalable air interface design assist in enhancing data rates. Considering the volume of traffic expected in the next generation cellular networks, 5G system must deploy a minimum of 10 times improvement in data rates as against LTE-Advanced's target of 1 Gb/s.

8.3 Spectral Efficiency

Spectrum is a limited resource that is being depleted by the continuous growth of cellular networks. Therefore, efficient use of spectrum would mean the optimized application of bandwidth as to maximize the transmission of data. There are three main components to attaining higher spectral efficiency: small-cell deployment, massive MIMO and advanced interference management. With efficient integration of these technology solutions 5G target of 10 times current rate of spectral efficiency would yield about 30 bps/Hz/cell.

8.4 Energy Efficiency

Cellular networks consume as much as 0.5 % of global energy [11]. Reference [12] projects a leap from current 5 billion connected wireless devices to between 50 and 500 billion devices by the time of 5G. Also rising demands for improved wireless

capacity will escalate energy utilization. Therefore, boosting energy efficiency is paramount to the beyond 4G networks.

8.5 Cell Throughput

Aside the projected improvement in capacity and data rates, achievable throughputs per user needs a significant boost. This is important because throughput represents the rate of successful message delivery across the transmission channel.

8.6 Latency

Latency is important in maintaining acceptable performance especially in delay sensitive transmissions such as voice and video. It must observe tight latency conditions of the physical layer processing to allow sufficient time for the Medium Access (MAC) layer scheduler tasks. With the anticipated increase in data rates, a decrease in latency is required to support higher data rates. End-user round-trip time (RTT) is less than 5 ms as defined in the LTE standard. The next generation wireless networks with a factor of 5 latency reduction should have uplink (end-user) RTT in the region of less than 1 ms and downlink (base station) less than 0.5 ms [13]. Latency reduction means considerable modifications on the air interface. Components such as frame structure, HARDQ and control signal timing constitute the major structure of the air interface which will be altered to achieve improvement in RTT. Again, because latency grows with distance it is a faction of physical space. Hence the proposed small-cell structure of 5G will further boost the attainment of this latency requirement.

9 System Design Solutions for 5G

This paper will follow a procedure for planning mobile networks that groups the basic phases into three.

1. Planning or dimensioning
2. Detailed radio network planning
3. Operation and Optimization.

Radio access is an integral part of any cellular network. It establishes the link between UE and the core network. To meet this requirement, the network has to provide satisfactory capacity and coverage. For the purpose of this paper, possible solutions for 5G will be proposed. Then cell characteristics (number of cells and

users) will be determined for the city of Oxford in England. This analysis will only cover the first two phases of the three radio network planning phases described above.

10 Physical Layer Design

The design comprises of large scale MIMO antenna technology, interference reduction schemes (JT CoMP and ICIC), Hybrid Automatic repeat Request (HARQ) and fast link adaptation. For the Uplink and downlink Orthogonal Frequency Division Multiplexing (OFDM) is utilized for modulation due to its multipath reduction potentials and support of MIMO. Time Division Duplex (TDD) mode is employed against Frequency Division Duplex (FDD) because of its ability to estimate channels based on orthogonal pilot tones sent by user terminals, hence avoid incurring extra training (feedback) overheads by the use of additional antennas. The assumption for this design is that all Access Points (APs) and UEs are synchronized so that they enjoy identical information of the frame timing.

11 Frame Structure

To attain the 5G requirement the frame structure should meet the following conditions:

- Enable large scale antennas. Large scale MIMO can be attained when antennas are miniaturized and compressed. This is made possible when the frame structure supports reduced latency. The deployment of large scale antennas helps to enhance data rate by mitigating co-channel interference.
- Support for low latency, below 1 ms and low power consumption, sustaining longer battery life. Low latency frame structure enables shorter wake-up time and longer sleeping time. By sleeping longer, battery life is saved and hence prolonged.
- Enable frequency reuse and coordination. Due to the frequency reuse factor of one co-channel interference would pose a limiting factor in terms of 5G performance.
- The 5G frame structure should also be able to support novel communication links beyond the conventional AP–UE type of communication to new methods of communication such as Machine Type Communication (MTC) (Fig. 4).

The proposed 5G design solution for this paper has selected the same frame structure as [14]. At the sides of the link, a small guard period (GP) is positioned at each possible switch. This is to provide alternate support for the on and off transitions. The frame consists of two main parts—the control and data parts. The first is for control and the other part for data. There is a separation of time between

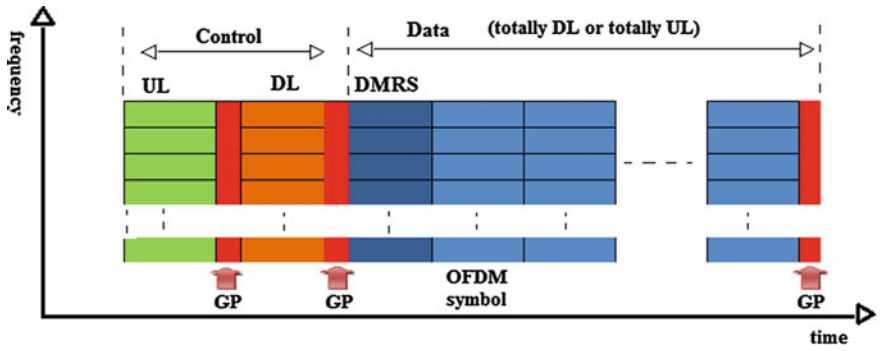

Fig. 4 Physical layer subframe structure

control and data parts. This is for a number of reasons. Power consumption is reduced by the UE as the receiver chain can go to sleep when commands are not received. Also pipeline processing can be enhanced as user equipment can simultaneously process control and data commands at the same time. This saves cost and time hence aiding latency reduction.

Some control commands are mapped to the control symbols. For instance, scheduling request (for UL), scheduling grant (for DL), modulation and coding scheme, Rank Indicator (RI)—this positions the quantity of streams to be deployed. This information can be symbolized in bits and encoded with some sort of modulation technique.

In the data part, the first symbol is set aside for channel estimation purposes called DeModulation Reference Symbols (DMRS). The entire data part transmission is either wholly UL or DL. This means that the data plane exclusively Tx or Rx at any given instance [10]. For the DMRS, the Zadoff-chu sequences will be preferred due to its favorable cross-correction characteristics, which support concurrent estimation of channel responses to the various interfering APs/UEs within the data part. Hence it brings stability to the interference pattern of the frame structure [14].

The latency requirement can be attained given 0.25 ms frame duration, HARQ and optimized scheduling design. The length time of the subframe can be determined with the equation

$$T_{sf} = (2 \times N_{ctrl\_s} + N_{data\_s}) \times (T_{Symbol} + T_{CP}) + 3 \times T_{GP} \quad (1)$$

where,

T_{sf}	Subframe length
N_{ctrl_s}	No. of control symbols
N_{data_s}	No. of data symbols
T_{Symbol}	Length of OFDM symbol
T_{CP}	Cyclic prefix duration
T_{GP}	Guard period duration.

Going by this design, 3 Time Division Duplex cycles are required for user equipment initiated data transmission. These are Uplink data transmission, Scheduling grant—Downlink, and request scheduling—Uplink. These 3 cycles requires a total time period of 0.75 ms. Also RTT of HARQ plus processing time equally requires 0.75 ms.

12 Physical Layer Parameters

Table 3 shows the physical layer parameters for the proposed 5G system solution. At the system level the most probable method of attaining greater spectral efficiency beyond current rate is the use of small-cells and large scale antenna arrays that support as much as 8 MIMO. With the above numerology, this paper is presuming a baseline carrier bandwidth of 200 MHz. The design will support the aggregation of multiple carriers towards attaining the required maximum throughput target when combined with a minimum of 4 × 4 MIMO and 256QAM modulation. The sub-carrier spacing is as much as 4 times more than that LTE-A, which translates to as many times fewer symbol duration. The design supports backward compatibility; with Access Point transmit power considerably lower than LTE BSs. Hence, guard period tends to have short GP in terms of on and off transitions.

The subframe length can be calculated as follows.

From Eq. (1)

$$T_{sf} = (2 \times N_{ctrl\_s} + N_{data\_s}) \times (T_{Symbol} + T_{CP}) + 3 \times T_{GP}$$

where, $N_{ctrl\_s} = 1$, $N_{data\_s} = 12$, $T_{Symbol} = 16.67$, $T_{CP} = 1$, $T_{GP} = 0.89$.

$$T_{sf} = 250\,\mu s$$

Table 3 Subframe requirements for 5G solution [19]

Proposed possible solution for 5G	
Carrier bandwidth (MHz)	200
Carrier spacing (KHz)	60
Length of symbol (μs)	16.67
TTI duration (ms)	0.25
FFT size	4096
Effective subcarriers	3000
No. of guard periods	3
Symbols per frame	14
Duration of cyclic prefix (μs)	1
Duration guard period (μs)	0.89
Overhead	6.67
HARQ processes	4

Percentage overhead per 0.25 ms subframe can be determined as follows:

$$\text{Overhead} = ((2 \times N_{ctrl\_s} \times T_{Symbol} + (2 \times N_{ctrl\_s} + N_{data\_s}) \times T_{CP} + 3 \times T_{GP})/T_{sf}) \times 100$$

$$\text{Overhead} = (50.01/250) \times 100 = 20\,\%.$$

13 Coverage Calculation

The coverage calculation targets the Oxford area with the following statistics.

Oxford Population: 151,900
Oxford Area: 45.59 km^2
Population density: 3293 km^2 [15].

This paper considers a modified Stanford University Interim model (SUI), as the propagation model for this project. This modified model is selected because of its ability to reliably estimate path loss for high millimeter wave frequencies. The well known models such as Okumura, Free Space Path Loss (FSPL), Hata/COST321 models do not provide reliable estimates when using millimeter wave frequencies. Another advantage for the choice of the modified Stanford University Interim is its modeling of different terrains, one of which suits Oxford city for which the dimensioning is being carried out. The terrain parameters used in this paper agrees with those of [16–18].

The model is formulated as follows:

$$PL_{SUI,Mod}[dB](d) = \alpha_{NLOS}\, x\, (PL_{SUI}(d) - PL_{SUI}(d_0)) + PL(d_0) + X_\sigma$$

where,

α_{NLOS}	Mean slope correction factor
$PL_{SUI}(d)$	$PL(d_0) + 10n \log_{10}(d/d_0) + X_{fc} + X_{Rx} + X_\sigma$
$PL_{SUI}(d_0)$	$PL(d) + 10n\log_{10}(d_0/d) + X_{fc} + X_{Rx} + X_\sigma$
$PL(d_0)$	$20\log_{10}(4\pi d_0/\lambda)$
N	$a - b \times h_{Tx} + c/h_{Tx}$
X_{fc}	$6 \times \log_{10}(f_{MHz}/2000)$, fc > 2 GHz
X_{Rx}	$-10.8 \times \log_{10}(h_{Rx}/2)$
λ	carrier wavelength in meters
$PL(d_0)$	free space path loss in dB at a close-in reference distance d_0
d	distance between transmitter and receiver in meters
h_{Tx}	base station height
h_{Rx}	mobile station height
X_{fc} and X_{Rx}	frequency and receiver heights correction factors

Table 4 SUI terrain types

Terrain type	Environment	Terrain parameters
A	Hilly/moderate to heavy tree density	a = 4.6, b = 0.0075, c = 12.6
B	Flat/moderate tree density	a = 4, b = 0.0065, c = 17.1
C	Flat/light tree density	a = 3.6, b = 0.005, c = 20

X_σ shadowing effect, $8.2 < \sigma < 10.6$ dB
C Speed of light
f frequency
a, b, and c constants modelling terrain type (Table 4)

where,

d = 150 m, h_{Rx} = 1.5 m, h_{Tx} = 20 m, d_0 = 50 m, f = 28,000 MHz, X_σ = 9.0, terrain type B, λ = C/f, f = frequency, α_{NLOS} = 0.88 (Slope correction factor selected from the model)
X_{Rx} = 1.35
X_{fc} = 6.88
N = 4.73
$PL(d_0)$ = 95.1 dB ($20\log_{10}(4\pi d_0/\lambda)$)
$PL_{SUI}(d)$ = 134.93 dB ($PL(d_0) + 10n\log_{10}(d/d_0) + X_{fc} + X_{Rx} + X_\sigma$)
$PL_{SUI}(d_0)$ = 99.33 dB ($PL(d) + 10n\log_{10}(d_0/d) + X_{fc} + X_{Rx} + X_\sigma$)
$PL_{SUI,Mod}[dB]\ (d) = \alpha_{NLOS} \times (PL_{SUI}\ (d) - PL_{SUI}\ (d_0)) + PL(d_0) + X_\sigma$
$PL_{SUI,Mod}[dB]\ (d) = 0.88 \times (134.93 - 99.33) + 95.1 + 9$
$PL_{SUI,Mod}$ [dB] (d) = 135.4 dB.

14 Number of Cell Sites

The modified SUI propagation model gives a path loss of 135.4 dB for d = 0.15 km.

$$\text{Area of the Hexagonal shape for one site} = ((3\sqrt{3})/2)d^2$$

where d = 150 m (0.15 km).

The distance of 150 m is selected based on the size of Oxford city and the propagation model. Millimeter wave frequencies are suitable for small-cells due to its high frequency and attenuation at longer distances.

$$\text{Area of one hexagonal cell site} = ((3\sqrt{3})/2)(0.15^2) = 0.39\,\text{km}^2$$

But Oxford area = 45.59 km^2.
Hence number of cell site for coverage = 45.59/0.39 ≈ 117 cells.

15 Throughput Calculation

To calculate the required throughput, an understanding of the system is important. The system for which throughput is sort has a central processing node deploying a 20 × 20 MIMO and 200 MHz channel bandwidth.

Peak data rate = no. Resource Elements (RE) × no. bits per modulation symbol
Resource Element = no. of Subcarriers × no. of symbols = 12 × 14 = 168
Since 10 % of channel bandwidth = guard band
Effective bandwidth for 200 MHz = 180 MHz
Bandwidth of Resource Block (RB) = no. subcarriers x subcarrier spacing = 12 × 60 = 720 kHz
Resource block = 180 MHz/720 kHz = 250
Peak data rate = number of REs/subframe × no. of bits per modulation

$$\text{For 256 QAM} = 16\,\text{bits}$$
$$= (168 \times 250) \times 16 = 672000\,\text{bits}/1\,\text{ms} = 672\,\text{Mbps}$$

Using 20 × 20 MIMO scheme
20 × 672 = 13.440 Gbps
Applying 20 % overhead leads to the effective data rate
13.44 Gbps × 0.8 = 10.75 Gbps.

16 Traffic Capacity Calculation

Population density for Oxford = 3293 km^2
Assumptions

10 % subscription to network
5 % simultaneous usage of network
At 10 Gb/s data rate

3293 × 10 % × 5 % × 10 Gbps = 165 Gbps/km^2
Capacity required for one square kilometer = 165 Gbps
Number of cells per square kilometer = 1/0.39 = 2.56
Number of users per cell = 3293/2.56 = 1286.3 users
Cell capacity = 165 Gbps/2.56 = 64.45 Gbps
Mean Traffic capacity per user = 64.45 Gbps/1286.3 = 50.1 Mbps.

17 Spectral Efficiency

The maximum spectral efficiency (SE) using various modulation schemes can be calculated with the formulation

$$SE = (1 - O_c) \times N_{SF} \times N_{RB} \times N_{SC} \times b_S \times R_{MIMO}/BW \quad (3)$$

where,

O_c	Control overhead
N_{SF}	no. of subframe per second
N_{RB}	no. resource blocks
N_{SC}	no. subcarriers
b_S	modulation bits/symbol with maximum coding rate
R_{MIMO}	MIMO rank
BW	Bandwidth.

The 5G spectral efficiency requirement of 10 Gbps is achievable with a combination of various specifications. Using Eq. (3), spectral efficiency is attainable with 350 MHz bandwidth, 6 × 6 MIMO and 64 QAM. Also 8 × 8 MIMO with 200 MHz bandwidth and 256 QAM can yield the required spectral efficiency. The 200 MHz bandwidth requires as much as 50 bits/s/Hz.

18 Main Findings and Conclusion

The expected techniques and technology for the future 5G networks were enumerated and analyzed. The key drivers for Beyond 4G (B4G) in terms of applications were also highlighted and analyzed.

A 5G design solution was proposed. Aspects of the capacity and range were given. Some of these include number of cell sites, path loss estimation, traffic capacity and throughput calculations.

However, the proposed solution could be improved upon. This is because path loss estimation models for mm-W has not been widely tested. Further improvements on the modified SUI model could lead to better path loss predictions, especially in the higher frequency range.

References

1. Prakash B, Satoshi Nagata S, Campoy L, Berberana I, Derham T, Liu G, Shen X, Zong P, Yang J (2012) LTE-advanced: an operator perspective. IEEE Commun Mag 104–114
2. Dreslinski RG, Wieckowski M, Blaauw D, Sylvester D, Mudge T (2010) Near-threshold computing: reclaiming Moore's law through energy efficient integrated circuits. Proc IEEE 98(2)

3. Rost P, Bernardos CJ, De Domenico A, Di Girolamo M, Lalam M, Maeder A, Sabella D, Wübben D (2014) Cloud technologies for flexible 5g radio access networks. IEEE Commun Mag 2014(52):68–76
4. Hu QR, Qian Y (2014) An energy efficient and spectrum efficient wireless heterogeneous network framework for 5G systems. IEEE Commun Mag 52:94–101
5. Boccardi F, Heath Jr RW, Lozano A, Marzetta TL, Popovski P (2014) Five disruptive technology directions for 5G. IEEE Commun Mag 74–80
6. Dahlman E et al (2014) IWPC evolutionary and disruptive visions towards ultra high capacity networks. White paper version 1.1
7. Jungnickel V, Manolakis K, Zirwas W, Panzner B, Braun V, Lossow M, Sternad M, Apelfröjd R, Svensson T (2014) The role of small cells, coordinated multipoint, and massive MIMO in 5G. IEEE Commun Mag 52:44–51
8. Talwar S, Choudhury D, Dimou K, Aryafar E, Bangerter B, Stewart K (2014) Enabling technologies and architectures for 5G wireless. IEEE MTT-S International Microwave Symposium (IMS) 1–4. doi: 10.1109/ MWSYM. 2014. 6848639
9. Raaf B, Tiirola E, Marsch P, Wichman R (2011) Vision for beyond 4G broadband radio systems. In: 22nd international symposium on personal, indoor and mobile radio communications. IEEE, New York, pp 2369–2373
10. Lähetkangas E, Pajukoski K, Tiirola E, Hämäläinen J, Zheng Z (2012) On the performance of LTE-advanced MIMO: how to set and reach beyond 4g targets. In: European wireless
11. Tombaz S, Vastberg A, Zander J (2011) Energy- and cost-efficient ultra-high-capacity wireless access. IEEE Wirel Commun 18(5)
12. G radio Access (2013) Ericsson white paper
13. Nanan J-C, Stern B (n.d.) Small cells call for scalable architecture. Freescale white paper
14. Mogensen P, Pajukoski K, Tiirola E, Lähetkangas E, Vihriälä J, Vesterinen S, Laitila M, Berardinelli G, Da-Costa GWO, Garcia LGU, Tavares FML, Cattoni AF (2013) 5G small cell optimized radio design. In: Globecom 2013 workshop—emerging technologies for LTE-advanced and beyond-4G, pp 111–116
15. Oxford City Council Population Statistics (2014) http://www.oxford.gov.uk/PageRender/decC/Population_statistics_occw.htm. Viewed on 14, Sept 2014
16. HashibSiddique A, Arifuzzman AKM, Tarique M (2013) Performance study of IEEE 802.16d under Stanford University Interim (SUI) Channel. Int J Comput Netw Commun (IJCNC) 5(2)
17. Sulyman AI, Nassar AM, Samimi Mk, MacCartney Jr GR, Rappaport TS, Abdulhameed Alsanie A (2014) Radio propagation path loss models for 5G cellular networks in the 28 GHz and 38 GHz millimeter-wave bands IEEE communications magazine 2014
18. Stanford University Interim (2014) http://www.xirio-online.com/help/en/sui.html. Viewed on 14 Sept 2014
19. Frank H, Ball P (2015) Mobile networks beyond 4G. In: Proceedings of the world congress on engineering 2015, WCE 2015, 1–3 July, 2015, London, UK. Lecture Notes in Engineering and Computer Science, pp 649–652

Indoor Localisation Using Multiple Fingerprint Maps

Pedro Mestre, Joao Cordeiro and Carlos Serodio

Abstract Fingerprinting is a location estimation technique, used in indoor applications, where information about wireless signals (e.g. RSS value) are mapped into spatial coordinates. Because WiFi is an ubiquitous communication technology, supported by Commercial Off-The-Shelf devices, Fingerprinting localisation algorithms based on WiFi are suitable for LBS applications. Although Fingerprint can lead to good results, it is not an error free technique. A source of interference that decreases the accuracy of Fingerprinting performance is the end-user, which can be seen as an obstacle that dynamically fades the Signal Strength. RSS fluctuations caused by the user can be wrongly interpreted as "the user moved", when in fact the user might have not moved at all, simply rotated 180°. To cope with this problem it is presented an approach to Fingerprinting Location using multiple Fingerprint Maps, which are built including the user direction information. The correct map (or a combination of maps) can be used during the on-line phase to increase the Location Estimation Algorithm accuracy.

Keywords Fingerprinting · Indoor localisation · Magnetic sensor · Navigation · Propagation models · RSS

P. Mestre (✉) · C. Serodio
Centre for the Research and Technology of Agro-Environmental and Biological Sciences, CITAB, University of Trás-os-Montes and Alto Douro, UTAD, Quinta de Prados, 5000-801 Vila Real, Portugal
e-mail: pmestre@utad.pt
URL: http://www.utad.pt

C. Serodio
e-mail: cserodio@utad.pt
URL: http://www.utad.pt

P. Mestre · C. Serodio
Algoritmi Research Centre, Guimaraes, Portugal

J. Cordeiro
University of Trás-os-Montes and Alto Douro, UTAD, Quinta de Prados, 5000-801 Vila Real, Portugal
e-mail: jtpcordeiro@gmail.com
URL: http://www.utad.pt

S.-I. Ao et al. (eds.), *Transactions on Engineering Technologies*,
DOI 10.1007/978-981-10-1088-0_34

1 Introduction

In indoor environments, where GPS based localisation cannot be used, alternative techniques must be considered. One of such techniques is Fingerprinting, which is the most used method for indoor localisation [3].

Fingerprinting comprises two distinct phases [2, 7, 10]: the off-line phase where information about wireless signals are acquired and stored in a database; the on-line phase where the location is estimated, by comparing data stored in the database and data collected on that moment. During the on-line phase it is used a Fingerprint Map (FM), generated using data collected during the off-line phase. The Location Estimation Algorithm (LEA) uses the FM information to map spatial and signal domains to estimate the mobile node coordinates.

As long as it is possible to have access to the incoming wireless signal properties, such as the Received Signal Strength (RSS) value, any wireless technology can be used for Fingerprinting-based localisation. However, if the objective is to develop Location Based Services (LBS) for use with smartphones, a wireless technology supported by such devices must be used. It also must be taken into account that better accuracy values are obtained for shorter range communications [9].

Because WiFi (IEEE802.11) is an ubiquitous technology, available on most smartphones, it is a good choice when creating localisation systems based on consumer electronics products. According to [3] Wireless Local Area Network (WLAN) based localisation systems are dominant indoors. Also such systems have the advantage of not requiring new or proprietary hardware.

Even though good results can be obtained using Fingerprinting localisation based on WLAN, this is not an error free technique. Wireless signals are absorbed by obstacles, including the human body, so users may influence the RSS values. When holding a smartphone, the user will cause the fading of wireless signals irradiated by the Access Points (AP) that are located behind him/her.

As a consequence of this radiation absorption by the user, if an FM is built using data collected only in one direction, it will not be very useful in a real-life application, because during the on-line phase the user might be facing the opposite direction.

A simple (and commonly used) solution to cope with this problem is to acquire data (during the off-line phase) facing different directions (the user rotates 360° while acquires the FM data). The resulting FM can be calculated by averaging all the acquired values.

Another, and more efficient solution, would be to use the most suitable information collected during the off-line phase. Instead of creating a single FM, multiple maps can be generated (one per direction, e.g. North, South, East and West) and at the on-line phase the most suitable map (or set of maps) can be used by the Location Estimation Algorithm. Most of the recent smartphones have a magnetic sensor that can be used to estimate the user's direction.

Collecting data to build an FM is a time consuming task, if more maps are added (which will be the case), then more time is needed to collect data. This can be

overcome by building the FM using propagation models, as presented in [8]. Using this solution it is only needed to add the user as an obstacle and generate the FM.

In this paper it is presented an approach to location estimation using multiple FM as presented by the authors in [5], and the performance of this approach is assessed both using Fingerprint Maps generated with real data acquired in the testing scenario and generated using propagation models. In the presented tests four maps are generated (North, South, East and West) and the assessment of the method feasibility is made using three of the classic LEA: Nearest Neighbour; k-Nearest Neighbour; Weighted k-Nearest Neighbour. To select the best map(s) to be used by the LEA, information provided by the magnetic sensor of an Android smartphone is used.

2 Directional Fingerprint Maps

In this section it will be presented the rational behind the use of multiple FM, the implemented algorithms to choose the correct map and how the maps can be generated without the need to collect RSS values.

2.1 User Interference

During the off-line phase, data must be collected at each spatial point that will be used in the FM. These data include the value of the power that the mobile node receives from the fixed references. When WiFi is used, these references are the network Access Points. The power received by the mobile node, from each AP, is given by Eq. 1:

$$P_r = P_t + G_t + G_r - PL_{tot} \tag{1}$$

where P_r is the received power (in dBm), G_t and G_r the gains of the transmitting and the receiving antennas (in dB or dBi) and PL_{tot} is the summation of all losses that electromagnetic waves suffer while travelling between the transmitter and the receiver (in dB).

In Eq. 1, the total path loss (PL_{tot}) is the result of the free-space path loss and losses due to the presence of obstacles between the transmitter and the receiver. Free-space path loss can be expressed as a function of the distance between the two wireless nodes [1] (Eq. 2):

$$PL(d) = PL(d_0) + 10N\log\left(\frac{d}{d_0}\right) + X_\sigma \tag{2}$$

where N represents the path loss exponent (which may vary according to the structure of the building [4]), d_0 is an arbitrary distance, X_σ denotes a Gaussian variable with zero mean and standard deviation σ.

Losses due to the presence of obstacles are caused by obstacles found in buildings. Propagation models like COST and Motley-Keenan consider the attenuation due to walls and furniture [8]. However there are other obstacles inside a building that can attenuate wireless signals. The user that is holding the smartphone will also absorb electromagnetic waves. In the literature it can be found that the absorption by a single human body may cause an attenuation as much as 3.5–5.0 dB [2, 11].

Let us consider that for indoor $N = 3$ [4] and $d_0 = 1$ m [8], using Eq. 2, an excess attenuation 5.0 dB is the equivalent to the user moving 1.78 m. This will obviously have a negative impact of the LEA performance and decrease the location estimation precision.

2.2 *Multiple Fingerprint Maps*

Because it is not feasible to force the user to face the direction at which the FM data was acquired, the proposed solution is to build multiple maps, and during the on-line phase, select the best map(s) to be used by the LEA. For this solution to be possible it is needed to know the user's direction, both during the on-line and off-line phases of Fingerprinting-based localisation.

Nowadays, using a smartphone, it is relatively easy to know which direction the user (or the smartphone) is facing, e.g. using the magnetic sensor as a compass. If the azimuth value is also stored in the database when FM data is collected, then it will be possible to build multiple maps.

It is not feasible to collect data in every direction because too much data would have to be collected, at each spatial point, to build multiple Fingerprint Maps. Also the azimuth value reported by the sensor has slight changes, even when the smartphone is not moving. The trigonometric circle can be divided into n slices (n is a small value). If $n = 1$ then we have the "traditional" FM based on the average of data collected in all directions. In Fig. 1 it is presented an example with $n = 4$.

As an example in Fig. 1 the four directions are North, South, East and West. It is not mandatory to use these directions. Any direction can be used, as long as the following conditions are met:

- Directions are fixed, and the same for all spatial points, otherwise it will not be possible to build a reliable set of maps;
- The trigonometric circle is divided evenly in n slices. Each slice has an amplitude (in °) given Eq. 3.

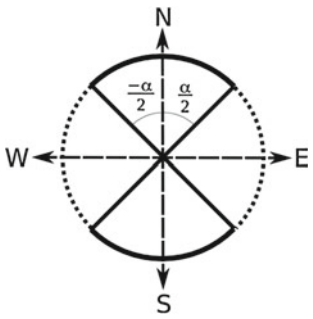

Fig. 1 Example using 4 slices

$$\alpha = \frac{360^\circ}{n}. \tag{3}$$

To choose the best map(s) to use with the LEA, two approaches have been considered:

- Direct Map—Only one map is chosen, based on the azimuth value;
- Weighted Maps—The contribution of each map to the final location estimation is calculated as a function of the azimuth value.

One of the objectives of the authors is to maintain compatibility with previously implemented location methods, i.e., the multi Fingerprint Maps can be used with any LEA, without the need to modify it.

2.2.1 Direct Maps

With Direct Maps, from the set of n maps that are built, only one FM is selected. This selection is based on the azimuth values reported by the magnetic sensor. The selected FM is fed to the LEA that estimates the user's location (Fig. 2). From the LEA point of view, there is only one FM.

Let us consider that data was collected facing n directions ($d_1, d_2, \ldots, d_n$, with $0^\circ \leq d_i \leq 360^\circ$), map i is selected if the current azimuth value (β) meets the condition:

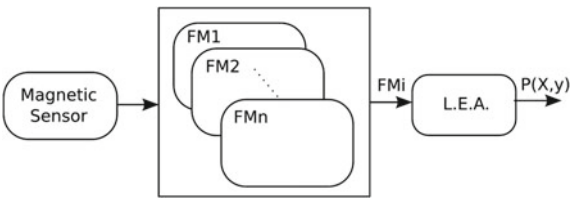

Fig. 2 Working principle of the "Direct Maps" method

$$d_i - \frac{\alpha}{2} < \beta \leq d_i + \frac{\alpha}{2} \tag{4}$$

This is a simple solution, that requires the same computational power as the original LEA. There is only one additional step, which requires low computing power: select the most suitable FM based on the azimuth value.

2.2.2 Weighted Maps

Because the azimuth value might not be stable, in the above method if its value is too close to the boundary values ($d_i - \frac{\alpha}{2}$ or $d_i + \frac{\alpha}{2}$) the algorithm could be constantly alternating between two maps.

In these conditions, the best choice could be using information of FM_i and FM_{i-1} or FM_i and FM_{i+1}. This is the working principle of Weighted Maps. Based on the current azimuth it is calculated the contribution that each map will have in the final estimation of the user's location (Fig. 3). Then an weighted average of all coordinates estimated by the LEA (one per map) is calculated, to estimate the user's coordinates.

In this work a linear weight function, Eq. 5, based on the angular distance of the azimuth value to the reference value is used.

$$w_i = \begin{matrix} 1 - \frac{|d_i - \beta|}{\theta}, & 0 \leq |d_i - \beta| \leq \theta \\ 0, & |d_i - \beta| > \theta \end{matrix} \tag{5}$$

where w_i is the weight of map i, β and d_i are as above and θ is a value chosen by the developer. The value used for θ, together with n, define the maximum number of maps that are considered in the location estimation. For example if $n = 4$ and $\theta = 45°$, then 2 maps are used.

For each map (i) that meets the condition $w_i > 0$, the user's location is estimated (without considering the weight). The final user's coordinates is then calculated as in Eq. 6:

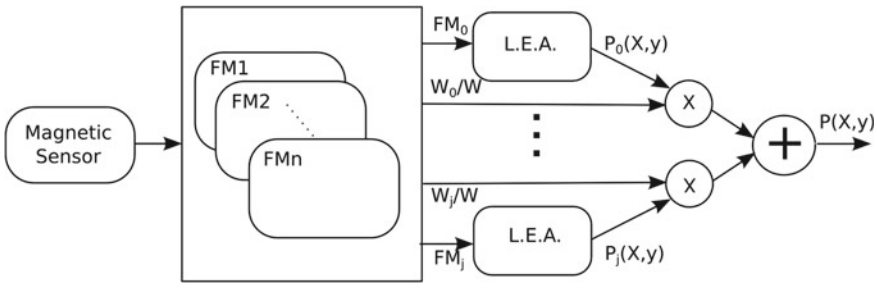

Fig. 3 Working principle of the "Weighted Maps" method

$$P(x,y) = \sum_{i=0}^{j-1} \frac{w_i}{w} \times P(x,y)_i \tag{6}$$

where $P(x,y)$ is the estimated user's location, j is the number of maps that meets the condition $w_i > 0$ and $P(x,y)_i$ is the user's location estimated using map i and w the summation of all weights.

Because the location is estimated for each map, it is possible to use multiple maps with Location Estimation Algorithms that were not developed to use it. Each execution of the LEA is independent.

Compared with the previous solution, the computational time is increased (j times). However a possible alternative would be to generate a new FM, e.g. by doing an weighted average of the maps, for each execution of the LEA. If the maps have many points, the computational requirements would also be increased (for each point an FM had to be created) and the memory requirements would also increase (to store $n + 1$ maps).

2.3 Generating the FM Using Propagation Models

Because collecting data to generate multiple FM is a very time consuming task, the Fingerprint Maps can be obtained by simulation, i.e., using propagation models to predict the RSS values at each point of the FM. To build such maps we have to consider the effect of the free-space attenuation, the attenuation due to obstacles (e.g. walls) and the user interference.

Because of the results obtained in [8], to model the FM it was used the a modified Motley-Keenan model, which is based on Motley-Keenan model, Eq. 7:

$$PL(d) = PL(d_0) + 10N\log\left(\frac{d}{d_0}\right) + \sum_{i=1}^{N} k_i L\omega_i \tag{7}$$

where:

- k_i: the number of walls of type i;
- $L\omega_i$: attenuation factor for walls of type i.

The above model does not consider wall thickness, so the adjusted model of Eq. 8 was considered:

$$PL(d) = PL(d_0) + 10N\log\left(\frac{d}{d_0}\right) + \sum_{i=1}^{N} k_i L_{0i} 2^{\log_3\left(\frac{\varepsilon_i}{\varepsilon_{0i}}\right)} \tag{8}$$

where:

- L_{0i}: is the attenuation of a reference wall with thickness ε_0;
- k_i: is the number of type i walls that have thinness ε_i.

To the above model we have also to add the attenuation due to the presence of the user. It was considered that the user is always facing the mobile terminal, so the user acts as an obstacle, with constant attenuation, between the mobile terminal and the Access Points behind him/her.

Also a random value (X_σ) must be added to the final RSS values, as in Eq. 2. These values add some randomness to the FM, making it more similar to the real values typically found in Fingerprint Maps acquired using a mobile terminal.

3 Testing Scenario and Conditions

To assess the feasibility of the proposed methods, data was collected in a building at the Campus of the University of Trás-os-Montes and Alto Douro. These data were used to generate the Fingerprint Maps and to off-line test the "Direct Map" and "Weighed Maps" methods.

In Fig. 4 it is depicted the map of the area where data was collected. In the map are marked the spatial points where RSS samples were acquired and the location of the reference Access Points. At each spatial point of the map, data was collected facing

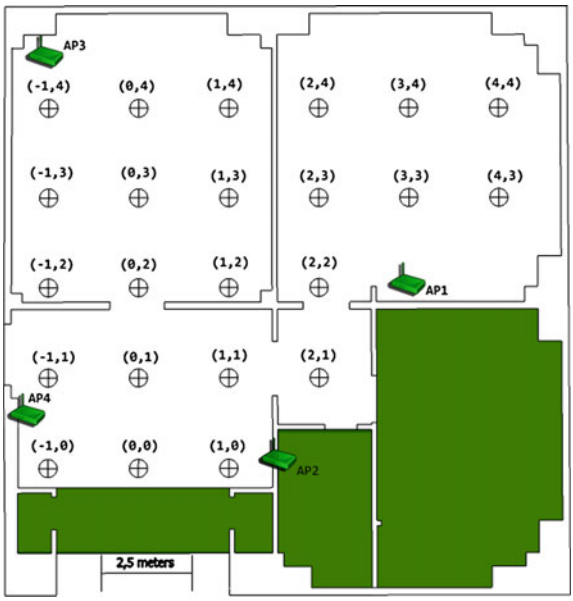

Fig. 4 Map of the testing scenario

four directions: North, South, East and West. At each direction 20 samples of the received power of all AP, the azimuth and the magnetic field values were recorded.

To collect data it was used an Android smartphone running an application developed by the authors for these tests. Because all the tests must be made using the same data, no data processing was made in real-time with this application. All data was stored in XML (eXtensible Markup Language) files and processed off-line.

To compare the performance of the proposed methods with other methods to generate the FM, in the present work the following classic LEA were used:

- Nearest Neighbour (NN)—it is assumed that the current coordinates of the mobile node (in the spatial domain) are the coordinates of the nearest point (in the signals domain);
- k-Nearest Neighbour (kNN)—the k nearest neighbours (in the signals domain) are selected, and then it is assumed that the mobile node coordinates (in the spatial domain) is the average of the spatial coordinates of those k points;
- Weighted k-Nearest Neighbour (WkNN)—similar to kNN, however an weighted average is used to estimate the user's coordinates.

Results presented in Sect. 4 were obtained considering $k = 3$ for kNN and WkNN, and, as in [9] the used weights (from the nearest to the furthest point) were 0.7, 0.2 and 0.1.

4 Numerical Results

In this section are presented the results obtained by the proposed methods, using data collected at the testing scenario. First are presented reference values, obtained in tests made for performance comparison. These reference tests also allow to demonstrate how the presence of the user can influence the location estimation accuracy. After, are presented the results that were obtained using the methods proposed in this paper.

Results obtained with the "Direct Map" and "Weighted Maps" (both for FM built using acquired data and FM built using propagation models) are divided into two subsections. First are presented the results that were obtained using four maps (N, S, E and W) and the user facing the same directions. After, are presented the results of two other tests where the same four maps were used, but the with user facing one of eight possible directions (N, NE, E, SE, S, SW, W and NW).

For all tests are shown the normalized values for the Precision, Standard Deviation, Maximum Error and Minimum Error, obtained using the three LEA.

Table 1 Results using the FM based on all directions

	NN	kNN	WkNN
Prec.	1.36	1.27	1.29
St. Dev.	0.97	0.72	0.79
Max. Err.	6.40	5.21	5.76
Min. Err.	0.00	0.00	0.10

4.1 Reference Values

Because one alternative to the use of multiple maps is to build a single FM, based on data collected in all directions, the first test was made with such an FM. The FM used in the test, which results are presented in Table 1, was built by averaging RSS data collected in the four directions.

These values are presented here as reference values, and will be used for performance comparison.

The next test consisted in generating an FM per direction and do the location estimation of an user facing the same direction as the FM, during the on-line phase. Results of this test are presented in Table 2. This is not a feasible solution for a real-life location system, however it can be used as the best case scenario. These are the best values that can be achieved using multiple maps.

Comparing data on Table 2 with data on Table 1 it can be concluded that considering a global FM with data collected in all directions, the results are worse than when the correct directional FM is used. These results validate that the solutions presented in this paper can improve the user's location estimation.

Results of another test, made to demonstrate the user influence in the precision of the location system, are presented on Table 3. In this test four FM are used, one per direction, and the user is rotating. Analysing data it can be concluded that the user presence has a negative impact in the system precision, but not in the accuracy.

Table 2 Results obtained using one FM per direction

	North/north			South/south			East/east			West/west		
	NN	kNN	WkNN	NN	kNN	WkNN	NN	kNN	WkNN	NN	kNN	WkNN
Prec.	1.12	1.14	1.11	1.24	1.22	1.19	1.26	1.16	1.20	1.25	1.12	1.16
St. Dev.	1.10	0.71	0.83	1.09	0.67	0.78	1.09	0.68	0.82	1.05	0.61	0.76
Max. Err.	5.00	4.03	4.38	6.40	5.21	5.04	5.83	3.54	4.58	4.12	3.67	3.96
Min. Err.	0.00	0.00	0.10	0.00	0.00	0.10	0.00	0.00	0.10	0.00	0.00	0.10

Table 3 Results using an FM per direction and user facing four directions

	North/all			South/all			East/all			West/all		
	NN	kNN	WkNN	NN	kNN	WkNN	NN	kNN	WkNN	NN	kNN	WkNN
Prec.	1.44	1.30	1.34	1.54	1.35	1.41	1.52	1.30	1.38	1.44	1.27	1.30
St. Dev.	1.02	0.75	0.83	1.06	0.75	0.84	1.00	0.74	0.81	1.00	0.72	0.78
Max. Err.	5.10	4.71	4.88	6.40	5.21	5.92	6.40	5.43	6.03	6.40	5.66	5.02
Min. Err.	0.00	0.00	0.10	0.00	0.00	0.00	0.00	0.00	0.10	0.00	0.00	0.10

As it was expected the results obtained using an FM based on the average values of all directions (Table 1) are better than those obtained with single direction FM (Table 3).

4.2 Multiple Maps Using Four Directions and FM Built Using Acquired Data

The first set of tests using the proposed methods are presented in Table 4. For all these tests the FM was generated the real data acquired in the testing scenario. In this table are shown the results of a test using Direct Maps (a single map is chosen). In these tests four FM were generated (one per direction), the user's location was estimated with the user facing all the four directions (N, S, E and W), and the FM was automatically selected by the method.

Comparing the obtained data with Table 1, better results are achieved with directional maps, as it was expected. However, even though the user was not

Table 4 Results using directional FM (Direct Map) with four directions and FM built using acquired data

	NN	kNN	WkNN
Prec.	1.22	1.16	1.17
St. Dev.	1.08	0.67	0.80
Max. Err.	6.40	5.21	5.04
Min. Err.	0.00	0.00	0.10

Table 5 Results using weighted FM with four directions and FM built using acquired data

	NN	kNN	WkNN
Prec.	1.20	1.16	1.15
St. Dev.	0.98	0.65	0.76
Max. Err.	6.40	5.15	5.08
Min. Err.	0.00	0.00	0.04

Table 6 Results using directional FM (Direct Map) with eight directions and FM built using acquired data

	NN	kNN	WkNN
Prec.	1.47	1.21	1.26
St. Dev.	0.85	0.62	0.75
Max. Err.	4.47	3.40	3.98
Min. Err.	0.00	0.00	0.14

Table 7 Results using weighted FM with eight directions and FM built using acquired data

	NN	kNN	WkNN
Prec.	1.20	1.16	1.15
St. Dev.	0.98	0.65	0.76
Max. Err.	6.40	5.15	5.08
Min. Err.	0.00	0.00	0.04

moving while acquiring data, the obtained results are worse than those where the FM was chosen manually (Table 2). This is because the azimuth value reported by the magnetic sensor is not stable.

Using weighted maps (Table 5), there is a slight improvement of the precision (comparing to Table 4) and an improvement of the accuracy in comparison to the FM generated with all data (Table 1).

4.3 Multiple Maps Using Eight Directions and FM Built Using Acquired Data

In this set of tests it is considered that the user might not be facing any of the directions used to build the FM. The Fingerprint Maps are the same as above (N, S, E and W) but for the user's location four new directions are added (NE, SE, SW and NW). As for the previous tests the used FM were obtained using real data acquired in the testing scenario.

These are limit conditions, because four slices are considered ($\alpha = \theta = 90°$). The newly added direction fall directly at the boundary between the Fingerprinting Maps. So this can be considered as a worse case scenario where the first method will constantly switch between maps. So for both methods it is expected a worse performance in comparison to results presented in Tables 4 and 5, and a better performance than using a single FM with all data (Table 1). In fact, analyzing Table 6 it can be concluded that those assumptions are true, except for the precision values with Nearest Neighbour Algorithm.

Results obtained using weighted maps are shown in Table 7. As it was expected these results are better than the above. There is an improvement of the location precision and accuracy. There is a slight increase of both the maximum error value though.

Table 8 Results using directional FM (Direct Map) with four directions and FM built using propagation models

	NN	kNN	WkNN
Prec.	1.55	1.39	1.44
St. Dev.	0.99	0.81	0.86
Max. Err.	5.83	5.68	5.66
Min. Err.	0.00	0.00	0.10

Table 9 Results using weighted FM with four directions and FM built using propagation models

	NN	kNN	WkNN
Prec.	1.53	1.39	1.43
St. Dev.	0.97	0.80	0.85
Max. Err.	5.83	5.67	5.66
Min. Err.	0.00	0.00	0.14

4.4 Multiple Maps Using Four Directions and FM Built Using Propagation Models

To assess the feasibility of FM generated using propagation models, are presented in this section two sets of tests. The first set, which results are presented in Table 8, corresponds to tests made using Direct Maps, and the second corresponds to tests made using weighted maps (Table 9). In these tests the FM was generated using propagation models and data acquired in the testing scenario was used to estimate the location.

Both methods had a similar performance, and for simulated FM there is no apparent advantage in using weighted maps instead of directional maps.

Comparing data from these tests with data of the previous testes (with all real data), including the reference tests, results are worse. Nevertheless these are not disappointing results taking into consideration that there is the advantage of not having to manually collect data from the scenario. Also, in the worse case we have a difference of 19 cm (for NN) when comparing to data of Table 1, which for most indoor location applications is suitable.

Table 10 Results using directional FM (Direct Map) with eight directions and FM built using propagation models

	NN	kNN	WkNN
Prec.	1.34	1.18	1.20
St. Dev.	0.75	0.60	0.65
Max. Err.	3.61	3.73	3.58
Min. Err.	0.00	0.00	0.10

Table 11 Results using weighted FM with eight directions and FM built using propagation models

	NN	kNN	WkNN
Prec.	1.30	1.16	1.18
St. Dev.	0.70	0.59	0.62
Max. Err.	3.54	3.41	3.29
Min. Err.	0.00	0.00	0.03

4.5 Multiple Maps Using Eight Directions and FM Built Using Propagation Models

The last two sets of tests (Tables 10 and 11) were made considering eight directions, the same as in Sect 4.3. However in these two tests the FM was generated using propagation models.

In a first analysis to the data it can be concluded that the results are better than those obtained with only four directions and simulated FM.

Weighted maps (Table 11) had worse performance than the version using real data (Table 7), and direct maps (Table 10) had a better performance in comparison to the tests made using real data (Table 6).

Both tests had better results than those made with real data, presented as reference values (Table 1).

5 Conclusion and Future Work

If the user's direction is known, as well as the direction at which data to build the FM was collected, it is possible to decrease the location error. Two methods based on the direction information, compatible to existing LEA that were developed without having the user direction information, were presented and their performance was assessed.

Comparing the results obtained using a single FM (average) and the multi map approach, it was obtained an improvement of 10.3 % for Nearest Neighbour, 8.7 % for k-Nearest Neighbour and 9.30 % for Weighted k-Nearest Neighbour.

Obviously that the user, in a real life application, will not be facing exactly the same direction at which the FM was collected. Even in these conditions, there is an improvement on the LEA performance (except for Nearest Neighbour in this particular testing scenario).

If instead a comparison is made with results obtained using an FM which includes only data collected in one direction, the precision improves by 22.08 % for Nearest Neighbour, 14.07 % for k-Nearest Neighbour and 18.44 % for Weighted k-Nearest Neighbour.

By using multiple maps it was possible to improve the performance of the LEA, however there is a drawback, related to the amount of data that must be collected. To build more maps, it must exist in the database more data. Because collecting

data to build an FM is a time consuming task, tests were also made using propagation models, considering the user direction and the user influence in the signal propagation.

Comparing results obtained using real data and simulated FM, it can be concluded the use of Fingerprint Maps with direction information obtained using real data are obviously better. However the FM generated using propagation models (containing user direction information) have a better performance than real data FM without user direction information. The precision values are improved by 4.46 % for Nearest Neighbour, 8.66 % for k-Nearest Neighbour and 8.52 % for Weighted k-Nearest Neighbour. Taking into consideration the advantages of using Fingerprint Maps generated using propagation models, these can be considered good results.

Further improvements of the the maps generated by propagation models, or even to maps collected using other mobile devices, can be made using Direct Search Methods as presented in [6].

References

1. Andersen J, Rappaport T, Yoshida S (1995) Propagation measurements and models for wireless communications channels. IEEE Commun Mag 33(1):42–49
2. Bahl P, Padmanabhan VN (2000) Radar: an in-building RF-based user location and tracking system. In: Proceedings of the nineteenth annual joint conference of the IEEE computer and communications societies, INFOCOM 2000, 26–30 March 2000, Tel Aviv, vol 2, pp 775–784. doi:10.1109/INFCOM.2000.832252
3. Deak G, Curran K, Condell J (2012) A survey of active and passive indoor localisation systems. Comput Commun 35(16):1939–1954. doi:10.1016/j.comcom.2012.06.004
4. Evennou F, Marx, F (2005) Improving positioning capabilities for indoor environments with WiFi. In: IST Summit
5. Mestre P, Cordeiro J, Serodio C (2015) Multi fingerprint map for indoor localisation. In: Proceedings of the world congress on engineering 2015, WCE 2015, 1–3 July, 2015, London, U.K. Lecture Notes in Engineering and Computer Science, pp 599–604
6. Mestre P, Reigoto L, Correia, A, Matias J, Serodio C (2012) RSS and LEA adaptation for indoor location using fingerprinting. In: Proceedings of the world congress on engineering 2012, WCE 2012, 4–6 July, 2012, London, U.K. Lecture Notes in Engineering and Computer Science, pp 1334–1339
7. Serodio C, Coutinho L, Pinto H, Mestre PA (2011) Comparison of multiple algorithms for fingerprinting using IEEE802.11. In: Proceedings of the world congress on engineering 2011, WCE 2011, 6–8 July, 2011, London, U.K. Lecture Notes in Engineering and Computer Science, pp 1710–1715
8. Serodio C, Coutinho L, Reigoto L, M J Correia A, Mestre P (2012) A lightweight indoor localization model based on Motley-Keenan and cost. In: Proceedings of the world congress on engineering 2012, WCE 2012, 4–6 July, 2012, London, U.K. Lecture Notes in Engineering and Computer Science, pp 1323–1328
9. Silva P, Pinto H, Serodio C, Monteiro J, Couto C (2009) A multi-technology framework for lbs using fingerprinting. In: 35th Annual conference of IEEE on industrial electronics, 2009. IECON'09, pp 2693–2698. doi:10.1109/IECON.2009.5415434
10. Taheri A, Singh A, Agu E (2004) Location fingerprinting on infrastructure 802.11 wireless local area networks. In: Proceedings of the 29th annual IEEE international conference on local

computer networks, LCN'04. IEEE Computer Society, Washington, DC, pp 676–683. doi:10.1109/LCN.2004.74

11. Youssef M, Mah M, Agrawala A (2007) Challenges: device-free passive localization for wireless environments. In: Proceedings of the 13th annual ACM international conference on mobile computing and networking, MobiCom'07. ACM, New York, pp 222–229. doi:10.1145/1287853.1287880

Extended Performance Research on Wi-Fi IEEE 802.11 a, b, g Laboratory Open Point-to-Multipoint and Point-to-Point Links

J.A.R. Pacheco de Carvalho, H. Veiga, C.F. Ribeiro Pacheco and A.D. Reis

Abstract The increasing importance of wireless communications, involving electronic devices, has been widely recognized. Performance is a crucial issue, leading to more reliable and efficient communications. Laboratory measurements were performed about several performance aspects of Wi-Fi (IEEE 802.11 a, b, g) Open point-to-multipoint links. Our study contributes to the performance evaluation of this technology, using new available equipments (V-M200 access points from HP and WPC600N adapters from Linksys). New detailed results are presented and discussed, namely at OSI levels 4 and 7, from TCP, UDP and FTP experiments: TCP throughput, jitter, percentage datagram loss and FTP transfer rate. Comparisons are made to corresponding results obtained for Open point-to-point links. Conclusions are drawn about the comparative performance of the links.

Keywords IEEE 802.11a · IEEE 802.11b · IEEE 802.11g · Open point-to-multipoint links · Open point-to-point links · Wi-Fi · Wireless network laboratory performance measurements · WLAN

J.A.R.P. de Carvalho (✉) · C.F. Ribeiro Pacheco · A.D. Reis
Unidade de Detecção Remota, Universidade da Beira Interior,
6201-001 Covilhã, Portugal
e-mail: pacheco@ubi.pt

C.F. Ribeiro Pacheco
e-mail: a17597@ubi.pt

A.D. Reis
e-mail: adreis@ubi.pt

H. Veiga
Centro de Informática, Universidade da Beira Interior, 6201-001 Covilhã, Portugal
e-mail: hveiga@ubi.pt

S.-I. Ao et al. (eds.), *Transactions on Engineering Technologies*,
DOI 10.1007/978-981-10-1088-0_35

1 Introduction

Contactless communications techniques have been developed using mainly electromagnetic waves in several frequency ranges, propagating in the air. The importance and utilization of Wi-Fi and FSO have been growing. They are important examples of wireless communications technologies.

Wi-Fi is a microwave based technology providing for versatility, mobility and favourable prices. The importance and utilization of Wi-Fi has been increasing for complementing traditional wired networks. Both ad hoc mode and infrastructure mode are possible. In this case an access point, AP, permits Wi-Fi electronic devices to communicate with a wired based LAN through a switch/router. Thus a WLAN, based on the AP, is created. At the personal home level a WPAN allows personal devices to communicate. Point-to-point (PTP) and point-to-multipoint (PTMP) 2.4 and 5 GHz microwave links are used, with IEEE 802.11a, 802.11b, 802.11g and 802.11n standards [1]. The increasing use of the 2.4 GHz band is leading to growing interferences. Therefore, the 5 GHz band is receiving considerable attention, in spite of larger absorption and shorter ranges. Wi-Fi communications are not significantly sensitive to rain or fog, as wavelengths are in the range 5.6–12.5 cm. On the contrary, FSO communications have been found to be affected by rain or fog, as the typical wavelength range for the laser beam is 785–1550 nm.

Nominal transfer rates up to 11 (802.11b), 54 Mbps (802.11 a, g) and 600 Mbps (802.11n) are specified. CSMA/CA is the medium access control. There are studies on wireless communications, wave propagation [2, 3], practical implementations of WLANs [4], performance analysis of the effective transfer rate for 802.11b point-to-point links [5], 802.11b performance in crowded indoor environments [6].

Performance has been seen as a fundamental issue, resulting in more reliable and efficient communications. New telematic applications are specially sensitive to performances when compared to traditional applications. Requirements have been given [7].

Wi-Fi security is very important. Microwave radio signals travel through the air and can be easily captured by virtually everyone. Several security methods have been developed to provide authentication such as, by increasing order of security, WEP, WPA and WPA2. Several performance measurements have been made for 2.4 and 5 GHz Wi-Fi Open [8, 9], WEP [10, 11], WPA [12, 13] and WPA2 [14, 15] links, as well as very high speed FSO [16]. It is important to investigate the effects of network topology, increasing levels of security encryption on link performance and compare equipment performance for several standards. In the present work new Wi-Fi (IEEE 802.11 a, b, g) results arise, using Open links, namely through OSI levels 4 and 7. Performance is evaluated in laboratory measurements of Open PTMP links using new available equipments. Comparisons are made to corresponding results obtained for Open PTP links. The present work is an extension of [17].

In prior and actual state of the art, several Wi-Fi links have been investigated. Performance evaluation has been considered as a crucially important criterion to assess communications quality. The motivation of this work is to evaluate performance in laboratory measurements of Open PTMP links using new available equipments. Comparisons are made to corresponding results obtained for Open PTP links. This contribution permits to increase the knowledge about performance of Wi-Fi (IEEE 802.11 a, g) links [4–6]. The problem statement is that performance needs to be evaluated under several topologies. The solution proposed uses an experimental setup and method, permitting to monitor signal to noise ratios (SNR) and noise levels (N) and measure TCP throughput (from TCP connections) and UDP jitter and percentage datagram loss (from UDP communications).

The rest of the paper is structured as follows: Sect. 2 is about the experimental details i.e. the measurement setup and procedure. Results and discussion are given in Sect. 3. Conclusions are drawn in Sect. 4.

2 Experimental Details

The measurements used a HP V-M200 access point [18], with three external dual-band 3×3 MIMO antennas, IEEE 802.11 a/b/g/n, software version 5.4.1.0-01-9867 and a 100-Base-TX/10-Base-T Allied Telesis AT-8000S/16 level 2 switch [19]. Two PCs were used having a PCMCIA IEEE.802.11 a/b/g/n Linksys WPC600N wireless adapter with three internal antennas [20], to enable (three-node) PTMP links to the access point. In every type of experiment, interference free communication channels were used (ch 36 for 802.11a; ch 8 for 802.11 b, g). This was checked through a portable computer, equipped with a Wi-Fi 802.11 a/b/g/n adapter, running NetStumbler software [21]. No encryption was activated in the AP and the wireless adapters of the PCs. The experiments were made under far-field conditions. No power levels above 30 mW (15 dBm) were required, as the wireless equipments were close.

A versatile laboratory setup has been planned and implemented for the PTMP measurements, as shown in Fig. 1. It involves two wireless links to the AP. At OSI level 4, measurements were made for TCP connections and UDP communications using Iperf software [22]. For a TCP connection (TCP New Reno, RFC 6582, was used), TCP throughput was obtained. For a UDP communication with a given bandwidth parameter, UDP jitter and percentage loss of datagrams were determined. Parameterizations of TCP packets, UDP datagrams and window size were as in [14]. One PC, with IP 192.168.0.2 was the Iperf server and the other, with IP 192.168.0.6, was the Iperf client. Jitter, which represents the smooth mean of differences between consecutive transit times, was continuously computed by the server, as specified by the real time protocol RTP, in RFC 1889 [23]. Another PC, with IP 192.168.0.20, was used to control the settings in the AP.

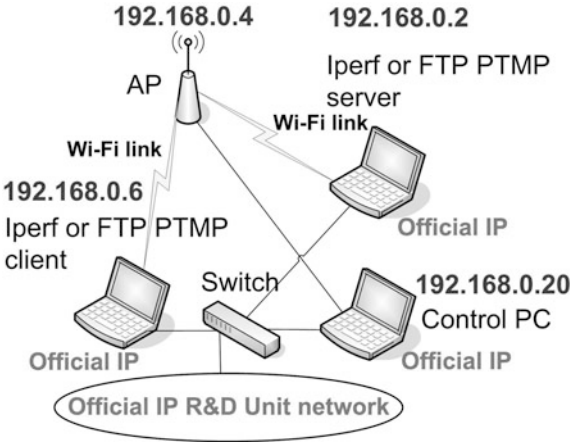

Fig. 1 Experimental laboratory setup scheme [17]

The scheme of Fig. 1 was also used for FTP measurements, where FTP server and client applications were installed in the PCs with IPs 192.168.0.2 and 192.168.0.6, respectively.

The server and client PCs were HP nx9030 and nx9010 portable computers, respectively, running Windows XP Professional. They were configured to optimize the resources allocated to the present work. Batch command files have been re-written to enable the new TCP, UDP and FTP tests.

The results were obtained in batch mode and written as data files to the client PC disk. Every PC had a second network adapter, to permit remote control from the official IP University network, via switch.

3 Results and Discussion

The access point and the wireless network adapters of the PCs were manually configured for each standard IEEE 802.11 a, b, g with typical nominal transfer rates (1, 2, 5.5, 11 Mbps for 11b; 6, 9, 12, 18, 24, 36, 48, 54 Mbps for 11 a, g). For every fixed transfer rate, data were obtained for comparison of the laboratory performance of the PTMP and PTP links at OSI levels 1 (physical layer), 4 (transport layer) and 7 (application layer) using the setup of Fig. 1. For each standard and every nominal fixed transfer rate, an average TCP throughput was determined from a set of experiments. This value was used as the bandwidth parameter for every corresponding UDP test, resulting in average jitter and average percentage datagram loss.

At OSI level 1, signal to noise ratios (SNR, in dB) and noise levels (N, in dBm) were measured. The measured data were similar for both experiment types. Typical values are shown in Fig. 2.

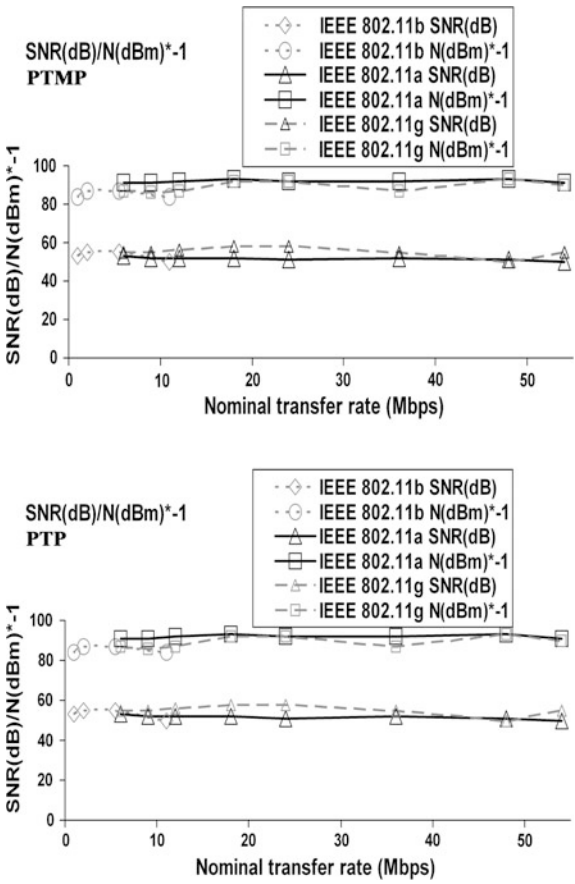

Fig. 2 Typical SNR (dB) and N (dBm); open PTMP and PTP links

Table 1 Average Wi-Fi (IEEE 802.11 a, b, g) open results; PTMP and PTP links

Link type	PTMP			PTP		
Parameter/IEEE standard	802.11b	802.11a	802.11g	802.11b	802.11a	802.11g
TCP throughput (Mbps)	1.5 ± 0.0	8.1 ± 0.2	6.5 + 0.2	3.2 + 0.1	15.0 + 0.5	13.9 ± 0.4
UDP-jitter (ms)	4.2 ± 0.7	2.8 ± 0.2	4.3 ± 0.6	5.6 + 0.3	2.2 + 0.1	3.1 + 0.9
UDP-% datagram loss	1.3 ± 1.0	1.2 ± 0.1	1.7 ± 0.2	1.2 + 0.2	1.4 + 0.1	1.5 + 0.1

The main average TCP and UDP results are summarized in Table 1, both for PTMP and PTP links. The statistical analysis, including calculations of confidence intervals, was carried out as in [24].

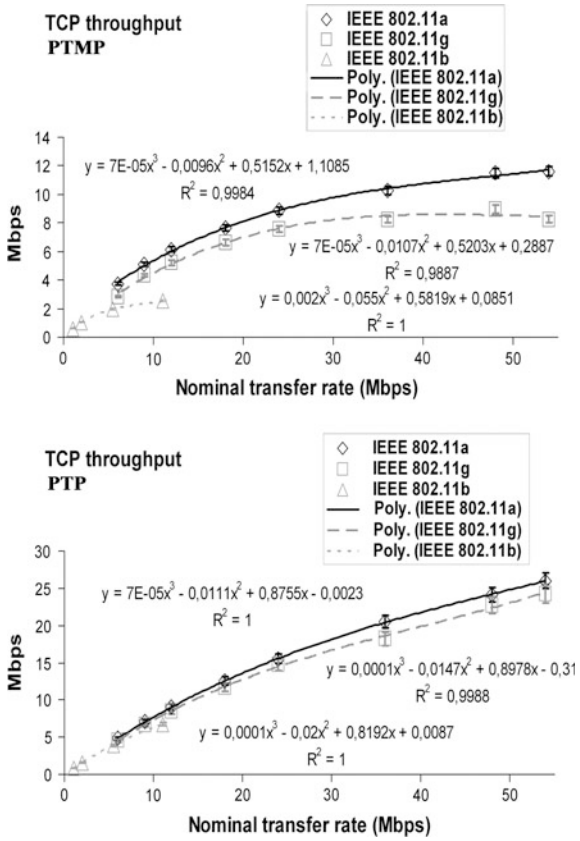

Fig. 3 TCP throughput results (y) versus technology and nominal transfer rate (x); open PTMP and PTP links

In Fig. 3 polynomial fits were made (shown as y versus x), using the Excel worksheet, to the 802.11 a, b, g TCP throughput data for PTMP and PTP links, respectively, where R^2 is the coefficient of determination. It gives information about the goodness of fit. If it is 1.0 it means a perfect fit to data. It was found that, on average, the best TCP throughputs are for 802.11a and PTP links (Table 1).

In Figs. 4 and 5, the data points representing jitter and percentage datagram loss were joined by smoothed lines. It was found that, on average, jitter performances are generally better for PTP than for PTMP links (Table 1). The best average performances were for 802.11a, both for PTP and PTMP links.

Concerning average percentage datagram loss, performances were generally found as better for PTP than for PTMP links (Table 1). The best average performances were for 802.11b, both for PTP and PTMP links.

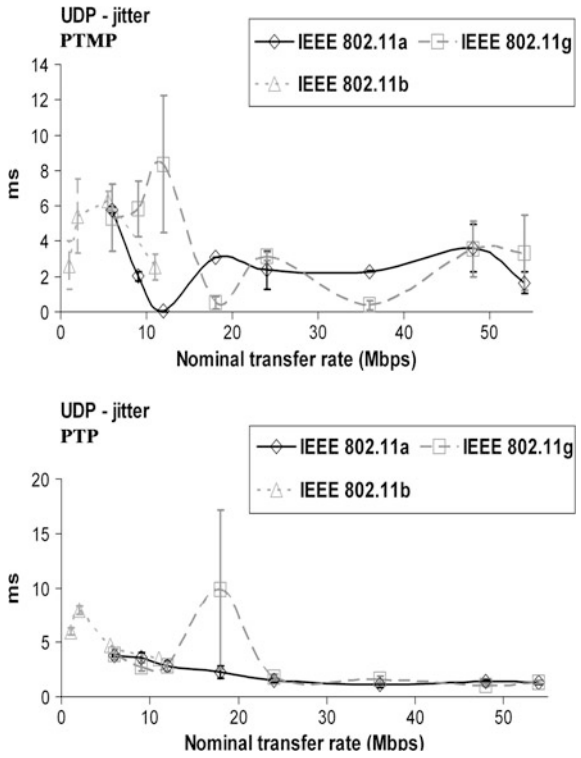

Fig. 4 UDP—jitter results versus technology and nominal transfer rate; open PTMP and PTP links

In comparison to PTP links, TCP throughput, jitter and percentage datagram loss were generally found to show performance degradations for PTMP links, where the processing requirements for the AP are higher so as to maintain links between PCs.

Additional experiments were carried out, involving four nodes (one AP, two client PCs and a control PC). These four-node PTMP (4N-PTMP) experiments were for simultaneous connections/communications between the two clients and the server. PTP was a particular case where the client was client1 and the server was the control PC. In comparison to PTMP links, TCP throughput, jitter and percentage datagram loss were generally found to show higher performance degradations for 4N-PTMP links. This is illustrated in Fig. 6 for TCP throughput.

At OSI level 7 we measured FTP transfer rates versus nominal transfer rates, configured in the wireless network adapters of the PCs, for the IEEE 802.11 a, b, g standards. The result for every measurement was an average of several experiments involving a single FTP transfer of a binary file with a size of 100 Mbytes. The FTP results show similar trends as those found for TCP throughput.

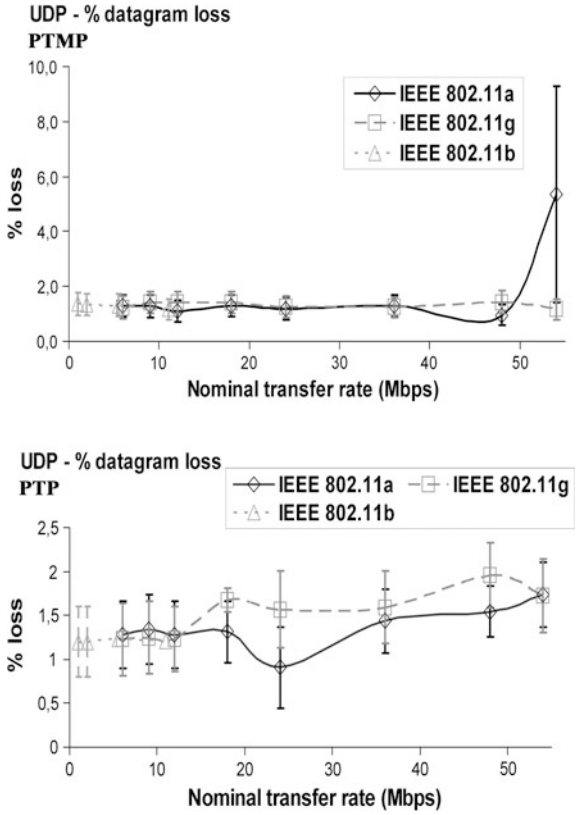

Fig. 5 UDP—percentage datagram loss results versus technology and nominal transfer rate; open PTMP and PTP links

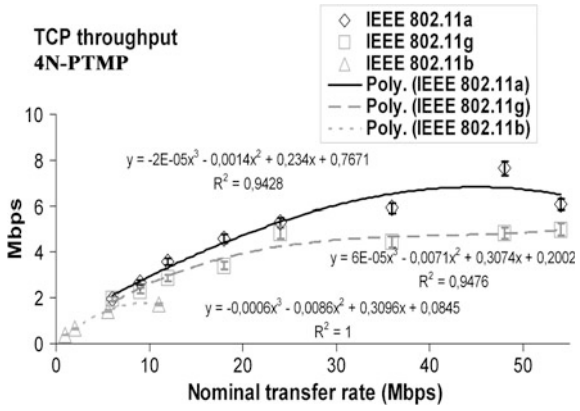

Fig. 6 TCP throughput results (y) versus technology and nominal transfer rate (x); open 4N-PTMP links

4 Conclusions

In the present work a versatile laboratory setup arrangement was planned and implemented, that permitted systematic performance measurements of new available wireless equipments (V-M200 access points from HP and WPC600N adapters from Linksys) for Wi-Fi (IEEE 802.11 a, b, g) in Open PTMP links.

Through OSI layer 4, TCP throughput, jitter and percentage datagram loss were measured and compared for every standard to corresponding results obtained for Open PTP links. In comparison to PTP links, TCP throughput, jitter and percentage datagram loss were generally found to show performance degradations for PTMP links, where the AP experiments higher processing requirements so as to maintain links between PCs.

From four-node PTMP (4N-PTMP) experiments it was found that, in comparison to PTMP links, TCP throughput, jitter and percentage datagram loss generally show higher performance degradations.

At OSI layer 7, FTP performance results have shown similar trends as those found for TCP throughput.

Further performance studies are planned using several equipments, topologies, security settings and noise conditions, not only in laboratory but also in outdoor environments involving, mainly, medium range links.

Acknowledgment Supports from University of Beira Interior and FCT (Fundação para a Ciência e a Tecnologia)/PEst-OE/FIS/UI0524/2014 (ProjectoEstratégico-UI524-2014) are acknowledged.

References

1. IEEE 802.11a, 802.11b, 802.11g, 802.11n, 802.11i standards; http://standards.ieee.org/getieee802. Accessed 10 Jan 2011
2. Mark JW, Zhuang W (2003) Wireless communications and networking. Prentice-Hall Inc., Upper Saddle River, NJ
3. Rappaport TS (2002) Wireless communications principles and practice, 2nd edn. Prentice-Hall Inc, Upper Saddle River, NJ
4. Bruce WR III, Gilster R (2002) Wireless LANs end to end. Hungry Minds Inc, NY
5. Schwartz M (2005) Mobile wireless communications. Cambridge University Press, Cambridge
6. Sarkar NI, Sowerby KW (2006) High performance measurements in the crowded office environment: a case study. In: Proceedings of ICCT'06-international conference on communication technology, pp 1–4. Guilin, China, 27–30 Nov 2006
7. Monteiro E, Boavida F (2002) Engineering of informatics networks, 4th edn. FCA-Editor of Informatics Ld., Lisbon
8. de Carvalho JARP, Gomes PAJ, Veiga H, Reis AD (2008) Development of a university networking project. In: Putnik GD, Cunha MM (eds) Encyclopedia of networked and virtual organizations. IGI Global, Hershey, PA (Pennsylvania), pp 409–422
9. de Carvalho JARP, Veiga H, Gomes PAJ, Ribeiro Pacheco CF, Marques N, Reis AD (2010) Wi-Fi point-to-point links-performance aspects of IEEE 802.11 a, b, g laboratory links. In:

Ao SI, Gelman L (eds) Electronic engineering and computing technology, series: lecture notes in electrical engineering, vol 60. Springer, Netherlands, pp 507–514
10. de Carvalho JARP, Veiga H, Marques N, Ribeiro Pacheco CF, Reis AD (2011) Wi-Fi WEP point-to-point links-performance studies of IEEE 802.11 a, b, g laboratory links. In: Ao SI, Gelman L (eds) Electronic engineering and computing technology, series: lecture notes in electrical engineering, vol 90. Springer, Netherlands, pp 105–114
11. de Carvalho JARP, Ribeiro Pacheco CF, Reis AD, Veiga H (2014) Extended performance studies of Wi-Fi IEEE 802.11 a, b, g laboratory WEP point-to-multipoint and point-to-point links. In: Ao SI, Gelman L (eds) Transactions on engineering technologies: world congress on engineering. Springer, Gordrecht, pp 563–572
12. de Carvalho JARP, Veiga H, Marques N, Ribeiro Pacheco CFF, Reis AD (2011) Performance measurements of IEEE 802.11 b, g laboratory WEP and WPA point-to-point links using TCP, UDP and FTP. In: Proceedings of applied electronics 2011–16th international conference, pp 293–298. University of West Bohemia, Pilsen, Czech Republic, 7–8 Sept 2011
13. de Carvalho JARP, Veiga H, Ribeiro Pacheco CF, Reis AD (2013) Extended performance studies of Wi-Fi IEEE 802.11 a, b, g laboratory WPA point-to-multipoint and point-to-point links. In: Yang GC, Ao SI, Gelman L (eds) Transactions on engineering technologies: special volume of the world congress on engineering. Springer, Gordrecht, pp 455–465
14. de Carvalho JARP, Veiga H, Ribeiro Pacheco CF, Reis AD (2012) Performance evaluation of Wi-Fi IEEE 802.11 a, g WPA2 PTP links: a case study. In: Lecture notes in engineering and computer science: proceedings of the world congress of engineering 2012, WCE 2012, pp 1308–1312. London, UK, 6–8 July 2012
15. de Carvalho JARP, Veiga H, Ribeiro Pacheco CF, Reis AD (2014) Performance evaluation of IEEE 802.11 a, g laboratory WPA2 point-to-multipoint links. In: Lecture notes in engineering and computer science: proceedings of the world congress of engineering 2014, WCE 2014, pp 699–704. London, UK, 2–4 July 2014
16. de Carvalho JARP, Marques N, Veiga H, Ribeiro Pacheco CFF, Reis AD (2010) Performance measurements of a 1550 nm Gbps FSO link at Covilhã City, Portugal. In: Proceedings of applied electronics 2010–15th international conference, pp 235–239. University of West Bohemia, Pilsen, Czech Republic, 8–9 Sept 2010
17. de Carvalho JARP, Ribeiro Pacheco CF, Reis AD, Veiga H (2015) Performance evaluation of IEEE 802.11 a, g laboratory open point-to-multipoint links. In: Lecture notes in engineering and computer science: proceedings of the world congress of engineering 2015, WCE 2015, pp 611–615. London, UK, 1–3 July 2015
18. HP V-M200 802.11n Access Point Management and Configuration Guide (2010) http://www.hp.com. Accessed 15 Jan 2015
19. AT-8000S/16 Level 2 Switch Technical Data (2009) http://www.alliedtelesis.com. Accessed 10 Dec 2010
20. WPC600N Notebook Adapter User Guide (2008) http://www.linksys.com. Accessed 10 Jan 2012
21. NetStumbler Software (2005) http://www.netstumbler.com. Accessed 21 Mar 2011
22. Iperf Software (2003) http://dast.nlanr.net. Accessed 10 Jan 2008
23. Network Working Group (1996) RFC 1889-RTP: a transport protocol for real time applications; http://www.rfc-archive.org. Accessed 10 Feb 2008
24. Bevington PR (1969) Data reduction and error analysis for the physical sciences. Mc Graw-Hill Book Company

From 3GPP LTE to 5G: An Evolution

Oluwadamilola Oshin, Matthew Luka and Aderemi Atayero

Abstract All-IP network architecture is fast becoming a norm in mobile telecommunications. The International Telecommunications Union—Radio communication sector (ITU-R) recognizes a technology as 4G after haven met the International Mobile Telecommunications Advanced (IMT-A) specification of a minimum of 100 Mb/s downlink data rate for high mobility and 1 Gb/s for low mobility. The Long Term Evolution specified by the 3GPP, provides a minimum downlink data rate of 100 Mb/s and marks a new beginning in Radio Access Technologies (RATs). It also notably implements an all-IP network architecture, providing higher data rates, end-to-end Quality of Service (QoS) and reduced latency. Since the first release of the LTE standard (3GPP release 8), there have been a number of enhancements in subsequent releases. Significant improvements to the standard that enabled LTE to meet the IMT-A specifications were attained in release 10, otherwise known as LTE-Advanced. Some of the enhancements such as the use of small cells (known as femtocells) are envisioned to be the basis of fifth generation (5G) wireless networks. Thus, it is expedient to study the LTE technology and the various enhancements that will shape the migration towards 5G wireless networks. This paper aims at providing a technical overview of 3GPP LTE. With a brief overview of its architecture, this paper explores some key features of LTE that places it at the forefront in achieving the goals of wireless access evolution, enabling it to become a key element of the ongoing mobile internet growth. The migration to 5G may be radical, thus some enabling technologies that will shape the 5G cellular networks are also examined.

O. Oshin (✉) · A. Atayero
EIE Department, Covenant University, Km 10, Idiroko Road,
Ota, Ogun State, Nigeria
e-mail: damilola.adu@covenantuniversity.edu.ng

A. Atayero
e-mail: atayero@covenantuniversity.edu.ng

M. Luka
Department of Electrical and Electronics Engineering,
Modibbo Adama University of Technology, Yola, Nigeria
e-mail: matthewkl@mautech.edu.ng

S.-I. Ao et al. (eds.), *Transactions on Engineering Technologies*,
DOI 10.1007/978-981-10-1088-0_36

Keywords 4G · 5G · E-UTRAN · GSM · IMT-A · LTE · LTE-A · UMTS

1 Introduction

LTE is designed to meet the IMT-2000 requirements set out by International Telecommunications Union—Radio communication sector (ITU-R). As at February 2014, the Global mobile Suppliers Association (GSA) confirmed a total of 274 LTE networks launched in 101 countries thus far, with majority deployed on the 1800 MHz frequency band [1]. LTE is a phenomenal technology—it enables operation under a vast set of conditions and still delivers excellent performance. LTE (Long Term Evolution) was developed and standardized by 3GPP as Release 8. It builds on 3GPP GSM/UMTS cellular concept and uses E-UTRAN (Evolved-UMTS Terrestrial Radio Access Network) as its radio access: it is therefore sometimes referred to as E-UTRAN. Compared to previous 3GPP telecommunication standards, LTE marks a departure from the normal circuit switched or a combination of circuit and packet switched networks, to an all-IP/packet-based network. LTE is a wireless access technology, which provides high quality experience. 3GPP LTE is a significant advancement in cellular technologies. The motivations for LTE as outlined by 3GPP are: need to ensure the continuity of competitiveness of the 3G system for the future, user demand for higher data rates and quality of service, packet-switched optimized system, continued demand for cost reduction in terms of both capital and operational expenditure (CAPEX and OPEX), low complexity and to avoid unnecessary fragmentation of technologies for paired and unpaired band operation [2]. The spectrum bandwidth of LTE is scalable with subsets of 1.4, 3, 5, 10, 15 and 20 MHz using the 20 MHz bandwidth, LTE is capable of achieving peak data rate of 100 Mbps in the downlink and up to 50 Mbps in the uplink for a 1×2 antenna configuration. The spectrum efficiency and throughput are up to 3–4 times better for the forward link and 2–3 times better for the reverse link than 3GPP release 6. Latency is significantly reduced by using a flat architecture with reduced number of network nodes. User plane and control latency are less than 30 and 100 ms respectively. Internetworking with backend systems such as 3GPP GERAN/UTRAN and non-3GPP systems such as WiMAX and Wi-Fi is supported via various interfaces. The use of self-organizing network operations, specification of uniform interfaces for multi-vendor interoperability and reduced terminal nodes are all envisioned to reduce cost. LTE also supports operation in both unpaired spectrum (Time Division Duplex) and paired spectrum (Frequency Division Duplex Modes). LTE supports Voice over Internet Protocol (VoIP) with an end-to-end quality of service comparable to that of UMTS circuit switched network [3]. Leveraging on these features LTE wireless access technology provides rich experience and high performance, connectivity, coverage and roaming, ecosystem richness, efficiency and cost effectiveness.

LTE-Advanced leverages on an increased bandwidth of up to 100 MHz to target a peak data rate of up 1 Gbps in the downlink and up to 500 Mbps in the uplink for low mobility scenarios. With support of up to 8×8 antenna configuration, LTE

advanced offers a peak spectral efficiency of up to 30 bps/Hz (approximately 2 times that of release 8) which translates into an improved user throughput. LTE-Advanced also supports higher mobility speeds of up to 350–500 km/h, which is a significant improvement over the 10 km/h mobility speed for release 8. The use of relay nodes (particularly layer 3 relay technology) significantly improves system coverage at a reduced cost [4]. In order to meet up with mobile traffic explosion, LTE-Advanced uses low cost small cells to improve system capacity. The use of small cells also improves user experience by reducing transmit-receive distance. The most obvious bottleneck for the currently deployed network to meet up with increasing traffic is scarcity of frequency spectrum. This challenge can be surmounted by using the vast spectrum in the millimetre band for 5G mobile network to support multi-gigabit communications services. The evolution towards 5G can be achieved by either continuous enhancements to the LTE radio access network or developing a new radio access network technology that departs from the concepts of LTE. Continuous enhancements to LTE will primarily focus on further enhancements to small cells and other general cellular enhancements for beyond release 13. For example in [5], MIMO-OFDM technology (on which LTE is based) was enhanced using an 8×16 antenna configuration in the 11 GHz frequency band to achieve a data rate of 10 Gbps. Defining a new Radio Access Technology (RAT) should prioritize the achievement of more gains over backward compatibility with LTE [6]. 5G is expected to combine sub 6 GHz and the band beyond 6 GHz to support extreme services such as low data Internet of Things applications to high data Ultra High Definition Video (UHDV) as illustrated in Fig. 1.

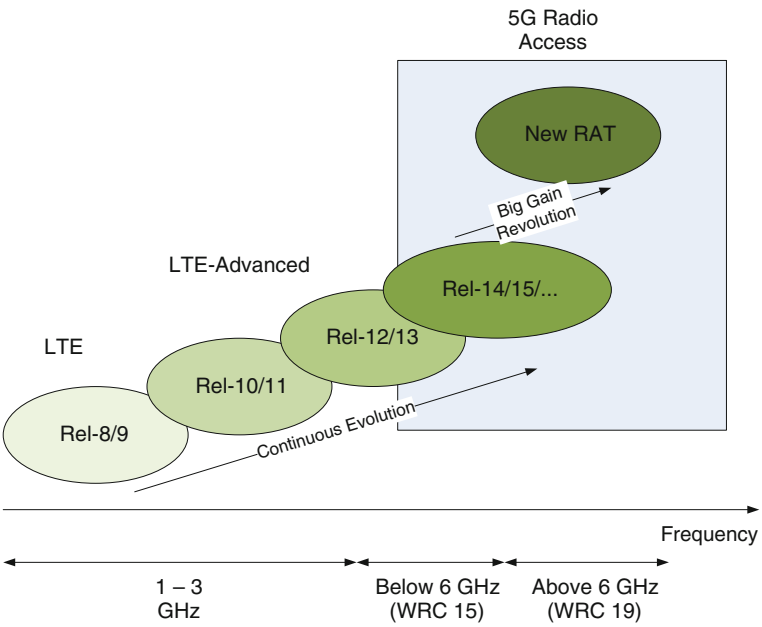

Fig. 1 Evolution paths from LTE to 5G

2 LTE Network Architecture

LTE network architecture is a generally simplified access network which marks a total departure from previous standards, characterized by the absence of a circuit-switched domain. It employs a non-hierarchical (distributed) structure. The LTE network architecture incorporates new network elements. As shown in Fig. 2, LTE network architecture can be sub-divided into three major groups: air interface, radio access network and core network. Transmission of data and control information between the user equipment (UE) and the evolved base stations (eNBs) take place within the air interface. LTE uses various mechanisms (as discussed later in this paper) within the air interface to provide highly reliable and efficient means of carrying out these operations.

The RAN of LTE consists only of a network of fully interconnected eNBs; hence the network is described as being flat or distributed. This RAN is called the E-UTRAN i.e. the Evolved-UMTS Terrestrial Radio Access Network. It is an evolved RAN from UTRAN, used by 3G networks but in LTE, all radio network controller (RNC) functions are transferred to the eNBs. Some of the functions of the eNB include:

- Radio Resource Management: This involves functions such as scheduling, dynamic allocation of resources, radio bearer control and mobility control.
- IP Header Compression.
- Security.
- Connection of users to the core network.

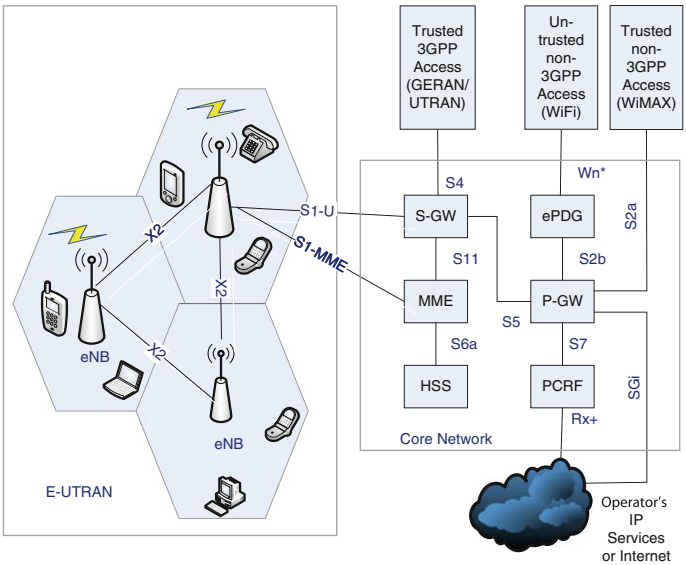

Fig. 2 LTE network architecture

The core network of LTE differed significantly from previous standards. All others had their core networks either entirely circuit switched or split into circuit switched domain and packet switched domain, but LTE core network is entirely packet switched and it is called the Evolved Packet Core (EPC). The EPC in conjunction with the E-UTRAN is called the Enhanced Packet System (EPS), whose details have been defined by 3GPP's study of System Architecture Evolution (SAE).

A Summary of the functional elements of the EPC are outlined below [7]:

- Mobility Management Entity (MME): this handles user authentication, it tracks and maintains the location of a user equipment, performs signalling operations, MME selection for inter-MME handovers.
- Serving Gateway (S-GW): while the MME handles control distribution functions, the S-GW handles data bearer functions where it handles user data functionality, routes and forwards data packets to the P-GW, performs mobility anchoring for inter-3GPP mobility and is responsible for lawful interceptions.
- Packet Data Network Gateway (P-GW or PDN-GW): It handles packet filtering for every user, allocation of IP addresses to the UEs, supports service level charging by collecting and forwarding call data records, handles DL data rate enforcement to ensure that a user does not surpass his traffic rate subscription level, provides interworking for the user plane, between some 3GPP access systems and all non-3GPP access systems, supports QoS differentiation between multiple IP flows. It is also capable of handling multiple lawful interceptions of user traffic to promote government intelligence services fighting criminal activities. The P-GW enforces PCRF policies.
- Home Subscriber Server (HSS): this is a major database, which houses all subscription-related information, to perform call control activities and session management functions.
- Policy and Charging Control Function (PCRF): The PCRF ensures QoS regulation within the network based on definite policies. It is responsible for framing policy rules from the technical details of Service Date Flows (SDFs) that will apply to the users' services, and then forwarding these rules to the P-GW for enforcement.
- Evolved Packet Data Gateway (ePDG): The ePDG provides interworking with un-trusted non-3GPP IP access systems. It ensures security by having a secured tunnel between the UE and the ePDG. It can also function as a local mobility anchor within un-trusted non-3GPP access networks.

As observed in Fig. 2, LTE uses interfaces as indicated for communication between its entities. In general, LTE network architecture implements a simplified, flat all-IP architecture which leads to reduced latency, reduced CAPEX and OPEX, increased scalability and efficiency among other benefits. Increased cost savings and increase capacity can be realized by using LTE *femtocells* known as Home eNodeB (HNB). Can be backhauled to the cellular operator network through a

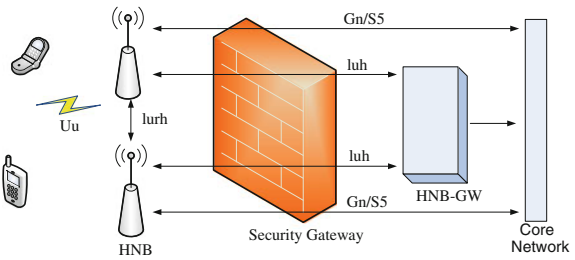

Fig. 3 HNB access radio access network reference model

broadband gateway such as fiber optic cable over the internet. The reference model of the HNB is shown in Fig. 3.

The HNB gateway is an optional entity that serves as a concentrator for HNB connections and as a Radio Network Controller (RNC) to the core network. Alternatively, the HNB can connect directly to the core network when a Local Gateway functionality is incorporated into it [8]. Enhancements to the HNB is very critical to the continuous evolution of the 3GPP LTE standard.

3 Enabling Technologies

LTE leverages on several technologies such as use of Orthogonal Frequency Division Multiplexing (OFDM) and Multiple Input Multiple Output (MIMO) antenna techniques to achieve the specified targets. Continuous improvements of these enabling technologies is the basis for the evolution of the LTE technology.

3.1 Multiplexing/Multiple Access Mechanism

The aim of multiplexing/multiple access mechanisms is to share scarce resources in order to achieve high capacity, by enabling simultaneous allocation of bandwidth/channel to multiple users. Multiplexing is a method by which multiple signals are transmitted at the same time in form of a single complex signal over a shared medium and then recovering the individual signals at the receiving end while Multiple access mechanisms define how the channel is shared in a finite frequency bandwidth i.e. it controls how to use (share) the radio resources efficiently. These operations take place within the air interface of the LTE network.

The OFDM is a data transmission multi-carrier modulation technique, which divides a high bit-rate data signal into several parallel low bit-rate data signals which are then modulated using an appropriate modulation scheme. OFDM is the core of LTE downlink transmission system. Majority of the striking features of LTE is made possible by its use of OFDM. The “low bit-rate multi-carrier” technique of OFDM, with a cyclic prefix added to it, makes the transmission robust to time

dispersion on the radio channel without the need for advanced and complex receiver channel equalization. In the downlink, this leads to reduced cost of terminal equipment and reduced power consumption as well. OFDM is also used due to its resilience to multipath delays and spread, its capability for carrying high data rates and its ability to support both FDD and TDD schemes. The concept of orthogonality can be illustrated by considering two OFDM modulation symbols α_{i1} and α_{i2} used to modulate time-limited complex signals (subcarriers):

$$\int_{mT_s}^{(m+1)T_s} \alpha_{i1}\alpha_{i2}^{*} e^{j2\pi k_1 \Delta f t - j2\pi k_2 \Delta f t} dt = 0 \quad \forall k_1 \neq k_2 \tag{1}$$

where $\Delta f = 1/T_s$ is the subcarrier spacing and $k.\Delta f$ is the sampling frequency which corresponds to the sampling frequency of the signal. In essence, OFDM transmission is the modulation of a set of orthogonal functions given by [9]:

$$\beta(t) = \begin{cases} e^{j2\pi k \Delta f t} & 0 \leq t < T_s \\ 0 & otherwise \end{cases} \tag{2}$$

In the downlink, the Base Station (BS) is the transmitter while the User Equipment (UE) only receives, therefore it does not have multiple access problems in terms of collisions. Fading is a natural characteristic of radio communication channels (either in time, frequency or space domain), resulting in rapid variations in radio channel quality. A derivative of OFDM—OFDMA is used in LTE downlink, where it combines functionalities of FDMA and TDMA. With OFDMA, the UE gets scheduled to a time slot and a frequency group (which makes the system resilient to frequency-selective fading) among other features, in order to send information. Using OFDMA, LTE can use channel-dependent scheduling to take advantage of the variations resulting in more efficient use of available radio resources. This creates a lot of flexibility and makes the system robust, as not all the requirements for transmission can be bad at the same time.

In the uplink, the UEs transmit to the BSs. Due to the high peak-to-average ratio (PAR) of OFDM (characterized by the high amount of power required by the RF power amplifier to push out the RF signal from the UE antenna to the BS), 3GPP was forced to adopt a different transmission scheme for LTE uplink. SC-FDMA, a hybrid scheme, was the solution—it combines the low PAR feature (which allows high RF power amplifier efficiency in the UEs, thereby reducing battery consumption for the UE) of single-carrier schemes with the resilience of multipath interference and the flexible subcarrier frequency allocation of OFDM technology [10].

3.2 Coding and Modulation

The reduced latency and high throughput of LTE is traceable to a number of mechanisms implemented in it. The physical/MAC layer of LTE adopts two key techniques: Hybrid Automatic Repeat reQuests (HARQ) and adaptive modulation and coding (AMC). These two techniques work together to give a very adaptive transport mechanism in LTE [11]. To handle re-transmission errors, LTE uses two loops: a fast HARQ inner loop with soft combining to take care of most errors and a robust selective-repeat ARQ outer loop to take care of residual errors [12, 13]. HARQ is a technique for both error detection and correction by identifying when transmission errors occur and facilitating retransmission from the source thereby ensuring that data is transported reliably from one network node to another. LTE uses Type-II HARQ protocols. LTE demonstrates dynamic resource allocation through link adaptation. Link adaptation is achieved using the AMC mechanism, with the aim of improving data throughput in a fading channel. AMC works by varying the downlink modulation technique depending on the channel conditions of each user. Given a good channel condition, the LTE system can use a higher order modulation scheme (64-QAM with 6 bits per symbol) or reduced channel coding, making the channel more spectrally efficient, and resulting in higher data rates. But as the channel becomes noisy due to signal fading or interference, the system selects a lower modulation technique (QPSK or 16-QAM with fewer bits per symbol) or stronger channel coding.

3.3 Radio Access Modes (Duplex Schemes)

A duplex scheme organizes how radio communication systems communicate in the two possible directions (uplink and downlink). 3GPP has specified LTE to operate in either unpaired spectrum for Time Division Duplex (TDD) called TD-LTE or paired spectrum for Frequency Division Duplex (FDD); where each has its pros and cons, therefore selection is made depending on the intended application.

LTE specifications emphasize on TD-LTE, as it presents significant advantages over LTE FDD. TD-LTE, asides many other advantages, provides an upgrade path for TD-SCDMA, it does not require a paired spectrum since uplink and downlink transmissions occur on the same channel making it highly spectrally efficient and TD-LTE also reduces hardware cost. LTE operation in FDD which is the same duplex method for GSM/UMTS, gives room for subscribers' migration to LTE.

LTE also supports half-duplex FDD at the UE. This mode allows the uplink and downlink to share hardware since they are never used simultaneously. The half duplex LTE FDD offers reduced complexity and therefore reduced cost [14].

3.4 Radio Channel Bandwidth

LTE is not only able to operate in different frequency bands, but can be implemented using different spectrum sizes. This makes it possible to harness the global wireless market and align with regional spectrum regulations and the obtainable spectrum. LTE implements a scalable radio channel bandwidth from 1.4 to 20 MHz with a subcarrier spacing of 15 kHz. The 20 MHz bandwidth will be required for optimum performance and to cope with the growth of the mobile internet. 3GPP has specified the LTE air interface to be "bandwidth agnostic" thereby allowing the physical layer to adapt to different spectrum allocation without severe impact on system operation.

LTE defines an enhanced mode of operation for broadcast/multicast services called eMBMS (Enhanced- Multimedia Broadcast/Multicast Service), yielding notable performance benefits compared to MBMS over WCDMA. LTE does this by enabling the support of MBSFN (Multimedia Broadcast over Single Frequency Network) yielding a possible subcarrier spacing of 7.5 kHz for standalone eMBMS operation using a dedicated carrier [15].

3.5 Multiple Antenna Techniques

Every terrestrial radio communication channel has data throughput limitations as defined by Shannon's theorem, and multipath interference. LTE networks are expected to provide high data rate in addition to high spectral efficiency; therefore, 3GPP included the use of multiple antenna techniques to provide additional robustness to the radio link [16]. Multiple antenna techniques take advantage of the effects of multipath interference to increase data throughput significantly within the channel's given bandwidth. The use of multiple antenna techniques introduces a concept called precoding, which is essential for obtaining the best data reception result at the receiver. It specifically maps the modulation symbols onto the different antennas. The basic principle of MIMO is illustrated in Fig. 4.

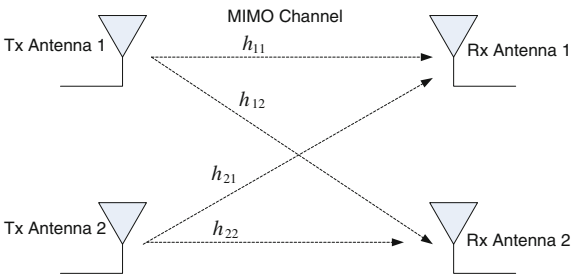

Fig. 4 Block diagram of a 2×2 MIMO system

The MIMO system for each subcarrier can be expressed as a system of linear equations which gives the relationship between the transmit antennas and the receive antennas. The relationship can be expressed in vector form as:

$$\vec{Y} = \begin{bmatrix} h_{11} & h_{12} \\ h_{21} & h_{22} \end{bmatrix} \vec{X} \tag{3}$$

In order to correctly recover the transmitted data, the receiver must estimate the channel response (channel state information) at each subcarrier for any pair of transmitted and received symbol. In selecting the type of multiple antenna technique to use, transmission modes were defined. 3GPP's Release 8 (LTE) specifies seven transmission modes (named TM1, TM2 etc.) for the downlink and one transmission mode for the uplink. These antenna techniques differ by the benefit they provide and the conditions required for their operation. The transmission modes differ in the number of layers or ranks and the number of antenna ports. The uplink transmission mode is Closed-loop switched antenna diversity.

MIMO is a generic term with several special cases and applications. When a point-to-point MIMO link between an eNB (base station) and a single user is involved, we have a case of single user MIMO (SU-MIMO). Multi-user MIMO (MU-MIMO) refers to use cases where several user equipment (UE) communicate with a single eNB using the same time and frequency—domain resources (David et al. 2009). Special cases of MIMO configuration include: Single-Input-Multiple-Output (SIMO), Multiple-Input-Single-Output (MISO). The main aim of the various MIMO configuration revolves around achieving either diversity gain, array gain or spatial multiplexing gain. Transmit/receive diversity involves the transmission/reception of redundant information on different antennas at each subcarrier. Diversity gain makes the link robust by mitigating the effect of multipath fading. In order words, diversity gain is aimed at improving the statistics of instantaneous Signal-to-Noise Ratio (SNR) in a fading channel. In LTE, transmit diversity gain is achieved using Space Frequency Block Codes (SFBCs) and Frequency Switched Transmit Diversity (FSTD). Beamforming is used to achieve array beamforming gain, by using multiple antenna to control the direction of wave front based on weighting the phase and magnitude of individual antenna signals [17]. Spatial multiplexing is designed to boost a link by transmitting non-redundant (independent) information on different antennas. The transmission modes for LTE based on these configurations are summarized in Table 1 [17].

3.6 Voice Over LTE/IP Multimedia Subsystem (IMS)

LTE implements an all-IP architecture; this implies that voice communication cannot be "business as usual" i.e. voice communication cannot be circuit-switched as it is with lower generation technologies. This problem also applies to SMS

Table 1 Transmission modes in LTE release 9

Transmission modes	Description	Remarks
1	Single transmit antenna	Single antenna port; port 0
2	Transmit diversity	2 or 4 antennas
3	Closed loop spatial multiplexing with cyclic delay diversity	2 or 4 antennas
4	Closed loop spatial multiplexing	2 or 4 antennas
5	Multi-user MIMO	2 or 4 antennas
6	Closed loop spatial multiplexing using a single transmission layer	1 layer (rank 1) 2 or 4 antennas
7	Beamforming	Single antenna port, port 5 (virtual antenna port, actual antenna configuration depends on implementation)
8	Dual-layer beamforming	Dual-layer transmission, antenna port 7 and 8

communication as well; therefore, new solutions for supporting voice and SMS on LTE network became an urgent need.

In order to provide these very crucial services, alliances were tasked to come up with solutions to these shortcomings, which are listed below:

- Circuit-Switched Fall-Back (CSFB): This method involves the use of a 2G/3G network alongside the LTE network. The LTE network is used for data services but on a call initiation, the network falls back to a 2G/3G circuit-switched connection while the LTE network (packet-switched) is suspended. For an SMS transmission, the mobile equipment uses an interface known as SGs (MME-MSC interface) which allows messages to be transmitted over an LTE channel.
- Simultaneous Voice—LTE (SV-LTE): This is very similar to the CSFB but in SV-LTE, the user device makes use of the 2G/3G network and the LTE network concurrently. Thus, when a call is initiated, it is routed through the circuit-switched 2G/3G connection while maintaining connection with the LTE network. This option requires the use of two radios simultaneously by the mobile device which causes a degrading impact on the battery life of the device.
- Over-the-top (OTT) VoIP: An example of an OTT VoIP solution is Skype. This concept led to the widespread usage of VoIP as a voice communication service and has advanced to an era of being pre-installed in smart phones. However, OTT VoIP solutions cannot guarantee satisfactory user experience in the absence of LTE coverage. OTT VoIP service providers do not have control over QoS in the wireless network, therefore, cannot ensure a good quality of

experience (QoE) under all load circumstances. It also lacks the capability of handing over to a circuit-switched connection.

- Voice over LTE via Generic Access (VoLGA): This method relies on the operating principles of 3GPP's Generic Access Network (GAN). The aim of GAN is to extend mobile services over a generic IP access network. For example, using Wi-Fi as an access technology to a 2G/3G network. In the case of LTE, VoLGA uses LTE as the access technology to a 2G/3G network. A GAN gateway provides a secure connection from the user to the mobile network operator's infrastructure. This connection serves as the channel for transmitting voice and other circuit-switched services such as SMS over the intermediate LTE network.
- Voice over LTE (VoLTE): This method implements 3GPP's IMS core network by deploying Multimedia Telephony (MMTel) on the IMS core as the solution for voice service delivery and other traditional circuit-switched services over the LTE network. VoLTE eliminates the need for fall-backs to 2G/3G voice, ensuring a truly flat all-IP LTE network. With VoLTE users are assured telecom grade voice and all forms of rich communication services on LTE-enabled devices. VoLTE defines three working interfaces:
  - The User Network Interface (UNI): This is the interface between the user device and the operator's network.
  - The Roaming Network Network Interface (R-NNI): This is the interface between the Home and Visited Network, for use in a roaming situation.
  - The Interconnect Network Network Interface (I-NNI): This is the interface between the networks of the two users making a call.

VoLTE has been accepted globally by a significant number of telecom industries as the standard for carrying voice, SMS and other related services over the LTE network [18].

3.7 Self-organizing Networks (SON)

The impact or functionality of a network is not just in its deployment and usage but in its ability to achieve operational excellence. This involves continuous end-to-end network management of the system i.e. seamless operation and consistent performance. Due to the increasingly expanding and evolving wireless network, there is a crucial need to automate this management process [19, 20]. In order to achieve this, LTE adopts SON techniques which enables the network to configure itself and manage the radio resources to achieve optimum performance at all times with minimal human supervision. SON techniques cover three main areas:

- Self Configuring: As a network expands and more eNBs are deployed, self configuring networks eliminate the need to go around configuring each one; rather, they are configured using automatic installation procedures.

- Self Optimizing: After configuration, self optimizing techniques adjust the network's operational characteristics based on measurement information collected from the UEs and eNBs, and use them to auto-tune the network to best meet its needs.
- Self Healing: In any system, faults are very likely to occur; however, the self healing capability of a network enables automatic detection and fault masking by changing relevant network characteristics. For example, edges of adjacent cells can be increased by raising power levels and changing antenna elevations.

4 LTE Technological Advancements

There are two groups of technological advancements on LTE Release 8, namely LTE Release 9 and LTE Release 10 [21]. Transmission Mode 8 (TM8), Dual Layer Beamforming, was added in LTE Release 9. LTE Release 9 also focuses on features that enhance the core network of LTE Release 8. These enhancements centre on:

- Location, broadcast and IMS emergency services using GPRS and EPS.
- Support of circuit switching services over the EPS of LTE.
- Home NB or eNB architecture considerations focusing on security, QoS, charging and access restrictions.
- IMS evolution.

LTE Release 10: This is the evolution of LTE to meet the IMT-A requirements defined by ITU. It is known as LTE-Advanced (LTE-A), and its focus is on higher capacity as outlined:

- Downlink peak data rate of 3 Gb/s and Uplink peak data rate of 1.5 Gb/s.
- Higher spectral efficiency on the downlink, from an upper limit of 16 bps/Hz in Release 8–30 bps/Hz in Release 10.
- Increased number of simultaneously active subscribers.
- Improved performance at cell edges.

LTE-A centres on three new techniques that enable it achieve the above-mentioned feats [22]:

- Carrier Aggregation (CA): The most basic method of increasing capacity is by adding more bandwidth. LTE-A is increased in bandwidth through aggregation of up to five component carriers of different bandwidths to form a maximum bandwidth of 100 MHz. This also provides LTE-A backward compatibility with Release 8 and Release 9 mobiles. Carrier aggregation can be used in both FDD and TDD schemes.
- Enhanced multiple antenna techniques: It adds a ninth transmission mode to the downlink called Eight Layer Spatial Multiplexing (8×8 MIMO), and adds a second transmission mode to the uplink (4×4 MIMO).

- Relay Nodes (RN): Relay nodes bring about the possibility of efficient heterogeneous network planning in LTE-A. The Relay Nodes are low power base stations that provide enhanced coverage and capacity at cell edges and can also provide connectivity to remote areas without the need for optical fibre cables.
- Coordinated Multipoint (CoMP) Transmission/Reception: This feature was finalized in Release 11. In this technique, multiple transmit and receive points provide coordinated transmission/reception. This transmission/reception is carried out jointly and dynamically across multiple cell sites, same site or within same or different eNBs. The primary purpose of CoMP is to improve the performance at cell edge.

The on-going enhancements in release 13 include additional enhancements for LTE to operate in the unlicensed spectrum and expansion of the carrier aggregation framework to support more than 5 component carriers. Other enhancements described in [23, 24] include:

- Enhancements for Machine-Type Communications (MTC) involves defining a new low complexity UE type that supports reduced support for downlink transmission modes, reduced bandwidth, reduced transmit power and very long battery life to support Internet of Things (IoT) markets.
- Improving multi-user transmission techniques using superposition coding for increasing spectral efficiency of the LTE system.
- Use of full dimension MIMO/Elevation Beamforming for improved spectral efficiency by the use of higher dimension MIMO of up to 64 antennas at the eNB and utilizing the vertical dimension for MIMO and beamforming operations.
- Improved indoor positioning accuracy and support for Single-cell Point-to-Multipoint (SC-PTM).

Table 2 gives a summary of the key characteristics of LTE at its inception and the current features of LTE as at today, LTE-A. However, recall that there are

Table 2 LTE—LTE-A comparison

Parameter	LTE	LTE-A
Frequency band	Country-dependent	Country-dependent
Downlink peak data rate	100–326 Mbps	1–3 Gbps
Uplink peak data rate	50–86 Mbps	500 Mbps–1.5 Gbps
Channel bandwidth (MHz)	1.4, 3, 5, 10, 15, 20	Up to 100 MHz
Peak spectral efficiency	16 bps/Hz downlink	30 bps/Hz downlink
Latency	~10 ms	Less than 5 ms

(continued)

Table 2 (continued)

Parameter	LTE	LTE-A
Duplex method	FDD and TDD (TD-LTE)	FDD and TDD (TD-LTE)
Multiplexing	OFDM	OFDM
Multiple access method	Downlink—OFDMA Uplink—SC-FDMA	Downlink—OFDMA Uplink—SC-FDMA
Modulation scheme	QPSK, 16-QAM, 64-QAM	QPSK, 16-QAM, 64-QAM
Multiple antenna technique	Up to 4 × 4 MIMO downlink	Higher order MIMO (8 × 8 MIMO downlink; 4 × 4 MIMO uplink)

improvements on the first release of LTE as already discussed in this sub-section, before the LTE Release 10 (LTE-A).

5 5G Enabling Technologies

The most obvious paths of evolution towards 5G radio access are improved spectrum efficiency, network densification and spectrum extension. As earlier noted [25], currently deployed networks are deployed in 1–3 GHz frequency band which eventually fall short of meeting the multi-gigabit requirements of future communication services such as Ultra-High Definition Video (UHDV) [26]. The millimeter wave (mmWave) frequency band from 30 to 300 GHz offers a huge bandwidth and consequently spectrum extension for mobile networks. Millimeter communications particularly in the 28, 38, 60 GHz and the E-band (71–76 and 81–86 GHz) bands will play a critical role in 5G applications such as small cell access, cellular access and wireless backhaul [27, 28]. Some of the key radio access technologies that will pave the way for 5G mobile communications include:

- Further enhancements to low power small cells to provide network densification.
- The use of massive MIMO and large number of miniaturized antennas at high (mmWave) frequencies to provide significant increase in spectrum efficiency and user throughput.
- Use of new access techniques such as Filtered OFDM and Sparse Code Multiple Access (SCMA) to improve system efficiency, support energy saving, reduced latency and massive connectivity [29, 30].
- Use of more efficient coding schemes such as Polar codes, which can achieve Shannon capacity using a simple encoder and a successive cancellation decoder for a large code block size. Another perspective to coding in 5G is to use

network coding for interference management, which can improve security, throughput and robustness for routing of information through the network.
- Use of Full Duplex to support bi-directional communications without the use of time or frequency duplex is expected to double system capacity and reduce latency.
- Use of self-organizing network operation for a cost effective management of the massive network densification. The concept of Device-to-Device communication which allows direct communication between nearby device will depend relies on self-organizing network operations.

6 Conclusion

It is most evident that LTE gives sustainable and significant advantages over existing 3G technologies and also offers the most efficient and feasible evolution path as user/operator network demands mature. The LTE technology has undergone a significant evolution from its first release, which was aimed at meeting the IMT-2000 requirements to achieving and even exceeding the IMT-Advanced (4G) requirements. These technologies will continue to play a critical role in the new frequency spectrum below 6 GHz expected to be allocated for mobile communications at the World Radio Conference (WRC) 2015. However, for the spectrum band above 6 GHz which is expected to be allocated at WRC in 2019, a new radio access technology may be necessary. Thus 5G which is the next frontier of a broader ICT ecosystem that will enhance mobile internet and empower Internet-of-Things (IoT) will be heterogeneous across frequency spectrum. The lower frequency bands (below 6 GHz) can be used as the primary band of 5G spectrum for wide area network coverage. The high frequency bands can be used for Ultra Dense Networking and flexible backhauling. The high frequency bands are also expected to use enhanced smalls cells due to high attenuation associated with these frequencies.

References

1. GSA confirms 1800 MHz as the most popular LTE band; LTE1800 used in over 37 % of networks (Online). Available: http://www.gsacom.com/news/gsa_367.php. Accessed 11 Nov 2014
2. Oni OO, Atayero AA, Idachaba FE, Alatishe AS (2014) LTE networks: benchmarks, prospects and deployment limitation. In: Lecture notes in engineering and computer science: proceedings of the world congress on engineering 2014, WCE 2014, pp 422–427. London, UK, 2–4 July 2015
3. Gessner C, Roessler A, Kottkamp M (2012) UMTS long term evolution (LTE)—technology introduction. In: Application note, 2012 (Online). Available: cdn.rhode-schwarz.com/pws/dl_

downloads/dl_application/application_notes/1ma111/1MA111_4E_LTE_technology_introduction.pdf. Accessed 14 Nov 2015
4. Iwamura M, Takahashi H, Nagata S (2010) Relay technology in LTE-advanced. NTT Docomo Tech J 12(2):29–36
5. Suyama S, Shen J, Oda Y (2014) 10 Gbps outdoor transmission for super high bit rate mobile communications. NTT Docomo Tech J 15(4):22–28
6. 5G radio access: requirements, concept and technologies. In: DOCOMO 5G white paper, 2014 (Online). Available: https://www.nttdocomo.co.jp/english/corporate/technology/whitepaper_5g/. Accessed 11 Nov 2015
7. Flore D (2009) LTE RAN architecture aspects I. In: IMT advanced evaluation, 2009 (Online). Available: ftp://www.3gpp.org/workshp/2009-12-17_ITU_R_IMT-Adv_eval/docs/pdf/REV-090005 LTE RAN architecture aspects.pdf. Accessed 13 Nov 2015
8. ETSI TS 125 467 (2013) Universal mobile telecommunications systems (UMTS); UTRAN architecture for 3G home node B (HNB). ETSI, 2013
9. Erik D, Stefan P, Johan S (2011) 4G LTE/LTE-advanced for mobile broadband. Elsevier, Oxford
10. Poole I (2015) LTE OFDM, OFDMA SC-FDMA and modulation. In: Radio electronics (Online). Available: www.radio-electronics.com/cellulartelecomms/long-term-evolution. Accessed 10 Nov 2015
11. 3GPP long term evolution system overview, product development and test challenges. In: Agilent technologies application note, 2009 (Online). Available: www.ccontrol.ch/cms/upload/applikationem/LTE/5989-8139EN.pdf. Accessed 13 Nov 2015
12. Anders F, Jonsson T, Lundevall M (2008) The LTE radio interface—key characteristics and performance. In: IEEE Symposium on PIMRC, 2008, pp 1–5
13. Astely D, Dahlman E, Fursuskar A, Jading Y, Lindstrom M, Parkvall S (2009) LTE: the evolution of mobile broadband. IEEE Commun Mag 44(4):44–51
14. Yonis AZ, Abdullah MFL, Ghanim MF (2012) LTE-FDD and LTE-TDD for cellular communications. In: Progress in electromagnetics research symposium proceedings, 2012
15. 3G Americas (2007) UMTS evolution from Rel-7 to Rel-8—HSPA and SAE/LTE. In: White paper, 2007 (Online). Available: www.3g4g.co.uk/Lte/LT_WP_0707_3GAmericas.pdf. Accessed 13 Nov 2015
16. Shapira Y (2013) LTE multiple antenna techniques, 2013 (Online). Available: www.exploregate.com/video.aspx?video_id=4
17. Schulz B (2011) LTE transmission modes and beamforming. In: Rhode and Schwarz white paper, 2011 (Online). Available at: http://www.rohde-schwarz.cz/file_17063/1ma186. Accessed 15 Nov 2015
18. Warren D (2010) Roaming in LTE and voice over LTE. In: GSM association, 2010 (Online). Available: www.3gpp.org. Accessed 16 Nov 2015
19. Atayero AA, Adu IO, Alatishe AA (2014) Self organizing networks for 3GPP LTE. In: Murgante B, Misra S, Rocha AMAC, Torre C, Rocha JG, Falcao MI, Taniar D, Apduhan BO, Gervasi O (eds) Computational science and its applications-ICCSA. Springer, pp 242–254
20. Feng S, Seidel E (2008) Self-organizing networks (SON) in 3GPP long term evolution, Nomor research, Munich, Germany, May 2008. In: White paper, 2008 (Online). Available: www.nomor.de/home/technology/white-papers/self-organizing-networks-in-long-term-evolution. Accessed 10 Nov 2014
21. 3G Americas (2009) The mobile broadband evolution: 3GPP release 8 and beyond HSPA+, SAE/LTE and LTE-advanced. In: White paper, 2009
22. Atayero AA, Luka MK, Orya MK, Iruemi JO (2011) 3GPP long term evolution: architecture, protocols and interfaces. Int J Inf Commun Technol Res 1(7):306–310
23. Nokia Network (2015) LTE release 12 and beyond. In: Nokia networks white paper (Online). Available: networks.nokia.com/system/files/document/nokia_lte_a_evolution_white_paper.pdf. Accessed 16 Nov 2015
24. Flore D (2015) Evolution of LTE in release 13 (Online). Available: www.3gpp.org. Accessed 16 Nov 2015

25. Adu OI, Atayero AA (2015) 3GPP LTE: an overview. In: Lecture notes in engineering and computer science: proceedings of the world congress on engineering 2015, WCE 2015, pp 616–621. London, UK, 1–3 July 2015
26. Elkashlan M, Duong TQ, Chen H-H (2015) Millemeter-wave communications for 5G-part 2: applications. IEEE Commun Mag 53(1):166–167
27. Niu Y, Li Y, Jin D, Su L, Vasilakos AV (2015) A survey of millimeter wave (mmWave) communications for 5G: opportunities and challenges. Springer Wirel Netw 21(8):2657–2676
28. Oshin OI, Oni O, Atayero A, Oshin B (2014) Leveraging Mmwave technology for mobile broadband/internet of things. In: IAENG transactions on engineering technologies, lecture notes in electrical engineering. Springer International Publishing, 2014
29. 5G: new air interface and radio virtualization. In: Huawei white paper, 2015 (Online). Available: www.huawei.com/minisite/has2015/img/5g_radio_whitepaper.pdf. Accessed 15 Nov 2015
30. Nikopour H, Yi E, Bayesteh A, Au K, Hawryluck M, Baligh H, Ma J (2014) SCMA for downlink multiple access of 5G wireless networks. Globecom 2014:3940–3945

Wireless Body Area Network for Cycling Posture Monitoring

António José de Freitas Maio and José Augusto Afonso

Abstract This work presents the design and implementation of a wireless body area network based on Bluetooth Low Energy (BLE) which enables the integration of multiple sensor nodes into a smartphone-based system in order to monitor the posture of cyclists. The wireless posture monitoring system presented in this chapter obtains the orientation in space of each body segment in which the sensor nodes are placed and calculates the trunk angle, the knee angle and the angle of inclination of the road. This system collects raw sensor data from accelerometers, magnetometers and gyroscopes and sends the data via BLE to an Android smartphone, which plays the role of central station and performs the data processing concerning the posture calculation. This chapter describes the development of the hardware and software of the sensor nodes, which are based on the CC2540 BLE system-on-chip, as well as the development of the Android application. Experimental results concerning the measurement of the posture of a cyclist are provided in order to validate the implementation.

Keywords Android · Bluetooth low energy · Cycling · Inertial sensors · Mobile sensing · Posture monitoring · Wireless body area networks

1 Introduction

Body posture monitoring is an emerging area of study and development, with applications in areas such as sports, healthcare and entertainment. Posture monitoring systems based on wireless body area networks (WBANs) [1] present several advantages compared to conventional systems based on cameras. Unlike the latter,

A.J. de Freitas Maio · J.A. Afonso (✉)
CMEMS-UMinho R&D Center, University of Minho, 4800-058 Guimarães, Portugal
e-mail: jose.afonso@dei.uminho.pt

A.J. de Freitas Maio
e-mail: a60142@alunos.uminho.pt

S.-I. Ao et al. (eds.), *Transactions on Engineering Technologies*,
DOI 10.1007/978-981-10-1088-0_37

the former can be used in uncontrolled environments, under any lighting conditions and without line of sight to the receptor.

WBANs require small-sized wireless sensors that can be conveniently placed in the user's body, as well as low power consumption hardware and energy efficient protocols, in order to provide adequate battery lifetime [2]. Sensor nodes in a WBAN normally send the collected data to a central station, such as a personal computer, with capacity to process and store the data. With the technological advancement, smaller personal devices, such as smartphones, also started to become suitable for these tasks, with the advantage of greater portability.

The posture of an athlete during the cycling activity can dramatically influence his performance. Several studies in this area were made, either with elite athletes or amateur cyclists. The aero position, where the cyclist adopts a lowered position with the trunk almost horizontal and the arms extended forward with elbows tucked in, has the advantage of reducing the drag imposed by wind resistance. However, in [3], the authors conclude that the upright position allows higher VO2, ventilation, heart rate, and workload for untrained cyclists performing with maximal effort. Moreover, the upright position makes the cycling exercise less costly during steady state. In [4], the authors conclude that the posture has a very large effect on the performance of active cyclists during constant-load exercises.

Besides the trunk posture, the performance of cyclists can be affected if the angle of the knee is not the most correct. In [5], anaerobic tests were performed with trained and untrained cyclists. Results show that the seat should be adjusted to allow the leg to be flexed by 25–35° for untrained cyclists, in order to contribute to the prevention of injuries and increase the performance.

Mobile sensing is an attractive emerging area of research and development [6, 7] that uses sensor data collected by users' smartphones to extract relevant information. Some of these research works are applied to cycling, monitoring sensor data from the bicycle, the user's body or the environment [8–10].

BikeNet [8] is a project that performs the mapping of user experience based on various sensors adapted to a conventional bicycle using a network of wireless sensors based on the IEEE 802.15.4 standard. In order to provide the interface between the sensor network and a smartphone, this system uses an IEEE 802.15.4/Bluetooth gateway. Data collection focuses on parameters such as noise and carbon dioxide levels, speed, geographical location and user's stress level. The cyclist's posture is not monitored.

The Copenhagen Wheel project [9] developed a wheel that can be adapted in a conventional bicycle in order to turn it into an electric bike. An iPhone smartphone communicates with the central part of the wheel (hub) using Bluetooth, providing geographical location services and allowing the user to manually lock/unlock the bike, change the gear and adjust the level of actuation of the electric motor. This system does not collect any physiological data from the cyclist.

This chapter, which provides a revised and extended version of a previous paper [11], presents a system that allows the real-time monitoring of the posture of cyclists through the use of wireless sensor nodes placed on the body of the cyclists. The developed sensor nodes, which are composed by two boards (sensor module

and wireless module), send the collected data to an application developed for Android smartphones. The sensor module integrates 3-axis accelerometers, magnetometers and gyroscopes.

The wireless communication between the sensor nodes and the smartphone is based on Bluetooth Low Energy (BLE) [12], which is a wireless technology optimized for ultra-low power consumption, designed to be used on devices that have to operate for long periods without having to replace or recharge their batteries. BLE is a new technology that is currently only available on some recent smartphones. However, similarly to previous Bluetooth versions, the trend is for BLE to be integrated on most smartphones in the future. In contrast, IEEE 802.15.4/ZigBee [13, 14], which is an alternative low power wireless technology, generally lacks smartphone support.

This chapter is organized as follows: The next section provides a description of all the components of the developed system, including the hardware of the sensor nodes, the code implemented in the nodes and the smartphone application. Section 3 describes the process for calculating the relevant posture angles. In Sect. 4, experimental results are presented and discussed. Finally, Sect. 5 presents the conclusions.

2 Developed System

2.1 System Overview

The cycling posture monitoring system presented in this chapter is composed of two main physical components: a smartphone (central station) and multiple wireless sensor nodes on the body of the cyclist, which communicate using BLE, as shown in Fig. 1.

Fig. 1 Architecture of the developed cycling posture monitoring system

Each sensor node has the task of collecting raw posture data from the body segment where it is placed. The sensor node is composed by two boards: sensor module and wireless module. Each sensor module integrates three sensors: accelerometer, magnetometer and gyroscope, which generate data on each of the three axes: *x*, *y*, *z*. The accelerometer provides the inclination angle between the accelerometer position and the gravity field, the magnetometer provides the angular difference between its position and the magnetic field of the Earth, and the gyroscope compensates errors in the calculation through the detection of rotational movements.

In order to monitor the posture of cyclists, three sensor nodes are placed in the user's body: one on the chest, in order to measure the inclination of the trunk relative to the horizontal plane; one on the upper leg and one in the lower leg, to obtain the knee angle. In order to calculate the trunk angle (relative to the bicycle), it is necessary to measure the inclination of the bicycle. For this purpose, we chose to use the sensors integrated on the smartphone, which is placed on the bicycle handlebar, taking advantage of the available equipment and thus avoiding the use of another sensor node.

The raw data from the sensor modules are sent via BLE to the developed application on a BLE compatible (Bluetooth Smart Ready) smartphone. Besides performing the basic functions of a Bluetooth connection, the application is capable of calibrating the sensors and calculating the posture angles (pitch, roll and yaw) for each body segment based on the raw data. Based on this information, the application provides the trunk and knee angles of the cyclist. This posture information can be visualized on the application, stored on the smartphone, or sent to a remote computer in real-time using Wi-Fi or a mobile data connection.

2.2 Sensor Node Hardware

The wireless module of the sensor node, shown in Fig. 2a, is a Texas Instruments CC2540EM module, which contains a CC2540 SoC (System-on-Chip) [15], an external antenna, two 20-pin connectors that provide access to the pins of the CC2540, and auxiliary components. The CC2540 integrates, in the same chip, an 8051-based microcontroller with 8 kB RAM and 128 kB of flash memory and a BLE transceiver, which operates in the 2.4 GHz frequency band with a data rate of 1 Mbps. The current sensor node prototype is relatively large due to the size of the external antenna. However, the size of the sensor node can be easily reduced in the future with the use of a wireless module with integrated antenna, such as the Panasonic PAN1720. Since this module is also based on the CC2540 SoC, the same embedded code developed for this prototype could be used without the need of changes.

The top and bottom views of the developed sensor module are shown in Fig. 2b, c, respectively. Its three sensors are divided into two distinct units. The InvenSense MPU-6000 (Motion Processing Unit) contains an accelerometer, a gyroscope, a

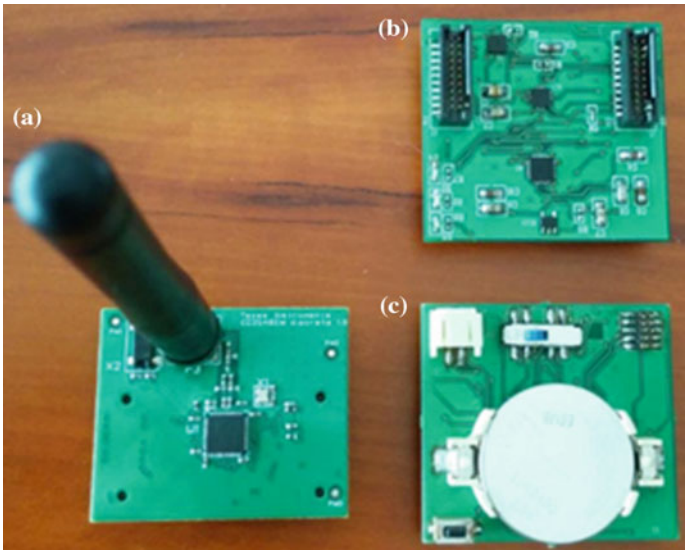

Fig. 2 Sensor node hardware: **a** Wireless module. **b** Sensor module *top* view. **c** Sensor module *bottom* view with the battery

digital motion processor (DMP) and an I2C bus. The accelerometer has a sample resolution of 16 bits, its range is programmable to ±2, ±4, ±8 or ±16 g and its output data rate can be between 4 Hz and 1 kHz. In this case, we used is a range of ±2 g, which provides a sensitivity of 61.0 μg/LSB. The I2C bus allows the MPU-6000 to access data from an external sensor, which in the case of this system is a Honeywell HMC5883L magnetometer. This high resolution magnetometer contains a 12-bit ADC which provides a resolution of 5 milligauss for a range of ±8 gauss, allowing between 1 and 2 degrees of compass precision.

Data acquisition from the sensors to the CC2540 was performed using the SPI (Serial Peripheral Interface) interface of the MPU-6000 chip.

2.3 Embedded Code

The code developed for the sensor nodes was based on the BLE protocol stack provided by Texas Instruments, version BLE-CC2540-1.3.2. In order to provide adequate communication between two BLE stations in the context of this system, we created a service to send periodic notifications from peripheral stations to the central station, i.e., from slaves to the master. This service is implemented in the peripheral station, which takes the role of GATT (Generic Attribute Profile) server, whereas the central station acts as GATT client.

The service created contains only one characteristic, whose value is a 20-byte data frame, and a descriptor (CCC—Client Characteristic Configuration) that activates the mode of periodic notification sending (0 × 0001). We used notifications instead of the indications because the former does not require further exchange of packets between the master and the slave after the data transmission for the acknowledgement, so the overhead is lower, making the transmission process more efficient. Figure 3 presents the flowchart of the data transmission process from the peripheral station to the central station.

This process starts at the BLEPeripheral_Init bloc, which is responsible for parameter initialization at the GAP layer with respect, for example, to the role of the device (in this case peripheral), definition of the advertising interval and initialization of the attributes of the GATT layer, more specifically the services implemented. In the next phase, BLEPeripheral_ProcessEvent processes all events that

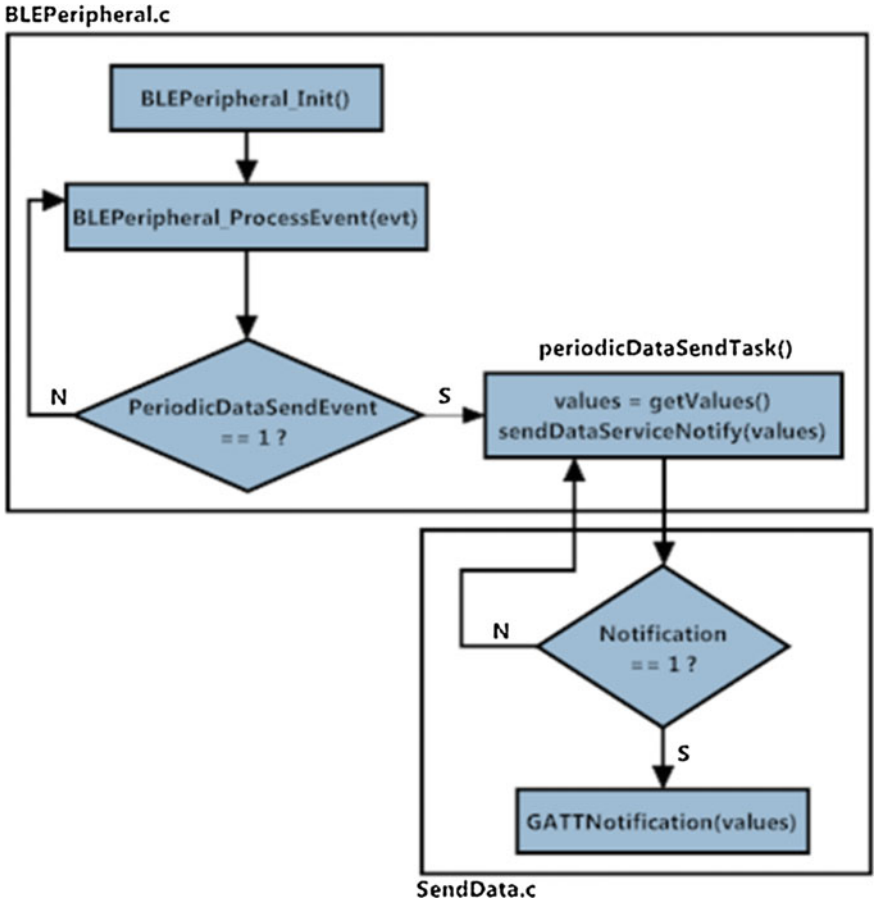

Fig. 3 Flowchart of the data transmission at the peripheral station

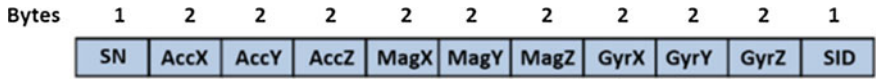

Fig. 4 Data frame payload of the BLE interface

are triggered. In the case of the firmware implemented, whenever an event concerning the periodic data transmission is detected the periodicDataSendTask block is called. This block is responsible to collect the values of the sensors, place them in the data frame payload and call the service created, SendDataServiceNotify. After verifying if notifications are enabled, this service calls the GATT_Notification function to send the information to the central station.

Data acquisition from the sensor module using SPI can be made using one of three different methods: polling of status bits, interrupt, or DMA [16]. Initially, the idea was to use the DMA controller of the BLE stack for data acquisition, but this controller defines a type of packet that does not match the format accepted by the MPU-6000. Therefore, we implemented a function, based on the method of polling of status bits, to read/write the data through SPI without resorting to the BLE stack.

After the acquisition of raw data from the sensors, the program constructs the payload of the data frame to be sent to the central station, which is shown in Fig. 4. Each sensor is sampled at 16 bits, which means that 2 bytes are required to represent the x, y and z values from each sensor, resulting in 18 bytes. Each frame includes also a sequence number (SN) and a sensor identifier (SID) to allow the smartphone application to properly identify the origin of the data from the different sensor nodes. Therefore, the length of the payload is 20 bytes, which corresponds exactly to the maximum allowed BLE payload, at application level, for transmission of notifications.

The sampling rate of the sensors modules was set to 30 Hz, which corresponds to a frame rate of 30 fps, a value typically used by motion capture applications [17]. The BLE connection interval parameter was set to 100 ms and the slave latency was set to zero, which means that each sensor generates three samples per 100 ms. Since it is not possible to send this amount of data in a single notification, each peripheral station has to send three notifications (data frames) per connection event.

2.4 Smartphone Application

The Android application was developed and tested using a Google Nexus 5 smartphone with Android v4.4 (KitKat). This application aims to monitor the posture of amateur or professional cyclists during training or competition. The smartphone assumes the role of central station and provides a user interface. It receives the sensor information collected from the monitored body segments and calculates the angles of the torso and knees and the inclination of the road in real-time, according to the process described in the next section. It has the capacity

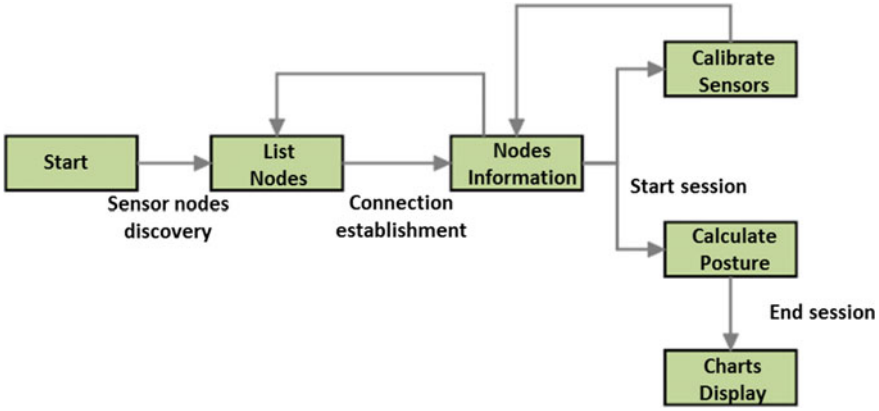

Fig. 5 Main blocks of the developed smartphone application

to store the data, display a chart of the monitored angles or forward the data to a remote computer. This application uses the Google BLE API, which has the advantage of compatibility with the majority of the most recent Android smartphones.

When started, the application begins the BLE device (sensor nodes) discovery process, and proceeds to the connection establishment. Once connected, it is possible to collect data from the sensor nodes. Once the nodes are calibrated and placed on the body, a training/competition session can be started. During a session, the values of the measured parameters referred in Sect. 3 are calculated in real-time and stored in the smartphone. The behavior of these parameters along the time can also be viewed through charts.

Figure 5 illustrates the main blocks of the developed smartphone application, which correspond to the Android activities.

The first block, "Start", corresponds to the main activity, and represents the initial screen of the application. The block titled "List Nodes" corresponds to the activity "DevicesList", which lists all sensor nodes found via BLE. After establishing the connection, the activity that provides the sensor nodes information is "InfoSensor", which corresponds to the "Nodes Information" block. The blocks "Calibrate Sensors" and "Calculate Posture" correspond to the activities "Calibrate" and "Posture", respectively. Finally, the "Charts Display" block, which comprises the activities "Results" and "Graph", allows the presentation of results regarding the posture calculation.

For the implementation of BLE technology in the application, as GATT client, we used a set of methods already available in a base application provided by Google through the Android Developers site. This base application consists of various BLE-related activities for discovery of compatible devices, establishment of connection to a GATT server, and receiving data in the form of notifications

(GATT notifications). The methods inherent to these tasks are included in a service called BluetoothLeService.

The BluetoothAdapter object is required in all activities that use Bluetooth. It represents the Bluetooth adapter (radio interface) of the device itself, and it is through this object that the Android application can interact with Bluetooth.

After activation of the Bluetooth interface, the device discovery process is done using the startLeScan() method from the BluetoothAdapter object. As the device discovery process is demanding in terms of energy consumption, it is automatically suspended after 4 s, which is enough time to find all the sensor nodes in this system. Anyway, a new scan can be performed by pressing the "Scan" button in the activity "DevicesList". This activity presents the name of each BLE device found, along with its MAC address.

The process of connection establishment between the GATT client and the GATT server is done using the connectGatt() method. This method returns an instance of BluetoothGatt object, which allows performing various client-side operations. The activity "InfoSensor" presents the data received from the sensor nodes, as well as the respective services and features that are supported by the GATT server, and communicates with the BluetoothLeService application service.

2.5 Sensor Modules Calibration

Before the sensor modules of the system are used for the first time, they require calibration. This process, which can be performed using the developed smartphone application, consists on obtaining the maximum and minimum readings of the accelerometer, magnetometer and gyroscope along the axes x, y and z, and storing them in a specific file. After that, the file becomes available to be used during the cycling activities, in order to normalize the raw sensor data for the calculation of the pitch, roll and yaw angles. Figure 6 shows the calibration screen of the activity "Calibration". For each axis, the current value is shown in black and the value stored when the respective button is pressed is shown in red. The gyroscope values are not being used; therefore its minimum and maximum values are not accurate.

3 Posture Calculation

The three angles that describe the orientation of each sensor node on the respective body segment are pitch, roll and yaw. Pitch and roll are calculated using the normalized vector of the accelerometer values for each axis (a_x, a_y, a_z), whereas yaw is obtained by the horizontal components (X_h and Y_h) of the Earth's magnetic field. The equations representing the pitch, roll and yaw are, respectively:

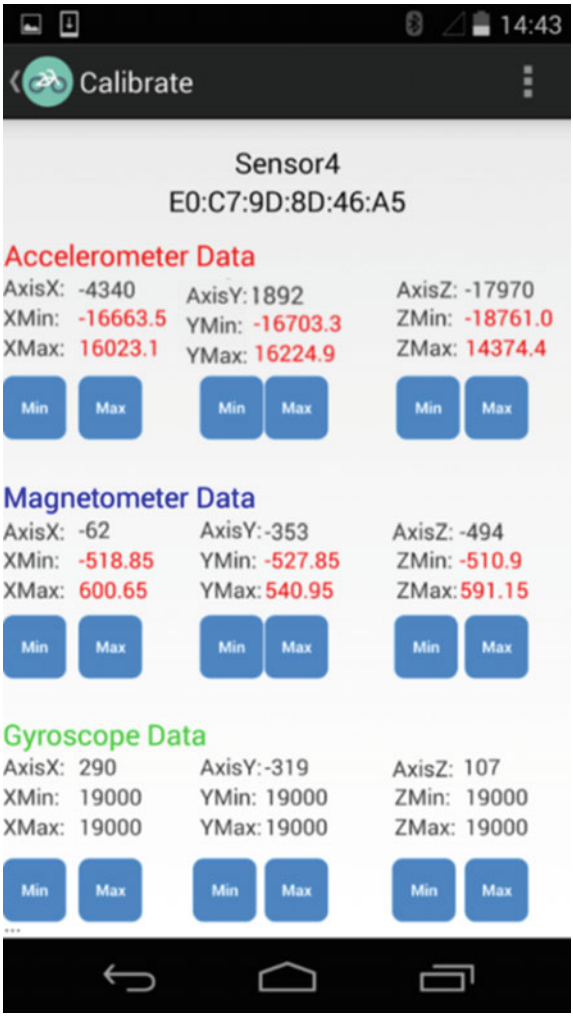

Fig. 6 Sensor calibration panel of the smartphone application

$$Pitch = arctan\left(\frac{a_y}{\sqrt{a_x^2 + a_z^2}}\right) \tag{1}$$

$$Roll = arctan\left(\frac{-a_x}{-a_z}\right) \tag{2}$$

$$\text{Yaw} = arctan\left(\frac{X_h}{Y_h}\right) \tag{3}$$

For the sensor node placed in the trunk, the pitch angle obtained in (1) provides the inclination of the trunk with respect to the horizontal plane. In order to obtain

the trunk angle with respect to the bicycle, it is necessary to calculate the difference between the pitch and the angle of inclination of the bicycle, which is measured with the smartphone placed on the handlebar. This angle is calibrated before the start of the cycling activity by placing the bicycle in a horizontal terrain and pressing a button in the application which sets the angle to zero.

The other two sensor nodes are used to measure the knee angle. For this purpose, one node is placed in the upper leg and the other is placed on the lower leg. The knee angle between these two body segments is given by (4).

$$A_{knee} = arccos \frac{\vec{V}_{upperLeg} . \vec{V}_{lowerLeg}}{\left\| V_{upperLeg} \right\| \left\| V_{lowerLeg} \right\|} \tag{4}$$

For the calculation of the orientation vectors $v_{upperLeg}$ and $v_{lowerLeg}$, the values of pitch, roll and yaw for both sensor nodes are calculated at each instant and multiplied by the rotation matrix in each axis. The rotation matrices for each axis are represented by $R_x(\alpha)$, $R_y(\theta)$ e $R_z(\tau)$ in (5), (6) and (7), respectively. α, θ e τ represent the angle of rotation about the x, y and z axis, respectively.

$$R_X(\alpha) = \begin{bmatrix} 1 & 0 & 0 \\ 0 & \cos\alpha & -\sin\alpha \\ 0 & \sin\alpha & \cos\alpha \end{bmatrix} \tag{5}$$

$$R_Y(\theta) = \begin{bmatrix} \cos\theta & 0 & \sin\theta \\ 0 & 1 & 0 \\ -\sin\theta & 0 & \cos\theta \end{bmatrix} \tag{6}$$

$$R_Z(\tau) = \begin{bmatrix} \cos\theta & -\sin\tau & 0 \\ \sin\tau & \cos\tau & 0 \\ 0 & 0 & 1 \end{bmatrix} \tag{7}$$

4 Results and Discussion

In order to verify the results of the measurement of the angles calculated by the developed system during cycling activities, three sensor nodes were placed on the appropriate parts of the body of an athlete, as shown in Fig. 7.

According to the convention adopted in this chapter, the inclination of the bicycle during a climb corresponds to a positive angle, whereas during a descent this angle has negative values. Regarding the trunk angle, a forward reclining means positive values and reclining back generates negative values. The knee angle has a value of 180° when the leg is fully extended, and as the cyclist bends the leg, the value of this angle decreases.

Fig. 7 Sites of placement of the sensors on the athlete's body: torso (*left*) and leg (*right*)

In order to assess if the trunk angle with respect to the bicycle remains the same regardless of the inclination of the bicycle, a scenario where this inclination changes with time was tested. During the first seconds, the athlete's torso is upright and the bicycle is in a horizontal terrain. Then the athlete bends the torso forward 40°, keeping this position in relation to the bicycle until the end of the test, while the bicycle follows its route on the terrain, first uphill and then downhill. As Fig. 8 shows, the trunk angle remained the same regardless of the positive and negative variations on the angle of inclination of the bicycle.

In order to evaluate the variation of the knee angle during a cycling activity, a second test was performed in a scenario where the athlete maintains an aerodynamic position in a horizontal terrain. The seat height in relation to the height of the pedals is an important factor to ensure maximum performance. The goal is that the athlete does not fully stretch his legs or otherwise bends them too much while pedaling.

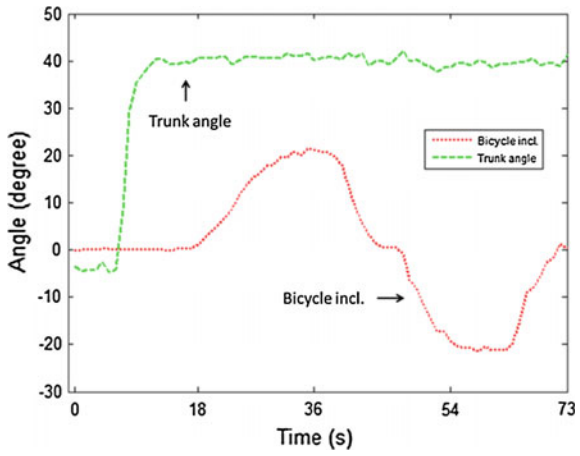

Fig. 8 Measurements of the trunk angle with variations on the angle of inclination of the bicycle along the time

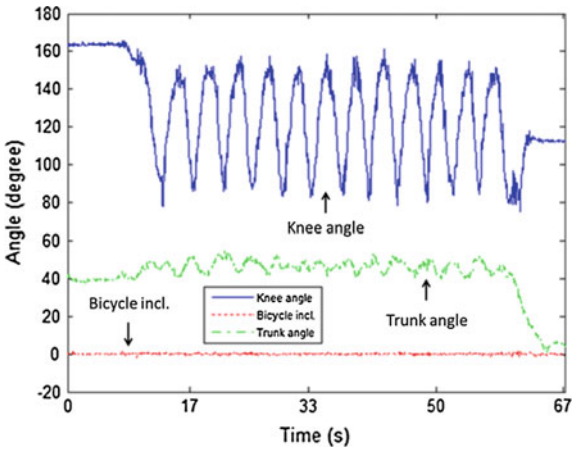

Fig. 9 Measurements of the knee and trunk angle while resting and pedaling on a horizontal terrain

Figure 9 presents the results of this test. Initially, without pedaling and with the leg almost fully extended, the knee angle has a value close to 160°. After 8 s the athlete starts pedaling and the knee angle oscillates between 80 and 150° until the athlete stops pedaling. During this time, the measured values for trunk angle are around 40 to 50°. There is some variation in this angle during the test due to the effort exerted by the athlete during pedaling.

5 Conclusion and Future Work

Cycling performance is significantly affected by the body posture. This chapter proposed a system that monitors the posture of cyclists in real-time through the use of sensor nodes placed on the user's body, which send the raw data via BLE to an Android smartphone, where it is processed in order to extract the posture angles. Unlike posture measurement systems based on cameras, this system does not require line of sight or controlled lighting conditions. Due to its portability, it can be used either by amateur or professional athletes, during training or competition.

Currently, the gyroscopes of the sensor modules are not being used. Their data are acquired via SPI and are received the application, but are not used along with the accelerometer and magnetometer readings in the calculations. In the future the gyroscope readings may be used to compensate eventual measurement errors, in order to contribute to enhance the accuracy in the calculation of the posture.

In the future this system will be integrated into another developed Android application [18] which provides a georeferenced database with measurements of several relevant cycling parameters, such as route, velocity, torque, cadence, power output and heart rate, and offers the functionalities of visualization current and past routes in a map, share data with friends, join or create events, and locate friends.

The data collected by this application may be uploaded to a remote database, where it can be accessed later using the mobile app or a web browser.

When used with electric bicycles (EBs), this system may be enhanced to allow the automatic control of the effort exerted by the cyclist [19]. The developed system may also be integrated in a mobile cockpit application [20] that provides useful personalized information to the cyclist related with the EB's use, including EB range prediction and information regarding available public transport.

Acknowledgment This work has been supported by FCT (Fundação para a Ciência e Tecnologia) in the scope of the project: UID/EEA/04436/2013.

References

1. Patel M, Wang J (2010) Applications, challenges, and prospective in emerging body area networking technologies. IEEE Wirel Commun 17(1):80–88
2. Chen M, Gonzalez S, Vasilakos A, Cao H, Leung VCM (2011) Body area networks: a survey. Mob Netw Appl 16(2):171–193
3. Ashe MC et al (2003) Body position affects performance in untrained cyclists. Br J Sports Med 37(5):441–444
4. Egaña M, Green S, Garrigan EJ, Warmington S (2003) Effect of posture on high-intensity constant-load cycling performance in men and women. Eur J Appl Physiol 96(1):1–9
5. Peveler W, Pouders J, Bishop P (2007) Effects of saddle height on anaerobic power production in cycling. J Strength and Condition Res 21(4):1023–1027
6. Khan WZ, Xiang Y, Aalsalem MY, Arshad Q (2013) Mobile phone sensing: a survey. IEEE Commun Surv Tutorials 15(1):402–427
7. Lane ND et al (2010) A survey of mobile phone sensing. IEEE Commun Mag 48(9):140–150
8. Eisenman SB et al (2009) BikeNet: a mobile sensing system for cyclist experience mapping. ACM Trans Sens Netw 6(1):1–39
9. Outram C, Ratti C, Biderman A (2010) The Copenhagen Wheel: an innovative electric bicycle system that harnesses the power of real-time information and crowd sourcing. In: Proceedings of EVER'2010, Monaco, Mar 2010
10. Walker W, Aroul ALP, Bhatia D (2009) Mobile health monitoring systems. In: Proceedings of the 31st annual international conference of the IEEE EMBS, pp 5199–5202. Minneapolis, Minnesota, USA, Sept 2009
11. Maio A, Afonso JA (2015) Wireless cycling posture monitoring based on smartphones and bluetooth low energy. In: Lecture notes in engineering and computer science: proceedings of the world congress on engineering 2015, WCE 2015, pp 653-657. London, UK, 1–3 July 2015
12. Gomez C, Oller J, Paradells J (2012) Overview and evaluation of Bluetooth low energy: an emerging low-power wireless technology. Sensors 12(9):11734–11753
13. IEEE Std 802.15.4-2006 (2006) Part 15.4: wireless medium access control (MAC) and physical layer (PHY) specifications for low-rate wireless personal area networks (WPANs), 2006
14. Mihajlov B, Bogdanoski M (2011) Overview and analysis of the performances of ZigBee-based wireless sensor networks. Int J Comput Appl 29(12):28–35
15. Texas Instruments Datasheet (2013) 2.4-GHz bluetooth low energy system-on-chip, CC2540F128, CC2540F256, June 2013
16. Johnsrud S, Sundet T (2009) CC111xFx, CC243xFx, CC251xFx and CC253xFx SPI. Design Note DN113, Texas Instruments, 2009

17. Moeslund TB, Hilton A, Kruger V (2006) A survey of advances in vision-based human motion capture and analysis. Comput Vis Image Underst 104:90–126
18. Oliveira DS, Afonso JA (2015) Mobile sensing system for georeferenced performance monitoring in cycling. In: Lecture notes in engineering and computer science: proceedings of the world congress on engineering 2015, WCE 2015, pp 269–273. London, UK, 1–3 July 2015
19. Afonso JA, Rodrigues FJ, Pedrosa D, Afonso JL (2015) Automatic control of cycling effort using electric bicycles and mobile devices. In: Lecture notes in engineering and computer science: proceedings of the world congress on engineering 2015, WCE 2015, pp 381–386. London, UK, 1–3 July 2015
20. Ferreira JC, Monteiro V, Afonso JA, Afonso JL (2015) Mobile cockpit system for enhanced electric bicycle use. IEEE Trans Industr Inf 11(5):1017–1027

Reducing Power Consumption of Wireless Sensor Networks Using Double Pseudo-coded Pilot Periods to Detect Collided Packets

Fawaz Alassery, Walid K.M. Ahmed and Victor Lawrence

Abstract Power conservation algorithms play very important role in order to extend the lifetime of WSN nodes, where typically such algorithms attempt at saving power by applying the power saving technique at either the transmitter or the receiver side. In this context, this paper represents a receiver approach for alleviating power consumption of WSNs. Unlike other power consumption techniques, instead of decoding every received signal at the receiver which consume too much power our technique is based on studying received packets at a sink node (a receiver), so it can make a fast decision to detect a collision without the need for full-decoding of received packets. In our technique, the receiver can determine when the transmitted signals can be decoded without wasting precious power decoding transmitted signals suffering from collisions. We present a complexity and power-saving comparison between our novel technique and conventional full-decoding (for a select coding scheme) to demonstrate the significant power and complexity saving advantage of our technique. In addition, we also demonstrate how to tune various design parameters in order to allow a system designer multiple degrees of freedom for design trade-offs and optimization.

Keywords Efficient techniques in WSNs · Low complexity protocols · Packets collision · Pilot periods transmission · Power consumption techniques · WSN protocols

F. Alassery (✉)
Computer Engineering Department, Taif University, Taif,
Makkah al-Mukarramah Region, Saudi Arabia
e-mail: falasser@tu.edu.sa

W.K.M. Ahmed (✉) · V. Lawrence (✉)
Electrical and Computer Engineering Department,
Stevens Institute of Technology, Hoboken, NJ 07037, USA
e-mail: walidmail@yahoo.com

V. Lawrence
e-mail: victor.lawrence@stevens.edu

S.-I. Ao et al. (eds.), *Transactions on Engineering Technologies*,
DOI 10.1007/978-981-10-1088-0_38

1 Introduction

In wireless networks the most popular strategies to deal with packet collisions use the combination between carrier sensing and collision avoidance. In carrier sensing, all nodes in the network share the same transmission medium, a node starts with listening to the medium before transmitting its own packets in a pre-specified time period, which is determined by an access point (e.g. a central node in WSNs). If the state of the transmission medium is busy, a node takes a random bakeoff time and then continues transmitting its packets in order to avoid collisions with other nodes which are listening and contending for the medium as well. However, when the collision avoidance fails to detect corrupted packets, network resources such as the channel bandwidth and the system throughput will be wasted and decreased respectively due to the fact that some corrupted packets are still transmitted in their entirety. This situation may exacerbate since the rate of collision may increase with increasing the number of transmitters (e.g. sensors which have packets ready to transmit) [1].

There are various sources of overhead power consumption in WSNs. For example, sensor nodes consume power when in idle mode, i.e., waiting and listening for packets to be received, but not transmitting. Another cause for overhead energy loss in WSNs is the reception of packets which are not addressed to a node, and re-transmission of control packets, which is considered as protocol overhead. One of the main sources of overhead power consumption in wireless sensors, which is the focus of this paper, is collision detection. When multiple sensors transmit at the same time, their transmitted packets collide at the central node (a receiver) [2]. However, until the central node has expended the required power and processing-time to detect the received packet, it wouldn't know that the packet is invalid and corrupted due to collision [3].

In this paper, we propose a suite of novel, yet simple and power-efficient technique to detect a collision without the need for full decoding of the received packet. Our novel approach aims at detecting collision through fast examination of a short snippet of the received packet via a relatively small number of computations over a small number of received IQ samples. Hence, operating directly at the output of the receiver's analog-to-digital-converter (ADC) and eliminating the need to pass the signal through the entire demodulator and decoder line-up. Accordingly, our novel technique not only reduces processing complexity and hence power consumption, but it also reduces the latency (or delay) incurred to detect a collision since it operates on only a small number of samples in the beginning of a received packet instead of having to buffer and process the entire packet as is the case with a full-decoding approach. In addition, we show that with a relatively short measurement period, our technique can achieve low False-Alarm and Miss probabilities, resulting in a reliable collision-detection mechanism. We also demonstrate how to tune various design parameters in order to allow a system designer multiple degrees of freedom for design trade-off and optimization.

For the remainder of this paper, we shall refer to our proposed technique as the "Pilot Periods, or PP" method. We shall also refer to the traditional full-decoding methods as "FD" methods.

The remainder of this paper is organized as follows. Section two investigates related works. Section three describes our proposed system. In section four we define the technique. In section five, we compare the computational complexity of our technique against commonly used full decoding technique (i.e. Max-Log-Map Algorithm). In section six, we discuss the results of the simulations used to model our system for different scenarios. Finally, we offer our conclusions in section seven.

2 Related Works

Some coding schemes that benefit from traditional communication networks may not perform well in WSN's [4]. For example, LDPC codes have been attracting a great deal of research interest in WSN's [5]. LDPC codes can be decoded either with soft-decision or hard-decision decoding algorithms which have low computational complexity (less number of real operations) in comparison with equivalent Viterbi algorithm [5]. Soft-decision decoding in LDPC codes implemented by iterative decoding based on Brief Propagation (BP) algorithm. However, the implementation of BP algorithms in WSN's is still restricted due to the computational complexity as well as consuming power for check nodes, which are responsible for decoding packets (e.g. central nodes) [6].

Most full decoding algorithms entail going through the entire complex receiver's front-end digital processing (e.g., for RF impairment correction …etc.) and modem demodulation, synchronization and decoding processing only to discover that the received packet has been corrupted by collision. Therefore, current collision detection mechanisms have largely been revolving around direct demodulation and decoding of received packets and deciding on a collision based on some form of a frame error detection mechanism, such as a CRC check. The obvious drawback of full detection of a received packet is the need to expend a significant amount of energy and processing complexity in order to fully-decode a packet, only to discover the packet is illegible due to a collision. These facts would contradict the critical design goal of WSN's which have limited power recourses.

3 System Description

We assume a WSN where a number of intermediate sensors are deployed arbitrarily to perform certain functionalities including sensing and/or collecting data and then communicating such information to a central (access) sensor node. The central node may process and relay the aggregate information to a backbone network.

There are N wireless sensors that communicate to the central sensor node, where at any point in time, multiple sensors may accidentally transmit simultaneously and cause a collision. Without loss of generality, we shall assume for the sake of argument that one sensor is denoted a "desirable" sensor, while the rest of the colliding sensors become "interferers".

A commonly accepted model for packet arrivals, i.e., a packet is available at a sensor and ready to be transmitted, is the well-known Bernoulli-trial-based arrival model, where at any point in time, the probability that a sensor has a packet ready to transmit is P_{Tr}.

The actual design details and choice of the multiple access mechanism, e.g., slotted or un-slotted Aloha, are beyond the scope of this paper and irrelevant to the specifics of the techniques proposed herein.

Upon the receipt of a packet, the central node processes and evaluates the received packet and makes a decision on whether the packet is a collision-free (good) or has suffered a collision (bad). In this paper, we propose a suite of fast collision detection techniques where the central node evaluates the statistics of the received signal's IQ samples at the output of the receiver's analog-to-digital converter (ADC) directly using simple discrimination metrics, as will be explained in more detail in the following section, saving the need to expend power and time on the complex modem line-up processing (e.g., demodulation and decoding). If the packet passes the discrimination metric test, it is deemed collision-free and undergoes all the necessary modem processing to demodulate and decode the data. Otherwise, the packet is deemed to have suffered a collision, which in turn triggers the central node to issue a NACK message per the mechanism and rules mandated by the specific multiple-access scheme employed in the network.

4 Technique Description

Let's define the kth received signal (complex-valued) IQ sample at the access node as [10]:

$$y_k = x_{0,k} + \sum_{m=1}^{N-1} x_{m,k} + n_k$$

where

$$y_k = y_{k,I} + jy_{k,Q}, \quad j = \sqrt{-1},$$
$$x_{0,k} = x_{0,k,I} + jx_{0,k,Q}$$

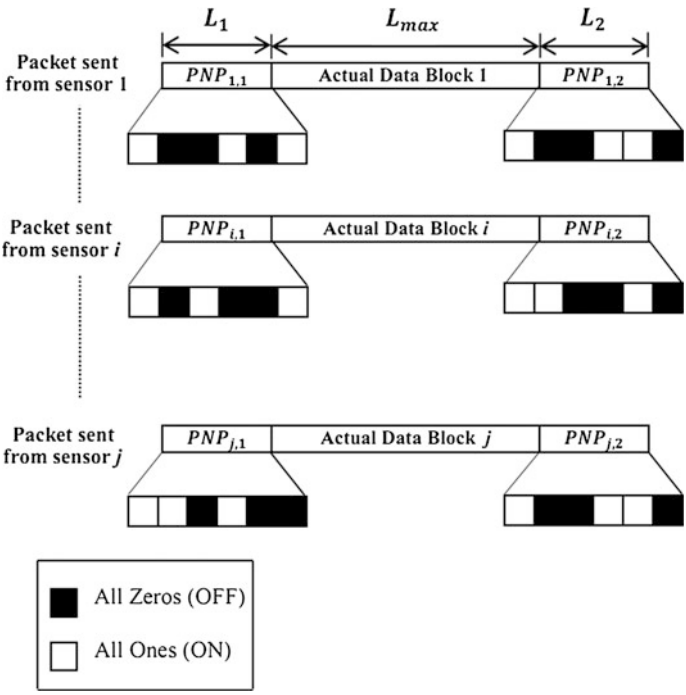

Fig. 1 Example of a packet structure for the double pseudo-coded ON-OFF pilot periods

is a complex-valued quantity that represents the k^{th} IQ sample component contributed by the desired sensor, while

$$x_{m,k} = x_{m,k,I} + jx_{m,k,Q}; \quad m = 1, \ldots, N-1$$

is the kth IQ sample component contributed by the mth interfering (colliding) sensor. Finally, $n_k = n_{k,I} + jn_{k,Q}$ is a complex-valued Additive-White-Gaussian Noise (AWGN) quantity (e.g., thermal noise).

We propose three time-averaging statistical discrimination (SD) metrics that are applied to the envelope value, $|y_k| = \sqrt{y_{k,I}^2 + y_{k,Q}^2}$, of the received IQ samples at the central node. Our approach is based on double pseudo-coded ON-OFF Pilot Periods (PP) transmission per packet. Figure 1 depicts a pictorial illustration of the packet structure for the double pilot periods scheme. In our PP technique we assume the following:

- A distinct sequence per sensor. That is, $PNP_{i,1} \neq PNP_{j,1}$ and $PNP_{i,2} \neq PNP_{j,2}$; $i \neq j$.
- $PNP_{j,1}$ and $PNP_{j,2}$ must have the same duty-cycles (i.e. D_1 and D_2 respectively) for all 1 $1 \leq j \leq N$.

- The length of the actual data block is L_{max}, the length of the first pilot period ($PNP_{j,1}$) is L_1, and the length of the second pilot period ($PNP_{j,2}$) is L_2.
- L_1 is divided into v_1 slots which include v_{Z_1} all zeros slots and v_{O_1} all ones slots, i.e., we assume the same ratio of v_{Z_1} to v_{O_1}, i.e. 50 %, as well as different ratio, e.g., 30, 40 %, etc.
- L_2 is divided into v_2 slots which include v_{Z_2} all zeros slots and v_{O_2} all ones slots, i.e., we assume the same ratio of v_{Z_2} to v_{O_2}, i.e. 50 %, as well as different ratio, e.g., 30, 40 %, etc.
- Each slot in the first and second pilot period has the same number of samples, i.e., $\omega_1\omega_1$ and ω_2 respectively. Accordingly, we evaluate different length of L_1 and L_2 based how many v, d, ω_1 and ω_2 (i.e. $L_1 = v \times \omega_1$ and $L_2 = d \times \omega_2$). In our design we try to minimize L_1 and L_2 as much as possible and ensure the SD approach would still work reliably (i.e. short pilot periods). For example, we assume $v = 8$ slots/period, d = 7 slots/period, $\omega_1 = 2$ samples/slot and $\omega_2 = 3$ samples/slot, so $L_1 = 16$ samples/period and $L_2 = 21$ samples/period. (It can be tuned as required by a designer).
- The central node is aware of what transmitted $PNP_{j,1}$ and $PNP_{j,2}$ periods to expect for each sensor.
- We evaluate various "soft" decision percentages when decoding the pilot periods at the central node (i.e.$\aleph_1$ and $\aleph_2$ for the first and second pilot periods respectively). We quantify the effect and performance versus different $\aleph_1$ and $\aleph_2$ such as 60,70 and 90 % (it can be tuned as required by a designer).
- The relative power is assumed to be the average power for the actual data block to the average power for the pseudo-coded ON-OFF pilot periods. It can be defined as:

$$\eta_{Pilot} = \frac{\left(\frac{1}{L_{max}} \sum_{i=L_1+1}^{L_1+L_{max}} P_i\right)}{\left(\frac{1}{L_1} \sum_{j_1=1}^{L_1} P_{j_1} + \frac{1}{L_2} \sum_{j_2=L_1+L_{max}+1}^{L_1+L_{max}+L_2} P_{j_2}\right)} \tag{1}$$

$$P_i = \left|y_{k_i}^2\right|^2; \quad i = L_1+1, L_1+2, \ldots, L_1+L_{max}$$

$$P_{j_1} = \left|y_{k_{j_1}}^2\right|^2; \quad j_1 = 1, 2, \ldots, L_1$$

$$P_{j_2} = \left|y_{k_{j_2}}^2\right|^2; \quad j_2 = L_1+L_{max}+1, L_1+L_{max}+2, \ldots, L_1+L_{max}+L_2$$

In the double pilot periods approach, the central node needs to decode (i.e. through Maximum Likelihood (ML) detection [7]) both pilot sequences for each received packet and compare them with the pre-stored look-up table (code-book) of all the valid sequences (i.e. δ_1 and δ_2 for the first and second pilot periods respectively). If the sequence of the first decoded pilot period match $\aleph_1$ (or more) of any pre-stored sequence (δ_1) and the second decoded pilot period match $\aleph_2$ (or more) of any pre-stored sequence (δ_2), then the received packet is a collision-free packet, and vice versa.

Now, for a collision-free packet, the relative power (η_{Pilot}) is compared with a pre-specified threshold value that is set based on a desired Signal-to-Interference-plus-Noise Ratio (*SINR*) cut-off assumption, $SINR_{cut\_off}$. For the pre-specified threshold level (γ), we generate a 100,000 Monte-Carlo simulated snapshots of interfering sensors where for each snapshot we compute the PP approach value (i.e. η_{Pilot}) for the received *SINR* and compare it with various threshold levels.

That is a system designer pre-evaluates the appropriate threshold value that corresponds to the desired $SINR_{cut\_off}$. If η_{Pilot} is higher than the threshold value, then the PP scheme value reflects a SINR that is less than $SINR_{cut\_off}$ and the packet is deemed not usable, and vice versa. Accordingly, a "False-Alarm" event occurs if the received SINR is higher than $SINR_{cut\_off}$ but the PP scheme erroneously deems the received SINR to be less than $SINR_{cut\_off}$. On the other hand, if the PP scheme deems the SINR to be higher than $SINR_{cut\_off}$ while it is actually less than $SINR_{cut\_off}$, a "Miss" event is encountered. Miss and False-Alarm probabilities directly impact the overall system performance as will be discussed in the following sections. Therefore, it is desired to minimize such probabilities as much as possible.

In the following we show how to decode the double pseudo-coded ON-OFF pilot periods through the Maximum Likelihood (ML) detection. Let the transmitted block be x_k; $k = (1, 2, \ldots, L_1)$, $(L_1 + 1, \ldots, L_1 + L_{max})$, $(L_1 + L_{max} + 1, \ldots, L_1 + L_{max} + L_2)$ and the received block be y_k; $k = (1,2,\ldots, L_1)$, $(L_1 + 1, \ldots, L_1 + L_{max})$, $(L_1 + L_{max} + 1, \ldots, L_1 + L_{max} + L_2)$. As mentioned earlier, the kth received signal (complex-valued) IQ sample at the central node is:

$$y_k = x_{0,k} + \sum_{m=1}^{N-1} x_{m,k} + n_k$$

where $x_{0,k}$ is a complex-valued quantity that represents the kth IQ sample component contributed by the desired sensor, while $x_{m,i}$ is the kth IQ sample component contributed by the mth interfering (colliding) sensor. Finally, n_k is a complex-valued Additive White Gaussian Noise (AWGN) quantity. Accordingly, the channel transition probability density function (pdf) $P(y_k|x_k)$ is:

$$P(y_k|x_k) = \frac{1}{(2\pi\sigma^2)^{L_2}} \exp\left(-\frac{1}{2\sigma^2}\sum_{k=1}^{L_2}|y_k - x_k|^2\right) \tag{2}$$

Hence, ML detection algorithm needs to maximize $P(\bar{y}_{k_1} \mid \bar{x}_{k_1})$ and $P(\bar{y}_{k_2} \mid \bar{x}_{k_2})$ for the first and second pilot periods respectively similar to that defined in (2) for all received packets, where in this case $\bar{y}_{k_1}$ is the vector for the first pilot period received by the central node, and $\bar{x}_{k_1}$ is the vector for the first pilot period transmitted by a sensor, $\bar{y}_{k_2}$ is the vector for the second pilot period received by the central node, and $\bar{x}_{k_2}$ is the vector for the second pilot period transmitted by a sensor. Equivalently, ML detector can maximize the log-likelihood function for both pilot periods as follows:

$$\mathcal{F}_{r_1} \propto (\mathrm{P}(\bar{y}_{k_1}|\bar{x}_{k_1})) = -\sum_{k=1}^{L_1} |\bar{y}_{k_1} - \bar{x}_{k_1}|^2$$

$$\mathcal{F}_{r_2} \propto (\mathrm{P}(\bar{y}_{k_2}|\bar{x}_{k_2})) = -\sum_{k=L_1+L_{max}+1}^{L_2} |\bar{y}_{k_2} - \bar{x}_{k_2}|^2$$

The following procedures implement the ML detection for our proposed double pseudo-coded ON-OFF pilot periods approach:

1. Start with $k_1 = 1$ and $k_2 = 2$.
2. Calculate

$$\mathcal{F}_{r_1} = -\sum_{k=1}^{L_1} |\bar{y}_{k_1} - \bar{x}_{k_1}|^2 \quad \text{and} \quad \mathcal{F}_{r_2} = -\sum_{k=L_1+L_{max}+1}^{L_2} |\bar{y}_{k_2} - \bar{x}_{k_2}|^2$$

3. Store $\mathcal{F}_{r_1}$ and $\mathcal{F}_{r_2}$.
4. Increment k_1 and k_2 by one.
5. If $k_1 = L_1 + 1$ and $k_2 = L_2 + 1$ go to step 7.
6. Go to step 2.
7. Find the sequences that correspond to the largest $\mathcal{F}_{r_1}$ and $\mathcal{F}_{r_2}$ and declare them as the detected sequences (i.e. $PNP_{j,1}$ and $PNP_{j,2}$).

As mentioned earlier, if the sequences $PNP_{j,1}$ and $PNP_{j,2}$ match $\aleph_1$ and $\aleph_2$ (or more) of any pre-stored sequences δ_1 and δ_2 respectively, then the corresponding received packet is declared as a collision free packet. For the collision free packet, η_{Pilot} is compared with a pre-specified threshold level (i.e. set based on $SINR_{cut\_off}$) in order to analyze packets' statistics (i.e. False-Alarm and Miss probabilities).

5 Power Saving and System Throughput Analysis

To analyze the power saving of our proposed PP system we introduce the following computational complexity metrics:

$$F_B = S + P_{miss}F \tag{3}$$

$$F_G = S + (1 - P_{FA})F \tag{4}$$

In above formulas, S is the number of computational operations incurred in our proposed approach, while F is the number of computational operations incurred in a full-decoding approach, P_{miss} and P_{FA} are the probabilities of Miss and False-Alarm events respectively. Hence, F_B represents the computational complexity for the case where the central node makes a wrong decision to fully-decode the received packet (i.e., declared as a collision-free packets) while the packet should has been rejected

(i.e., due to collision). On the other hand, F_G is the computational complexity for the case where the central node makes a correct decision to fully decode received packet.

In addition, and for the comparison purposes, we introduce the following formulae in order to compare the computational complexity saving achieved by our proposed PP approach (i.e. T_{PP}) over the FD approach (i.e. T_{FD}):

$$T_{PP} = F_B P_{collision} + F_G P_{no\_collision} \tag{5}$$

$$T_{FD} = F \tag{6}$$

In above formulae, $P_{collosion}$ and $P_{no\_collosion}$ are the probabilities of collision and no-collision events respectively. $P_{collosion}$ and $P_{no\_collosion}$ have been obtained via Monte-Carlo simulation as follows: A random number of interfering sensors (maximum of 30 sensors) is generated per a simulation snapshot, where each sensor is assumed to have a randomly received power level at the access node (to reflect a random path loss/location effect). The generation of the interfering sensors is based on a Bernoulli trial model where it is assume that the probability of a packet available for transmission at a sensor (hence the existence/generation of the sensor for the snapshot at hand) is equal to α. If the total SINR is found to be worse than the cut-off limit, a collision is assumed and vice versa. For our numerical example in this section we used $\alpha = 0.3$ and $SINR_{cut\_off} = 5$ dB. Also, we typically generate more than 100,000 snapshots in order to achieve a reliable estimate of the collision probabilities. For the aforementioned choices of α and $SINR_{cut\_off}$, we found the collision probabilities to be $P_{collosion} = 0.3649$ and $P_{no\_collosion} = 0.6351$.

5.1 Comparing with Full Decoding

In order to assess the computational complexity of our PP scheme, we first quantize our metrics calculation in order to define fixed-point and bit-manipulation requirement of such calculations. We also assume a look-up table (LUT) approach for the logarithm calculation. Note that the number of times the algorithm needs to access the LUT equals the number of IQ samples involved in the metric calculation. Thus, our algorithm only needs to perform addition operations as many times as the number of samples. Hence, if the number of bits per LUT word/entry is equal to M at the output of the LUT, our algorithm needs as many M-bit addition operations as the number of IQ samples involved in the metric calculation.

As a case-study, we compare the complexity of our PP scheme with the complexity of a FD algorithm assuming a Max-Log-Map Algorithm. Max-Log-Map has been an attractive choice for WSNs [8]. Authors in [9] measure the computational complexity of Max-Log-Map (per information bit of the decoded codeword) based on the size of the encoder memory. It has been shown in [9] that for a memory length of λ, the total computational complexity per information bit can be estimated as:

$$F_{\text{Max\_Log-MAP}} = 15 \times 2^{\lambda} + 17 \tag{7}$$

In contrast, our PP system does not incur such complexity related to the size of the encoder memory. In addition, our PP system avoids other complexities required by a full decoding such as time and frequency synchronization, Doppler shift correction, fading and channel estimation, etc., since our SD scheme operates directly at the IQ samples at the output of the ADC "as is". Finally, the FD approach requires buffering and processing of the entire packet/codeword while our PP scheme needs only to operate on a short portion of the received packet.

Now let's compute the computational complexity for our SD approach. Let's assume that the IQ ADCs each is D bits. Also, let's assume a $(\cdot)^2$ operation is done through a LUT approach to save multiplication operations. In addition, let's also assume that the square-root, $\sqrt{\cdot}$, is also done through a LUT approach. Hence, each of the I^2 and Q^2 operations consume of the order of D bit-comparison operations to address the $(\cdot)^2$ LUT. Then, if the output of the LUT is G bits, it follows that we need about G bit additions for an $I^2 + Q^2$ operation. Let's assume that the $\sqrt{\cdot}$ LUT has G bits for input addressing and K output bits. Then, we need about $G + 1$ bit-comparison operations to address the $\sqrt{\cdot}$ LUT. Finally, for simplicity, let's assume that a bit comparison operation costs as much as a bit addition operation. Accordingly, the total number of operations needed to compute the $\left(\sqrt{I^2 + Q^2}\right)$ for one IQ sample is:

$$2D + G + (G + 1) = 2D + 2G + 1 \tag{8}$$

However, our approach is based on calculating the power for the pilot periods and the actual data period per packet. So, the total number of operations needed to compute the $(I^2 + Q^2)$ for one IQ sample (E) is:

$$E = 2D + G \tag{9}$$

If we assume the IQ over-sampling rate (OSR) to be Z (i.e., we have Z samples per information symbol), then we need about $Z \times G$ bit additions to add the Z $(I^2 + Q^2)$ values for every information symbol. Hence, for one information symbol, we need a total of:

$$(2D + G) \times Z + Z \times G = (2D + 2G)Z \tag{10}$$

Now if we assume an M-ary modulation (i.e., $\log_2(M)$ information bits are mapped to one symbol), then the computational complexity per information bit can be computed as:

$$S/\text{InfoBit} = \frac{(2D + 2G)Z}{\log_2(M)} \tag{11}$$

For example, in order to show the complexity saving of our SD scheme, let's assume a QPSK modulation scheme ($M = 4$). Also, let's assume $Z = 2$ (2 samples per symbol), and $D = G = 12$ bits, which represents a good bit resolution. Also, let's assume a memory size of $\lambda = 4$ for the Max-Log-MAP. Using the formulae (7), it follows the Max-Log-MAP FD algorithm costs 257 operations per an information bit, while our PP scheme based on formula (11) costs only 48 operations per an information bit, which represents an 81 % saving on the computational complexity.

In addition, in a no-collision event, the PP scheme check would represent a processing overhead. Nonetheless, our PP approach still provides a significant complexity saving over the FD scheme as demonstrated by the following example. Table 1 in the Appendix shows the probability of Miss and False-Alarm to be 0.0313 and 0.0315, respectively for QPSK, $\aleph_1 = \aleph_2 = 70\ \%$, and a 50 bits measurement period. Now, based on formulae (3) and (4), F_B and F_G (per information bit) for our PP approach will equal:

$$\begin{aligned} F_B &= S + P_{miss} F_{\text{Max}-\text{Log}-\text{MAP}} = 48 + 0.0313 \times 257 \\ &= 56 \text{ Operations/Info Bit} \\ F_G &= S + (1 - P_{FA}) F_{\text{Max}-\text{Log}-\text{MAP}} = 48 + (1 - 0.0315) \times 257 \\ &= 296 \text{ Operations/Info Bit} \end{aligned}$$

For the comparison purposes between our PP approach and FD algorithms (i.e. the Max-Log-MAP algorithm), formulae (5) and (6) are used to find the computational complexity when no-collision is detected:

$$\begin{aligned} T_{PP} &= F_B P_{collosion} + F_G P_{no\_collosion} \\ &= 56 \times 36.49\ \% + 296 \times 63.51\ \% = 208 \text{ Operations/Info Bit} \\ T_{FD} &= F_{\text{Max}-\text{Log}-\text{MAP}} = 257 \text{ Operations/Info Bit} \end{aligned}$$

Hence, the complexity savings (in number of operations per information bit) against the Max-Log-MAP algorithm becomes:

$$\Delta_{PP}\% = (T_{FD} - T_{PP})/T_{FD} = (257 - 208)/257 = 19.06\ \%$$

Note that the above complexity saving calculations, in fact, represent a lower bound on the saving since the above calculations did not take into account the modem line-up operational complexity in order to demodulate and receive the bits in their final binary format properly (i.e., synchronization, channels estimation, etc.).

6 Results and Discussion

We have generated 100,000 simulation snapshots where each snapshot generates a random number of sensors up to 30 sensors with random power assignments (or equivalently path loss, i.e., assignments). All proposed metrics exhibit robust

performance. In our study, we have evaluated QPSK, and 8PSK modulation schemes versus various measurement durations, sampling rates and metric numerical (fixed-point) quantization levels to reflect the effects of practical implementation constraints.

Our proposed technique has a low sensitivity to deviations of the received SINR from the assumed set-point which is 5 dB (i.e.$SINR_{cut\_off}$). The technique works reliably and able to determine if the packet is in collision or not. That is if the SINR is well below or above the set-point, the received signal statistics are expected to also be less confusing to the discriminator anyway and the algorithm shall perform reliably.

Figures 2 and 3 show the Miss and False-Alarm probabilities versus the choice of the technique comparison threshold level (i.e., above which we decide the packet is in collision or not) for the proposed technique when signals belong to QPSK modulation scheme and various design choices which are described below the figures. As shown in the figures, the intersection point of the False Alarm and Miss curves, can be a reasonable point to choose the threshold level in order to have a reasonable (or balanced) consideration of the Miss and False-Alarm probabilities, but certainly a designer can refer to the Appendix in order to choose an arbitrarily different point for a different criterion of choice.

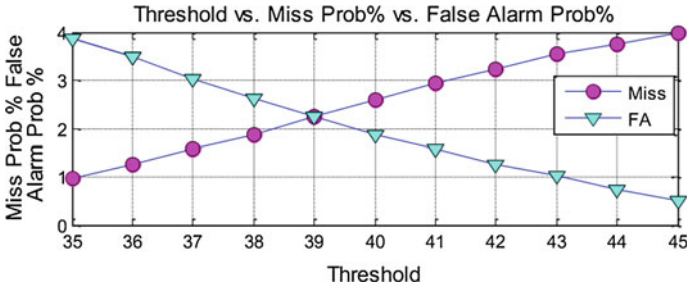

Fig. 2 Miss probability = 2.25 % versus False-Alarm probability = 2.25 % versus threshold = 39.0, $\Delta_{SINR} = \pm 1$ dB, $SINR_{cut\_off} = \pm 5$ dB, QPSK, measurement period = 500 bits, $L_1 = L_2 = 16$ samples, $\frac{v_{Z_1}}{v_{O_1}} = \frac{v_{Z_2}}{v_{O_2}} = 50\ \%$, $\aleph_1 = \aleph_2 = 70\ \%$

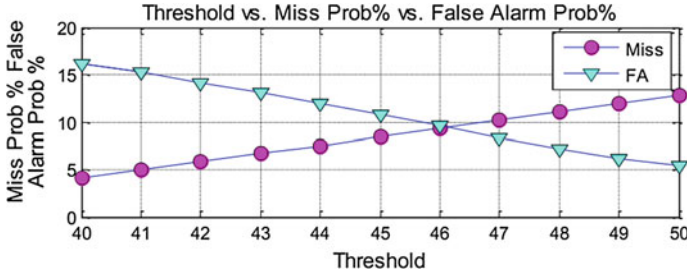

Fig. 3 Miss probability = 9.88 % versus. False Alarm probability = 9.96 % versus. threshold = 46.0, $\Delta_{SINR} = \pm 1.5$ dB, $SINR_{cut\_off} = \pm 7$ dB, QPSK, measurement period = 500 bits, $L_1 = L_2 = 16$ samples, $\frac{v_{Z_1}}{v_{O_1}} = \frac{v_{Z_2}}{v_{O_2}} = 50\ \%$, $\aleph_1 = \aleph_2 = 60\ \%$

7 Conclusion

In this paper we propose a novel simple power-efficient collision detection scheme for WSNs and analyze its performance. Our scheme is applied directly at the receiver's ADC IQ signal output to determine if the received signal represents a valid interference-free packet or corrupted due to collision. We also analyze and demonstrate the amount of power saving achieved by our scheme compared to the full-decoding algorithm (i.e. Max-Log-MAP algorithm). As demonstrated by the numerical results and performance analysis, our novel scheme offers much lower computational complexity and short measurement period to full-decoding, with minimal impact on throughput, which can also be arbitrarily minimized per the system designer's choice of parameter setting and trade-offs.

Acknowledgment This work has been partially sponsored by Taif University of the Kingdom of Saudi Arabia.

Appendix

In this appendix, we provide more detailed performance results for our proposed schemes. We test two modulation schemes (i.e. QPSK and 8PSK) (Tables 1 and 2).

Table 1 QPSK—double pseudo-coded ON-OFF pilot periods scheme

R	B	Z	G	$\frac{v_Z}{v_O}$	L	V	ℵ (%)	Δ_{SINR} (dB)	P_{FA} (%)	P_{MISS} (%)	γ
50 Bits	4	2	8	0.5	16	82	60	±1	11.22	11.12	45.0
								±1.5	10.30	10.33	44.0
	10	8	7	0.4	14	228	60	±1	11.98	12.03	53.0
								±1.5	11.54	11.51	54.0
	4	2	8	0.5	16	82	70	±1	2.44	2.41	45.0
								±1.5	2.23	2.22	44.0
	10	8	7	0.4	14	228	70	±1	3.15	3.13	52.0
								±1.5	2.80	2.87	53.0
	4	2	8	0.5	16	82	90	±1	0.24	0.21	37.0
								±1.5	0.17	0.16	36.0
	10	8	7	0.4	14	228	90	±1	0.14	0.15	48.0
								±1.5	0.09	0.09	50.0

(continued)

Table 1 (continued)

R	B	Z	G	$\frac{v_Z}{v_O}$	L	V	ℵ (%)	Δ_{SINR} (dB)	P_{FA} (%)	P_{MISS} (%)	γ
500 Bits	4	2	8	0.5	16	532	60	±1	10.12	10.20	40.0
								±1.5	9.94	9.91	40.0
	10	8	7	0.4	14	2028	60	±1	11.44	11.45	54.0
								±1.5	10.22	10.20	54.0
	4	2	8	0.5	16	532	70	±1	2.25	2.25	39.0
								±1.5	2.02	2.04	39.0
	10	8	7	0.4	14	2028	70	±1	3.04	3.02	49.0
								±1.5	2.33	2.39	49.0
	4	2	8	0.5	16	532	90	±1	0.10	0.10	37.0
								±1.5	0.04	0.05	39.0
	10	8	7	0.4	14	2028	90	±1	0.12	0.13	48.0
								±1.5	0.08	0.08	48.0

Table 2 8PSK—double pseudo-Coded ON-OFF pilot periods Scheme

R	B	Z	G	$\frac{v_Z}{v_O}$	L	V	ℵ (%)	Δ_{SINR} (dB)	P_{FA} (%)	P_{MISS} (%)	γ
50 Bits	4	2	8	0.5	16	64	60	±1	10.32	10.31	48.0
								±1.5	9.13	9.13	48.0
	10	8	7	0.4	14	156	60	±1	11.38	11.33	59.0
								±1.5	10.12	10.11	59.0
	4	2	8	0.5	16	64	70	±1	1.92	1.91	47.0
								±1.5	1.32	1.31	48.0
	10	8	7	0.4	14	156	70	±1	3.05	3.01	58.0
								±1.5	2.50	2.51	58.0
	4	2	8	0.5	16	64	90	±1	0.15	0.16	43.0
								±1.5	0.09	0.10	43.0
	10	8	7	0.4	14	156	90	±1	0.93	0.90	56.0
								±1.5	0.22	0.24	56.0
500 Bits	4	2	8	0.5	16	364	60	±1	9.14	9.10	49.0
								±1.5	8.71	8.76	49.0
	10	8	7	0.4	14	1356	60	±1	10.24	10.22	60.0
								±1.5	9.12	9.10	60.0
	4	2	8	0.5	16	364	70	±1	2.03	2.01	41.0
								±1.5	1.12	1.14	41.0
	10	8	7	0.4	14	1356	70	±1	2.94	2.92	58.0
								±1.5	1.63	1.69	58.0
	4	2	8	0.5	16	364	90	±1	0.09	0.08	41.0
								±1.5	0.03	0.03	41.0
	10	8	7	0.4	14	1356	90	±1	0.11	0.11	57.0
								± 1.5	0.07	0.06	57.0

References

1. Dam TV, Langendoen K (2003) An adaptive energy-efficient MAC protocol for wireless sensor networks. In: The First ACM conference on embedded networked sensor systems (Sensys'03), Los Angeles, CA, USA, Nov 2003
2. Miranda J, Gomes T, Abrishambaf R, Loureiro F, Mendes J, Cabral J, Monteiro JL (2014) A wireless sensor network for collision detection on guardrails. In: IEEE 23rd international symposium on industrial electronics (ISIE), pp 1430–1435, 1–4 June 2014
3. Li L, Maunder RG, Al-Hashimi BM, Hanzo L (2013) A low-complexity turbo decoder architecture for energy-efficient wireless sensor networks. IEEE Trans Very Large Scale Integr (VLSI) Syst 21(1):14–22
4. Zorzi M, Rao RR (2004) Coding tradeoffs for reduced energy consumption in sensor networks. In: 15th IEEE international symposium on personal, indoor and mobile radio communications (PIMRC 2004), vol 1, pp 206–210, 5–8 Sept 2004
5. Zhang H, Yuan D. Wang C-X (2008) An improved normalized BP based decoding algorithm for LDPC codes. In: IET 2nd international conference on wireless, mobile and multimedia networks (ICWMMN 2008), pp 223–226, 12–15 Oct 2008
6. Sartipi M, Fekri F (2004) Source and channel coding in wireless sensor networks using LDPC codes. In: 2004 first annual IEEE Communications Society conference on sensor and ad hoc communications and networks (IEEE SECON 2004), pp 309–316, 4–7 Oct 2004
7. Wang K, Chen Y, Alouini M-S. Xu F (2014) BER and optimal power allocation for amplify-and-forward relaying using pilot-aided maximum likelihood estimation. IEEE Trans Commun 62(10):3462–3475
8. Kim WT, Bae SJ, Kang SG, Joo EK (2000) Reduction of computational complexity in two-step SOVA decoder for turbo code. In: Global telecommunications conference (GLOBECOM'00), IEEE, vol 3, pp 1887–1891
9. Robertson P, Villebrun E, Hoeher P (1995) A comparison of optimal and sub-optimal MAP decoding algorithms operating in the log domain. IEEE international conference on communications (ICC'95), Seattle, Gateway to Globalization, vol 2,, pp 1009–1013, June 1995
10. Alassery F, Ahmed WKM, Sarraf M, Lawrence V (2015) Novel low-complexity and power-efficient techniques for fast collision detection in wireless sensor networks. In: Lecture notes in engineering and computer science: proceedings of the World Congress on Engineering 2015, pp 627–633, 1–3 July 2015

Microstrip Patch Antenna

Performance Comparison for Rectangular and Circular Shaped Patch

Nsikan Nkordeh, Francis Idachaba, Oluyinka Oni and Ibinabo Bob-Manuel

Abstract The demand for smaller, conformable antennas with desired properties has made antenna Engineers to device better ways of making antennas. The patch antenna comes to the rescue, as it provides the features needed in antennas used in the telecoms, meteorological and military industries, where light weight low profile antennas are required. The Microstrip patch antennas comes in different shapes and configuration, the most common being circular and rectangular. The Microstrip patch antenna gives a relatively satisfactory antenna radiation pattern vis-à-vis the size and has different feeding methods used to ensure low return loss. The Patch antenna is conformal in shape as it 'blends in' with the aesthetics of devices it is used in. This chapter takes a close look at the performance characteristics of the rectangular and circular Microstrip antennas, comparing different antenna parameters like directivity, E and H planes Half Power Beam Width (HPBW) vis-à-vis the dimensions and size (area of patch). Five frequencies (0.9, 1.8, 1.9, 2.3 and 2.4 Ghz) are used in computing the configurations-these frequencies correspond to that of GSM, LTE and Bluetooth; results from this paper can be used in building practical antennas for phones and laptops or any Bluetooth enabled device.

Keywords Circular patch · Dielectrics · Directivity · Electromagnetic and magnet plane · Microstrip patch antenna · Rectangular · Resonant frequency

N. Nkordeh (✉) · F. Idachaba · O. Oni
EIE Department, Covenant University, Km 10, Idiroko Road, Ota, Ogun, Nigeria
e-mail: nsikan.nkordeh@covenantuniversity.edu.ng

F. Idachaba
e-mail: francis.idachaba@covenantuniversity.edu.ng

O. Oni
e-mail: oluyinka.oni@covenantuniversity.edu.ng

I. Bob-Manuel
Kakatar Group, Maitama, Abuja, Nigeria
e-mail: ibinabo.bobmanuel@gmail.com

S.-I. Ao et al. (eds.), *Transactions on Engineering Technologies*,
DOI 10.1007/978-981-10-1088-0_39

1 Introduction

Antenna is a device that transforms travelling waves in a conductor to propagating electromagnetic waves in free space; it is the connection between the transmission lines and the free space. Antenna exhibits the property of reciprocity- i.e., an antenna will maintain the same property in a communication link irrespective of whether it is operating as a transmitter or as a receiver. Antennas have become ubiquitous in this digital age, as it provides the coverage for connectivity through its radiation pattern. Microstrip antennas are desirable due to their light weight, conformability and low cost. The Microstrip antenna is made up of a very thin metallic patch placed a small fraction of wavelength above a ground plane in a dielectric substrate ($h < \lambda_o$, usually $0.003\ \lambda_o \leq 0.005\lambda_o$), where $\lambda_o =$ free space wavelength. [1]. For example the rectangular patch antenna is approximately a-one half wavelength long section of a rectangular Microstrip line [2]. Microstrip Patch Antenna are typically used at frequencies between 1 and 100 GHz [2].

The Microstrip patch antenna is designed so its pattern maxima is normal to the patch; this can be achieved by choosing the appropriate excitation technique.

The Microstrip patch antenna consist of a radiating patch on one side of the dielectric substrate which has a ground plane on the other side. Microstrip Patch Antenna come in conformable shapes like square, rectangle, elliptical, circular etc.

Microstrip Patch Antennas radiate primarily because of the fringing fields between the patch edge and the ground plane. In the design of patch antennas, there has to be a compromise between antenna's dielectrics value, dimensions (i.e. thickness and size) and antenna performance-these variables affect the antenna performance. [3] For good antenna performance, a dielectric with low value but high thickness is required, as this provide better efficiency, larger bandwidth and better radiation. However, such a design leads to antenna of larger size. In order to reduce the size, a higher dielectric constant should be used, but this results in a Microstrip with less efficiency and narrow bandwidth due to its high quality factor [4].

Microstrip Patch Antenna generally have very high quality factor (Q) .High Quality factor, which is inherent in Microstrip Patch Antenna leads to lower efficiency and narrow bandwidth [5]. The Quality Factor represents the loss associated with the antenna; increasing the thickness of the dielectric substrate will reduce Q, but this will increase the size of the MPA. The surface wave contribution responsible for high Q can be reduced by the use of photonic bandgap structure [6]. To achieve high performance like high bandwidth, high efficiency, high gain vis-a-vis a conformably small size, the feeding method used is very important (Fig. 1, Table 1).

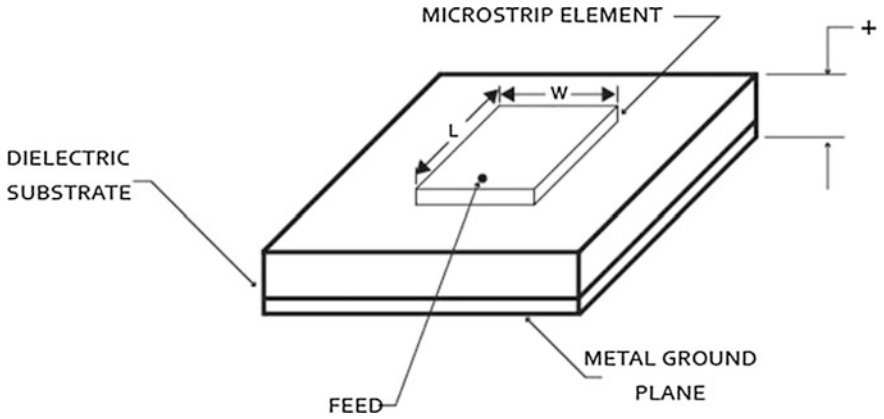

Fig. 1 Rectangular microstrip-antenna element

Table 1 Advantages and disadvantages of microstrip patched antenna

	Major advantages of microstrip patch antenna	Major disadvantages of microstrip patched antenna
1	Light weight and low volume	Narrow bandwidth
2	Supports both dual and triple frequency operation	Low efficiency
3	Supports both linear and circular polarization	Low gain
4	Low fabrication cost	Extraneous radiation from feeds and junctions, Surface wave excitation
5	Low profile planar configuration	Poor end fire radiator except for tapered slot antenna; Lower power handling capacity

2 Operation of a Microstrip Patch Antenna

A Microstrip Patch Antenna is made of a radiating patch placed on a dielectric substrate, with a ground plane on the other side as shown in Fig. 2. The EM waves fringe off the top parts into the substrate, reflecting off the ground plane and radiate off into the air [1]. Electromagnetic radiation occurs mainly due to the fringing fields between the patch and the ground at the edges; this is because the dimensions of the patch are finite along the length and width. The amount of fringing depends on the ratio of patch length (L) and substrate height (h) . Since for Microstrip antennas $L/h \gg 1$, fringing is reduced; this must be taken into account when designing as this influences the resonant frequency of the antenna. The region between the conducting patch and the ground plane acts as the region between a transmission line and the ground plane with both ends open, which leads to a standing waves in the dielectric. In designing a Microstrip Patch Antenna, we obtain both the effective dielectric constant (ε_{reff}) and dielectric (ε_r) [7]. The ε_{reff} is needed to account for the fringing

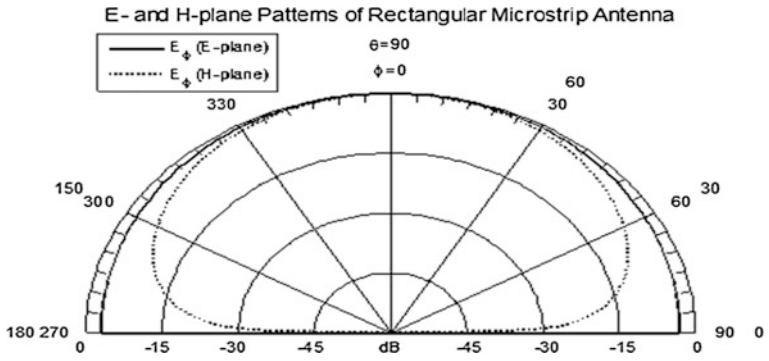

Fig. 2 Rectangular MPA: E-H Resonant Freq = 0.9 Hz, dielectric = 4.5, substrate height = 0.25 cm

fields and the wave propagation in the line. Most of the fields lie in the substrate while others line in the air; the phase velocity in air and in the substrate will be different, which makes it impossible for it to support pure Electric-Magnetic (TEM) mode of transmission. In analysis, we assume the quasi-TEM mode of transmission. The value of the effective dielectric constant is usually constant at low frequencies, increasing monotonically as frequency increases, and ends up approaching the value of the dielectric constant at higher frequencies. For $W/h > 1$,

$$\varepsilon_{reff} = \frac{\varepsilon_r + 1}{2} + \frac{\varepsilon_r - 1}{2}\left[1 + 12\frac{h}{W}\right]^{-1/2} \tag{1}$$

The fringing effect causes the Microstrip patch look electrically bigger than its physical dimensions. In the analysis of the Patch, we take this into account by assuming an extension to the patch at both ends (for rectangular/square patch) ΔL; ΔL is a function of the effective dielectric constant, ε_{reff}, and the width-to-height ratio (W/h) and can be represented by the ratio

$$\frac{\Delta L}{h} = 0.412\frac{\left(\varepsilon_{reff} + 0.3\right)\left(\frac{W}{h} + 0.264\right)}{\left(\varepsilon_{reff} - 0.258\right)\left(\frac{W}{h} + 0.8\right)} \tag{2}$$

For the dormant TM_{010} *mode*, the effective Length of the patch is given by

$$L_{eff} = L + 2\Delta L \tag{3}$$

The resonant frequency is given by

$$(f_r)_{010} = \frac{1}{2L\sqrt{\varepsilon_r}\sqrt{\mu_0\varepsilon_0}} = \frac{v_0}{2L\sqrt{\varepsilon_r}} \tag{4}$$

v_0 is the velocity of light in free space. Equation (4) does not take account of the fringing effect. When the fringing effect is taking care of, (4) becomes

$$\begin{aligned}(f_{rc})_{010} &= \frac{1}{2L_{eff}\sqrt{\varepsilon_{reff}}\sqrt{\mu_0\varepsilon_0}} = \frac{1}{2(L+\Delta L)\sqrt{\varepsilon_{reff}}\sqrt{\mu_0\varepsilon_0}} \\ &= q\frac{1}{2L\sqrt{\varepsilon_r}\sqrt{\mu_0\varepsilon_0}} = q\frac{v_0}{2L\sqrt{\varepsilon_r}}\end{aligned} \tag{5}$$

where

$$q = \frac{(f_{rc})_{010}}{(f_r)_{010}} \tag{6}$$

q is called the fringing factor, i.e. length reduction factor.

Note: As the substrate height increases, fringing also increases and leads to larger separation between the radiating edges and the lower resonant frequencies.

Feeding method is a critical issue when designing Microstrip patch antenna, as this has great influence on the performance of the patch, especially its radiation pattern [8]. The main feeding methods used in Microstrip patch antennas are: Microstrip line, Coaxial probe, Aperture coupling and Proximity feed.

Procedure: Specify ε_r, f_r (in Hz) and h

After these parameters have been specified, determine the effective dielectric constant ε_{reff}, using (1). The width of the patch, W, is calculated using:

$$W = \frac{1}{2f_f\sqrt{\mu_0\varepsilon_0}}\sqrt{\frac{2}{\varepsilon_r+1}} = \frac{v_0}{2f_r}\sqrt{\frac{2}{\varepsilon_r+1}} \tag{7}$$

Once W is calculated, use (2) to determine ΔL, the extension of the length due to fringing. The actual length of the path L is determined using the formula

$$L = \frac{1}{2f_r\sqrt{\mu_0\varepsilon_0}\sqrt{\varepsilon_{reff}}} - 2\Delta L \tag{8}$$

3 Design of Circular Microstrip Patch Antenna

The circular Microstrip antenna can be analyzed conveniently using the cavity model, it is modelled as a cavity, the modes supported by the circular patch antenna can be found by modelling the patch, the ground plane and the material between the two as a circular cavity. The dominant mode is TM^z_{110} where z is taken perpendicular

to the patch; the model analysis assumes that substrate height is small ($h \ll \lambda$). Using the TM^z_{110} mode, the resonant frequency is given by

$$(f_r)_{110} = \frac{1.8412}{2\pi\sqrt{\mu\varepsilon}} = \frac{1.8412 v_0}{2\pi a\sqrt{\varepsilon_r}} \tag{9}$$

where v_o is the speed of light in free space

Note: Eq. (9) does not take note of fringing effect.

In designing the circular Microstrip patch antenna, a correction is introduced by using an effective radius, a_e instead of the actual radius, a where

$$a_e = a\left\{1 + \frac{2h}{\pi a\varepsilon_r}\left[\ln\left(\frac{\pi a}{2h}\right) + 1.7726\right]\right\}^{1/2} \tag{10}$$

Due to the fringing effect, which gives rise to (8), the resonant frequency (9) for the dominant TM^z_{110} would have to be modified to

$$(f_r)_{110} = \frac{1.8412 v_0}{2\pi a_e\sqrt{\varepsilon_r}} \tag{11}$$

The actual radius, a is found using

$$a = \frac{F}{\left\{1 + \frac{2h}{\pi\varepsilon_r F}\left[\ln\left(\frac{\pi F}{2h}\right) + 1.7726\right]\right\}^{\frac{1}{2}}} \tag{12}$$

where F is given by

$$F = \frac{8.791 \times 10^9}{f_r\sqrt{\varepsilon_r}} \tag{13}$$

3.1 Design Procedure

1. Specify the ε_r,f_r (in Hz), and h (in cm)
2. Determine, the actual radius a of the patch using (12) and then proceed to determine effective radius a_e by using (10).

3.2 Simulation

Having gone through the analysis and design procedures for the circular and rectangular Microstrip patch antennas, Mathlab will be used in comparing some antenna characteristics of both rectangular and circular patch antenna

f_r (Ghz) = Resonant frequency
ε_r = Dielectric constant of substrate
h (cm) = Height of substrate
W (cm) = Physical width of patch
L_e (cm) = Effective length of patch
L (cm) = Physical length of patch
R (cm) = Physical radius of patch
R_e (cm) = Effective radius of patch
E-HPBW = E-plane high power beam width
H-HPBW = H-plane high power beam width

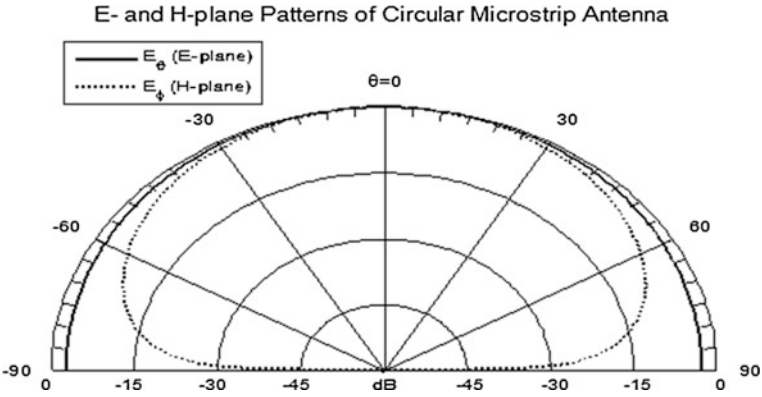

Fig. 3 Circular MPA: E-H Resonant Freq = 0.9 Hz, dielectric = 4.5, substrate height = 0.25 cm

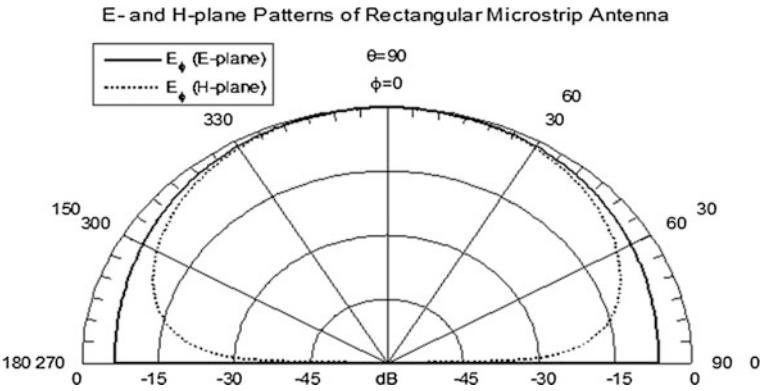

Fig. 4 Rectangular MPA: E-H plane pattern: Resonant Freq = 0.9 Hz, dielectric = 2.32, substrate height = 0.25 cm

Plots for different both rectangular and circular patch antennas with the following parameters as variables where taken: Resonant Frequency, Dielectrics and Substrate height. The following plots were obtained (Figs. 3, 4, 5, 6, 7, 8 and 9).

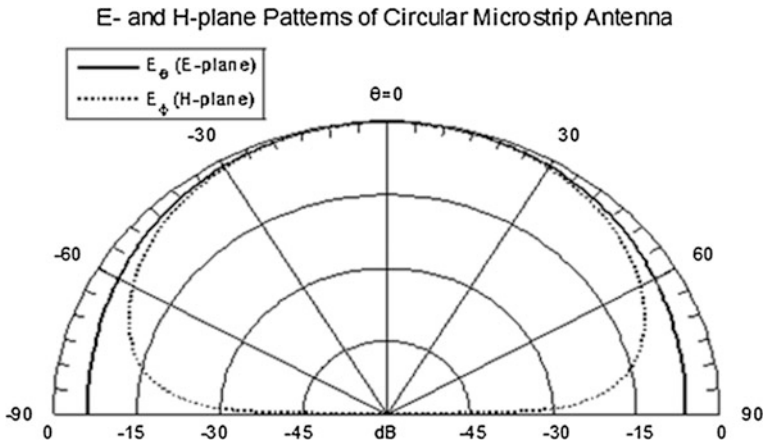

Fig. 5 Circular MPA: E-H plane pattern: Resonant Freq = 0.9 Hz, dielectric = 2.32, substrate height = 0.25 cm

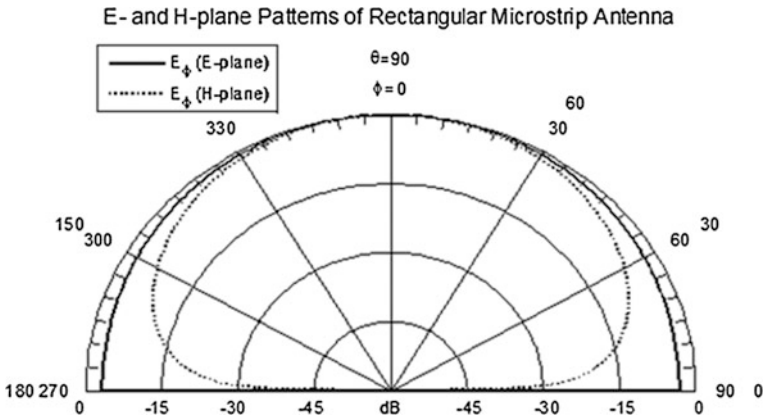

Fig. 6 Rectangular: E-H plane: Resonant Freq = 1.8 Hz, dielectric = 4.5, substrate height = 0.25 cm

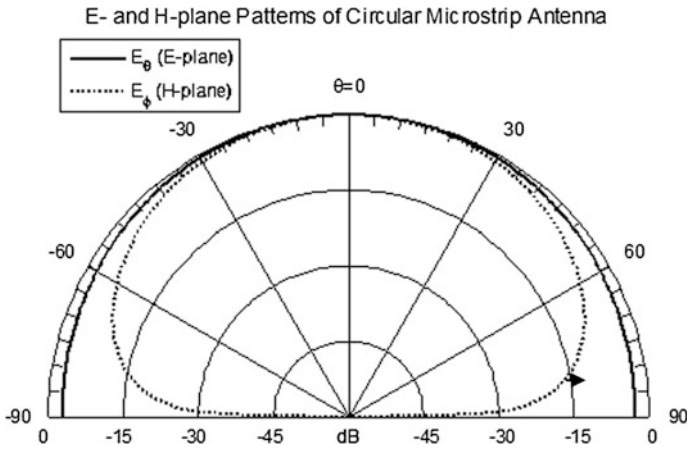

Fig. 7 Circular: E-H plane: Resonant Freq = 1.8 Hz, dielectric = 4.5, substrate height = 0.25 cm

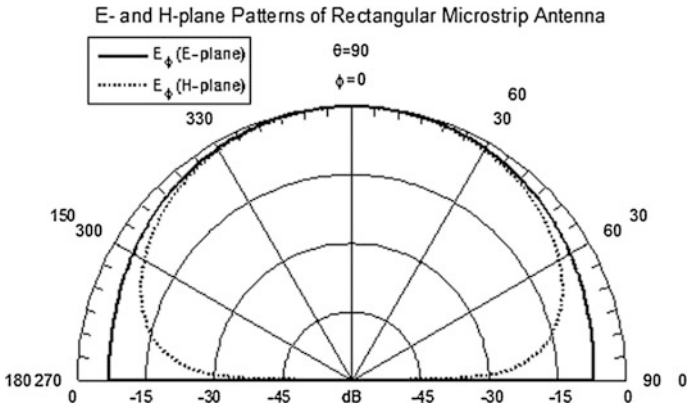

Fig. 8 Rectangular: E-H plane: Resonant Freq = 2.4 Hz, dielectric = 2.32, substrate height = 0.25 cm

4 Results and Conclusion

In this work, specific frequencies have been chosen-0.9, 1.8, 1.9, 2.3 and 2.4 GHz-these frequencies corresponds to that of GSM, LTE and BLUETOOTH. These frequencies are very important in designing antennas for Mobile Phone and Bluetooth-enabled devices. Two types of materials, roger (with a relative dielectrics ε_r of 4.5) and duroid (with a relative dielectrics, ε_r of 2.32) have been used as substrate. Tables 2 and 3 shows how the choice of dielectric constant affects different antenna parameters at these four important frequencies for a rectangular and a circular

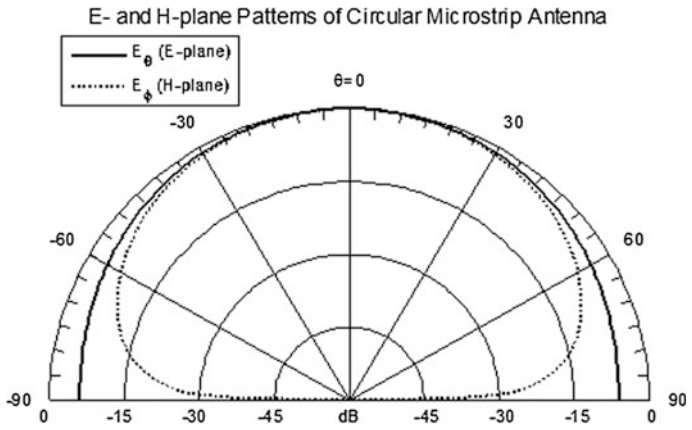

Fig. 9 E-H plane: Resonant Freq = 2.4 Hz, dielectric = 2.32, substrate height = 0.25 cm

Table 2 Data table for rectangular patch antenna

f_r (Ghz)	ε_r	h (cm)	y_0 (cm)	W (cm)	L_θ (cm)	L (cm)	Surface area (m^2)	E-HPBW (deg)	H-HPBW (deg)	Direct ivity (dB)
0.9	4.5	0.25	1.5	10.05	8.05	7.82	78.59	180	80	5.98
0.9	2.3	0.25	1.5	12.93	11.09	10.84	140.21	96	76	7.03
1.8	4.5	0.25	1.5	5.025	4.1	3.87	19.44	180	80	6.02
1.8	2.3	0.25	1.5	6.47	5.61	5.35	34.61	94	76	7.07
1.9	4.5	0.25	1.5	4.7607	3.8892	3.6598	17.42	180	80	6.02
1.9	2.3	0.25	1.5	6.1275	5.3217	5.0622	26.94	94	76	7.073
2.3	4.5	0.25	1.5	3.9328	3.2335	3.005	11.81	180	80	6.032
2.3	2.3	0.25	1.5	5.0619	4.4141	4.1551	18.34	94	76	7.088
2.4	4.5	0.25	1.5	3.77	3.1	2.88	10.84	180	80	6.03
2.4	2.3	0.25	1.5	4.85	4.23	3.98	19.28	94	76	7.09

Table 3 Data table for circular patch antenna

f_r (Ghz)	ε_r	h (cm)	y_0 (cm)	R (cm)	R_θ (cm)	Surface area (m^2)	E-HPBW (deg)	H-HPBW (deg)	Directi vity (dB)
0.9	4.5	0.25	1.5	4.52	4.606	44.59	180	84	6.041
0.9	2.3	0.25	1.5	6.23	6.417	61.53	96	80	7.248
1.8	4.5	0.25	1.5	2.23	2.304	21.99	180	84	6.043
1.8	2.3	0.25	1.5	3.05	3.212	30.15	96	80	7.253
1.9	4.5	0.25	1.5	2.107	2.183	13.95	180	84	6.043
1.9	2.3	0.25	1.5	2.888	3.044	26.19	96	80	7.254
2.3	4.5	0.25	1.5	1.732	1.804	9.423	180	84	6.044
2.3	2.3	0.25	1.5	2.367	2.516	17.6	96	80	7.257
2.4	4.5	0.25	1.5	1.66	1.73	16.36	180	84	6.044
2.4	2.3	0.25	1.5	2.26	2.41	22.35	96	80	7.257

Microstrip Patch antenna [9]. A common trend is noticed in this work—to obtain a smaller patch antenna (in terms of size, amount of material used), a material of higher dielectrics (the Rogers dielectric 4.5 gives an antenna of smaller size than duroid the dielectric) needs to be used, for both the rectangular and circular Microstrip patch antenna. In this era of miniaturization, incorporating a small antenna in a mobile phone or any device is a desired quality. When compared with each other, to obtain the same directivity, a circular Microstrip Patch antenna will need less size (material) than the corresponding rectangular one at any particular frequency. For example, from the table, to get a directivity ≈6 dB, at frequency of 0.9 GHz using Rogers, $\varepsilon_r = 4.5$ (for a rectangular 5.98 dB), we need a patch antenna with material area of 78.59 m^2 while for a circular patch operating at the same frequency, we need a patch is material area of 44.59 m^2. This is a significant result, both in material savings size conformity and aesthetics, as it shows that high miniaturization can be achieved by using circular Microstrip Patch than rectangular (in a ratio ≈1:2).

Directivity is a quantitative measure of an antenna's ability to concentrate radiated power per unit solid angle in a certain direction; it is a very important antenna parameter especially in RADAR systems [10]. Microstrip Patch antennas generally have low directivity when compared to dipoles and some other types of antenna due to their relatively large High Power Bandwidth (HPBW) both in the E and H planes [11]. From the tables and plots, the use of material with lower dielectric constant improves the directivity, both for circular a rectangular Microstrip patch (hence at any frequency duroid gives a better result than Roger).

In conclusion, this chapter has shown that circular Microstrip patch antenna gives better performance, enhance the concept of miniaturization when compared to the rectangular Microstrip Patch antenna [5]. While it has been shown that circular Microstrip Patch gives better performance than rectangular, it exhibit more difficulties in feeding method, and the probe feeding method seems to be the best for circular Microstrip patch [5].

References

1. Braaten BD (2009) Modeling multiple printed antenna embedded in stratified uniaxial anisotropic dielectrics. Dissertation submitted to the Graduate Faculty of the North Dakota State University of Agriculture and Applied Science
2. Balanis CA (2005) Antenna theory, analysis and design, 3rd edn. Wiley, New York. ISBN 978-0-471-66782-7
3. Braaten BD, Roy S, Nariyal S, Al Aziz M, Chamberlain NF, Irfanullah I, Reich MT, Anagnostou DE (2013) A self-adapting flexible (Selflex) antenna array for changing conformal surface applications. IEEE Trans Antenna Propagation 61(2)
4. Blakes LV, Long MW (2008) Antenna fundamental, design, measurement. Scitech Publishing Inc., Daryaganz
5. Nkordeh N, Idachaba F, Oni O (2015) Microstrip patch antenna: comparing performance of a rectangular and a circular patch at LTE bluetooth and GSM frequencies. In: Proceedings of the World Congress on Engineering 2015 (WCE 2015), vol I, London, UK, pp 658–663, July 1–3 2015

6. Krauss JD, Marhefka RJ (Nov 12 2001) Antennas for all application, 3rd edn. McGraw-Hill Science/Engineering/Math
7. Kirar AS, Jadaun VS, Sharma PK (2013) Design a circular microstrip patch antenna for dual band. Int J Electron Commun Comput Technol (IJECCT) 3(2)
8. Vardhana Reddy CV (2009) Design of linearly polarized rectangular microstrip patch antenna using IE3d/PSO. A thesis submitted in partial fulfillment of the requirements for the degree of Bachelor of Technology in Electronics and Communication Engineering. Department of Electronics and Communication Engineering National Institute of Technology, Rourkela
9. Edling T Design of circular polarized dual band patch antenna. Masters thesis for Uppsala Universitet, Sweden
10. Ahamed M, Bhowmik K (June 2012) Shahidulla M Rectangular microstrip patch antenna at 2GHZ on different dielectric constant for pervasive wireless communication. Int J Electr Comput Eng (IJECE) 2(3), pp. 417–424 ISSN: 2088-8708
11. Paul B, Mridula S, Aanandan CK, Mohanan P (2014) A new microstrip patch antenna for mobile communications and bluetooth applications
12. Bhatnagar GD, Saini S, Saxena VK, Joshi LM (2011) Design of broadband circular patch Microstrip patch antenna with diamond shape slot. Indian J Radio Space Phys 40:275–281
13. Majumder A (2013) Rectangular microstrip patch antenna using coaxial probe feeding technique to operate in S-band. Int J Eng Trends Technol (IJETT) 4(4)